Study on Interaction between Rocking-Wall System and Surrounding Structure

A DISSERTATION
SUBMITTED TO THE FACULTY OF
UNIVERSITY OF MINNESOTA
BY

Qingzhi Liu

IN PARTIAL FULFILLMENT OF THE REQUIREMENTS
FOR THE DEGREE OF
DOCTOR OF PHILOSOPHY

Catherine E.W. French

December 2016

Acknowledgements

I would like to express the deepest appreciation to my supervisor, Professor Catherine French. Her continued enthusiasm, broad knowledge, and thoughtful consideration for the details have been central to this dissertation and my career development. Without her guidance and persistent encourage this dissertation would not have been possible. I also would like to acknowledge her family for the generous support during my stay in Minnesota.

I would like to thank Professor Sri Sritharan in Iowa State University, Assistant Professor Sriram Aaleti in University of Alabama, Assistant Professor Rick Henry in University of Auckland, graduate students Maryam Nazari and Jonathan Watkins. It was a great pleasure to work with all of them in the rocking-wall project.

I would like to thank Professor Carol Shield, the staff in the MAST Laboratory Paul Bergson, Rachel Gaulke, Christopher Bruhn and Michael Boldischar, graduate students Tanner Swenson, Brock Hedegaard, Ben Dymond and John Gervais, undergraduate students Sam Konieczny, Mike Larson, Aaron Fortunato and Anna Flintrop for their assistance during the experimental testing. Without their contribution, the two large-scale assemblage tests would not be successfully finished.

Thank you to my parents who have supported me through this study. My wife, Zheng, I would not have made it through without your endless encouragement and full understanding. Even if we lived and studied two thousand miles away from each other, I never felt lonely with you accompanying in my heart.

Abstract

Reinforced concrete (RC) special structural walls have proven to be an effective means of resisting lateral loads in structural systems. They are detailed to dissipate energy through the development of plastic hinge regions. Although few buildings with special structural walls have collapsed in recent earthquake events greatly limiting the number of casualties, tremendous economic loss has been encountered due to irreparable structural damage. Compared to special structural walls, rocking-wall systems have demonstrated superior seismic performance with excellent self-centering and greatly reduced damage. This innovative structural system was proposed decades ago, but limited effort had been put into investigating the interaction mechanism between rocking-wall systems and the surrounding structure (e.g. floors and columns). This limitation has prevented this system from becoming popularized in practice.

Two large-scale structural assemblages, which consisted of rocking-wall systems and surrounding structures, were tested under quasi-static loading to investigate the interaction mechanism. A PreWEC (Precast Wall with End Columns) system was used as the rocking-wall system in the two tests. The PreWEC system consisted of a rocking wall and end columns adjacent to the wall with energy dissipating elements “O-connectors” connecting the two components together.

A surrounding rigid-connected structural system constructed using cast-in-place concrete was used in test specimen PFS1. The structure was designed to investigate an upper bound interaction between the PreWEC system and the surrounding structure. It featured gravity columns and an unbonded post-tensioned floor system with rigid wall-floor connections. PFS1 exhibited reasonable self-centering characteristics and excellent energy dissipating capabilities. Although some localized damage occurred to the floor adjacent to the wall ends, fast re-occupation of the structure was possible with little damage to the wall and structural integrity of the floor maintained. Three-dimensional constraint effects of the floor on the rocking wall were found to be significant in the test, especially when transverse constraint from parallel structural elements existed close to

the wall. A three-dimensional numerical model of the unbonded post-tensioned floor was proposed and validated using the test data. Design recommendations for the rigid wall-floor connections were proposed to alleviate the damage to the floor.

A surrounding precast structural system was used in test specimen PFS2 designed to minimize the interaction between the PreWEC system and the surrounding structure. It featured precast edge columns and a floor system formed by precast untopped planks. Special precast wall-floor connections that isolated the floor from the vertical movement of the wall were used in PFS2. The existence of the end columns provided a unique gravity load transfer path toward the wall frame line, while isolating the floor from the wall. This greatly increased the flexibility in floor-plan layout and space planning of the building. PFS2 was almost "damage-free" and "self-centered" after the design drift (2%), thus immediate re-occupation of the precast structure might be feasible after seismic events. Design recommendations were proposed for the end columns, the special wall-floor connections and the plank-beam connections, which were key components in the precast rocking-wall structure.

Although the base moment of the PreWEC system used in PFS1 was similar to that used in PFS2, the strength and the energy dissipation capacity of PFS1 were much larger than those of PFS2. The gravity load transfer path and constraint effect from surrounding structure were the two key factors that contributed to the difference. A general criterion that accounts for both factors is proposed to ensure the self-centering of rocking-wall structures.

The advantages and disadvantages of using the rigid or the special isolation wall-floor connections are summarized. Design recommendations for rocking wall panels, energy dissipating elements, and the interface grout layer are presented.

Table of Contents

List of Tables

List of Figures

NOTATION

Roman characters:

A = Empirical parameters for defining stress-strain curves of confined concrete

A_{ch} = Cross-sectional area of a structural member measured to the outside edges of transverse reinforcement, in.^{2}

A_g = Gross area of concrete sections of walls and end columns, in.^{2}

A_{lr} = Volume of longitudinal steel (unit length), in.^{2}

A_{mgbeam} = Cross-sectional area of mega beams, in.^{2}

A_{ps} = Area of prestressing steel in flexural tension zone, in.^{2}

A_{rod} = Cross-sectional area of threaded rods in end columns, in.^{2}

A_s = Cross-sectional area of longitudinal reinforcement, in.^{2}

A_{scol} = Cross-sectional area of steel columns, in.^{2}

A_{sh} = Total cross-sectional area of rectangular hoop reinforcement, in.^{2}

A_{st} = Area of longitudinal reinforcement in end columns, in.^{2}

$A_{s,max}$ = Maximum allowable tensile reinforcement, in.^{2}

$A_{s,min}$ = Minimum allowable tensile reinforcement, in.^{2}

A_{strand} = Cross-sectional area of a post-tensioned strand, in.^{2}

A_{strap} = Cross-sectional area of strap plates, in.^{2}

A_{truss} = Cross-sectional area of steel trusses, in.^{2}

A_{sx}= Total area of transverse bars running in x direction, in.^{2}

A_{sy}= Total area of transverse bars running in y direction, in.^{2}

A_{CV} = Gross area of concrete section bounded by web thickness and length of section in the direction of shear force considered, in.^{2}

A_{PT_hole} = Cross-sectional area of PVC pipes in walls and end columns, in.^{2}

A_{PT_slab} = Cross-sectional area of a 3/8” PT strand, in.^{2}

b = Width of compression face of member, in.

b_c = Core dimension to centerlines of perimeter hoop in x direction; Cross-sectional dimension of member core measured to the outside edges of the transverse reinforcement area, in.

b_{cp} = Width of cover plates at “dogbone” section, in.

b_{plank} = Width of precast planks, in.

b_w = Width of cross sections of transverse beams, in.

B = Empirical parameters for defining stress-strain curves of confined concrete

c = Neutral axis depth of walls, in.

c_{base} = Neutral axis depth at the base of walls, in.

$c_{cut-off}$ = Neutral axis depth of walls where steel confinement is not effective, in.

c_{design_wall} = Neutral axis depth of walls at 2% design drift, in.

c_{design_Ecol} = Neutral axis depth of end columns at 2% design drift, in.

$c_{\max\_wall}$= Neutral axis depth of walls at maximum expected drift, in.

$c_{wall\_3\%}$ = Neutral axis depth of walls at 3% drift, in.

c_{Ecol_C} = Neutral axis depth of end columns at compressed side of walls, in.

c_{Ecol_T} = Neutral axis depth of end columns at uplift side of walls, in.

c'' = Neutral axis depth of walls from centerline of steel confinement at design drift, in.

C = Compressive force acting on concrete at wall/grout interface, kip

d = Distance from extreme compressive fiber to centroid of longitudinal reinforcement in tension; One half of width of walls in jointed wall system, in.

d_{bot} = Distance from bottom surface of floor (mega beams/trusses) to core of bottom LVDT (SP) attached to floor (mega beams/trusses), in.

d_c= Core dimension to centerlines of perimeter hoop in y direction, in.

d_{col_E} = Distance from east surface of edge columns to the core of the LVDT (SP or DCDT) on the east side of edge columns, in.

d_{col_W} = Distance from west surface of edge columns to the core of the LVDT (SP or DCDT) on the west side of edge columns, in.

d_{mgbeam} = Depth of mega beams, in.

d_p = Distance from extreme compressive fiber to centroid of prestressing steel, in.

d_{scol} = Depth of steel columns, in.

d_{st} = Distance between centroid of PT strands and resultant compression force in the slab, in.

d_{top} = Distance from top surface of floor (mega beams/trusses) to core of top LVDT (SP) attached to floor (mega beams/trusses), in.

d_{truss} = Depth of steel trusses, in.

d_A = Elemental area of a cross section above the neutral axis, in.^{2}

d_{NWPT} = Distance between wall center and action line of resultant compression force, in.

d_{O_E} = Distance between the O-connectors attached to the east side of the wall and action line of resultant compression force, in.

d_{O_W} = Distance between the O-connectors attached to the west side of the wall and action line of resultant compression force, in.

d_1 = Distance from top bonded reinforcement to the N.A., in.

D_{slab} = Lateral displacement at top of edge column,s in.

$D_{elastic}$ = Elastic deformation at top of edge columns, in.

$D_{plastic}$ = Pastic deformation at top of edge columns, in.

E_c = Young's modulus of concrete, ksi

E_s = Young's modulus of steel materials (e.g. rods, rebar, cover plates and steel beams), ksi

E_{strand} = Young's modulus of prestressing steel, ksi

f = Stress-strain response of PT strands, ksi

f_c = Stress in stress-strain curves of concrete, psi

f_c' = Compressive strength of unconfined concrete, psi

f_{cc}' = Compressive strength of confined concrete, psi

f'_g = Compressive strength of grout, ksi

f'_{l1}= Effective lateral confining pressure in x direction, psi

f'_{l2}= Effective lateral confining pressure in y direction, psi

f_{ps} = Stress in prestressing steel at nominal flexural strength, ksi

f_{pu} = Specified tensile strength of prestressing steel, ksi

f_{py} = Specified yield strength of prestressing steel, ksi

f_{se} = Effective stress in prestressing steel, ksi

f_y = Specified yield strength of reinforcement and strap plates, ksi

f_{y_rod} = Specified yield strength of rods in end columns, ksi

f_{yt} = Specified yield strength of transverse reinforcement, ksi

F = Lateral force on top of walls and columns, kip

F_{cls} = Vertical resistance at free edge of slabs, kip

$F_{crosshead}$ = Concentrated lateral force applied by MAST crosshead, kip

F_{design_slab} = Initial PT force per foot provided by strands (E-W direction), kip

F_i = Initial PT force in jointed wall system; initial PT force of strands in slabs; concentrated lateral force on each story, kip

$F_{initial\_rod}$ = Initial force of threaded rods in end columns, kip

F_{slab_PT} = Initial PT force in each strand in scaled floors (E-W direction), kip

$F_{wall\_2\%}$ = Forces of strands in walls at 2% design drift, kip

F_{y_strap} = Yield strength of strap plates, kip

F_{BS} = Nominal shear capacity of a BS Italia connection, kip

F_C = Resisting force in energy dissipating elements in jointed wall system, kip

F_{Ecol_T} = Force in threaded rod of end columns on uplift side of walls, kip

F_{Ecol_C} = Force in threaded rod of end columns on compression side of walls, kip

F_{JVI} = Nominal shear capacity of JVI Mini V connections, kip

$F_{PT\_initial}$ = Initial PT force in walls at the beginning of tests, kip

$F_{PT\_1\%}$ = PT forces after 1% drift cycles, kip

F_{V_PT} = Shear resistance provided by PT strands, kip

G = Shear modulus of steel materials, ksi

h_{cc} = Distance between wall base and cut-off section, in.

h_w = Height of rocking walls, in.

h_x = Maximum center-to-center horizontal spacing of crossties or hoop legs on all faces of columns, in.

H = Height of each story in prototype buildings, ft.

H_{col} = Height of edge columns, in.

H_{cr} = Height of strain concentration at the corners of rocking walls, in.

$H_{specimen}$ = Height of specimens, ft.

H_w= Height of rocking walls, in.

i_{slab} = Flexural stiffness of floors, kip/in

I_{col} = Moment inertia of columns, in.^{4}

I_{gross}= Gross moment of inertia of walls, in.^{4}

I_{mgbeam} = Moment of inertia of mega beams, in.^{4}

I_{scol} = Moment of inertia of steel columns, in.^{4}

I_{slab}= Moment of inertia of slabs, in.^{4}

I_{strap} = Moment of inertia of strap plates, in.^{4}

I_A = Moment of inertia of cross-sectional area, in.^{4}

k_e= Confinement effective coefficient

k_w= Lateral stiffness of walls in PFS1 and PFS2, kip/in

l_{cr}= Width of confinement reinforcement, in.

l_w = Length (width) of rocking walls, in.

L_{hinge} = Plastic hinge length of edge columns, in.

L_{rod} = Total length of rods in end columns, in.

L_{slab}= Length of slabs; Span of slabs, in.

$L_{strands}$ = Total length of strands in walls; Length of strands in slabs, in.

L_{strap} = Length of strap plates between weld and edge of planks, in.

L_{s_eb} = Length of strap plates between end of strap plates and edge of planks at floor-edge beam connections, in.

L_{s_tb} = Length of strap plates between end of strap plates and edge of planks at floor-transverse beam connections, in.

M_{cls} = Moment at fixed edge of slabs, kip-in

M_{col} = Moment resistance of edge columns under sustained axial loads, kip-in

$M_{cut-off}$ = Moment at the section of walls where steel confinement is not effective, kip-in

M_{design_wall} = Moment resistance of walls and O-connectors at 2% design drift, kip-in

M_{left} = Moment resistance provided by the left wall panel in jointed wall systems, kip-in

M_{max_wall}= Base moment resistance of walls at maximum expected drift, kip-in

M_{mgbeam_cp} = Moment resistances provided by cover plates of mega beams, kip-in

M_{mgbeam_middle} = Moment in the middle section of mega beams, kip-in

M_{pr} = Probable flexural strength of walls at wall-foundation interface, kip-in

M_{right} = Moment resistance provided by the right wall panel in jointed wall systems, kip-in

M_{scol_B} = Moment at the bottom of steel columns, kip-in

M_{scol_T} = Moment at the top of steel columns, kip-in

M_{single} = Base moment of a single rocking wall panel, kip-in

M_{slab} = Concentrated moment demand on the floor at wall-floor connections, kip-in

M_{slaved} = Slaved moments applied by MAST crosshead, kip-ft

$M_{specimen}$ = Base moment of test specimens, kip-in

M_{strap} = Moment in strap plates, kip-in

M_{strap_eb} = Moment in strap plates at floor-edge beam connections, kip-in

M_{strap_tb} = Moment in strap plates at floor-transverse beam connections, kip-in

M_{strap_y} = Yield moment of strap plates, kip-in

M_y = Yield moment of floors, kip-in

M_{BASE} = Moment at the base of walls generated by external lateral loads and external lateral moments applied by the crosshead, kip-in

M_E= Maximum moment provided by energy dissipating elements, kip-in

M_{Ecol_C} = Moment resistance of end columns at compressed side, kip-in

M_{Ecol_T} = Moment resistance of end columns at uplift side, kip-in

M_{FO} = Moment resistance of O-connector far from rotation point, kip-in

M_N = Moment resistance provided by axial loads in walls, kip-in

M_O = Moment resistance of O-connectors, kip-in

M_{O_E}= Moment resistance provided by O-connectors attached to east side of walls, kip-in

M_{O_W}= Moment resistance provided by O-connectors attached to west side of walls, kip-in

M_{PreWEC}= Moment resistance of PreWEC systems, kip-in

M_{PB} = Base moment of scaled prototype building, kip-in

M_{PT} = Moment resistance provided by post-tensioned loads on walls, kip-in

M_{PT_i}= Moment provided by initial effective PT forces on walls, kip-in

M_S= Maximum moment provided by surrounding structure, kip-in

M_{SU} = Total resisting moment of surrounding structure; resisting moments from floors, kip-in

M_W = Moment resistance provided by self-weight of walls, kip-in

n = Dimensionless parameters for controlling shape of stress-strain curve of concrete

n_{strand}= Number of strands in walls and unbonded PT slab

n_{strap}= Number of straps across floor-edge beam connections

$n_{\#2}$ = Number of #2 wires in floor

n_{BS} = Number of BS Italia connections

n_{FO} = Number of O-connectors away from rotation point

n_{JVI} = Number of JVI Mini V connections

n_{NO} = Number of O-connectors near rotation point

n_{PT_slab} = Number of strands in scaled floors (E-W direction)

N_{mgbeam_cp} = Axial force in mega beams deduced by strain gages on cover plates, kip

N_{mgbeam_middle} = Axial force in mega beams deduced by strain gages on flanges, kip

N_{scol_B} = Axial force in steel columns deduced by gages at the bottom of steel columns, kip

N_{scol_T} = Axial force in steel columns deduced by gages at the top of steel columns, kip

N_{slip} = PT loss due to slip of strands in walls, kip

N_{strap} = Axial force in strap plates, kip

N_{truss} = Axial forces in steel trusses, kip

N_{wall} = Axial load applied to walls, kip

N_G = Axial load on walls, kip

N_{G_Ecol} = Axial load on end columns, kip

N_{PT} = PT force recorded in walls, kip

$N_{PT\_2\%}$ = PT force expected in walls at 2% drift, kip

P_{total} = Total compression force at wall corners, kip

p = Parameter controlling shape of stress-strain curves

Q = Statical moment of area of mega beams, $in.^3$

r = Coefficient to determine equivalent rectangular block; Dimensionless parameters for controlling shape of stress-strain curves of concrete

R_{FO} = Vertical resistance from O-connectors away from rotation point, kip

R_{NO} = Vertical resistance from O-connectors near rotation point, kip

R_V = Base shear resistance of rocking walls, kip

R_{YO} = Yield resistance of O-connectors, kip

s = Center-to-center spacing of transverse reinforcement; horizontal distance between wall-floor connections and rotation point of walls, in.

s_{col}= Gage length of LVDT (string pot or DCDT) attached to edge columns, in.

s_{col_rebar} = Distance between rebar in the east and the west side of edge columns, in.

s_l = Average gage length of LVDTs attached to the top and the bottom of slabs, in.

s_o = Center-to-center spacing of transverse reinforcement, in.

s_{scol_gage}= Distance between top and bottom strain gages on steel columns, in.

s_1 = Gage length of first row of LVDTs attached to slabs, in.

s_2 = Gage length of second row of LVDTs attached to slabs, in.

s_{BS} = Distance between BS Italia connections and compressive end of walls, in.

s_{FO}= Distance between O-connectors away from rotation point and wall end, in.

$s_{L1\_FWE\_V}$ = Distance between LVDT L1_FWE_V and wall end, in.

s'= Clear vertical spacing between hoop bars, in.

sf = Scale factor

S_{O_E} = Distance between east O-connectors and adjacent wall end, in.

S_{O_W} = Distance between west O-connectors and adjacent wall end, in.

t = Thickness of rocking walls, Depth of end columns and edge columns; Thickness of mega beam web; Thickness of strap plates, in.

t_{cp} = Thickness of cover plates, in.

t_{plank} = Thickness of planks, in.

t_{slab} = Thickness of slabs, in.

t_w'' = Distance between centerline of steel confinement in the direction of wall thickness, in.

V_{col} = Shear force in edge columns, kip

V_{floor} = Horizontal design forces transferred to walls, kip

V_{mgbeam} = Shear force in mega beams, kip

V_n = Nominal shear resistance of walls, kip

V_{scol} = Shear force in steel columns, kip

$V_{specimen}$ = Base shear of test specimens, kip

V_{PB} = Base shear of scaled prototype buildings, kip

V_{TB} = Volume of top blocks, in.^{3}

V_{WALL} = Volume of walls, in.^{3}

w_{slab} = Width of scaled floors, in.

w_{wall} = Width (length) of rocking walls, in.

w'_i= Clear transverse spacing between longitudinal bars, in.

w_{Ecol} = Width of end columns, in.

$w_{Edgecol}$ = Width of edge columns, in.

W_w = Self weight of wall and top block, kip

W_{Ecol} = Self weight of end columns, kip

$\bar{x}$ = Parameter related to confinement effect

y_i = Perpendicular distance from neutral axis to elemental area, in.

Greek characters:

α = Equivalent rectangular block constant

α_c = Coefficient defining relative contribution of concrete strength to nominal wall shear strength; Equivalent rectangular block constant for confined concrete

α_{fcol} = Rotation at top of fixed-base edge columns, rad

α_o= Overstrength factor for energy dissipating elements

α_{rcol} = Rotation at top of rocking edge columns, rad

α_{strap} = Rotation of strap plates on precast floors, rad

α_{strap_eb} = Maximum rotation of strap plates at floor-edge beam connections, rad

α_{strap_tb} = Maximum rotation of strap plates at floor-transverse beam connections, rad

$\alpha_{Edgecol}$ = Rotation of edge columns, rad

α_{Endcol} = Rotation of end columns, rad

α_T = Thermal coefficient, 1/K

β = Equivalent rectangular block constant for concrete; Rotation at top of columns

β_1 = Equivalent rectangular block constant for unconfined concrete

β_c= Equivalent rectangular block constant for confined concrete

β_0= Overstrength factor of surrounding structure

β_{Eplank} = Rotation of east edge planks, rad

β_{Wplank} = Rotation of west edge planks, rad

Δ = Vertical deformation of floors at wall ends, in.

Δ_{beam_B} = Extension or shortening recorded by LVDTs mounted on bottom flange, in.

Δ_{beam_T} = Extension or shortening recorded by LVDTs mounted on top flange, in.

Δ_{cls} = Vertical deformation of floors at free edges, in.

$\Delta_{design\_2\%}$ = Elongation of strands in walls at 2% design drift, in.

Δ_{bot} = Shortening or extension recorded by LVDTs below slabs, in.

Δ_{col_E} = Extension/shortening of LVDT (SP or DCDT) on east side of edge columns, in.

Δ_{col_W} = Extension/shortening of LVDT (SP or DCDT) on west side of edge columns, in.

Δ_l = Elongation of strands in each panel in jointed wall systems, in.

$\Delta_{relative\_disp}$ = Relative vertical displacement between wall and slab, in.

$\Delta_{rod\_2\%}$ = Elongation of rods in end columns at 2% design drift, in.

$\Delta_{rod\_5\%}$ = Elongation of rods in end columns at 5% drift, in.

Δ_{struss_T} = Extension or shortening recorded by LVDT mounted on top surface, in.

Δ_{top} = Extension or shortening recorded by LVDT above slab, in.

Δ_{truss_B} = Extension or shortening recorded by LVDT installed on bottom surface, in.

Δ_{uplift_endcol} = Uplift of end columns, in.

$\Delta_{uplift\_edgecol}$ = Uplift of edge columns, in.

Δ_{uplift_slab} = Uplift of slab at the location of LVDT L1_FWE_V, in.

Δ_{uplift_wall} = Uplift of wall at the location of LVDT L1_FWE_V, in.

Δ_{BS} = Uplift of wall at the location of BS Italia connections, in.

Δ_F = Increased forces in walls in jointed wall systems, kip

Δ_{FO} = Relative vertical deformation of O-connectors away from rotation point, in.

Δ_{NO} = Relative vertical deformation of O-connectors near rotation point, in.

Δ_{PT} = Elongation of PT strands in walls, in.

Δ_T = Magnitude of varied temperature, K

$\Delta_{1\%}$ = Residual gap opening recorded after 1% drift cycles, in.

ε_b = Strain in bottom reinforcement, in./in.

ε_c = Strain in stress-strain curves; Strain in extreme compressive concrete fiber, in./in.

ε_c' = Strain at compressive strength of concrete f_c', in./in.

ε_{cc} = Strain at peak strength of confined concrete, in./in.

ε_{conc} = Maximum strain in extreme compressive concrete fiber, in./in.

ε_{cp_B} = Strain in dogbone section of bottom cover plate, in./in.

ε_{cp_T} = Strain in dogbone section of top cover plate, in./in.

$\varepsilon_{initial}$ = Initial compressive strain in walls and end columns generated by PT forces; initial strain in PT strands in walls, in./in.

ε_{mgbeam_B} = Strain in bottom flange of mega beams, in./in.

ε_{mgbeam_T} = Strain in top flange of mega beams, in./in.

$\varepsilon_{rebar\_E\_i}$ = Strain in rebar on east side of edge columns (i=3,5,7,9,11), in./in.

$\varepsilon_{rebar\_W\_j}$ = Strain in rebar on west side of edge columns (j=4,5,8,10,12), in./in.

$\varepsilon_{rod\_5\%}$ = Strain in rods in end columns at 5% drift, in./in.

ε_{scol_BBf} = Strain in bottom flange at bottom of steel columns, in./in.

ε_{scol_BTf} = Strain in top flange at bottom of steel columns, in./in.

ε_{scol_TBf} = Strain in bottom flanges at top of steel columns, in./in.

ε_{scol_TTf} = Strain in top flanges at top of steel columns, in./in.

ε_{strand} = Strain in prestressing steel, in./in.

ε_{strap_B} = Strain in bottom surface of strap plates, in./in.

ε_{strap_T} = Strain in top surface of strap plates, in./in.

ε_{su} = Ultimate strain in steel confinement, in./in.

ε_{truss_N} = Strain in north surface of trusses, in./in.

ε_{truss_S} = Strain in south surface of trusses, in./in.

ε_{unconf}= Crushing strain of unconfined concrete, in./in.

ε_y = Yield strain in reinforcement or prestressing steel, in./in.

ε_H = Strain in horizontal gage of rosette, in./in.

ε_I = Strain in 45° inclined gage of rosette, in./in.

ε_V = Strain in vertical gage of rosette, in./in.

$\varepsilon_1(x,p)$ = Strain distribution along unbonded strands (assuming "bonded" strands), in./in.

$\varepsilon_{1,ave}(p)$ = Average strain in post-tensioned strands, in./in.

$\varepsilon_{1,max}(p)$ = Maximum strain in post-tensioned strands, in./in.

$\varepsilon_{1\%}$ = Strain in PT strands after 1% drift cycles, in./in.

σ_c = Compressive stress in extreme concrete fiber, psi

$\sigma_{design\_2\%}$ = Stress in strands of walls at 2% design drift, ksi

$\sigma_{initial}$ = Initial stress of strands in walls and unbonded PT slab, ksi

$\sigma_{initial\_rod}$ = Initial stress of rods in end columns, ksi

$\sigma_{rod\_2\%}$ = Stress in rods in end columns at 2% design drift, ksi

σ_{strand} = Stress in prestressing steel, ksi

$\sigma_{1,max}(p)$ = Maximum stress in post-tensioned strand, ksi

$\sigma_{1,ave}(p)$ = Average stress in post-tensioned strand, ksi

θ = Rotation angle of walls; Rotation angle of end columns; Lateral drift of walls, rad

θ_{col} = Rotation of edge columns, rad

θ_{design} = Rotation of walls at design drift, rad

θ_l = Local rotation of slabs, rad

θ_{l1}= Local rotation obtained from first row of LVDTs on slabs, rad

θ_{l2}= Local rotation obtained from second row of LVDTs on slabs, rad

θ_{max}= Maximum expected drift of walls, rad

θ_{mgbeam} = Rotation of mega beams, rad

θ_s = Rotation over a longer gage length of LVDTs on floors, rad

θ_{truss} = Rotation of steel trusses, rad

θ_{TBW} = Rotation recorded by TBW on bottom portion of walls, rad

θ_{TTW} = Rotation recorded by TTW on top portion of walls, rad

λ = Modification factor reflecting reduced mechanical properties of lightweight concrete (all relative to normal weight concrete of the same compressive strength)

μ = Coefficient of friction between wall and grout beneath walls; Amplification coefficient for rotation at top of fixed-base edge columns

φ = Curvature of cross sections, 1/rad

φ_{col_a} = Average curvature of edge columns, 1/rad

φ_{col_l} = Local curvature of edge columns, 1/rad

φ_l = Local curvature of slabs, 1/rad

φ_s = Average curvature over a longer gage length of LVDTs on slabs, 1/rad

φ_{strap} = Curvature in strap plates due to flexural bending, 1/rad

∅ = Shear strength reduction factor

$\emptyset_{max}$= Plastic curvature at maximum expected drift, 1/rad

ρ = Ratio of reinforcement area to gross concrete area

ρ_{cc} = Ratio of volume of longitudinal steel to volume of concrete core

$\rho_{flexural}$ = Ratio of flexural bending of walls to rotation of walls

ρ_x = Ratio of volume of steel confinement to volume of confined concrete core (x direction)

ρ_y = Ratio of volume of steel confinement to volume of confined concrete core (y direction)

ρ_{min} = Minimum ratio of reinforcement area to gross concrete area

ρ_p = Ratio of to A_{ps} to bd_p; Ratio of ratio of $n_{strand}A_{strand}$ to $W_{slab}d_p$

ρ_G = Density of concrete, lbs/ft^3

$\gamma_{rosette}$ = Shear strains deduced from rosette, in./in.

ν = Poission's ratio of steel materials

CHAPTER 1. Introduction

1.1 Overview

Reinforced concrete (RC) shear walls have proven to be an effective means of resisting lateral loads in structural systems without collapse. Special structural walls are detailed to dissipate energy through the development of plastic hinge regions that enable structural engineers to design for lower lateral forces than would be expected if the structure were to remain elastic. This provides an upfront economic benefit in the design of the structure, but the energy dissipation is typically associated with significant permanent damage in a large seismic event. This methodology is effective for life safety, but can cause tremendous economic losses including large permanent residual drifts (Wood et al. 1987).

Fig. 1-1 shows reinforcement details of a typical special structural wall tested in the laboratory. As shown in the figure, the longitudinal rebar are continuous across the base of the wall and the foundation. A constant axial load was input to the wall to simulate the gravity load carried by the wall and lateral cyclic displacement was applied to the top of the wall. The hysteretic behavior of the tested wall is shown in Fig. 1-2. As shown in the figure, significant residual displacement was observed when the wall was unloaded from the peak displacements to zero applied loads. On the other hand, the energy dissipation capability of the wall, which was represented by the area enclosed by the hysteretic curves, was large. Fig. 1-3 shows the damage of the structural wall after 1.5% lateral drift. As shown in the figure, extensive cracks were distributed at the base of the wall (plastic hinge regions) alongside crushing of the concrete. Yielding and fracture of the longitudinal rebar was also observed in the test. Large repair costs were expected for the damaged wall.

Besides the repair and reconstruction costs of the damaged structural wall structures, many businesses suffer large costs associated with the inability to reoccupy their offices

quickly. These economic losses underscore the need to develop structural concepts to minimize the damage and the residual drift of buildings after seismic events.

Unlike conventional RC structural walls, rocking walls are typically not connected to the foundation with continuous mild reinforcement. Rather, the walls are clamped to the foundation using unbonded post-tensioned (PT) strands. When the walls are subjected to lateral loads, they rock about the corners, causing a separation at the interface initiating at the opposite corner, and the strands provide a restoring force to self-center the walls. To inhibit yielding due to the elongation of the strands caused by the gap opening, the strands are unbonded over their length. A sketch of the rocking wall concept is shown in Fig. 1-4.

Five rocking wall panels using unbonded PT bars were tested at Lehigh University (Perez 2004). The test setup is shown in Fig. 1-5. Fig. 1-6 shows the hysteretic behavior of the second specimen (TW5). As shown in the figure, little residual drift exists in the wall and self-centering is realized. Compared to regular shear walls, the energy dissipation capability of the tested rocking wall was relatively small because of limited damage in the wall: only minor concrete cover spalled at the corners of the wall and yielding of the PT bars occurred at high drift levels (1.5% to 2%). Fig. 1-7 shows the damage in the rocking wall after 6% drift.

A specimen (PTT) representing a typical post-tensioned precast concrete wall with tendons unbonded over the wall height was tested at the National Institute of Standards and Technology (NIST) (Erkmen and Schultz 2007). Fig. 1-8 shows the test specimen. In-plane horizontal displacements, overturning moment, and a constant vertical force were applied to the tested wall. Fig. 1-9 shows the hysteretic behavior of the specimen (curves termed “Experiment”). Similar to the behavior of specimen TW5 discussed above, self-centering was realized, and the energy dissipation capacity was stable but small.

The lack of energy dissipation capability of the rocking walls might lead to large lateral displacement and high acceleration of the structure, which would be detrimental. To increase the energy dissipation capacity of the rocking walls, supplementary elements were added to the rocking walls, which formed “rocking-wall systems.” Fig. 1-10

illustrates the rocking-wall system concept. As shown in the figure, if additional energy dissipating elements ("fuses") are added to the rocking walls, the approximate bilinear hysteretic curve of the wall (the minor damage in the wall and the yielding of the strands neglected) will be changed to ideal flag-shaped hysteretic curves, which have both self-centering and energy dissipation capabilities.

A number of experimental studies of the rocking-wall systems with different types of additional energy dissipating elements have been conducted (Priestley et al. 1999, Aaleti et al. 2011, Restrepo et al. 2007, Smith et al. 2011). For example, a proof test of Precast Wall with End Column ("PreWEC"), one type of rocking-wall systems using oval-shaped steel plates ("O-connectors") as energy dissipating elements, was completed at the National Center for Research on Earthquake Engineering (NCREE) in Taiwan (Aaleti and Sritharan 2011). Test results indicated that the rocking-wall system performed exceptionally well with excellent energy dissipation and self-centering ability. Detailed discussion of different types of rocking-wall systems is given in the literature review of Chapter 2.

1.2 Research Objectives

The majority of existing research, including the proof test in NCREE of the PreWEC system, focused on isolated rocking-wall systems. Limited effort had been put into investigating the interaction between the rocking-wall systems and surrounding structures, such as floors and gravity columns. It has been one of the main drawbacks preventing rocking-wall systems from being used in practice.

It is apparent that the interaction between the rocking-wall systems and surrounding structures is inevitable, because the shear forces need to be transferred from the floor diaphragms to the vertical elements of the lateral-force-resisting system (e.g., rocking wall). When the gravity loads from the floors are also carried by rocking walls (i.e., the floor is rigidly connected to the rocking wall), the interaction becomes more complicated. On one hand, the gravity load can increase the self-centering capability of the rocking wall (if the resultant gravity load does not move beyond the resultant compression force in the wall at large drifts). On the other hand, the rocking of the wall can impose a large

deformation demand on the floor, which might cause floor damage. The damaged floor might constrain the rocking wall from self-centering and increase the residual drift of the entire building.

Therefore, accounting for the interaction between the rocking-wall system and surrounding structure is essential to ensure the self-centering and functionality of a building after a major seismic event. Furthermore, the rocking behavior of the wall might have significant impact on the floor and gravity columns.

To investigate the interaction mechanism, two large-scale assemblages that used different types of wall-floor connections were designed to maximize (Specimen PFS1) and minimize (Specimen PFS2) the interactions between the rocking-wall system and surrounding structure. "PreWEC" systems were used as the rocking-wall systems in both tests.

Specimen PFS1 consisted of a rocking wall that carried gravity loads (i.e., bearing wall), cast-in-place (CIP) gravity columns, and a CIP unbonded post-tensioned floor system to promote the interaction with the wall. PFS1 also featured energy dissipating elements "O-connectors" that were attached between the rocking wall and adjacent side tubes pinned at the base block.

Specimen PFS2 was entirely precast and designed to minimize the interaction. It consisted of a rocking wall (non-bearing wall) that only transferred lateral loads from the floors, precast gravity columns and a precast floor system formed by solid planks. A unique connector system provided lateral load transfer between the floor and the rocking wall, isolating the floor from the vertical movement of the wall. The system also featured rocking end columns adjacent to the wall that carried the gravity loads from the floor and connected with the "O-connectors."

The two tests were conducted in the MAST laboratory to study the upper bound and lower bound interaction between the rocking-wall system and the surrounding structures. Test results were utilized in the following aspects: (1) Analyze and compare the overall performance of the two specimens; (2) Analyze the behaviors of individual structural components in the two specimens; (3) Validate proposed finite element models; (4) Propose design recommendations of rocking-wall structures.

1.3 Thesis Outline

This thesis is separated into the following chapters:

Literature Review: Chapter 2 provides an extensive literature review of rocking-wall structures. Existing experimental and numerical studies of isolated rocking-wall systems and rocking-wall structures are presented. Design guidelines of rocking-wall systems (ITG 5-2) and design details practically used in existing tests are also discussed.

Experimental Program: Chapter 3 provides an overview of the two large-scale assemblages tested in the MAST laboratory. The prototype building of the specimens is introduced first, followed by the design and construction of the two specimens. The material properties of the two specimens are also presented in this chapter.

Instrumentation Plan and Loading Protocol: Chapter 4 summarizes the instrumentation plan of the two specimens. Associated drawings containing different types of instrumentation are given. Purpose of the instrumentation and data process methods are presented. Loading protocols of the two tests are also introduced in this chapter.

Finite Element Modeling of the Test Specimens: Chapter 5 provides an overview of the finite element modeling of the test specimens. Commercial software ABAQUS is used for the simulation. Material models, element types and some simulation techniques used in the models are presented.

Test Observations and Data Analysis for PFS1: Chapter 6 describes the test observations and data analysis for the first specimen (PFS1) that used rigid wall-floor connections. Overall behaviors of PFS1 are discussed first, followed by local behaviors of every structural component in PFS1. The numerical models described in Chapter 5 are also validated in this chapter.

Test Observations and Data Analysis for PFS2: Chapter 7 describes the test observations and data analysis for the second specimen (PFS2) that used special vertical movement isolated wall-floor connections. Both overall and local behaviors of PFS2 are discussed.

Comparison of PFS1 and PFS2: Because the prototype building of the two specimens was the same and they were designed to have similar base moment resistances, a direct comparison of the two specimens was made possible. Chapter 8 makes a comparison of the overall behaviors of the two specimens, including stiffness, strength and self-centering capacities. Different damage occurred to the two specimens is also summarized and discussed in this chapter.

Design Recommendations: Chapter 9 discusses the proposed design recommendations for PreWEC systems, rocking-wall structures using rigid wall-floor connections as well as vertical movement isolated connections.

Summary and Conclusions: Chapter 10 summarizes main conclusions of the thesis and provides recommendations for future studies.

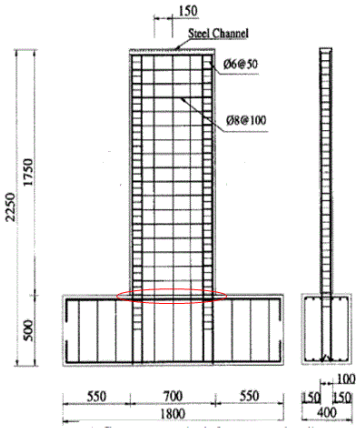

Fig. 1-1 Reinforcement details of a shear wall specimen (Zhang and Wang 2000)

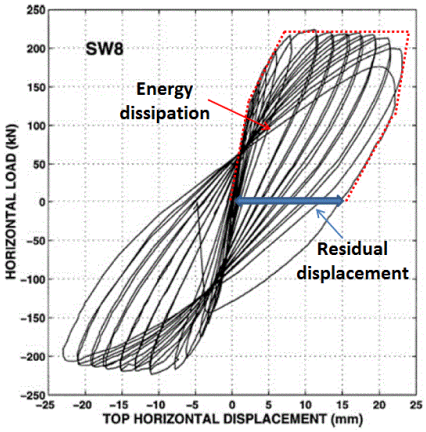

Fig. 1-2 Hysteretic curve of a shear wall specimen (Zhang and Wang 2000)

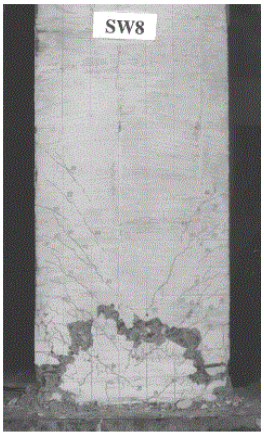

Fig. 1-3 Damage of a shear wall specimen (Zhang and Wang 2000)

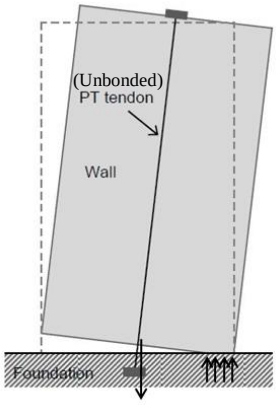

Fig. 1-4 Sketch of rocking wall concept (Henry 2011)

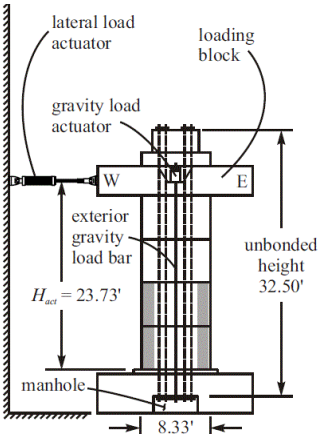

Fig. 1-5 Test setup (Perez 2004)

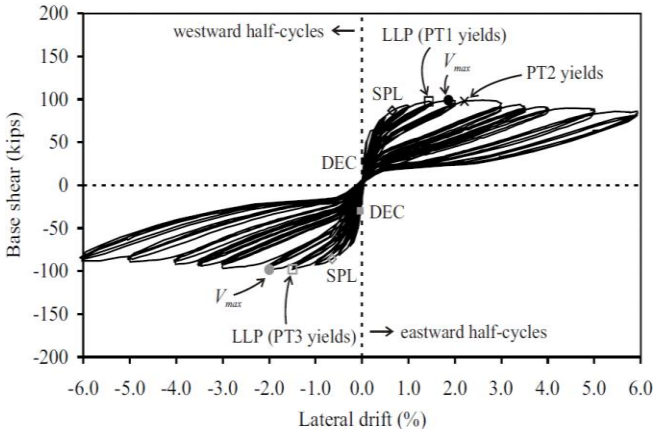

Fig. 1-6 Cyclic response of TW5 (Perez 2004)

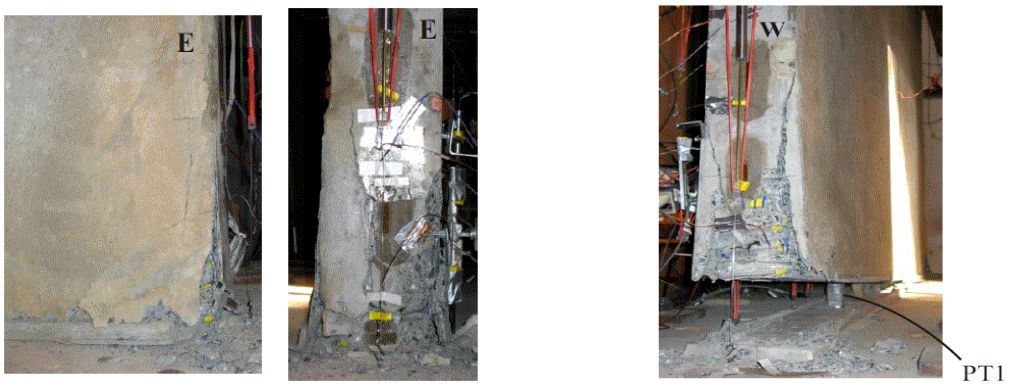

(a) East end after 6% drift (b) West end after 6% drift

Fig. 1-7 Damage of the wall in tests of rocking walls at Lehigh University (Perez 2004)

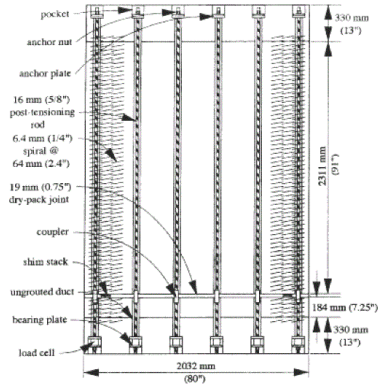

Fig. 1-8 Specimen of a post-tensioned wall (Erkmen and Schultz 2007)

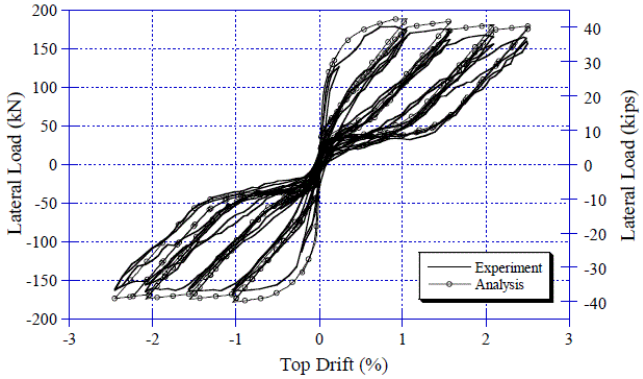

Fig. 1-9 Experimental and analytical response for the specimen PTT (Erkmen and Schultz 2007)

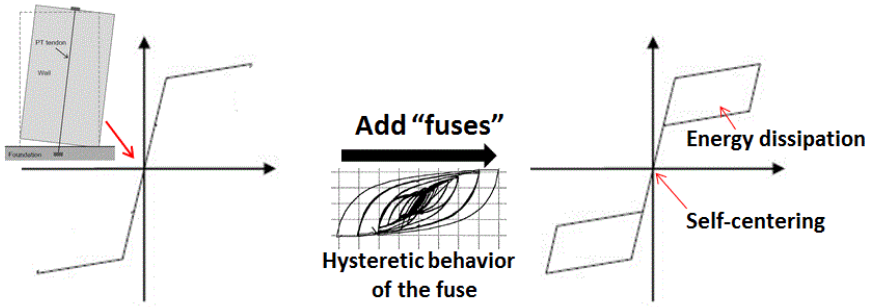

Bilinear hysteretic curve **Flag-shaped hysteretic curve**

Fig. 1-10 Ideal hysteretic curves for rocking walls and rocking-wall systems

CHAPTER 2. Literature Review

An extensive literature review of rocking-wall structures and their components is provided in this chapter. Other pertinent literature associated with the research presented in this thesis is summarized in the associated chapters. Section 2.1 reviews existing experimental studies on three types of rocking-wall systems, including jointed wall systems, hybrid wall systems and Precast Wall with End Columns (PreWEC) systems. Section 2.2 summarizes and discusses existing computational techniques of modeling rocking-wall systems. To implement rocking-wall systems in buildings, it is important to understand rocking-wall structures including the interaction between the rocking-wall systems and surrounding structural systems (e.g. floors and gravity frames) and their impact on the performance of the buildings. Section 2.3 summarizes and discusses existing experimental and numerical studies on rocking-wall structures. Section 2.4 compares existing design guidelines of rocking-wall systems (ITG 2009) with the design details practically used in those experimental studies.

2.1 Experimental Studies of Rocking-Wall Systems

2.1.1 Jointed Wall System

A joint US-Japan research program PRESSS (PREcast Seismic Structural Systems) was conducted in the 1990's to investigate jointed precast concrete structures. The concept of jointed wall systems was proposed and tested in the PRESSS program.

Fig. 2-1 shows a sketch of a jointed wall system featuring three adjacent precast wall panels each made of a series of panels stacked on top of each other. A layer of grout is placed between the base of the walls and the foundation, and the wall panels are clamped to the foundation using unbonded post-tensioning strands to provide self-centering forces to the walls. The three vertical wall panels are connected to each other using special connectors to dissipate energy. When the walls are displaced laterally, the special connectors are deformed as shown in Fig. 2-2 due to the relative vertical displacement between adjacent walls.

In the PRESSS program, stainless steel U-shaped flexural plates (UFP) were used as the special connectors. Component tests had shown that the U-shaped flexural plates provided stable and significant amount of energy dissipation when they were subjected to relative vertical deformation (Schultz and Magana 1996). Fig. 2-3 shows the detail of the tested U-shaped flexural plates. Fig. 2-4 shows the hysteretic behavior obtained from the component tests.

As shown in Fig. 2-5, the jointed wall system used in the PRESSS program included two unbonded post-tensioned precast walls, which were connected along the vertical interfaces by UFP (Priestley et al. 1999). Fig. 2-6 shows the base moment-lateral displacement (measured at the fifth floor) response for the specimen in the wall direction of the building. As shown in the figure, although residual displacement was observed, the specimen exhibited reasonable self-centering characteristics. A reasonable amount of energy was dissipated by the specimen, which was believed to be mainly contributed by the UFP. Damage of the rocking walls only included minor spalling of the cover concrete in the corners, which was not significant.

2.1.2 Hybrid Wall System

Fig. 2-7 illustrates an example of a hybrid wall system. Different from jointed wall systems where multiple vertical walls are used and connected along the vertical interfaces by energy dissipating elements (e.g., UFP), a single vertical precast rocking wall (made of multiple stacked wall elements) was used in the hybrid wall system with mild reinforcement used as energy dissipating elements. As shown in the figure, when the wall rocks laterally, the gap opening at the base of the wall elongates the rebar; when the wall moves back, the closing of the gap compresses the rebar back to its original length. The hysteretic behavior of the rebar provided a source of energy dissipation.

Three identical half-scale precast concrete wall specimens were tested at the University of Canterbury (Restrepo and Rahman 2007), which included hybrid systems. The first specimen was a single rocking wall without energy dissipating elements and the other two specimens were hybrid wall systems with different amounts of energy dissipating elements. Dogbone-shaped mild reinforcement was used for the energy dissipating

elements. The “dogbone” segment of the rebar was machined over a specified length to enable the development of tensile yielding and identical compressive force in the “dogbone” portion without buckling. The top non-milled segment of the rebar, which protruded from the foundation, was grouted into a duct pre-embedded in the wall and was intended to remain elastic.

Fig. 2-8 shows the test setup. The three specimens were tested under pseudo-static cyclic loading. A constant gravity load was applied to the third specimen but no gravity load was applied to the first two specimens. The hysteretic behavior of the first specimen is shown in Fig. 2-9. As shown in the figure, the hysteretic behavior is characterized by an approximate nonlinear elastic relationship, which was similar to the performance observed for single rocking walls.

After adding the energy dissipating elements in the second and the third specimens, typical flag-shaped hysteretic behaviors of the two specimens were observed with negligible residual displacement and significant energy dissipation was mainly contributed by the milled bars. Fig. 2-10 and Fig. 2-11 show the hysteretic curves for the second and the third specimens alongside damage of the wall observed in the tests. As shown in the figures, minor spalling of concrete cover was observed in the wall toe, which was believed to be repairable. Confinement in the boundary elements of the walls successfully prevented significant crushing of the concrete. It was also observed that the strength of the third specimen was much larger than that of the second specimen, which was believed to be mainly due to the additional gravity load applied on the third specimen.

Although the hybrid wall systems performed well in the test, one disadvantage of the system was that the energy dissipating mild reinforcement was not easily replaced after they yielded or fractured in the earthquake event. One solution was to install additional mild reinforcement across the wall and foundation but leave them ungrouted during construction. These reserved rebar could be grouted after the earthquake event and provide the demanded energy dissipation capacity to the rocking wall. However, this solution would reduce the cost-effectiveness of the hybrid wall system.

2.1.3 Precast Wall with End Columns (PreWEC)

As described in Section 2.1.1, the jointed wall performed well in the test with greatly reduced residual drifts, reasonable energy dissipation capability and limited damage in the wall. However, the implementation of the system was limited in practice. To install the energy dissipating elements, the jointed wall system would have to consist of at least two panels. Compared to a monolithic reinforced concrete wall with the same dimension, the division of the wall into several panels greatly reduced the length of the lever arm between the post-tensioned strands and the compression block in the corners of the wall, which resulted in a loss of moment resisting capacity and a reduction cost-effectiveness of the jointed wall system.

Fig. 2-12 compares the base moment provided by a single rocking wall panel and a jointed wall system of the same width (4*d*), which includes two panels and an energy dissipating element between the vertical faces of the jointed wall. The analysis is aimed to demonstrate that the moment resistance of a single wall is decreased when it is divided into multiple panels. To simplify the analysis, the following assumptions were made: (1) the initial PT force in the single wall ($2F_i$) was equal to the total initial PT force in the jointed wall system ($F_i + F_i$); (2) the walls were assumed to rock about the tip of the wall, so the lever arm of the PT strands in any wall was equal to half of the width of the wall; (3) the strands remained elastic in the walls and the increased PT forces were proportional to the elongation of the strands ($2\Delta_l$ for the single wall and Δ_l for each panel in the jointed wall system); (4) the action line of the resistance from the energy dissipating element, which providing resisting force, F_C, in the jointed wall system along the edge of the wall went through the rotation point of the left panel; (5) the resistance from the energy dissipating element (F_C) was smaller than $F_i + \Delta_F$ to prevent the left panel from being picked up; (6) the self-weight and the external gravity load were not considered.

The base moment of the single wall (M_{single}) about the rotation point is:

$$M_{single} = (2F_i + 2\Delta_F)2d = 4(F_i + \Delta_F)d \tag{2.1}$$

The base moment of the jointed wall system is:

$$M_{left} + M_{right} = (F_i + \Delta_F)d + [(F_i + \Delta_F)d + F_C \cdot 2d] \\ = 2(F_i + \Delta_F)d + 2F_C d \tag{2.2}$$

Where M_{left} = Moment resistance provided by the left wall panel; M_{right} = Moment resistance provided by the right wall panel. Because $F_C < F_i + \Delta_F$ as mentioned earlier, it was deduced that $M_{left} + M_{right} < M_{single}$. The base moment of the jointed wall system was smaller than that of the single wall.

To improve the performance of jointed wall systems, the Precast Wall with End Columns (PreWEC) system was developed (Aaleti and Sritharan 2011). Fig. 2-13 shows a sketch of the PreWEC system. It includes a precast wall and two steel, concrete or composite end columns. Similar to the precast wall, the two end columns are clamped to the foundation by unbonded post-tensioned strands or high strength rods. They are connected to the wall along the vertical interface by energy dissipating connectors. Compared to the width of the individual wall in the jointed wall systems, the PreWEC wall width is greatly increased. It leads to a larger lever arm between the post-tensioned strands and the compression block in the corner of the wall and a larger base moment resistance. With additional moment resistance provided by the energy dissipating connectors, the moment capacity of the PreWEC can be designed to be similar to that of a monolithic reinforced concrete wall with the same dimensions.

Because large inelastic strains can be developed during the process of rolling steel plates, stainless steel material was used to manufacture the U-shaped flexural plates (UFP) in the jointed wall system. Drawbacks of the UFP include high cost and unpredictable behavior due to the inelastic strain developed during the manufacturing process. Although the UFP performed well in the PRESSS program, a different type of energy dissipating element, Oval-shaped flexural plate connectors (O-connectors) were used in the PreWEC system. Fig. 2-14 shows an O-connector connected to the wall and the end column. The O-connectors were manufactured by direct laser cutting from mild steel plates, resulting in lower cost and more predictable behavior. Different from UFP which are installed inside the joints between adjacent panels (Fig. 2-3), the O-connectors are connected to the surfaces of the wall and the end column. As shown in Fig. 2-14, the

O-connectors are welded to embedded plates in the wall and the surface of the steel end column.

A series of component tests of the O-connectors were conducted at Iowa State University to investigate their performance. Fig. 2-15 shows the setup of the component test using an MTS testing frame. A U-shaped steel frame was attached to the loading grip on the top of the MTS testing frame. An H-shaped assemblage was installed to the fixed base grip of the MTS frame. To eliminate eccentric loading, four O-connectors (two in the front and two in the back) were welded to the U-shaped frame and the H-shaped assemblage. When the loading grip moved in the vertical direction and the fixed base grip stood still, the O-connectors were deformed due to the relative movements between the loading grip and the fixed base grip, which were similar to the deformations of the O-connectors in the test. To prevent the O-connectors from buckling, four horizontal tubes were installed as shown in the figure. The O-connectors were under displacement controlled cyclic loading and Fig. 2-16 shows the measured force-displacement response of a tested O-connector. As shown in the figure, the O-connector exhibited a stable and excellent energy dissipating capability. The same test setup was used in Chapter 5 for the calibration of the finite element model of O-connectors.

A proof of concept test was completed through a large-scale PreWEC specimen at the National Center for Research on Earthquake Engineering (NCREE) in Taiwan. Fig. 2-17 shows an overview of the test specimen. The specimen included a 72 in. long, 6 in. thick precast wall and two 8 in. by 6 in. concrete filled steel tube end columns. A 1 in. gap was reserved between the wall and each end column. The total height of the PreWEC was 258 in. Five pairs of O-connectors were installed along each vertical joint between the wall and the end columns (20 O-connectors in total). Fig. 2-18 shows the dimension of the 0.395 in. thick O-connector used in the test.

Fig. 2-19 shows the plan view of the PreWEC specimen at the base. As shown in the figure, the wall and end columns were anchored to the foundation by 12 and 3 pieces of 0.6 in. diameter post-tensioned strands, respectively. The initial prestress of the strands in the wall and the two end columns were $0.67f_{pu}$, $0.66\ f_{pu}$ and $0.68f_{pu}$, respectively, where f_{pu} was the specified tensile strength of the strands.

Fig. 2-20 shows the loading protocol of the test. As shown in the figure, the first four cycles of loading were under force-control mode, when the wall was about to be uplifted. Pseudo-static cyclic displacement-controlled loading protocol was applied to the specimen for the rest of the test. Fig. 2-21 shows the damage condition of the test specimen at 3% drift. As shown in the figure, only minor spalling of concrete cover was observed in the corners of the wall and the majority of the wall remained intact. The O-connectors were deformed and dissipated energy as expected. Fig. 2-22 shows the measured force-displacement curve of the specimen and the associated envelope curve. As shown in the figure, the rocking wall performed well with excellent energy dissipation and reasonable self-centering capability. It was also reported that the strength of the tested PreWEC system was 15% higher than that of a comparable monolithic reinforced concrete shear wall, demonstrating the improved performance over jointed wall systems.

2.2 Numerical Studies of Rocking-Wall Systems

Several computational techniques have been used with different finite element software to simulate the behavior of rocking walls, such as lumped plasticity models, fiber-based models and solid element models.

2.2.1 Lumped Plasticity Model

A lumped plasticity model with a combination of multiple non-linear springs was used to model the PreWEC system using Ruaumoko (Henry 2011). Ruaumoko is a non-linear dynamic structural analysis program developed by researchers at the University of Canterbury, New Zealand. It is capable of elastic and inelastic analyses of two- and three-dimensional structures subjected to dynamic loadings. Various line, plate and spring elements are included in the model with an extensive library of hysteresis rules, enabling it to be used to simulate complicated nonlinear characteristics of structures.

Fig. 2-23 shows the model, which includes an arrangement of seven non-linear rotational springs at the base of the wall. Table 2-1 lists the hysteresis rule used and associated function for each spring. As shown in Fig. 2-24, the simulation results closely

matched the hysteretic response of the PreWEC specimen, especially for the recorded residual drifts.

Using the validated numerical model, a series of dynamic analyses were conducted to assess the self-centering performance of the PreWEC system. An extensive parametric matrix was developed, which varied the fundamental period of the structure, quantity of energy dissipating elements, viscous damping, seismic hazard level, and earthquake ground motion. Because dynamic analysis is beyond the scope of this dissertation, the results from the dynamic analyses are not presented.

2.2.2 Fiber Model

Fiber models were firstly proposed by Kurama et al. (1999) to simulate the hysteretic response of rocking walls using DRAIN-2DX (Prakash and Powell 1993). DRAIN-2DX is a general-purpose computer program developed by researchers at the University of California, Berkeley. It is suitable for nonlinear static and dynamic analysis of plane structures. Its element library includes truss, beam-column and panel elements.

Fig. 2-25 shows the wall and associated numerical models. As shown in the figure, the model includes fiber elements for the wall panels and truss elements for the unbonded tendons.

The cross sections of the wall were composed of fibers. The property of each fiber included a uniaxial stress-strain material model, an area and a location. Rebar fibers were not included to simulate reinforcement in the wall that was not continuous across the horizontal wall-foundation joint. Different uniaxial stress-strain models were assigned to the unconfined concrete fibers and confined concrete fibers in the boundary elements.

To simulate the gap opening between the wall and the foundation when the wall uplifted, the tensile strength of the concrete fibers was neglected. The reduction in the stiffness of the wall due to the gap opening was simulated by the zero stiffness of the concrete fibers when they went into tension.

The unbonded post-tensioning tendons were simulated by truss elements. As shown in the figure, kinematical constraint was imposed between the nodes of truss elements and those of the fiber elements. At the roof level, all degrees-of-freedom of the truss element

nodes were constrained to the fiber element nodes to model the post-tensioning anchorages. At the floor levels, only horizontal degree-of-freedom was constrained between the truss element nodes and the fiber element nodes to ensure the tendons and the wall panels had the same lateral displacements. The vertical and rotational degrees-of-freedom were not constrained because the tendons were unbonded from the wall. The post-tensioning forces of the wall were simulated by initial tensile forces in the truss elements.

The fiber models were capable of accounting for axial-flexural interaction and simulating hysteretic response of the wall with detailed definition of the hysteresis rules of the material models for the tendons and concrete.

The reliability of the fiber model was verified by Perez et al. (2007) using data from five rocking wall panels tested at Lehigh University. Fig. 2-26 shows the test setup and the associated fiber model. Different from the fiber model proposed by Kurama, only one truss element was used to simulate each tendon and it was constrained to the wall only on the top node. The bottom of the truss element was simulated as a pin connection to the foundation. Fig. 2-27 compares the recorded hysteretic behavior of the second specimen (curve Exp.) with the simulation results. FM (monotonic) and FM (cyclic) represent the pushover curve and the hysteretic curves obtained from the fiber model. As shown in the figure, the fiber models well predicted the test.

2.2.3 Solid Element Model

Detailed finite element software ABAQUS (Dassault 2011) has been successfully used to simulate the hysteretic response of rocking walls, including the half-scale PreWEC test specimen at NCREE and the tested hybrid wall system in the DSDM project discussed in Section 2.3.3 (Henry 2011, Belleri et al. 2013).

ABAQUS is powerful commercial software for finite element analysis. It includes different types of elements (solid, shell, beam and truss) with a broad library of material models, including models suitable to simulate cracking and damage of the concrete (concrete smeared cracking model and concrete damaged plasticity model). It is also capable of simulating complicated contact problems with its sophisticated contact

elements. Furthermore, it has both implicit and explicit solvers, which are suitable for static and dynamic analyses (Dassault 2011).

Fig. 2-28 shows an overview of the detailed ABAQUS model for the PreWEC specimen proposed by Henry (Henry 2011). Solid elements C3D8R were used to simulate the wall, the fiber grout layer, the O-connectors, and the two end columns. The unbonded PT tendon was simulated by truss elements (T3D2). The longitudinal and transverse reinforcement in the wall were not modeled, assuming the wall did not have any nonlinear flexural or shear deformation.

Fig. 2-29 shows modeling details of the wall near the base. As shown in the figure, steel channels at the corners of the wall were modeled using solid elements. The bottom plate of the channel was "embedded" in the wall and "contact" elements were assigned between the two side plates of the channel and the surfaces of the wall. Fig. 2-30 shows the modeling details of one of the O-connectors. Steel plates "embedded" in the wall and the welds of the O-connectors were modeled using solid elements. "Tie" constraints were applied to the welds to rigidly connect the O-connectors to the steel plates and the end columns.

Concrete damage plasticity model was used for the concrete material. Different stress-strain responses were assigned to the confined and unconfined concrete. Elastic material was assigned to the fiber grout assuming that it was stronger than the confined concrete in the wall and remained elastic. Plasticity model with combined isotropic and kinematic hardening was used for the steel material.

Special contact elements were defined between the wall and the fiber grout. Because the wall did not pierce into the fiber grout, "hard contact" was used for the normal behavior of the contact elements. "Rough" tangential behavior was assigned to the contact elements because shear sliding of the wall was avoided in the test.

The explicit solver of ABAQUS was used with the lateral displacement slowly enforced to the top block to solve the convergence problem caused by the complicated contact boundary condition. The PT force was slowly applied by subjecting the bottom node of the tendon to a velocity condition to elongate the tendon to minimize the inertia effect.

Fig. 2-31 compares the hysteretic response of the specimen (termed “Test”) with that of the finite element modeling (termed “FEM”). As shown in the figure, the FEM well predicted the test results. Other than the overall behavior, the accuracy of the model was further validated by comparing local responses of the specimen with those from the finite element model, including stress of the tendon, neutral axis depth and base rotation of the wall, compressive strains of the concrete in the wall corners and connector displacements.

A similar modeling approach using ABAQUS was also adopted and verified by the shake table test of a rocking-wall structure in the DSDM project (Belleri et al. 2013) described in 2.3.3.

2.2.4 Discussion of Numerical Studies of Rocking-Wall Systems

In this section, the three computational techniques (lumped plasticity, fiber-based and solid element) are further discussed with respect to the following factors: computational cost, complexity of the models and output results.

The computational cost of lumped plasticity models, which include the cost to establish the model and to run analysis, is low because of the use of nonlinear springs. The springs are macro-elements and only simulate the overall behavior of rocking-wall systems (e.g. moment, rotation). Thus, no material models are needed for the concrete, the steel reinforcement and the steel tendons. Although the model can capture overall behavior, it has the following disadvantages: (1) the calibration of the model is empirical, which is mainly based on existing test results and requires a great amount of trial-and-error. (2) the local responses of the structure cannot be obtained, such as the stress (strain) distribution in the cross sections of the wall, the stress in the tendons, and the uplift of the wall, etc. (3) The plastic behavior of the structure is concentrated in the nonlinear springs and does not spread to other elements along the height of the wall.

The computational cost of fiber models is slightly higher than that of plasticity models, because the stress-strain responses of all the fibers in each cross section of the wall are to be integrated during the analysis. Material models are needed for the confined and unconfined concrete fibers, the steel fibers (if they are continuous across the wall-foundation interface as in the hybrid wall system), and the steel tendons. Compared to the lumped plasticity model, it has the following advantages: (1) the calibration of the model is less empirical, because the

material models for the concrete and the steel can be determined directly from associated material tests; (2) the fiber model can capture the overall behavior and local responses of the rocking-wall systems; (3) the plastic behavior of the structure can be spread to other elements along the height of the wall.

The fiber model assumes that plane sections remain plane; however, this assumption might not be correct at the base of the wall, where the gap opening occurs and localized compression forces spread out. Thus, the fiber model cannot accurately capture the local stress and strain in the walls adjacent to the wall-foundation interface, which might result in discrepancies in other local responses, such as neutral axis depth and stress in the tendons.

The computational costs of solid element models are much higher than those of plasticity and fiber models. A great number of nodes are generated after meshing the structural components into elements. Consequently, it requires more time to establish solid element models and they require more computational time. Despite the high computational cost, solid element models are better able to capture the local stress and strain distribution in the walls adjacent to the wall-foundation. Moreover, pre-processing and post-processing of the data are more convenient with some of the user-friendly interfaces of solid element computational tools (e.g., ABAQUS).

2.3 Experimental and Numerical Studies on Rocking-wall structures

2.3.1 Overview

Although the excellent performance of rocking-wall systems had been successfully validated as discussed in Section 2.1 and Section 2.2, it is important to investigate the interaction between rocking-wall systems and their surrounding structural systems before implementing the rocking-wall system into buildings. However, due to the cost and complexity, only a few system tests of rocking-wall structures, which include both a rocking-wall system and surrounding structural system, have been conducted to date.

In this section, three large-scale rocking-wall structures are described, including: PRESSS test of a five-story, two-bay by two-bay precast building (Priestley et al. 1999); DSDM test of a three-story, four-bay by one-bay precast building (Schoettler 2010); E-Defense test of a four-story, two-bay by one-bay post-tensioned concrete building (Nagae

et al. 2011). Vertical movement isolation connections were used in the first two specimens (PRESSS and DSDM) to minimize the wall-floor interaction and rigid wall-floor connections were used in the E-Defense test. The summaries of each test include an overview, description of rocking wall-floor connection and gravity frames in the wall plane, and test results.

2.3.2 System Test in the PRESSS Project

2.3.2.1 Overview

The main goal of the PRESSS (PREcast Seismic Structural Systems) project was to develop design guidelines for precast hybrid frames and precast jointed wall systems in high seismic regions. The hybrid frames are beyond the scope of this dissertation. The 60%-scale five-story two-bay by two-bay specimen included a jointed wall system with pre-topped double tees in the N-S direction. Fig. 2-32 shows a plan view of the test specimen. As shown in the figure, the pre-topped double tee was placed parallel to the wall. The elevation view of the specimen was shown in Fig. 2-5.

2.3.2.2 Rocking Wall-Floor Connection

The connections between the double tees and the wall were designed to permit free relative vertical movement and free relative rotation, yet transfer horizontal diaphragm forces to the wall. A special connection was designed specifically for the specimen. Because the connection was not practical, it was not the focus of the test and no photos of the connection detail were found in the literature. The special connection can be seen in Fig. 2-5.

2.3.2.3 Gravity Frames in the Wall Plane

In the frame line of the wall, non-seismic precast gravity frames were used. Because of the use of the special connections discussed in Section 2.3.2.2, the gravity loads on the double tees were expected to be transferred to the gravity frames shown in Fig. 2-5. Unbonded steel tendons were placed in the gravity columns. They were post tensioned to emulate the sustained gravity loads. The longitudinal mild reinforcement of the columns was continuous across the column-foundation connection. Thus, the base connections of the columns were expected to be fixed connections.

2.3.2.4 Test Results

Test results showed that the special wall-floor connections performed well when the specimen was deformed to 3% drift in the wall direction. They successfully isolated the double tees from the rocking walls. No further investigation about the wall-floor interaction was found in the literature.

2.3.3 Shake Table Test in the DSDM project

2.3.3.1 Overview

The goal of the DSDM (Diaphragm Seismic Design Methodology) project was to develop a proper procedure to design precast diaphragms. Fig. 2-33 shows the full-scale three-story specimen. As shown in the figure, two precast hybrid walls were used as the primary lateral load resisting systems in the transverse direction. Columns and spandrel beams formed four bays of the structure in the longitudinal direction. Three types of floors, including composite double tee diaphragm, non-composite hollow-core diaphragm, and pre-topped double tee diaphragm, were used from the first story to the third story, respectively. Similar to the PRESSS specimen, the three-story floors were all oriented parallel to the wall.

2.3.3.2 Rocking Wall-Floor Connection

Similar to the PRESSS structure, the wall-floor connections used in the DSDM test were also designed to permit free relative vertical movement and free relative rotation, yet transfer horizontal forces from the floors to the wall. Commercial product PSA connectors were used for the wall-floor connections. Fig. 2-34 shows the detailing of a PSA connector. The detail of an installed PSA connector is shown in Fig. 2-35. As shown in Fig. 2-35(a), a vertically slotted channel was pre-embedded in the wall. An anchor strap with a welded threaded rod was screwed into the slot channel and welded to a pre-embedded plate in the floor, as shown in Fig. 2-35(b) and (c).

2.3.3.3 Gravity Frames in the Wall Plane

Similar to the PRESSS structure, precast gravity frames were used in the frame line of the wall. Because of the use of PSA connectors, the gravity loads on the precast floors

were expected to be transferred to the gravity frames. The columns were post-tensioned to emulate the sustained gravity loads.

Typical precast column base connections recommended by Precast Concrete Institute (PCI) were used in the specimen (PCI 2004). The longitudinal reinforcement at the bottom of the precast column was welded to a steel base plate. The plate was fixed to the foundation by four 3/8 in. diameter A36 bolts at the four corners of the column.

2.3.3.4 Test Results

The PSA connectors got jammed after an MCE (maximum considered earthquake) input because the travel stroke was exceeded due to large wall uplifts. The floors were picked up, which was evident by the dislodged bearing pads. Minor cracking was observed in the flange of the pre-topped double tee slabs at the wall-to-floor connection when the floors were picked up. The connectors had to be repaired before the next test by adding an angle with vertical slots in the wall to extend the vertical stroke.

Permanent deformation of the anchor bolts was observed in Fig. 2-36(a). Under this condition, slack was created in the connection such that the bolts would not be engaged immediately when the columns were displaced laterally. The base connection of the column changed from a fixed connection to a semi-rigid connection. At higher drift levels, the column anchor bolts fractured and the grout beneath the base plate also crushed at the corner, as shown in Fig. 2-36(b).

Because the focus of the DSDM project was to propose design guidelines for precast diaphragms, no further investigation of the wall-floor interaction was found in the literature.

2.3.4 Shake Table Test at E-Defense

2.3.4.1 Overview

Shaking table tests of a full-scale post-tensioned (PT) concrete building were conducted at the world's largest shake table (E-Defense) in Japan (Nagae et al. 2011). A reinforced concrete (RC) building of comparable dimensions was also tested on the shake table next to the PT building. A photo of the test setup is shown in Fig. 2-37. The goal of the test was to investigate the performance of the two buildings which had been designed

by the latest code requirements and detail recommendations in Japan and the U.S. Because the two specimens were tested on the shake table at the same time, a direct visual comparison of the two systems could be made.

2.3.4.2 Rocking Wall-Slab Connection

For the PT specimen, the lateral resisting system consisted of two unbonded post tensioned walls and unbonded PT frames in the wall direction. Precast double tee slabs with topping were used as the floor system.

In the wall direction, a precast half-beam was clamped to the wall panel by a post-tensioned tendon. The other half-beam was cast with the topping of the double tee slabs, which formed an indirect wall-slab connection as shown in Fig. 2-38(a). The detail of the wall-floor connection in the wall direction is shown in Fig. 2-39.

In the direction perpendicular to the wall plane, multiple inserts pre-embedded in the wall panel were connected to the mesh rebar in the topping of the slab, which formed a direct wall-slab connection as shown in Fig. 2-38(b). The detail of the wall-floor connection in the direction perpendicular to the wall plane is shown in Fig. 2-40. The wall-floor connection was considered as a rigid connection because it transferred both shear and gravity forces from the floor into the wall.

2.3.4.3 Gravity Frames in the Wall Plane

Typical PT frame details in Japan were used for the gravity frames in the wall plane. At the column base, eight high-strength steel rebar extended into the foundation. The column base connections were considered as fixed connections.

2.3.4.4 Test Results

Test results showed that complete self-centering response (zero residual displacement at the end of the record) was achieved for all three test trials. Documented damage of the PT specimen is shown in Fig. 2-41, including minor concrete spalling at the wall toe with the core concrete still adequately confined; damage in the 1st story and the 2nd story column bases; damage in the web of the double tee floor near the wall-floor connection and the floor-column connections. No further investigation about the wall-floor interaction was found in the literature

2.3.5 Numerical Study of Rocking-Wall Structures

Very few numerical studies of rocking-wall structures were found in the literature. Two ABAQUS models of a four-story building, which included a PreWEC system, slabs and gravity columns, were established by Henry (2011) to investigate the interaction between the wall and the surrounding structural systems. An ABAQUS model of the PreWEC system alone was also established for comparison. The accuracy of the ABAQUS model of the PreWEC system had been validated as discussed in Section 2.2.3. Fig. 2-42 shows one of the models for the four-story building. To simplify the building models, the beam-column joints and the column bases were all considered as pinned connections.

The only difference between the two building models was the wall-floor connection used. In the first model, rigid wall-floor connections were used, which were simulated by "embedding" the overlapped portion of the floors into the wall. In the second model, vertical movement isolated connections were used, which were simulated by only coupling the horizontal degree of freedoms of the floors with those of the wall.

Due to the complexity of the building models, only monotonic pushover analysis was performed. Fig. 2-43 and Fig. 2-44 show the deformation shapes of the two building models. As shown in Fig. 2-43, the floors were deformed at the wall-floor connections. On the other hand, because the vertical displacement was isolated between the wall and the floors in the second building model, the floors were not influenced by the rocking of the wall, as shown in Fig. 2-44.

The monotonic base moment versus lateral wall drift curves of the two building models (termed "Building: CIP floor" and "Building: Isolated floor") and the PreWEC alone (termed "Wall only") are shown Fig. 2-45. As shown in the figure, the moment resistance of the first building model, which used the rigid wall-floor connections for CIP floor, was significantly increased by approximately 50% at 3% drift, compared to that the of "Wall only" for the PreWEC system alone. On the other hand, the moment resistance of the second building model was nearly identical to that of the "Wall only" model.

The simulation results revealed that the responses of rocking wall buildings can be dramatically different because of the use of different wall-floor connections, which generated different wall-floor interaction.

2.3.6 Discussion of the Experimental and Numerical Studies of Rocking-Wall Structures

Experimental studies of the interaction between the rocking-wall systems and surrounding structural systems have been limited. Vertical movement isolation connections were used in both PRESSS and DSDM projects: an impractical connection was used specifically in the PRESSS project and a commercial product (PSA connector) was used in the DSDM project. In both tests, the connection performed well (although ran out of travel in the DSDM project) and successfully isolated the floors and the walls. However, no in-depth studies of the wall-floor interaction in the two system systems were found. Only one system test (E-Defense) with rigid wall-floor connections was found in the literature. However, because of the complexity and diverse purposes of the shake table test, existing publications (Tanyeri et al. 2012, Tuna et al. 2012) were not related to the wall-floor interaction to the author's knowledge.

The numerical studies conducted by Henry (2011) demonstrated that the moment resistances of buildings with rigid wall-floor connections were much higher than those of buildings with vertical movement isolated connections. If the wall-floor interaction is neglected during design, the wall may have premature failure (e.g., shear failure and shear sliding). Moreover, the floors with rigid connections are expected to encounter extensive damage according to the analysis. Although not shown by the numerical simulation because only monotonic pushover analysis was performed, it was not difficult to predict that the self-centering capability of the rocking-wall system would vary with different types of wall-floor connections. Failure to account for the impact from wall-floor interaction might also result in the loss of the self-centering characteristic of rocking-wall structures, which is one of the most appealing features for this type of structure.

In summary, no systematic studies have been conducted on the interaction between rocking-wall systems and surrounding structural systems, which not only would impact

the overall performance of the rocking-wall structures, but also might impact the design of rocking walls and surrounding structural systems. The potential damage to the floors and columns caused by the rocking behavior of the walls has been observed in existing tests but not further studied. Therefore, in-depth experimental and numerical studies focusing on wall-floor interaction will help to further understand the seismic performance of the whole building incorporating rocking-wall systems, which are the main purpose of this dissertation. Design recommendations for rocking-wall systems and wall-floor connections are proposed in Chapter 9 following the experimental and numerical simulations. The research will be very beneficial to popularize the application of rocking-wall structures in practice.

2.4 Design Guidelines and Details of Rocking-Wall Systems

2.4.1 Overview

Specific design guidelines for the rocking-wall structures had not been included in Building Code Requirements for Structural Concrete (ACI 318-11) due to limited experimental and analytical work of the innovative system. However, earthquake-resistant design of ACI 318-11 specifies that "a reinforced concrete structural system not satisfying the requirements of this chapter shall be permitted if it is demonstrated by experimental evidence and analysis that the proposed system has strength and toughness equal to or exceeding those provided by a comparable monolithic reinforced concrete structure satisfying this chapter."

Innovation Task Group 5 (ITG-5) was set up by the American Concrete Institute (ACI) to provide guidance on the application of the aforementioned code requirement to the experimental and analytical work of unbonded post-tensioned precast wall systems. Two documents were published by ITG-5, including ITG-5.1 "Acceptance Criteria for Special Unbonded Post-Tensioned Precast Structural Walls Based on Validation Testing and Commentary" and ITG-5.2 "Requirements for Design of a Special Unbonded Post-Tensioned Precast Shear Wall Satisfying ACI ITG-5.1 (ACI ITG-5.2-09) and Commentary" in chronological order.

ITG-5.1 defines minimum acceptance criteria for unbonded post-tensioned precast concrete walls based on experimental evidence. The document outlines the design procedure of the specimen, test modules, test methods and test report. It regulates that no fewer than two modules shall be tested; the test modules shall be subjected a sequence of displacement-controlled cycles at least to 3% drift and three fully reversed cycles shall be applied at each drift angle.

ITG-5.2 defines design requirements of unbonded post-tensioned rocking-wall systems, including coupled walls by coupling devices that connect adjacent vertical boundaries of shear walls (i.e., jointed wall system) and uncoupled walls by energy-dissipating reinforcement that crosses the interface between the base of the wall and the foundation (i.e., hybrid wall system). The document also describes materials used in the rocking-wall systems, structural system requirements for walls and design requirements for coupling devices in jointed wall systems.

Because ITG-5.1 and ITG-5.2 were created mainly based on experimental and analytical work of jointed wall systems and hybrid wall systems that had been conducted, the interaction between the rocking-wall system and surrounding structural system was not considered in the documents for the following reasons: (1) In the PRESSS project where the jointed wall system was used, the wall-floor interaction was minimized by the special connection adopted between the wall and the precast floor; (2) No system test using a hybrid wall system had been conducted when the two documents were created. Therefore, it is beneficial to investigate the performance of the wall in the rocking-wall structures using rigid wall-floor connections, where the wall-floor interaction is maximized.

Furthermore, due to limited experimental and analytical work, the design recommendations included in ITG-5.2 were not complete even if the wall-floor interaction was not considered. For example, there was no design recommendation about the height of the boundary element in ITG-5.2, which is an important factor to be considered. For some design parameters, including the amount of required longitudinal, transverse and confining reinforcement, the relevant requirements for special structural walls in ACI 318-11 were recommended to be used. However, the mechanism of rocking

walls is quite different than that of special structural walls. Design recommendations for special structural walls might not be adaptable for rocking walls. In addition, special detailing of rocking walls, such as adding external steel channels in the corners of the wall to further confine the concrete in the corners, were adopted by several tests of rocking-wall systems, but they are not included in ITG-5.2.

Because of the incompleteness of ITG-5.2 recommendations and the lack of specific design guidelines, the design of the rocking walls has varied in different tests. In the following section, recommendations provided by ITG-5.2 are discussed in detail, followed by a summary of design details which were different from ITG-5.2 in some of the tests.

2.4.2 Design Details in ITG-5.2

Design details of rocking walls in ITG-5.2 mainly included the following: longitudinal reinforcement, transverse (shear) reinforcement and shear sliding resistance, confinement reinforcement and external armor plates in wall corners, initial stress level of PT strands, and grout layer beneath the wall.

Longitudinal reinforcement

Section 3.3.1 suggests that reinforcement in the boundary elements shall comply with 21.2.5 of ACI 318-05, which regulates the type of reinforcement allowed.

Section 4.4.10 (a) suggests that reinforcement shall be provided around the perimeter of the panel that provides a nominal tensile strength of not less than 6 kips per horizontal foot of panel to control concrete cracking.

Shear reinforcement and shear sliding resistance

Section 5.5.1 suggests that nominal shear strength of the wall shall be calculated as specified in 21.7.4.1 and 21.7.4.2 of ACI 318-05, and shear reinforcement shall be provided as required by 21.7.4.3.

Section 5.5.3 suggests that the shear sliding resistance shall be taken as μC, where C is the compressive force acting on the concrete at the interface and the coefficient of friction μ shall be taken as 0.5; the shear sliding resistance shall be greater than the base shear

causing M_{pr}, where M_{pr} is the probable flexural strength of the wall at the wall-foundation interface and computed in accordance with Section 5.6.3.8.

Confinement reinforcement and external armor plates in wall corners

Because large concentrated compression forces concentrate at the corners of the wall, design of confinement reinforcement is believed to be a key factor for the performance of rocking walls. Section 5.6.3.6 recommends that the compressed concrete shall be confined by transverse reinforcement satisfying the requirements of 21.7.6.4(c) of ACI 318-05. Section 5.6.3.6 also suggests that the transverse reinforcement shall extend horizontally from the extreme compression fiber a distance not less than $0.95c$, and not less than 12 in., where c is the neutral axis depth. However, no recommendation of the height of the confinement is included in the document.

Other than the confinement reinforcement, no other special detailing (e.g., steel channels or steel plates) are required in wall corners in the ITG-5.2.

Initial stress of the PT strands

Section 3.3.3 recommends that the effective stress in the PT strands shall not be less than $0.3f_{pu}$ to prevent strand slippage, where f_{pu} is the specified tensile strength of the strands.

Section 4.4.7 suggests that the maximum stress in the PT strands shall be less than the specified yield strength f_{py} at the design drift angle to ensure no slip of the wall relative to the foundation and no permanent residual drift of the wall.

Grout layer beneath the wall

Section 5.8 suggests that fiber or polypropylene shall be added to the grout to increase the toughness; the specified strength of the grout layer shall be larger than the greater of f'_c and $0.4f'_{cc}$, where f'_c is the specified strength of unconfined concrete and f'_{cc} is the strength of the confined concrete.

2.4.3 Summary of Design Details in Existing Experiments

In this section, design details of rocking walls are summarized for three tests. Hybrid wall systems were used in the tests conducted at the University of Notre Dame and

University of California San Diego (DSDM project). The PreWEC system was used in the NCREE test.

2.4.3.1 Notre Dame Test (Brian et al. 2009, 2011)

A 0.4-scale "hybrid" precast concrete wall specimen was tested under reversed cyclic lateral loading. The test provided an assessment of the seismic design and analysis of the wall by using the experimental results.

Longitudinal reinforcement

Wire mesh reinforcement was used in the wall and the amount was designed based on Section 4.4.10 (a) of ITG-5.2 to control concrete cracking.

Shear reinforcement and shear sliding resistance

The design of shear reinforcement followed Section 5.5.1 of ITG-5.2, which directly adopted the requirements in ACI 318-05. The examination of shear sliding resistance of the wall followed Section 5.5.3 of ITG-5.2.

Design of the confinement reinforcement and external armor plates in wall corners

The amount and spacing of the confinement reinforcement was designed to ensure that the compressive strain demand on the confined concrete at the maximum expected drift could be achieved. The compressive strain demand was calculated by the following equation:

$$\epsilon_{conc} = \emptyset_{max} c_{\max\_wall} = \frac{\theta_{max}}{0.06 H_w} c_{\max\_wall} \quad (2.3)$$

Where $\emptyset_{max}$= plastic curvature at the maximum expected drift; ϵ_{conc}= maximum strain in the extreme compressive concrete fiber; $c_{\max\_wall}$= neutral axis depth of the wall at the maximum expected drift; θ_{max}= the maximum expected drift; H_w= height of the wall.

The equation was derived assuming $0.06H_w$ was the "plastic hinge height" for the rocking wall and the plastic curvature was uniformly distributed over the plastic hinge height (Thomas and Sritharan 2004).

The width of distributed confinement reinforcement in the test followed the recommendations in ITG-5.2. The height of distributed confinement reinforcement in the test was not found in the literature.

External armor plates were not used in the corners of the tested wall. The purpose was to minimize the differences of the test specimen from typical construction.

Initial stress of the PT strands

A strand strain limit of 0.01 was used in the design of the strands in the tested wall. The strands were expected to remain mostly in the linear-elastic range through the maximum expected drift regulated in Section 4.3.4 of ITG-5.2, which was higher than the design drift regulated in ITG-5.2. The average initial tendon stress was designed to be $0.55f_{pu}$.

Grout layer beneath the wall

Polypropylene-reinforced grout with a 7-day compressive strength of 4.5 ksi was used. The grout was designed to be weaker than the unconfined wall panel concrete (4.8 ksi) to provide a soft contact surface at the base. It did not conform to the requirement in ITG-5.2.

2.4.3.2 DSDM Project (Belleri et al. 2013, 2014, Schoettler 2010)

The DSDM project has been discussed in Section 2.3.3. The design of the wall panel is described in detail in this section.

Longitudinal reinforcement

Different from regular design, a strut-and-tie model was used to design the layout of the longitudinal reinforcement of the tested wall in the DSDM project, which resulted in a longitudinal reinforcement ratio 0.38% in the unconfined region and 3.22% in the confined region (12 in. by 8 in.). The main purpose of the high reinforcement ratio in the confined region was because the bars located in the compression zone would share the compressive force with the concrete, thus reducing the neutral axis depth. Moreover, special headed bars were used because heads on these bars enhanced the bar compressive force transfer through the bedding mortar into the footing.

Shear reinforcement and shear sliding resistance

Transverse hoops spaced at 8 in. were provided as shear reinforcement. They were designed based on recommendations provided by Perez (Perez 2004) to prevent separation of confined regions from the region containing post-tensioning and energy

dissipation ducts. The hoops consisted of No. 3 transverse hoops spanning the entire wall length and provided continuity between these regions.

Additional outside shear keys were set back 0.12 in. from the wall toes to limit unanticipated shear sliding of the wall. Moreover, the wall base was roughened to increase the base shear resistance.

Confinement reinforcement and external armor plates in wall corners

The amount and spacing of the confinement reinforcement was designed to ensure that the maximum compressive strain demand on the confined concrete could be achieved. The compressive strain demand was calculated by the following equation:

$$\epsilon_{conc} = \frac{\theta_{design} c_{design\_wall}}{c_{design\_wall}} = \theta_{design} \quad (2.4)$$

Where θ_{design} = rotation of the wall at the design drift, which was approximately equal to the lateral drift of the wall; c_{design_wall} = neutral axis depth at design drift.

The above equation assumed that due to the rotation of the wall, the extreme compressive fiber at the wall toe was shortened by $\theta_{design} c_{design\_wall}$; the compressive strain was constant over a distance c_{design_wall} along the height of the wall above the foundation, thus resulted in $\epsilon_{conc} = \theta_{design}$.

It was believed that because of the gradual occurrence of concrete residual strains at the wall toes, walls with neutral axis depths larger than 15% of the wall length resulted in loss of initial stiffness on rocking even if the corners of the walls were heavily confined. Moreover, walls with a large neutral axis depth can compromise the stability of the compressed chord. Sudden buckling and failure of a rocking wall, with a neutral axis depth of about 30% of the wall length was observed in a test (Perez 2004). Therefore, it was suggested by Rahman and Restrepo that the neutral axis (N.A.) depth of the tested wall should be restricted to within 15% of the wall length to ensure hysteretic response stability and geometrical stability (Restrepo and Rahman 2007). The width of distributed confinement reinforcement of the wall in the DSDM project was 12 in., which was equal to 12.5% of the 8-ft. wall length (Restrepo and Rahman 2007).

The height of distributed confinement reinforcement was about 12 in., which was equal to the neutral axis depth. It was based on the aforementioned assumption when determining the amount and spacing of the confinement reinforcement: the compressive strain was constant over a distance c_{design_wall} along the height of the wall above the foundation.

The extreme end of each wall toe was armored with a 9 in. long, 7 in. wide and 1/2 in. thick embedded steel plate. Four 14 in. long No. 6 deformed bars were welded to the embedded plate. Although the main purpose of the vertical plate was to protect the concrete toe from impact against shear keys set back 0.12 in. from the wall toe, the plate essentially replaced the concrete cover that could spall as a result of the expected high compressive strain and also provided additional confinement to the core concrete.

Initial stress of the PT strands

The initial stress of the PT strands was about 0.24 to 0.37f_{pu} in different phases of testing, which was very low. It did not conform to Section 3.3.3 of ITG-5.2: the effective stress in the PT strands shall not be less than 0.3f_{pu} to prevent strand slippage. It was believed that the strands were stressed low for the purpose to prevent damage to the strands and reuse the specimen through multiple phases of testing.

However, fracture of strands was observed in the test with a low average strand stress of 0.45f_{pu} (Belleri et al. 2014). As reported, the strand failure might have been caused by the process of seating the tendons: the five strands were simultaneously seated with post-tensioning jacks, rather than seating each strand individually as is done in practice. It might result in uneven wedge seating and thus an uneven distribution of tendon forces. It was recommended to grout the strand duct ends after post-tensioning.

Grout layer beneath the wall

Polypropylene fiber grout was used beneath the wall. The strength of the grout (7 ksi, 35 days) was slightly smaller than that of the unconfined concrete in the wall (7.76 ksi, 28 days). It did not conform to the requirement in ITG-5.2. During the test, it was observed that when some fiber grout spalled, concrete damage at the wall toe was limited to cosmetic spalling of concrete cover.

2.4.3.3 NCREE Test (Aaleti and Sritharan 2011)

The NCREE test has been discussed in Section 2.1.3. The design of the wall panel is described in detail in this section.

Longitudinal reinforcement

The amount of longitudinal reinforcement in the wall was designed to satisfy the minimum longitudinal steel ratio requirements in Section 21.7.2.1 of ACI 318-05, which was different from that required in Section 4.4.10 (a) of ITG-5.2.

Shear reinforcement and shear sliding resistance

The design of shear reinforcement and the examination of shear sliding resistance followed Section 5.5.1 and 5.5.3 of ITG-5.2, respectively.

Confinement reinforcement and external armor plates in wall corners

The amount and spacing of the confinement reinforcement was designed to ensure that the compressive strain demand on the confined concrete at the maximum expected drift could be achieved. The compressive strain demand was calculated by the following equation:

$$\epsilon_{conc} = c_{\max\_wall}\left(\frac{M_{max,wall}}{E_c I_{gross}} + \frac{\theta_{max}}{0.06 H_w}\right) \quad (2.5)$$

Where $M_{\max\_wall}$= base moment resistance of the wall at the maximum expected drift; E_c= Young's modulus of concrete; I_{gross}= gross moment of inertia of the wall; θ_{max}= the maximum expected drift (1.5 times the design drift); H_w= height of the wall.

The above equation was derived by equating the total displacement of a precast wall with that of an equivalent monolithic wall. A detailed derivation of the equation was described in the work of Thomas and Sritharan (2004).

The width of distributed confinement reinforcement in the test was determined by the following equation:

$$l_{cr} = c_{\max\_wall}\left(1 - \frac{\epsilon_{unconf}}{\epsilon_{conc}}\right) \quad (2.6)$$

Where l_{cr}= width of the confinement reinforcement; ϵ_{unconf}= crushing strain of the unconfined concrete.

The equation was derived based on the following assumptions: (1) A linear strain distribution existed in the compression region at the wall corners; (2) the confinement should extend to the region where the concrete strains were greater than the crushing strain of the unconfined concrete.

The height of distributed confinement reinforcement in the test followed Section 21.7.6.2 (b) in ACI 318-05 for special reinforced concrete walls. The boundary elements were provided over the bottom 72 in. height of the wall.

In addition to the confinement reinforcement, a 2 ft. long, 1/4 in. thick steel channel was attached near the corners of the wall to minimize the spalling of the concrete.

Initial stress of the PT strands

The initial stress of the strands in the wall was $0.67f_{pu}$, which followed the requirement in ITG-5.2 to remain elastic at 2% design drift.

Grout layer beneath the wall

A high strength steel fiber reinforced grout was placed at the interface between the foundation and the wall. The nominal strength of the fiber grout was 14 ksi, which was expected to be larger than the strength of confined concrete in the tested wall (13 ksi).

2.4.4 Discussion of Current Design Details of Rocking-wall structures

Table 2-2 lists and compares design details of the rocking walls in the three tests. As shown in the table, inconsistency with the ITG-5.2 existed in the design of the walls: (1) amount and spacing of the steel confinement were designed based on the maximum compressive demand on the concrete and different equations for calculating the demand were proposed; (2) the width of the confinement in DSDM and NCREE was not determined in accordance with ITG-5.2. The former was determined empirically from test observation (Perez 2004, Restrepo and Rahman 2007) and the latter assumed a linear distribution of the strain in the corners; (3) special detailing was used in the corners of the walls in DSDM and NCREE to protect the wall toes, although it was not required in ITG-5.2; (4) the strength of the grout beneath the wall was weaker than that of the unconfined concrete in the wall in ND and DSDM, which did not conform to ITG 5.2.

Because there were no related recommendations in ITG-5.2 for some of the design details, the requirements for special structural walls in ACI 318-11 or requirements established based on the results existing tests were sometimes used. Examples included detailing the amount of longitudinal rebar in the wall and the height of the steel confinement. However, because the mechanism of rocking walls is different from that of special structural walls, the design recommendations for special structural walls might not be adaptable for rocking walls.

Table 2-1 Hysteresis rules and functions of the springs (Henry 2011)

Spring	Hysteresis rule	Function
W1	Multi-linear elastic	Wall base PT response
W2	Degrading bilinear elasto-plastic	Wall base hysteresis area
RD1a	Modified Tekada	Residual drift offset (1st force limit)
RD1b	Revised Origin centered	Residual drift unloading stiffness correction (1st force limit)
RD2a	Modified Tekada	Residual drift offset (2nd force limit)
RD2b	Revised origin centered	Residual drift unloading stiffness correction (2nd force limit)
C	Bounded Ramberg-Osgood	Connector hysteresis response

Table 2-2 Summary of design details in existing tests

	Reinforcement					Special detailing in the corners of the wall	Initial stress of strands	Fiber grout layer
	Longitudinal	Shear	Confinement					
			Amount and spacing	Height	Width			
ND	ITG-5.2 4.4.10 (a)	ITG-5.2	Related to ϵ_{conc} Eq. (2.3)	Not found	ITG-5.2, $0.95c_{max,wall}$	No	ITG-5.2 $0.55f_{pu}$	Weaker
DSDM	Strut-tie model	Empirical	Related to ϵ_{conc} Eq. (2.4)	Equal to the N.A. depth, 12 in.	Empirical, less than 15% of wall width	Vertical plates at side face of walls	Low $0.24\ f_{pu}$ to $0.37f_{pu}$	Weaker
NCREE	Section 21.7.2.1 ACI 318-05	ITG-5.2	Related to ϵ_{conc} Eq. (2.5)	Section 21.7.6.2 (b) ACI 318-05, 72 in.	Related to ϵ_{conc} Eq. (2.6)	Steel channels at the wall corners	ITG-5.2 $0.67f_{pu}$	Stronger

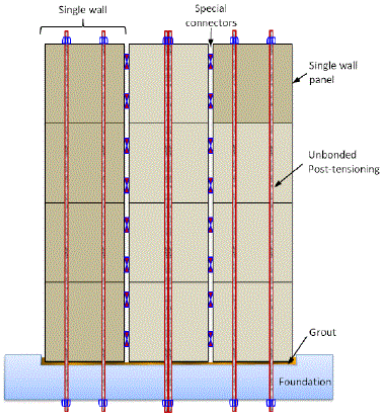

Fig. 2-1 Sketch of a jointed wall system (Aaleti and Sritharan 2009)

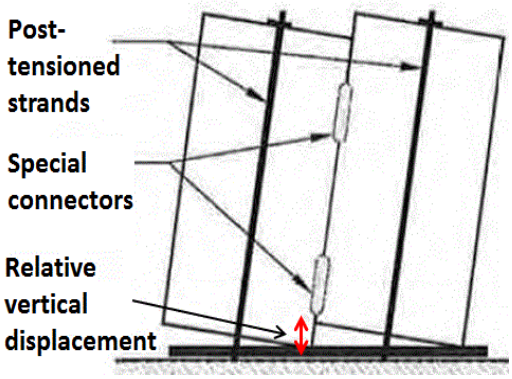

Fig. 2-2 Relative vertical displacement between two displaced rocking wall panels (Aaleti and Sritharan 2009)

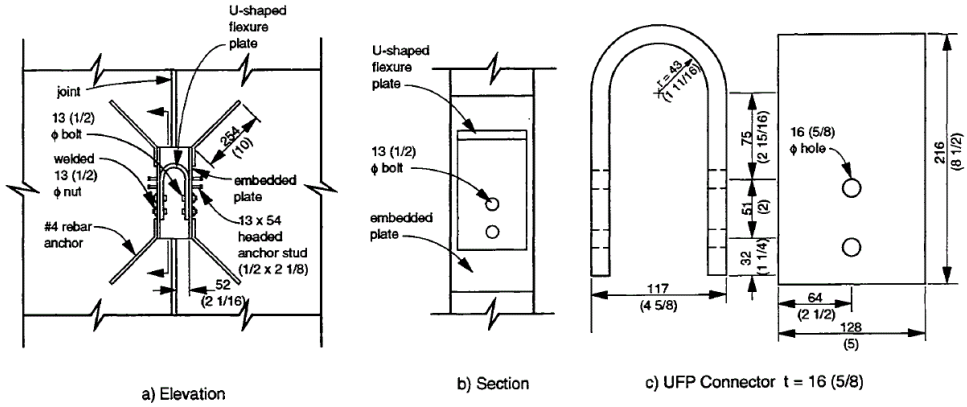

Fig. 2-3 Design details of the U-shaped flexural plates (Schultz and Magana 1996)

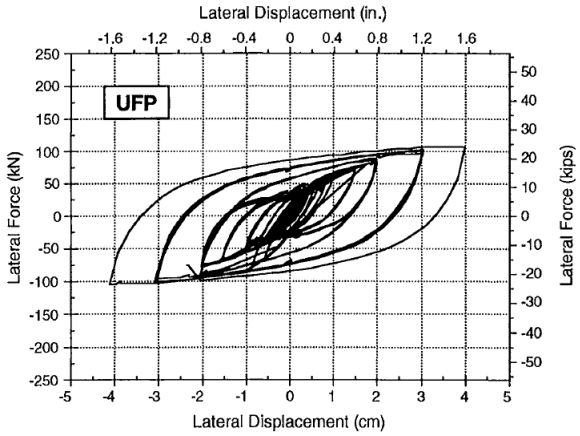

Fig. 2-4 Lateral force – lateral displacement response of the U-shaped flexural plates (Schultz and Magana 1996)

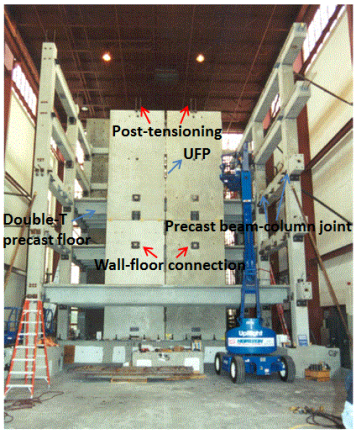

Fig. 2-5 Jointed wall system in the PRESSS program (Priestley et al. 1999)

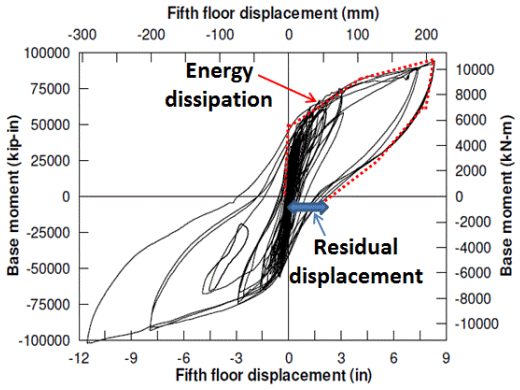

Fig. 2-6 Base moment – top displacement response for the PRESSS jointed wall test specimen (Priestley et al. 1999)

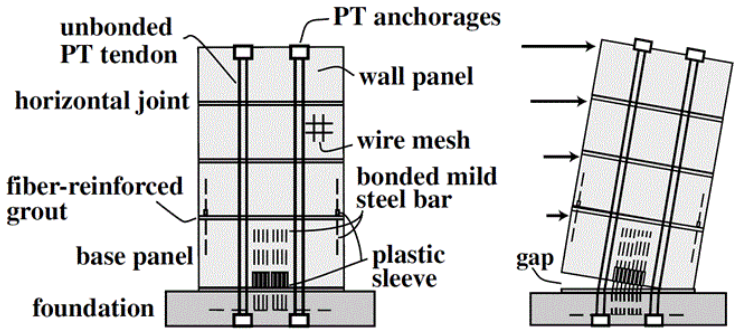

Fig. 2-7 Rocking wall with rebar dissipater (Smith et al. 2011)

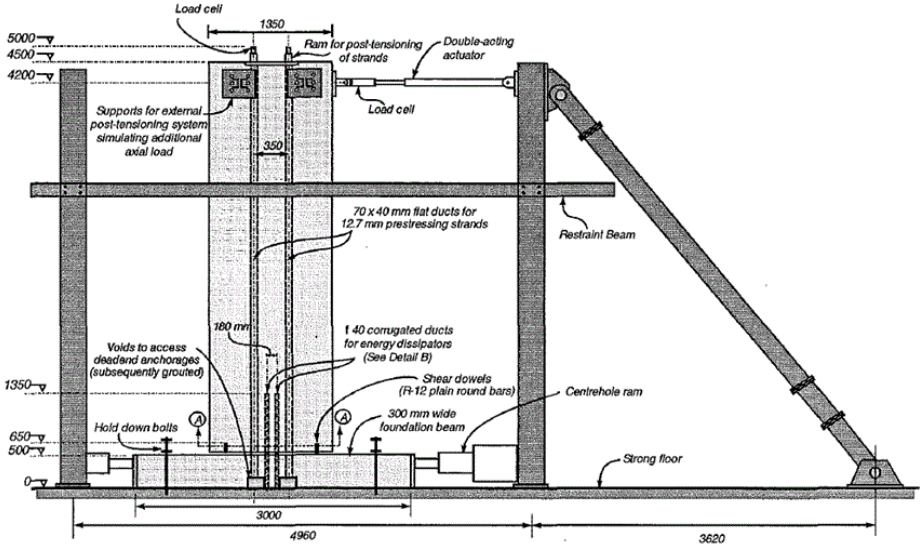

Fig. 2-8 Test setup for the specimen of hybrid wall system (Restrepo and Rahman 2007)

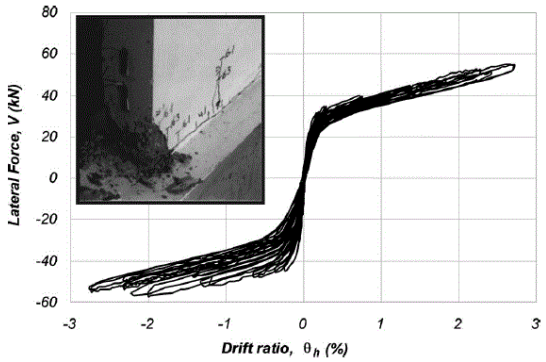

Fig. 2-9 Lateral force – drift ratio response of the first specimen without energy dissipating rebar (Rahman and Restrepo 2007)

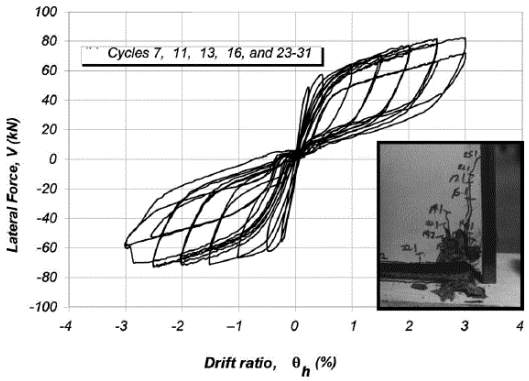

Fig. 2-10 Lateral force – wall drift ratio response of the second specimen without gravity load (Rahman and Restrepo 2007)

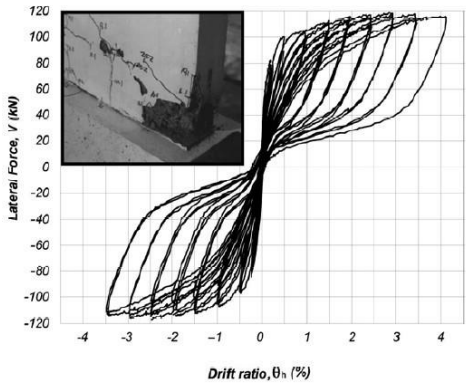

Fig. 2-11 Lateral force – wall drift ratio response of the third specimen with gravity load (Rahman and Restrepo 2007)

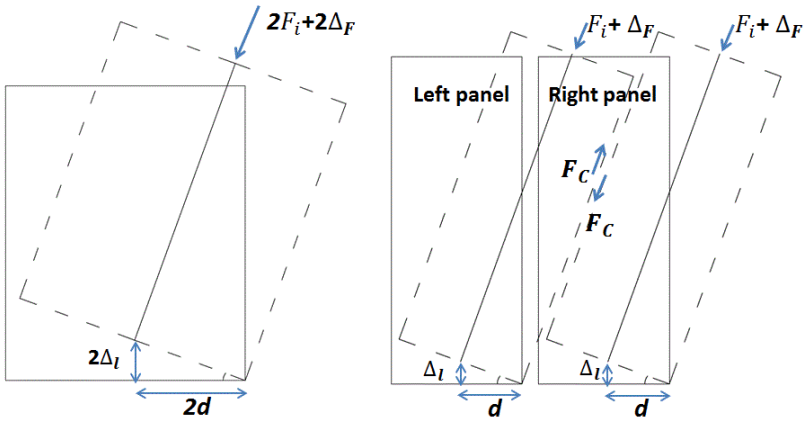

Fig. 2-12 Illustration of the disadvantage of jointed wall systems

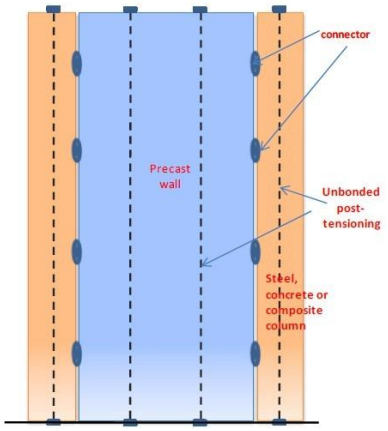

Fig. 2-13 Precast Wall with End Columns (Aaleti and Sritharan 2011)

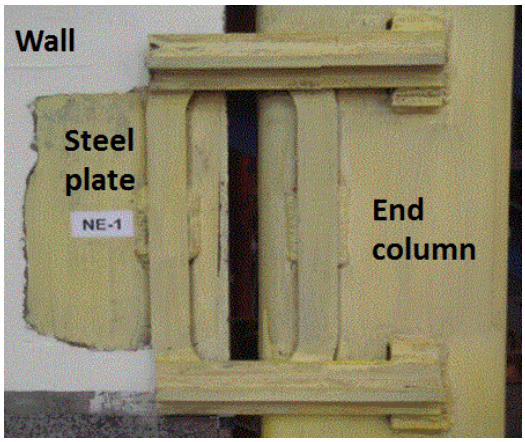

Fig. 2-14 Connection for an O-connector in PreWEC system (Aaleti and Sritharan 2011)

Fig. 2-15 Test setup for the O-connectors

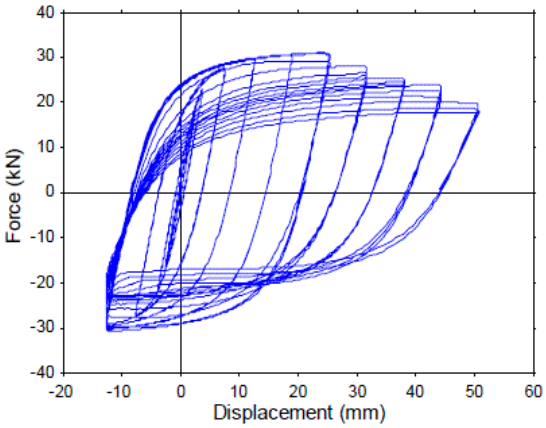

Fig. 2-16 Force-displacement response of an O-connector (Henry 2011)

Fig. 2-17 Test setup of the PreWEC test in NCREE (Aaleti and Sritharan 2011)

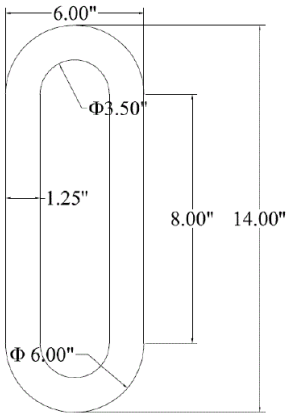

Fig. 2-18 Dimension of the O-connector (Henry 2011)

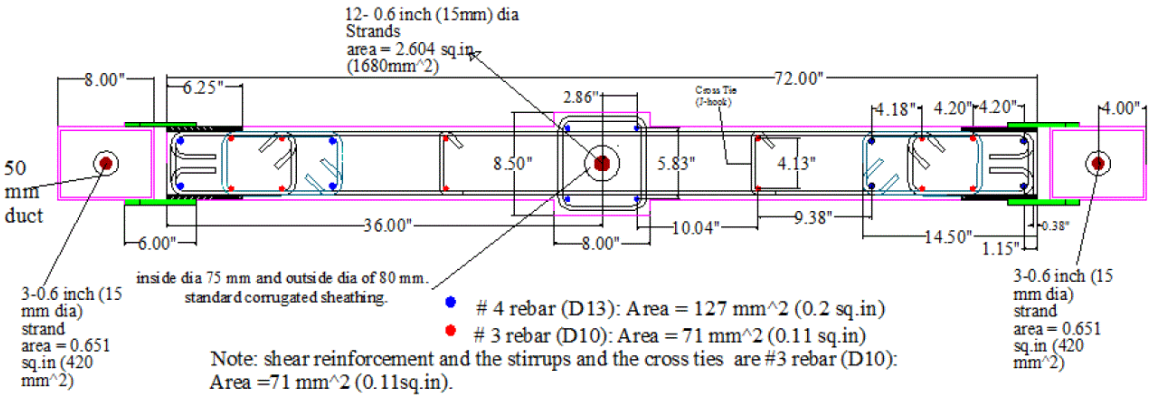

Fig. 2-19 Plan view of the PreWEC specimen (Aaleti and Sritharan 2011)

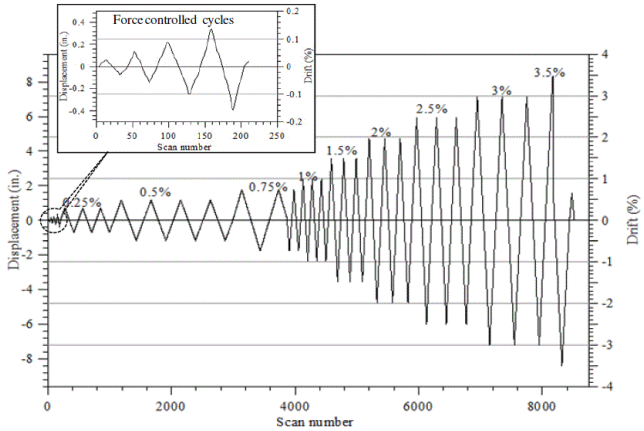

Fig. 2-20 Loading protocol of the PreWEC test (Aaleti and Sritharan 2011)

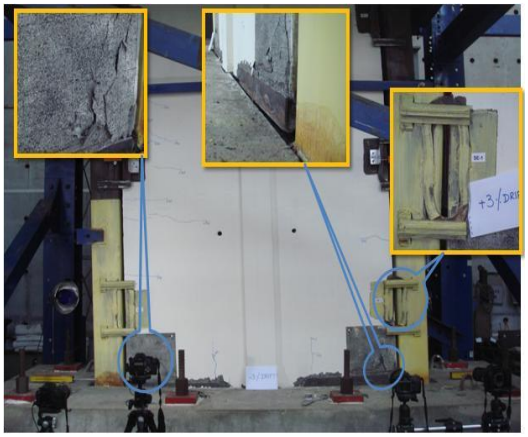

Fig. 2-21 Damage of the PreWEC specimen at 3% drift (Aaleti and Sritharan 2011)

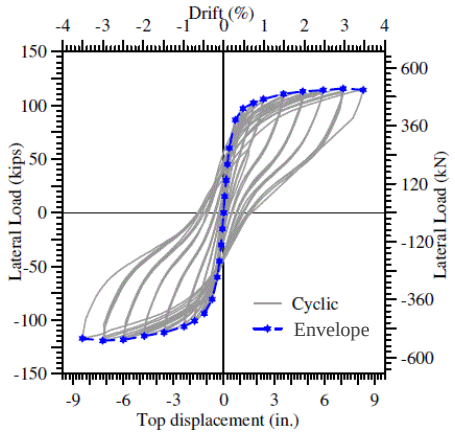

Fig. 2-22 Lateral load – top displacement response of the PreWEC specimen (Aaleti and Sritharan 2011)

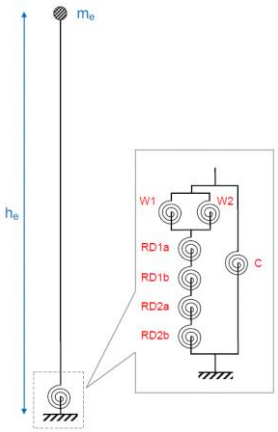

Fig. 2-23 Lumped plasticity model for the PreWEC system (Henry 2011)

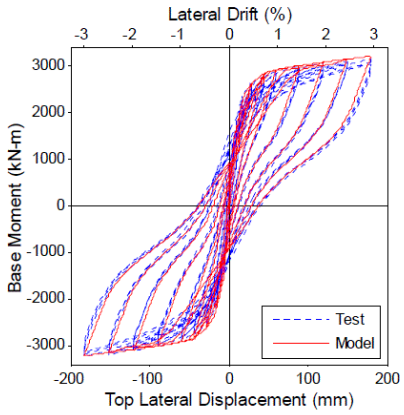

Fig. 2-24 Base moment – top lateral displacement response of the test and the lumped plasticity model (Henry 2011)

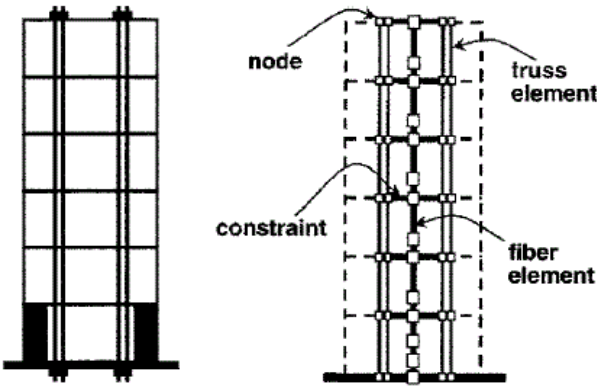

Fig. 2-25 Fiber model for a rocking wall panel (Kurama et al. 1999)

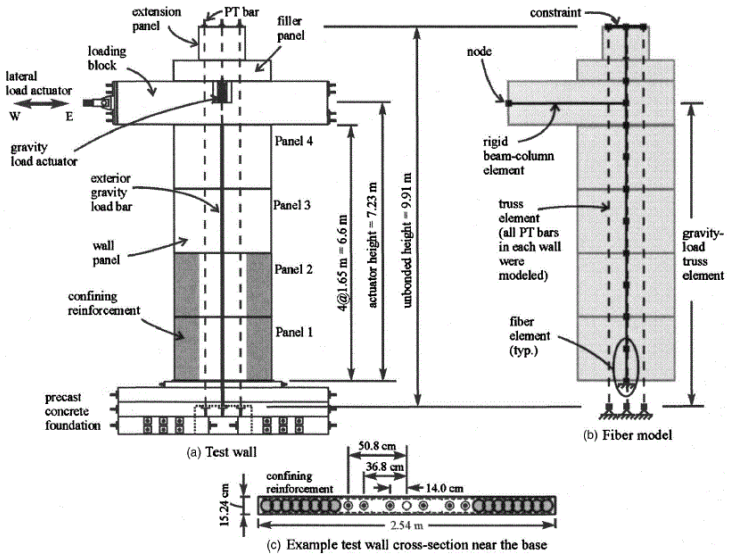

Fig. 2-26 Test setup and the fiber model of the test (Perez et al. 2007)

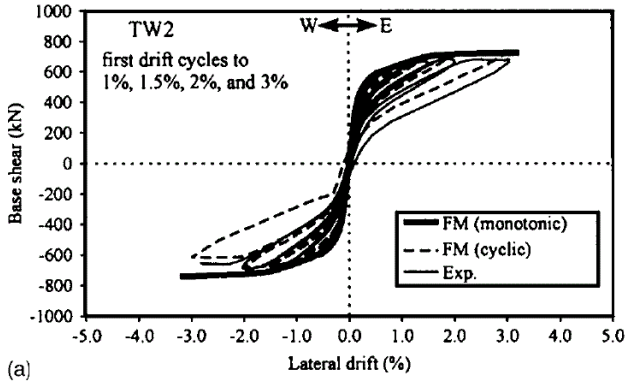

Fig. 2-27 Base shear – lateral drift response of the test and the fiber model (Perez et al. 2007)

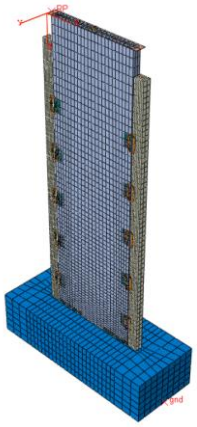

Fig. 2-28 Solid element model of the PreWEC specimen (Henry 2011)

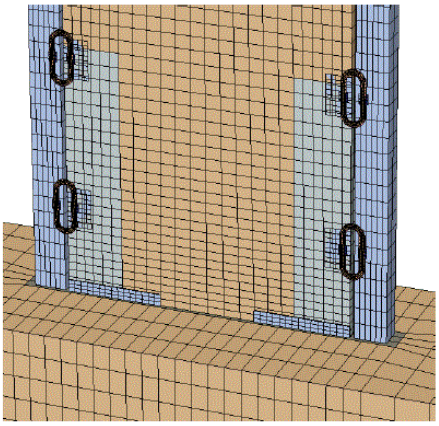

Fig. 2-29 Detail of the PreWEC model near the wall base (Henry 2011)

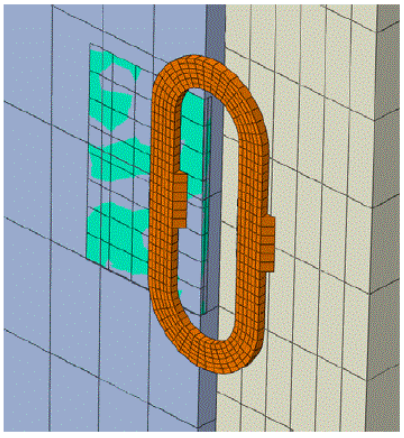

Fig. 2-30 Detail of the O-connector model (Henry 2011)

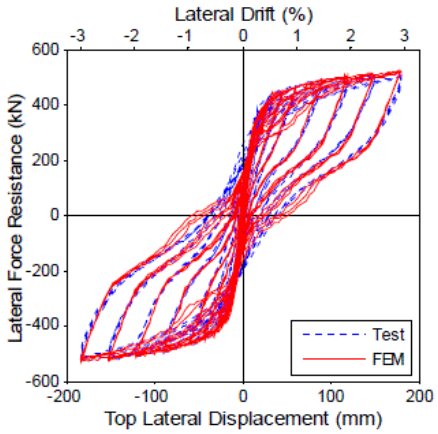

Fig. 2-31 Lateral force – top lateral displacement response of the test and the solid element model (Henry 2011)

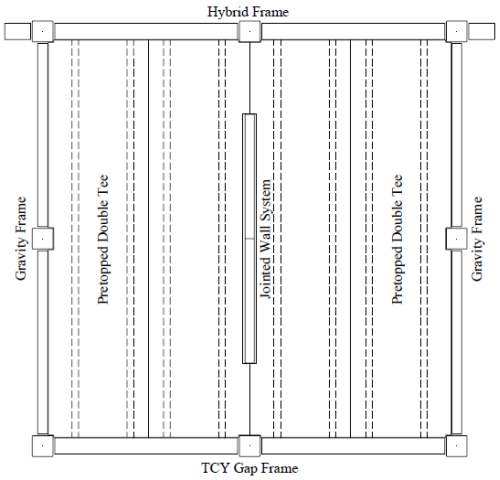

Fig. 2-32 Plan view of the test specimen (Priestley et al. 1999)

Fig. 2-33 Test setup of the shake table test (Schoettler 2010)

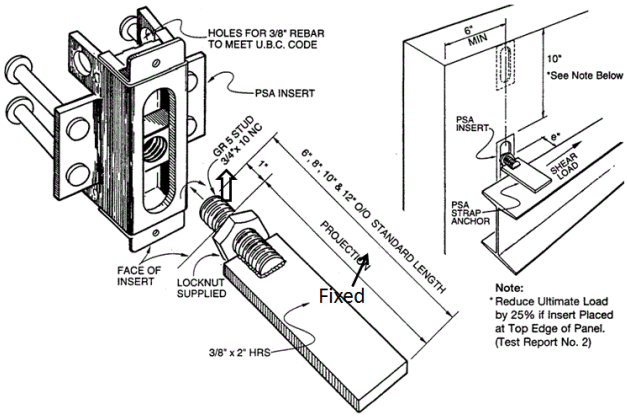

Fig. 2-34 Detailing of PSA connector (JVI company)

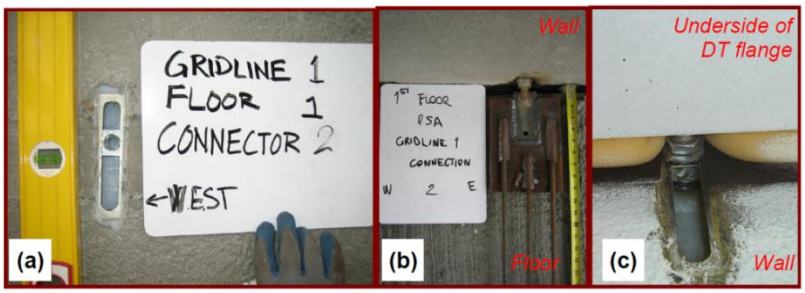

Fig. 2-35 Wall-to-floor connection (a) vertical slot (b) anchor strap (c) underside view of the connection (Schoettler 2010)

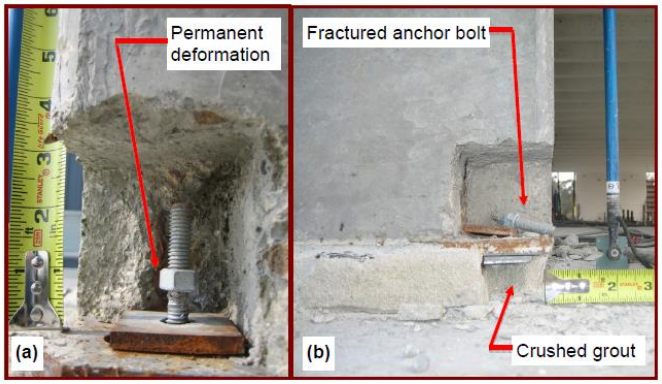

Fig. 2-36 Column anchor bolt fractured and grout crushed (Schoettler 2010)

Fig. 2-37 E-defense shaking table tests (PT specimen on the left) (Tanyeri et al. 2013)

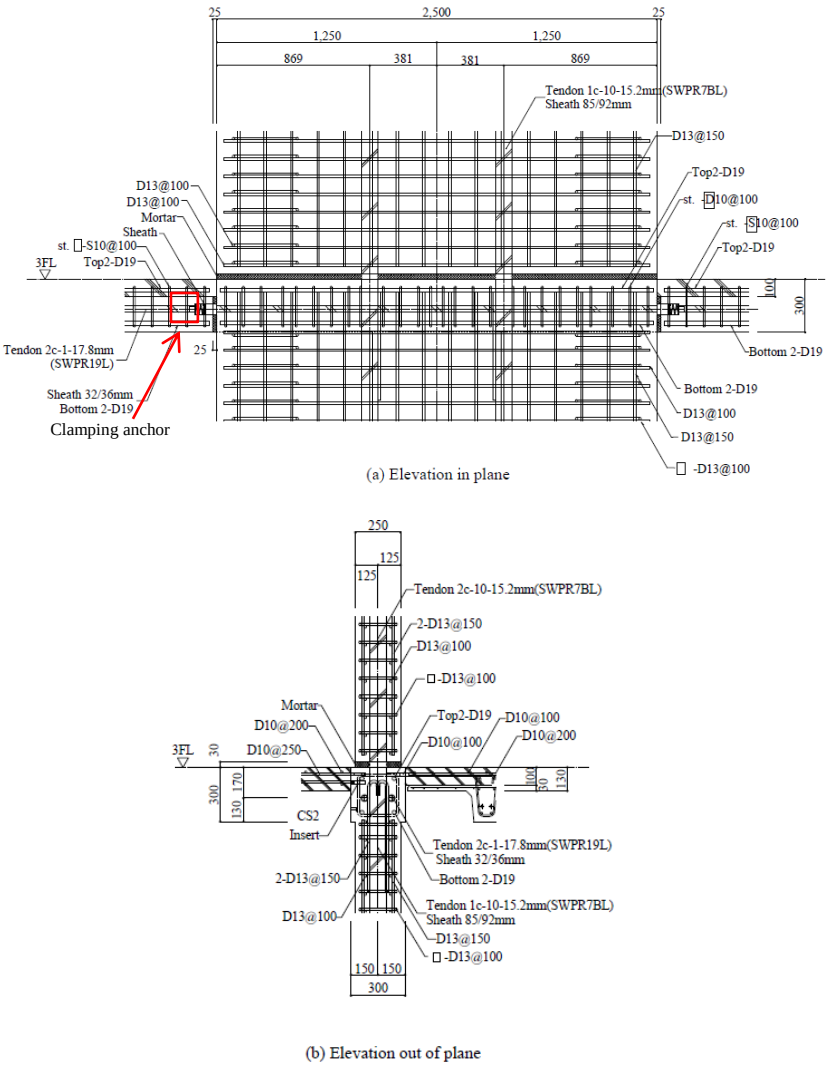

Fig. 2-38 Detail of PT wall – floor interface (Nagae et al. 2011)

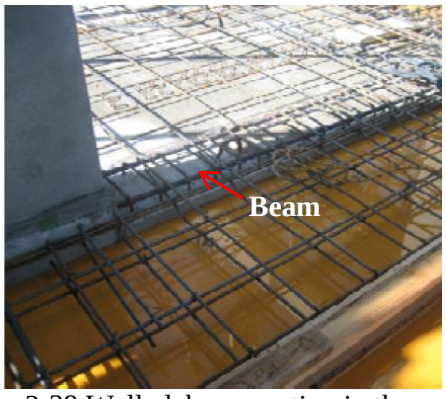

Fig. 2-39 Wall-slab connection in the wall direction (Nagae et al. 2011)

Fig. 2-40 Wall-slab connection in the transverse direction (Nagae et al. 2011)

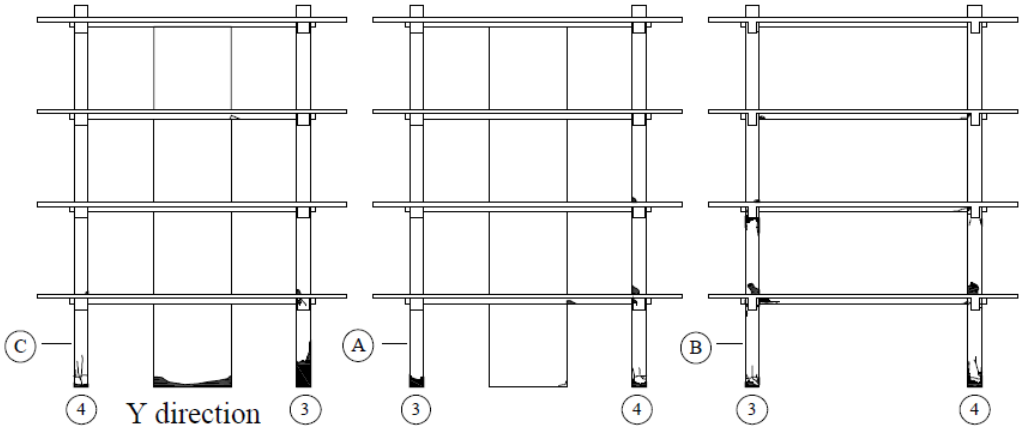

Fig. 2-41 Damage of the PT specimen after JMA-Kobe-100% test (Nagae et al. 2012)

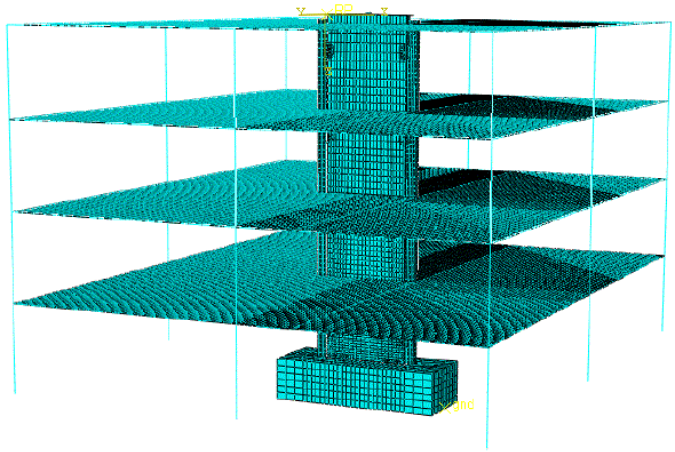
Fig. 2-42 Model of the rocking-wall structure with PreWEC system (Henry 2011)

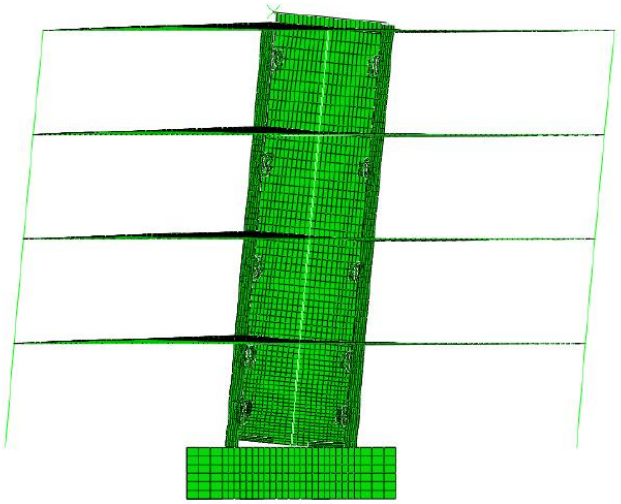
Fig. 2-43 Building in the model with rigid wall-floor connections (Henry 2011)

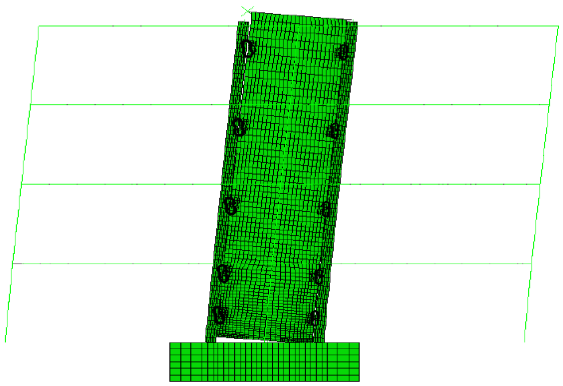

Fig. 2-44 Building in the model with special wall-floor connections (Henry 2011)

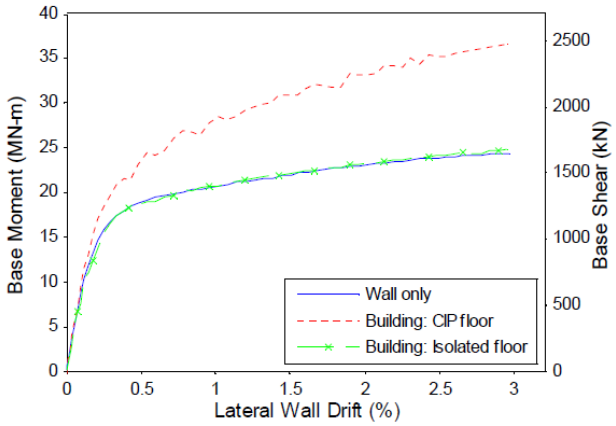

Fig. 2-45 Base moment versus lateral wall drift response of the three models (Henry 2011)

CHAPTER 3. Experimental Program

This chapter summarizes the design and construction of the two one-third scale structural assemblages tested at the MAST laboratory (Multi-Axial Subassemblage Testing - NEES@UMN facility). Section 3.1 gives a brief description of the prototype building for the two test specimens (PFS1 and PFS2). The boundary conditions of the test specimens are described in Section 3.2. Sections 3.3 and 3.4 describe the design and construction of the first specimen (PFS1). Sections 3.5 and 3.6 describe the design and construction of the second specimen (PFS2). Section 3.7 summarizes the material properties in the two specimens.

3.1 Prototype Building

The prototype structure for the laboratory test was a six-story office building developed by a practicing structural engineer in the State of California. The lateral force resisting system used in the building consisted of rocking walls in one direction and special moment frames in the orthogonal direction. The building had three spans in the direction parallel to the wall plane and five spans in the orthogonal direction.

Two different floor systems were investigated for the same prototype building to bound the interaction between the surrounding structural system and the rocking-wall system. The structural system expected to have significant interaction with the rocking-wall system (represented by test specimen PFS1) featured a cast-in-place (CIP) unbonded post-tensioned slab that transferred gravity as well as lateral loads to the wall. The structural system (represented by test specimen PFS2) that was expected to exhibit minimal interaction with the rocking wall, outside of the transmission of lateral forces, featured special vertical movement isolated connectors.

Plan views of the two types of floor systems are shown in Fig. 3-1 and Fig. 3-2 for the unbonded PT slab and the precast slab with vertical movement isolated connectors, respectively. The unbonded PT floor system (Fig. 3-1) was assumed to be an 8-1/2 in. thick cast-in-place two-way slab supported by both the rocking walls and special moment

frames. The wall was a bearing wall and sustained the gravity loads from tributary floor areas. The precast slab (Fig. 3-2) was assumed to consist of 8-1/2 in. thick hollow core planks that spanned between precast girders and edge beams. Because the precast girders were supported by the columns adjacent to the wall, the gravity loads from the tributary floor area of the wall were transferred to the columns adjacent to the wall (the wall was a non-bearing wall). The typical height of the floor was 12 feet. The elevation view of the prototype structure is shown in Fig. 3-3.

The typical area per floor in the prototype building was about 9,000 square feet, with assumed superimposed dead and live loads of 30 and 60 psf, respectively. Lateral design loads for the building were determined by IBC 2009. The building was assigned to Seismic Design Category D. The seismic coefficients were taken as Site Class: D (Stiff soil); S_s (short-period spectral response acceleration): 1.0 g; S_1 (1-second period spectral response acceleration): 0.4 g; F_a (site coefficient for short periods): 1.0; F_v (site coefficient for 1-second period): 1.5; I_E (important factor): 1.0; R (response modification coefficient): 5.0; Ω_0 (system overstrength factor): 2.5; C_d (deflection amplification factor): 5.0. The estimated period of the building was 0.6 second. The design base shear in the E-W direction for the building was 1,756 kips and the base moment was 1,103,700 kip-in. In the E-W direction, four rocking walls resisted the lateral loads. Assuming the base shear and base moment was evenly distributed to the four walls, each wall was required to carry design shears and base moments of 439 kips and 275,924 kip-in, respectively. For the one-third scale test structures, these design forces scaled by 1/9 for shear and 1/27 for moment to values of 49 kips and 10,219 kip-in, respectively.

The Precast Wall with End Columns, termed “PreWEC,” was used for the rocking-wall system. Design of the PreWEC system was based on the “Performance Verification of the PreWEC Concept and Development of Seismic Design Guidelines” (Aaleti 2011). Fig. 3-4 shows the detail for the PreWEC system in the prototype structure. The wall panel was 246 in. wide and 18 in. thick. The end columns were 24 in. wide and 18 in. thick. A 1-1/2 in. gap was reserved between the wall and the end column. Eight energy dissipating elements “O-connectors” were placed in each story and forty-eight in total were used for

the building. The number of O-connectors was determined to achieve 14% hysteretic damping for the building.

Forty-five and nine 0.6 in. diameter 7-wire GR270 strands were post-tensioned to a stress level of $0.8f_{py}$ to clamp the wall and the end columns to the foundation, respectively. The number of PT strands and the initial stress were determined to satisfy the design base moment and base shear.

For the first specimen (PFS1), the end columns which were originally placed next to the east and west wall end were moved to the north and south surface of the wall (termed "side columns"), as shown in Fig. 3-5. The purpose of moving the end columns was to explore the performance of another style of PreWEC system. The new PreWEC simplified the construction of the side columns and gave designers a second option. As shown in Fig. 3-5, there were 12 O-connectors between a side column and the front surface of the wall. Because there were four side columns in total (two side columns adjacent to the front and the back surface of the wall), there were 48 O-connectors in total in the prototype for PFS1.

For the second specimen (PFS2), the layout of the PreWEC was the same as that in Fig. 3-4. As shown in the figure, two end columns are placed adjacent to the ends of the wall. There were 12 O-connectors connected to the front surface and another 12 to the back surface of each end column. Therefore, 24 O-connectors were connected between each end column and the wall. There were also 48 O-connectors in the prototype for PFS2 in total.

The special moment frame was used to resist all lateral loads in the N-S direction (orthogonal to the wall plane). The columns in the east and west edge of the floor were 24 in. wide and 36 in. deep. Two columns that were 24 in. wide and 24 in. deep were placed in the mid span in the north and south edge of the floor. The columns were designed based on the force demand in the N-S direction.

3.2 Test Specimen Boundary Conditions

This section describes the representative section of the prototype structure that was selected for testing and the associated boundary conditions. For both test structures, PFS1

and PFS2, which were one-third scale assemblages of the prototype structure, two types of boundary conditions were investigated in the transverse direction. The transverse boundary conditions simulated the effects of the adjacent lateral force resisting systems (e.g., parallel walls or parallel frames) through the use of props as discussed in Section 3.2.1. In the vertical direction, to increase the speed of construction and reduce the cost of test specimen, only one floor was fabricated. The remaining floors were simulated through the use of "mega beams" or steel trusses (pin-connected steel tubes) in PFS1 and PFS2, respectively. These elements were designed to emulate the behavior of the missing floors (Section 3.2.2). The top and bottom of the test specimens employed top and bottom base blocks, respectively, to attach the specimen to the MAST crosshead and strong floor to apply the (6DOF) load/deformation reversed cyclic loading to the structure (Section 3.2.3).

3.2.1 Boundary Conditions in the Transverse Direction

A single frame line of the prototype building was selected for testing as shown within the box in the plan views of Fig. 3-6 and Fig. 3-7 that bound the test specimen. The absence or addition of props as shown in the figures simulated the effect of adjacent wall systems rocking in phase (Fig. 3-6) and columns on adjacent frame lines that constrained the uplift of the rocking wall (Fig. 3-7), respectively.

For the case where the rocking walls were assumed to rock in phase, the north and south edges of the specimen boundary in Fig. 3-6 were simulated as free edges, where the floor was not subject to differential vertical deflection relative to the adjacent rocking wall.

The other boundary condition case of adjacent frame lines with columns was simulated with props. The columns were expected to have negligible elongation and thus inhibit uplift of the floor. Four stiff props were pin-pin connected to the free edges of the floor and the laboratory strong floor. Fig. 3-7 shows the props attached to the slabs to simulate the constraint from parallel frame columns in PFS1. The four props were attached or removed at both north and south boundary edges of the floor at the same time to maintain

symmetry of the specimen. The props were also adopted in PFS2 to serve the same purpose.

As shown in the plan view in Fig. 3-7, the props were located at mid-span of the floor. Assuming the mid-span of the floor was close to the inflection point in the transverse direction, internal moment was about zero at the edge of the floor in the test specimen but shear forces existed. The props, when present, were designed to provide only axial constraint to the floor. Hollow structural tube (HSS 4×4×1/4) was used as the main body of the prop. The HSS tube was expected to remain elastic and had negligible elongation during the test. A clevis hinge was formed at the base of the prop to ensure free in-plane rotation. A rod end (AURORA KW-16-1) with rotatable ball was used at the top of the prop. The rotatable ball enabled the prop to rotate 17 degrees in the out-of-plane direction, which was sufficient to ensure the free out-of-plane rotation of the prop. Drawings of the prop are given in the Appendix A.

3.2.2 Boundary Condition along the Height of the Building

Existing tests have validated that lightly post-tensioned rocking walls rotate similar to rigid bodies under lateral loads (Henry, 2011). Consequently, floor slabs at different stories are expected to undergo similar vertical movements and in-plane rotations at the wall-floor interface as long as the wall-floor connections are the same in each story. To simplify the construction of the test specimen, only the 1st story floor slab was constructed as a representative floor for the tests, as shown in Fig. 3-8. This figure shows just the physically modeled portion of the floor system; the remainder of the floors were physically simulated using steel mega beams for PFS1 (Section 3.3.3) and steel trusses for PFS2 (Section 3.5.5). The two different floor systems required two different types of systems to emulate the effects of the missing floors.

3.2.3 Connecting the Specimen to the MAST Crosshead and Strong Floor

Fig. 3-9 shows the MAST advanced six degree-of-freedom (6DOF) control testing system that can be operated with some degrees of freedom in displacement control and others in force control to simulate desired boundary conditions and loading conditions on

large-scale test specimen. To connect the test specimen to the MAST crosshead, a top block was constructed between the crosshead and the wall panel in both tests. The top block was tied to the crosshead by twelve pre-tensioned high strength 1-1/2 in. diameter threaded rods. It was connected to the wall with ten No.6 rebar that protruded from the wall. Fig. 3-10 shows the drawings of the top blocks in both tests. A 13-in. deep opening was reserved at the top of the top block for the wedge plate of the PT strands and the load cell.

To connect the specimen to the MAST strong floor, base blocks were used and served as foundations for the walls and columns in the two tests. The base blocks for the walls were tied to the strong floor with sixteen pre-tensioned high strength 1-1/2 in. diameter threaded rods. A 5-in. deep pocket was formed in the base block for the wall in PFS1. Fiber grout was poured into the pocket as the wall sat on shims in the pocket. The bottom face of the wall was about 3-1/2 in. lower than the top face of the base block. The pocket was designed to confine the grout layer and prevent potential shear sliding of the wall in the in-plane and out-of-plane directions. A blockout was created near the west wall end to observe the local behavior at the wall corner and the fiber grout layer. Fig. 3-11 and Fig. 3-12 show the drawings of the base block for the wall in PFS1. A 9-in. deep opening was reserved at the base of the base block for the wedge plate of the PT strands.

To simulate a different type of construction technique, the pocket was eliminated in the base block for the wall of PFS2. The fiber grout was directly poured above the base block as the wall sat on shims above the base block. Short vertical dowels were cast into the base of the wall that fit in ducts within the base block. The dowels served to prevent the wall from “walking” in the transverse direction when orthogonal loads were applied to the wall preventing potential shear sliding of the wall in the in-plane and out-of-plane directions. The ducts were oversized to ensure the dowels would not inhibit the rocking of the wall.

The base blocks for each of the columns were tied to the strong floor with four pre-tensioned high strength 1-1/2 in. diameter threaded rods. Fig. 3-13 shows the drawings for the base blocks for the columns in PFS1. The base of the rebar cages of the columns in PFS1 were cast together with the base block, which formed rigid column base

connections. The column cages were embedded into the base block 21 in., long enough to fully develop the No. 3 rebar in the columns. In PFS2, the base blocks were constructed with four 1-1/4 in. diameter high-strength threaded rods protruding from the top of each column base block. Precast columns with steel base plates were bolted to the base blocks using the threaded rods.

3.3 Design of PFS1

PFS1 was a one-third scale model of the rocking-wall frame line of the prototype building (Fig. 3-2) that represented a system expected to exhibit significant interaction between the rocking-wall system and the surrounding structural system. An overview photo of PFS1 is shown in Fig. 3-14. The plan view of PFS1 is shown in Fig. 3-15. Fig. 3-16 through Fig. 3-19 show elevation views of the specimen. As shown in the figures, the specimen consisted of a rocking-wall system (rocking wall and O-connectors) that featured a bearing wall, an unbonded PT slab, mega beams, steel columns, reinforced concrete columns and edge beams. Design of each structural component is presented in detail in the following sections.

3.3.1 PreWEC System

As mentioned in Section 3.1, the modified version of the PreWEC system (i.e., rocking wall with side columns) was used in PFS1. It consisted of a rocking-wall system that carried gravity loads (i.e., bearing wall), four “side columns” (i.e., steel tubes pinned at the base) adjacent to the wall and “O-connectors” energy dissipating elements. Fig. 3-20 shows a detailed elevation view of the rocking-wall system. Fig. 3-21 shows the plan view of the wall at the base. The tested wall that was directly scaled from the wall in the prototype building was 90 in. wide and 6 in. thick. The height of the wall was chosen to be 224 in. After accounting for the length of the strands within the top block and the base block, the overall unbonded length for the strands was about 280 in. It was close to the unbonded length in the scaled wall from the prototype building (12 ft. ×12 in./ft.×6 stories /3= 288in.).

Design of the rocking-wall system was mainly based on the design requirements for special structural walls in Section 21.9 of ACI 318-11 as well as requirements for design of a special unbonded post-tensioned precast shear wall in ITG 5.2. Design of the rocking-wall system included the following: (1) Quantity of PT strands and initial PT stress; (2) Design of the boundary element; (3) Design of the shear reinforcement; (4) Examination of shear sliding resistance at the wall base; (5) Energy dissipating elements. The special detailing of the wall at the wall-floor connection is discussed following design of the rocking-wall system.

Quantity of PT strands and initial PT stress - The required design strengths in the tested wall should be taken equal to the design forces, discussed in Section 3.1, divided by the appropriate under-capacity (ϕ) factors (0.75 for shear and 0.9 for flexure). This led to required nominal shears and moments of 49 kips /0.75=65 kips and 10,219 kip-in/0.9=11,354 kip-in, respectively.

The amount of initial prestress forces in the wall of PFS1 was selected to ensure the nominal shears and moments of the rocking-wall system were satisfied. Five 1/2 in. diameter 7-wire GR270 strands that were prestressed to a stress level of $0.58f_{pu}$ were used in PFS1. Following the "Performance Verification of the PreWEC Concept and Development of Seismic Design Guidelines," (Aaleti 2011) the predicted base moment resistance of the rocking-wall system including the effect of the O-connectors at 2% design drift was 10,866 kip-in, which was within 4% of the demand. The calculation procedure for determining the moment capacity is outlined in Appendix B1. It should be noted that the moment capacity was determined by eliminating the gravity load (N_{wall}) in Appendix B1, where the effect of the gravity load on the wall was not considered. This was thought to be conservative, and in the case of seismic events with large vertical accelerations, it may be prudent to ignore the effect of the gravity load on the moment resistance.

If the effect of the gravity load on the flexural capacity of the wall was taken into consideration in PFS1, as discussed in Appendix B2, the base moment of the rocking-wall system increased to 15,509 kip-in. This value was 36% larger than the design base moment (11,354 kip-in).

The initial prestress in the PT strands was selected to ensure the strands would remain elastic at 2 design drift (ITG 2009). This requirement was satisfied in both conditions (without or with the effect of the gravity loads), as validated in Appendix B1 and B2.

Design of the boundary element - Design of the boundary element was based on the requirements of boundary elements in Section 21.9.6 of ACI 318-11. The confinement in the wall corners consisted of a #3 stirrup and a #3 crosstie at a 2-in. spacing, as shown in Fig. 3-21. The spacing satisfied the maximum spacing limit of 1/3 minimum member dimension (thickness of the wall, 6 in.). In addition, a 14-in. long steel channel C6x10.5 was installed on each side of the wall to protect the wall corners. The stiff steel channel not only confined the concrete in the wall corner, but also might spread the compression force to a larger area.

Design of the shear reinforcement - Design of the shear reinforcement followed Section 21.9.4 in ACI 318-11. As mentioned in Section 3.1, the design base shear for the rocking-wall system was 49 kips, which led to a required shear resistance of 49 kips/0.75=65 kips. The shear resistance capacity of the wall is calculated as follows when the shear reinforcement is not considered:

$$V_n = A_{CV}\alpha_c\lambda\sqrt{f_c'} = 90\times6\times2.0\times\frac{1.0\sqrt{6{,}000}}{1000} \approx 84\ kips > 65\ kips, \quad (3.1)$$

$$\alpha_c = 2.0, H_w/l_w = 224/90 \approx 2.5 > 2 \quad (3.2)$$

Where V_n = Nominal shear resistance of the wall; α_c = Coefficient defining the relative contribution of concrete strength to nominal wall shear strength; λ = Modification factor reflecting the reduced mechanical properties of lightweight concrete, all relative to normal weight concrete of the same compressive strength; H_w= Height of the rocking walls; l_w = Length (width) of entire wall.

Therefore, only the minimum shear reinforcement was needed due to the small design base shear. The spacing satisfied the maximum spacing limit of 18 in. in ACI 318-11. To be conservative, two layers of #3 mesh reinforcement were placed at a spacing of 14 in., serving as the shear reinforcement in PFS1.

Examine shear sliding at the wall base - If the base shear demand of the wall is greater than the sliding shear capacity of the wall, it leads to slip at the base joint, which has

detrimental effects such as possibly kinking the post-tensioning strands. Moreover, the re-centering capability of the wall is lost with a shear sliding failure mode. Therefore, shear sliding should be avoided during the design.

According to Section 5.5.3 in ITG 5.2, a coefficient of friction of 0.5 can be assumed at the interface between the wall base and the fiber grout. The shear sliding resistance provided by the compressive force from the PT strands at the base of the wall was:

$$F_{V\_PT} = \mu N_{PT} = 0.5\times 0.58 f_{pu} n_{strand} A_{strand} = 0.5\times 0.58\times 270\times 5\times 0.153 \approx 60 kips < 65\ kips \quad (3.3)$$

Where F_{V_PT} = Shear resistance provided by the PT strands, μ = Coefficient of friction between the wall and the grout beneath the wall; N_{PT} = Force in the PT strands; n_{strand}= Number of strands in the wall; A_{strand} = Cross-sectional area of each strand

It should be noted that this check did not include the effect of the gravity load, when included, the sliding shear resistance became 124 kips. To be discussed in Section 4.5.1, the gravity load was applied to the tested wall in most of the testing phases in PFS1. Therefore, shear sliding was not expected to occur in PFS1.

Energy dissipating elements - To increase the energy dissipation capacity of the wall, eight oval shaped energy dissipating elements "O-connectors" were added to the wall, which formed the rocking-wall system. The number of O-connectors was determined by assuming the resisting moment from the O-connectors in the test specimen were about 1/27 of that in the prototype building at the design drift. As shown in Fig. 3-22, it was expected that the relative vertical deformations of the O-connectors near the rotation point (inverted triangle mark in the figure) was much smaller than those generated by the O-connectors away from the rotation point, generating a relatively small resisting forces ($R_{NO} < R_{FO}$) and resisting moments, where R_{NO} is the resistance provided by the O-connectors near the rotation point and R_{FO} is that provided by the O-connectors near far from the rotation point. Therefore, only the O-connectors located away from the rotation point were considered in the following calculation.

At 2% design drift, the O-connectors located away from the rotation point were expected to have yielded. As shown in Fig. 3-22, the moment resistances of the O-connectors away from the rotation point of the wall were:

$$M_{FO} = n_{FO} R_{YO} \left(l_w - s_{FO} - \frac{\beta c_{design\_wall}}{2} \right) \quad (3.4)$$

Where M_{FO} = Moment resistance of the O-connector far from the rotation point; n_{FO} = Number of O-connectors away from rotation point; R_{YO} = Yielding resistance of an O-connector; s_{FO}= Distance between the O-connectors and the wall end

Because the O-connectors of the same dimensions were used in the prototype building and PFS1, R_{YO} in the equation above is the same. The length of the wall in PFS1 (l_w) was 1/3 of that in the prototype building; the distance from the O-connections to the edge of the wall in the specimen (s_{FO}) was also 1/3 of that in the prototype building. Assuming the N.A. depth of the wall in the specimen (c_{design_wall}) was about 1/3 of that in the prototype building; the moment arm of the resistance of the O-connectors in PFS1 was also about 1/3 of that in the prototype building. Using the equation above, the moment resistance of an O-connector in the specimen was thus about 1/3 of that in the prototype building.

To render the resisting moments from all O-connectors in PFS1 to be 1/27 of those in the prototype building, the number of O-connectors in PFS1 was reduced to 1/9 of those in the prototype building. As mentioned in Section 3.1, there were 48 O-connectors assumed in the prototype building, 12 O-connectors between each side column and the wall. After dividing by 9 and choosing an integral number ($12/9 \approx 1.3$), it was decided that two O-connectors should be installed between each end column and the surfaces of the wall. The length of the side column was constrained to not extend beyond the 1st floor to simplify the construction of the CIP floor, as shown as "HSS Tube" in Fig. 3-16.

Fig. 3-23 shows details of the O-connectors. The O-connector was connected to the wall and the side columns (HSS tubes) adjacent to the wall. One side of the O-connector was welded to a 3/8 in. plate (SP-1 in Fig. 3-20) that was pre-embedded in the wall and the other side to the surface of the steel tube. Each steel tube was welded to a clevis hinge, which was free to rotate in the wall plane. To prevent the O-connector from potential out-of-plane buckling which was observed in the component test (Henry 2011), a threaded rod running through the front steel tube, the wall and the back steel tube was used to connect them together. When the wall rocked, the O-connectors were deformed

by the relative vertical displacement between the wall and the steel tube and dissipated energy. Tests have exhibited stable and excellent energy dissipation capacity of the O-connectors under this circumstance (Henry 2011).

Special detailing of the wall to accommodate connections - As shown in Fig. 3-20, corrugated sleeves were pre-embedded in the wall to accommodate the placement of the reinforcement and the strands in the floor that needed to pass through the wall. Eight #3 reinforcement protruded from the wall at approximately 4 ft. from the foundation and were to be cast into the floor slab to satisfy integrity reinforcement requirements (two top and two bottom rebar projecting from the plane of the wall). The embedment reinforcement at top of the wall transferred the forces from the mega beam (Section 3.2.2 and Section3.3.3.4) into the wall. One layer of ten #5 mild reinforcement protruded from the top of the wall were to be fed into the holes in the top block, which connected the wall to the top block after the holes being grouted.

3.3.2 Unbonded Post-Tensioned Floor Slab

A CIP unbonded PT slab was used as the floor system in PFS1 (only the 1st story slab was constructed in the specimen). The dimension of the tested slab was directly one-third scaled from the slab in the prototype building, except that the slab thickness was 3 in., which was a little larger than the scaled down thickness ($8.5/3 \approx 2.8$ in.). Fig. 3-24 shows the plan view of the floor. As shown in the figure, the PT strands are shown in black; the rebar in green represent the bonded rebar on the top; the rebar in red represent the rebar on both top and bottom of the slab; the rebar in blue represent the bottom rebar; the rebar in magenta represent the shear-friction rebar; the rebar in cyan represent the additional rebar required for PT slab detailing. Fig. 3-25 and Fig. 3-26 show the reinforcement and strand distribution in the three cross sections in the N-S direction. Fig. 3-27 and Fig. 3-28 show the reinforcement and strand distribution in the three cross sections in the E-W direction. Design of the strands and the reinforcement are presented below.

In the prototype design, the PT strands were distributed in the E-W direction (parallel to the wall plane). According to Section 18.12.4 of ACI 318-11, the spacing of tendons shall not exceed the smaller of eight times the slab thickness and 5 ft. For the scaled floor

in PFS1, the spacing of tendons should not exceed 20 in., which was the smaller of 24 in. (eight times the slab thickness) and 20 in. (1/3 scaled of 5 ft.) In PFS1, six strands with a spacing of 18 in. were used in the scaled floor of 10 ft. wide.

In the prototype design, the distributed strands were required to provide 13 kip per foot initial PT force. The PT forces provided the required minimum average effective prestress of 125 psi in the slab according to Section 18.12.4 in ACI 318-11.

The initial PT force required in each of the six strands in the scaled floor is calculated below:

$$F_{slab\_PT} = \frac{F_{design\_slab}}{sf \cdot n_{PT\_slab}} w_{slab} = \frac{13}{3\times6}\times10 \approx 7.2\ kip \quad (3.5)$$

Where F_{slab_PT} = Initial PT force in each strand in the scaled floor (E-W direction), F_{design_slab} = Initial PT force per foot provided by the strands (E-W direction) in the design, sf = Scale factor, n_{PT_slab} = Number of strands in the scaled floor (E-W direction), w_{slab} = Width of the scaled floor.

Grade 250 3/8 in. diameter strands were used in PFS1. The nominal cross-sectional area of the strand was 0.08 in^2, thus each strand was prestressed to 0.36f_{pu} to provide the required 7.2 kip initial PT force.

In the prototype design, the PT strands were banded in the N-S direction (perpendicular to the wall plane) and required to provide 346 kip initial post-tensioned force close to each wall end. The scaled floor in PFS1 was reinforced with four strands banded at each wall end in the N-S direction. Each strand was prestressed to 0.48f_{pu}, which provided the required initial PT force 9.6 kip (346 kip/ scale factor 9/ 4 strands).

The design of the anchorage region was based on both ACI 318-11 and ACI 352.1R-11. For the distributed strands in the E-W direction, a 3 in. × 3 in. × 3/8 in. steel plate was pre-embedded in the slab to resist the local force of each strand. The bursting force of the strand was resisted by the edge beam. For the banded strands in the N-S direction, a 25 in. × 3 in. × 3/8 in. long steel plate was pre-embedded in the slab to resist the local force from the four strands. Four additional longitudinal #3 mild reinforcement and five #2 U-shaped wires were placed at the anchorage region as recommended in 6.1.7 in ACI 352.1R-11 to resist the bursting force from the banded strands, shown in Fig. 3-29.

The single long plate used to anchor the banded tendons in the N-S direction (transverse to the wall) was recommended by the PT installers to ease congestion in the region of the banded tendons and to provide a more uniform prestress. The plate had an unanticipated effect on the curvature of the slab in the longitudinal direction during testing because it limited changes in curvature in the vicinity of the plate.

Minimum bonded mild reinforcement was placed in the slab in the E-W direction based on the requirements in Section 18.9.3 of ACI 318-11. At the floor-edge beam connection, eight 2 ft. long #3 rebar were placed at the top of the floor, as shown in Fig. 3-24. Two rebar were located at each corner of the floor and spaced 2 in. apart; four rebar were distributed at the floor-column connection with 4 in. spacing. For structural integrity purposes, two of the four rebar at the top of the floor and two additional #3 rebar at the bottom of the floor extended into the columns at the floor-column connection. Fig. 3-30 shows the bonded reinforcement at the west slab-edge beam connection. Similar layout of the rebar was used across the wall-floor connection in the E-W direction.

Initially the slab was designed with PreWEC system that had end columns next to the rocking wall. Two transverse strands and two rebar of the slab in the N-S direction passed through the end columns based on the structural integrity requirements in Section 18.12.6 in ACI 318-11 and Section 6.3.1 in ACI 352.1R-11. When it was decided to use side tubes to attach the “O-connectors” rather than end columns, the strands and the rebar were maintained to pass through the wall ends. The wall-floor connection is shown in Fig. 3-31 and Fig. 3-32. Because the props were assumed to behave like columns with pin-pin connections at both ends, the arrangement of the reinforcement and the strands at the prop-floor connection was similar to that at the wall-floor connection, as shown in Fig. 3-29.

Additional mesh reinforcement at bottom of the slab was placed at a spacing of 24 in. in the longitudinal direction and 32 in. in the transverse direction based on engineering practice of the consulting engineer who developed the prototype design; although it was not required by the existing code. Four #3 rebar were distributed along the 90-in. long wall-floor interface and located at mid-depth of the floor to serve as shear-friction reinforcement to transfer the lateral loads into the wall (in this case, as the lateral loads

were applied through the MAST crosshead to the rocking wall, the wall transferred the loads to the slab). The final layout of the reinforcement and strands is shown in Fig. 3-33.

3.3.3 Mega Beams

3.3.3.1 Design of the Mega Beam

Existing tests have validated that lightly post-tensioned rocking walls rotate like a rigid body under lateral loads (Henry 2011). The floor slabs at different stories undergo similar vertical movements and in-plane rotations at the wall-floor interface as long as the wall-floor connections are the same in each story. To simplify the construction of the test specimen, only the 1st story unbonded PT slab was constructed as a representative floor. A "mega beam" concept was implemented in the structure to simulate the constraint of the five missing upper-story CIP floors of the prototype. Fig. 3-34 shows the mega beam with cover plates used in the MAST test. The mega beam featured pinned connections at its ends to transmit shear and special dogbone-shaped cover plates that created a tension-compression force couple to simulate the predicted total moment resistance of the five upper-story floors. The calculation of the predicted moment resistance of the floor was based on the assumptions that all bonded reinforcement in the slab cross section yielded and the PT stress was equal to the recommended f_{ps} from Eqn. 18-2 in ACI 318-11. The calculation process is given in Appendix C.

3.3.3.2 Component Test of the Mega Beam

A proof of concept test for the mega beam was conducted to characterize its behavior and uncover any potential problems before implementing it in the PFS1 test specimen. The details of the component test are shown in Fig. 3-35, and a photo is provided in Fig. 3-36. Based on the results of the component tests, some changes were made to the mega beam cover plate to improve its performance in PFS1. The modified cover plate is shown in Fig. 3-34 and is discussed in the next section. Fig. 3-37 shows the moment-rotation results from the component test, termed "Component_Test," The moment was obtained by multiplying the input load from the actuator by the distance between the centroid of the actuator and the base of the cover plates. Two bilinear curves termed "5×Floor@Wall" and "5×Floor@Edge beam" are superimposed in the figure. These

curves represent the five times the predicted moment resistance of the floor at the wall-floor and floor-edge beam connections assuming elastic-perfect plastic behavior of the floor. As shown in the figure, the maximum moment resistance of the mega beam was close to five times the predicted moment resistance of the slab at both connections, which proved the design purpose. The result from a detailed finite element model of the tested mega beam is also shown in the figure and it matched well with the test result.

3.3.3.3 Improvement of the Mega Beam

Although the design purpose of the mega beam was proven, improvement was made learning from the test observation. A 1/2 in. gap existed between the mega beam and the steel tabs at the pin connection for construction tolerance, as shown in Fig. 3-38. The wood stick shown in the figure was placed to demonstrate the gap and not used during the test. As a result, the mega beam could move along the gap; twist of the mega beam was observed during the component test, as shown in Fig. 3-39. Because the cover plate was still in either tension or compression and the mega beam only resisted shear force, the test result showed that the twisting did not have a large impact on the moment resistance. To prevent the same problem occurring in the test of PFS1, two washer plates were inserted into the gap when installing the mega beam to the pin connection.

The component test was terminated when fracture of the cover plates occurred at the corner of the “dogbone” region, as shown in Fig. 3-40. It was believed that stress concentration at the sharp corners was the main cause of the fracture. The laser cutting technique used in fabricating the cover plates might also result in residual stress in the cover plates, which could have been another cause of the failure. As shown in Fig. 3-37, the ultimate rotation of the mega beam was about 0.035 rad, which was expected to be achieved when the lateral drift of PFS1 was only 1.5%. To prevent the early fracture of the dogbone-shaped cover plates, the dogbone region was redesigned to have fillet corners with smooth transitions from the full section to the trimmed down section. A rough shape of the cover plate was cut out using the laser cutting technique and then ground down to the desired shape. The improvements were expected to increase the ductility of the cover plate. The improved mega beam used in the assemblage test was shown in Fig. 3-34.

3.3.3.4 Connectivity to the Wall Panel

The embedment at top of the wall in Fig. 3-20 was reserved for connecting the mega beam. The drawings of the mega beam end plate and the steel embedment are given in Fig. 3-41 and Fig. 3-42, respectively. Twelve bolts connected the mega beam end plate to the embedment. Twelve A706 No.6 rebar was welded to the embedment and used to transfer the load into the surrounding concrete in the wall. The staggered rebar cutoffs anchoring the embedment were intended to prevent stress concentrations (e.g., splitting) in the wall at a discontinuity; the staggers served to distribute the load into a larger region of the wall.

3.3.4 Steel Columns

3.3.4.1 Design of the Steel Column

A steel column was installed above the 1st story RC column to connect the mega beam and to withstand the large concentrated moment at the beam-column joint that simulated yielding of the five floors. To render the moment distribution in the 1st story gravity column of the specimen similar to that of the scaled prototype structure, the steel column extended three stories to diminish the large concentrated moment along the steel column and move the inflection point to correspond with the expected location relative to the 1st story beam-column joint (i.e., half story above). Wide flange steel columns, W16x67, about 11 ft. long were used in the test.

3.3.4.2 Connectivity to the Mega Beam

Twelve bolts were used to connect the flange of the steel column to the mega beam end plate. Four stiffeners were welded to the web of the steel column which were parallel to the cover plates to prevent local buckling of the flange and the web.

3.3.5 Edge Columns and Edge Beams

The dimensions of the tested reinforced concrete edge columns and edge beams were directly scaled from those in the prototype building. Fig. 3-43 and Fig. 3-44 show the cross sections of the columns and the edge beams in the test, respectively. Fig. 3-45 and Fig. 3-46 show the elevation views of the column and edge beam. As mentioned before,

the base of the rebar cages for the columns were built and cast together with the base block, forming rigid column base connections. The 1st story columns, edge beams and the unbonded PT slab were cast together.

A short RC column 16 in. long was built between the 1st story RC column and the steel column. The purpose of the short column was to prevent congestion of the rebar in the 1st story beam-column joint. The rebar in the 1st story RC column were continuous to the top of the short column, which integrated the short column with the 1st story column. Four high strength 3/4 in. diameter threaded rods of 22 in. long were embedded in the steel cages of the short column. The rods were used to connect to the steel plate at the base of the steel column. Fig. 3-47 and Fig. 3-48 show the plan view and elevation view of the connection.

3.4 Construction of PFS1

3.4.1 Construction of the Base Block and the Top Block for the Wall

The rebar cages of the base block and the top block were assembled in the structural lab. Fig. 3-49 shows the assembled rebar cage of the base block sitting in the formwork. A blockout made of lumber was placed in the middle of the cage to form the pocket for the wall in the base block. A blockout made of foam was placed near the end of the wood blockout to form an opening to enable visualization of the performance of the corner of the wall and the fiber grout during testing. PVC pipes were placed in the base block for three purposes. As shown in the figure, one PVC pipe was placed in the middle of the cage, which created a through hole for the unbonded PT strands of the wall. The three PVC pipes covered by red tape were used to create holes for grouting between the base block and the strong floor in the MAST laboratory. Two rows of PVC pipes which were covered by grey tape were used to create holes for threaded rods. The threaded rods were used to tie the base block down to the strong floor in the MAST laboratory.

Fig. 3-50 shows the formed pocket in the base block. As shown in the figure, there were two lumber blocks placed in the pocket. The wall sat on the blocks, which served as shims, when the steel fiber grout was poured into the pocket. Black foam with a hole was

placed in the middle of the pocket. The foam was used to prevent the fiber grout falling into the through hole in the base block, which was used for the unbonded PT strands of the wall.

Fig. 3-51 shows the assembled rebar cage of the top block sitting in the formwork. Sleeves were placed in the middle of the cage to create holes, which were used to accommodate the rebar that protruded from the wall. After grouting the rebar in the holes, the wall was connected to the top block.

Fig. 3-52 shows the special detailing of the PT anchor used in both the bottom and top base blocks. As shown in the figure, a steel embedment was placed in the middle, which was used to sustain the large concentrated force of the PT strands. The steel embedment is shown in Fig. 3-53. The external wedge plate, which held the strand wedges, is shown in Fig. 3-54. It fitted into the bottom surface of the steel embedment and was installed during the post-tensioning operation. As shown in Fig. 3-52, spiral reinforcement was used to confine and strengthen the concrete in the local region of the steel embedment. A PVC pipe was placed above the embedment to create a through hole for the unbonded PT strands.

3.4.2 Construction of the Base Block for the Edge Columns

Fig. 3-55 shows the built base block for the edge column. As shown in the figure, a PVC pipe was placed in the middle of the column cage, which was for the unbonded PT threaded rod used to simulate the gravity load on the edge column. The steel cage of the edge column was cast into the base block, as a cast-in-place column would be cast into the foundation. As shown in Fig. 3-56, commercial product Weldcrete Bonding Agent was uniformly spread on the base of the edge column to increase the bond between the base block and the edge column. A monolithic connection between the column and the base block was expected after casting the concrete into the formwork for the column.

3.4.3 Construction of the Wall Panel

The wall panel was constructed in a precasting plant (Molin Concrete). The two steel cages for the boundary elements of the wall were constructed first with strain gages and

concrete gages attached, as shown in Fig. 3-57 and Fig. 3-58. The wood formwork for the wall was built on a flat steel bed. As shown in Fig. 3-59 and Fig. 3-60, the steel channels used to armor the wall corners at the base and the steel embedment at the top of the wall to accommodate attachment of the mega beam were installed in place, followed by placing the two finished steel cages at the wall boundaries, as shown in Fig. 3-61. The embed plates used to attach the O-connectors are also shown in the photo. Mesh reinforcement and a PVC pipe for the unbonded PT strands were then installed, shown in Fig. 3-62. Lastly, foam and corrugated sleeves were glued to the bed to reserve holes in the wall, as shown in Fig. 3-63, to accommodate later access including placement of transverse slab reinforcement. When casting concrete into the formwork, twenty-four concrete cylinders and 6 concrete beams were fabricated for the future material testing. The steel bed was vibrated to help the concrete flow into the formwork, especially the congested wall corners. The finished wall is shown in Fig. 3-64. The whole construction process took about a day.

3.4.4 Erect the Wall and Form Fiber Grout Layer

The precast wall was shipped to the MAST laboratory one week after it was cast. As shown in Fig. 3-65, the wall was tilt up by two cranes working together. The MAST laboratory crane held up the top of the wall with a steel spreader beam and an external truck crane held the bottom of the wall. The wall was lifted and then rotated vertically. After the wall was tilt up, it was moved and then sat above two shims in the pocket of the base block. A total station was used to level the wall in 3D space, shown in Fig. 3-66. Lateral supporting EFCO frames were built around the wall to stabilize it.

Fiber grout, 1-1/2 in. thick, was poured into the pocket of the base block with the wall in place, as shown in Fig. 3-67. To ensure a smooth contact, the grout was over-poured into the pocket 1/2 in. higher than the bottom face of the wall. Commercial product PAGEL V1A with nominal 28-day strength of 13 ksi was used for the fiber grout. The nominal strength of the fiber grout was chosen to be about twice the nominal concrete strength of the wall, which satisfied Section 5.8 in ITG-5.2 (ITG 2009). Nine cube samples were made when pouring the fiber grout for future material testing.

It was noteworthy that the fiber grout was mixed in the MAST laboratory using handheld blenders. Several grout samples were made and broken for examination before the test. It was observed that in some samples the steel fiber settled to the bottom of the grout. The strength of the fiber grout was found to be smaller than expected under this circumstance.

3.4.5 Install the Top Block

The top block was craned onto the wall panel three days after the fiber grout was poured, when the grout was expected to have cured. Plain grout was pasted between the top block and the wall to create a smooth contact, shown in Fig. 3-68. The holes in the top block which accommodated the reinforcement protruded from the wall were filled using fiber grout, as shown in Fig. 3-69.

3.4.6 Post-tensioning the Wall Panel

After the top block was installed, five PT strands were slowly put through the aligned holes in the top block, the wall and the base block. To prevent the strands from tangling inside the holes, tapes of different colors were used to mark the top and bottom of every strand.

After receiving the calibrated post-tensioning jack from DSI Company, the gage pressure of the hydraulic pump corresponding to 20, 30, 40, 50, 60 and 70 and 100% of the target PT force (120 kips) was calculated and prepared before the PT date. Two small hydraulic jacks sat on the ground to hold the wedge plate at the base of the top block in place, as shown in Fig. 3-70. Initial seating of the wedges at the bottom was performed by using a hammer to tap the wedges into the wedge plate, as shown in Fig. 3-71. The post-tensioning jack was craned to the top of the top block and put in place. As shown in Fig. 3-72, a load cell (i.e., blue cylinder beneath the plate) was installed to monitor the PT force in the strands.

The post-tensioning procedure was monitored by comparing the PT force derived from the gage pressure readings to the recorded force in the load cell at 20, 30, 40, 50, 60 and 70% of the target PT force. The elongation of the strands was also measured by a steel

ruler to examine the reliability of the achieved PT force, as shown in Fig. 3-73. Power seating was conducted after 70% of the target PT force was achieved to reduce the seating loss. The final recorded PT force after releasing the strands was 119.3 kips, which was close to the target PT force of 120 kips. Table 3-1 shows the recorded values during the post-tensioning process. At the beginning of the test date of PFS1, the recorded PT force in the strands was 112.5 kips, which was about 6.8 kips smaller than the PT force at the post-tensioning date due to the PT loss.

3.4.7 Construction of the Floor Slab and the 1st Story Frame Reinforcing Cages

As discussed in Section 3.3.2, for scaling purposes, it was desired to use 3/8 in. diameter strand for the unbonded PT in the PFS1 floor slab. However, it was not commercially available. Instead, the 3/8 in. unbonded PT strands were created for the project by uniformly greasing 3/8 in. prestressing strand with the ExxonMobil lubricant, wrapping the strand by duct tape and placing it in split plastic tubing at the MAST laboratory. Each strand was checked to ensure that it slid well inside the tube. The length of the distributed strands in the E-W direction was 24 ft. and that of the banded strands in the N-S direction was 14 ft. The fabricated strands were longer than the length (20 ft.) and width (10 ft.) of the floor, which provided space for the anchors and the load cell at each end.

Formwork with shoring was built for the CIP slab, the 1st story RC columns and the edge beams. The banded transverse strands in the slab were placed in position first, followed by the distributed longitudinal strands and the mild reinforcement. Rebar chairs of different heights were mounted to the slab to support the curved tendons as well as the rebar.

As mentioned in Section 3.2.3, the steel cages for the reinforced concrete columns were built together with the column base blocks. Formwork for the columns was assembled around the steel cages after the base blocks were placed in position. For the edge beams, the stirrup and crossties on one side of the steel cage were tied to the longitudinal rebar on the ground. The semi-finished steel cage was placed through the beam-column joint.

The stirrup and crossties on the other side of the steel cages were finished inside the formwork of the edge beam.

3.4.8 Cast the Slab and the 1st Story Frame

Before casting the slab, high strength injectable mortar (Hilti HIT-RE 500-SD) was used to fill the corrugated sleeves through the wall, as shown in Fig. 3-74. Only the holes with mild reinforcement were filled. Commercial product Weldcrete Bonding Agent was uniformly spread on the wall at the wall-floor interface to increase the bond between the wall and the slab. As shown in Fig. 3-75, temporary aluminum rods were used for guiding a piece of lumber to screed the slab surface.

The slab, the 1st story reinforced concrete columns, and the edge beams were cast together. Commercial concrete with a nominal strength of 5 ksi was ordered for casting the slab. Twenty-four concrete cylinders and six concrete beams, as shown in Fig. 3-76, were made for future material testing. Two vibrators were used to ensure adequate concrete flow and consolidation in the structure. Although the concrete was cast in the laboratory, it was important to finish the entire operation in a short time due to the cold weather in January. Although the concrete was pumped to the formwork inside the heat controlled laboratory, the concrete-mixing truck was located outside the laboratory in the frigid environment. Eight people, including the MAST staff, undergraduate researchers, and project members participated in the casting process. Fig. 3-77 shows a photo taken during casting. Care had to be taken in casting the slab that the reinforcement was not disturbed because of the tight tolerances in the 3-in. slab. Overall, the operation went very well. Fig. 3-78 shows the finished surface of the floor slab.

3.4.9 Cast the Short Column above the 1st Story Column

After the concrete in the slab had cured (2 weeks later), the 16-in. short column above the PT slab was cast. Before casting, the top surface of the 1st story RC column was roughened by chipping the hardened concrete to increase the bond. Moreover, Weldcrete Bonding Agent was uniformly spread on the top surface of the 1st story RC column to

further increase the bond. Twelve concrete cylinders and three concrete beams were made for future material testing.

3.4.10 Post-tensioning of the Floor and Weld the O-connectors

Post-tensioning the slab was conducted a week after casting the short columns. A local post-tensioning company conducted the operation. Fig. 3-79 and Fig. 3-80 show the strands running in the longitudinal (in-plane) and the transverse (out-of-plane) directions of the test structure, respectively. As shown in the figures, small donut-shaped chucks with wedges were used to anchor the strands. The chucks used for the small 3/8 in. diameter strands were the same as those used to anchor PT "railing" cables in parking garages. Load cells were installed on selected strands to measure the post-tensioning forces. A small steel plate was placed between the chuck and each load cell to ensure the full contact. The wedges were tapped into the chuck using a small pipe during the initial seating, as shown in Fig. 3-81. Similar to the post-tensioning process for the strands in the wall, the gage pressures of the calibrated post-tensioning jack were calculated in advance for the target PT forces. Yellow paint was sprayed onto each strand before the post-tensioning procedure, which was used to measure the elongation of the strand. The recorded elongation was used to examine the reliability of the recorded PT forces in the strands where the load cells were installed. It also correlated with the gage pressure applied to the strands without load cells, which gave guidance for determining the PT force in the strands. Fig. 3-82 shows placing the jack for the post tensioning operation for the slab.

The post-tensioning order is denoted in Fig. 3-83. The distributed strands were post-tensioned first, followed by the banded strands. The operation started from the strands in the middle of the slab and then toward the edges of the slab in a symmetrical way. The purpose was to achieve a uniformly distributed stress in the slab. Strands (5 and 13) were re-stressed at their other ends because the load cell readings showed that the PT force decreased significantly after the seating loss. Strands (2 and 4) were re-stressed at their other ends as well because the elongation of the strands after the first pull indicated that they did not achieve the target PT force. Table 3-2 and Table 3-3 summarize the stages of

the post-tensioning operation in the longitudinal and transverse directions, respectively. The column “Final force after seating” in the table shows the final PT readings recorded by the load cells. The column “Final elongation after seating” shows the final recorded elongation of each strand.

PT losses occurred between the post-tensioning date and the test date. Table 3-4 summarizes the recorded PT loss obtained as the difference between the PT recorded on the day of tensioning (after seating) and on the day of test. The loss was attributed to creep and shrinkage of the concrete.

After post-tensioning the floor, a welder from the structural laboratory at Iowa State University conducted the welding operation, connecting the O-connectors to the wall and the adjacent HSS tubes. The welding detail is shown in Fig. 3-23.

3.4.11 Install the Steel Columns and the Mega Beams

Steel columns were craned onto the short columns. The steel column was connected to the short column with the four threaded rods pre-embedded in the short column. The mega beams were the last pieces installed for the specimen. The mega beams were craned into position and connected to the steel columns and walls, as shown in Fig. 3-84. When installing the mega beams, the west mega beam fit tightly in between the wall and the west steel column; whereas the east mega beam was placed between the wall and the east steel column without difficulty. To prevent the potential twist of the mega beam as well as the steel column, EFCO was built around the steel column to provide lateral support, as shown in Fig. 3-85.

3.5 Design of PFS2

PFS2 was a one-third scale model of the rocking-wall frame line of the prototype building (Fig. 3-2) that represented a system expected to exhibit minimal interaction between the rocking-wall system and the surrounding structural system. An overview photo of PFS2 is shown in Fig. 3-86. The plan view of PFS1 is shown in Fig. 3-87. Fig. 3-88 through Fig. 3-91 show elevation views of the specimen. As shown in the figures, the specimen consisted of a rocking-wall system that included a non-bearing wall, end

columns and O-connectors, a precast floor slab that was formed by twelve pieces of precast planks, steel trusses, precast concrete columns, transverse beams and edge beams. Design of each structural component is presented in detail in the following sections.

3.5.1 PreWEC System

As mentioned in Section 3.1, the regular PreWEC system (i.e., rocking wall with end columns) was used in PFS2. It consisted of a rocking-wall system that did not carry gravity loads (i.e., non-bearing wall), two end columns adjacent to the wall and "O-connectors" energy dissipating elements. Fig. 3-92 shows a detailed elevation view of the wall, and Fig. 3-93 through Fig. 3-96 show plan views of the wall at different cross sections annotated in Fig. 3-92. The wall was 68 in. wide and 6 in. thick and had 10 in. wide and 6 in. thick end columns in the plane of the wall with a 1 in. gap between, such that the combined footprint of the rocking wall with end columns (90 in. wide and 6 in. deep) was the same as that of the rocking wall of PFS1. The height of the tested wall in PFS2 was 219-1/2 in. Although the same prototype building was used for PFS1 and PFS2, the wall in PFS2 was 4-1/2 in. shorter than that in PFS1. Because there was no pocket in the base block of PFS2 and the fiber grout layer was directly formed above the top surface of the base block where the wall sat.

Similar to PFS1, design of the rocking-wall system in PFS2 was mainly based on the design requirements for special structural walls in Section 21.9 of ACI 318-11 as well as requirements for design of special unbonded post-tensioned precast shear walls in ITG 5.2. Design of the rocking-wall system included the following: (1) Quantity of PT strands and initial PT stress; (2) Design of the boundary element; (3) Design of the shear reinforcement; (4) Examination of shear sliding resistance at the wall base; (5) Rebar for preventing out-of-plane movement (6) Energy dissipating elements. Special detailing at the 1st story wall-floor and the 2nd story wall-tube connections is discussed following design of the rocking-wall system.

Quantity of PT strands and initial PT stress - In the design of PFS2, there was a miscommunication and the required design strengths were taken as the value of the design forces, without incorporation of the undercapacity factors. So rather than taking

the required nominal shears and moments as 49 kips/0.75=65 kips and 10,219 kip-in/0.9=11,354 kip-in, respectively, the demands were assumed to be 49 kips and 10,219 kip-in.

Seven 1/2 in. diameter 7-wire GR270 strands were prestressed to a stress level of $0.65f_{pu}$. Following the "Performance Verification of the PreWEC Concept and Development of Seismic Design Guidelines," the predicted base moment resistance of the rocking-wall system was about 10,579 kip-in, which was about 4% larger than the assumed design base moment of the rocking-wall system in the scaled prototype structure (10,219 kip-in) and 7% lower than the correct demand (11,354 kip-in). The calculation procedure is outlined in Appendix B3. As shown in Appendix B3, the contribution from the two end columns to the moment resistance of PreWEC system was only 6.4%, which was small. The amount of initial prestress was selected to ensure the strands would remain elastic at 2% design drift, which is validated in Appendix B3.

As mentioned in Section 3.3.1, the base moment of the rocking-wall system in PFS1 was 10,866 kip-in if the gravity load on the wall was not considered. It was very close to the base moment of the rocking-wall system in PFS2, where the gravity load was transferred to the end columns and contributed little to the base moment of the rocking-wall system. The difference was only about 2.7%:

$$\left|\frac{10866-10579}{10579}\right| \times 100\% \approx 2.7\%$$

It allowed for a direct comparison of the behaviors of the two specimens to demonstrate the impact from different gravity load transfer paths. The comparison of the two specimens is discussed in detail in Chapter 8.

Design of the boundary element - Design of the boundary element in PFS2 was the same as that of PFS1 discussed in Section 3.3.1. The confinement in the wall corners consisted of a #3 stirrup and a #3 crosstie at a 2-in. spacing. Similar to PFS1, a 14-in. long steel channel C6x10.5 was installed on each side of the wall to protect the wall corners.

Design of the shear reinforcement - As mentioned above, the assumed design base shear for the tested rocking-wall system was taken as 49 kips due to a miscommunication. The

actual demand was 65 kips. The shear resistance capacity of the wall in PFS2 is calculated as follows when the shear reinforcement is not considered:

$$V_n = A_{CV}\alpha_c\lambda\sqrt{f_c'} = 68\times6\times2.0\times\frac{1.0\sqrt{6{,}000}}{1000} \approx 63\ kips > 49\ kips, \quad (3.6)$$
$$where\ \alpha_c = 2.0, H_w/l_w = 224/68 \approx 3.3 > 2$$

The nominal capacity was just slightly less than the actual demand (65 kips). Only the minimum shear reinforcement was needed for both the assumed and actual demand. Similar to PFS1, two layers of #3 mesh reinforcement placed at a spacing of 14 in. served as the shear reinforcement.

Examine shear sliding at the wall base - Assuming a coefficient of friction 0.5 at the interface between the wall base and the fiber grout, the shear sliding resistance provided by the compression force from the PT strands at the base of the wall was:

$$F_{V\_PT} = \mu N_{PT} = 0.5\times0.65 f_{pu} n_{strand} A_{strand}$$
$$= 0.5\times0.65\times270\times7\times0.153 \approx 94\ kips > 49\ kips \quad (3.7)$$

Shear sliding was not expected to occur even if the actual demand (65 kips) was assumed.

Rebar for preventing out-of-plane movement - Different from the wall in PFS1, four additional #5 mild rebar were embedded at the base of the wall, as shown in Fig. 3-92. The rebar protruded from the base of the wall and fed into holes reserved in the base block. The rebar was used to guide the wall to ensure it would not "walk" when subject to out-of-plane loading. Locating the dowels in the wall and the receiving holes in the base block was deemed to be the way the system would be constructed in the field. If the dowels did not align with the holes in the base block, new holes could be drilled in the base block to accommodate the deviation more readily than drilling new holes in the thin wall. The fiber grout was prevented from filling the holes in the base block and the rebar were unbonded in the holes. The size of the holes was selected to ensure the rebar would not contact the edge of the holes when the lateral drift of the specimen was 5% in the in-plane direction, which was the upper limit of the lateral displacement applied throughout the test.

Energy dissipating elements - Eight “O-connectors” were attached to the wall and the end columns, which formed the PreWEC system. Each O-connector was welded to pre-

embedded plates in the wall and the end columns. To prevent potential out-of-plane buckling of the O-connectors, horizontal strap plates extended over the top and bottom of the O-connectors. The strap plates were welded to small square plates as thick as the O-connectors (to keep the straps parallel to the O-connectors), and the square plates were welded to pre-embedded plates in the end column as shown in Fig. 3-97 (a). Fig. 3-97 (b) shows a photograph of the O-connector in the test. Because the O-connector would deform more when the wall uplifted, to prevent the O-connector moving out of the bounds of the strap, the bottom strap was wider than the top strap as shown in the photo.

Special detailing of the wall to accommodate connections - Different from PFS1, where a rigid-connected CIP floor system was used to simulate an upper bound interaction between the wall and the surrounding structure, the floor in PFS2 simulated the lower bound interaction with vertical movement isolated connections (BS Italia connections). A total of four connections were used to connect the wall to the floor (two on each side of the wall). The connections transferred horizontal shears while allowing for relative vertical deformation between the wall and the floor system. The BS Italia vertical movement isolated connections consisted of slotted channels embedded in the wall that accommodated the vertical movement of the connections, as shown in Fig. 3-92. The other components of the BS Italia connection are discussed in Section 3.5.4. As shown in Fig. 3-96, V-shaped #4 rebar were placed around each slotted insert to spread the local concentrated force into a larger area of the wall.

As shown in Fig. 3-92, two steel plates, which were 6 in. wide, 10 in. high and 3/8 in. thick, were embedded in the wall to connect with the steel trusses used to simulate the effect of the missing floors in the test specimen. Because the steel truss element was pin-connected to the wall, the steel plate was expected to only sustain an axial force from the steel tube. Four #3 rebar were welded to the back of the plate and embedded in the wall to transfer the axial force from the steel truss element into the wall.

Different from PFS1, where the O-connectors were attached to side columns (HSS tubes) adjacent to the wall, PFS2 featured prestressed end columns in the PreWEC system to attach the O-connectors. The design of the end column is described in detail in Section 3.5.2.

3.5.2 End Columns

End columns were placed 1 in. away from the wall for construction tolerance. In the prototype building, the end columns were precast reinforced concrete columns with a dimension of 30 in. wide and 18 in. deep. After being scaled down, the dimension of the end columns in the test specimen was 10 in. wide and 6 in. deep. The depth of the end columns was the same as that of the wall (6 in.), which had two benefits: (1) the PreWEC (Precast rocking Wall with End Columns) was appealing architecturally because it resulted in a planar surface, and (2) it accommodated installation of the O-connectors to the surfaces of the wall and end columns.

The height of the six-story end column in the prototype building was 864 in. high. After scaling to one-third, the height of the end column in the specimen should have been 288 in. However, because there was only one representative precast floor constructed (for time and cost considerations), the height of the tested end columns was reduced to 78 in. Steel truss elements were used to represent the boundary condition provided by the other floors as discussed in Section 3.5.5. The end columns extended above the 1st story floor and below the steel truss elements. Two O-connectors were connected to each end column with one below the floor and the other above the floor.

End columns in the PreWEC system serve two purposes: connect energy dissipating O-connectors and carry gravity load from tributary area of the rocking walls. Under different loading directions, the directions of the O-connector forces acting on the end column are different. As shown in Fig. 3-98,when the system is loaded to the east, the O-connectors on the west side of the wall pull up the west end column, but the O-connectors on the east side of the wall compress the east end column. The opposite is true for loading to the west.

Design of the end columns should consider both the force equilibrium conditions and moment equilibrium conditions. For the force equilibrium conditions, the tie-down force in the west end column, which includes the prestressed force and the gravity load carried by the end column, should be greater than the forces of the O-connector to prevent the end columns being pulled up. If the end columns lose contact with the base block,

damage to the secondary structural elements (e.g. floor and partition wall etc.) might occur. It is an important factor to be considered when determining the lower bound PT forces in the end column.

On the other hand, the total compression force at the corner of the east end column includes the tie-down forces and the forces of the O-connector. Concrete crushing might occur in the corner of the east end columns because of the large compressive force. Moreover, because the moment arm between the prestressed rod and the resultant compressive force in the corner of the column is small due to a short column width, end columns contribute little to the total moment resistance of the PreWEC system. Applying high PT forces in end columns will not effectively increase the total moment resistance of the PreWEC system.

Therefore, it is recommended to apply the lower bound PT force in the threaded rod to decrease the likelihood of potential damage. Applying the lower bound PT force also decreases the required size of the threaded rod, which saves materials and reduces the cost.

Other than force equilibrium conditions, moment equilibrium conditions of the end columns are another important factor to be considered when determining the lower bound PT forces in the end column. As shown in Fig. 3-99, the line of action of the gravity loads may be out of the bounds of both end columns, which generates an overturning moment (P-delta effect) on the end columns. On the other hand, the resistances of O-connectors might generate an overturning or self-centering moment on the end columns depending on the relative location of the O-connectors and the rotation point of the end columns. To maintain the stability of the end columns, the self-centering moment provided by the prestress forces (and possibly O-connectors) should be larger than the overturning moment generated by the gravity load (and possibly O-connectors) for both end columns.

As shown in Fig. 3-98, for the east end column, the resistance of O-connectors generates a self-centering moment on the east end column before yielding (while they are elastic). Therefore, the self-centering moment was provided by both the prestressed forces and the O-connectors in the east end columns. On the other hand, the resistances of the O-connectors might generate an overturning or self-centering moment on the west

end column depending on the relative location of the O-connectors and the rotation point. Because the O-connectors were very close to the compression side of the end column, their contribution to the self-centering or overturning moment was negligible. The self-centering moment was primarily provided by the prestressed forces in the west end columns. When the initial prestress forces in the east and west end column were the same, the self-centering moment of the west end column was smaller than that of the east end column, which decided the lower bound PT force from the moment equilibrium condition.

To conclude, both force and moment equilibrium conditions of the end column connected to the uplift side of the wall should be considered in determining the lower bound PT force, which shall be the larger under both equilibrium conditions.

Design of the end columns is discussed in detail in the following, including: Lower bound prestressed force in the threaded rod; Design of the threaded rod specifically for the test specimen; Longitudinal reinforcement in the end columns; Confinement of the end columns.

Lower bound prestress force in the threaded rod – The lower bound threaded rod prestress force was the prestress level that was required to inhibit uplift and overturning of the end columns in the tests.

Force equilibrium condition

As discussed above, the tie-down force in the end column, which includes the prestress force and the gravity load carried by the end column, should be greater than the resistances of the O-connectors. Therefore, the prestressed force in the end column shall be governed by the following equation:

$$F_{Ecol\_T} + N_{G\_Ecol} > n_{FO} R_{FO} \tag{3.8}$$

Where F_{Ecol_T} = Prestressed force in the threaded rod; N_{G_Ecol} = Axial load in the end column, including self-weight of the end column and tributary floors (2.8 kip) n_{FO} = Number of the O-connectors attached on the end column away from rotation point of the wall (n_O = 4 in PFS1); R_{FO} = Vertical resistance from O-connectors away from rotation point, assuming it was equal to the yielding resistance of the O-connectors (9.5 kips);

Substitute the above numbers into the equation,

$$F_{Ecol\_T} > n_{FO}R_{FO} - N_{G\_Ecol} = 4\times 9.5 - 2.8 = 35.2\ kips \quad (3.9)$$

Moment equilibrium condition

As discussed above, the line of action of the gravity load sustained by the end columns may be beyond the resultant compressive force in the end column, which generates an overturning moment (P-delta effect) on the end columns. Because there was only one story floor in the test specimen and no distributed mass was placed on the floor, no external gravity load except the self-weight was transferred to the end column. The overturning moment was negligible in PFS2.

To conclude, the lower bound prestress force in the threaded rod was 35.2 kips for the test specimen.

Design of the threaded rod specifically for the test specimen - Although the lower bound prestress force was 35.2 kips, it was decided to prestress the rod in the tested end column to 64 kips. It was equal to one half of the external gravity load applied to the rocking wall in PFS1. This load accounted for the load from the tributary areas of the six floors in the scaled building that would be required to be carried by the end columns. As shown in Fig. 3-99, one disadvantage of using the prestressed rods to simulate the gravity loads is that the action line of the prestressed rods always passes through the center of the end column, which is different from that of the gravity loads. It provides additional resisting moment to the end column instead of overturning moment. However, as calculated in Appendix B3, the contribution from the two end columns to the moment resistance of PreWEC system was only 6.4%, which was small. Therefore, the impact of using prestressed rods to simulate the gravity loads on the end columns was expected to have a negligible effect on the overall behavior of the specimen.

ASTM A193 Grade B7 threaded rods of 1-1/2 in. diameter were selected for the tested end columns. The nominal yield strength of the rod was 105 ksi. The cross-sectional area of the rod was 1.045 in. The rods were post-tensioned to 64 kips and the initial stress in the rods was 61 ksi. The dimension of the threaded rods was selected to ensure the rod would remain elastic throughout the entire test (maximum lateral drift was 5%), as shown in the following.

As shown in Appendix B3, the N.A. depth of the west end column (1.5 in. at 2% drift), which is pulled up by the O-connectors (for eastward displacement of the wall), is smaller than that of the east end column (2.5 in. at 2% drift) which is compressed by the O-connectors. Therefore, the elongation of the rod in the west end column is expected to be higher than that in the east end column. If the rod in the west end column does not yield at 5% drift, the rod in the east end column should not yield either. The stress in the rods at 5% drift is calculated below.

Assuming the N.A. depth of the west end column is 1.8 in. at 5% drift, the elongation of the rod is:

$$\Delta_{rod\_5\%} = \left(\frac{w_{Ecol}}{2} - c_{Ecol\_T}\right)\theta = \left(\frac{10}{2} - 1.8\right) \times 0.05 = 0.16\ in. \tag{3.10}$$

Where $\Delta_{rod\_5\%}$ = Elongation of rods in end columns at 5% drift, w_{Ecol} = Width of end columns, c_{Ecol_T} = Neutral axis depth of the end column at the uplifted side of the wall. The strain in the rod at 5% drift is:

$$\begin{aligned} \varepsilon_{rod\_5\%} = \sigma_{initial\_rod} + \frac{\Delta_{rod\_5\%}}{L_{rod}} &= \frac{64}{29000 \times 1.045} + \frac{0.16}{126.5} \\ &= 0.0033 < \frac{f_{y\_rod}}{E_s} = \frac{105}{29000} \approx 0.0036, not\ yield \end{aligned} \tag{3.11}$$

Where $\varepsilon_{rod\_5\%}$ = Strain in rods in end columns at 5% drift, $\sigma_{initial\_rod}$ = Initial stress of rods in end columns, $\Delta_{rod\_5\%}$ = Elongation of rods in end columns at 5% drift, L_{rod} = Total length of rods in end columns, f_{y_rod} = Specified yield strength of rods in end columns

Verify the N.A. depth of the west end column assumed above:

$$\begin{aligned} c_{Ecol\_T} &= \frac{E_S \varepsilon_{rod\_5\%} A_{rod} + N_{G\_Ecol} - n_{FO} R_{FO}}{\alpha \beta f'_{cc} t} \\ &= \frac{29000 \times 0.0033 \times 1.045 + 2.8 - 4 \times 9.5}{0.92 \times 0.96 \times 1.35 \times 5 \times 6} \approx 1.8\ in. \\ &= 1.8\ in., O.K. \end{aligned} \tag{3.12}$$

Where A_{rod} = Cross-sectional areas of threaded rods, t = Thickness of end columns

Therefore, the 1-1/2 in. threaded rod was not expected to yield in the end columns throughout the test.

Longitudinal reinforcement in the end columns - It was believed that the longitudinal reinforcement in the rocking end columns served the following purposes: support skeleton of the confinement reinforcement; resist the compression force along with the concrete in the end column; and control cracking in the end column.

To satisfy the above design purposes, four rebar were placed in the four corners of the end columns to serve as the skeleton for the confinement reinforcement. They also could assist in carrying the concentrated compression forces in the corners of the columns.

No existing guidelines were found for designing the longitudinal reinforcement in the end columns. To be conservative, the minimum amount of longitudinal reinforcement required by Section 21.6 of ACI 318-11 ("Special moment frame members subjected to bending and axial load") was used for design. According to the code, area of longitudinal reinforcement, A_{st}, shall not be less than $0.01A_g$ or more than $0.06A_g$, where A_g is the gross area of the end columns.

$$0.01A_g = 0.01\times6\times10 = 0.6\ in^2; 0.06A_g = 3.6\ in^2 \tag{3.13}$$

Choose four #4 rebar in the end column. The area of longitudinal reinforcement, A_{st}, is:

$$0.6\ in^2 < A_{st} = 4\times0.2 = 0.8\ in^2 < 3.6\ in^2, O.K. \tag{3.14}$$

Confinement reinforcement at the base of end columns - The confinement reinforcement of the end columns was also designed following Section 21.6 of ACI 318-11.

Spacing of the confinement

According to Section 21.6.4.3: Spacing of the transverse reinforcement shall not exceed the smallest of (a), (b), and (c):

(a) One-quarter of the minimum member dimension;

(b) Six times the diameter of the smallest longitudinal bar; and

(c) s_o, as defined by

$$s_o = 4 + \left(\frac{14 - h_x}{3}\right) \tag{3.15}$$

The value of s_o shall not exceed 6 in. and need not be taken less than 4 in.; h_x = maximum center-to-center horizontal spacing of crossties or hoop legs on all faces of the column.

For the end column, one-quarter of the minimum member dimension (6 in., depth of the column) is 1-1/2 in.; six times the diameter of the smallest longitudinal bar (1/2 in., #4 rebar) is 3 in.; maximum center-to-center horizontal spacing of crossties or hoop legs on all faces of the column is 8-3/4 in. and s_o=5.75 in. The smallest of (a), (b), and (c) is 1-1/2 in., which was used as the spacing of the confinement reinforcement in the end columns.

Amount of the confinement

In the tested end columns, #2 wire at a spacing of 1-1/2 in.is utilized. The amount of transverse reinforcement is examined as follows to satisfy Section 21.6.4.4 (b) of ACI 318-11: The total cross-sectional area of rectangular hoop reinforcement, A_{sh}, shall not be less than required by the following two equations:

$$A_{sh} \geq 0.3 \frac{s * b_c f_c'}{f_{yt}} \left[\left(\frac{A_g}{A_{ch}} \right) - 1 \right] \tag{3.16}$$

$$A_{sh} \geq 0.09 \frac{s * b_c f_c'}{f_{yt}} \tag{3.17}$$

Where A_{sh} = Total cross-sectional area of rectangular hoop reinforcement, s = Center-to-center spacing of transverse reinforcement, b_c = Cross-sectional dimension of member core measured to the outside edges of the transverse reinforcement, f_{yt} = Specified yield strength of transverse reinforcement, A_{ch} = Cross-sectional area of a structural member measured to the outside edges of transverse reinforcement.

Eq. (3.16) and Eq. (3.17) are calculated below in the direction along the depth of the end column (6 in.):

$$A_{sh} \geq 0.3 \frac{s * b_c f_c'}{f_{yt}} \left[\left(\frac{A_g}{A_{ch}} \right) - 1 \right]$$

$$= 0.3 \times \frac{1.5 \times (6 - 0.5 \times 2) \times 5}{90} \times [\frac{6 \times 10}{(6 - 0.5 \times 2) \times (10 - 0.5 \times 2)} - 1]$$

$$= 0.042 \text{ in}^2$$

$$A_{sh} \geq 0.09 \frac{s * b_c f_c'}{f_{yt}} = 0.09 \times \frac{1.5 \times (6 - 0.5 \times 2) \times 5}{90} = 0.0375 \text{ in}^2$$

Therefore, the total area of the confinement in the direction along the depth of the end column shall be more than 0.042 in^2. The total cross-sectional area of the two legs of #2 wire stirrup is $2 \times 0.049 = 0.098\ in^2 > 0.042\ in^2$, O.K.

Eq. (3.16) and Eq. (3.17) are calculated below in the direction along the length of the end column (10 in.):

$$A_{sh} \geq 0.3 \frac{s * b_c f_c'}{f_{yt}} \left[\left(\frac{A_g}{A_{ch}} \right) - 1 \right]$$

$$= 0.3 \times \frac{1.5 \times (10 - 0.5 \times 2) \times 5}{90} \times [\frac{6 \times 10}{(6 - 0.5 \times 2) \times (10 - 0.5 \times 2)} - 1]$$

$$= 0.075\ in^2$$

$$A_{sh} \geq 0.09 \frac{s * b_c f_c'}{f_{yt}} = 0.09 \times \frac{1.5 \times (10 - 0.5 \times 2) \times 5}{90} = 0.0675\ in^2$$

Therefore, the total area of the confinement in E-W direction of the end column shall be more than 0.075 in^2. The total cross-sectional area of the two legs of #2 wire stirrup is $2 \times 0.049 = 0.098\ in^2 > 0.075\ in^2$, O.K.

Fig. 3-100 shows the plan view of the end columns. Fig. 3-101 shows the elevation views of the end columns, viewing from the directions parallel to the width and depth of the end columns, respectively. As shown in the figures, steel plates were embedded in the end columns where O-connectors would be welded. Two small plates, one above and the other below the steel plate for each O-connector, were reserved for the horizontal strap plates as shown in Fig. 3-97.

3.5.3 Transverse Beams Cast with the End Columns

Transverse beams were attached to the end columns to support the precast planks. With the vertical movement isolation connections between the plank and the wall, the tributary load that the wall would have carried would be transferred by the transverse beams to the end columns.

Steel angles attached to transverse beams - To support the precast planks, steel angles (4×4×1/2) were attached to the transverse beams, as shown in Fig. 3-88 denoted as "Angle corbel." The edge beams attached to the columns had similar angles denoted

"Angle ledge" in the figure. Because there was no external mass distributed on the planks during the tests, only self-weight of the planks was transferred to the steel angles.

In PFS2, L-shaped steel angles (4×4×1/2) were used. The steel angles with the selected dimension were expected to remain elastic because of the small force demand and no strain gages were attached to the angles.

Design of the transverse beams - Because there was only self-weight of the planks and that of the steel angles that was transferred to the transverse beams, minimum amounts of longitudinal reinforcement and confinement reinforcement were used when designing the transverse beams. The transverse beams were expected to remain elastic when the props were not attached to them.

According to Section 21.5.2.1 of ACI 318-11, at every section of a flexural member, for top as well as for bottom reinforcement, the amount of reinforcement shall not be less than that given by Eq. (10.3) and $200b_w d/f_y$. At least two bars shall be provided continuously at both top and bottom. Eq. (10.3) is described in Section 10.5.1 of ACI 318-11: At every section of a flexural member where tensile reinforcement is required by analysis the area of the tensile reinforcement shall not be less than that given by:

$$A_{s,min} = \frac{3\sqrt{f_c'}}{f_y} b_w d = \frac{3\times\sqrt{5{,}000}}{60{,}000}\times 10\times 7.5 = 0.27 \text{ in}^2, \quad (3.18)$$

$$A_{s,min} = 200 b_w d/f_y = 200\times 10\times 7.5/60{,}000 = 0.25 \text{ in}^2 \quad (3.19)$$

Where $A_{s,min}$ = Minimum allowable tensile reinforcement, b_w = Width of the cross section of the transverse beam, d = Distance from extreme compression fiber to centroid of longitudinal tension reinforcement

Moreover, according to Section 21.5.2.1 of ACI 318-11, the reinforcement ratio shall not exceed 0.025. The upper bound of the area of the tensile reinforcement is:

$$A_{s,max} = 0.025 b_w d = 0.025\times 10\times 7.5 = 1.88 \text{ in}^2 \quad (3.20)$$

Where $A_{s,max}$ = Maximum allowable tensile reinforcement

Choose two #4 rebar in the bottom and the top of the transverse beam, the total cross-sectional are is 2 × 0.2 = 0.4 in^2, which is between the lower and the upper bound of the required amount of rebar.

Fig. 3-102 shows the plan view of the transverse beam. Fig. 3-103 shows the elevation view of the transverse beam. Because the transverse beam was symmetrical with the center, only one half of the transverse beam is shown in Fig. 3-103. As shown in the figure, there were three types of steel plates embedded in the transverse beams, serving different purposes. The steel plates facing the side surfaces of the transverse beams (transverse beam-plank) were used to connect the steel angles, which were welded to the plates. One steel plate (transverse beam-prop) with four nuts welded on the back was placed at the end of the transverse beams to connect the prop. The nuts were used to accommodate the threading rods from the props for connection. The steel plates (tack welded to 3/8" strap plate) facing the top surfaces of the transverse beams were used to connect the steel straps, which are discussed in Section 3.5.4.

3.5.4 Precast Floor Slab

In the prototype building, precast planks were used as the floor system. The dimensions of the planks used in the test were directly one-third scaled from those used in the prototype building. The floor included the following components: precast planks, plank-to-plank connections, plank-to-beam connections and plank-to-wall connections.

Precast planks - As shown in Fig. 3-104, twelve pieces of precast planks were used in PFS2 to form the modeled 1st floor. Depending on the location of the planks, the twelve pieces of planks were categorized into four types: Planks 1 through Plank 4 as shown in Fig. 3-105 through Fig. 3-108, respectively.

As shown in the figures, one layer of #2 wire mesh reinforcement at a spacing of 6 in. in both directions was placed on top and on bottom of the planks. According to Section 10.5.4 of ACI 318-11, maximum spacing of the flexural reinforcement shall not exceed three times the thickness or 18 in. Because the tested planks were 3 in. thick, the maximum spacing should be smaller than 9 in. The 6 in. spacing adopted in the design satisfied the requirement.

Because the planks were expected to remain elastic throughout the test, only the minimum required shrinkage and temperature reinforcement was used. According to Section 7.12.2.1 of ACI 318-11, area of shrinkage and temperature reinforcement shall

provide at least the following ratios of reinforcement area to gross concrete area, but not less than 0.0014: For slabs where reinforcement with yield stress exceeding 60,000 psi (specified yield strength of #2 wire was 80,000 psi),

$$\rho_{min} = \frac{0.0018\times60{,}000}{f_y} = \frac{0.0018\times60{,}000}{80{,}000} = 0.00135 < 0.0014 \quad (3.21)$$

Where ρ_{min} = Minimum ratio of reinforcement area to gross concrete area

For the edge planks, there were five #2 wires on top and bottom of the planks in the loading direction:

$$\rho = \frac{n_{\#2}A_s}{b_{plank}t_{plank}} = \frac{10\times0.049}{29.75\times3} = 0.0055 > 0.0014, \text{O. K.} \quad (3.22)$$

Where ρ = Ratio of reinforcement area to gross concrete area, $n_{\#2}$ = Number of #2 wires in the floor, b_{plank} = Width of the precast planks, t_{plank} = Thickness of the plank, A_s = Cross-sectional area of the #2 wire

For the middle planks, there were also five #2 wires at the top and bottom of the planks in the loading direction:

$$\rho = \frac{n_{\#2}A_s}{b_{plank}t_{plank}} = \frac{10\times0.049}{26.375\times3} = 0.0062 > 0.0014, \text{O. K.} \quad (3.23)$$

Plank-to-plank connections - Commercial products, JVI Mini V connections, were used as the plank-to-plank connections. As shown in Fig. 3-109(a), the connection consisted of two flat angled faces with tabs to anchor them into adjacent concrete panels and one round bar. Fig. 3-109(b) shows the JVI Mini V connections installed in the planks. Fig. 3-110 shows the drawing of the JVI Mini V connections. As shown in the figure, the tabs of the JVI Mini V connections were embedded in the two adjacent planks separately. The flat plates of the two inserts were inclined, forming a gap between adjacent planks that could hold the round bar. The round bar was welded to the two flat plates and connected the planks together. The V-shaped green lines shown in Fig. 3-105 through Fig. 3-108 represent the embedded flanges in each plank. As shown in the figures, two U-shaped #2 wires (red lines) were placed across the tabs in each plank to distribute local forces transferred by JVI Mini V connections.

According to the design documents, the maximum horizontal force in the floor of the prototype building was 439 kips in the E-W direction (in the direction of the wall plane in Fig. 3-2). Assuming the horizontal force was evenly distributed to the four walls and the amplifier for torsion effects was 1.1 used by the engineer in the design, the maximum horizontal design force transferred to each wall was:

$$V_{floor} = \frac{439}{4} \times 1.1 \approx 121\ kips \tag{3.24}$$

Where V_{floor} = Horizontal design force transferred to each wall

According to the product manual, the nominal shear capacity of a JVI Mini V connection was 8.7 kips. Assuming the horizontal design force was transferred from the floor to the wall through the JVI Mini V connections through both sides of the wall and the shear strength reduction factor was 0.6, the number of JVI Mini V connections required along each side of the wall was:

$$n_{JVI} = \frac{V_{floor}}{2\emptyset F_{JVI}} = \frac{121}{2 \times 0.6 \times 8.7} \approx 12 \tag{3.25}$$

Where n_{JVI} = Number of JVI Mini V connections, $\emptyset$ = Shear strength reduction factor, F_{JVI} = Nominal shear capacity of a JVI Mini V connection.

Therefore, 12 JVI Mini V connections were used along each side of the wall in the prototype building; 4 JVI Mini V connections were used for each of the three panels in the E-W direction. The spacing of the JVI Mini V connections was 720/12=60 in. 720 in. was the total length of the diaphragm in the E-W direction.

Because there were no scaled products available, the same JVI Mini V connections used in the prototype buildings were used in the test specimen. To prevent the plank from twisting, at least two JVI Mini V connections were needed along each plank-to-plank connection. To be conservative, it was decided to use three connections at each plank-to-plank interface, as shown in Fig. 3-104. The number of connections was selected to ensure that there were two connections along each plank-to-plank interface even when one of the three connections failed, so that the structural integrity of the entire floor was maintained.

Plank-to-beam connections - Strap plates were used on top of the planks to connect the precast planks to the edge beams and the transverse beams. According to the force equilibrium condition at the floor-column joint shown in Fig. 3-111, the forces that the strap plates sustained were equal to the difference between the shear forces in the adjacent edge columns above and below the floor. Conservatively, it was assumed that the shear force in the edge column above the floor was zero and the edge column below the floor formed plastic hinges on the top and the bottom. The maximum possible forces that the strap plates would sustain were achieved under this circumstance. The shear force in the edge column below the floor is calculated as follows:

$$V_{col} = \frac{M_{col}}{H_{col}/2} = \frac{11299}{144/2} \approx 157\ kips \tag{3.26}$$

Where M_{col} = Moment resistance of the edge column under sustained axial loads; H_{col} = Height of the edge column (144 in.). M_{col} was calculated using the sectional analysis module in OpenSees and the calculation process is shown in Appendix E. The maximum possible forces that the strap plates would sustain was V_{col}.

If the steel strap plates with a dimension of 4 in. wide, 6 in. long and 3/8 in. thick were used at the floor-edge beam connection, the nominal yield strength for each strap plate (A36 steel material) was:

$$F_{y\_strap} = f_y A_{strap} = 36 \times 4 \times \frac{3}{8} = 54\ kips \tag{3.27}$$

Where F_{y_strap} = Nominal yield strength for each strap plate, A_{strap} = Cross-sectional area each the steel strap

The number of strap plates required at the floor-edge beam connection is calculated:

$$n_{strap} = \frac{V_{col}}{F_{y\_strap}} = \frac{157}{54} \approx 3 \tag{3.28}$$

To be conservative, it was decided to use two strap plates in each edge plank. Because there were four planks at the plank-to-edge beam connections, there were eight steel plates in total at the plank-to-edge beam connections.

At the plank-to-transverse beam connections, long steel strap plates, which were 4 in. wide, 17 in. long and 3/8 in. thick, were welded to the embedded plates in the planks on

either side of the transverse beams and to the transverse beams. The long strap plate was anchored to the two adjacent planks and tack welded to the transverse beam to avoid buckling of the plate. Similar to the plank-to-edge beam connections, two long strap plates were used for each plank and there were eight steel strap plates at the plank-to-transverse beam connections.

Because the dimensions of the strap plates were already very small, it was difficult to further scale them down to be used in the test specimen. It was decided to use the strap plates of the same dimension in the specimen. The number of strap plates used in the specimen was also the same as that used in the prototype building. The purpose was to ensure that there were two strap plates at each end of each plank in case one of them failed, so that the structural integrity of the entire floor was maintained. Fig. 3-112 and Fig. 3-113 show the plank-to-edge beam and plank-to-transverse beam connections in the test specimen, respectively. As shown in both figures, a strip of 1/8 in. thick Korolath shim layer was placed between the planks and the steel angle, which was used to protect the local contact region of the plank. Fig. 3-114 and Fig. 3-115 show the finished plank-to-edge beam and plank-to-transverse beam connections in the test specimen respectively.

The rectangles marked by cyan lines in Fig. 3-105 through Fig. 3-108 represent the embedded steel plates in each plank. As shown in the figures, U-shaped #2 wires (red lines) were placed around each plate to distribute local forces transferred by strap plates.

Plank-to-wall connections - Commercial products, BS Italia connections, were used for plank-to-wall connections. As shown in Fig. 3-116, the BS Italia connectors consisted of a vertical slotted channel with a rotatable stud, a V-shaped plate and a high strength threaded bolt. The slotted channel was embedded in the wall and the V-shaped plate was welded to the steel plates pre-embedded in the planks. As shown in Fig. 3-117, the high strength bolt went through the hole in the V-shaped plate and was screwed into the rotatable stud in the slot channel to connect the two pieces together. Because the stud was able to slide vertically along the channel, the planks were isolated from the vertical uplift of the wall. In the horizontal direction, the V-shaped plate came into contact with the channel transferring horizontal forces between the planks and the wall.

In the sections below, the location of the BS Italia connections is discussed first, followed by the discussion of the number of BS Italia connections used.

Existing component tests of BS Italia connections (Watkins 2013) show that the connections are able to fully isolate the floor if the uplift at the connector location is limited to 1 in. The BS Italia connections were placed 48 in. away from the wall ends. The location was selected to ensure the uplift at the connector location was smaller than 1 in. until 3% drift such that the floor would be fully isolated from the wall at least at the design drift (2%).

Performing the similar iteration process described in Appendix B3, it was found that the N.A. depth of the wall was 6.8 in. at 3% drift. The maximum uplift at the connector location was calculated as follows:

$$\Delta_{BS} = \left(s_{BS} - c_{wall\_3\%}\right)\theta = (40 - 6.8) \times 0.03 \approx 1\ in., O.K. \tag{3.29}$$

Where Δ_{BS} = Uplift of the wall at the location of the BS Italia connection, s_{BS} = Distance between the BS Italia connection and the compressed wall end, $c_{wall\_3\%}$ = Neutral axis depth of walls at 3% drift

As mentioned earlier at "Plank-to-plank connections" section, the maximum horizontal design force transferred to each wall was about 121 kips. According to the existing component test of BS Italia connections, the measured shear capacity of one BS Italia connection was about 50 kips (Watkins 2014). Therefore, the required number of BS Italia connections was:

$$n_{BS} = \frac{V_{floor}}{F_{BS}} = \frac{121}{50} \approx 2.4 \tag{3.30}$$

Where n_{BS} = Number of BS Italia connections, F_{BS} = Nominal shear capacity of a BS Italia connection

To maintain symmetry, four BS Italia connections were used in the prototype building. Because there were no scaled products available, the same BS Italia connections used in the prototype building were used in the test specimen. As shown in Fig. 3-104, two BS Italia connections were placed back to back on each side of the wall. Because the force transferred to each BS Italia connection was not large, the BS Italia connection was not expected to be damaged in the test.

The rectangles marked by green lines in Fig. 3-108 represent the embedded steel plates in Plank 4 for the BS Italia connections. As shown in the figures, two U-shaped #3 rebar (green lines) were placed around each plate to distribute local shear forces transferred by the BS Italia connections. Other than the U-shaped rebar, a V-shaped #3 rebar (magenta line) was placed parallel to the steel plate in the plane of the slab to distribute potential tensile forces transferred by the BS Italia connections during out-of-plane loading.

3.5.5 Steel Truss

Assuming both the wall and the end columns rotated like rigid bodies, the floors at different stories were expected to undergo similar vertical movements and in-plane rotations as long as the plank-transverse beam and plank-edge beam connections were the same in each story.

To simplify the construction of the test specimen, only the 1st story precast floor was constructed as a representative floor. Because the planks were connected to the wall by the vertical movement isolated connections and they were pin-connected to the transverse beams as well as edge beams, the constraint from the five missing upper story floors on the wall was not significant. Steel truss elements fabricated with tubes (4×4×1/4) that were pin-connected to the wall and the gravity columns were used in the second story of the specimen, only to preserve proper boundary conditions for the 1st story gravity columns. The clevis hinge shown in Fig. 3-23(a), which was used in PFS1, was reused for the pin connection of the 2nd story steel truss element in PFS2.The steel trusses were expected remain elastic during the test.

3.5.6 Edge Columns and Edge Beams

The dimensions of the tested reinforced concrete edge columns and edge beams were directly scaled from those in the prototype building. Therefore, they were the same as those in PFS1, as discussed in Section 3.3.5.

Different from PFS1 where CIP edge columns and edge beams were used, precast edge column and edge beam assemblages were constructed at a precasting plant and installed in PFS2 at the MAST laboratory. Typical detailing recommended by the PCI Design

Handbook (PCI 2004) was used for the precast edge columns. Fig. 3-118 shows the plan view of the column base connection. Fig. 3-119 and Fig. 3-120 show the elevation views of the column base connections. As shown in the figures, longitudinal rebar of the precast column were welded to a steel base plate; the steel plate was connected to the base block using four 1-1/4 in. diameter threaded rods; grout was poured between the base plate and the base block to form a smooth contact surface. As will be discussed in Section 4.5.2, the nuts for the 1-1/4 in. rods were not connected in the first two phases of testing to promote rocking behavior of the edge columns; similar to the rocking wall concept, the rocking column concept was anticipated to alleviate potential damage in the edge columns. In the following testing phases, the nuts were tightened, rigidly connecting the edge columns to their respective base blocks.

During construction, the steel cage of the edge columns was assembled at the MAST lab before sending to the precasting plant, where the assembled steel cages were welded to the steel base plates. However, it was found that the welding operation was difficult to perform because the base of the longitudinal rebar was uneven and the confinement reinforcement limited accessibility. Consequently, the quality of the weld was difficult to control. In practice, longitudinal rebar or anchors should be welded to the steel base plate and subsequently embedded into the column prior to casting. The better accessibility for welding with this approach would promote better weld quality. The impact of the construction procedure on the performance of the edge columns will be discussed in detail in Section 7.6.

Similar to PFS1, threaded rods were placed inside the edge columns and post-tensioned to 31 kips to simulate the gravity loads from tributary areas of the six story floors. Different from PFS1 where 3/4 in. diameter rods were used, 1 in. diameter rods were used in PFS2. The purpose was to prevent the rods from yielding, which was easier to monitor during the test.

3.6 Construction of PFS2

3.6.1 Construction of the Base Block of the Wall

The steel cage of the PFS2 wall base block was similar to that of PFS1, with a couple of exceptions. Only the different detailing of the PFS2 base block is discussed here.

As shown in Fig. 3-121, because no pocket was reserved in the base block in PFS2, the fiber grout was poured above the top surface of the base block. Neither the wood blockout for pocket nor the foam blockout for the observation opening was needed in the PFS2 base block.

Six oval-shaped corrugated sleeves were embedded in the base block. The sleeves were 3-1/8 in. wide and 4-1/2 in. long. Two of the sleeves were used to accommodate the unbonded threaded rods in the end columns adjacent to the wall, as shown in Fig. 3-122. The other four sleeves were used to accommodate the rebar that protruded from the base of the wall, as shown in Fig. 3-123. The sleeves were carefully placed to ensure that the longer dimension (4-1/2 in.) was in the in-plane loading direction. It was designed to prevent the rebar from contacting the edge of the holes to drifts up to 5% during the in-plane loading. The purpose of the rebar was to keep the wall from "walking" on the base block because of the lack of a pocket for the wall.

The top block of PFS2 was nearly identical to that of PFS1, except that the locations of the corrugated sleeves in the top block were different. Because PFS2 was shorter in plan than PFS1 to accommodate the end columns, the rebar protruded from the wall into the top block from different locations than those of PFS1. The PT anchors used in both the bottom and the top base blocks of PFS2 were the same as those in PFS1.

3.6.2 Construction of the Base Block for the Edge Columns

Fig. 3-124 shows the steel cage built for the edge column base block. As shown in the figure, a corrugated sleeve was placed in the middle of the column cage. It was used to accommodate the 1 in. diameter unbonded threaded rod, which would be post-tensioned to simulate the gravity load on the edge column. Four 1-1/4 in. diameter threaded rods were placed in the steel cage, which were used to connect to the steel base plate of the

edge columns. A small bearing plate was connected to each threaded rod at the base of the base block, which anchored the rod to the base block after casting the concrete.

Fig. 3-125 shows the built base block after casting the concrete. As shown in the figure, only a fraction of the 1 in. PT threaded rod extended beyond the base block, but the total length of the edge column was about 96 in. (two stories high). A coupler nut was used to connect the short rod with the rest portion of the rod. The four 1-1/4 in. diameter rods used to attach the edge column base plate extended about 6 in. beyond the base block. The 6 in. extension length was selected to accommodate a 1 in. thick fiber grout layer, a 1-1/2 in. thick steel base plate of the column and 1-1/2 high bolt nuts with additional 2 in. tolerance.

3.6.3 Construction of the Wall Panel

As for PFS1, the PFS2 wall panel was also constructed in the precasting plant (Molin Concrete). The construction process was similar to that described in Section 3.4.1 for the PFS1 wall. Only the different detailing of the PFS2 wall is discussed in this section.

The slotted channels of the four BS Italia connections were pre-embedded in the wall. Fig. 3-126 shows the slotted channels of the BS Italia connections. Because the thickness of the slotted channels was 3-1/4 in., the total thickness of two slotted channels installed back to back was 6-1/2 in., which was larger than the designed depth (thickness) of the wall (6 in.). To accommodate placement of the slotted channels, a portion of the wall where the BS Italia slotted channels were to be located was thickened to 7 in. As shown in Fig. 3-127, 1/2 in. thick plywood sheets were glued to the casting bed with a 15-in. strip cutout to reserve an additional 1/2 in. depth on the back face of the wall. Directly above the strip on the back face, as shown in Fig. 3-128, the side formwork of the wall was 1/2 in. higher over a 15 in. length; that with two steel angles installed across the wall panel at the ends of the extended side formwork created a 1/2 in. thickened region on the top face of the wall.

As shown in Fig. 3-129, two U-shaped rebar were placed around the embedded slotted channel to spread the concentrated load to a larger area of the wall. The steel embedment for the 2nd story steel truss element is shown in Fig. 3-130.

The finished PFS2 wall cage is shown in Fig. 3-131. The four #5 rebar which protruded from the base of the wall (to prevent the wall from walking and to serve as a guide) are also shown in the figure. The cast wall is shown in Fig. 3-132. As shown in Fig. 3-133, the protective cap over the embedded BS Italia slotted channel was pried off after the concrete in the wall was cured. The thickened portion of the wall with slotted channels is shown in Fig. 3-134.

3.6.4 Erect the Wall and Form Fiber Grout Layer

The precast wall was shipped and tilted up in the MAST laboratory. After the wall was tilted up, it sat above two shims on the base block. A total station was used to level the wall in 3D space; lateral supporting EFCO frames were built around the wall to stabilize it.

A rectangular wood formwork with a dimension of 69 in. long, 8 in. wide and 1-1/2 in. high was built around the wall. At this stage, the formwork was built only for the fiber grout beneath the wall but not for the end columns. The fiber grout extended 1/2 in. from each end of the wall (68 in. long).

The fiber grout was poured into the formwork on the base block with the wall in place. To ensure a smooth contact, the grout was over-poured into the pocket 1/2 in. higher than the bottom face of the wall. The product PAGEL V1A in PFS1 was used for the fiber grout. Different from PFS1 where the grout was 1-1/2 in. thick, the grout layer in PFS2 was only 1 in. thick. It was expected that when the grout layer was thinner, the settling of the fiber grout might be mitigated and make the fiber grout stronger.

3.6.5 Install the Top Block and Post-tension the Wall Panel

The top block was craned onto the wall panel after the fiber grout was cured. Similar to PFS1, plain grout was pasted between the top block and the wall to create a smooth contact. The holes in the top block which accommodated the reinforcement that protruded from the wall were filled using fiber grout.

After the top block was installed, seven PT strands were slowly put through the aligned holes in the top block, the wall, and the base block. Similar post-tensioning procedure to

that of PFS1 was followed. Table 3-5 shows the recorded values during the post-tensioning process. As shown in the table, the PT force after release was 185 kip, which was very close to the target PT force (188 kip). At the beginning of the test date of PFS2, the recorded PT force in the strands was 177.3 kips, which was about 7.7 kips smaller than the PT force at the post-tensioning date due to the PT loss.

3.6.6 Install the End Column and the Transverse Beam

During fabrication of the end columns and transverse beams, it was found that the west end column encountered consolidation issues in the stirrup confined region, as shown in Fig. 3-135. Because multiple concrete gages were placed in the base of the end column, the concrete in those regions was not properly stirred, which caused the consolidation issues. High strength grout was filled into the void to repair the columns. It was noteworthy that the poor concrete was not chipped away before putting high strength grout due to a tight schedule of construction in the precasting plant. Although the columns appeared to be repaired, some poor pockets might exist in the columns.

The two precast end column and transverse beam assemblages were shipped to the MAST laboratory after they cured. Each assemblage was lifted by the crane and positioned next to the wall, as shown in Fig. 3-136. A 1-1/2 in. diameter threaded rod was slowly put through the hole in the end column and the base block and fit into the threaded hole in the pre-embedded plate in the base block.

As shown in Fig. 3-137, wood formwork with a dimension of 12-1/2 in. long, 8 in. wide, 1-1/2 in. high was built around the base of the end column. The fiber grout extended 2 in. beyond the end column (away from the wall), and it extended 1/2 in. from the other end of the end column (toward the wall) connecting with the existing fiber grout layer beneath the wall. Fig. 3-138 shows the fiber grout layer beneath the end column. Although not shown in the figures, a lumber spacer (4×4×1-1/2 approximately) with a hole in the middle was placed between each end column and the base block to prevent the grout falling into the base block.

The end column was post-tensioned after the fiber grout cured. As shown in Fig. 3-139, a load cell was installed on the 1-1/2 in. diameter threaded rod on top of the end column

to monitor the PT force. The PT forces recorded when pre-tensioning the rods were 69.2 kips and 70.8 kips in the east and the west end columns, respectively. At the beginning of the test date of PFS2, these PT forces had dropped to 60.8 kips and 61.8 kips in the east and the west end columns, respectively, due to losses.

3.6.7 Install the Edge Column and the Edge Beam

The two precast edge column and edge beam assemblages were shipped to the MAST laboratory after they cured. Before assembling the edge column and the edge beam with the base block of the edge column, a piece of 1 in. rod (110 in. long) was connected to the existing short rod protruding from the base block through a coupler nut. The edge column and edge beam assemblages were craned and placed above the base block, with the 1 in. rod being fed into the hole in the edge column and the four 1-1/4 in. rods through the holes of the column base plate, as shown in Fig. 3-140.

After pre-tensioning the nuts of the 1 in. rod, the edge columns were temporarily rigidly connected to the base block. The entire assemblage was lifted by the crane and positioned on the strong floor of the MAST laboratory.

Wood formwork with a dimension of 20 in. wide, 8 in. deep, 1-1/2 in. high was built around the base of the edge column. Fiber grout was poured into the formwork 1/2 in. higher than the bottom of the base plate, creating a smooth contact between the base plate and the base block. Similar to the construction of end columns, a lumber spacer (4×4×1-1/2 approximately) with a hole in the middle was placed between each edge column and the base block to prevent the grout falling into the base block. Fig. 3-141 shows the cured fiber grout layer beneath the edge column.

The edge column was post-tensioned after the fiber grout cured. Similar to the end columns, a load cell was installed on the 1 in. diameter threaded rod on top of each edge column to monitor the PT force. The recorded PT forces when pre-tensioning the rods were 31.3 kips and 31.4 kips in the east and the west edge columns, respectively. Because of the PT loss, the recorded PT forces in the east and the west edge columns both decreased to about 28.7 kips at the beginning of the test date of PFS2.

3.6.8 Install the Precast Planks

The twelve pieces of precast plank were shipped to the MAST laboratory after they cured. They were lifted and placed onto the steel angles of the transverse beam and the edge beam by a fork lift. Each plank was positioned to ensure they were parallel to each other and the gaps between the planks and the edge beam and the transverse beam were uniform across the connections, as shown in Fig. 3-142.

Multiple field welding tasks were completed in sequence: plank to plank connections (JVI Mini V), the plank to edge beam connections (strap plates), plank to plank and transverse beam connections (strap plates), and plank to wall connections (BS Italia).

As shown in Fig. 3-143, between each pair of planks there were three gaps along the longitudinal edges formed by the embedment of the JVI Mini Vs. Because the gaps were inclined, weldable round bars fit snugly into the gaps. The round bars were welded to the embedment in both planks to connect them together.

Steel straps were carefully placed onto the embedded plates of the planks and the edge beams as well as the transverse beams, as shown in Fig. 3-144. They were welded on both ends to form the longitudinal connections across the transverse edges of the planks.

The bolt of the BS Italia connections was placed through the V-shaped connectors and fitted into the rotatable studs in the slotted channels, as shown in Fig. 3-145. The two legs of each V-shaped connector were welded to the embedded plate in the plank, forming the plank-wall connections.

3.6.9 Weld the O-connectors and Install the Steel Trusses

After finishing the welding tasks for the precast floor system described above, the eight O-connectors were welded to the end columns and the wall, as shown in Fig. 3-146. The welding operation was performed by a welder from a local construction company. The 2^{nd} story steel trusses were craned onto the finished floor and attached between the wall and the edge columns, as shown in Fig. 3-147. The construction of the entire specimen was completed.

3.7 Material Properties in PFS1 and PFS2

A summary of the material properties in PFS1 and PFS2 is given in Table 3-6, Table 3-7 and Table 3-8 for the strands, steel, and concrete, respectively. Brief descriptions of the materials used in the two tests are provided below.

3.7.1 PT Strands

The wall PT strands consisted of 1/2 in. diameter 7-wire Grade 270 strands. The strands in the two tests came from the same batch. The 3/8 in. diameter strands were only used in the unbonded PT slab in PFS1. The mill of certification for the two types of strands is given in Table 3-6.

3.7.2 Mild Reinforcement and No.2 Wire

The tension tests for the mild reinforcement and the wire were conducted in the 200 kip MTS loading frame in the Galambos Structural Engineering Laboratory, as shown in Fig. 3-148. The testing procedure followed the requirements in the Annex A9 of ASTM A370-12a. Each sample was cut to approximately 22 in. length and mounted between the loading grips. As shown in the figure, an extensometer was mounted to the rebar sample to measure the average strain over the gage length. Strain gages were also attached to some rebar samples to measure the local strain. Because failure of the strain gages was generally observed when the strain was in excess of 20,000 με, the strain recorded by the extensometer was used to obtain the stress-strain curve of the rebar and the wire. The readings from the strain gages were used to validate the average strain obtained from the extensometer, in case slip or malfunction of the extensometer occurred during the loading.

The testing procedure followed the requirements in ASTM A370-12a. A slow loading rate of 0.0625 in. per minute was used to pull the samples to fully capture the yielding plateau of the steel. When the steel material started to harden, the loading rate was increased twice to shorten the testing time. To protect the extensometer, it was removed

when the stresses of the samples barely increased after the hardening. The test continued until the sample fractured and the ultimate stress was recorded.

No. 3 weldable mild reinforcement conforming ASTM A706 was used in the walls, RC gravity (edge and end) columns, and RC beams in the two tests. The bars were fabricated from the same batch for the two tests. Fig. 3-149 shows the stress-strain curves of the #3 rebar obtained from the material testing. As shown in the figure, three samples were tested and the results were consistent.

No. 5 rebar weldable mild reinforcement was used in the boundary elements of the walls in the two tests. They were fabricated from the same batch for the two tests.

No. 2 wires were used for the stirrups and crossties in the RC gravity (edge and end) columns and RC beams in both tests. They were also used as the mesh reinforcement in the planks in PFS2.

3.7.3 Steel Coupons

The 200 kips MTS loading frame was also used for pulling the steel coupons, as shown in Fig. 3-150. Three types of steel coupons were tested, including the O-connectors in the two tests, the mega beam cover plates in PFS1, and the steel straps in PFS2. The testing procedure followed the requirements in ASTM A370-12a. Because the gage length of the coupons was smaller than that of the rebar samples, the loading rate was decreased to 0.01 in. per minute to fully capture the yielding plateau of the steel. When the steel coupons started to harden, the loading rate was increased twice. The test continued until the coupon fractured and the ultimate stress was recorded.

3.7.3.1 O-connectors in PFS1 and PFS2

The O-connectors used in both specimens were from the same batch. Four coupons were made from the same material. Fig. 3-151 shows the stress-strain curves obtained from the coupon test. As shown in the figure, three coupons were tested and the results were consistent.

3.7.3.2 Cover Plates in PFS1

Two coupons were made from the same steel plate that was used to fabricate the mega beam cover plates in the component test as well as the PFS1 system test. Because the

maximum thickness of the steel coupons that the loading grips could hold was 3/4 in., the 7/8 in. coupons were ground down to 3/4 in. thick. The grinding process should not change the material property of the steel coupons.

3.7.3.3 Strap Plates in PFS2

Three coupons were made from the same batch of material used to fabricate the strap plates in PFS2.

3.7.4 Concrete

Standard 4 x 8 in. concrete cylinders were made in every concrete casting activity. Compression tests following ASTM C39/C39M were conducted to measure the compressive strength of concrete. Split-cylinder tests following ASTM C496/C496M were conducted to obtain the splitting tensile strength of concrete. Standard 6 in. × 6 in. × 24 in. concrete prisms were produced to obtain the flexural tensile strength of the concrete following the ASTM C78/C78M testing procedure.

Three separate concrete casting activities were conducted in PFS1, including the wall panel, the unbonded PT slab with 1st story frames, and the short story columns. Three separate concrete casting activities were conducted in PFS2, including the wall panel, the east rocking column together with the west gravity column and the east rocking column together with the west gravity column. The material properties given in Table 3-8 represent the average strength of the concrete obtained from the respective samples tested. Table 3-9 lists the casting dates, the MAST testing dates and the material testing dates. Note there was some lag between the MAST testing dates and the material testing dates due to inaccessibility to the material test equipment.

3.7.5 Fiber Grout

Standard 2 in. cube samples were made when pouring the fiber grout into the pocket of the base block in PFS1. Compression tests of the cube samples were conducted to obtain the compressive strength. The test procedure followed ASTM C109/C109M. Because the molds for the grout sample were not available when pouring the fiber grout in PFS2, the

cube samples were not made in PFS2. The strength results from the fiber grout samples are given in Table 3-8.

Table 3-1 Stages of PFS1 wall post-tensioning process

Target PT stress	Target load (kip)	Target DSI gage pressure (psi)	Estimated actual DSI gage pressure (psi)*	Estimated load based on gage pressure (kip)	Load cell reading (kip)	Measured elongation (in)	Expected elongation (in)**
20%	24	526.3	600	27.8	26.3	0.125	0.316
30%	36	789.5	750	34.7	33	0.1875	0.474
40%	48	1052.3	1000	46.3	46.5	0.375	0.632
50%	60	1313.7	1300	60.1	59.2	0.5625	0.790
60%	72	1575.2	1575	72.8	70.1	0.6875	0.948
70%	84	1836.6	1825	84.4	82.5	0.875	1.106
Power Seating	84	0	0	0.0	9.4	0.6875	0.964
100% + PT loss	129.4	2789.2	2875	133.0	129	1.5625	1.878
After release		0	0	0	119.3	1.375	

* Because the dial gage on the jack was crude, it was difficult to get it to the exact targeted pressure. This column shows the estimated jack pressure based on the reading from the dial gage.

** Initial Length of the strands = 280 in.

Table 3-2 Stages of PFS1 slab post-tensioning process in the longitudinal direction (target load after seating loss: 7.2 kip)

Order of stressing	Strand end #	Initial stress (gage pressure, psi)	Force before seating (k)	Force after seating (k)	Elongation after seating (in.)	2nd stress (gage pressure, psi)	Force before 2nd seating (k)	Final force after seating (k)	Final elongation after seating (in.)
1	1	950	5.4 W [-4.6 E*]	3.67 W [-3.7 E]	5/8	1753 (9.76 k target)	10.4 W [-9.0 E]	8.0 W [-8.0 E]	1-1/8
2	2	950	N/A	N/A	5/16	1750	N/A	N/A	3/4
3	3	1150	5.4	1.95	7/16	2037 target (11.48 k target) 2100 actual	11.1	7.9	1-1/8
4	4	1150	N/A	N/A	1/2	2100	N/A	N/A	7/8
5	5	1150	-5.6[1]	-3.22	9/16	1860 target (10.41 k target) 1900 actual	-10.3	-6	7/8
6	6	1150	N/A	N/A	7/16	2100	N/A	N/A	1-1/16
7	7(5)**	2100	N/A [-10.9 W]	N/A -9.1	1/4	N/A	N/A	N/A	1-1/8
8	8(4)**	1800	N/A	N/A	0	2100	N/A	N/A	7/8
9	9(2)**	2100	N/A	N/A	1/2	N/A	N/A	N/A	1-1/4

* Note a couple of load cells had negative readings (wiring issue)

** Number in parentheses indicates strand end number at opposite end (W end)

Table 3-3 Stages of PFS1 slab post-tensioning process in the transverse direction (target load after seating loss: 9.6 kip)

Order of stressing	Strand End #	Initial stress (gage pressure, psi)	Force before seating (k)	Force after seating (k)	Elongation after seating (in.)	2nd stress (gage pressure, psi)	Force before 2nd seating (k)	Final force after seating (k)	Final elongation after seating (in.)
10	10	1200	6.87	3.75	5/16	2350 (13.36 k target) 2300 actual	14.0	7.9	5/8
11	11	2500	16.5	14.2	7/8	N/A	N/A	14.2	7/8
12	12	2750	15.7	11.7	1	N/A	N/A	11.7	1
13	13	1500	8.9	6.5	5/16	2230 target 2300 actual	12.8	10.5	3/4
14	14	2400	N/A	N/A	13/16	N/A	N/A	N/A	13/16
15	15	2400	N/A	N/A	¾	N/A	N/A	N/A	3/4
16	16	2400	N/A	N/A	11/16	N/A	N/A	N/A	11/16
17	17	2400	N/A	N/A	3/4	N/A	N/A	N/A	3/4
18	18(10)*	2400	N/A [14.5 S]	N/A [7.9]	0	2700	N/A [16.1]	N/A [10]	11/16

* Number in parentheses indicates strand end number at opposite end (S end).

Table 3-4 PT losses between the PT tensioning and test date

Measure	E–W longitudinal direction (kips)				N–S transverse direction (kips)			
date	FPTW1	FPTW2	FPTW3	FPTW4	FPTSE1	FPTSE2	FPTSE3	FPTSE4
PT date	8.00	7.90	6.00	8.00	10.50	7.90	14.20	11.70
Test date	7.59	6.99	6.07	5.40	8.73	8.08	12.07	9.68
PT loss	-0.41	-0.91	0.07	-2.60	-1.77	0.18	-2.13	-2.02

Table 3-5 Stages of PFS2 wall post-tensioning process

Target PT stress	Target load (kip)	Target DSI gage pressure (psi)	Estimated actual DSI gage pressure (psi)	Load cell reading (kip)	Measured elongation (in)
20%	38	840	850	40	0.5625
50%	94	2040	2040	94	1.188
Power Seating	64	0	0	80	1
100% + PT loss	202	4350	4440	202	2.3125
After release	188	0	0	185	2.125

Table 3-6 Strand mill certification

Application	Size (in.)	Grade	Tested modulus (Mpsi)	Actual area (in^2)	Yield point (lbf)	Breaking strength (lbf)	Elongation (%)
Wall (PFS1 & PFS2)	1/2	270	29.1	0.152	40,038	42,952	5.20
Floor (PFS1, N-S)	3/8	250	28.5	0.0798	20,400	23,100	6.26
Floor (PFS1, E-W)	3/8	250	29.0	0.0813	21,133	22,797	5.47

Table 3-7 Material properties of the steel reinforcement

Specimen	Material	Designation and location	f_y (ksi)	f_u (ksi)	ε_{sh} (%)	ε_{su} (%)
PFS1 & PFS2	Strand	GR270 1/2 in. wall	263.4	282.6	-	5.2
PFS1		GR250 3/8 in. PFS1 slab	255.6	289.5	-	6.3
PFS1 & PFS2	Reinforcement	GR60 #3 wall & column	66.5	86.4	2.08	11
PFS1 & PFS2		GR60 #5 wall	68.1	95.5	0.92	16.5
PFS1	Wire	#2 column	90.5	-	-	-
PFS2		#2 column & planks	85.5	-	-	-
PFS1	PFS1 Mega Beam cover	GR36 7/8 in. mega beam	49.3	79.7	0.71	20.8
PFS2	PFS2 steel strap	GR36 3/8 in. steel strap	47.0	74.6	1.32	16.0
PFS1 & PFS2	O-connector	GR36 7/16 in. wall	60	73.2	1.87	21.2

Table 3-8 Material properties of the concrete

Specimen	Material	Designation and location	f_c (ksi)	f_{t_split} (ksi)	f_{t_beam} (ksi)	E_c (ksi)
PFS1	Concrete	Nominal 6 ksi wall	11.226	0.9	-	6,410
		Nominal 5 ksi slab & 1st story column	7.045	0.563	0.766	4,503
		Nominal 5 ksi 2nd story column	6.694	0.579	0.757	4,734
	Fiber grout	Nominal 13 ksi foundation	8.647	-	-	-
PFS2	Concrete	Nominal 6 ksi wall	10.389	0.653	0.559	5,586
		Nominal 5 ksi East PreWEC end column & West edge column & planks	8.261	0.537	0.633	5,328
		Nominal 5 ksi West PreWEC end column & East edge column & planks	8.841	0.606	0.58	5,243

Table 3-9 Summary of the casting date, MAST test date and material test date

Specimen	Casting activity	Casting date	MAST testing date	Material testing date
PFS1	Wall panel	09/27/2013	03/12/2014 - 03/24/2014	05/20/2014 - 06/03/2014
	Unbonded PT CIP slab & 1st story frames	01/08/2014		05/20/2014 - 05/28/2014
	Short columns	01/15/2014		05/20/2014 - 05/22/2014
PFS2	Wall panel	03/04/2014	05/12/2014 - 05/22/2014	05/27/2014 - 05/29/2014
	East rocking column & West gravity column	04/04/2014		05/27/2014 - 05/29/2014
	West rocking column & East gravity column	04/06/2014		05/27/2014 - 05/29/2014

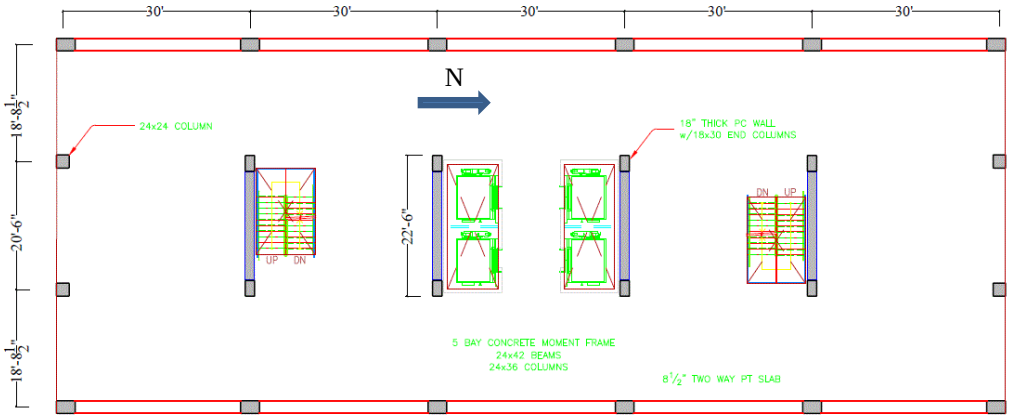

Fig. 3-1 Plan view of the prototype building using unbonded PT slabs

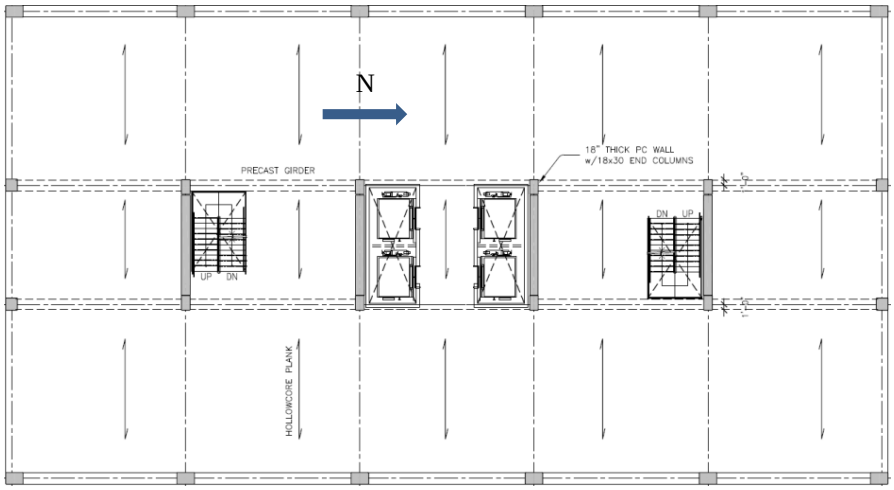

Fig. 3-2 Plan view of the prototype building using precast hollow core planks

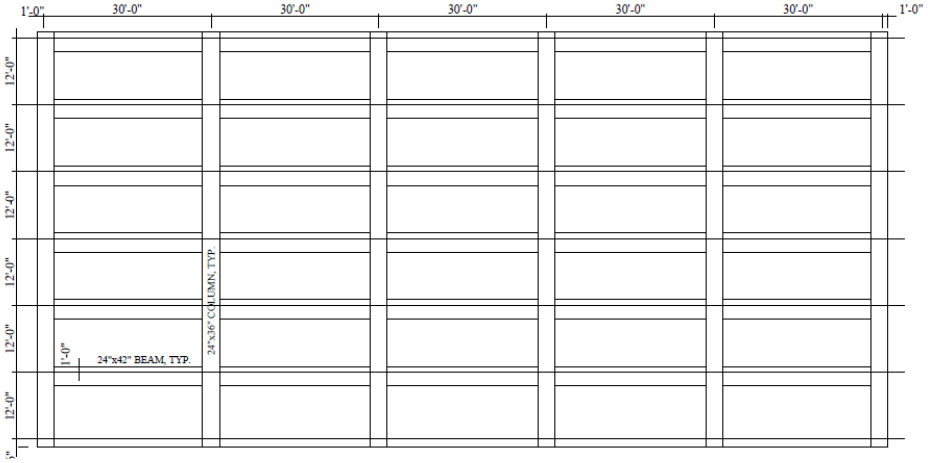

Fig. 3-3 Elevation view of the prototype building

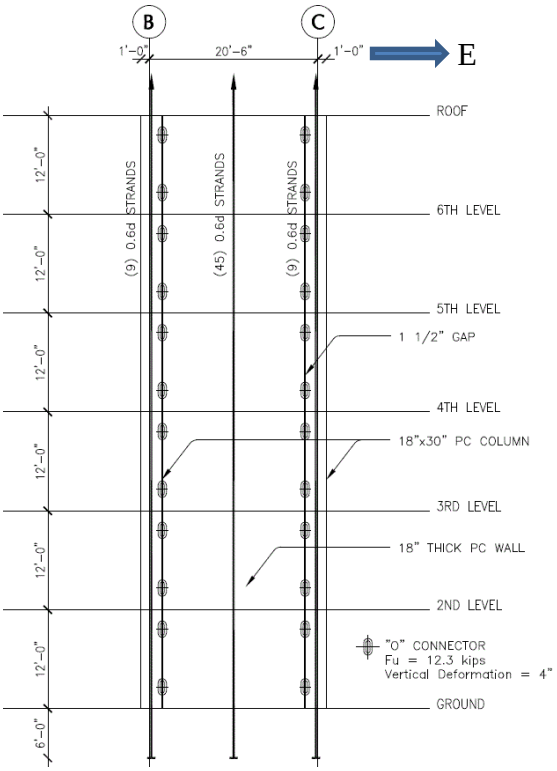

Fig. 3-4 PreWEC system with end columns

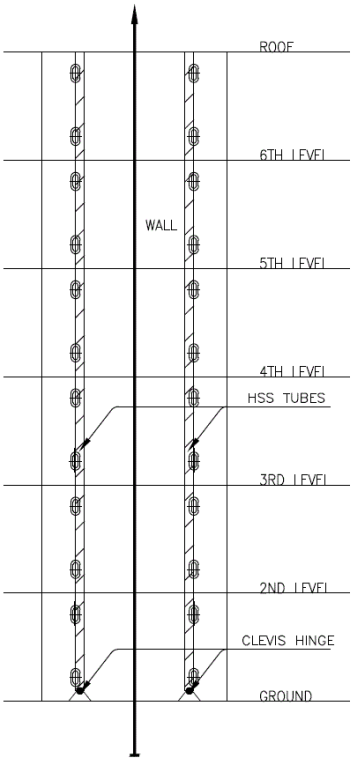

Fig. 3-5 PreWEC with side columns

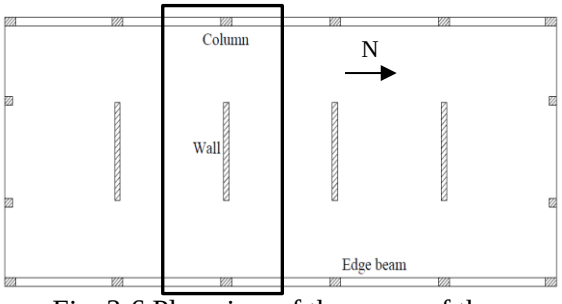

Fig. 3-6 Plan view of the scope of the specimen (No props)

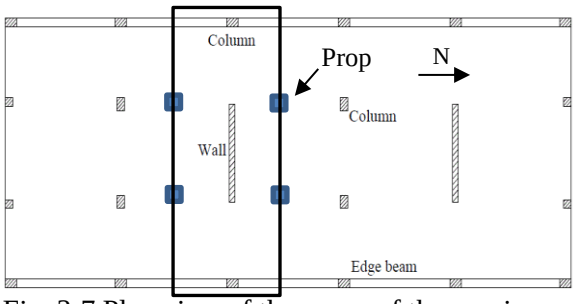

Fig. 3-7 Plan view of the scope of the specimen (With props)

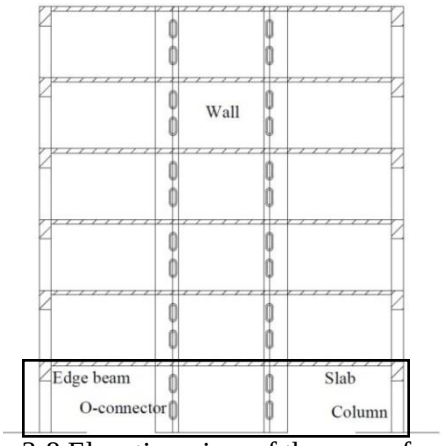

Fig. 3-8 Elevation view of the scope for the specimen PFS1 and PFS2

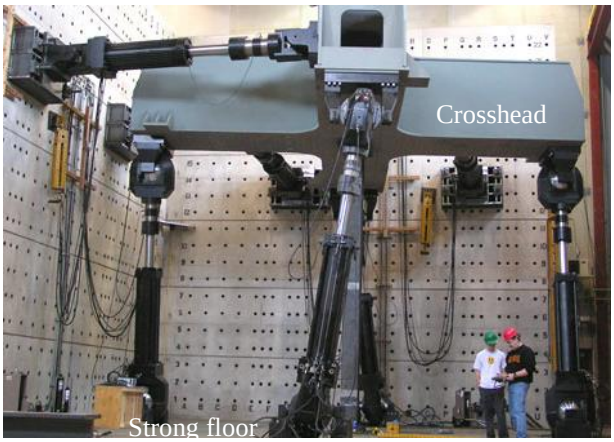

Fig. 3-9 MAST 6DOF control testing system

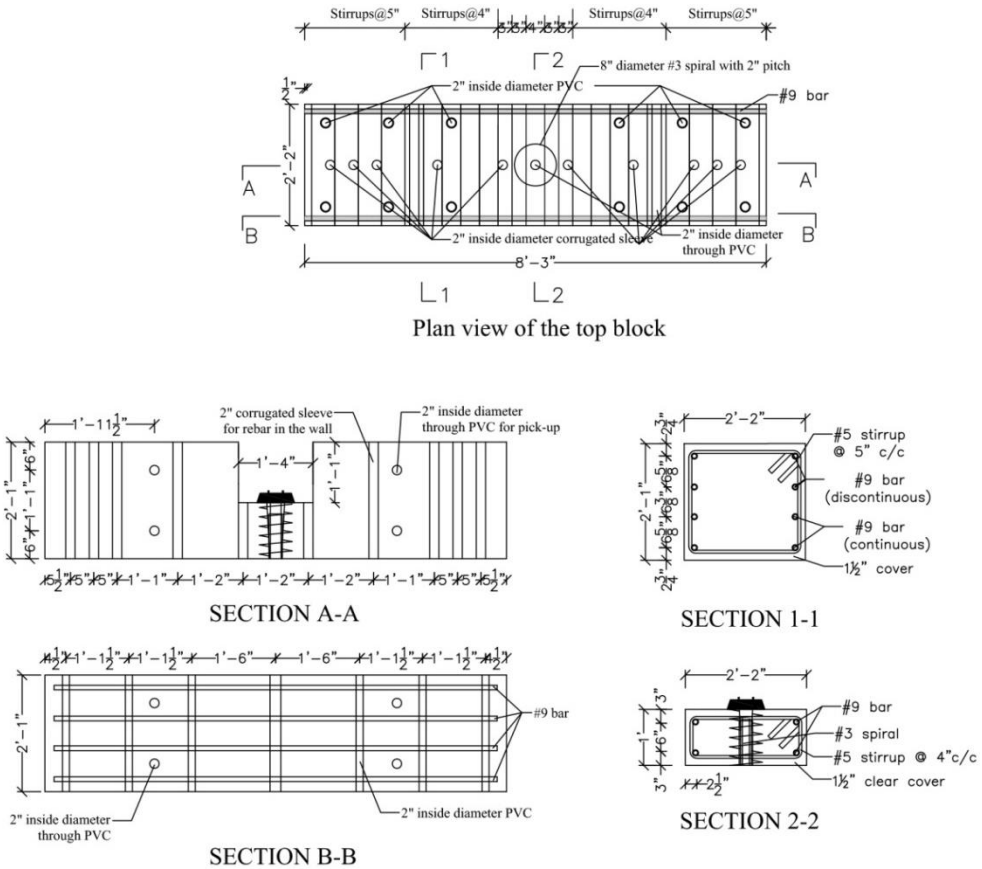

Fig. 3-10 Design of the top blocks

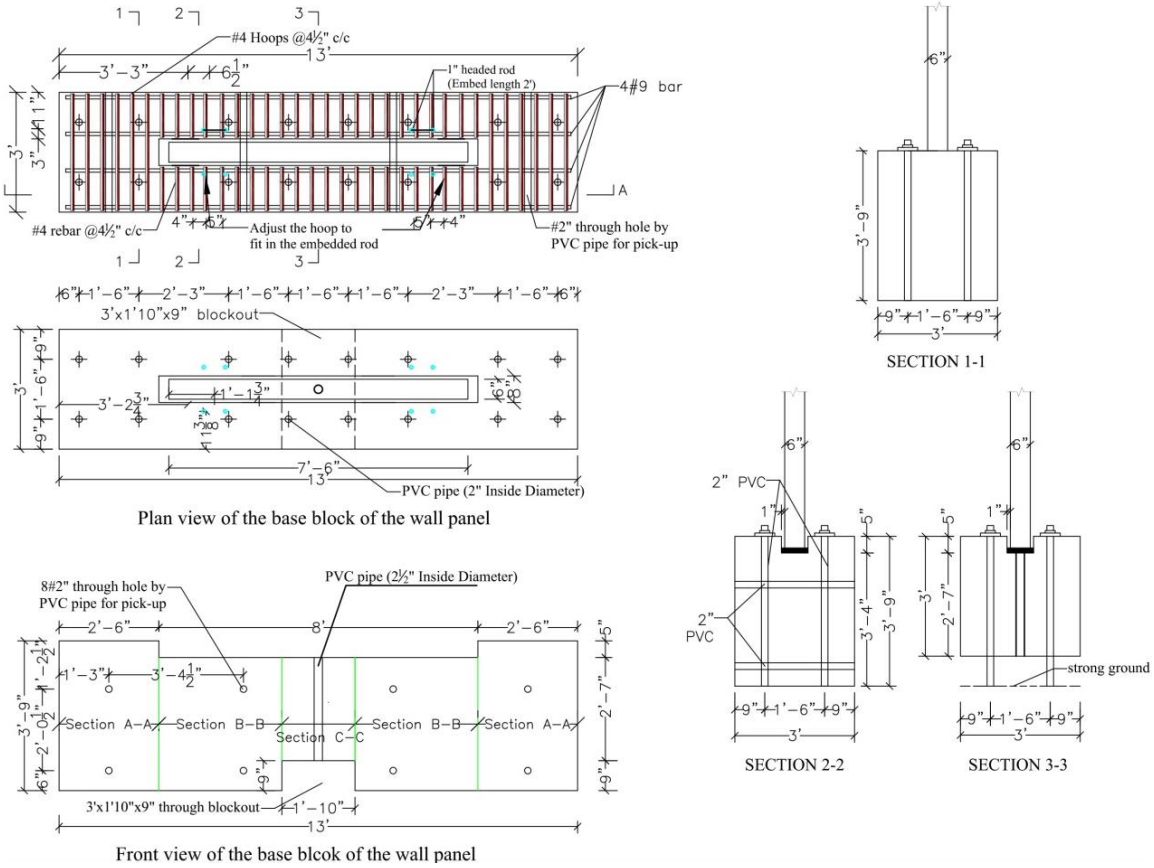

Fig. 3-11 Plan and sectional views of the rocking wall base block for PFS1

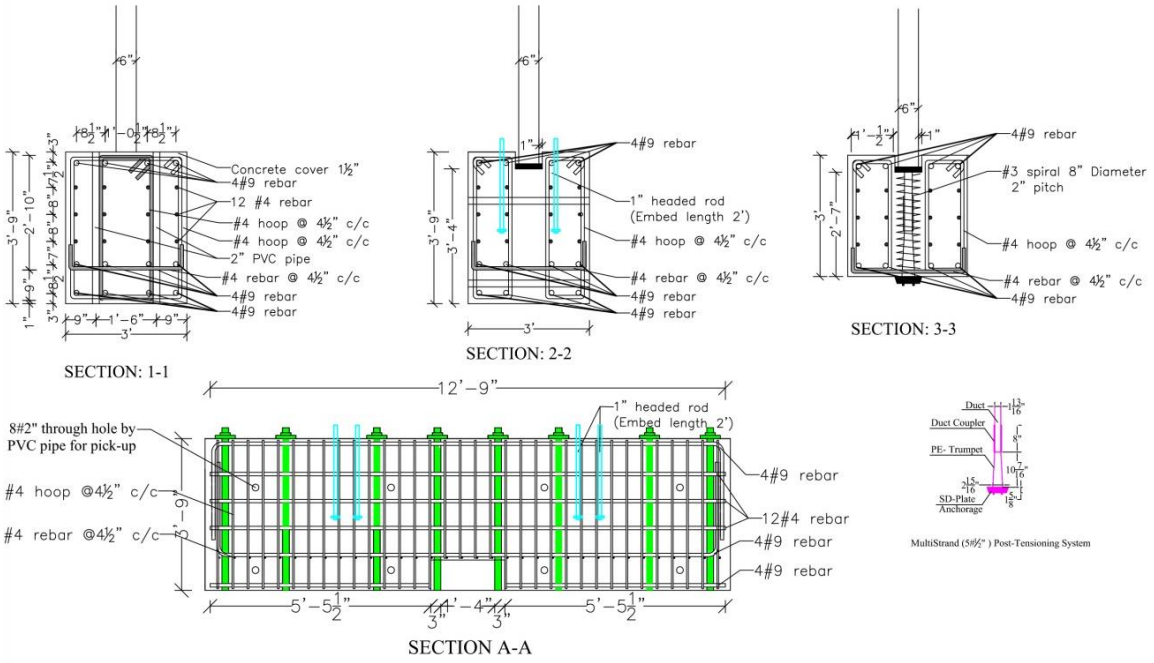

Fig. 3-12 Reinforcement details of the rocking wall base block for PFS1

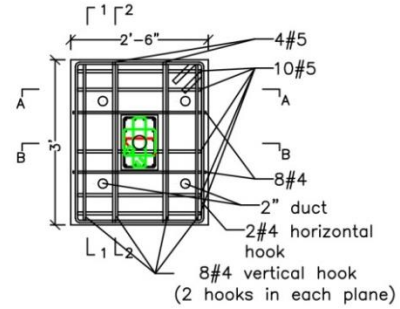

Plan view of the base block of gravity column

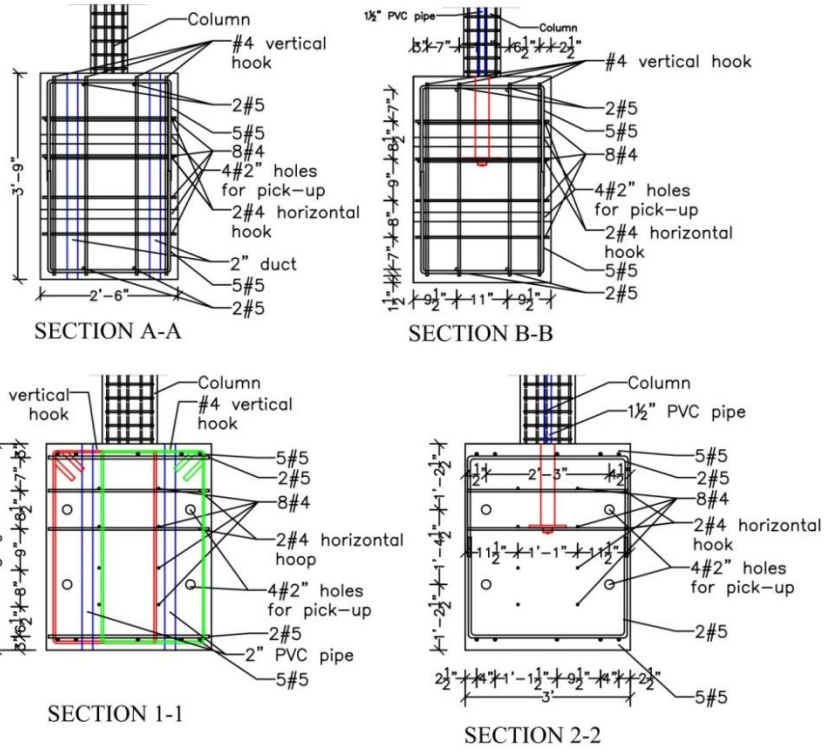

Fig. 3-13 Details of the column base blocks for PFS1

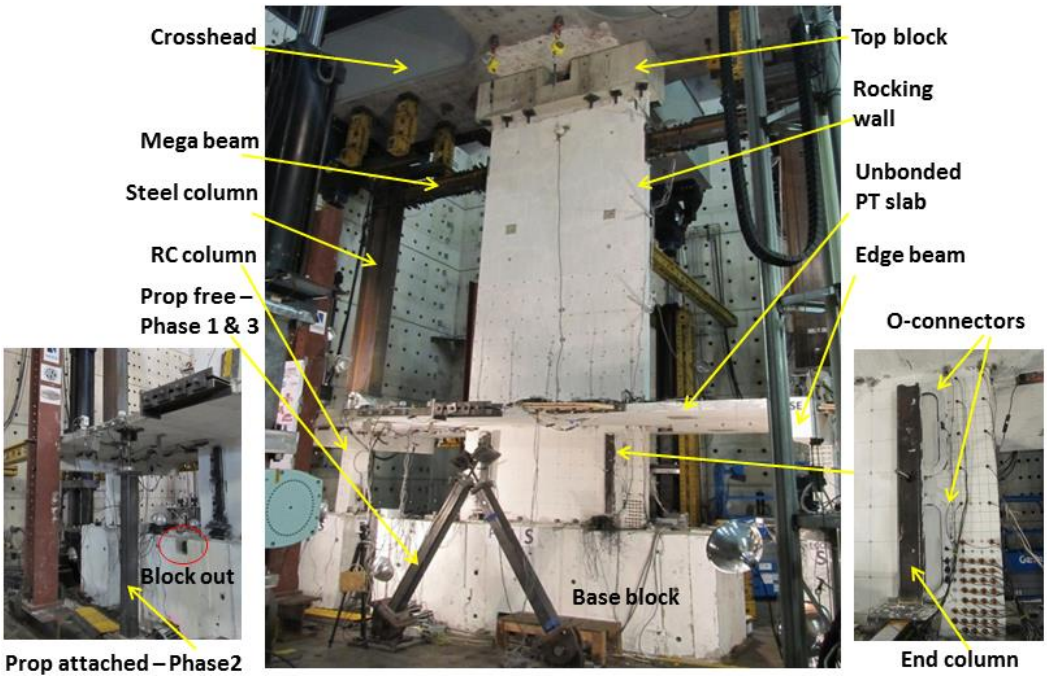

Fig. 3-14 Overview of PFS1

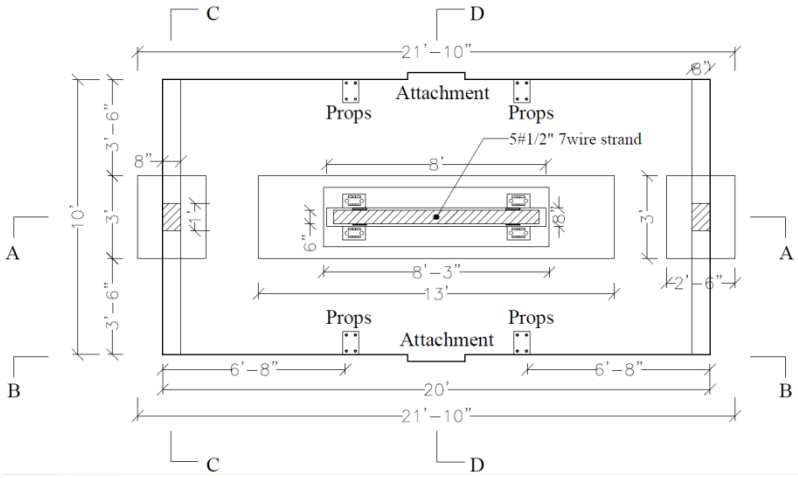

Fig. 3-15 Plan view of PFS1

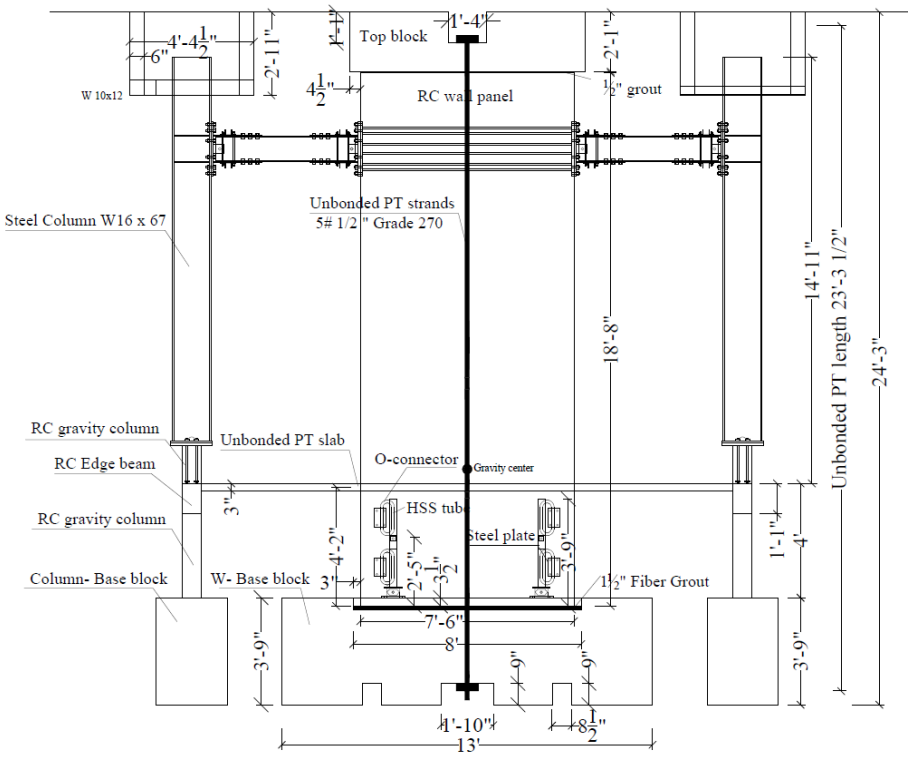

Fig. 3-16 Elevation view of PFS1 at Section A-A

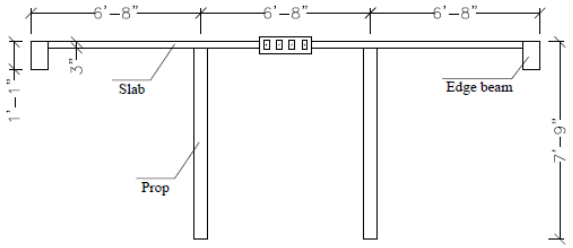

Fig. 3-17 Elevation view of PFS1 at Section B-B

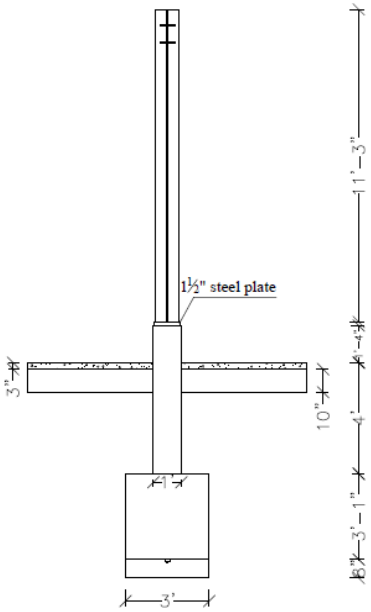

Fig. 3-18 Elevation view of PFS1 at Section C-C

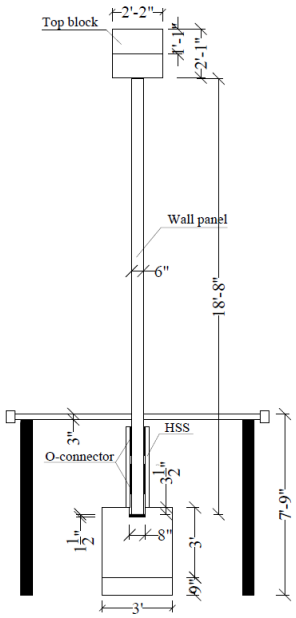

Fig. 3-19 Elevation view of PFS1 at Section D-D

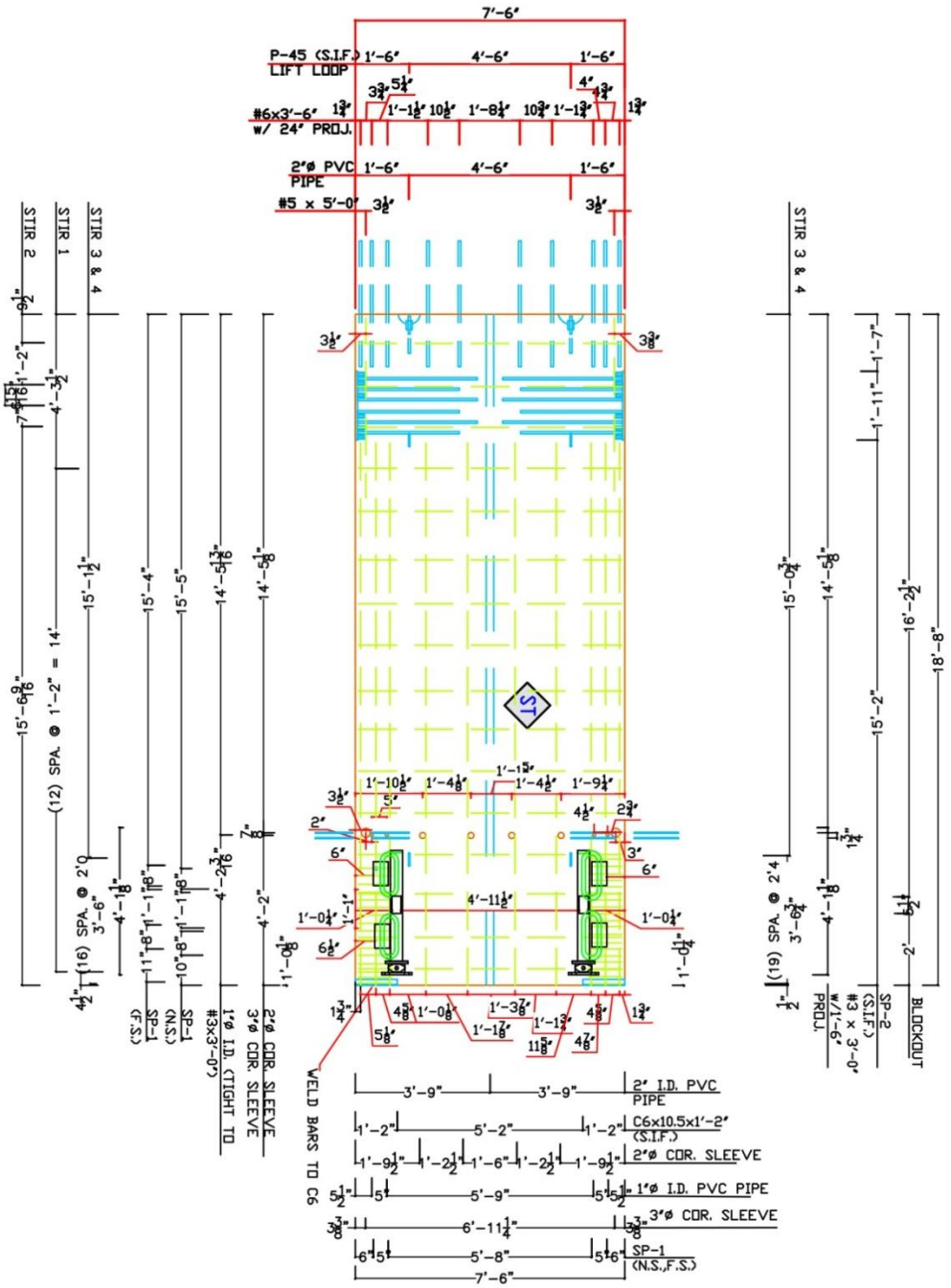

Fig. 3-20 Detailed elevation view of PFS1 PreWEC system (Drawing from precaster)

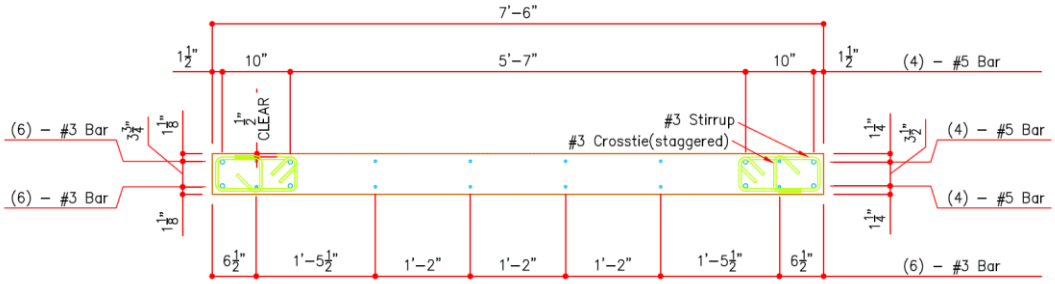

Fig. 3-21 Cross section of PFS1 wall panel at the base

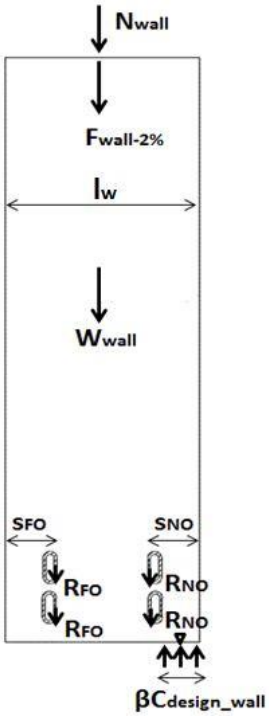

Fig. 3-22 Load distribution in the rocking-wall system

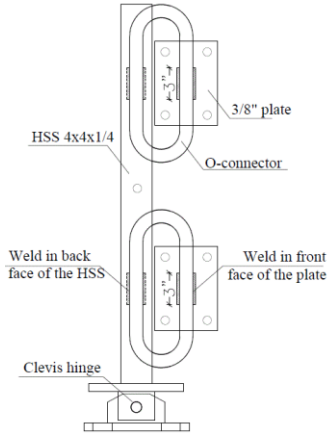

(a) Connection of the O-connector and the HSS tube

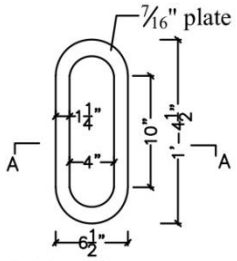

(b) Design of the O-connector

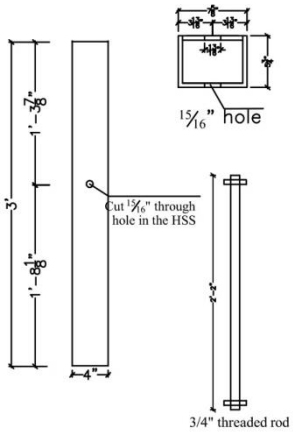

(c) Design of the HSS tube

Fig. 3-23 Detail of the O-connectors in PFS1

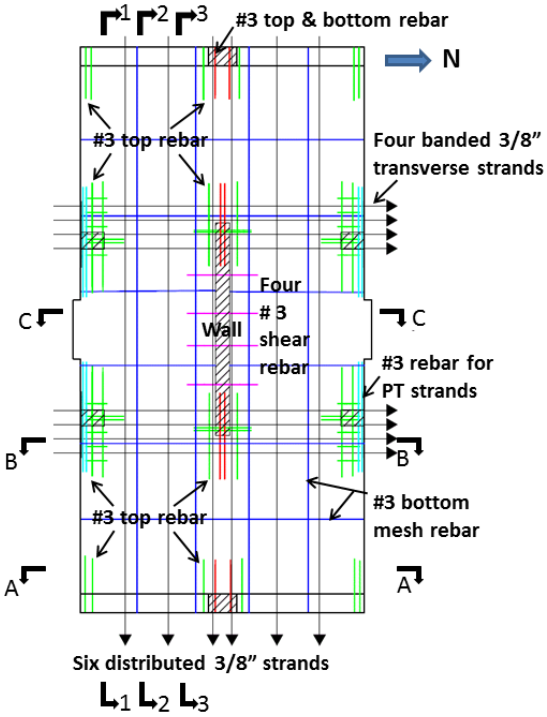

Fig. 3-24 Plan view of the floor slab in PFS1

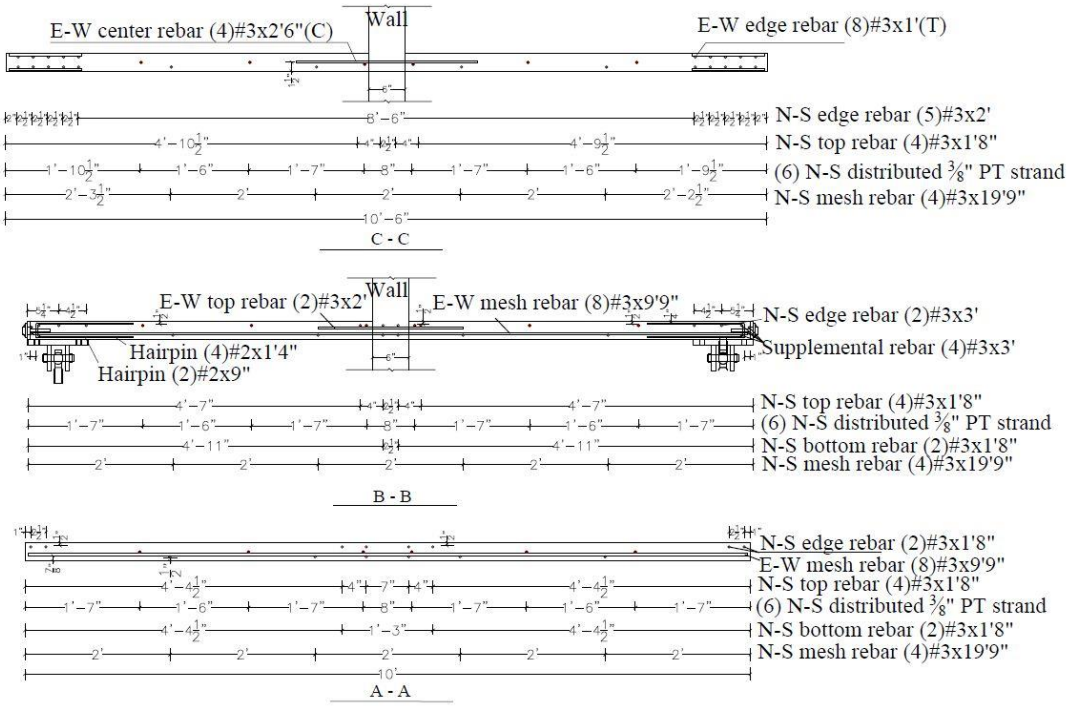

Fig. 3-25 Reinforcement layout at the A-A, B-B and C-C slab cross sections

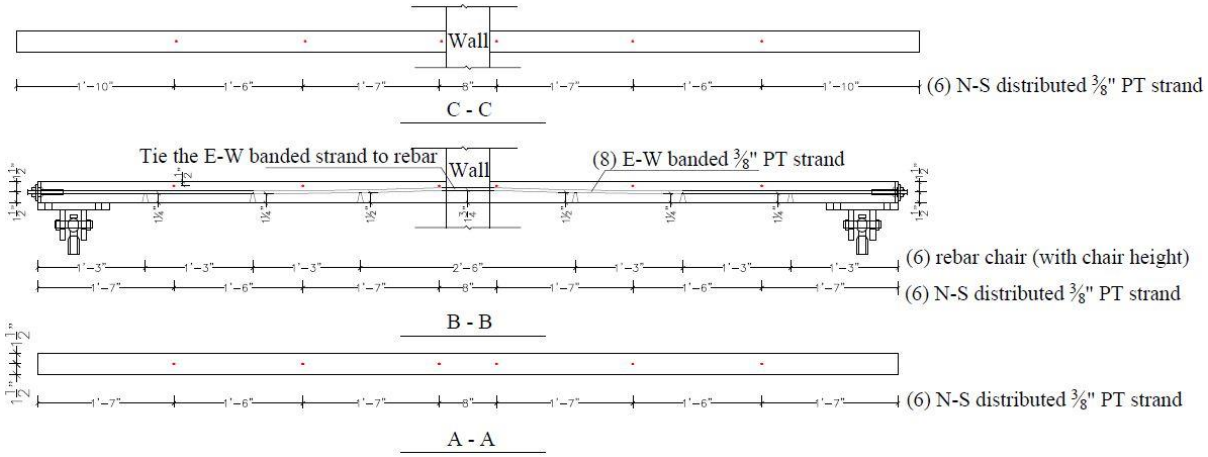

Fig. 3-26 Strand layout at the A-A, B-B and C-C slab cross sections

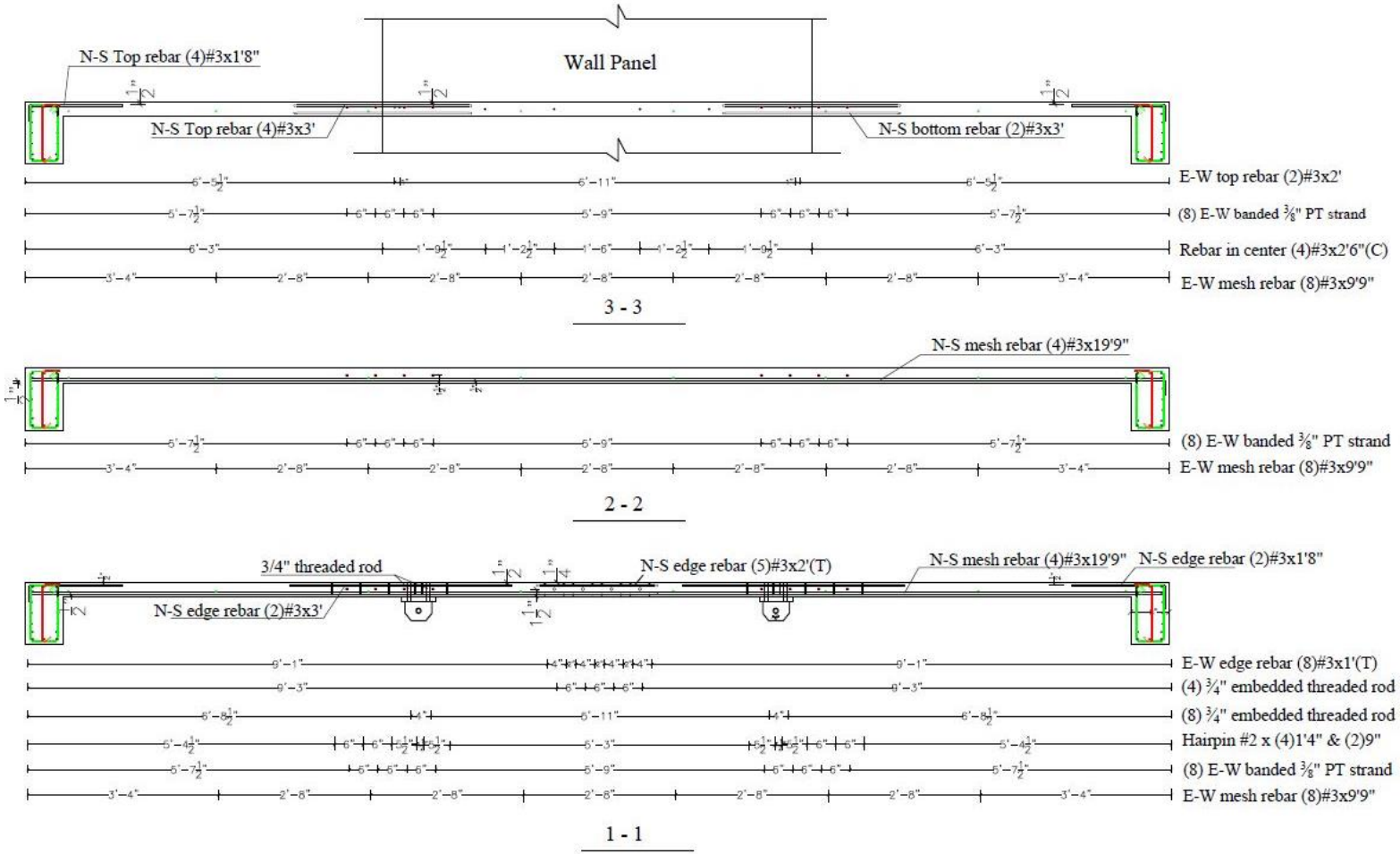

Fig. 3-27 Reinforcement layout at the 1-1, 2-2 and 3-3 slab cross sections

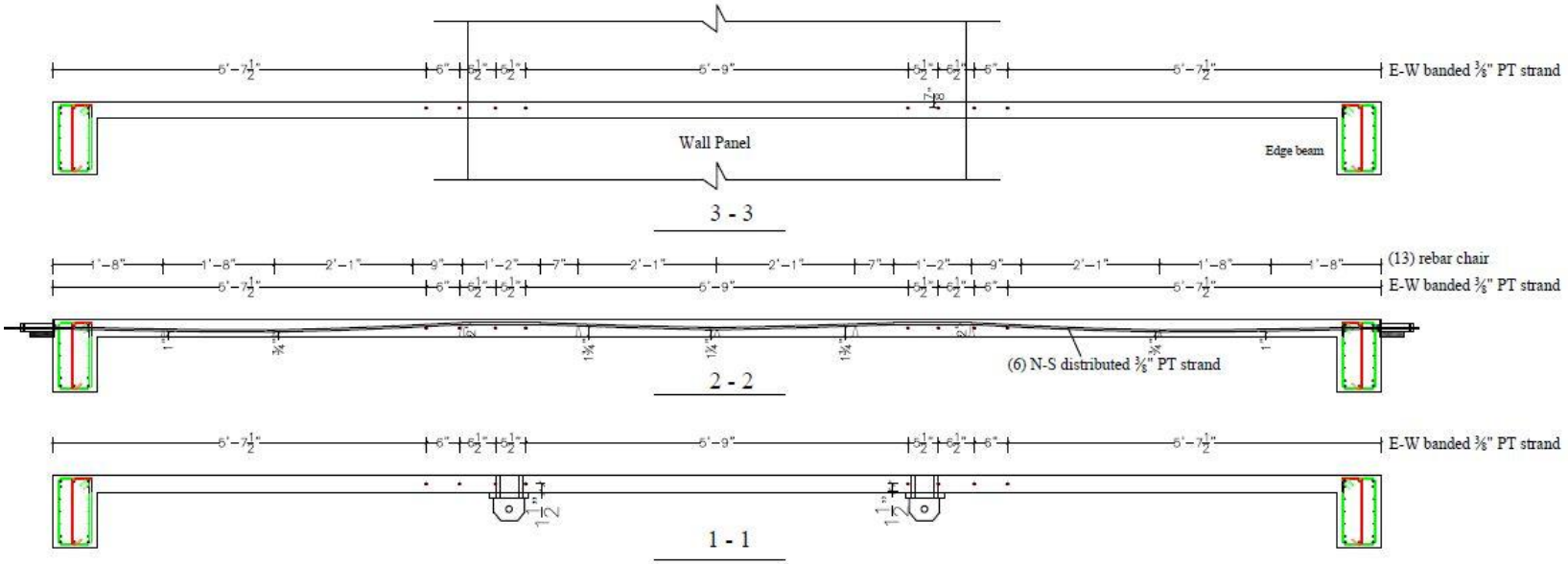

Fig. 3-28 Strand layout at the 1-1, 2-2 and 3-3 slab cross sections

Fig. 3-29 Anchorage zone of the transverse strands

Fig. 3-30 Bonded rebar at floor-column connection

Fig. 3-31 Strand and rebar layout at the wall-floor connection

Fig. 3-32 Strand and rebar of the slab running through the wall

Fig. 3-33 Layout of the reinforcement and strands of the floor slab before casting

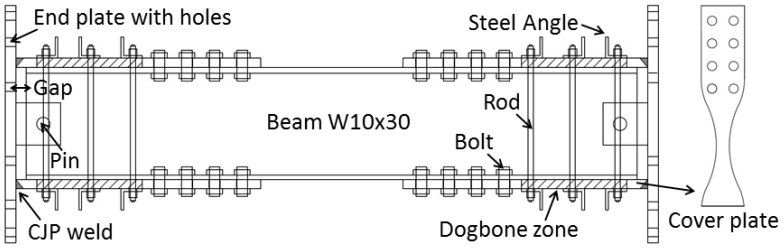

Fig. 3-34 Detail of the PFS1 mega beam with cover plates

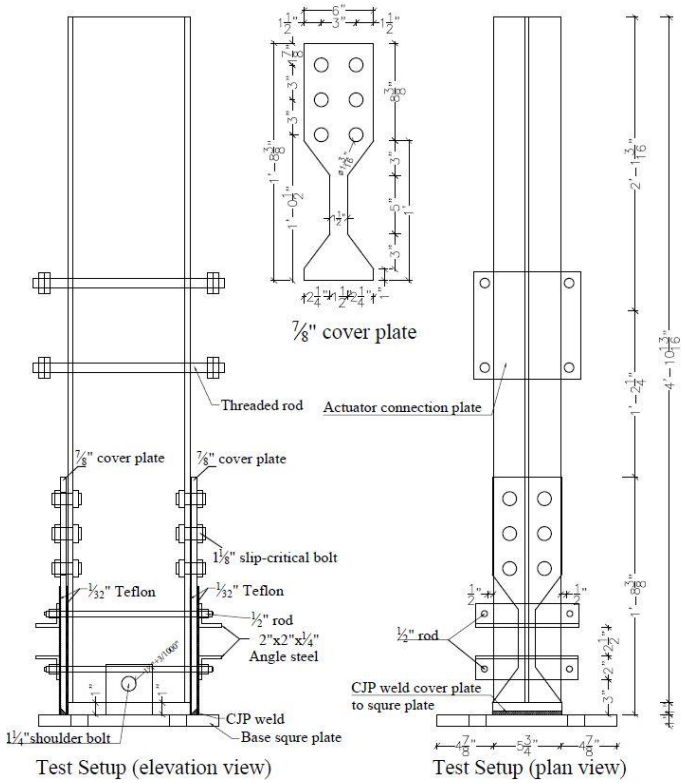

Fig. 3-35 Details of the mega beam used in the component test

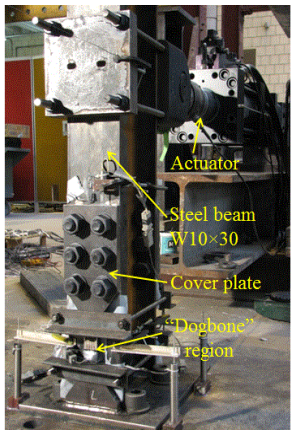

Fig. 3-36 Mega beam component test setup

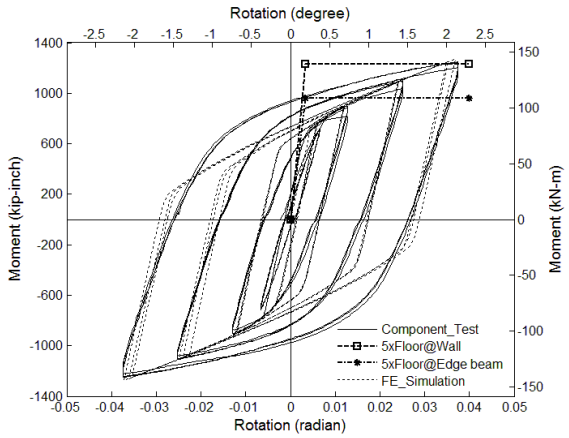

Fig. 3-37 Mega beam component test result compared to predicted behavior of the slab

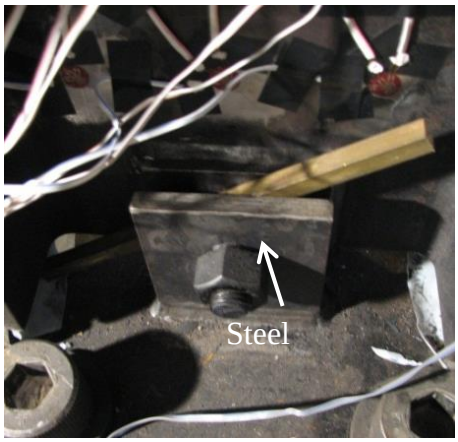

Fig. 3-38 Gap between the beam and the tabs

Fig. 3-39 Twist of the mega beam

Fig. 3-40 Fracture of the cover plate

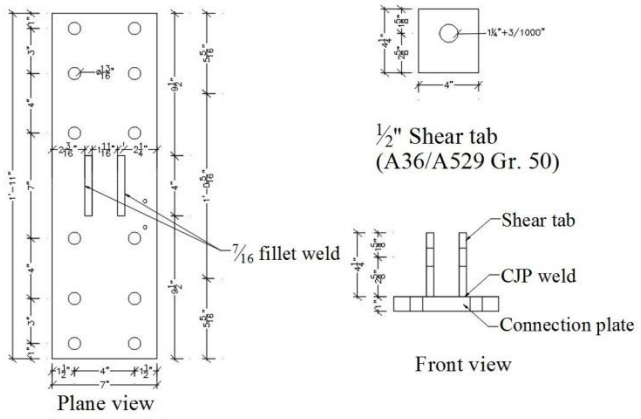

Fig. 3-41 Design of the mega beam end plate

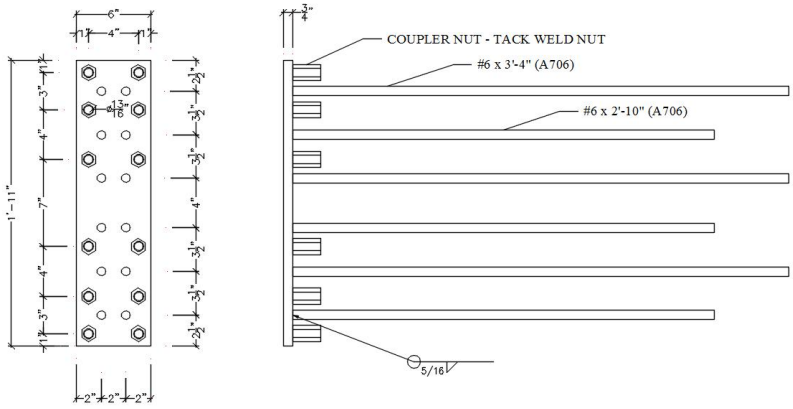

Fig. 3-42 Detail of the steel embedment in the wall

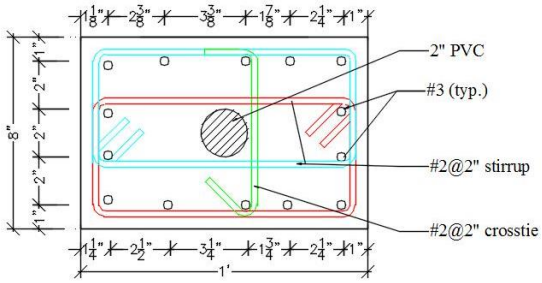

Fig. 3-43 Cross section of the RC column

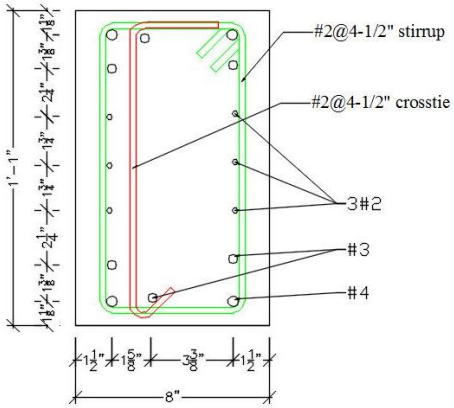

Fig. 3-44 Cross section of the edge beam

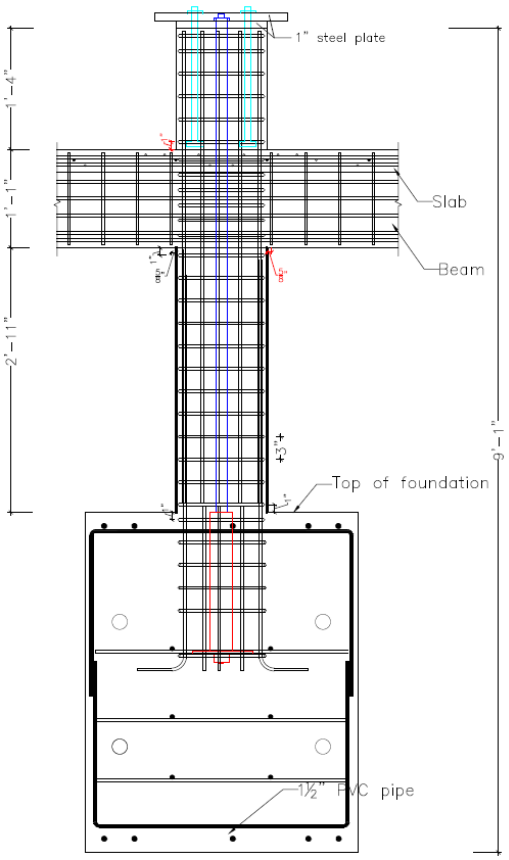

Fig. 3-45 Elevation view of the column and edge beam in E-W direction

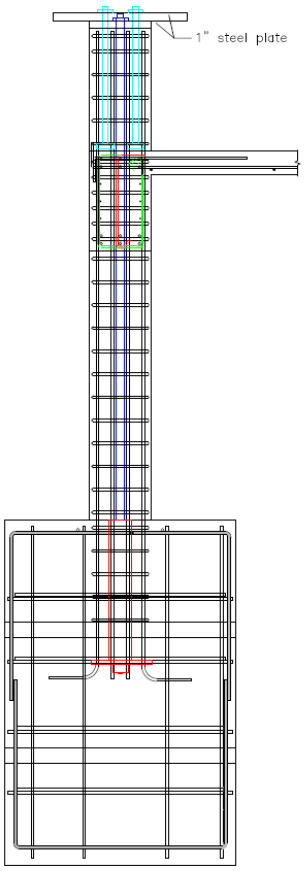

Fig. 3-46 Elevation view of the column and edge beam in N-S direction

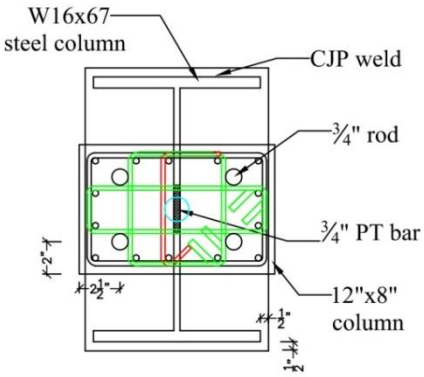

Fig. 3-47 Plan view of steel column – RC column connection

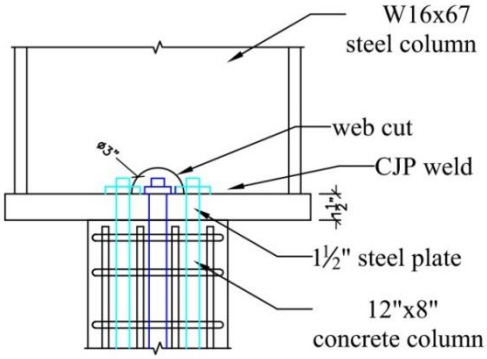

Fig. 3-48 Elevation view of steel column – RC column connection

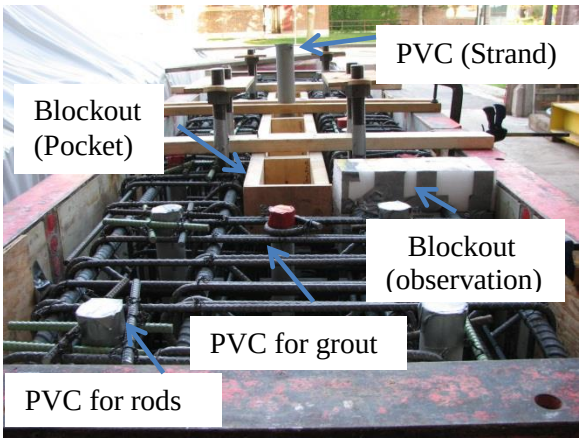

Fig. 3-49 Rebar cage for the wall base block

Fig. 3-50 Formed pocket in the base block

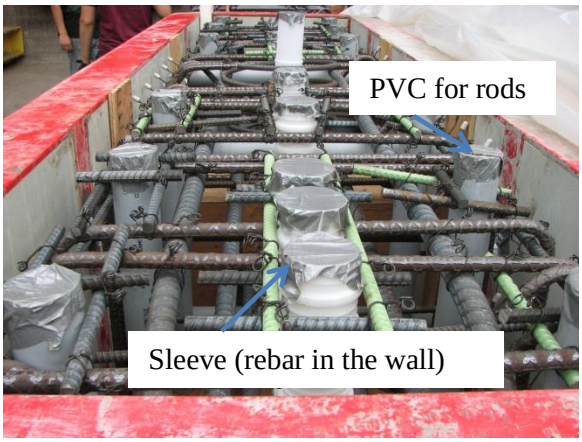

Fig. 3-51 Rebar cage for the wall base block

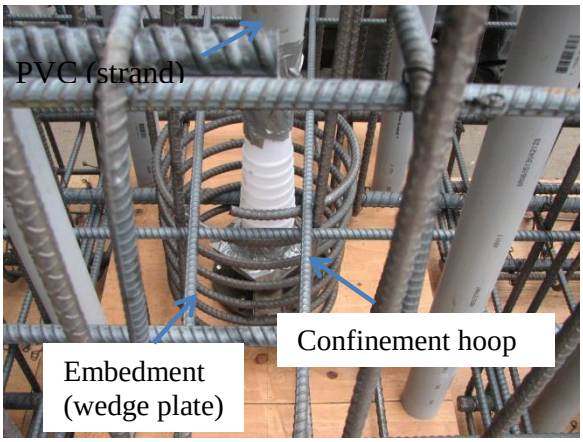

Fig. 3-52 Special detailing for the PT anchor

Fig. 3-53 Embedment in the base/top blocks

Fig. 3-54 External wedge plate

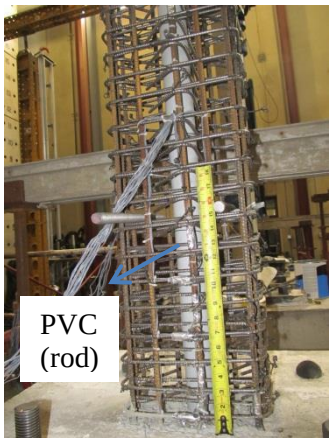

Fig. 3-55 Cast base block for the edge column

Fig. 3-56 Weldcrete at the base of the column

Fig. 3-57 Steel strain gages on the boundary element of the wall

Fig. 3-58 Concrete strain gages in the boundary element of the wall

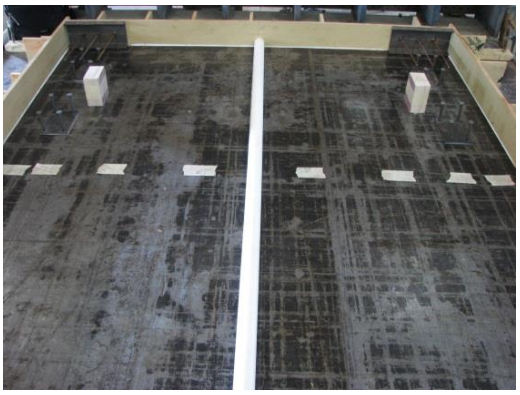

Fig. 3-59 Steel channels in the wall corners

Fig. 3-60 Steel embedment at top of the wall

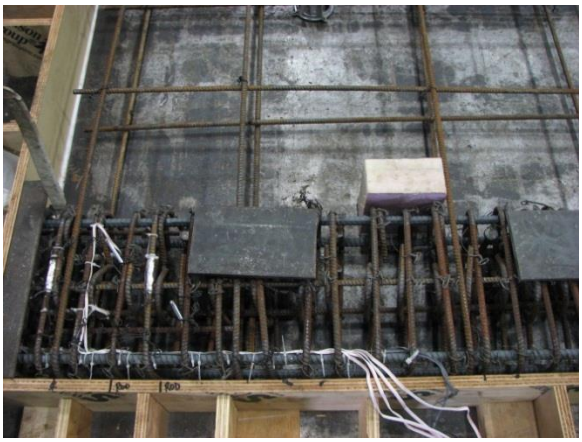

Fig. 3-61 Boundary element in the wall corner

Fig. 3-62 Mesh reinforcement in the wall

Fig. 3-63 Finished steel cage of the wall

Fig. 3-64 Cast wall panel

Fig. 3-65 Tilting up the wall

Fig. 3-66 Leveling the wall

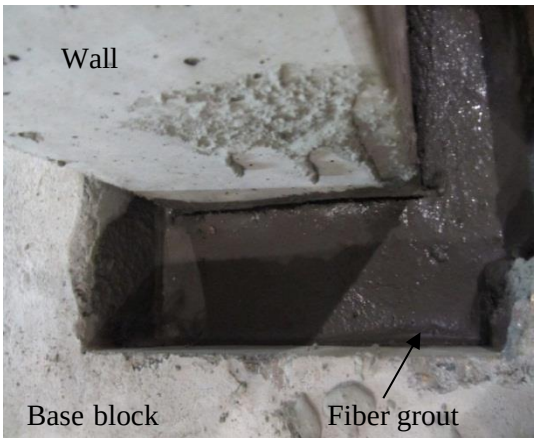

Fig. 3-67 Pouring steel fiber grout into the pocket

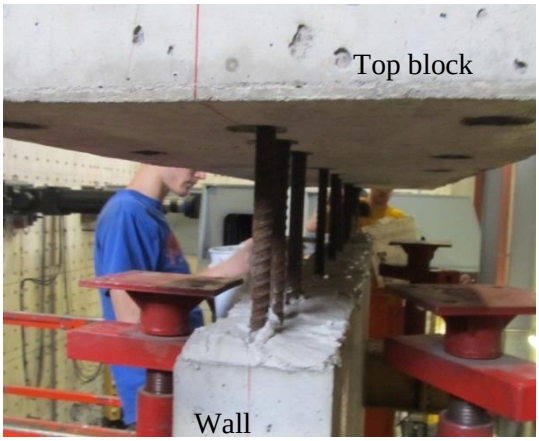

Fig. 3-68 Grouting the wall-top block interface

Fig. 3-69 Grouting the rebar in the top block

Fig. 3-70 Supporting the bottom wedge plate

Fig. 3-71 Tapping wedges into the wedge plate

Fig. 3-72 Placement of the post-tensioning jack

Fig. 3-73 Measuring elongation of the strands

Fig. 3-74 Injecting mortar to grout reinforcement through the wall

Fig. 3-75 Temporary aluminum rods for leveling the surface of the slab

Fig. 3-76 Preparing cylinders and beams

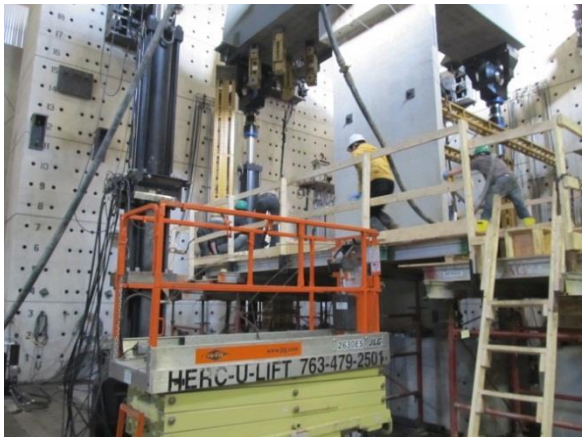

Fig. 3-77 Casting the PT floor slab

Fig. 3-78 Finished floor slab

Fig. 3-79 Strands in longitudinal direction

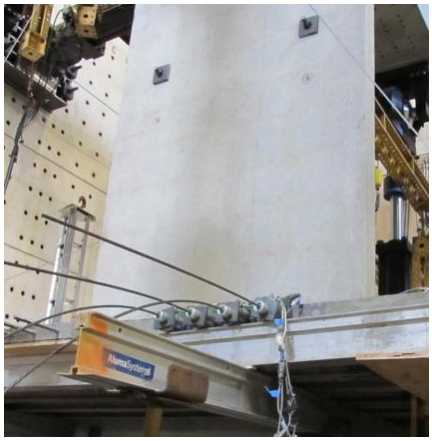

Fig. 3-80 Strands in transverse direction

Fig. 3-81 Initial seating of the wedges

Fig. 3-82 Placing the post-tensioning jack

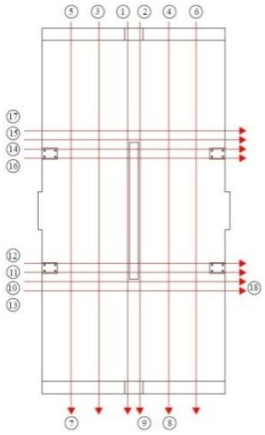

Fig. 3-83 Sequence of post tensioning the slab

Fig. 3-84 Installing the mega beam

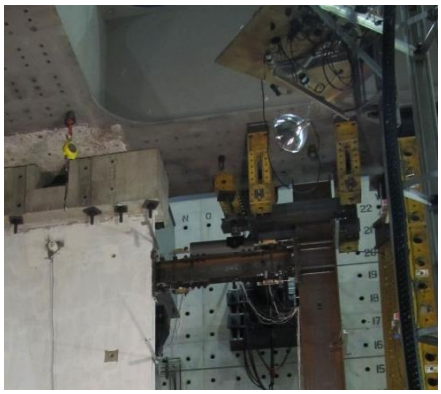

Fig. 3-85 Lateral support for steel columns

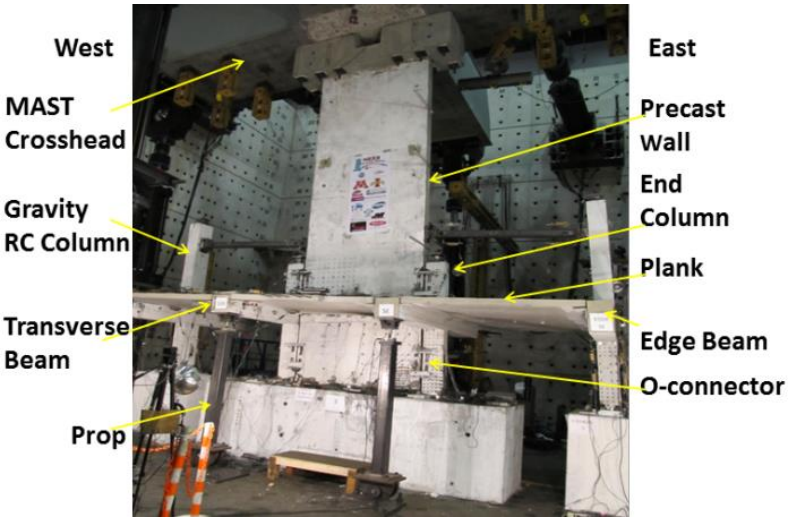

Fig. 3-86 Overview of PFS2

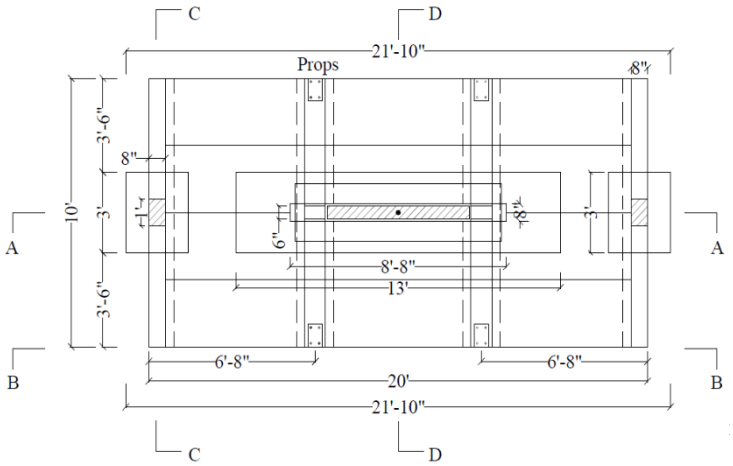

Fig. 3-87 Plan view of PFS2

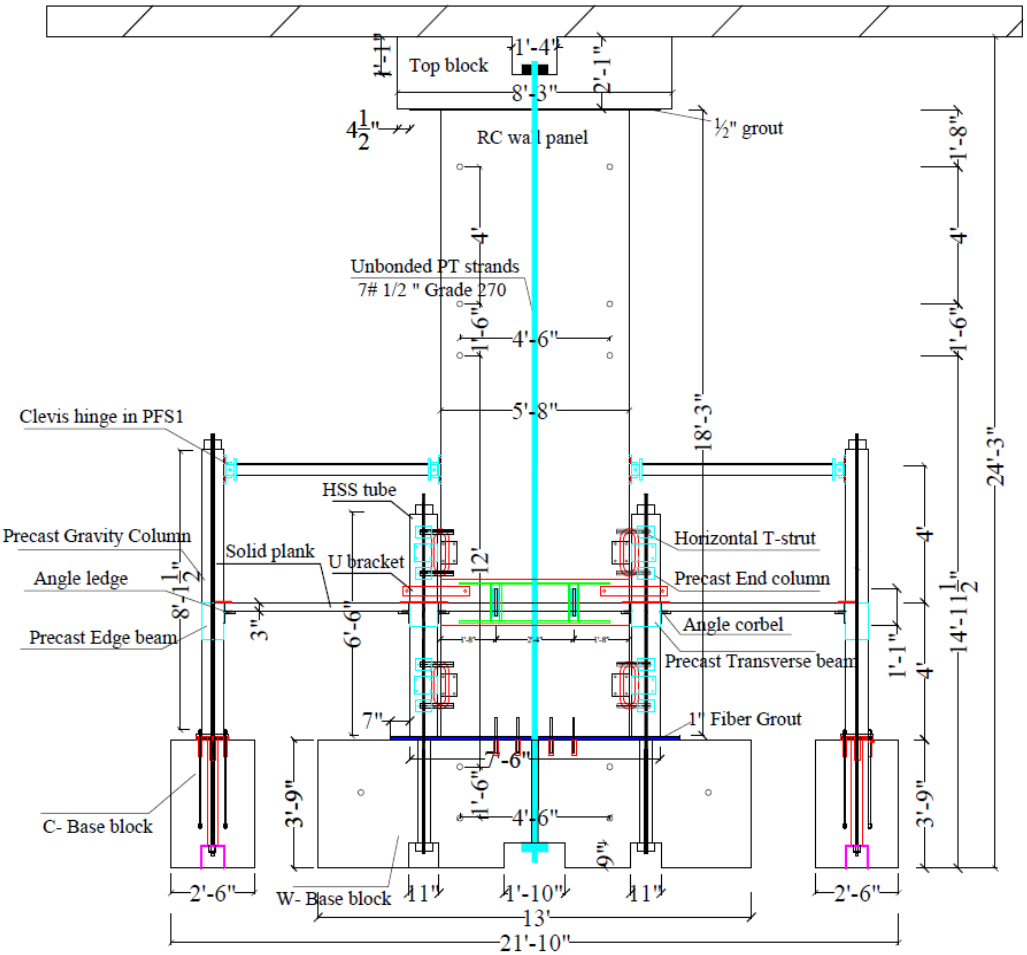

Fig. 3-88 Elevation view of PFS2 at Section A-A

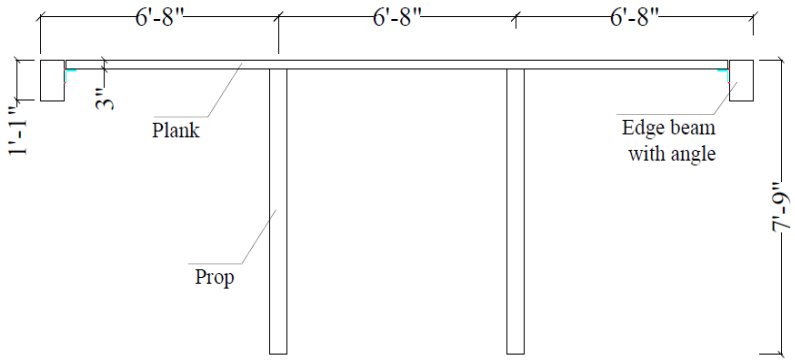

Fig. 3-89 Elevation view of PFS2 at Section B-B

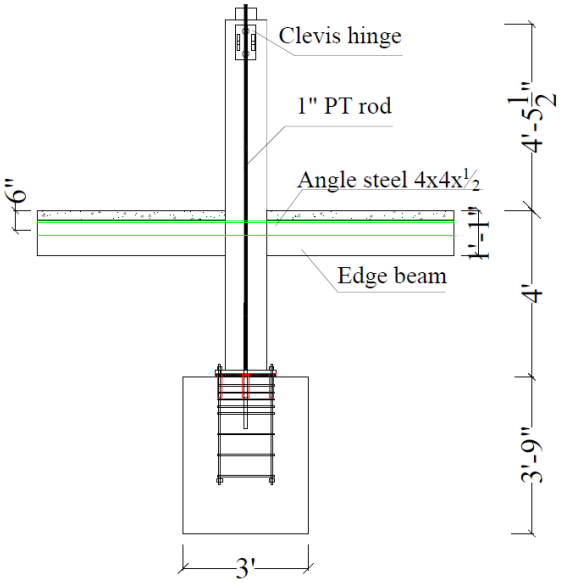

Fig. 3-90 Elevation view of PFS2 at Section C-C

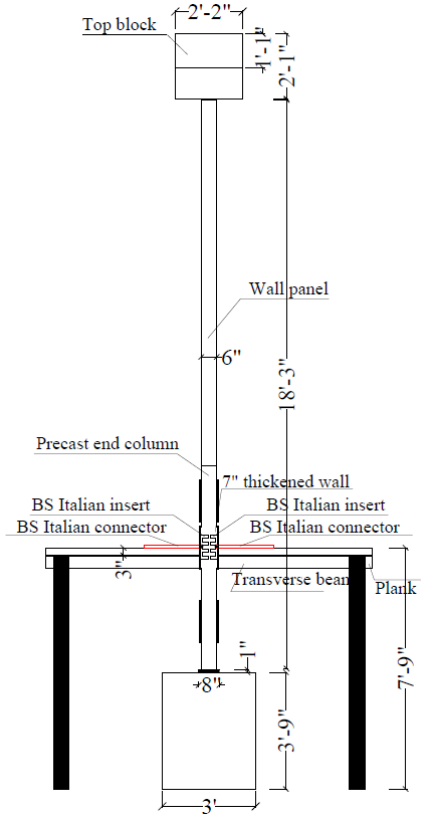

Fig. 3-91 Elevation view of PFS2 at Section D-D

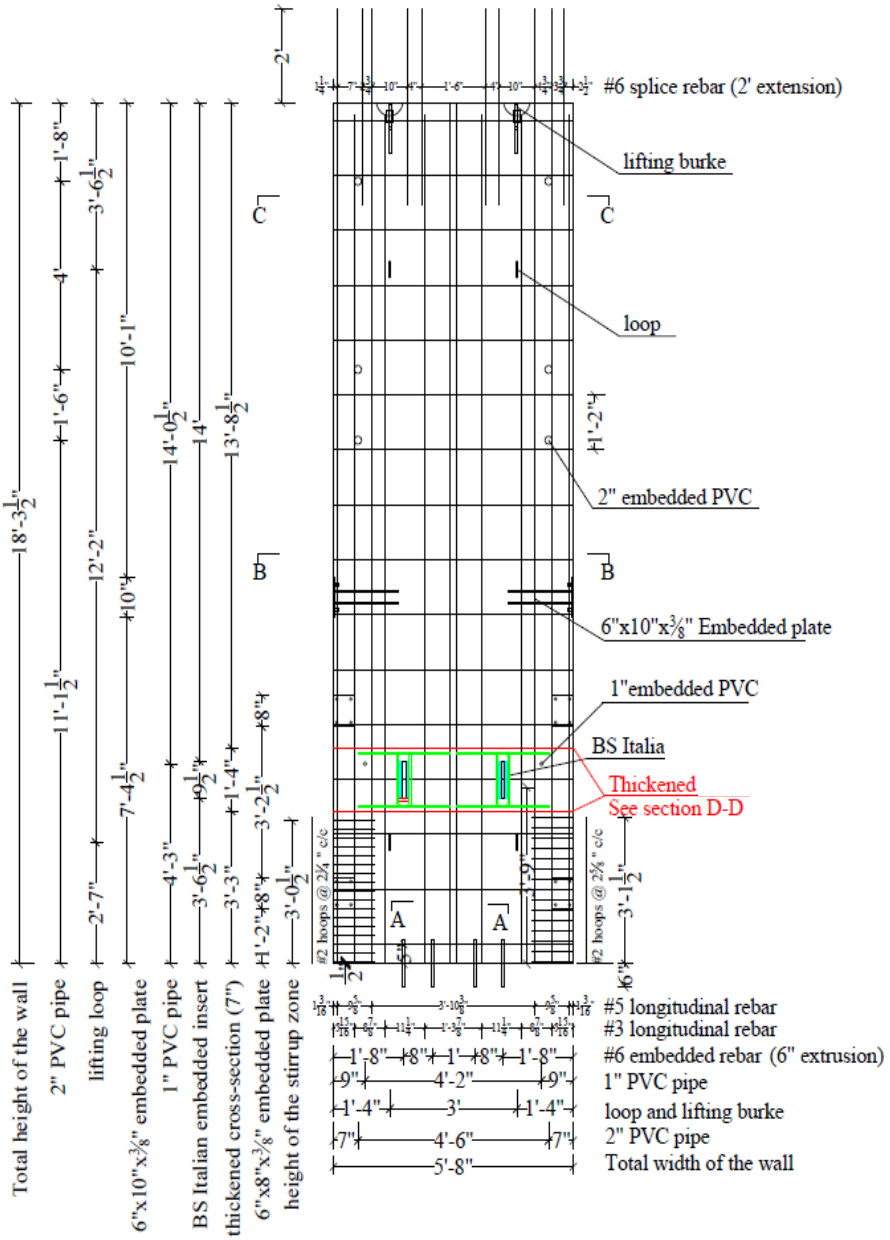

Fig. 3-92 Detailed elevation view of PFS2 wall panel

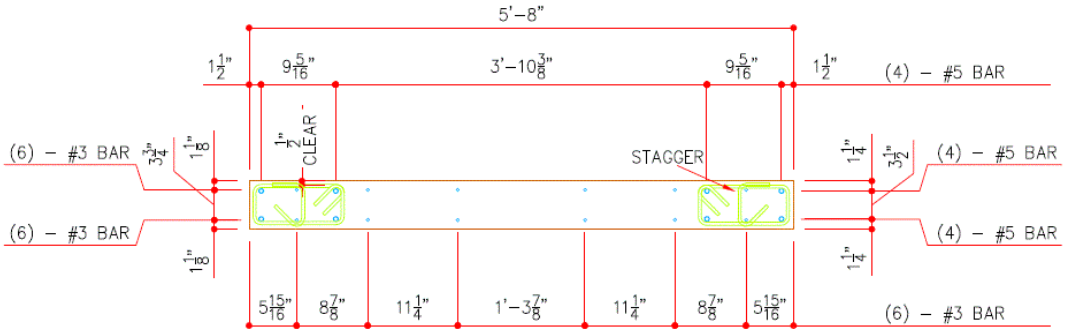

Fig. 3-93 Cross section A-A of PFS2 wall panel

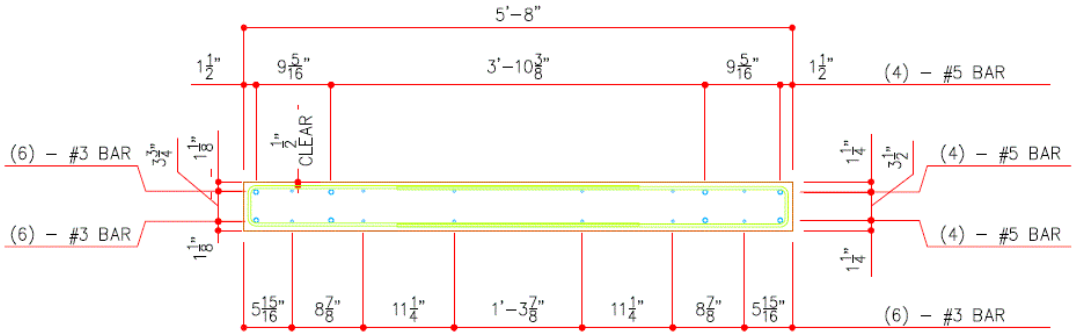

Fig. 3-94 Cross section B-B of PFS2 wall panel

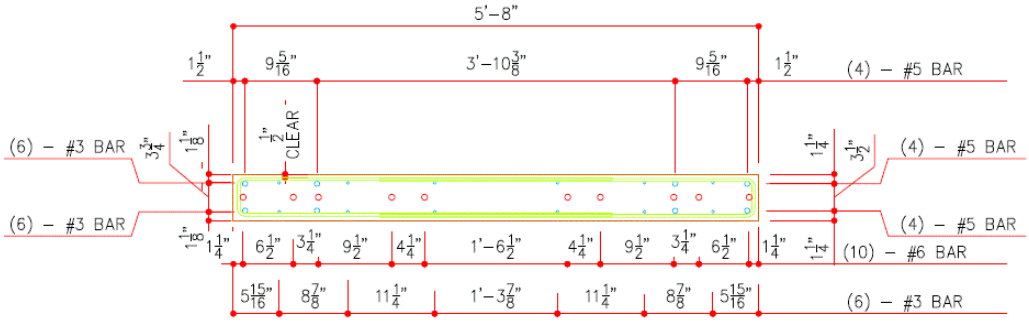

Fig. 3-95 Cross section C-C of PFS2 wall panel

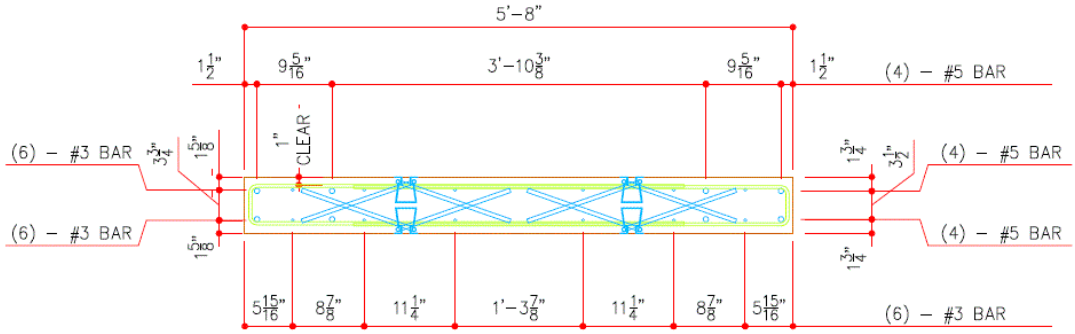

Fig. 3-96 Thickened cross section D-D of PFS2 wall panel

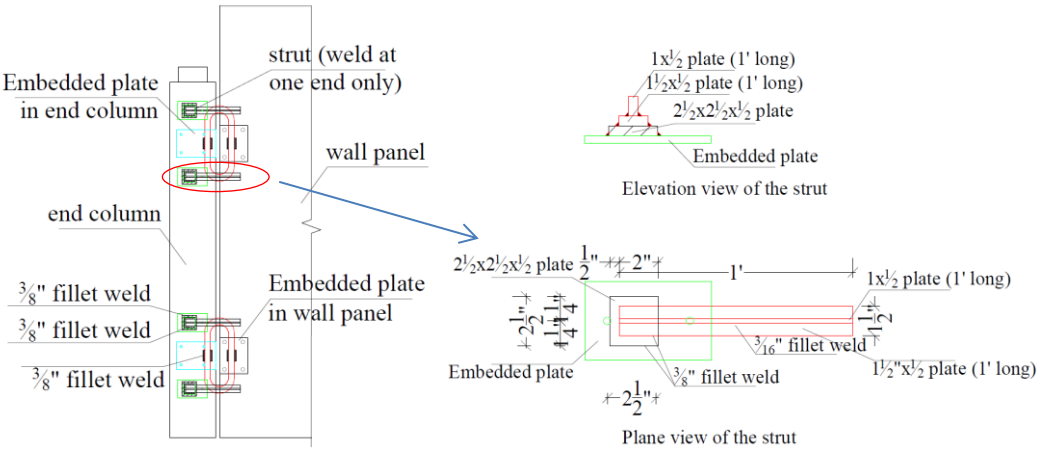

(a) Detail of the O-connectors in PFS2

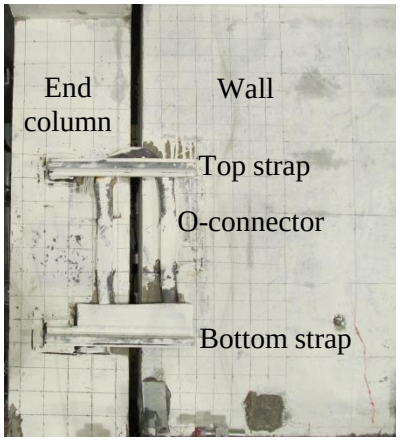

(b) O-connectors and strap plates (angles) in PFS2

Fig. 3-97 Details of the O-connectors in the design and PFS2

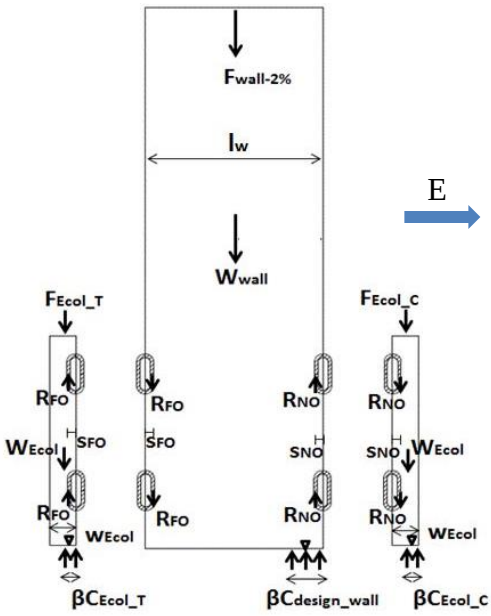

Fig. 3-98 Load distribution in the PreWEC system in PFS2

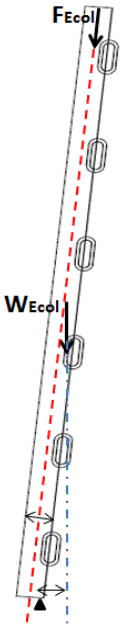

Fig. 3-99 Prestress forces and gravity loads in end columns

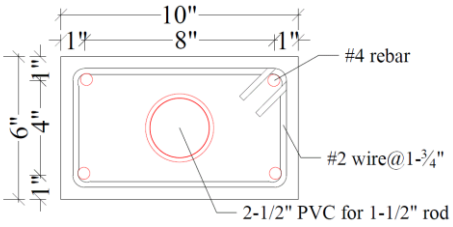

Fig. 3-100 Plan view of end columns

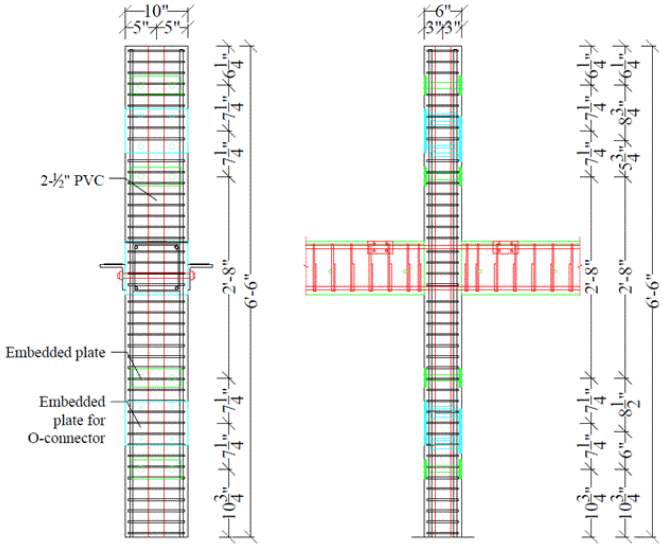

Fig. 3-101 Elevation view of end columns

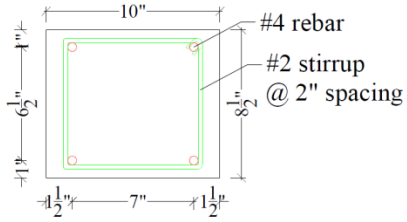

Fig. 3-102 Cross section of transverse beam

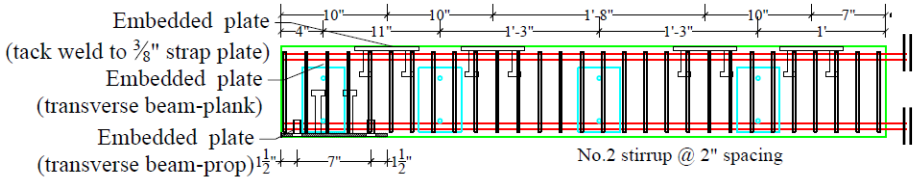

Fig. 3-103 Elevation view of the transverse beam (half of beam shown due to symmetry)

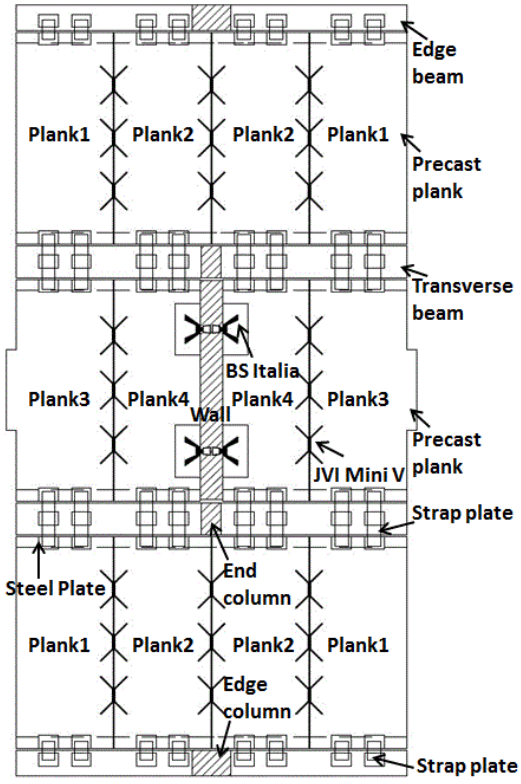

Fig. 3-104 Plan view of PFS2 precast floor

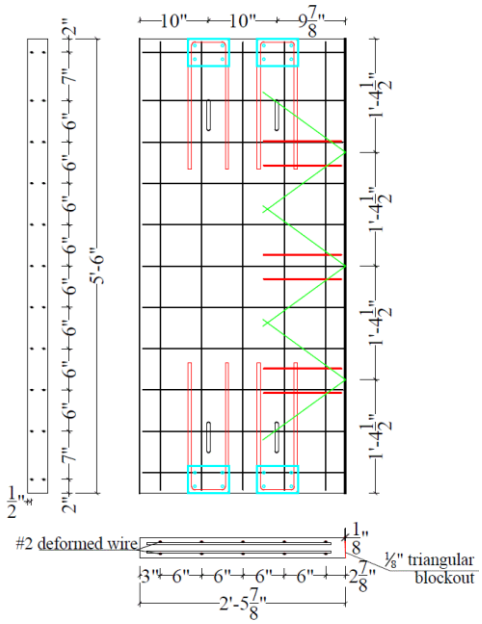

Fig. 3-105 Detail of Plank1

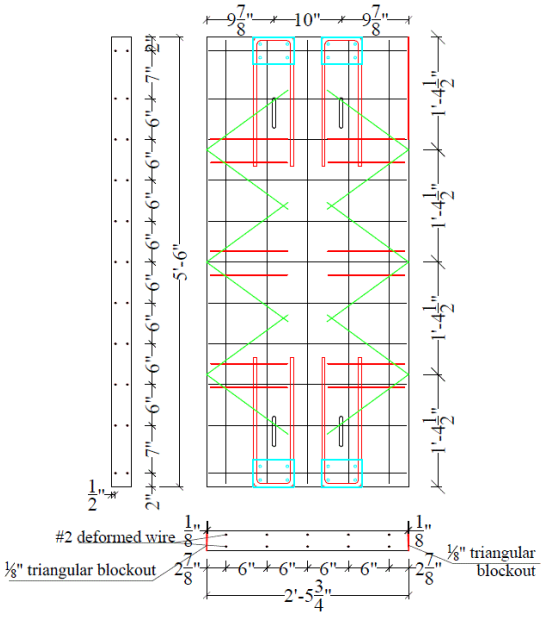

Fig. 3-106 Detail of Plank2

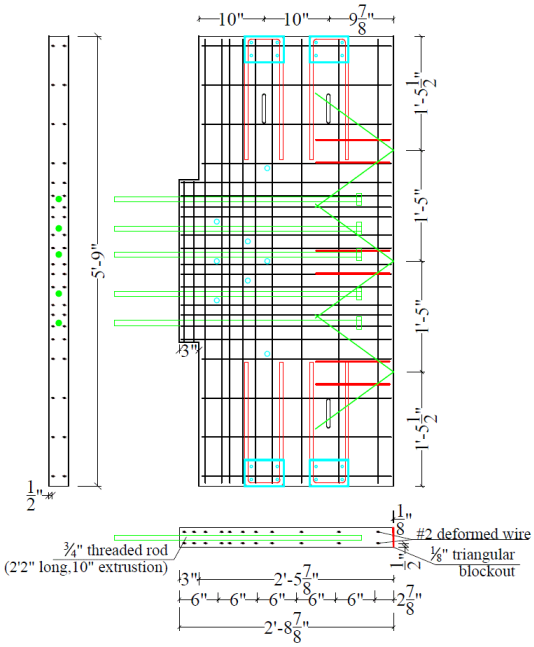

Fig. 3-107 Detail of Plank3

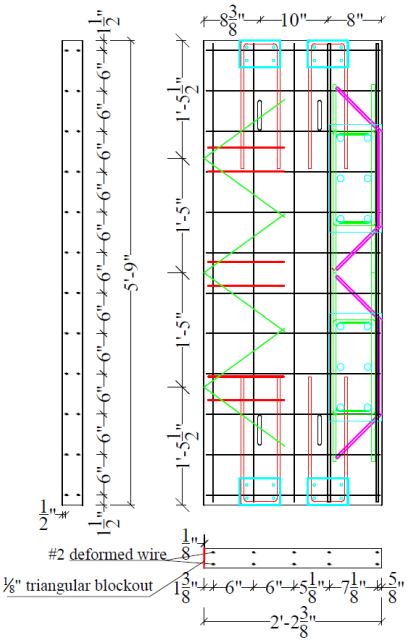

Fig. 3-108 Detail of Plank4

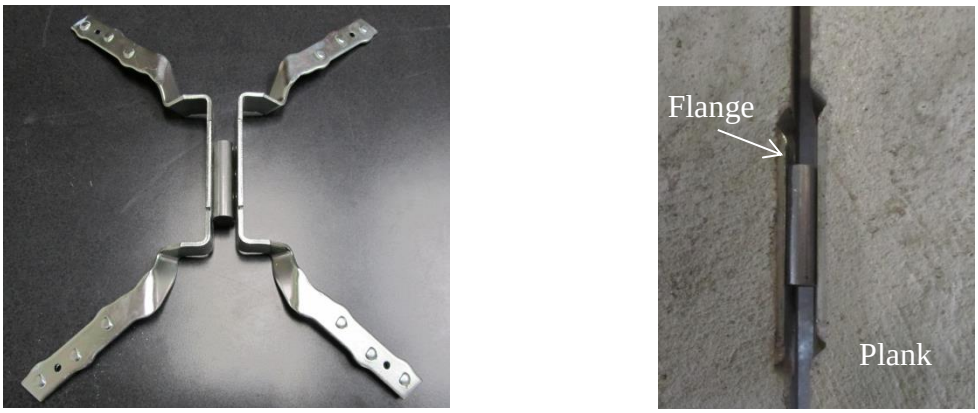

(a) JVI Mini V product (b) JVI Mini V installed in planks

Fig. 3-109 Details of JVI Mini V connections

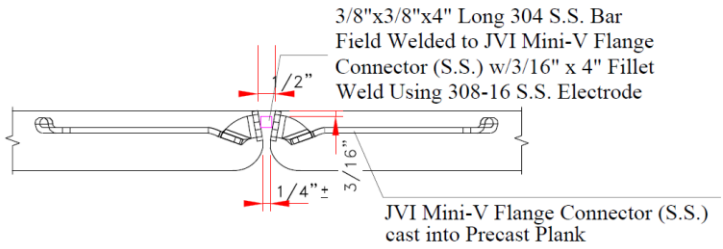

Fig. 3-110 Detail of installed JVI Mini V connection

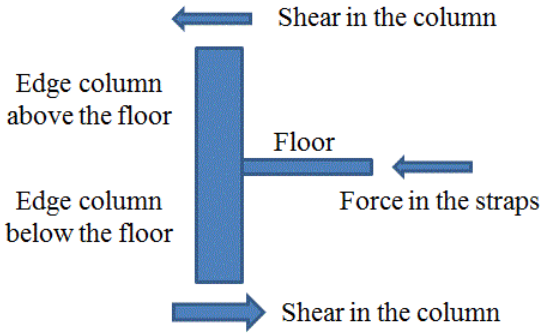

Fig. 3-111 Force equilibrium condition at the floor-column joint

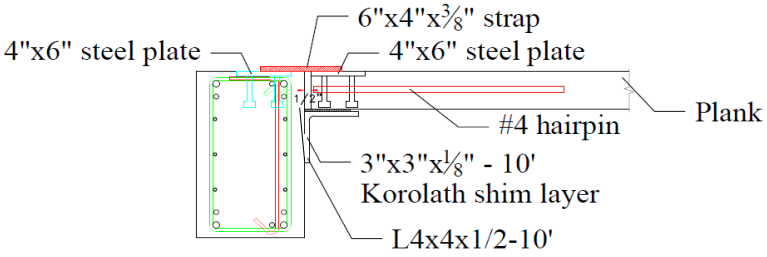

Fig. 3-112 Detail of plank-edge beam connection

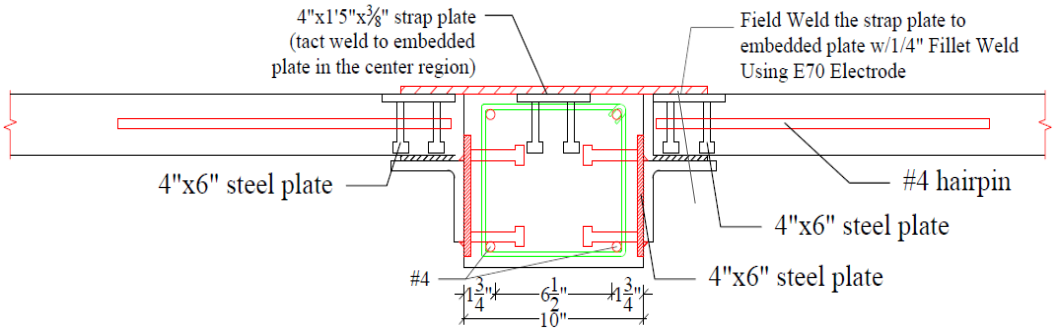

Fig. 3-113 Detail of plank-transverse beam connection

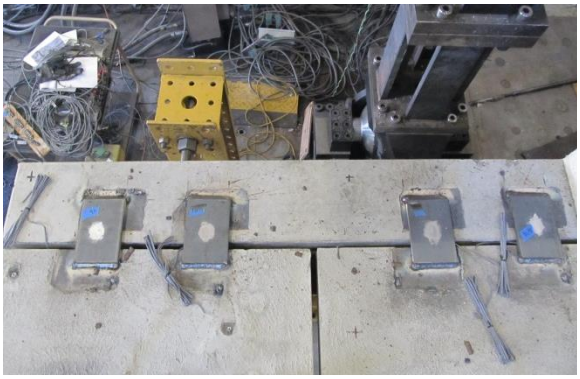

Fig. 3-114 Plank-edge beam connection

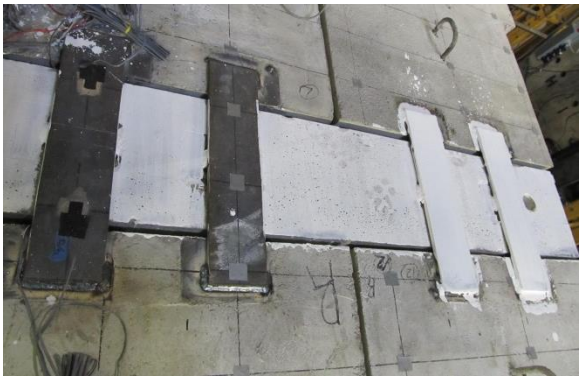

Fig. 3-115 Plank-transverse beam connection

Fig. 3-116 Components of BS Italia connection

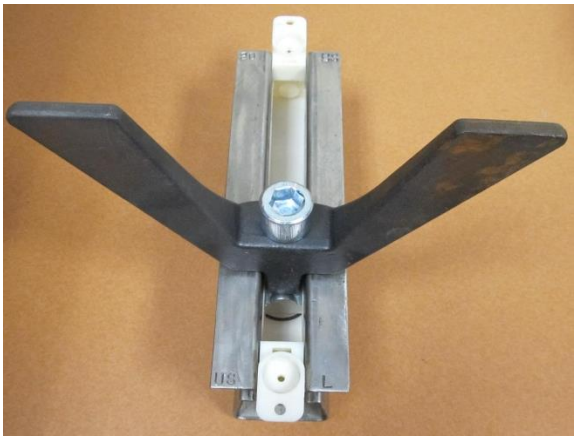

Fig. 3-117 Assemblage of BS Italia connection

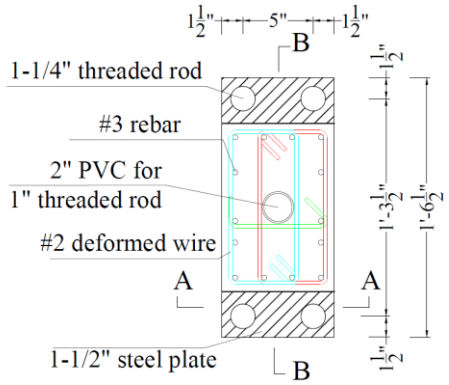

Fig. 3-118 Plan view of edge column base connection

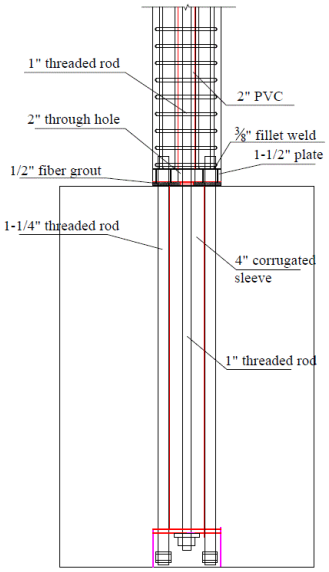

Fig. 3-119 Elevation view of column base connection (Section A-A)

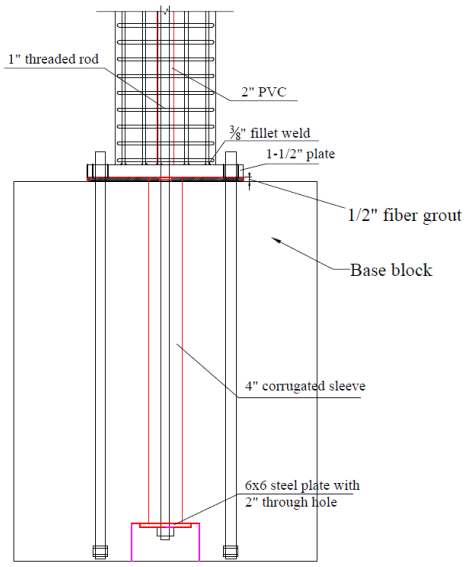

Fig. 3-120 Elevation view of column base connection (Section B-B)

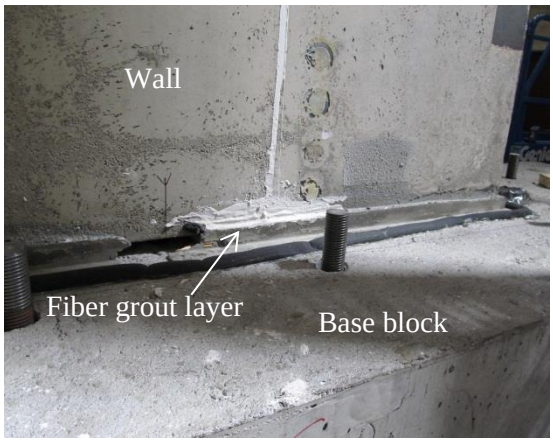

Fig. 3-121 PFS2 wall base block

Fig. 3-122 Sleeves for end columns

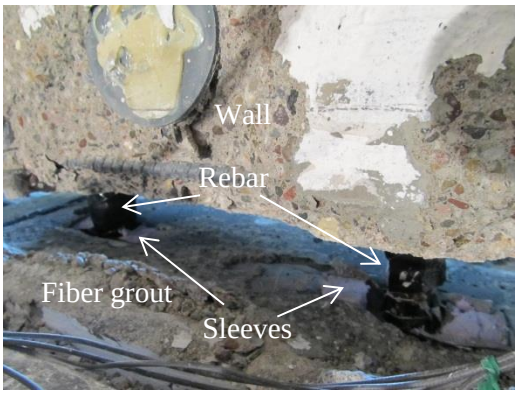

Fig. 3-123 Sleeves in the base block for rebar protruding from the wall base

Fig. 3-124 Rebar cage of the base block for edge columns

Fig. 3-125 Casting base block of edge columns

Fig. 3-126 BS Italia slotted channel

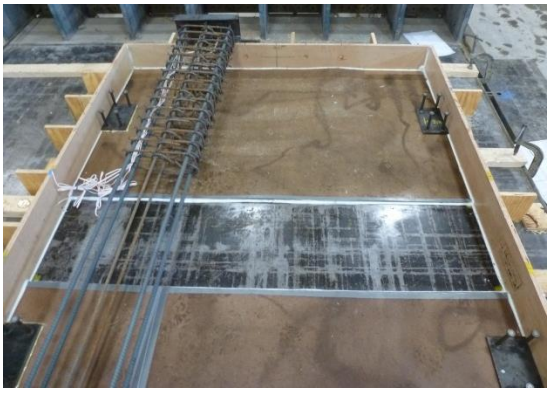

Fig. 3-127 PFS2 wall formwork

Fig. 3-128 Extended side formwork of wall

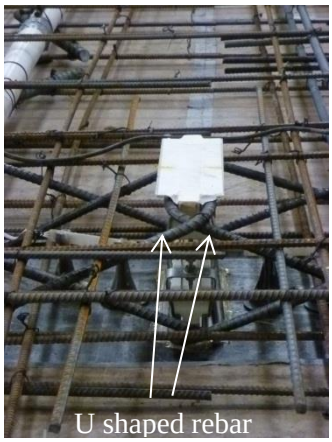

Fig. 3-129 U-shaped rebar for channel

Fig. 3-130 Steel plate for 2nd story tube

Fig. 3-131 Finished cage for PFS2 wall

Fig. 3-132 Cast wall in PFS2

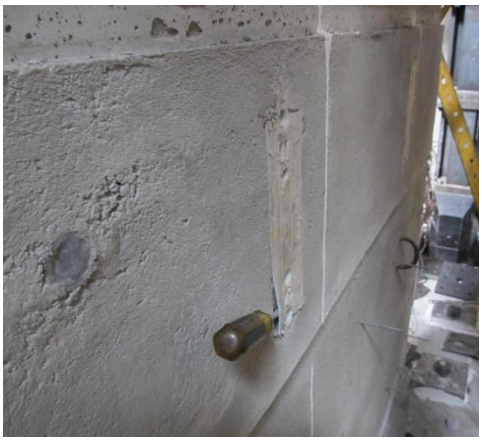

Fig. 3-133 Slotted channel in cast wall

Fig. 3-134 Slotted channel before the test

Fig. 3-135 Concrete consolidation

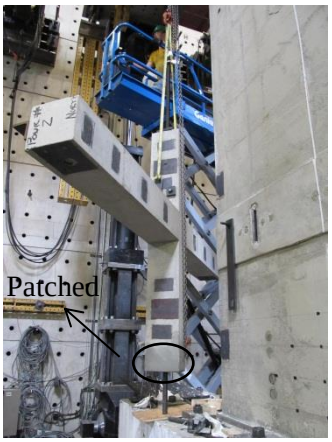

Fig. 3-136 Installation of west end column

Fig. 3-137 Formwork for grout

Fig. 3-138 Cured fiber grout layer

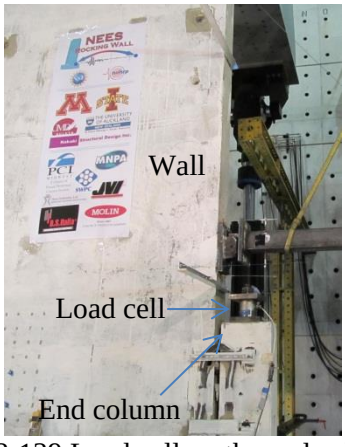

Fig. 3-139 Load cell on the end column

Fig. 3-140 Installation of edge column

Fig. 3-141 Finished edge column base

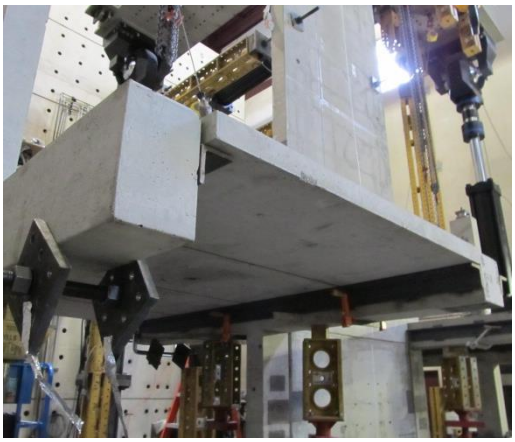

Fig. 3-142 Installation of precast planks

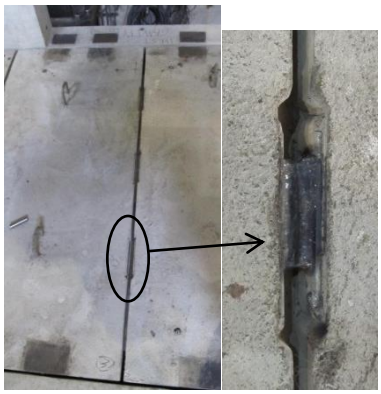

Fig. 3-143 Plank-plank connection

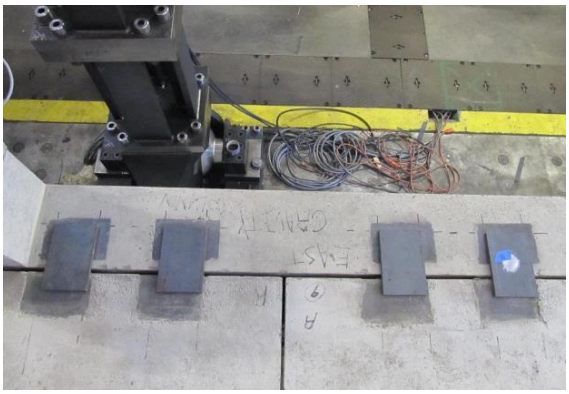

Fig. 3-144 Strap plates prior to welding

Fig. 3-145 BS Italia before welding

Fig. 3-146 Welding O-connectors

Fig. 3-147 Installing 2nd story steel trusses

Fig. 3-148 Test setup for testing mild reinforcement

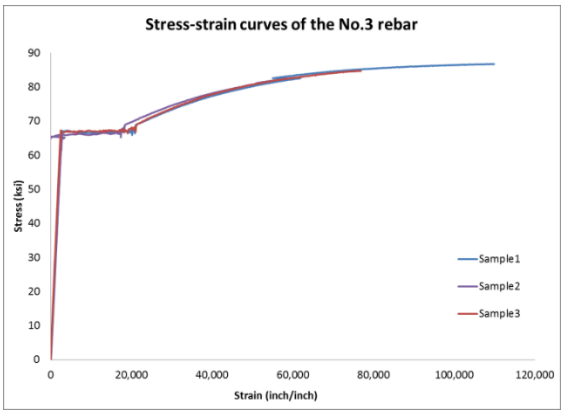

Fig. 3-149 Stress-strain response of No.3 rebar

Fig. 3-150 Test setup for steel coupons

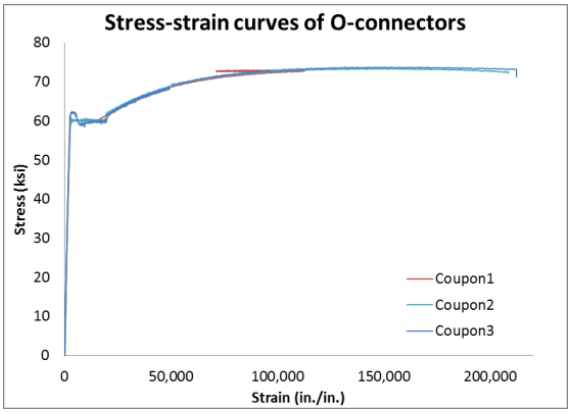

Fig. 3-151 Stress-strain response of O-connector

CHAPTER 4. Instrumentation Plan and Loading Protocol

This chapter describes the instrumentation plans and the loading protocols for the two assemblage tests, PFS1 and PFS2. Section 4.1 gives an overview of the instrumentation used in the test and introduces the instrumentation nomenclature. Section 4.2 summarizes the instrumentation that served similar purposes in the two tests. Section 4.3 and 4.4 describe the instrumentation designed specifically for PFS1 and PFS2, respectively. Section 4.5 describes the loading protocols in the two tests. Fig. 4-1 through Fig. 4-14 show the instrumentation used in PFS1. Fig. 4-15 through Fig. 4-30 show the instrumentation used in PFS2. It should be noted that the positive in-plane loading direction in these figures ("positive y") corresponded to the east, and the positive out-of-plane loading direction ("positive x") corresponded to the south.

4.1 Overview of the Instrumentation

Different types of instrumentation were used in the tests, including load cells, tiltmeters, Linear Variable Differential Transformers (LVDTs), string pots, Direct Current Displacement Transducers (DCDT), Krypton and Optotrak systems, and resistive steel and concrete strain gages.

The forces in the PT strands and the PT threaded rods were measured by load cells. Tiltmeters were used to measure the rotation of the wall and the columns in each test. The displacement and the deformation of the specimen were measured by LVDTs, string pots and DCDTs. Two Krypton systems and one Optotrak system were also used to monitor the movements of the specimen. These devices were capable of determining the 3D positions of LED sensors attached to the structure. Resistive strain gages attached to the reinforcement (steel gages) and embedded in the concrete (concrete gages) were used to measure local strains in the specimen.

Nomenclature was developed to describe each instrument by its type and location in accordance with the following conventions. LC stands for load cells, followed by the location, orientation and number in order (if applicable). For example, LC-FPTSE4 denotes: Load Cell on the Floor; PT strands in the Southeast quadrant #4. The symbol

"T" stands for tiltmeters, followed by the location. For example, TTW denotes: Tiltmeter on the Top portion of the Wall. The symbol "L" and "SP" stand for LVDT and string pot, respectively, followed by measurement range, location, orientation and number in order (if applicable). For example, L1-EC1FB-E denotes: +/- 1 in. LVDT on the East Column at the 1st Floor Base on the East face. SP10-ECBASE denotes: 10 in. string pot on the East Column Base. DCDTs were used only in PFS2. There were only 10 DCDTs used in PFS2, thus they were named by the number in order. SG and CG stand for resistive strain gages attached to the steel (SG) and embedded in the concrete (CG), followed by location, orientation and number in order (if applicable). For example, SG-WCOL-L1 represents the first Steel strain Gage on the West Column on the Longitudinal reinforcement. CG-W2 represents the Second Concrete strain Gage in the West corner of the wall. There were approximately 300 digital channels used in the data acquisition system in both tests, excluding the Krypton and Optotrak systems. All information of the instrumentation is summarized in Appendix D.

4.2 Instrumentation for Similar Purposes in the Two Specimens PFS1 and PFS2

The instrumentation that served similar purposes in the two test specimens is summarized in this section. To make the description more organized, it is categorized by different structural components, including wall panel, edge columns, O-connectors and props. The outline of the description is: Types of the instrumentation, purpose of the instrumentation and the associated data processing methods.

4.2.1 Wall Panel

4.2.1.1 Lateral Displacement of the Wall

As shown in Fig. 4-1, five string pots (SP2_EW0, SP10_EW1, SP20_EW2, SP20_EW3 and SP30_EW4) were affixed to the wall in PFS1 to measure the lateral movement of the wall along its height. As shown in Fig. 4-15, because the PreWEC end column was in the way of the string of SP10_EW1, it was removed and only four string pots (SP2_EW0, SP20_EW2, SP20_EW3 and SP30_EW4) were used in PFS2.

By plotting the readings of the string pot along the height of the wall at different peak drifts, the deformed shape of the wall was obtained. The readings of SP2_EW0 were used to examine potential sliding of the wall at the base.

4.2.1.2 Rotation of the Wall Panel

As shown in Fig. 4-1 and Fig. 4-15, two tiltmeters (TTW and TBW) were mounted on the walls in both tests. One tiltmeter was attached on the upper portion of the wall while the other was attached below the floor slab. The tiltmeters were used to monitor both in-plane and out-of-plane rotations of the wall. The readings from the tiltmeters were directly used for data analysis.

The flexural rotation of the wall was expected to increase along the height of the wall in general. TBW was located close to the base of the wall, where the rotation of the wall caused by the flexural bending of the wall was expected to be small. By comparing the readings from the two tiltmeters, the significance of flexural bending of the wall to the total lateral displacement of the wall was investigated. The portion of the rotation caused by flexural bending of the wall to the rotation of the wall ($\rho_{flexural}$) on the top could be obtained as follows:

$$\rho_{flexural} = \frac{\theta_{TTW} - \theta_{TBW}}{\theta_{TTW}} \tag{4.1}$$

Where θ_{TTW} = Rotation recorded by TTW on the top portion of the wall, θ_{TBW} = Rotation recorded by TBW on the bottom portion of the wall.

4.2.1.3 Forces in the PT Strands

As shown in Fig. 4-1 and Fig. 4-15, a load cell (LC-WALL) was used to monitor the forces in the PT strands of the wall in both tests. The load cell was installed in a recess in the top block. The PT force in the wall was an important indicator of structural performance that was directly related to the moment resistance and the self-centering capability of the wall. The load cell was used to measure the initial PT force at the beginning of the test after seating losses, measure the PT force at peak drifts and the residual PT force when the wall returned to the upright position (termed “zero displacement position” in the following). By dividing the recorded PT forces by the cross-sectional area of the strands, the average stress in the strands was obtained. It was

used to monitor the yielding and the potential fracture of the strands. The load cell readings were directly used for data analysis.

4.2.1.4 Neutral Axis Depth of the Wall

As shown in Fig. 4-2, a group of six LVDT was used to measure the gap opening across wall-foundation interface (L2_EW1, L2_EW2, L1_EW3, L1_WW3, L2_WW2 and L2_WW1) in PFS1. As shown in Fig. 4-16, a group of five LVDT was used in PFS2 (L2_EW1, L2_EW2, L1_CW, L2_WW2 and L2_WW1). It was found that L2_WW2 did not work in either test, thus it was excluded from the data analysis.

By plotting the readings of the LVDTs across the width of the walls, the gap opening of the wall was obtained. Moreover, the neutral axis depth of the wall was obtained by extrapolating the LVDT readings to the edge of the wall. The intersection point where the vertical displacement was equal to zero was the point where the wall was assumed to lose contact with the foundation. The distance between the intersection point and the adjacent wall end was identified as the neutral axis depth. The neutral axis depth was an important parameter that was related to the strains developed in the extreme compressive fiber at the wall tip.

4.2.1.5 Relative Displacement at the Wall-Floor Connections

In PFS1, two LVDTs (L05-FWE-V and L05-FM-V) were used to measure the relative vertical displacement between the wall and the slab, and two LVDTs (L05-FWE-H and L05-FM-H) were used to measure the relative horizontal displacement between the wall and the slab. The LVDTs are shown in Fig. 4-2. The test data was used to examine the potential vertical and horizontal shear sliding at the wall-floor connections.

In PFS2, only two LVDTs (L05-FWE-V and L05-FM-V) were used because of the limited amount of available LVDTs.

4.2.1.6 Strain Distribution in the Wall

As shown in Fig. 4-3, four concrete strain gages were placed in each wall corner in PFS1. Three gages were at the bottom and within the range of steel confinement to investigate the compressive strain distribution in the wall corners. The fourth gage was above the one near the tip to monitor the strain distribution along the height of the wall.

Because the strain gage readings were not recorded during the post-tensioning operation, the strain gages were under precompression that was not initially monitored. Consequently, the recorded tensile strains would be larger than the actual strain. Assuming the initial axial force was uniformly distributed across the wall base, the initial compressive strain could be estimated:

$$\varepsilon_{initial} = \frac{N_b}{E_c l_w t} \tag{4.2}$$

Where N_b = Axial load on the wall base; E_c = Young's modulus of concrete (Table 3-8); l_w = Width of the wall; t = Thickness of the wall.

In PFS1, the axial load at the wall base included the initial PT force at the beginning of the test (112.5 kip, Section 3.4.6) and self-weight of the wall and the top block (16 kip). The initial strain is calculated:

$$\varepsilon_{initial\_PFS1} = \frac{112.5 + 16}{6{,}410 \times 90 \times 6} = 3.7 \times 10^{-5} = 37\ \mu\varepsilon$$

In PFS2, the axial load at the wall base included the initial PT force at the beginning of the test (177.3 kip, Section 3.6.5) and self-weight of the wall and top block (13 kip). The initial strain:

$$\varepsilon_{initial\_PFS2} = \frac{177.3 + 13}{5{,}586 \times 68 \times 6} = 8.3 \times 10^{-5} = 83\ \mu\varepsilon$$

The actual strain in the wall was assumed to be the recorded strains from the strain gages minus the initial average compression strain in the respective tests.

As shown in Fig. 4-17 for PFS2, other than the gages in the wall corners, four more groups of concrete gages were placed along the height of the wall to investigate the force flow in the wall. Gages CG-EWBC2/CG-CEWB2/CG-CWWB2 and CG-EWBC3/CG-CEWB3/CG-CWWB3 were located in the region close to the wall corner, which was expected to be disturbed, where plane section was assumed to not remain plane. By plotting the readings from CG-EWBC1-1, CG-EWBC2 and CG-EWBC3 with respect to the locations along the height of the wall at different peaks, the strain distribution along the height of the wall was obtained. Gages CG-EWBC4/CG-CEWB4/CG-CWWB4 and CG-EWBC5/CG-CEWB5/CG-CWWB5 were located in the region of the wall which was expected to be undisturbed, where plane sections were expected to remain plane. By

plotting the three gages in each group with respect to their locations along the width of the wall, information about the strain distribution across the width of the wall was obtained. It was expected to be close to a linear distribution.

As shown in Fig. 4-2, a group of four LVDTs (L01_NE_WE, L01_NE_EM, L01_NE_WM and L05_NW_EE) were placed along the north face in the mid-height of the first story wall in PFS1. The strains in the wall were calculated through dividing the LVDT readings by the gage length of the LVDT, which is listed in Table D-1 in Appendix D. By plotting the calculated compressive strains with respect to the locations of the LVDTs along the width of the wall, information about the strain distribution across the width of the wall could be obtained.

4.2.1.7 Strains in the Transverse Confinement Reinforcement at the Wall Corners

As shown in Fig. 4-3, strain gages were attached to the stirrups in the boundary elements of the wall to monitor the confinement effect in PFS1. If high compressive strains were developed in the concrete at the wall corners, the stirrups were expected to be stretched and the strain gages would have noticeable readings. By plotting the strain gage readings along the height of the boundary elements, the region where the confinement took effect was obtained, which provided an indication of the strain distribution along the wall height. Similar strain gages were used in one of the wall boundary elements in PFS2, as shown in Fig. 4-17.

4.2.2 Edge Columns and Edge Beams

4.2.2.1 Lateral Displacement of the Edge Columns

As shown in Fig. 4-1 and Fig. 4-15, a group of three string pots (SP2-ECBASE, SP10-ECEB and SP10-EC1) was attached along the height of the first story east edge column to monitor its deformed shape in the two tests. The readings of SP2-ECBASE were used to examine the potential shear sliding at the column base.

4.2.2.2 Rotation and Average Curvature at the Base and Top of Columns

As shown in Fig. 4-2, a pair of LVDTs (L1-EC1FB-E/L1-EC1FB-W) and a pair of SPs (SP2-EC1FT-E/SP2-EC1FT-W) were attached to the bottom and the top of the east edge column. The LVDTs were mounted between the east edge column body and the base

block. The string pots were mounted at the joint of the east edge column and the edge beam. For the west edge column, a pair of LVDTs (L1-WC1FB-E/L1-WC1FB-W)) was attached between the edge column body and the base block. The gage length of the LVDTs and the string pots is given in Table D-1 in Appendix D. The recorded data were used to measure the rotations and deduce the average curvatures of the edge columns at both ends.

In PFS2, precast edge columns with steel base plates were used. The total rotation of the precast edge columns at the base included the rotation of the base plate and that of the edge column body. As shown in Fig. 4-16, a pair of LVDTs (L1-WC1FB-E/L1-WC1FB-W) was mounted between the west edge column body and the base block. It measured the total rotation of the west edge column. A pair of displacement transducers (DCDT5/DCDT8) was mounted between the steel base plate and the base block to measure the rotation of the base plate. For the east edge column, a pair of LVDTs (L1-EC1FT-E/L1-EC1FT-W) was mounted at the top of the east edge column to measure the rotations of the edge column at the floor-column joint. The LVDTs (L1-EC1FB-E/L1-EC1FB-W) were mounted between the east edge column body and the base block. They were used to measure the total rotation of the east edge column at the base. The gage lengths of the LVDTs and the DCDTs is listed in Table D-2 in Appendix D.

The rotations and the average curvatures of the edge column were obtained through the following equations:

$$\theta_{col} = \frac{\Delta_{col\_W} - \Delta_{col\_E}}{t + d_{col\_E} + d_{col\_W}} \tag{4.3}$$

$$\varphi_{col\_a} = \frac{\theta_{col}}{s_{col}} \tag{4.4}$$

Where θ_{col} = Rotation of the edge column, Δ_{col_W} = Extension or shortening of the LVDT (string pot or DCDT) on the west side of the edge column, Δ_{col_E} = Extension or shortening of the LVDT (string pot or DCDT) on the east side of the edge column, t = Depth of the edge column in the in-plane loading direction, d_{col_E} = Distance from the east surface of the edge column to the core of the LVDT (string pot or DCDT) on the east side of the edge column, d_{col_W}= Distance from the west surface of the edge column to

the core of the LVDT (string pot or DCDT) on the west side of the edge column, φ_{col_a} = Average curvature, s_{col}= Gage length of the LVDT(string pot or DCDT).

The average curvature was used to monitor the formation of plastic hinges and correlate with local curvatures deduced by the strain gage readings, which is discussed in the next section.

4.2.2.3 Local Strains and Curvature Distribution in the Edge Columns

Strain gages were attached to the rebar in the edge columns in both tests. The readings of the steel strain gages were used to judge the yielding of the longitudinal rebar. By investigating the strain gage readings that varied along the height of the edge column, the formation of the plastic hinge at the base of the edge column was monitored.

The layout of the steel strain gages attached to the reinforcement in the edge columns in PFS1 is shown in Fig. 4-4 and Fig. 4-5. Nine gages placed within 6 in. (half of the width of the column) from the edge column base in PFS1 (SG-ECOL-L11/L12/L13, SG-ECOL-L3 to SG-ECOL-L8). Multiple pairs of strain gages were placed on the edge column rebar in the base block (SG-ECOL-L1/L2), at the top of the first story edge column (SG-ECOL-L9/L10), and at the bottom of the second story edge column (SG-ECOL-L15/L16).

The layout of the steel strain gages attached to the reinforcement in the edge columns in PFS2 was similar to that of PFS1, as shown in Fig. 4-18 through Fig. 4-21. Different from PFS1, four concrete strain gages were embedded at the base of each edge column. Because the gage length of the concrete strain gages was about 2-3/8 in., which was much larger than that of the steel strain gages (1/8 in.), the readings from the concrete gages were only used to deduce an average strain over the gage length in the edge columns. Two figures of each edge column viewing from two orthogonal directions are used to better illustrate the locations of the concrete gages.

Assuming strain compatibility was valid for the cross sections of the edge columns, local curvatures could be obtained using a pair of strain gages located at similar heights in the cross section:

$$\varphi_{col\_l} = \frac{\varepsilon_{rebar\_E\_i} - \varepsilon_{rebar\_W\_j}}{s_{col\_rebar}} \tag{4.5}$$

Where φ_{col_l} = Local curvature of the edge column, $\varepsilon_{rebar\_E\_i}$ = Strain gage readings of the rebar on the east side of the edge column (i=3,5,7,9,11), $\varepsilon_{rebar\_W\_j}$ = Strain gage readings of the rebar on the west side of the edge column (j=4,5,8,10,12), s_{col_rebar} = Distance between the rebar in the east and the west side of the edge column.

Local curvature distribution along the height of the edge columns was monitored by these strain gage pairs in the edge columns. The local curvatures were also used to examine the reliability of the average curvatures obtained from the LVDTs (string pots or DCDTs) discussed in the previous section.

Three strain gages (SG-WCOL-T1/T2/ T3) were attached to the stirrups in the edge column to monitor the confinement effect in both tests. Fig. 4-6 shows the arrangement in the west edge column in PFS1. By plotting the strain gage readings along the height of the edge columns, the region where the confinement took effect was obtained.

4.2.2.4 PT Force in the Edge Columns

In PFS1, a 3/4 in. diameter high strength threaded rod in the first story edge column was post-tensioned to simulate the gravity load from the tributary area of the floor. Because the edge column was directly connected to the steel column above, load cells were not able to be installed on top of the first story edge column. Instead, four strain gages (two vertical and two horizontal) were attached to the threaded rod to measure the axial strain in the rod. A small portion of the rod was ground to create a smooth surface for the attachment of the strain gages. To validate the feasibility of this method, a component test of a threaded rod with four strain gages attached was conducted before the assemblage test. A factor that converted the strain gage readings to the axial force in the rod was obtained and input to the data acquisition system of PFS1 test.

In PFS2, a 1 in. diameter high strength threaded rod in each edge column was post-tensioned to emulate the gravity loads from the tributary area of the floor. A load cell was installed on top of each edge column to measure the axial load in the rod. The load cell readings were used directly for data analysis.

4.2.3 O-connectors

4.2.3.1 Relative Vertical Displacement

Existing tests have shown that the hysteretic behavior of the O-connectors was well predicted by numerical models as long as the relative vertical displacements of the O-connectors was known (Henry 2011). Assuming the wall rocked like a rigid body, the four O-connectors on the same side of the wall were expected to similar relative vertical deformations. As shown in Fig. 4-2, two LVDTs (L2-NWOV and L2-NEOV) were used to measure the east and the west relative vertical deformations of the O-connectors between the wall and the end columns in PFS1. As shown in Fig. 4-16, only one LVDT (L2-NWOV) was used to measure the west relative vertical deformation in PFS2 due to the limited amount of LVDTs.

4.2.3.2 Strains at Critical Regions

Strain gages were attached to critical regions of the O-connectors where large strains were expected, as shown in Fig. 4-7 for PFS1 and Fig. 4-22 for PFS2. The strain gage readings were used to monitor the yielding and fracture of the O-connectors. The critical regions were determined by the numerical models (discussed in Section 5.4.3).

4.2.4 Props

A load cell was installed at the top of each prop to measure the individual forces in the props in both tests, including the varied axial forces at the peak drifts. By multiplying the axial forces by the distance between the props and the wall, the resisting moment on the wall from the floor in the transverse direction was obtained that was related to the strength and the self-centering behaviors of the specimens.

4.2.5 Krypton and Optotrak Systems

Two Krypton systems and one Optotrak system were used in both tests. Fig. 4-8 and Fig. 4-9 show the regions where the LEDs were attached to PFS1. Fig. 4-23 and Fig. 4-24 show the regions where the LEDs were attached to PFS2. Abundant data was generated

by the Krypton and Optotrak systems. They were used to validate the test data provided by other types of instrumentation in this dissertation.

After describing the instrumentation that served similar purposes in the two tests, the instrumentation used specifically for PFS1 and PFS2 is discussed in the following two sections.

4.3 Instrumentation for Specific Purposes in PFS1

4.3.1 Unbonded PT Slab

4.3.1.1 Rotation and Average Curvature Distribution of the Slab

As shown in Fig. 4-11, seven pairs of LVDTs distributed among series FCL, FEG and FCE were used to measure the rotation and average curvature distribution at the west floor-edge beam connections. Each pair of LVDTs included one above and one below the slab. The first row of LVDTs mounted across the floor-edge beam interface contained four pairs, while the other three pairs of LVDTs were placed in the second row and measured the deformation between the first and second row of LVDTs. The second row of LVDTs were placed across the sections where the bonded reinforcement was terminated and the potential secondary weak cross sections existed.

Similarly, two rows of LVDTs and string pots (Series of FWL1 and FWL2) were placed across the west wall-floor connections. Because long steel plates were used as a common anchor on the slab edge to distribute the bearing stresses of the four banded transverse PT tendons placed towards the wall tips, it was thought that the steel plates might locally constrain the flexural deformation of the slab in the longitudinal direction and affect the crack patterns. Consequently, LVDTs and SPs were arranged to cover potential cracks that were expected to develop across the edges of the wall and each end of the steel plate (L1-FWL1-T1/B1, L1-FWL1-T2/B2, SP2-FWL1-T3/B3, L01-FWL1-T4, L1-FWL2-T1/B1, L05-FWL2-T2/B2, SP2-FWL2-T3/B3, SP2-FWL2-T4/B4).

To investigate the constraint effect from parallel structural systems emulated by the props, three pairs of LVDTs distributed among series of FWT and FPT were used to

measure the rotation and the average curvature distribution at the wall-floor and the floor-prop connections in the transverse direction.

Due to limited instrumentation, only two pairs of LVDTs (Series of EFWL and EFCL) were placed at the east half of the floor: one was at the east wall-floor connection and the other was at the east floor-edge beam connection close to the edge column. The data recorded by these LVDTs was used to examine the reliability of the data recorded by the instrumentation for the west half of the floor.

The average curvatures of the slab were deduced by dividing the rotations obtained from each pair of LVDTs (or String Pots) with the gage length of the LVDTs (or String Pots), which is listed in Table D-1 in Appendix D. For example, the local curvature at the location of the L1-FWL1-T1/L1-FWL1-B1 was deduced:

$$\theta_l = \frac{\Delta_{top} - \Delta_{bot}}{t_{slab} + d_{top} + d_{bot}} \tag{4.6}$$

$$\varphi_l = \frac{\theta_l}{s_l} \tag{4.7}$$

Where θ_l = Local rotation of the slab, Δ_{top} = Extension or shortening recorded by the LVDT above the slab (e.g. L1-FWL1-T1), Δ_{bot} = Shortening or extension recorded by the LVDT below the slab (e.g. L1-FWL1-B1), t_{slab} = Thickness of the slab, d_{top} = Distance from the top surface of the slab to the core of the top LVDT (e.g. L1-FWL1-T1), d_{bot} = Distance from the bottom surface of the slab to the core of the bottom LVDT (e.g. L1-FWL1-B1), φ_l = Local average curvature of the slab, s_l = Average gage length of the top and the bottom LVDT (e.g. L1-FWL1-T1 and L1-FWL1-B1).

The average curvature distribution of the slab was used to investigate the potential damage of the floor in the two orthogonal directions. By comparing the average curvature distribution before and after the props were attached to the slab, the impact from the parallel structural systems was studied.

4.3.1.2 Local Strain Distribution of the Floor Slab

As shown in Fig. 4-12, strain gages were attached to the rebar in the floor slab to measure local strains in the floor. The strain gages attached to the longitudinal and transverse rebar are described separately in the following.

Strain gages on the rebar in the longitudinal direction

Five strain gages (SG-FEG-T0 through SG-FEG-T4) were attached to the top bonded rebar at the floor-edge beam connection. One strain gage SG-FEG-B1 was attached to the bottom bonded rebar at the floor-edge column interface. Two strain gages (SG-FEG-B2 and SG-FEG-B3) were attached to the bottom mesh rebar at the floor-edge beam connections. Two strain gages (SG-FEGE-B1 and SG-FEGE-B2) were attached to the bottom mesh rebar beyond the first row of strain gages to measure the strains in the region of the slab beyond the rebar cutoff points to investigate potential spread of plasticity beyond the cutoffs.

Two strain gages (SG-FWL-T1 and SG-FWL-T2) were attached to the top bonded rebar close to the wall. One strain gage SG-FWL-B1 was attached to the bottom bonded rebar at the wall-floor connection. Two strain gages (SG-FWL-B2 and SG-FWL-B3) were attached to the bottom mesh rebar. Two strain gages (SG-FPL-T1 and SG-FPL-T2) were attached to the top bonded rebar at the prop-floor connection.

Strain gages on the rebar in the transverse direction

Two strain gages (SG-FWT-T1 and SG-FWT-T2) were attached to the top rebar at the west wall end. One strain gage SG-FWT-C1 was attached to the shear-friction rebar that was in the middle of the slab. Two strain gages (SG-FWT-B1 and SG-FWT-B2) were attached to the bottom mesh rebar close the wall.

Six strain gages (SG-FPT-T1/SG-FPT-B2, SG-FPT-T2/SG-FPT-B3 and SG-FPT-T3/SG-FPT-B4) were attached to the top and bottom legs of the U-shaped #2 wire. As discussed in Section 3.3.2, the U-shaped wires were used to resist the bursting force for the banded PT strands. Two strain gages (SG-FPT-B1 and SG-FPT-B5) were attached to the bottom mesh rebar close to the prop.

Due to a limited amount of strain gage channels, only four discrete strain gages were attached to the rebar at the east half of the slab. SG-EFWL-T-Y was attached to the top

longitudinal rebar at the east wall-floor connection. Strain gages SG-EFWT-T1-Y and SG-EFWT-T2-Y were attached to the transverse rebar at the east wall-floor connection. A strain gage SG-EFCL-B-Y was attached to the longitudinal rebar at the east floor-column connection. The readings of these strain gages were used to examine the readings from the counterpart strain gages at the west side of the slab.

Other than the strain gages on the steel reinforcement, multiple concrete gages were mounted in the slab to monitor the strains in the slab developed during the post-tensioning operation. Six concrete gages (CG-L-SW, CG-L-WM, CG-L-NW, CG-L-SE, CG-L-EM and CG-L-NE) were used in the longitudinal direction and four concrete gages (CG-T-SW, CG-T-NW, CG-T-SE and CG-T-NE) were used in the transverse direction. However, it was observed that some concrete gages were bumped when casting the slab during construction. The readings of these concrete gages were excluded from data analysis.

4.3.1.3 PT Forces in the Unbonded PT Slab

As shown in Fig. 4-10, seven load cells were used to monitor the forces in the PT strands in the slab. LC_FPTW1 through LC_FPTW4 were used to measure the PT force in the E-W longitudinal strands. LC_FPTW3 and LC_FPTW4 were installed on the same strand to investigate the PT forces at different ends. LC_FPTSE1 through LC_FPTSE4 were used to measure the PT forces in the N-S transverse strands. The load cells were used to record the initial PT forces after seating losses, the PT forces at the beginning of the test, and measure the varied PT forces when the slab deformed due to the rocking of the wall and the residual PT forces when the wall returned to “zero displacement position.” The load cell readings were also used to investigate the three-dimensional constraint effect after the props were attached to the slab.

4.3.1.4 Deformed Shape of the Slab

As shown in Fig. 4-10, thirteen string pots were placed in two quadrants of the slab to measure the vertical deformation of the slab. However, it was found that deriving the actual vertical deformation of the slab from the readings of string pots was difficult. It was because other than the vertical deformation of the slab, the horizontal displacements

of the slab also contributed to the elongation of the string pot wire. The readings from these string pots were not used in the analysis in this dissertation.

4.3.2 Mega Beam with Cover Plates

4.3.2.1 Relative Rotation of the Mega Beams

As shown in Fig. 4-2, a pair of LVDTs was attached on each end of the east mega beam. L1-EMBT-W and L1-EMBB-W were used to measure the relative rotation between the mega beam and the wall. L1-EMBT-E and L1-EMBB-E were used to measure the relative rotation between the mega beam and the steel column. As discussed in Section 3.3.3.2, the behavior of the mega beam with cover plates was well predicted by the detailed finite element model. The moment resistances provided by the cover plates of the west mega beam at the beam-wall joint and the beam-steel column joint were deduced by inputting the recorded rotations of the mega beams to the numerical model of the mega beams.

The rotations of the mega beam were deduced by the following equation:

$$\theta_{mgbeam} = \frac{\Delta_{beam\_T} - \Delta_{beam\_B}}{d_{mgbeam} + d_{top} + d_{bot}} \tag{4.8}$$

Where θ_{mgbeam} = Rotation of the mega beam, Δ_{beam_T} = Extension or shortening recorded by the LVDT mounted on the top flange, Δ_{beam_B} = Extension or shortening recorded by the LVDT mounted on the bottom flange, d_{mgbeam} = Depth of the mega beam (10-1/2 in).

No LVDTs were attached to the west mega beam due to the limited amount of LVDTs. Instead, a tiltmeter (TBWSB) was used to measure the rotation of the west mega beam close to the steel column, as shown in Fig. 4-1. A tiltmeter (TBWSC) was attached to the top of the west steel column to measure its rotation, as shown in Fig. 4-1. By subtracting the readings of TBWSB by those of TBWSC, the rotations of the mega beam at the west beam-column joint were obtained.

4.3.2.2 Force Flow in the Mega Beam

As shown in Fig. 4-13, two strain gages were attached to each cover plate of the east mega beam for redundancy. Strain gages SG-EBWTP-M/SG-EBWTP-E and SG-

EBWBP-M/SG-EBWBP-E were attached to the top and the bottom cover plates close to the wall. SG-EBCTP-M/SG-EBCTP-E and SG-EBCBP-M/SG-EBC-BP-E were attached to the top and bottom cover plates close to the steel column. The strain gages measured the axial strains in the steel plate that were used to deduce the resisting moments at the two ends of the mega beam.

Two strain gages (SG-EBMT and SG-EBMB) were attached to the top and the bottom flanges to investigate the moments in the middle of the beam. Three rosettes (FRA-EBM-V/I/H, FRA-EBC-V/I/H and FRA-EBW-V/I/H) were attached to the web of the mega beam to investigate the shear strains in the mega beam: one was placed in the middle and the other two were placed at the two ends of the beam.

Fig. 4-14 shows the strain gages attached to the west mega beam. Due to limited strain gages, only one gage was attached to each cover plate of the west mega beam (SG-WBWTP-M, SG-WBWBP-M, SG-WBCBP-M and SG-WBCTP-M). One rosette FRA-WBM-V/I/H was attached to the web in the middle of the beam.

Before the cover plates yielded in the test, the resisting moment of the mega beam at the two ends could be deduced as follows:

$$M_{mgbeam\_cp} = \frac{E_s\left(\epsilon_{cp\_T} - \epsilon_{cp\_B}\right)}{2} \cdot (t_{cp} b_{cp}) \cdot (d_{mgbeam} + t_{cp}) \qquad (4.9)$$

Where M_{mgbeam_cp} = Moment resistances provided by the cover plates of the mega beam; E_s = Young's modulus of the steel; ϵ_{cp_T} = Strains in the dogbone section of the top cover plate; ϵ_{cp_B} = Strains in the dogbone section of the bottom cover plate; d_{mgbeam} = Depth of the mega beam, t_{cp} = Thickness of the cover plate (7/8 in.); b_{cp} = Width of the cover plate at the "dogbone" section (1-1/2 in.).

For the two strain gages attached to the top and the bottom flanges in the middle of the east mega beam, the moment of the beam was deduced as follows:

$$M_{mgbeam\_middle} = \frac{E_s\left(\epsilon_{mgbeam\_T} - \epsilon_{mgbeam\_B}\right)}{2} \cdot \frac{I_{mgbeam}}{d_{mgbeam}/2} \qquad (4.10)$$

Where M_{mgbeam_middle} = Moment in the middle section of the mega beam; ϵ_{mgbeam_T} = Strain in the top flange of the beam; ϵ_{mgbeam_B} = Strain in the bottom flange of the beam; I_{mgbeam} = Moment of inertia of the beam (170 in^4).

The strain gages on the flanges of the beam could be used to deduce the axial load in the mega beam as follows:

$$N_{mgbeam\_middle} = \frac{E_s\left(\epsilon_{mgbeam\_T} + \epsilon_{mgbeam\_B}\right)}{2} \cdot A_{mgbeam} \tag{4.11}$$

Where A_{mgbeam} = Cross-sectional area of the mega beam (8.84 in^2); N_{mgbeam_middle} = Axial force in the beam deduced by the strain gages on the flanges.

For the strain gage rosettes attached to the web of the mega beam, the shear force in the beam could be deduced as follows:

$$V_{mgbeam} = \frac{G\gamma_{rosette} I_A t}{Q}, \tag{4.12}$$

$$G = \frac{E_s}{2(1+\nu)}, \tag{4.13}$$

$$\gamma_{rosette} = \sqrt{2} \times \sqrt{(\epsilon_V - \epsilon_I)^2 + (\epsilon_H - \epsilon_I)^2} \tag{4.14}$$

$$Q = \int y_i d_A \tag{4.15}$$

Where V_{mgbeam} = Shear forces in the mega beam; G = Shear modulus of steel; $\gamma_{rosette}$ = Shear strains deduced from the rosette; I_A = Moment of inertia of the entire cross-sectional area; t = Web thickness (0.3 in); Q = Statical moment of area (18.1 in^3 in the middle of the beam); ν = Poission's ratio of steel materials (0.3); ϵ_V = Strain in the vertical gage of the rosette; ϵ_I = Strain in the 45° inclined gage of the rosette; ϵ_H = Strain in the horizontal gage of the rosette; d_A = Elemental area of the cross section above the neutral axis; y_i = Perpendicular distance from the neutral axis to the elemental area.

It was observed during the test that the cover plates of the mega beams yielded at small drift levels, thus it was difficult to obtain the resisting moments of the mega beams from the strain gage readings. As mentioned in the previous section, the numerical model of the mega beam was mainly used in this dissertation to investigate the resisting moments

provided by the mega beams. The rotations that were used in the numerical model were measured by the LVDTs and the tiltmeters discussed above.

4.3.3 Steel Columns

As shown in Fig. 4-7, three gages (SG-ESCBTF, SG-ESCBW-N and SG-ESCBBF) were attached to the bottom of the east steel column. As shown in Fig. 4-13, three gages (SG-ESCTTF, SG-ESCTW-N and SG-ESCTBF) were attached to the top of the east steel column. Because the steel column was expected to remain elastic throughout the test, the strain gages were used to deduce the moment, the shear and the axial load in the steel columns:

$$M_{scol\_T} = \frac{E_s\left(\epsilon_{scol\_TTf} - \epsilon_{scol\_TBf}\right)}{2} \cdot \frac{I_{scol}}{d_{scol}/2} \tag{4.16}$$

$$M_{scol\_B} = \frac{E_s\left(\epsilon_{scol\_BTf} - \epsilon_{scol\_BBf}\right)}{2} \cdot \frac{I_{scol}}{d_{scol}/2} \tag{4.17}$$

$$N_{scol\_T} = \frac{E_s\left(\epsilon_{scol\_TTf} + \epsilon_{scol\_TBf}\right)}{2} \cdot A_{scol} \tag{4.18}$$

$$N_{scol\_B} = \frac{E_s\left(\epsilon_{scol\_BTf} + \epsilon_{scol\_BBf}\right)}{2} \cdot A_{scol} \tag{4.19}$$

$$V_{scol} = \frac{\left(M_{scol\_T} - M_{scol\_B}\right)}{s_{scol\_gage}} \tag{4.20}$$

Where M_{scol_T} = Moment at the top of the steel column; ϵ_{scol_TTf} = Strain in the top flange at the top of the steel column; ϵ_{scol_TBf} = Strain in the bottom flange at the top of the steel column; I_{scol} = Moment of inertia of the steel column (954 in^4); d_{scol} = Depth of the steel column (16-3/8 in.); N_{scol_T} = Axial force in the steel column deduced by the gages at the top of the steel column; N_{scol_B} = Axial force in the steel column deduced by the gages at the bottom of the steel column; M_{scol_B} = Moment at the bottom of the steel column; ϵ_{scol_BTf} = Strain in the top flange at the bottom of the steel column; ϵ_{scol_BBf} = Strain in the bottom flange at the bottom of the steel column; A_{scol} = Cross-sectional area of the steel column (19.7 in^2); V_{scol} = Shear force in the steel column; s_{scol_gage}= Distance between the top and the bottom strain gages (95 in.).

Based on force equilibriums at the beam-column joint, the shear forces and the axial forces in the steel column were equal to the axial forces and shear forces in the connected mega beam, respectively. Therefore, the shear forces and the axial forces deduced from the readings of the strain gages on the steel column were used to obtain the axial forces and the shear forces in the mega beam. Because the steel columns were expected to remain elastic, the readings of the strain gages were effective throughout the test that provided an indirect way to investigate the behaviors of the mega beams.

4.4 Instrumentation for Specific Purposes in PFS2

4.4.1 PreWEC End Columns

The reinforcement in the PreWEC end columns was not continuous across the base block, thus the end columns were expected to behave like rocking columns. Four concrete gages were placed in the end columns near the base to monitor the strain distribution. To better illustrate the locations of the concrete gages, two figures of each end column viewing from two orthogonal directions are used: Fig. 4-25 and Fig. 4-26 are for the east end column; Fig. 4-27 and Fig. 4-28 are for the west end column. As shown in the figures, three gages were placed close to the bottom to investigate the compressive strain distribution in both in-plane and out-of-plane directions. The fourth gage was placed above the first row of the three gages to investigate the strain distribution along the height of the end column.

As shown in Fig. 4-25 and Fig. 4-27, three steel strain gages (SG-E_ECOL-T1/T2/ T3 and SG-W_ECOL-T1/T2/ T3) were attached to the stirrups in the east and the west end column base to monitor the confinement effect. By plotting the readings of the strain gages along the height of the end columns, the region where the confinement took effect was obtained.

4.4.2 Precast Floor

As shown in Fig. 4-29, four pairs of LVDTs distributed among series FCL and MFCL were placed at the west floor-edge beam connections. Each pair included an LVDT above

and below the slab. Because the precast planks were much stiffer than the connecting straps across the floor-edge beam connections, they were expected to behave like rigid bodies (the curvature of the planks was expected to be very small). The readings of the LVDTs were mainly used to investigate the rotation distribution across the floor-edge beam connections. Similarly, six pairs of LVDTs distributed among series FWL1, FWL and MFWL were used to investigate the rotation distribution across the floor-transverse beam connections.

Other than the LVDTs measuring the rotation of the planks, multiple LVDTs were mounted on the top surface of the planks to monitor the behaviors of the JVI Mini-V connectors. L05_FL_1, L05_FL_3 and L05_FL_5 were used to measure the potential shear sliding between adjacent planks. L05_FL_2, L05_FL_4 and L05_FL_6 were used measure the potential horizontal opening between adjacent planks.

Due to the limited amount of LVDTs, no LVDTs were placed on the east half of the floor.

As shown in Fig. 4-30, a large amount of strain gages was attached to the steel strap plates to monitor the force flow in the precast planks. Because the straps were expected to have flexural bending in the test, strain gages were attached to both top and bottom of the straps. The axial force and the bending moment of the strap plates were deduced as follows:

$$N_{strap} = \frac{E_s\left(\epsilon_{strap\_T} + \epsilon_{strap\_B}\right)}{2} \cdot A_{strap} \tag{4.21}$$

$$M_{strap} = \frac{E_s\left(\epsilon_{strap\_T} - \epsilon_{strap\_B}\right)}{2} \cdot \frac{I_{strap}}{t/2} \tag{4.22}$$

Where N_{strap} = Axial force in the strap; ϵ_{strap_T} = Strain in the top surface of the strap; ϵ_{strap_B} = Strain in the bottom surface of the strap; A_{strap} = Cross-sectional area of the strap (1.5 in^2); M_{strap} = Moment in the strap; I_{strap} = Moment of inertia of the strap (0.0176 in^4); t = Depth of the strap (3/8 in.).

There were no strain gages attached to some straps at the floor-transverse beam connections and floor-edge beam connections. Because the stiff planks were expected to move like rigid bodies, an assumption was made that the axial forces in the two straps

connected to the same plank were the same. By summing the axial forces of all of the strap plates at the floor-transverse beam connections, the horizontal force that was transferred to the BS Italia connectors was deduced.

4.4.3 Steel Mega Truss

As shown in Fig. 4-16, a pair of LVDTs was mounted on each end of the east steel truss. L1-EMBT-W and L1-EMBB-W were used to measure the relative rotation between the steel truss and the wall. L1-EMBT-E and L1-EMBB-E were used to measure the relative rotation between the steel truss and the second story edge column. The rotation of the steel truss was deduced by the following equation:

$$\theta_{truss} = \frac{\Delta_{truss\_T} - \Delta_{truss\_B}}{d_{truss} + d_{top} + d_{bot}} \tag{4.23}$$

Where θ_{truss} = Rotation of the steel truss, Δ_{struss_T} = Extension or shortening recorded by the LVDT mounted on the top surface, Δ_{truss_B} = Extension or shortening recorded by the LVDT installed on the bottom surface, d_{truss} = Depth of the steel truss (4 in.), d_{top} = Distance from the top surface of the mega truss to the top LVDT, d_{bot} = Distance from the bottom surface of the mega truss to the bottom LVDT

No LVDTs were mounted on the west steel truss. Instead, a tiltmeter (TBWSB) was used to measure the rotation of the west steel truss, as shown in Fig. 4-15. By subtracting the readings of TBWSB with the readings of TTW mounted on top portion of the wall, the total rotation of the west steel truss at the beam-wall joint could be obtained.

Because the steel truss was pinned-pinned connected at both ends, little moment was expected to be generated in the steel truss. Two strain gages were attached to each end of the steel truss to obtain its axial forces. The strain gages were on the north and south surface of the steel truss and located at mid-depth of the steel truss. The axial forces in the steel truss were obtained as follows:

$$N_{truss} = \frac{E_s\left(\varepsilon_{truss\_N} + \varepsilon_{truss\_S}\right)}{2} \cdot A_{truss} \tag{4.24}$$

Where N_{truss} = Axial forces in the steel truss; ε_{truss_N} = Strains in the north surface of the truss; ε_{truss_S} = Strains in the south surface of the truss; A_{truss} = Cross-sectional area of the truss (3.75 in^2).

The axial forces in the steel truss were used to investigate the force flow in specimen PFS2.

4.5 Loading Protocol and Testing Phases

4.5.1 Specimen PFS1

The test of PFS1 consisted of four phases. The specimen was under in-plane loading in the first three phases. The props were attached to the floor in Phase 2 and removed in Phase 3 when lateral displacements of high drift levels (i.e., in excess of 3%) were applied to PFS1. The specimen was under biaxial loading in phase 4. The boundary conditions of the four phases are summarized in Table 4.1. As shown in the table, a constant axial load 128 kips was input to the top block in the first three phases to simulate gravity load effects applied to the wall, and it was removed in Phase 4 (for safety considerations).

External lateral loads generated to achieve the programmed lateral displacements and external lateral resisting moments slaved to the external loads were applied to the top of the wall in the tests. The slaved moment was equal to 3.48 times the input lateral load in the crosshead throughout the test, and it was in the opposite direction of the input load. The amount and the direction of the slaved moment were discussed below.

The height of the scaled prototype building was 24 feet. The test specimen was 249-1/2 in. that was slightly shorter than the scaled prototype building. A compensating moment was required to keep the base moment and the base shear of the specimen equivalent to those in the scaled prototype building. Assuming an inverted triangular distribution of the lateral loads was applied to the prototype structure, the base moment and the base shear of the scaled prototype structure would be:

$$\begin{aligned} M_{PB} &= 6F_1 \cdot 6H + 5F_1 \cdot 5H + 4F_1 \cdot 4H + 3F_1 \cdot 3H + 2F_1 \cdot 2H + F_1 H \\ &= 91F_1 H \end{aligned} \tag{4.25}$$

$$V_{PB} = \int_{i=1}^{6} F_i = 6F_1 + 5F_1 + 4F_1 + 3F_1 + 2F_1 + F_1 = 21F_1 \quad (4.26)$$

Where M_{PB} = Base moment of the scaled prototype building, F_i = Concentrated lateral force on each story (i = [1, 6]), H = Height of each story (4 feet), V_{PB} = Base shear of the scaled prototype building.

The base moment and the base shear of the test specimen were:

$$M_{specimen} = F_{crosshead}H_{specimen} + M_{slaved} \quad (4.27)$$

$$H_{specimen} \approx 5.2H \quad (4.28)$$

$$V_{specimen} = F_{crosshead} \quad (4.29)$$

Where $M_{specimen}$ = Base moment of the specimen, $F_{crosshead}$ = Concentrated lateral force applied to the crosshead, $H_{specimen}$ = Height of the specimen, M_{slaved} = Slaved moment applied to the crosshead, $V_{specimen}$ = Base shear of the specimen.

Substitute $V_{specimen} = F_{crosshead} = V_{PB} = 21F_1$ and $H_{specimen} = 5.2H$ into the expression for the base moment of the specimen and equate it with M_{PB}:

$M_{specimen} = F_{crosshead}H_{specimen} + M_{slaved} = 21F_1 \times 5.2H + M_{slaved} = M_{PB} = 91F_1H$

Solve the equation and $M_{slaved} = -18.2\ F_1H = -0.867F_{crosshead}H = -3.48\ F_{crosshead}$ (Unit: kip-ft).

Fig. 4-31 and Fig. 4-32 show the in-plane and the out-of-plane loading protocols of PFS1, respectively. Three cycles at each drift level were applied until 2.5% drift in Phase 1 when an unexpected fracture of one strand wire occurred. To avoid further decreasing the PT forces in the wall, it was decided to attach the props to the slab and the second phase of testing was started (i.e., Phase 2). In Phase 2, two cycles at each drift level were applied until 2.5% drift and then three cycles at 3% drift followed. At the end of Phase 2, severe localized damage was observed at the wall-floor connections, which was believed to have been caused by the restraint provided by the props. For safety considerations, the props were removed in Phase 3 when high drift levels (3 cycles of 4% drift and 1 cycle of 5% drift) were applied to the specimen. Fig. 4-31 summarizes the in-plane loading protocol of PFS1.

A “butterfly-shaped” loading protocol was applied for the biaxial test in Phase 4. A lateral displacement of 4% drift was applied in the in-plane direction; a lateral displacement of 1.2% drift was applied in the out-of-plane direction. The choice of the appropriate loading combination was based on IBC: the design orthogonal loading combination was equal to “100 percent of the forces for one direction plus 30 percent of the forces for the perpendicular direction. The combination requiring the maximum component strength shall be used.” (IBC 2009) Displacement control was used in the test of PFS1, thus it was decided that the out-of-plane displacement applied to PFS1 was equal to 30% of the in-plane displacement during the biaxial loading. Similarly, the slaved moment in the out-of-plane direction was equal to -3.48 times the applied load in the out-of-plane direction. Fig. 4-32 shows the biaxial loading protocol in PFS1.

4.5.2 Specimen PFS2

The test of PFS2 consisted of twelve phases. Table 4.2 shows an outline of the different boundary conditions in the twelve testing phases. Because of the use of the vertical movement isolated connectors, no axial load was input to the specimen by the crosshead except during the last phase of testing.

The edge column base plates were not tightened to the base block in Phase 1 and Phase 2 to investigate the possibility of achieving a “damage-free” structure with the PreWEC system, rocking edge columns and precast floor systems. The damage was expected to be limited to the replaceable energy dissipating elements, the replaceable steel straps on the slab and the repairable damage in the concrete in the corners of the wall, PreWEC end columns and edge columns. During Phase 3 through Phase 12, the edge column base plates were tightened to the base block to emulate a more typical connection detail for the precast fixed-base edge columns.

The boundary conditions of with/without props were investigated by comparing the results in Phase 1 with those in Phase 2 (also Phase 3 with Phase 4). In Phase 5, the specimen was loaded to higher drift levels (4%) with fixed-base edge columns being used and props attached.

Biaxial loading was applied to the specimen in Phase 6. One cycle of butterfly-shaped loading at 2% drift was applied first, followed by two cycles of butterfly-shaped loading steps at 3% drift. Different from the biaxial loading protocol in PFS1, the drift level in the out-of-plane direction was the same as that in the in-plane direction in all biaxial loading phases in PFS2. The purpose was to investigate the behavior of PFS2 when it was loaded to a relatively large in-plane displacement with a comparable out-of-plane displacement.

In-plane loading was resumed in Phase 7 during which the specimen was loaded to 5% drift limited only by the displacement capacity of the facility.

Two BS Italia connections that were close to the east side of the wall were disconnected by torching them just prior to Phase 8. The purpose of removing the two connectors was to increase the shear force transferred to the remaining two BS Italia connections to investigate its vertical sliding performance under large shear forces. The specimen was displaced to 5% drift in this phase.

The steel mega trusses of the specimen were removed in Phase 9. The purpose was to further increase the shear force transferred to each of the two BS Italia connections.

The impact from the surrounding structures was reduced to the minimum in Phase 10 by the following operations: the props were removed; the nuts at the edge column base were removed; the PT forces in both edge columns and end columns were removed; the O-connectors were all torched. The purpose was to study the performance of an isolated rocking wall under biaxial loading in Phase 11.

In this phase, one cycle of butterfly-shaped loading was applied at 2% drift. One cycle of 3% in-plane loading was conducted afterwards to serve as a control to investigate the behavior before the following biaxial loading cycles. One cycle of butterfly-shaped and cloverleaf-shaped loading steps were applied at 3% drift. A half cycle of butterfly-shaped loading step at 3% drift was followed to compare with the results from the previous butterfly-shaped loading step and study the impact from cloverleaf-shaped loading step. A cycle of butterfly-shaped loading was applied at 4% drift to conclude Phase 11.

In Phase 12, a constant axial force (96.8 kips) was input to the specimen by the crosshead that emulated the gravity load from the tributary floor of the wall, assuming that the wall carried the gravity load despite of the usage of BS Italia connections. The

purpose of this phase was to study the impact from the gravity load on the moment resistance and self-centering capability of the rocking wall.

Table 4.1 Test phases of PFS1

Phases	Drift level (cycles per drift level)	Peak drifts (%)	With Props	Biaxial Loading	Gravity Load (kip)
1	0-2.5% (3)	0.05, 0.075, 0.1, 0.25, 0.5, 0.75, 1, 1.5, 2, 2.5	No	No	128
2	0-3% (2)	0.1, 0.25, 0.5, 0.75, 1, 1.5, 2, 2.5, 3	Yes	No	128
3	4% (1)	4	No	No	128
	5% (1)	5	No	No	
4	4% in plane 1.2% out of plane	4 in plane 1.2 out of plane	No	Butterfly	0

Table 4.2 Test phases of PFS2

Phases	Drift level (cycles per drift level)	Rocking / Fixed-base column	With Props	No. BS Italia connections	2nd story truss	Biaxial loading
1	0-2% (3)*	Rocking	No	Four	Yes	No
2	2% (1)	Rocking	Yes	Four	Yes	No
3	0-2% (3)*	Fixed-base	No	Four	Yes	No
4	2% (1)	Fixed-base	Yes	Four	Yes	No
5	2-4% (3)**	Fixed-base	Yes	Four	Yes	No
6	2% & 3% biaxial	Fixed-base	Yes	Four	Yes	Yes
7	4%-5% (3)***	Fixed-base	Yes	Four	Yes	No
8	5% (1)	Fixed-base	Yes	Two	Yes	No
9	5% (1)	Fixed-base	Yes	Two	No	No
10	5% (1)	Fixed-base	No	Two	No	No
11	3% & 4% biaxial	Fixed-base	No	Two	No	Yes
12	2% (1)	Fixed-base	No	Two	No	No

* Peak drifts in Phase 1 and Phase 3 in PFS2 were similar to those defined in Phase 1 of PFS1

** Peak drifts in Phase 5 in PFS2 included 2%, 2.5%, 3% and 4%.

*** Peak drifts in Phase 7 in PFS2 included 4% and 5%.

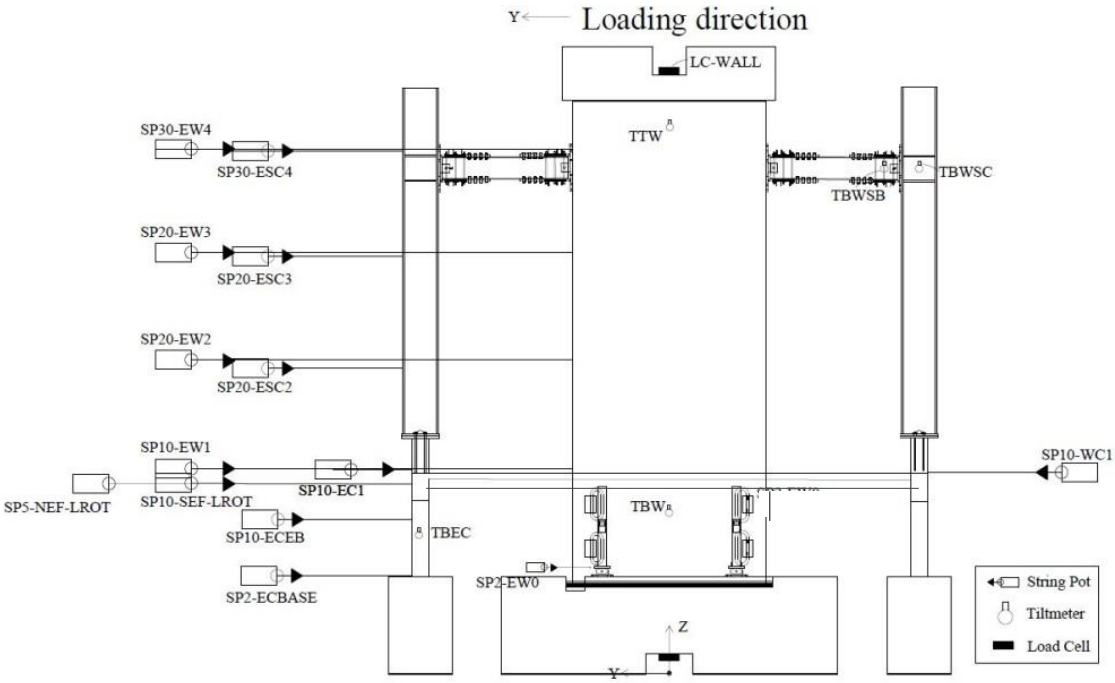

Fig. 4-1 Load cell, string pots and tiltmeters of PFS1 (Elevation view of the specimen)

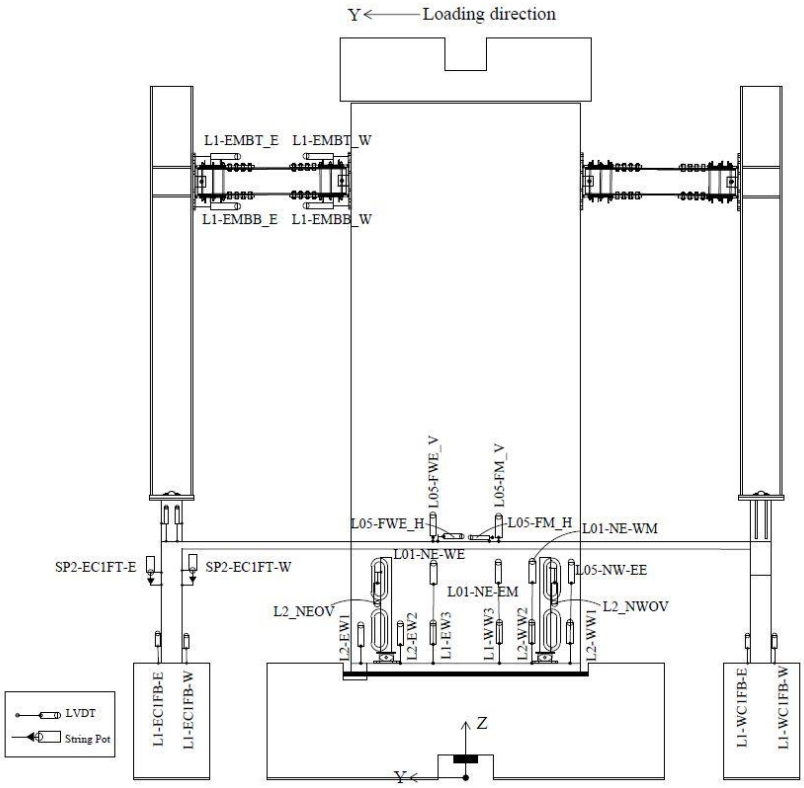

Fig. 4-2 LVDTs and string pots of PFS1 (Elevation view of the specimen)

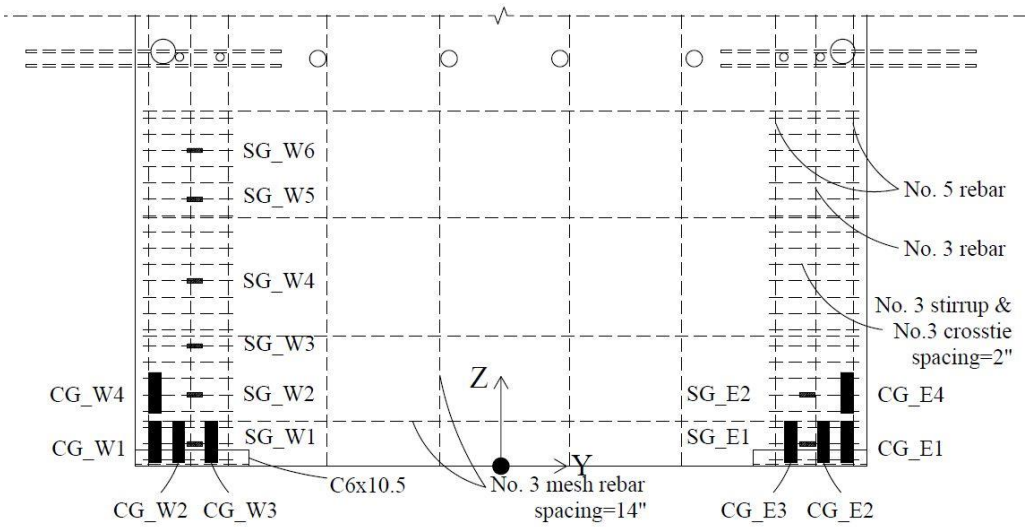

Fig. 4-3 Strain gages in the wall panel of PFS1

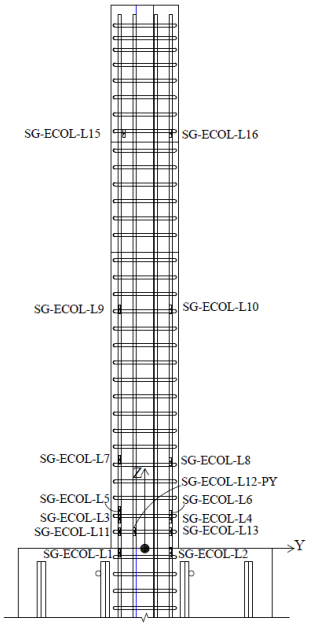

Fig. 4-4 Strain gages on the longitudinal reinforcement of east column

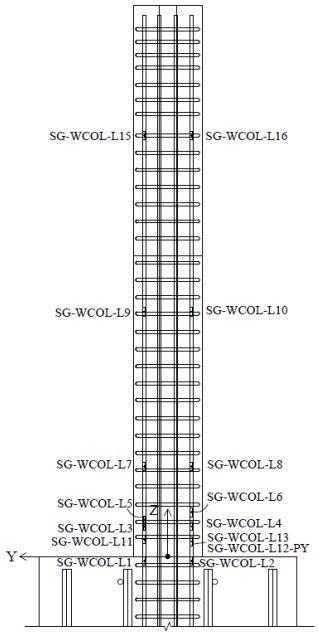

Fig. 4-5 Strain gages on the longitudinal reinforcement of the west column

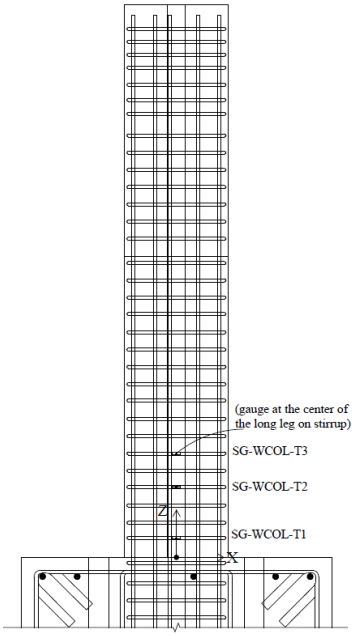

Fig. 4-6 Strain gages on the steel stirrups in the west column

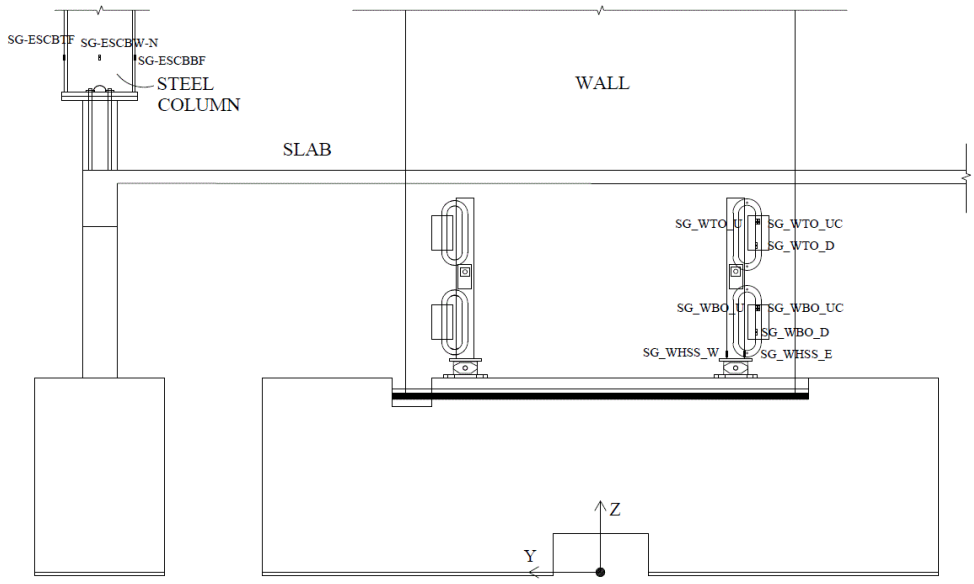

Fig. 4-7 Strain gages on the O-connectors and at the bottom of the steel column in PFS1

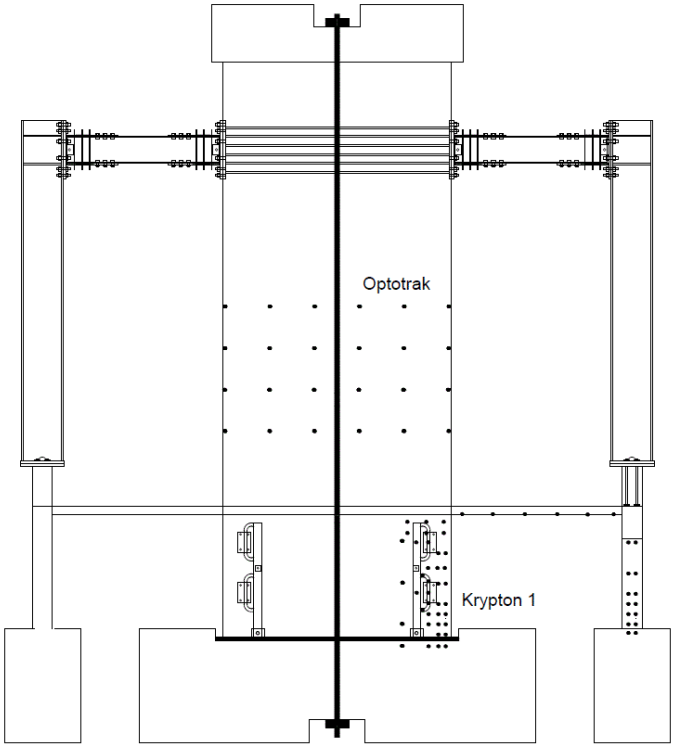

Fig. 4-8 Optotrak and Krypton system 1 on the wall and the column

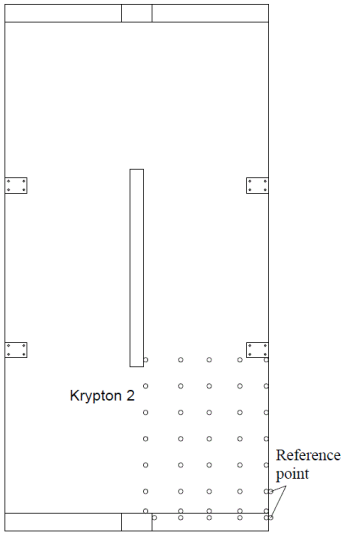

Fig. 4-9 Krypton system 2 on the unbonded PT slab (plan view from above)

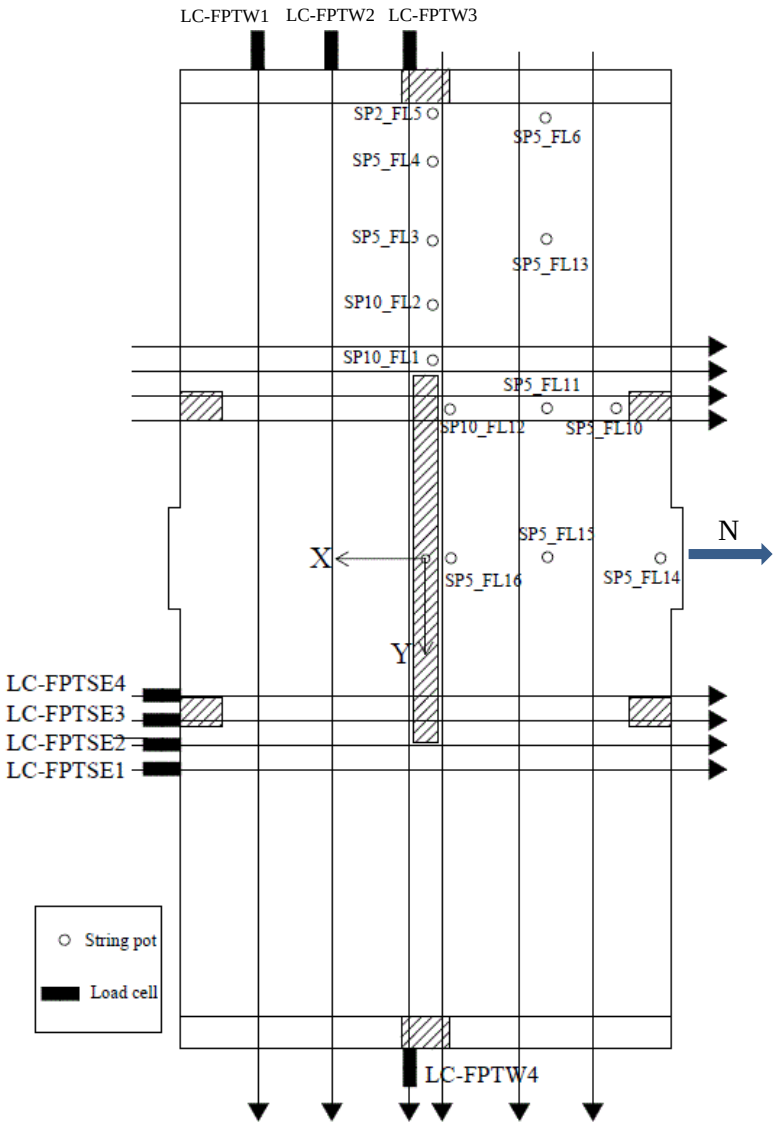

Fig. 4-10 String pots and load cells placed in the unbonded post-tensioned slab

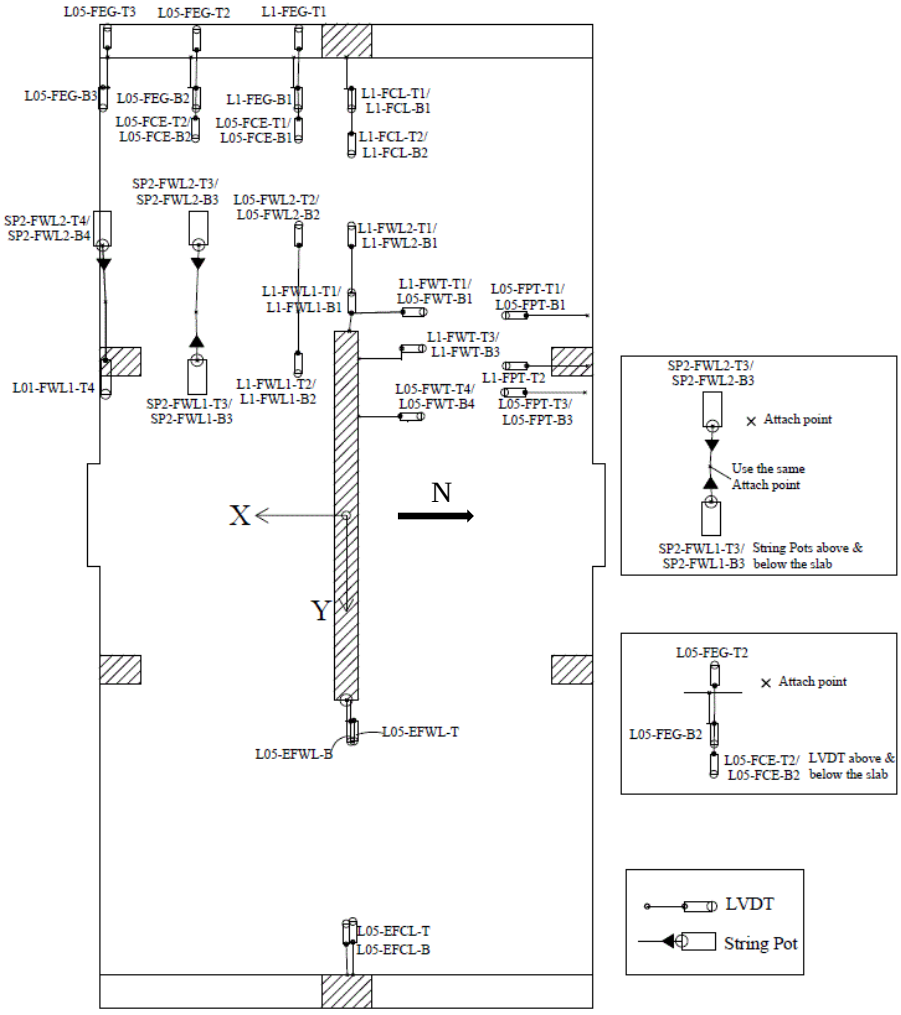

Fig. 4-11 LVDTs placed in the unbonded post-tensioned slab

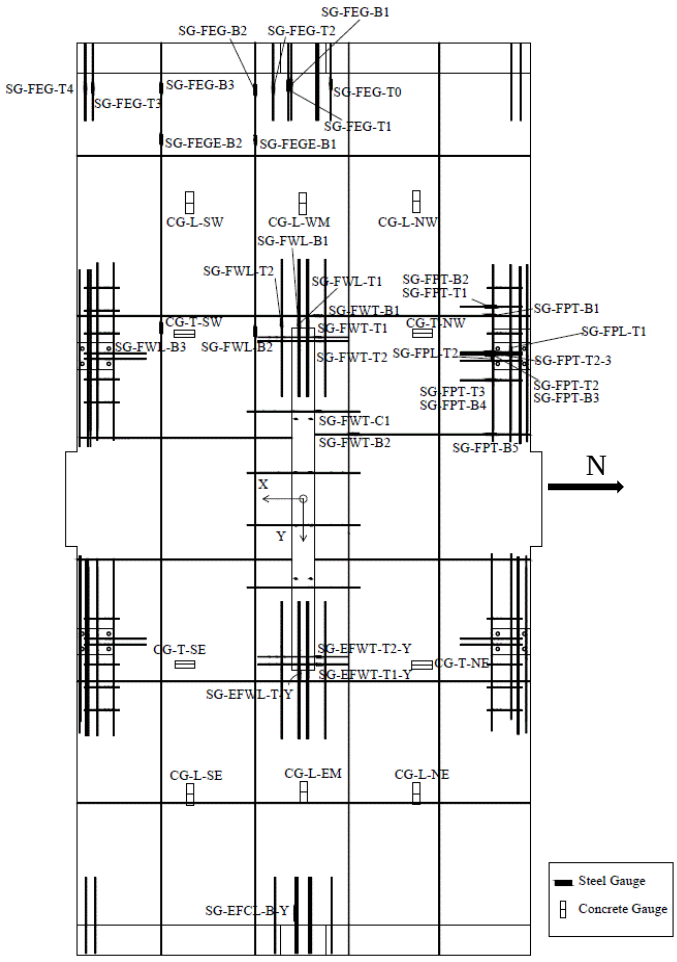

Fig. 4-12 Strain gages placed in the unbonded post-tensioned slab

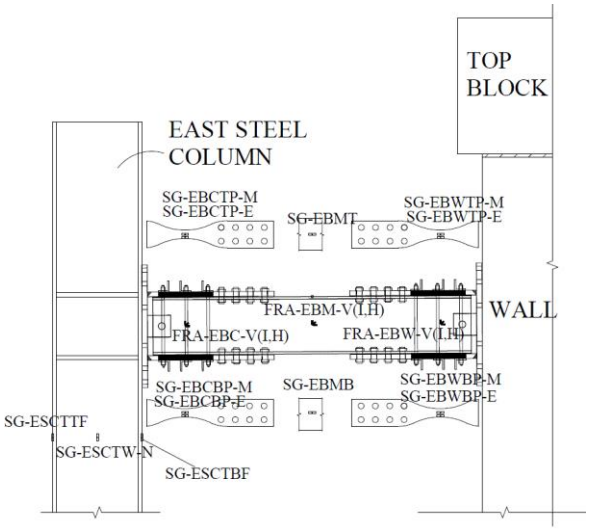

Fig. 4-13 Strain gages attached on the east mega beam and at the top of the east steel column

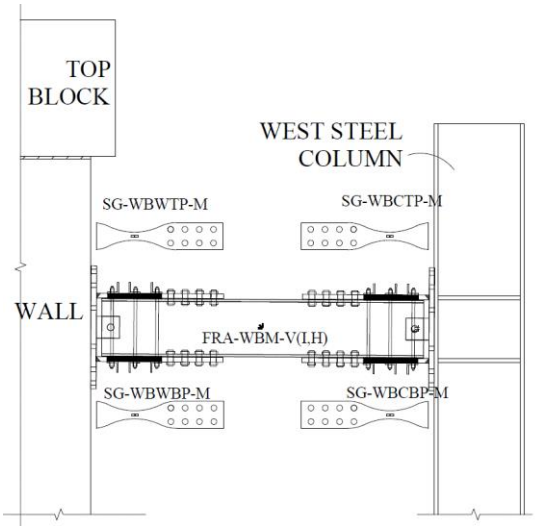

Fig. 4-14 Strain gages attached on the west mega beam

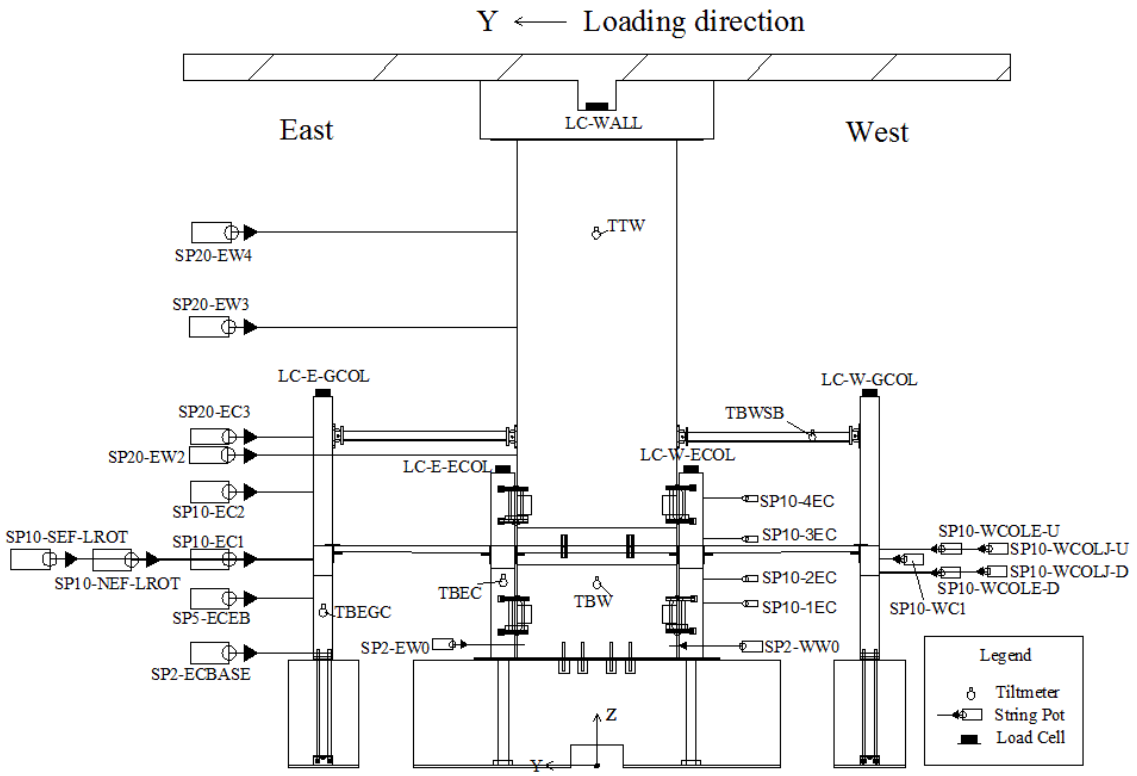

Fig. 4-15 Load cell, string pots and tiltmeters of PFS2 (Front view of the specimen)

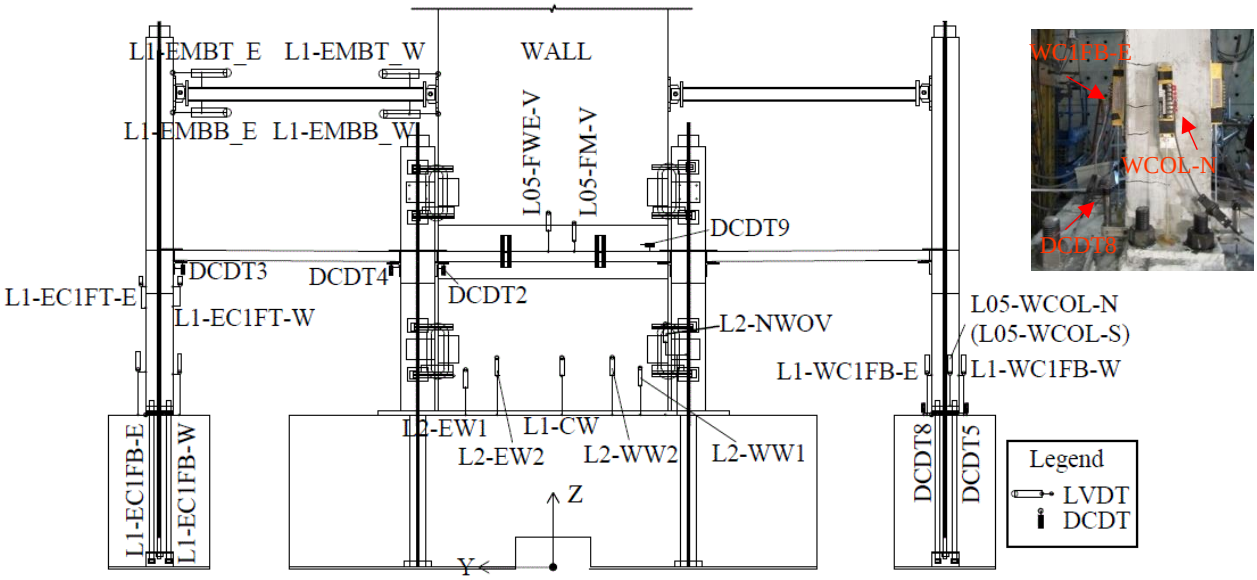

Fig. 4-16 LVDTs and DCDTs of PFS2 (Front view of the specimen)

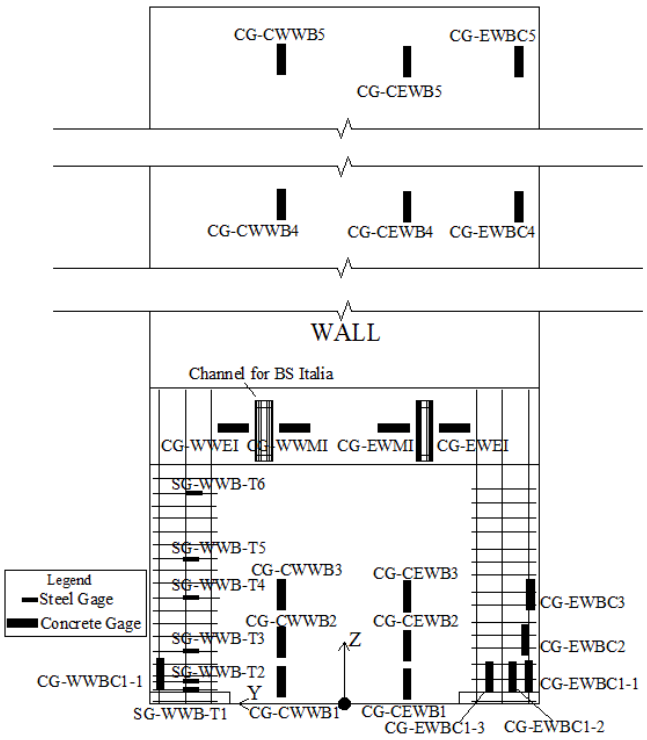

Fig. 4-17 Strain gages in the wall panel of PFS2

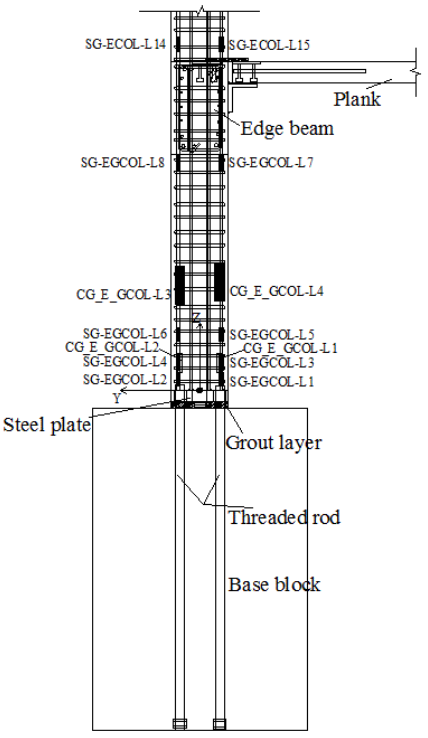

Fig. 4-18 Strain gages in the east gravity column (view from the south, loading direction)

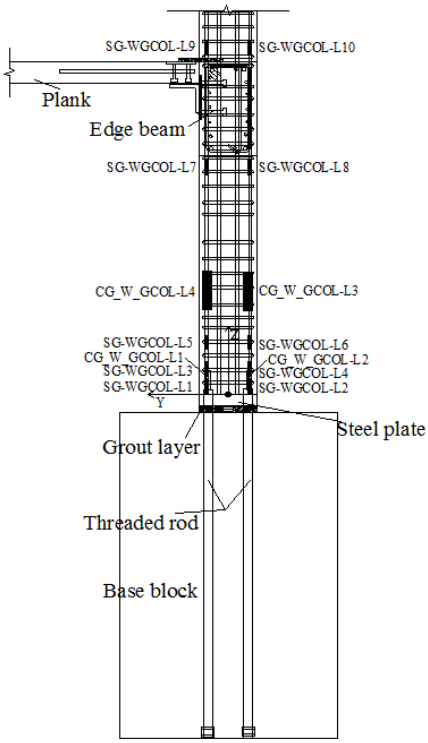

Fig. 4-19 Strain gages in the west gravity column (view from the south, loading direction)

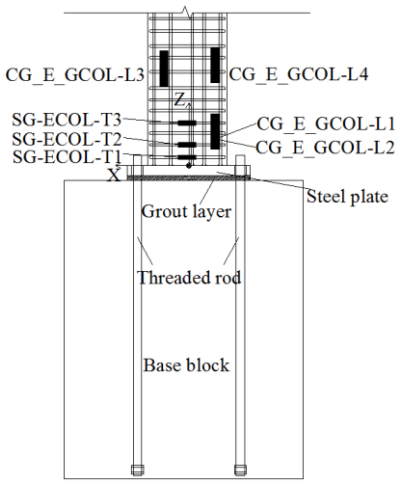

Fig. 4-20 Strain gages in the east gravity column (view from the east, transverse direction)

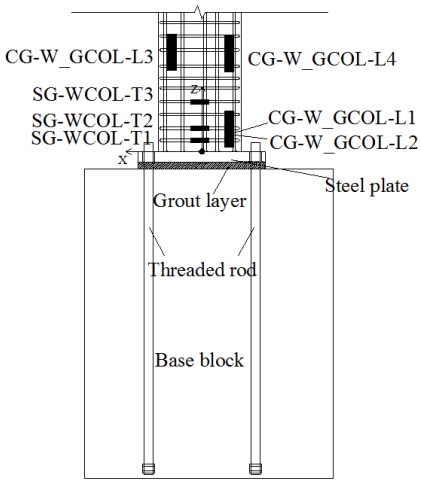

Fig. 4-21 Strain gages in the west gravity column (view from the east, transverse direction)

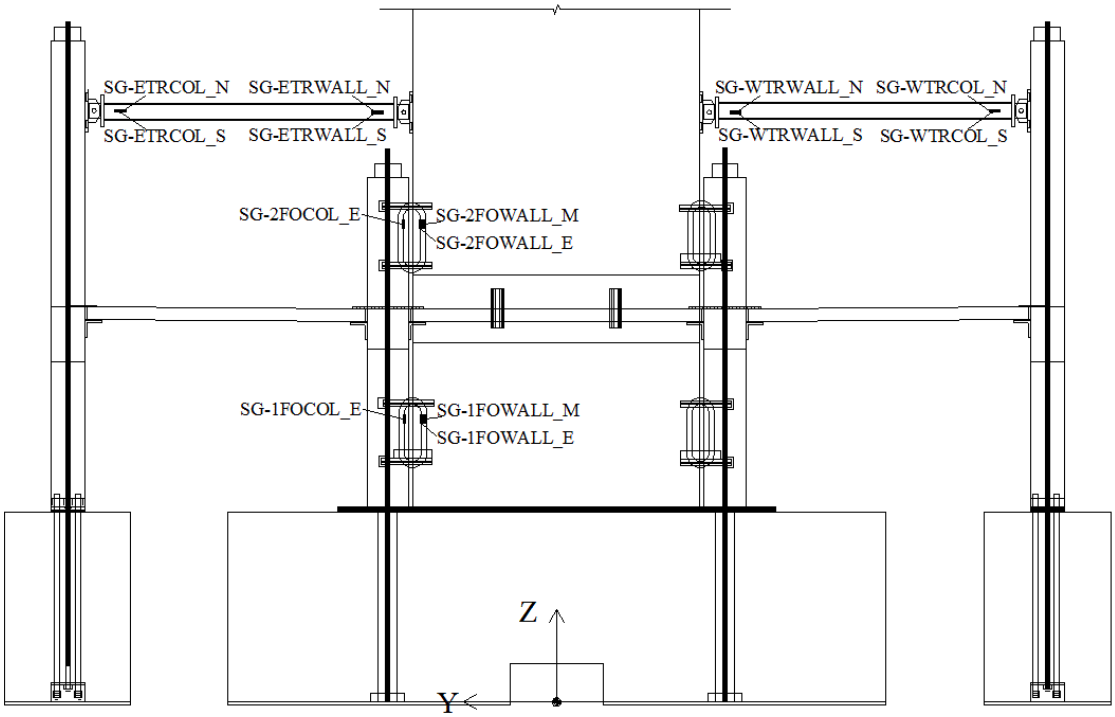

Fig. 4-22 Strain gages on the O-connectors and the mega beams in PFS2

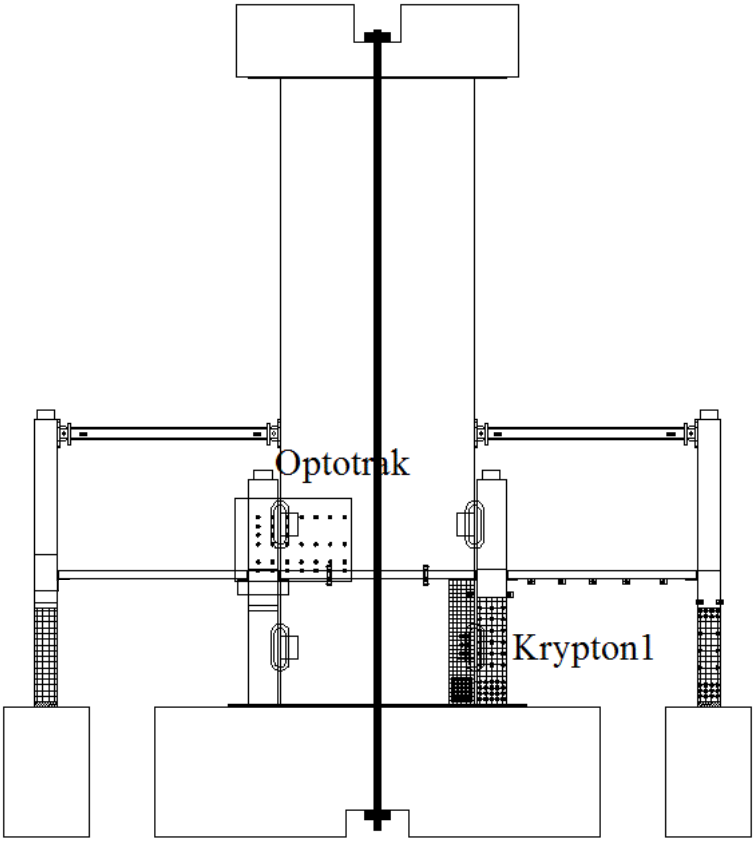

Fig. 4-23 Optotrak and Krypton system 1 on the wall and the columns

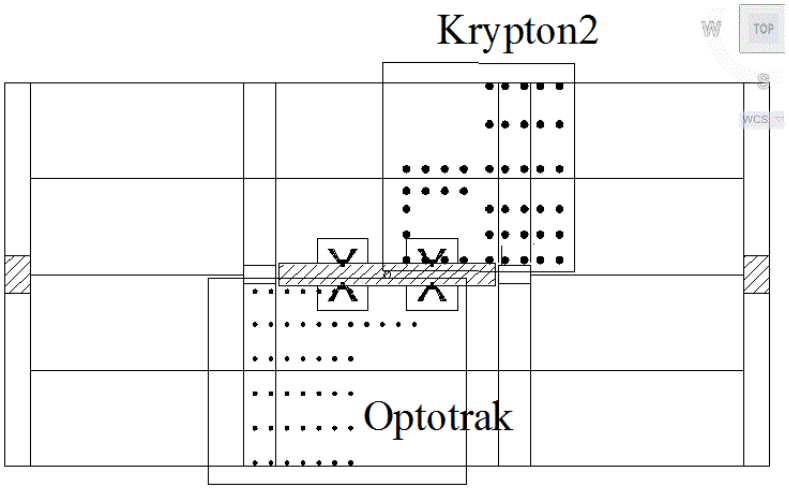

Fig. 4-24 Optotrak and Krypton system 2 on the slab

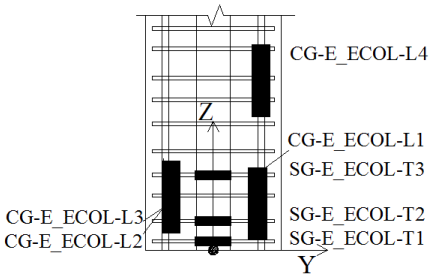

Fig. 4-25 Strain gages in the east end column (view from the south, loading direction)

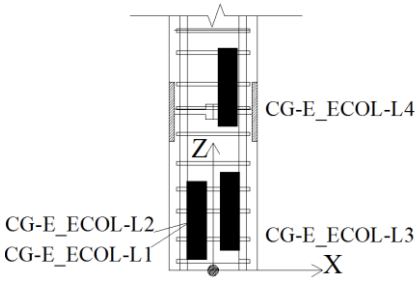

Fig. 4-26 Strain gages in the east end column (view from the east, transverse direction)

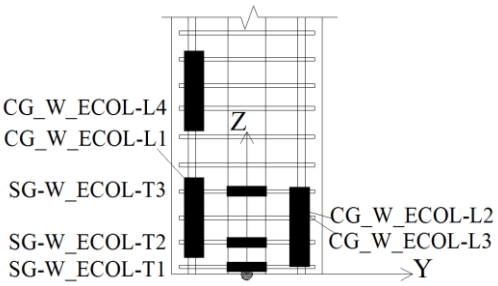

Fig. 4-27 Strain gages in the west end column (view from the south, loading direction)

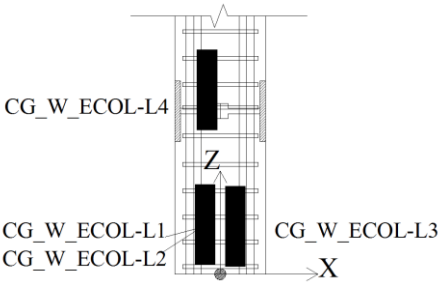

Fig. 4-28 Strain gages in the west end column (view from the east, transverse direction)

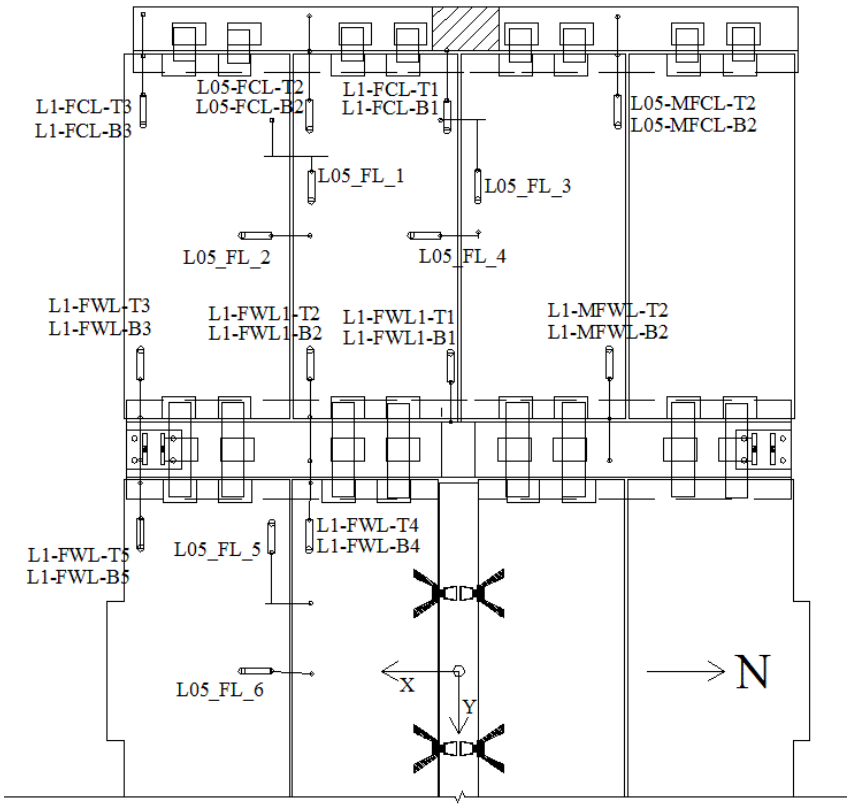

Fig. 4-29 LVDTs placed in the precast floor system

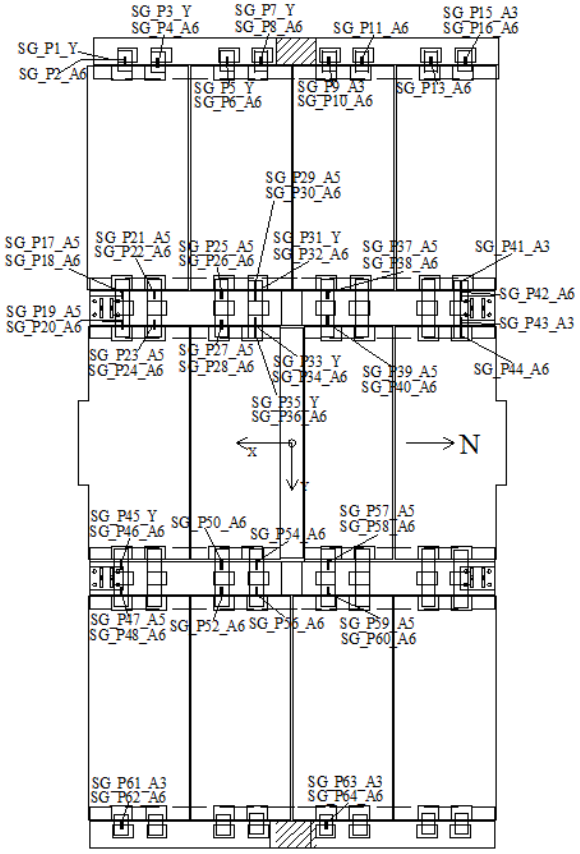

Fig. 4-30 Strain gages in the precast floor system

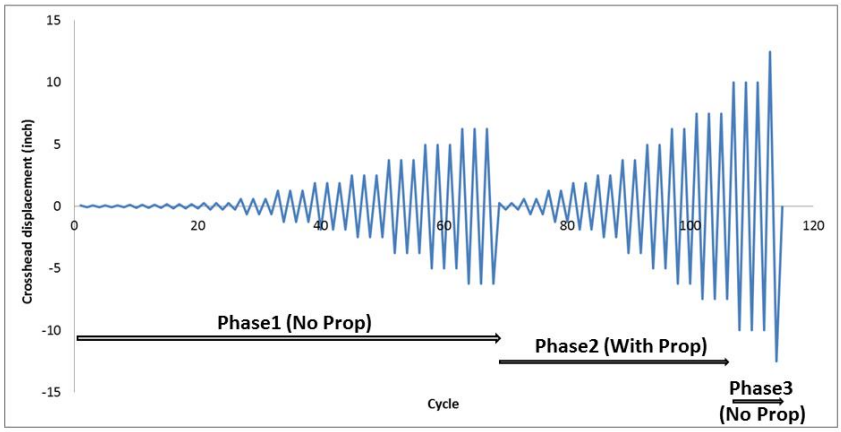

Fig. 4-31 In-plane loading protocol of PFS1

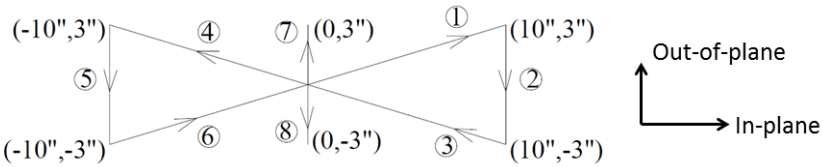

Fig. 4-32 Out-of-plane loading protocol of PFS1 (step 7 and 8 were repeated twice)

CHAPTER 5. Finite Element Modeling of the Test Specimens

This chapter describes the finite element modeling of the test specimens. The numerical models were built using commercial software ABAQUS (Dassault 2011). In this chapter, Section 5.1 describes the motivations of the numerical simulation. Section 5.2 gives a general introduction of the material models, element types, and computational solvers in ABAQUS. The parameters of the material models used in the simulation are summarized in Section 5.3.

The numerical model of PFS1 with rigid wall-floor connection is described in detail in Section 5.4 and 5.5. Section 5.4 describes the modeling of the PreWEC system and Section 5.5 describes the modeling of the surrounding structure in PFS1. In Section 5.4, special computational techniques to simulate prestressing forces, simulation of the wall-fiber grout contact, and verification of the model of the energy dissipating elements (O-connectors) are included. In Section 5.5, simulation of the unbonded PT slab, mega beam, edge columns, edge beams and props are included. Verification of the numerical model of PFS1 is described in Chapter 6 alongside test results from PFS1.

Because it was expected that little interaction occurred between the PreWEC system and the surrounding structure in PFS2 that used vertical movement isolation connections, no numerical models for the entire specimen PFS2 are built in this dissertation. A numerical model for the isolated PreWEC system tested in PFS2 is described in Section 5.6. The results of the model are compared to the test results of PFS2 in Chapter 7.

5.1 Motivation for the Numerical Simulations

5.1.1 Modeling of PFS1

A detailed finite element model, which included a PreWEC system using side columns, an unbonded post-tensioned slab, steel mega beams and steel columns, RC edge columns and edge beams, was built for PFS1. Fig. 5-1 shows an overview of the model.

Because of the complexity of the specimen and the limited amount of instrumentation, only parts of the specimen were instrumented. Moreover, some instrumentation might not function well before or during the test. Therefore, it might not be possible to obtain sufficient test data to analyze the behaviors of the specimen.

After validating the numerical model of PFS1 with results obtained from instrumented locations in the test structure, the model was used to understand some behaviors of the specimen that were not captured by the instrumentation. For example, it was expected that the contribution from the mega beams to the behavior of the specimen was significant because they represented the constraint of five-story floors in the scaled prototype building. However, there was less instrumentation on the west mega beam compared to the east mega beam. Using the validated model, the impact from the west mega beam could also be investigated. Other pertinent analysis using the validated numerical model, including the behavior of the PreWEC system and the impact from fractured mega beam cover plates, is discussed in the associated chapters in this dissertation.

5.1.2 Modeling of the Isolated PreWEC System in PFS2

Only a numerical model for the isolated PreWEC system was built in PFS2. The motivation was to investigate the effectiveness of the vertical movement isolation wall-floor connections used in PFS2. If the simulation results from the model were similar to the test results of PFS2, it would indicate that the special wall-floor connections functioned well to vertically isolate the floor from the wall in the test. Fig. 5-2 shows an overview of the model for the isolated PreWEC system.

5.2 General Introduction of the Finite Element Modeling in ABAQUS

In this section, an overview of the finite element modeling in ABAQUS is given. ABAQUS provides a broad library of material models and different types of elements. It is important to choose proper material models and element types in order to obtain accurate simulation results under reasonable computational cost. The material models and element types used in the models are discussed in Section 5.2.1. Different types of

interaction (e.g. contact elements) and constraints (e.g., tie, coupling and embedded) are included in ABAQUS to help assemble different structural components in the model. Section 5.2.3 gives a brief introduction to the interaction and constraints used in the models. Section 5.2.4 describes solution technique and mesh control of the models that are related to convergence and computational cost.

5.2.1 Material Models

A general introduction of the material models defined in ABAQUS is given in this section. Detailed parameters for the material models used in the numerical models in this study are provided in Section 5.3.

5.2.1.1 Steel Material Models

Structural elements made of steel that were simulated in the models included 1/2 in. diameter PT strands in the walls (PFS1 and PFS2), 3/8 in. diameter PT strands in the floor slab (PFS1), reinforcement and wires in the walls and the columns (PFS1 and PFS2), O-connectors (PFS1 and PFS2), steel cover plates (PFS1), short steel tubes (PFS1), steel plates in the wall (PFS1 and PFS2) and the end columns (PFS2).

Different material models were used for these structural elements. “Plasticity” model with combined kinematic/isotropic hardening was assigned to the elements that were expected to yield in the test. On the other hand, elastic material model with Young’s modulus of 29,000 ksi was assigned to the elements that were expected to remain elastic throughout the test. Table 5-1 lists the material models used for the different steel structural elements in the two models.

5.2.1.2 Concrete Material Models

Structural components made of concrete that were simulated in the models included the top blocks (PFS1 and PFS2), the wall panels (PFS1 and PFS2), edge columns and edge beams (PFS1 and PFS2), the floor slab (PFS1), and the end columns (PFS2).

Different material models were used for these structural components. Elastic models were assigned to the concrete in the top blocks because they were expected to remain elastic throughout the test. For other structural components that were expected to be damaged in the test, “Concrete damaged plasticity” model was used. Table 5-2 lists the

material models used for the different concrete structural components in the two models. The sophisticated "Concrete damaged plasticity" model in ABAQUS is described in detail in the following.

The concrete damaged plasticity model of ABAQUS provides a general capability for modeling concrete in different types of elements (e.g. beams, shells and solid elements). The model is a plasticity-based damage model for concrete. It is primarily used for the analysis of reinforced concrete structures and applications where concrete is subjected to monotonic and cyclic loading.

The following input parameters are required to complete the definition of the material model, including: uniaxial stress versus plastic-strain curve (both tension and compression branches), damage parameters (d_t and d_c) versus plastic-strain, weight factors (w_t and w_c) for stiffness recovery upon strain reversal, and parameters for defining the yield functions and flow rules of the concrete. The four groups of parameters are described below.

Uniaxial tensile stress versus plastic-strain curve

Fig. 5-3 shows the response of concrete in uniaxial tensile loading. The stress-strain curve follows a linear elastic relationship until the failure stress (σ_{t0}). The failure stress corresponds to the onset of cracks in the concrete. For the concrete in the test specimen, the flexural tensile strength of concrete measured from prism beam tests was used for σ_{t0}. Beyond the failure stress, the formation of cracks is represented with a softening stress-strain branch. For the reinforced concrete structures, it is recommended in ABAQUS that the strain softening after cracking reduces the stress close to zero at a total strain of about ten times the cracking strain.

Uniaxial compressive stress versus plastic-strain curve

Fig. 5-4 shows the response of concrete to uniaxial compressive loading. The stress-strain curve follows a linear elastic relationship until the initial yield (σ_{c0}). Beyond the initial yield, stress hardening occurs, followed by strain softening after the ultimate stress (σ_{cu}).

Different from steel materials whose complete stress-strain curves were directly obtained through the tensile test of the steel coupons, only the compressive strength of

the concrete materials was obtained from compression tests of concrete cylinders. To obtain a complete uniaxial stress-strain curve, the following equations proposed by Chang and Mander (1994) were used:

$$\frac{f_c}{f_c'} = \frac{n\frac{\epsilon_c}{\epsilon_c'}}{1+\left(n-\frac{r}{r-1}\right)\frac{\epsilon_c}{\epsilon_c'}+\frac{\left(\frac{\epsilon_c}{\epsilon_c'}\right)^r}{r-1}} \tag{5.1}$$

$$\epsilon_c' = \frac{(f_c')^{\frac{1}{4}}}{4{,}000} \tag{5.2}$$

$$n = \frac{46}{(f_c')^{\frac{3}{8}}} \tag{5.3}$$

$$r = \frac{f_c'}{750} - 1.9 \tag{5.4}$$

In Eq. (5.1) through Eq. (5.4), ϵ_c and f_c are the strain and associated stress in the stress-strain curve, f_c' is the compressive strength of the concrete obtained from the compression test of concrete cylinders, ϵ_c' represents the strain at the compressive strength, *n* and *r* are dimensionless parameters for controlling the shape of the curve. According to Eq. (5.1), a complete uniaxial stress-strain curve for the material model was obtained once f_c' was known from the material testing. It should be noted that f_c' in Eq. (5.1) was defined as σ_{cu} in Fig. 5-4.

In ABAQUS, the uniaxial stress-strain curve is required to be converted into stress versus plastic-strain curve before being assigned to the material model. The elastic strain of the concrete was taken as $0.45f'_c/E_c$ (Chang and Mander 1994) in the model. The plastic strain was obtained by subtracting the elastic strain from the total strain. The stress versus plastic strain curves were directly used for the unconfined concrete in the model, such as the concrete of the wall outside the boundary elements and that in the CIP floor slab.

Damage parameters (d_t and d_c) versus plastic-strain

After the concrete material was damaged, the unloading responses of the concrete would be different from those of undamaged concrete. In ABAQUS, damage parameters (d_t and d_c) are used to simulate this behavior. As shown in Fig. 5-5, when the concrete is

unloaded from any point on the strain softening branches (tension or compression), the weakened unloading response is represented with degraded unloading stiffness, which is characterized by the two damage variables (d_t and d_c). The two variables are assumed to be functions of plastic strains and specified in a tabular form for the material model. They can take values from 0, representing undamaged material, to 1, representing total loss of strength. Because there were no available test results of the concrete materials under cyclic loading, it was decided to use the default values ($d_t = 0$ and $d_c = 0$) in the numerical models of PFS1 and PFS2.

Because the numerical model of PFS1 was only subjected to monotonic loading (pushover), this simplification would not affect the results. In the case of PFS2, in which just the PreWEC was simulated, there was little damage to the wall; consequently, the default damage parameters of 0 were reasonable.

Weight factors (w_t and w_c) for stiffness recovery upon strain reversal

When the strain changes sign during a uniaxial cyclic test (from tension to compression or from compression to tension), there exists some recovery of the elastic stiffness. The recovery mechanism is very complex under uniaxial cyclic loading, involving the opening and closing of previously formed cracks.

In ABAQUS, two weight factors (w_t and w_c) are used to control the recovery of the tensile and compressive stiffness upon load reversal. The compressive stiffness is recovered on crack closure as the strain changes from tension to compression. However, the tensile stiffness is not recovered as the strain changes from compression to tension once crushing has developed. This behavior corresponds to $w_t = 0$ and $w_c = 1$, which are the default parameters recommended by ABAQUS. The default values were used in the numerical models of PFS1 and PFS2. Fig. 5-5 shows a uniaxial strain cycle using the default values.

Yield functions and flow rules of the concrete

The concrete damage plasticity model uses the yield function proposed by Lubliner et al. (1989) with the modifications by Lee and Fenves (1998). Non-associated potential plastic flow is used for the model. The flow potential for the model is the Drucker-Prager hyperbolic function. The yield functions and flow rules are already established in the

kernel of ABAQUS. A detailed description of the yield functions and flow rules can be found in the ABAQUS documentation and are not discussed in the dissertation.

5.2.1.3 Fiber Grout Materials

Although there were no specific material models designed for fiber grout in ABAQUS, it was expected that the behaviors of the fiber grout were similar to those of concrete. It was decided to use "Concrete Damaged Plasticity" model to simulate the fiber grout.

5.2.2 Element Types

Solid, shell and truss elements were used in the models. Table 5-3 lists the structural components simulated in the two models with associated elements types. In the table, C3D8R represents continuum, 3-dimensional and 8-node linear solid elements; S4R represents general 4-node linear shell elements; T3D2 represents 3-dimensional and 2-node linear truss elements.

5.2.3 Assemblage Techniques

After all the structural components of the test specimens were built using proper material models and element types, they were assembled to form the integrated model. Special contact elements and three types of constraint defined in ABAQUS, including tie, coupling and embedded, were used for the assemblage. Applications of these techniques are discussed in the following.

The precast wall directly sat above the fiber grout and there was no continuous bonded reinforcement across the interface between the wall and the fiber grout. Contact elements were assigned between the wall base and the top of the fiber grout layer to simulate the boundary conditions.

"Tie" is a constraint technique that ties two separate surfaces together and no relative motion between the two surfaces is allowed. For example, it was expected that no relative motions existed between the wall and the top block, thus "tie" constraint was assigned to the top surface of the wall and the bottom surface of the top block.

"Coupling" is a constraint technique to constrain the motions of a slaved surface to those of one control point. For example, the top surface of the top block was "coupling"

constrained to the top of the strands, thus the initial PT force applied to the strands was transferred to the top block.

"Embedded" is a constraint technique that constrains the translational degrees of freedom of embedded elements to those of host elements. For example, steel plates where the O-connectors were welded were embedded in the tested walls. In the models, the steel plates (simulated by shell elements) were "embedded" constrained to the wall panels (simulated by solid elements).

5.2.4 Solution and Mesh Control

5.2.4.1 Solution Control

The implicit solver of ABAQUS uses full Newton or quasi-Newton solution techniques to solve nonlinear equilibrium equations generated during the analysis. Using the implicit solver was always successful when conducting monotonic quasi-static analysis.

One aspect of the study was to investigate the self-centering performance of the rocking-wall structures. Cyclic quasi-static analyses are required in the numerical models to obtain the residual displacements of the walls when the external loads applied to the specimens were reduced to zero. However, when cyclic loads were applied to the models, severe convergence problems were encountered using the implicit solver, even when the convergence tolerances were increased. It was believed that the convergence problem was mainly attributed to the complicated contact conditions between the wall and the fiber grout under cyclic loadings.

As recommended by ABAQUS user manuals, the explicit solver is more suitable to perform quasi-static analysis under complicated contact conditions. The explicit solver performs a large amount of small time increments using central-difference time integration rules, which greatly improves the convergence of the problem. Therefore, the explicit solver of ABAQUS was used in this study. Because the explicit solver is typically used for dynamic loading, some factors that impacted the simulation are discussed in the following.

Loading steps

To reduce dynamic effects in the models (inertia forces and related damping effect), a separate loading phase over a time span of 5 seconds was used to apply gravity loads and PT forces to the walls in the numerical models of PFS1 and PFS2. The time span was selected after several trials that achieved a balance between accurate simulation results and reasonable computational time.

Similarly, external lateral displacements were slowly applied to the models to ensure that both accelerations and velocities of the models were small to mimic quasi-static analysis. After several trials, a loading speed of 1/2 in. per second was used in the models.

Stability limit

As indicated by ABAQUS user manuals, the central-difference operator adopted by the explicit solver is conditionally stable. The stability limit (the largest time increment that can be taken without causing rapidly growing errors) is proportional to the smallest element dimension in the model. The time increment in the analysis might be very short if mesh densities were large, resulting in high computational cost during a complete cyclic quasi-static analysis. Mesh control of the model is discussed in the following section.

5.2.4.2 Mesh Control

As discussed in the previous section, the computational cost is related to the density of the meshes when using the explicit solver. It was found that the dimensions of the O-connectors were relatively smaller than those of other structural components in the models. Thus, the mesh density of the O-connectors was a critical factor for mesh control. To reduce the computational cost, it was better to use relatively coarse meshes for the O-connectors provided that the simulation results were reasonably accurate. Optimization of the mesh density of the O-connectors is described in Section 5.4.3.3.

To improve the accuracy of the simulations, all structural components in the models were divided into regularly shaped regions to form quadrilateral-dominated elements. To capture local behaviors, finer meshes were assigned to the regions where plastic behaviors were expected to occur. For example, Fig. 5-6 shows the meshed wall panel.

As shown in the figure, all the elements are regular hexahedron; more elements are provided in the boundary elements of the wall compared to the rest regions of the wall.

5.3 Material Models Used in the Finite Element Models

As discussed earlier, three types of materials were used in the test, including steel, concrete and fiber grout. A general description of the material models used in ABAQUS has been given in Section 5.2.1.The input parameters for each material model, which were determined using available material properties from the material testing (described in Section 3.7), are discussed in detail in this section.

5.3.1 Input Parameters for Steel Material Models

The stress-strain curves of the steel materials were directly defined based on the measured curves from the material testing of steel samples. For example, Fig. 5-7 shows the input stress-strain curves alongside the measured curves of No.3 rebar. As shown in the figure, measured stress-strain responses from three samples of the No.3 rebar were very close. The curves defined in the numerical models consisted of average values from the three measured curves.

The input stress-strain curve of the 1/2 in. diameter strands in the wall was based on the values provided in the mill of certification from the manufacturer. Fig. 5-8 shows the stress-strain responses of the 1/2 in. strands.

Table 5-4 summarizes the stress-plastic strain pairs assigned to the steel materials in the models, including 1/2 in. strands, No. 3 and No. 5 rebar, No. 2 wires, O-Connectors, cover plates, 3/4 in. rods, 1 in. rods and 1/2 in. rods.

5.3.2 Input Parameters for Concrete Material Models

5.3.2.1 Unconfined Concrete

As mentioned in Section 5.2.1.2, concrete damage plasticity model was used to describe the concrete materials expected to be damaged. The input stress-strain curves of the unconfined concrete materials are given together with those of confined concrete in Section 5.3.2.2.

5.3.2.2 Confined Concrete

Increased strength and ductility of confined concrete

Compared to unconfined concrete, the strength and ductility of confined concrete are larger because of the confinement effect provided by steel confinement. However, the steel confinement was not simulated in the models because it would greatly increase the time for building the models and running the analysis. Instead, the stress-strain curves of the confined concrete were defined to account for the confinement effect. The confined concrete existed in the corners of the walls (PFS1 and PFS2), the edge columns (PFS1 and PFS2) and the end columns (PFS2).

The analytical model proposed by Mander et al. (1988) was used to deduce the stress-strain curves of the confined concrete:

$$\frac{f_c}{f'_{cc}} = \frac{p\frac{\epsilon_c}{\epsilon_{cc}}}{p - 1 + \left(\frac{\epsilon_c}{\epsilon_{cc}}\right)^p} \tag{5.5}$$

$$p = \frac{E_c}{E_c - \frac{f'_{cc}}{\epsilon_{cc}}}; \tag{5.6}$$

Where ϵ_c and f_c are the strain and the associated stress in stress-strain curves, f'_{cc} is the peak strength of the confined concrete, ϵ_{cc} represents the strain at the peak strength of the confined concrete, p is a parameter controlling the shape of the stress-strain curve, E_c is Young's modulus of concrete. To obtain the complete stress-strain curve of the confined concrete, the following two equations were proposed by Chang and Mander (1994) to calculate f'_{cc} and ϵ_{cc} of the confined concrete:

$$f'_{cc} = f'_c\left[1 + A\bar{x}\left(0.1 + \frac{0.9}{1 + B\bar{x}}\right)\right] \tag{5.7}$$

$$\epsilon_{cc} = \epsilon'_c\left[1 + 5\left(\frac{f'_{cc}}{f'_c} - 1\right)\right] \tag{5.8}$$

In Eq. (5.7) and Eq. (5.8), A and B are empirical parameters from experimental results; $\bar{x}$ is a parameter related to confinement effect; f'_c and ϵ'_c are the strength of the unconfined concrete and the associated strain. The equations to calculate A, B and $\bar{x}$ are shown below:

$$A = 6.8886 - (0.6069 + 17.275q)e^{-4.989q}; \tag{5.9}$$

$$B = \frac{4.5}{\frac{5}{A}(0.9849 - 0.6306e^{-3.8939q}) - 0.1} - 5; \tag{5.10}$$

$$\bar{x} = \frac{f'_{l1} + f'_{l2}}{2f'_c} \tag{5.11}$$

$$q = \frac{f'_{l2}}{f'_{l1}}\left(f'_{l1} \geq f'_{l2}\right) \tag{5.12}$$

$$f'_{l1} = k_e \rho_x f_{yt} \tag{5.13}$$

$$f'_{l2} = k_e \rho_y f_{yt};$$

$$\rho_x = \frac{A_{sx}}{sd_c}; \tag{5.14}$$

$$\rho_y = \frac{A_{sy}}{sb_c} \tag{5.15}$$

$$k_e = \frac{\left(1 - \sum_{i=1}^{m} \frac{(w'_i)^2}{6b_c d_c}\right)\left(1 - \frac{s'}{2b_c}\right)\left(1 - \frac{s'}{2d_c}\right)}{(1 - \rho_{cc})} \tag{5.16}$$

$$\rho_{cc} = \frac{A_{lr}}{b_c d_c} \tag{5.17}$$

Where f'_{l1}= Effective lateral confining pressure in x direction; f'_{l2}= Effective lateral confining pressure in y direction; k_e= Confinement effective coefficient; ρ_x = Ratio of the volume of transverse confining steel to the volume of confined concrete core in x direction; ρ_y= Ratio of the volume of transverse confining steel to the volume of confined concrete core in y direction; f_{yt}= Yield strength of the steel confinement; A_{sx}= Total area of transverse bars running in x direction; A_{sy}= Total area of transverse bars running in y direction; s= Center to center spacing of the hoop; b_c= Core dimension to centerlines of perimeter hoop in x direction; d_c= Core dimension to centerlines of perimeter hoop in y direction. s'= Clear vertical spacing between the hoop bars; w'_i= Clear transverse spacing between longitudinal bars; ρ_{cc}=Volume of longitudinal steel to volume of concrete core; A_{lr} = Volume of longitudinal steel (unit length).

To give an example of calculating the parameters in the confinement model, the peak strength f'_{cc} and the associated strain ϵ_{cc} of the confined concrete in the boundary element of the wall in PFS1 are deduced in the following.

Fig. 5-9 and Fig. 5-10 show the plan view and the elevation view of the wall boundary element. The measured strength of the unconfined concrete was 11.3 ksi. The cross-sectional area of No. 3 and No. 5 rebar were 0.11 and 0.31 in^2, respectively. The yield strength of the steel confinement f_{yh} was 66.5 ksi. The spacing of the confinement *s* was 2-5/16 in. (as-built average values). The core dimension to centerlines of perimeter hoop in x direction (b_c) and y direction (d_c) were 11 in. and 4.625 in., respectively. As shown in Fig. 5-9, the longitudinal rebar included 2 pieces of No. 3 and 4 pieces of No. 5 rebar, the volume of longitudinal steel to volume of the concrete core ρ_{cc} is calculated:

$$\rho_{cc} = \frac{A_{lr}}{b_c d_c} = \frac{4\times0.31 + 2\times0.11}{11\times4.625} = 0.029$$

Because there was one No. 3 stirrup running in x direction, ratio of the volume of transverse confining steel to the volume of confined concrete core in x direction ρ_x is:

$$\rho_x = \frac{A_{sx}}{s d_c} = \frac{2\times0.11}{2.3125\times4.625} = 0.0206$$

Because there was one #3 stirrup and one #3 tie running in y direction, ratio of the volume of transverse confining steel to the volume of confined concrete core in y direction ρ_y is:

$$\rho_y = \frac{A_{sy}}{s b_c} = \frac{2\times0.11 + 0.11}{2.3125\times11} = 0.013$$

The clear transverse spacing between longitudinal bars was 5 in., 5in., 3-5/8 in., 5 in., 5in. and 3-5/8 in. (as-built dimensions). The clear vertical spacing between the hoop bars (*s'*) was equal to center to center spacing of the stirrup (*s*) minus the diameter of the stirrup. Following the equations shown previously, the following calculations are conducted to obtain f'_{cc} and ϵ_{cc}:

$$k_e = \frac{\left(1 - \sum_{i=1}^{m} \frac{(w'_i)^2}{6b_c d_c}\right)\left(1 - \frac{s'}{2b_c}\right)\left(1 - \frac{s'}{2d_c}\right)}{(1 - \rho_{cc})}$$

$$= \frac{\left(1 - \frac{2\times(5^2 + 5^2 + 5^2)}{6\times 11\times 4.625}\right)\left(1 - \frac{2.3125 - 0.375}{2\times 11}\right)\left(1 - \frac{2.3125 - 0.375}{2\times 4.625}\right)}{(1 - 0.029)} = 0.435$$

$$f'_{l1} = k_e \rho_x f_{yh} = 0.435\times 0.0206\times 66.5 = 0.596\ ksi$$

$$f'_{l2} = k_e \rho_y f_{yh} = 0.435\times 0.013\times 66.5 = 0.376\ ksi$$

$$q = \frac{f'_{l2}}{f'_{l1}} = \frac{0.376}{0.596} = 0.631;\ \bar{x} = \frac{f'_{l1} + f'_{l2}}{2f'_c} = \frac{0.596 + 0.376}{2\times 11.226} = 0.043$$

$$A = 6.8886 - (0.6069 + 17.275q)e^{-4.989q} = 6.395$$

$$B = \frac{4.5}{\frac{5}{A}(0.9849 - 0.6306e^{-3.8939q}) - 0.1} - 5 = 2.167$$

$$f'_{cc} = f'_c\left[1 + A\bar{x}\left(0.1 + \frac{0.9}{1 + B\bar{x}}\right)\right]$$

$$= 11.226\times\left[1 + 6.395\times 0.043\left(0.1 + \frac{0.9}{1 + 2.167\times 0.043}\right)\right]$$

$$= 14.094\ ksi;$$

$$\epsilon_{cc} = \epsilon'_c\left[1 + 5\left(\frac{f'_{cc}}{f'_c} - 1\right)\right] = 0.00257\times\left[1 + 5\left(\frac{14.094}{11.226} - 1\right)\right] = 0.00585$$

By substituting the obtained f'_{cc} and ϵ_{cc} into Eq. (5.5), a complete stress-strain curve of the confined concrete can be obtained.

Adjusting model parameters to account for spalling of concrete cover

It has been experimentally observed that the concrete cover (i.e., concrete outside the confined regions) spalls under axial compression or combined compression and bending. In the test specimens, the thickness of the concrete cover was small (1/2 in.) compared to the full depth of the wall (6 in.) or the columns (8 in.). To prevent partitioning the models into small segments for the purpose of assigning different material models (unconfined and confined concrete), which would greatly increase mesh densities and the computation cost, the same material model for the confined concrete was assigned to the concrete

cover and the confined concrete core in the corners of the wall as well as the base of the columns.

Adjustment of the stress-strain responses of confined concrete was needed to account for this simplification. The adjustment was based on the following assumptions. First, the passive pressure provided by the confinement on the concrete core would not take effect until the compressive strength f'_c of the unconfined concrete was reached. Under this condition, the behavior of the unconfined concrete cover was similar to that of the confined concrete core. No modification was needed for the assigned material model when the strain was smaller than the yield strain (ϵ'_c). Second, the steel confinement started to be engaged beyond ϵ'_c. The concrete cover had spalled and the concrete core carried all of the compression forces. The assigned stress-strain response was modified to account for this effect. All stresses corresponding to the strains in excess of ϵ'_c were multiplied by a reduction factor to average the forces distributed over the respective cross section.

Although the compression zone of the cross sections (wall or columns) varied with different force (moment) demands and the reduction factor would also change, a fixed reduction factor was selected for simplicity. Fig. 5-11 (a), (b) and (c) show the spalled concrete cover region (hatched) in the corners of the wall (PFS1 and PFS2), at the base of the edge columns (PFS1 and PFS2) and the end columns (PFS2). The reduction factor was calculated by dividing the concrete core (measured from the centerlines of perimeter stirrup) to the total cross-sectional area. As shown in Fig. 5-11, three sides of the concrete cover were considered in the boundary elements of the wall; all four sides of the concrete cover were considered for the edge columns and end columns. The reduction factor for the wall, the edge columns and the end columns were 0.73, 0.76 and 0.69, respectively.

Summary of uniaxial stress-strain definitions for concrete materials

Fig. 5-12 through Fig. 5-18 summarize the input stress-strain curves of the concrete materials in the models, including the walls (PFS1 and PFS2), the edge columns (PFS1 and PFS2) and the end columns (PFS2). Because different batches of concrete were used when constructing the edge columns and the end columns, different stress-strain responses were defined.

In the figures, the curves “Unconfined concrete” are assigned to the unconfined concrete in structural components; the curves “Confined concrete” represent the responses of the confined core, but they were not directly used in the models. Instead, the curves titled with “Modified,” that were obtained through the averaging procedure described previously were assigned to the confined concrete.

5.3.3 Input Parameters for Fiber Grout Materials

As mentioned in Section 5.2.1.3, concrete damaged plasticity model was used for the fiber grout materials. Similar to concrete materials, only the compressive strength of the grout materials was obtained from compression tests of cube samples as shown in Table 3-8.

Eqn. (5.1) that was used for concrete materials was also used to deduce the uniaxial stress-strain curve for the grout. Because of the existence of the steel fibers, the grout was expected to be ductile. Therefore, it was assumed that the stresses were capped with increasing strains beyond the compressive strength. Fig. 5-19 shows the stress-strain curve of the fiber grout.

5.4 Modeling of the PreWEC System in PFS1

ABAQUS models had been used successfully to predict the hysteretic behaviors of the PreWEC system tested in NCREE, as discussed in Section 2.3.5. Similar simulation techniques were used when modeling the PreWEC system in PFS1, except the following changes: O-connectors were simulated by shell elements instead of solid elements (to be discussed in Section 5.4.3); “concrete damaged plasticity” model instead of elastic material model was assigned to the fiber grout because damage might occur to the grout.

Furthermore, different from the PreWEC system tested in NCREE (shown in Fig. 2-17), four side columns instead of two end columns were used in the PreWEC system in PFS1 (shown in Fig. 3-20). Each side column in PFS1 consisted of a steel tube and a clevis hinge, as shown in Fig. 3-23(a). The side column was pin-connected to the base block through the clevis hinge and rotated freely in the in-plane direction. In the model of PFS1, shell elements were used to simulate the steel tubes. To simulate the pin-

connection, translational degrees of freedom of the two nodes in the middle bottom of each steel tube were constrained, as shown in Fig. 5-20. By applying this constraint, the tubes did not move laterally but were free to rotate about the center. To simulate the welding between the O-connectors and the steel tubes, the edges of the O-connectors were tied to the adjacent surface of the steel tubes at the weld locations, as shown in Fig. 5-21.

5.4.1 Modeling Prestressing Forces

There were two different methods in ABAQUS to apply prestressing forces to strands that were modeled by truss elements. The first method was to define an initial prestress condition for the PT strands and the other method was to apply a temperature field to the PT strands. The two methods are discussed in the following.

5.4.1.1 Defining an Initial Prestress Condition

There was no direct computer-aided engineering (CAE) interface in ABAQUS to define an initial prestress condition for the PT strands. Instead, the following codes had to be manually written into the input file of the model:

[*INITIAL CONDITIONS, TYPE=STRESS, REBAR

Element number or Element set name, Rebar name, Prestress value]

This method was applicable only when the implicit solver of ABAQUS was used. When the explicit solver of ABAQUS was used, because the initial prestress was applied to the model in a transient time, the transient large force change in the models would result in unstable responses of the PT strands. Because the explicit solver was used in the simulation, this method was not used in the dissertation.

5.4.1.2 Applying a Temperature Field

By applying a low temperature field to the strands, the strands were shortened due to the thermal contraction. The strain generated by the varied temperature was:

$$\epsilon_T = \alpha_T \Delta_T \tag{5.18}$$

Where α_T = Thermal coefficient (6.7×10^{-6}/K for strands); Δ_T = Magnitude of varied temperature.

A “kinematic coupling” constraint was applied between the node of the truss (reference node) and the region of the top block (slaved region) where the prestressing force was transferred. The “kinematic coupling” constrained the motion of the slaved region to the rigid body motion of the reference node. When the strands were shortened because of the thermal contraction, the vertical movement was resisted by the top block. The resistance from the top block generated the tensile force in the strands in return that simulated the prestressing force.

Because the temperature field can be slowly applied to the strands within a load step in the model, this method could be used with the explicit solver of ABAQUS. This method was used in this study to apply the prestressing forces to the strands. A direct CAE interface existed under the module of “Load” in ABAQUS to apply the temperature field that greatly simplified the modeling process.

5.4.2 Modeling Contact between Wall and Fiber Grout

When a rocking wall moves laterally, the wall loses contact with the fiber grout and there exists a gap opening between the wall and the fiber grout. When the wall returns to its upright position, the contact is resumed and the gap opening is closed. Special contact elements were defined in ABAQUS to simulate this type of boundary condition.

The contact elements were assigned to the bottom surface of the walls and the top surface of the fiber grout. Tangential and normal behaviors were required in ABAQUS to define the property of the contact elements. Because the wall was not expected to penetrate the fiber grout, “hard contact” was used for the normal behavior of the contact. “Rough” tangential behavior was assigned to the contact elements assuming that shear sliding of the wall was avoided in the test.

5.4.3 Modeling of O-Connectors

O-connectors were important structural components in the PreWEC system that contributed to the strength and energy dissipating capacity of the system. In this section, a component test conducted for the O-connectors is described first, followed by the

calibration of the model of the O-connectors. Optimization of the O-connector mesh density is subsequently discussed.

5.4.3.1 Component Test

The O-connector tests conducted at Iowa State University (ISU), described in Section 2.1.3, were used to validate the numerical model of the O-connector.

Displacement control was used in the ISU experimental component tests. The relative vertical movements of the O-connector recorded in Phase 1, Phase 3, Phase 5 and Phase 7 of the second specimen (PFS2) were used as the loading protocol for the tests, as shown in Fig. 5-22. The testing phases in PFS2 are described in Section 4.5.2.

5.4.3.2 Numerical Simulation

Shell elements S4R (4-node shell element with reduced integration) were used to simulate the O-connectors. A combined kinematic and isotropic hardening model was used for the steel material. The stress-plastic strain pairs of the steel material shown in Table 5-4 were assigned to the material model. Instead of simulating the entire test setup, only one O-connector is simulated, as shown in Fig. 5-23. The star shows in the figure is the loading point of the model. A comparison of the average force-displacement responses of one O-connector measured in the test is plotted alongside the results from the numerical simulation in Fig. 5-24 and Fig. 5-25, respectively. Recorded relative vertical displacements of the O-connector are shown on the horizontal axis and the resistance of the O-connector is shown on the vertical axis.

In Phase 1, the numerical model provided an accurate estimation of the cyclic behavior of the O-connector as shown in Fig. 5-24. The model closely predicted the loading and unloading stiffness throughout the test and only slightly overestimated the strength of the O-connector in the positive loading direction (12% at 1.4 in.) and underestimated it in the negative peaks (8% at -0.2 in.). The model of the O-connectors was validated for this phase. The same element type and material model of the O-connectors were used in the model of PFS1 and PFS2.

In Phase 3, 5 and 7, the numerical model overestimated the strength of the O-connector in the positive loading direction but predicted it reasonably well in the negative loading direction, as shown in Fig. 5-25. It was believed that when larger relative vertical

displacement was applied to the O-connectors in the positive loading direction, damage in the O-connector was significant and the strength gradually degraded. The observed damage may have included cracking and fracture of the O-connector or the welding, which was not covered in the numerical model. Therefore, the strength of the O-connector predicted by the numerical model was larger than that recorded in the component test at higher drift levels.

5.4.3.3 Mesh of the O-connectors

As mentioned in Section 5.2.4.2, the mesh density of the O-connectors is a critical factor related to the computational cost. Relatively coarse meshes were recommended for the O-connectors provided that the simulation results were reasonably accurate.

Three models using different mesh densities were built to investigate the optimized solution, as shown in Fig. 5-26. The same loading protocol used in Phase 1 of the component test described in Section 5.4.3.1 was applied to the three models. The analysis results of the models and the test results are compared in Fig. 5-27. As shown in the figure, the results from the moderate meshed and the fine meshed models matched well with the test results. However, the results from the coarse meshed model were not reliable. To reduce computational cost, the moderate meshed model was used in the models of PFS1 and PFS2.

5.5 Modeling of Surrounding Structure in PFS1

After describing the simulation of the PreWEC system in PFS1 in Section 5.4, the simulation of the surrounding structure in PFS1 is described in this section, including: steel mega beams, steel columns, an unbonded post-tensioned slab, RC edge columns, edge beams, and props.

5.5.1 Steel Mega Beam and Steel Column

As discussed in Section 3.3.3, mega beams are used to simulate the constraint from five missing upper-story floors in the scaled prototype building. A proof of concept test was conducted to characterize the behavior of the mega beam before the assemblage test.

A detailed description of the component test is given in Section 3.3.3.2. The setup of the component test is shown in Fig. 5-28.

A numerical model of the component test is built as shown in Fig. 5-29. Shell elements S4R were used to simulate the cover plates, the end plates and the steel beam W10×30. A combined kinematic and isotropic hardening material model was used for the steel. The end plate was fixed at the base (no movement allowed).

To simulate the hinge connection between the beam and the end plate, a "kinematic coupling" constraint was established between the centroid of the end plate (red circle in Fig. 5-29) and the web of the steel beam with the three translational degrees of freedom being slaved. Under this constraint, the steel beam would freely rotate about the centroid of the end plate and the connection behaved like a pin.

In the numerical model, the edge of the cover plates is "tie" constrained to the end plate as shown in Fig. 5-29. As mentioned in Section 5.2.3, "Tie" constrained all six degrees of freedom of the slaved nodes with those of the reference nodes. The constraint matched the condition of the weld connections between the cover plates and the end plate. It was expected that the six slip-friction bolts would rigidly connect the cover plates to the flanges of steel beams. Thus, the bolt connections were also simulated by using "tie" constraint between the edges of the cover plates that were away from the end plate to the flanges of the steel beams.

A reference point (marked by star in Fig. 5-29) was introduced near the middle of the top edge of the beam. The loading protocol used in the component test was applied to the simulated beam through the reference point by coupling the horizontal movements of the reference point with the edge of the beam.

The base moment-lateral displacement curves from the numerical model and the component test are compared in Fig. 5-30. The base moment provided by the mega beam connection was obtained by multiplying the input loads from the actuator with the distance between the centroid of the actuator and the base of the cover plates. The lateral displacement was recorded by the actuator. As shown in the figure, the simulation results matched well with the test results and thus the model of mega beam connections was validated.

In the model of PFS1, the same element type and material model of the mega beam connections were used. The cover plates of the mega beam were “tie” connected to the steel columns that were simulated by using shell elements with elastic steel material models.

5.5.2 Modeling of Edge Columns and Edge Beams

As discussed in Section 5.2.2, truss elements were used to simulate the rebar in the edge columns and edge beams. The truss elements (rebar) were “embedded” in the solid elements (concrete) in the model. As mentioned in Section 5.2.3, “embedded” constrains the translational degrees of freedom of the embedded nodes to the interpolated values of the corresponding degrees of freedom of the host element. This technique was recommended by ABAQUS to simulate the rebar in the reinforced concrete structures.

When meshing the edge columns, the cross section of the edge columns was divided into 20 segments and each of the fourteen longitudinal rebar was located in a separate single segment. Furthermore, the mesh densities of the edge column and those of the rebar were the same along the height of the column, ensuring that each node of the truss element (rebar) was within a single cube of the solid element (concrete). These simulation techniques were used to improve the accuracy of the simulation.

5.5.3 Modeling Props

As discussed in Section 3.2.1, the props were designed to be rotatable in both in-plane and out-of-plane directions. There was little moment generated in the props. Truss elements (T3D2, A 2-node linear 3D truss) were used to simulate the props only providing axial constraint to the floor. Because the connection plates of the props were 7 in. wide and 10 in. long, a small region of the slab that had similar dimensions was slaved to the movement of the props by using the “kinematic coupling” constraint.

5.5.4 Unbonded Post-Tensioned Slab

In this section, existing modeling techniques of unbonded PT slabs are summarized in Section 5.5.4.1, followed by a comparison of these techniques in Section 5.5.4.2.

Through the comparison, the method of "Adjusting stress-strain responses of PT strands" was selected for this study. The method was validated through simulating a cantilever unbonded PT slab by using ABAQUS. Modeling of the unbonded PT slab in PFS1 is described in detail in Section 5.5.4.4, and the technique to simulate the rigid wall-floor connections is described in Section 5.5.4.5.

5.5.4.1 Existing Modeling Techniques

Using contact elements

Solid elements are used to simulate the slab and the strands when using this technique. To simulate the "unbonded" characteristic, contact elements are assigned between the slab and the strands.

Fig. 5-31 shows a model of unbonded PT slabs using contact elements in ABAQUS. The contact elements consisted of two matched surfaces of the strands and the surrounding concrete elements. Tangential and normal behaviors were assigned to the strands to define the properties of the contact elements. Because the strands would not penetrate the slab, "hard contact" was used for the normal behavior. "Frictionless" was used for the tangential behavior because the strands were expected to slide freely within the sheathing tube. Satisfactory simulation results were achieved using this technique (Ellobody and Bailey 2008).

Using link element

The slab is simulated using solid elements when using this technique, and truss elements are used to simulate the strands. To simulate the "unbonded" characteristic, link elements are introduced between the solid elements of the slab and the truss elements of the strands.

Fig. 5-32 shows a model of unbonded PT slabs using link elements. As shown in the figure, the link elements are special zero-length elements assigned to the coincident nodes of the solid elements of the concrete and the truss elements of the strands. Fig. 5-33 shows the details of a link element. As shown in the figure, *i* node connects the solid element and *j* node connects the truss element. Two orthogonal springs defined the properties of the link element. Extraordinarily large stiffness was assigned to the vertical spring to simulate the non-penetration property; bond-slip relationship was assigned to

the horizontal spring to simulate potential friction inside the sheathing tube. If the strands were assumed to slide freely, no bond resistance would be assigned to the horizontal spring. The proposed model was verified through a series of tests of unbonded PT beams (Vecchio et al. 2006).

Adjusting stress-strain responses of PT strands

Different from the previous two techniques where solid elements are used to simulate the slabs, shell elements are used in this technique. The PT strands are simulated by using "bonded" rebar layers. The benefit of using the "bonded" characteristic is that strain compatibility is valid when deducing the strains in the PT strand that significantly simplifies the modeling and analysis of the slab.

Because the "unbonded" strands are simulated by "bonded" rebar layers, discrepancies exist. In general, the maximum strain increment in the "bonded" strands would be larger than that in the "unbonded" strands due to large local deformations generated at critical sections of the slab. Correspondingly, the stresses in the "bonded" strands are expected to be larger than those in the "unbonded" strands.

One way to reduce the discrepancies is to adjust the stress-strain responses of the "bonded" strands. An iterative procedure was proposed by Kwak and Kim (2006) to adjust the stress-strain curves based on average strains and stresses in the "bonded" strands. An example is given below to demonstrate the procedure.

The example includes a simply-supported unbonded PT beam with a concentrated load in the middle, as shown in Fig. 5-34(a). Fig. 5-34(b) shows the strain distribution along the length of the beam assuming the strands are "bonded" to the beam. As shown in the figure, the strain is not uniformly distributed along the length with the maximum strain $\varepsilon_{1,max}(p)$ and the associated stress $\sigma_{1,max}(p)$ at the critical section in the middle of the beam:

$$\varepsilon_{1,max}(p) = max[\varepsilon_1(x,p)] \tag{5.19}$$

$$\sigma_{1,max}(p) = f(\varepsilon_{1,max}(p)) \tag{5.20}$$

The average strain $\varepsilon_{1,ave}(p)$ and the associated average stress $\sigma_{1,ave}(p)$ can be calculated by the following equations:

$$\varepsilon_{1,ave}(p) = \frac{1}{L_{strands}} \int_0^L \varepsilon_1(x,p)dx \tag{5.21}$$

$$\sigma_{1,ave}(p) = f(\varepsilon_{1,ave}(p)) \tag{5.22}$$

Where f = Stress-strain response of a strand; $L_{strands}$ = Total length of a strand between anchorages at both ends; $\varepsilon_1(x,p)$= Strain distribution along the strands obtained by assuming the strands are bonded.

Because $\varepsilon_{1,ave}(p)$ represents a uniform strain distribution along the full length of the beam, it better represents the "unbonded" characteristic of the PT strands. Kwak and Kim recommended adjusting the stress–strain curve of the strands on the basis of the strain $\varepsilon_{1,max}(p)$ at the critical section, because the behavior of the structural components, especially those at ultimate states, is dominated by the behavior at critical sections.

Fig. 5-35 shows adjusted stress-strain responses for "bonded" strands and those for a bare strand. As shown in the figure, the maximum stress $\sigma_{1,max}(p)$ corresponding to the maximum strain of $\varepsilon_{1,max}(p)$ for a bare strand (Point A) is revised to an average stress $\sigma_{1,ave}(p)$ at the same maximum strain $\varepsilon_{1,max}(p)$ (Point B). The non-uniform strain distribution $\varepsilon_1(x,p)$ with the maximum value $\varepsilon_{1,max}(p)$ of the "bonded" strand in the numerical model was averaged to simulate the "unbonded" strand in the PT beam. When the same procedure is repeated at different load levels, a complete stress–strain curve specifically adjusted for the "bonded" strands can be obtained.

The following procedure was proposed to apply this iterative procedure in the simulation. The numerical model of the beam with stress-strain response for the "bonded" strand was conducted first to obtain the aforementioned adjusted stress-strain responses. A second analysis of the same beam model using the adjusted stress–strain responses of the strand was conducted. The purpose of the second analysis of the model was to check that the unbonded characteristics of the strand were effectively represented. It was done by comparing the two maximum tendon stresses from the second analysis with the average stress in the PT strands corresponding to the average strain obtained through Eq. (5.21). If the difference of the two maximum stresses was large, the stress-strain responses needed to be re-adjusted based on the results from the second analysis.

The obtained re-adjusted stress-strain responses were used for the third iteration. The process was repeated until the difference of the two maximum stresses was relatively small.

Two continuous unbonded PT slabs tested by Burns et al. (1978) were used by Kwak and Kim to verify the reliability of the proposed technique. The simulation results matched well with the test results (Kwak and Kim 2006).

Other modeling techniques

Besides the three modeling techniques described above, some other techniques were also used by researchers to simulate unbonded PT slabs. For example, Lou et al. (2013) suggested that the contribution of unbonded strands to other structural components could be made by transforming the PT force into equivalent nodal loads acting on the model. Yu (2012) used a virtual tendon with spring elements to simulate the interaction between the strands and the concrete slab. Because these techniques are only applicable under specific circumstances, they are not as widely used as the three techniques discussed above.

5.5.4.2 Discussion of Existing Modeling Techniques

Contact elements and link elements had been successfully used by researchers to simulate the unbonded PT slab. However, because solid elements were used in both techniques to simulate the structural components (e.g. beams and slabs), a great amount of elements were generated in the model that resulted in high computational cost. When using the "contact elements," the PT strands of a small diameter were simulated by solid elements. Very small elements were generated when meshing the PT strands. As discussed in Section 5.2.4.2, the computational cost is directly related to the density of the mesh when using explicit solver. The small elements of the strands further increased the computational cost.

The problem was avoided when using the "link elements," because the strands were simulated by truss elements. However, to build link elements between the solid elements of the slab and the truss elements of the strands, the mesh of the solid elements and that of the truss elements was required to be arranged in a way that the solid elements shared nodes with the truss elements. It greatly increased the complexity of the mesh process.

Furthermore, the complexity of contact elements and link elements can cause convergence problems during the analysis. In summary, it was not advisable to use contact elements or link elements to simulate the unbonded PT slab for the studies in this dissertation.

When using the third technique, "adjusting stress-strain responses of PT strands," the unbonded PT slab was simulated by using shell elements that greatly reduced the amount of elements in the numerical models. Because no contact elements or link elements were used, less convergence problems were expected. This technique was used in this dissertation.

5.5.4.3 Modeling of a Cantilever Unbonded PT Slab

In this section, a cantilever unbonded PT slab is simulated using ABAQUS. The purpose is to introduce the associated modeling techniques in ABAQUS and validate the technique "adjusting stress-strain responses of PT strands" to model an unbonded PT slab.

Details of the cantilever unbonded PT slab are shown in Fig. 5-36. The slab was 10 ft. wide, 20 ft. long and 3 in. thick. Five 3/8 in. diameter, Grade 250 strands were evenly distributed along the width of the slab with a spacing of 20 in. The PT strands were placed in the middle layer of the slab cross section. The initial stress in the PT strands was 200 ksi. No bonded reinforcement was included in this simplified model.

The compressive strength of the concrete in the slab was 7,000 psi. The tensile strength of the concrete was assumed to be only 6 psi. The benefit of this assumption was to exclude the tensile contribution of uncracked concrete in the slab, which made it clearer in interpreting the simulation results.

In the following, general definitions of shell elements with "rebar layers" and the method to apply initial PT forces to the slab in ABAQUS are discussed first, followed by the iteration procedure to determine the adjusted stress-strain responses of the PT strands in the simplified model. The simulation results are then compared to the theoretical analysis results for validation.

Definitions of the shell elements for the slab with "rebar layers"

Shell elements were used to simulate the 3-in. thick concrete slab. Because the slab was expected to encounter large inelastic strains, 9 integration points were used along the thickness of the slab.

In ABAQUS, "rebar layers" were used in the shell elements to define the "bonded" rebar in the slab. In the model for the cantilever PT slab, the "unbonded" strands were modeled by "bonded" rebar layers. The following items were required to define a "rebar layer": material, area per bar, spacing, orientation angle and position.

"Material" referred to the material models assigned to the PT strands. The original stress-strain responses of the strand included: the yield strength was 230 ksi; the ultimate strength was 260 ksi and the associated plastic strain was 0.046; and the Young's modulus of the strand was 29000 ksi. The stress-strain responses were assigned to the PT strands to initiate the iteration process. They were adjusted by following the iteration procedure described in Section 5.5.4.1.

"Area per bar" referred to the cross-sectional area for the PT strand (0.0813 in^2).

"Spacing" referred to the average distance between two adjacent strands. It was directly calculated by dividing the width of the region containing the strands by the amount of the strands in the region (120 in. /5 strands = 24 in.).

"Orientation angle" referred to the angular orientation of the strands relative to the reference orientation. For the strands distributed along the width of the slab, the "orientation angle" was 90 degrees.

"Position" referred to the locations of the strand measured from the middle layer of the slab cross section. When positive values were assigned to the strands, it indicated that they were located above the middle layer. Because the strands were placed in the middle of the slab cross section, the "Position" was zero.

Applying initial PT forces to the strands

The method to apply initial PT forces to the strands in the wall has been described in Section 5.4.1. A similar method was used to apply initial PT forces to the strands in the slab. A temperature field was assigned to the slab containing the PT strands. Only the strands were assigned the property of thermal expansion, thus no thermal strains would

be generated in the concrete due to the assigned temperature field. Because the initial stress in the strands was 200 ksi, the temperature assigned to the slab was calculated as follows:

$$\Delta_T = \frac{\sigma_{initial}}{E_{strand}\alpha_T} = \frac{200}{29000 \times 6.7 \times 10^{-6}} \approx 1029\ K \tag{5.23}$$

Where Δ_T = Magnitude of varied temperature; $\sigma_{initial}$ = Initial stress in the strand; E_{strand} = Young's modulus of the strand; α_T = Thermal coefficient (6.7×10^{-6}/K for strands).

The PT strands were cooled down by -1029 K to initially compress the slab.

Adjusted stress-strain responses of longitudinal PT strands

Fig. 5-37 shows the model of the cantilever unbonded PT slab. One end of the slab was fixed and the other end was free. The free edge of the slab was vertically displaced to 5 in. The model where the original stress-strain responses were used for the PT strands ran for the first iteration.

Fig. 5-38 shows the strain distribution in the strand when the free edge was vertically displaced to 5 in. As expected, the slab was subjected to localized deformations at the fixed edge, where the strains in the "bonded" PT strands were larger than those away from the fixed edge. The strains would lead to increased stresses in the strands that were larger than the actual increased stresses when the strands were "unbonded" in reality.

To reduce the increased stresses in the PT strands under the large strain demands on the "bonded" PT strand, the following operations were conducted to adjust the stress-strain curve of the strands: (1) find the maximum strain in the strands ($\varepsilon_{max} = 0.00082$); (2) multiply the length of each strand segment ($L_i \approx 13.3\ in.$) with the associated strain (ε_i, shown in Fig. 5-38), and sum the results to obtain the total elongation of the strand ($\Delta L = \sum_{i=1}^{18} \varepsilon_i L_i = \approx 0.02\ in.$); (3) divide the total elongation of the strand (ΔL) by the total length of the strand ($L_{strand} = 240\ in.$) to obtain the average strain ($\varepsilon_{ave} = 0.000083$); (4) calculate the average stress in the strand associated with the average strain ($\sigma_{ave} = E_{strand}\varepsilon_{ave} = 0.000083 \times 29000 \approx 2.4\ ksi$); (5) record the maximum strain – average stress pair ($\varepsilon_{max}, \sigma_{ave}) = (0.00083, 2.4$); (6) add the initial strain and the initial stress pair ($\varepsilon_{ini}, \sigma_{ini}) = (0.0069, 200)$ generated by the initially applied temperature field to the

maximum strain – average stress $(\varepsilon_{max}, \sigma_{ave}) = (0.00083, 2.4)$ to obtain the adjusted strain - stress pair $(\varepsilon_{adjust}, \sigma_{adjust}) = (0.00773, 202.4)$. This was a point in the adjusted stress-strain curve of the PT strand that corresponded to the condition when the slab had 5 in. vertical deformation.

Other $(\varepsilon_{max}, \sigma_{ave})$ pairs in the adjusted stress-strain curve can be obtained by conducting the same operations when the slab was subjected to different vertical deformations. Fig. 5-39 shows a comparison of the original stress-strain curve of the PT strand with the adjusted curve after the first run. As shown in the figure, the stresses in the adjusted curve for the "bonded" PT strands start to slowly increase with increasing strains after the "initial stress" point. It well simulated the "unbonded" characteristic of the PT strands in the slab.

Using the adjusted stress-strain curve after the first run, the second run of the model was conducted. Fig. 5-40 shows a comparison of the original stress-strain curve with the adjusted curves after the first and second run. As shown the figure, the curve after the second run matches well with that after the first run, thus the third run of analysis is not necessary. The adjusted stress-strain curve after the second run was used as the stress-strain responses of the strands in the numerical model.

Theoretical analysis of the cantilever unbonded PT slab

To validate the numerical model, theoretical analysis of the cantilever unbonded PT slab was conducted for two cases. First, the response when the slab remained elastic (cracks did not open or zero stress at bottom fiber), and second, the upper bound moment resistance of the slab was calculated.

The strain distribution along the cross section of the slab is shown in Fig. 5-41 for the case when the bottom fiber reaches decompression (i.e., the tensile stress at the bottom fiber was close to zero). Because the deformation of the slab was small, it was expected that the PT force in the unbonded strand would remain almost constant.

The initial force in the PT strands when the cracks start to open is calculated:

$$F_i = n_{strand}\sigma_i A_{strand} = 5\times200\times0.0813 = 81.3\ kip \quad (5.24)$$

Where F_i = Initial PT force in the strands; n_{strand} = Number of the strands in the slab; A_{strand} = Cross-sectional area of the strand.

The moment resistance at the fixed-edge of the slab is calculated:

$$M_{cls} = F_i d_{st} = 81.3\times\left(\frac{3}{2}-\frac{3}{3}\right) \approx 41\ kip-in \tag{5.25}$$

Where M_{cls} = Moment at the fixed edge of the slab; d_{st} = Distance between the centroid of the strand and the resultant compression force in the cross section.

The vertical deformation at the free end of the cantilever slab is calculated:

$$\Delta_{cls} = \left(\frac{M_{cls}}{L_{slab}}\right)\frac{(L_{slab})^3}{3E_c I_{slab}} = \frac{41}{240}\times\frac{(240)^3}{3\times4503\times\frac{120\times3^3}{12}} \approx 0.32\ in \tag{5.26}$$

Where Δ_{cls} = Vertical deformation of the slab at the free edge; L_{slab}= Length of the slab; E_c= Young's modulus of the concrete in the slab; I_{slab}= Moment of inertia of the slab.

After calculating the response when the slab remains elastic, the upper bound moment resistance of the slab was calculated.

According to Equation (18-3) in ACI 318-11, for members with unbonded tendons and with a span-to-depth ratio greater than 35 (240 in. /3 in. = 80 > 35), the stress in the PT strand is calculated:

$$f_{ps} = f_{se} + 10{,}000 + \frac{f_c'}{300\rho_p} = 200{,}000 + 10{,}000 + \frac{7{,}000}{300\times1.3\times10^{-3}} \approx 228\ ksi \tag{5.27}$$

$$\rho_p = \frac{n_{strand}A_{strand}}{w_{slab}d_p} = \frac{5\times0.0813}{10'\times12"\times(3"-0.25"-0.375"/2)} \approx 1.3\times10^{-3} \tag{5.28}$$

Where ρ_p = Ratio of $n_{strand}A_{strand}$ to $w_{slab}d_p$; w_{slab}= With of the slab; d_p= Distance from extreme compression fiber to centroid of strands (0.25 in. was the concrete cover and 0.375 in. was the diameter of the strand); f_{ps} = Stress in prestressing steel at nominal flexural strength; f_{se} = Effective stress in the strand (equal to the initial stress in the model).

To derive the upper bound moment resistance of the slab, assuming the extreme compressive stress in the slab was 0.003 and the depth of the Whitney stress block $a_{cls}$is calculated:

$$a_{cls} = \frac{n_{strand} f_{ps} A_{strand}}{0.85 f_c' w_{slab}} = \frac{5\times228\times0.0813}{0.85\times7\times120} \approx 0.13\ in \tag{5.29}$$

The upper bound moment resistance of the slab (M_{cls}) and the associated vertical resistance at the free edge of the slab (F_{cls}) are calculated:

$$\begin{aligned} M_{cls} &= n_{strand} f_{ps} A_{strand} d_{st} = 5\times228\times0.0813\times\left(\frac{3}{2} - \frac{0.13}{2}\right) \\ &\approx 133\ kip - in \end{aligned} \tag{5.30}$$

$$F_{cls} = \frac{M_{cls}}{L_{slab}} = \frac{133}{240}\times1000 \approx 554\ kip \tag{5.31}$$

Fig. 5-42 shows a comparison of the results from the simulation and the theoretical analysis. As shown in the figure, the simulation matched reasonably well with the theoretical results when the slab remained elastic. In comparing the maximum vertical force obtained in the model to the predicted upper bound force, the model resulted in a 15% smaller force. It was found in the numerical model that when the slab was vertically deformed 5 in., the stress in the PT strands only increased to 203 ksi that was smaller than the value predicted by the code (228 ksi). This was believed to be the primary cause for the lower vertical resisting force in the model.

After validating the feasibility of using the technique “adjusting stress-strain responses of PT strands” to simulate the unbonded PT slab, the modeling of the floor slab tested in PFS1 is discussed in the next section.

5.5.4.4 Modeling of the Unbonded PT Slab Tested in PFS1

Design of the unbonded PT slab in PFS1 is discussed in Section 3.3.2. Fig. 5-43 shows the plan view of the slab. As shown in the figure, the slab includes the following structural elements: a 3 in. thick concrete slab, distributed strands in the E-W direction (in black color with arrow), banded strands near the wall ends in the N-S direction (in black color with arrow), discrete bonded reinforcement at the top and bottom of the slab (in green, red and cyan colors) at the wall-floor, floor-edge beam and floor-prop connections, distributed bonded reinforcement at the bottom of the slab (in blue color), and four No.3 shear-friction rebar along the N-S surfaces of the wall (in magenta color).

In the following, region dividing, applying initial PT forces and definitions of the shell elements with “rebar layers” are discussed.

Region dividing

As shown in Fig. 5-43, the slab contains multiple types of reinforcement and strands. To accurately simulate the distribution of the reinforcement and the strands, the slab was divided into different regions. Fig. 5-44 shows the divided slab in the model. The same properties of the west half of the slab were assigned to the east half of the slab assuming the slab was structurally symmetrical. Because most of the instrumentation was placed in the west half of the slab as discussed in Section 4.3.1, it was reasonable to use the as-built dimensions for the west half of the slab. Although the positions of the reinforcement (the strands) and the forces in the banded transverse strands in the east half of the slab were slightly different from those in the west half of the slab, this symmetrical assignment greatly simplified the modeling. Table 5-5 lists the properties of each slab region input to the model, including contained structural elements, area per bar, spacing, orientation angle and position.

Applying initial PT forces to the strands

Because the prestress forces varied in different strands, different temperature fields were assigned to different slab regions containing the strands. Only one temperature field can be assigned to each region. For the regions containing both longitudinal and transverse strands (i.e. zone Q, R, S, Q', R' and S'), the thermal expansion coefficient of the transverse strands ($\alpha_{exp\text{-tran}}$) was adjusted to generate appropriate initial PT forces in the transverse strands. For example, the initial PT force in the longitudinal strand in Zone S was 6.1 kip while the average initial PT force in the transverse strands in Zone S was 9.6 kip. Under the same temperature field assigned to Zone S, $\alpha_{exp\text{-}tran}$ was adjusted to $9.6/6.1\times\alpha_{exp\text{-}long}\approx 1.6\alpha_{exp\text{-}long}$, where $\alpha_{exp\text{-}long} = 6.7\times10^{-6}$ was the thermal expansion coefficient of the longitudinal strands. Table 5-6 lists the initial force, initial stresses, applied temperature and thermal expansion coefficient in the longitudinal and transverse strands in the model.

Definitions of the shell elements for the slab with "rebar layers"

To define "Material" for the bonded reinforcement and the PT strands, the stress-strain response discussed in Section 5.3.1 was assigned to the No.3 reinforcement and No.2

deformed wire in the slab. Adjusted stress-strain responses were assigned to the PT strands.

For the longitudinal rebar and the distributed strands, the "orientation angle" was 90 degrees. For the transverse rebar and the banded strands, the "orientation angle" was 0 degrees.

The as-built location of the rebar measured before the test was used to define "Position" for the reinforcement. The slab was divided into smaller regions, thus the continuous strands of curved profiles were divided into discontinuous segments. Because the slope of the strands in the 3-in. thick slab was very small, the highest and the lowest location of the strands in each segment were similar. Averaged as-built location was assigned to the divided strand segments at different heights along the thickness of the slab to simulate the curved profile.

After describing the techniques to simulate the floor slab in PFS1, the iteration procedure to determine the adjusted stress-strain response of both longitudinal and transverse PT strands is discussed in the following.

Adjusted stress-strain response of the longitudinal and transverse strands

As discussed previously, because the "unbonded" PT strands were simulated by "bonded" rebar layers, the stress-strain response of the "bonded" strand should be modified to reflect the "unbonded" characteristic. A numerical model of the test specimen PFS1 named "Model-A PFS1" was built to deduce the adjusted stress-strain curves of the strands. For Phase 1, the props were not included in the model as shown in Fig. 5-45(a). For Phase 2, the props were included in the model as shown in Fig. 5-45(b).

As shown in Fig. 5-43, the PT strands were distributed in the longitudinal direction (E-W) and banded in the transverse direction (N-S). Different adjusted stress-strain curves were assigned to the longitudinal and the transverse strands. The iteration process to deduce the adjusted stress-strain curve for the longitudinal strand in the "Model-A PFS1" (without props) is discussed below as an example.

For the first run of the model "Model-A PFS1," the material properties of the strands that were directly obtained from the mill of certification were used in the model.

The model was monotonically pushed to 2% design drift. Fig. 5-46 shows the strain distribution in the longitudinal strand that was closest to the wall (Vertical regions D' through Z3' and the corresponding regions on the east half of the wall shown in Fig. 5-44) at 2% drift. As expected, the slab was subjected to localized deformations at the wall-floor and the floor-edge connections, where the strains in the "bonded" strand segments were larger than those away from the connections.

To reduce the increased stresses in the strand under the large strain demands on the "bonded" strand, the following operations were conducted to adjust the stress-strain curve of the strand: (1) find the maximum strain in the strand ($\varepsilon_{max} = 0.0076$); (2) multiply the length of each strand segment (L_i) with the associated strain (ε_i) to obtain the total elongation of the strand ($\Delta L = 0.15\ in.$); (3) divide the total elongation of the strand (ΔL) by the total length of the strand ($L = 224\ in.$) to obtain the average strain ($\varepsilon_{ave} = 0.00068$); (4) calculate the average stress in the strand associated with the average strain ($\sigma_{ave} = E\varepsilon_{ave} = 0.00068 \times 29000 \approx 20\ ksi$); (5) record the maximum strain – average stress pair $(\varepsilon_{max}, \sigma_{ave}) = (0.0076, 20)$; (6) add the initial strain and stress pair $(\varepsilon_{ini}, \sigma_{ini}) = (0.0026, 75)$ generated by the assigned temperature field to the maximum strain – average stress $(\varepsilon_{max}, \sigma_{ave}) = (0.0076, 20)$ to obtain the adjusted strain - stress pair $(\varepsilon_{adjust}, \sigma_{adjust}) = (0.0102, 95)$. It was the point in the adjusted stress-strain curve of the PT strand corresponding to 2% drift.

Other strain - stress pairs in the adjusted curve could be obtained by conducting the same operations at different drifts. Fig. 5-47 shows a comparison of the original stress-strain curve from the mill of certification and the adjusted curve after the first run. As shown in the figure, the stresses in the adjusted curve for the "bonded" PT strands start to slowly increase with increasing strains after the "initial stress" point, demonstrating the "unbonded" characteristic of the PT strands in the tested floor slab.

Using the adjusted stress-strain curve, the second and the third run of the model was performed. Fig. 5-48 shows a comparison of the original stress-strain curve, the adjusted stress-strain curves after the first, second and third runs. As shown the figure, the curve after the third run matched well with that after the second run, thus the fourth run was not

necessary. The adjusted stress-strain curve after the third run was used for the longitudinal strands in “Model-A PFS1” for Phase 1 (without props).

A similar procedure was used to derive the adjusted stress-strain curve for the transverse strands in Phase 1. The only difference was that the strains in the transverse strand segments were used for the iteration process. Fig. 5-49 shows the strain distribution in the transverse strand (horizontal regions P to P’ shown in Fig. 5-44) at 2% drift after the first run of the model.

The same procedure was used to derive the adjusted stress-strain curve for the transverse strand. Fig. 5-50 shows a comparison of the original stress-strain curve, the adjusted stress-strain curves after the first run and the second run. As shown in the figure, the curve after the second run matched well with that after the first run, thus the third run was not necessary. The adjusted stress-strain curve after the second run was used for the transverse strand in “Model-A PFS1” for Phase 1.

Props were attached to the floor in Phase 2 of the test. It was believed that the props would change the deformation demands on the floor, especially in the transverse direction. Props were added to “Model-A PFS1” as shown in Fig. 5-45(b) to deduce the adjusted stress-strain curves of the strands in Phase 2. The same procedure described above was used.

Fig. 5-51 summarizes the different adjusted stress-strain curves for the longitudinal and the transverse strands in the numerical model “Model-A PFS1” for Phase 1 and Phase 2. They were used in the numerical models of PFS1 in Chapter 6 when validating the models with the associated test results.

5.5.4.5 Modeling of Rigid Wall-Floor Connections

Neither relative vertical nor horizontal slip was expected to occur at the wall-floor connections throughout the test of PFS1. In the numerical model of PFS1, the portion of the slab that contained rebar and strands going through the wall was “embedded” in the wall, as shown in Fig. 5-52. The “embedded” portion of the slab would move along with the wall.

5.6 Modeling of the PreWEC System in PFS2

A PreWEC system with regular end columns was used in PFS2. It consisted of a rocking wall, two post-tensioned end columns and the O-connectors. The modeling techniques of the tested PreWEC system in PFS2 were similar to those of the PreWEC system in NCREE (described in Section 2.2.3). A major difference between the PreWEC system in PFS2 and that in NCREE was that reinforced concrete end columns were used in PFS2, but concrete filled steel tubes were used as end columns in NCREE. No damage occurred to the concrete filled steel tubes, thus elastic material models were used to simulate the end columns in the model of the specimen in NCREE. On the other hand, it was expected that damage would occur in the end columns in PFS2, thus the damaged plasticity model was used to simulate the confined concrete in the end columns of PFS2. Simulation results of the isolated PreWEC system are discussed in Section 7.1.

Table 5-1 Material models for steel structural elements of the FE models

Specimen	Material model	Structural elements
PFS1	Plasticity	1/2 in. strands in the wall
		3/8 in. strands in the unbonded PT Slab
		Rebar in the wall, edge columns and edge beams
		O-connectors
		Cover plates of the mega beams
		Threaded rods in the edge columns
	Elastic	Mega beams W10x30
		Steel columns W16x67
		Short steel tubes for O-connectors
		Steel plates embedded in the wall
PFS2	Plasticity	1/2 in. strands in the wall
		Rebar in the wall and the end columns
		O-connectors
		Threaded rods in the end columns
	Elastic	Steel plates embedded in the wall
		Steel plates embedded in the end columns

Table 5-2 Material models for concrete structural components of the FE models

Specimen	Material model	Structural components
PFS1	Concrete damaged plasticity	Wall panel
		Floor slab
		Edge columns
		Edge beams
	Elastic	Top block
		Base block
PFS2	Concrete damaged plasticity	Wall panel
		End columns
		Edge columns
		Edge beams
	Elastic	Top/Base block

Table 5-3 Element types for structural components of the FE models

Models	Element types	Structural components
PFS1	C3D8R	Top block
		Base block of the wall
		Wall panel
		Fiber grout layer
		Edge columns and edge beams
	S4R	Mega beams with cover plates
		Steel columns
		Short steel tubes for the O-connectors
		O-connectors
		Plates embedded in the wall
		Unbonded PT slab
	T3D2	Strands in the wall and the slab
		Rebar in the wall, the edge columns and the edge beams
		Threaded rods in the edge columns
PreWEC In PFS2	C3D8R	Top block
		Base block of the wall
		Wall panel
		Fiber grout layer
		End columns
	S4R	Plates embedded in the wall and the end columns
		O-connectors
	T3D2	Strands in the wall and the unbonded PT slab
		Rebar in the wall and the end columns
		Threaded rods in the end columns and the edge columns

Table 5-4 Input stress-plastic strain pairs for the steel material models

	Elements	E_s (Mpsi)	Pair1 (με-ksi)		Pair2 (με-ksi)		Pair3 (με-ksi)		Pair4 (με-ksi)		Pair5 (με-ksi)	
			ε_p^*	f_y	ε_p	σ	ε_p	σ	ε_p	σ	ε_p	σ
PFS1 & PFS2	1/2 in. strand	29.1	0	247	0.0016	263	0.028	278	0.04	283	-	-
	#3 Rebar	29.0	0	67	0.0159	68	0.035	77	0.06	83	0.09	86
	#5 Rebar	29.0	0	68	0.0061	70	0.034	88	0.06	95	0.09	96
	#2 wire	29.0	0	91	0.0064	97	-	-	-	-	-	
	O-conn.	29.0	0	60	0.0166	61	0.047	71	0.20	72	-	-
PFS1	3/8 in.	29.0	0	230	0.046	260	-	-	-	-	-	-
	Cover	29.0	0	50	0.0064	51	0.035	76	0.21	80	-	-
	3/4 in.	29.0	0	105	0.1564	125	-	-	-	-	-	-
PFS2	#2 wire	29.0	0	86	0.0066	92	-	-	-	-	-	-
	1 in. rod	29.0	0	105	0.1564	125	-	-	-	-	-	-
	1/2 in.	29.0	0	105	0.1564	125	-	-	-	-	-	-

* ε_p = Plastic strain, $\varepsilon_p = \varepsilon - \varepsilon_e$, ε = total strain, ε_e = Yield strain
$\varepsilon_e = f_y/E$, f_y = Yield strength, E_s = Young's modulus

Table 5-5 Regions of the slab with "rebar layers" properties

Region of slab	Contained Structural elements	Area per bar (in^2)	Spacing (in.)	Orientation (°)	Position (in.)
A	Top discrete E-W rebar	0.11	6	90	0.875
B	Bottom distributed E-W rebar	0.11	24	90	-0.25
	E-W strand	0.0813	24	90	-0.25
C	E-W strand	0.0813	9	90	-0.25
D	Top discrete E-W rebar	0.11	12	90	0.25
	Bottom distributed E-W rebar	0.11	12	90	-0.875
	E-W strand	0.0813	12	90	-0.25
E	Top discrete E-W rebar	0.11	3	90	-0.125
	Bottom discrete E-W rebar	0.11	3	90	-0.75
A'	Top discrete E-W rebar	0.11	6	90	0.75
B'	Bottom distributed E-W rebar	0.11	24	90	-0.5
	E-W strand	0.0813	24	90	-0.25
C'	E-W strand	0.0813	9	90	-0.25
D'	Top discrete E-W rebar	0.11	12	90	0.125
	Bottom distributed E-W rebar	0.11	12	90	-1
	E-W strand	0.0813	12	0	-0.25
F	Bottom distributed N-S rebar	0.11	38	0	-0.75
G	Bottom distributed E-W rebar	0.11	24	90	-0.5

Region of slab	Contained Structural elements	Area per bar (in^2)	Spacing (in.)	Orientation (°)	Position (in.)
	Bottom distributed N-S rebar	0.11	38	0	-0.75
	E-W strand	0.0813	24	90	-0.5625
H	Bottom distributed N-S rebar	0.11	38	0	-0.75
	E-W strand	0.0813	9	90	-0.5625
I	Bottom distributed E-W rebar	0.11	12	90	-0.625
	Bottom distributed N-S rebar	0.11	38	0	-0.75
	E-W strand	0.0813	12	90	-0.5625
J	Bottom distributed N-S rebar	0.11	38	0	-0.75
F'	Bottom distributed N-S rebar	0.11	38	0	-0.75
G'	Bottom distributed E-W rebar	0.11	24	90	-0.5
	Bottom distributed N-S rebar	0.11	38	0	-0.75
	E-W strand	0.0813	24	90	-0.5625
H'	E-W strand	0.0813	9	90	-0.5625
	Bottom distributed N-S rebar	0.11	38	0	-0.75
I'	Bottom distributed E-W rebar	0.11	12	90	-0.5
	Bottom distributed N-S rebar	0.11	38	0	-0.75
	E-W strand	0.0813	12	90	-0.5625
K	Top discrete E-W rebar	0.11	3	90	1
	Bottom discrete E-W rebar	0.11	12	90	-0.625
	Bottom distributed N-S rebar	0.11	13	0	-0.75
	Top distributed N-S wire	0.049	6.5	0	1.25
	Bottom distributed N-S wire	0.049	6.5	0	-1.25
	N-S strand	0.0798	6.5	0	-0.0625
L	Bottom distributed E-W rebar	0.11	24	90	-0.8125
	Bottom distributed N-S rebar	0.11	13	0	-0.75
	E-W strand	0.0813	24	90	0.4375
	N-S strand	0.0798	6.5	0	-0.0625
M	Bottom distributed N-S rebar	0.11	13	0	-0.75
	E-W strand	0.0813	9	90	0.4375
	N-S strand	0.0798	6.5	0	0.0625
N	Top discrete E-W rebar	0.11	12	90	0.75
	Bottom distributed E-W rebar	0.11	12	90	-0.625
	E-W strand	0.0813	12	90	0.4375
	Bottom distributed N-S rebar	0.11	13	0	-0.75
	N-S strand	0.0798	6.5	0	0.1875
O	Top discrete E-W rebar	0.11	3	90	0.6875
	Bottom discrete E-W rebar	0.11	3	90	-0.875
	Bottom distributed N-S rebar	0.11	13	0	-0.75
	N-S strand	0.0798	6.5	0	0.4375

Region of slab	Contained Structural elements	Area per bar (in^2)	Spacing (in.)	Orientation (°)	Position (in.)
K'	Top discrete E-W rebar	0.11	3	90	0.6875
	Bottom discrete E-W rebar	0.11	12	90	-1
	Bottom distributed N-S rebar	0.11	13	0	-0.75
	Top distributed N-S wire	0.049	6.5	0	1.25
	Bottom distributed N-S wire	0.049	6.5	0	-1.25
	N-S strand	0.0798	6.5	0	-0.0625
L'	Bottom distributed E-W rebar	0.11	24	90	-0.8125
	Bottom distributed N-S rebar	0.11	13	0	-0.75
	E-W strand	0.0813	24	90	0.4375
	N-S strand	0.0798	6.5	0	-0.0625
M'	Bottom distributed N-S rebar	0.11	13	0	-0.75
	E-W strand	0.0813	9	90	0.4375
	N-S strand	0.0798	6.5	0	0.0625
N'	Top discrete E-W rebar	0.11	12	90	0.75
	Bottom distributed E-W rebar	0.11	12	90	-0.625
	E-W strand	0.0813	12	90	0.4375
	Bottom distributed N-S rebar	0.11	13	0	-0.75
	N-S strand	0.0798	6.5	0	0.1875
P	Top discrete E-W rebar	0.11	3	90	1
	Bottom discrete E-W rebar	0.11	12	90	-0.625
	Top discrete N-S rebar	0.11	6	0	0.5
	Top distributed N-S wire	0.049	4	0	1.25
	Bottom distributed N-S wire	0.049	4	0	-1.25
	N-S strand	0.0798	6	0	-0.0625
Q	Bottom distributed E-W rebar	0.11	24	90	-0.8125
	E-W strand	0.0813	24	90	0.6875
	N-S strand	0.0798	6	0	-0.0625
R	E-W strand	0.0813	9	90	0.6875
	N-S strand	0.0798	6	0	0.0625
S	Top discrete E-W rebar	0.11	12	90	0.75
	Bottom distributed E-W rebar	0.11	12	90	-0.75
	E-W strand	0.0813	12	90	0.6875
	Bottom discrete N-S rebar	0.11	6	0	0.375
	N-S strand	0.0798	6	0	0.1875
T	Top discrete E-W rebar	0.11	3	90	0.6875
	Bottom discrete E-W rebar	0.11	3	90	-0.875
	Bottom discrete N-S rebar	0.11	6	0	0.375
	N-S strand	0.0798	6	0	0.4375
P'	Top discrete E-W rebar	0.11	3	90	0.5625

Region of slab	Contained Structural elements	Area per bar (in^2)	Spacing (in.)	Orientation (°)	Position (in.)
	Bottom discrete E-W rebar	0.11	12	90	-0.625
	Top discrete N-S rebar	0.11	6	0	0.375
	Top distributed N-S wire	0.049	4	0	0.75
	Bottom distributed N-S wire	0.049	4	0	-1.375
	N-S strand	0.0798	6	0	-0.0625
Q'	Bottom distributed E-W rebar	0.11	24	90	-0.8125
	E-W strand	0.0813	24	90	0.6875
	N-S strand	0.0798	6	0	-0.0625
R'	E-W strand	0.0813	9	90	0.6875
	N-S strand	0.0798	6	0	0.0625
S'	Top discrete E-W rebar	0.11	12	90	0.75
	Bottom distributed E-W rebar	0.11	12	90	-0.75
	E-W strand	0.0813	12	90	0.6875
	Bottom discrete N-S rebar	0.11	6	0	0.375
	N-S strand	0.0798	6	0	0.1875
U	Top discrete E-W rebar	0.11	3	90	1
	Bottom discrete E-W rebar	0.11	12	90	-0.625
	Bottom distributed N-S rebar	0.11	20.5	0	-0.75
V	Bottom distributed E-W rebar	0.11	24	90	-0.75
	E-W strand	0.0813	24	90	0.4375
	Bottom distributed N-S rebar	0.11	20.5	0	-0.75
W	E-W strand	0.0813	9	90	0.4375
	Bottom distributed N-S rebar	0.11	20.5	0	-0.75
X	Bottom distributed E-W rebar	0.11	12	90	-0.625
	E-W strand	0.0813	12	90	0.4375
	Bottom distributed N-S rebar	0.11	20.5	0	-0.75
	Center N-S shear-friction rebar	0.11	20.5	0	-0.1875
Y	Center N-S shear-friction rebar	0.11	20.5	0	-0.1875
U'	Top discrete E-W rebar	0.11	3	90	0.5625
	Bottom discrete E-W rebar	0.11	12	90	-0.625
	Bottom distributed N-S rebar	0.11	20.5	0	-0.75
V'	Bottom distributed E-W rebar	0.11	24	90	-0.75
	E-W strand	0.0813	24	90	0.4375
	Bottom distributed N-S rebar	0.11	20.5	0	-0.75
W'	E-W strand	0.0813	9	90	0.4375
	Bottom distributed N-S rebar	0.11	20.5	0	-0.75
X'	Bottom distributed E-W rebar	0.11	12	90	-0.625
	E-W strand	0.0813	12	90	0.4375
	Bottom distributed N-S rebar	0.11	20.5	0	-0.75

Region of slab	Contained Structural elements	Area per bar (in^2)	Spacing (in.)	Orientation (°)	Position (in.)
	Center N-S shear-friction rebar	0.11	20.5	0	-0.1875
Z0	Top discrete E-W rebar	0.11	2.4	90	1.25
	Top discrete N-S rebar	0.11	3.125	0	1
	Bottom discrete E-W rebar	0.11	2.4	90	-0.75
	Bottom discrete N-S rebar	0.11	3.125	0	-1
Z1	Bottom distributed E-W rebar	0.11	24	90	-0.8125
	E-W strand	0.0813	24	90	0.1875
Z2	E-W strand	0.0813	9	90	0.1875
Z3	Bottom distributed E-W rebar	0.11	12	90	-0.8125
	E-W strand	0.0813	12	90	0.1875
	Center N-S shear-friction rebar	0.11	12.5	0	-0.1875
Z4	Center N-S shear-friction rebar	0.11	12.5	0	-0.1875
Z0'	Top discrete E-W rebar	0.11	2.4	90	1.25
	Top discrete N-S rebar	0.11	3.125	0	1
	Bottom discrete E-W rebar	0.11	2.4	90	-0.75
	Bottom discrete N-S rebar	0.11	3.125	0	-1
Z1'	Bottom distributed E-W rebar	0.11	24	90	-0.875
	E-W strand	0.0813	24	90	0.1875
Z2'	E-W strand	0.0813	9	90	0.1875
Z3'	Bottom distributed E-W rebar	0.11	12	90	-0.6875
	E-W strand	0.0813	12	90	0.1875
	Center N-S shear-friction rebar	0.11	12.5	0	-0.1875

Table 5-6 Initial force, initial stresses, applied temperature and thermal expansion coefficient in the longitudinal and transverse strands

Types of strands	Assigned region	Initial force (kip)	Initial stress (ksi)	Applied temperature (R)	Thermal expansion coefficient (in/(in▪K))
Distributed longitudinal strands (E-W)	B'-Z1'	7.6	93	-480	6.7×10^{-6}
	B-Z1	7.2	88	-454	
	C'-Z2'	7.0	85	-442	
	C-Z2	5.4	67	-344	
	D'-Z3'	6.1	75	-385	
	D-Z3	5.2	64	-330	
Banded transverse strands (N-E)	K-K' P-P'	9.5*	117	-385**	1.1×10^{-5}

* The initial force is selected as the average value of those in the four banded strands.
** The temperature field in banded strands is equal to that in D'-Z_3' (closest to the wall)

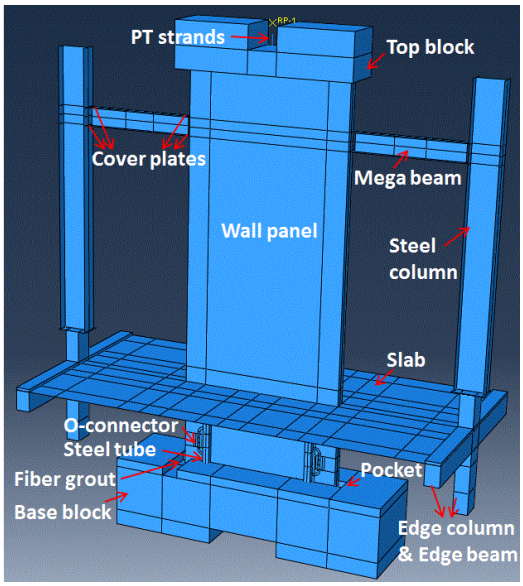

Fig. 5-1 Overview of the model of PFS1

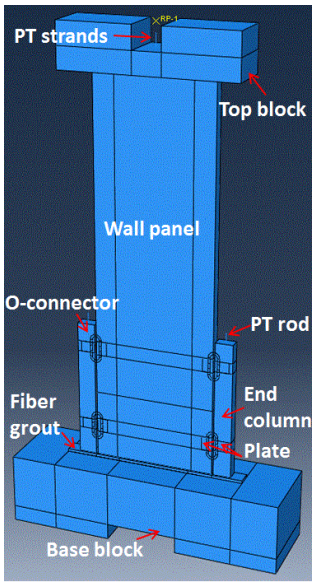

Fig. 5-2 Overview of PreWEC model in PFS2

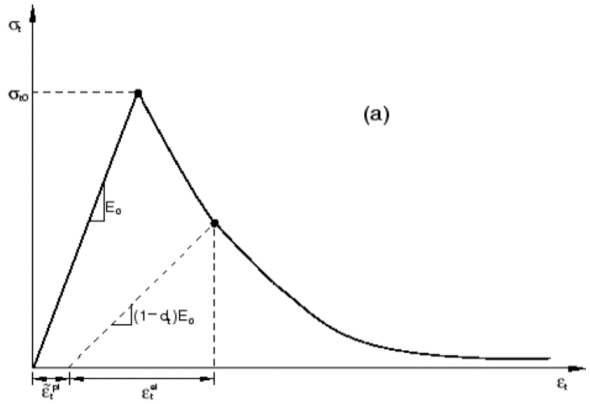

Fig. 5-3 Stress-strain response of the tension branch (Dassault 2011)

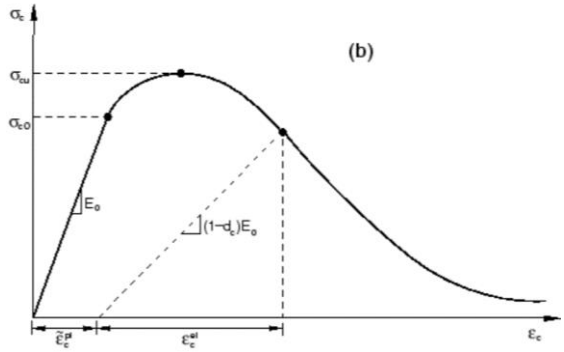

Fig. 5-4 Stress-strain response of the compression branch (Dassault 2011)

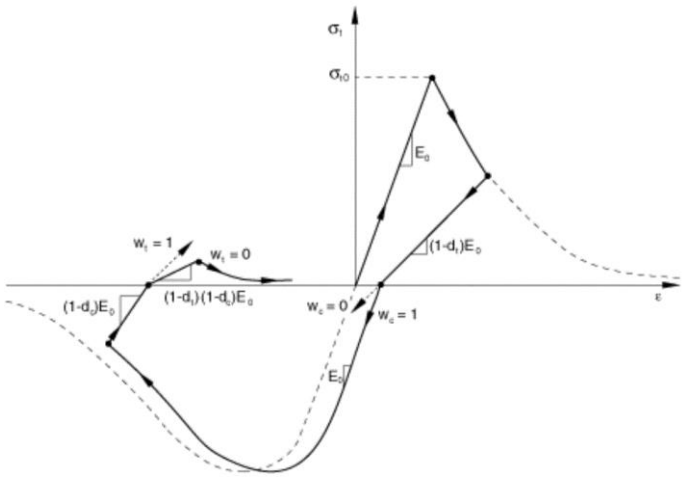

Fig. 5-5 Uniaxial stress-strain cyclic response using $w_t = 0$ and $w_c = 1$ (Dassault 2011)

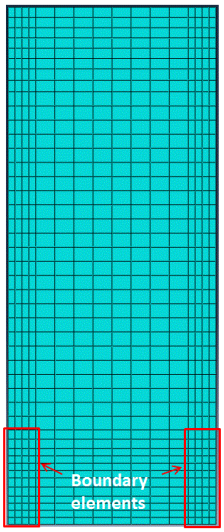

Fig. 5-6 Meshed wall panel in the model

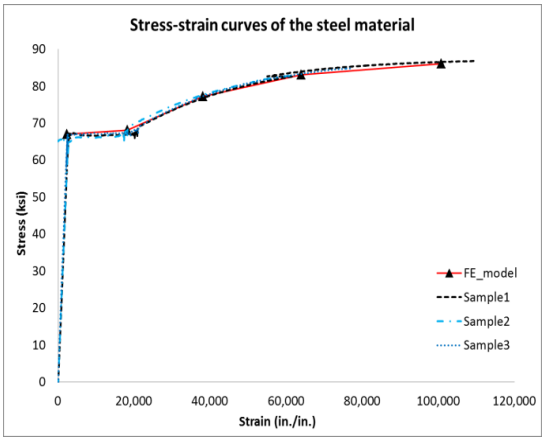

Fig. 5-7 Stress-strain responses of #3 Rebar

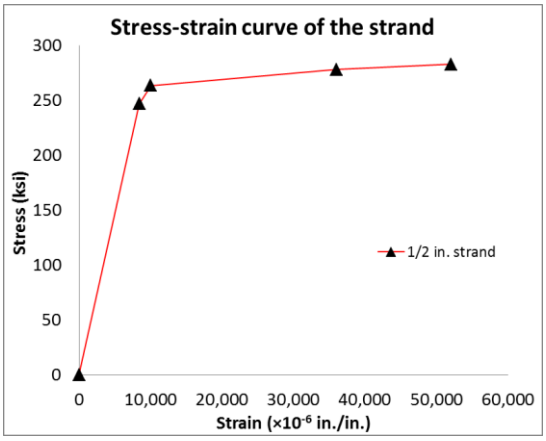

Fig. 5-8 Stress-strain responses of strands

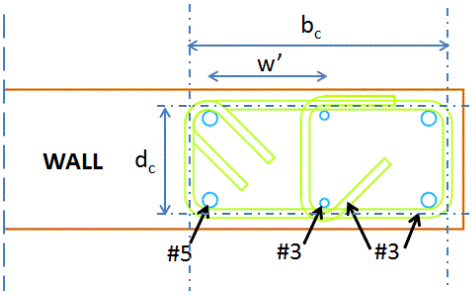

Fig. 5-9 A plan view of the wall corners

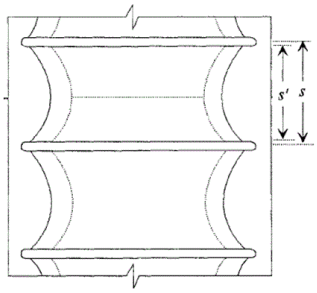

Fig. 5-10 An elevation view of the wall corners

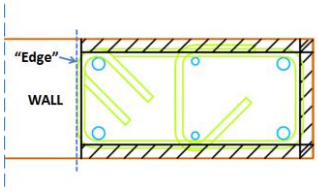

(a) Wall corners

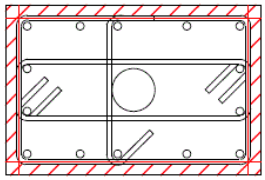

(b) Edge column bases

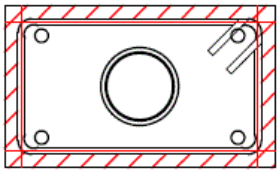

(c) End column bases

Fig. 5-11 Spalled concrete cover regions (hatched)

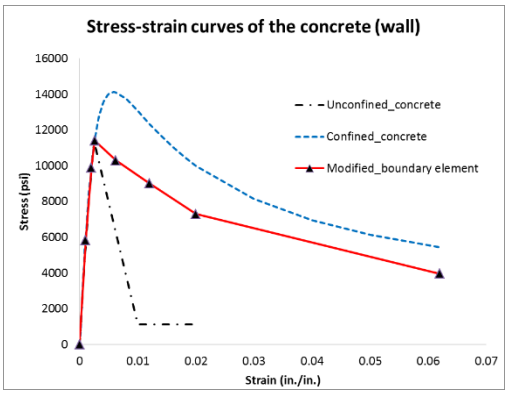

Fig. 5-12 Stress-strain response of the concrete in the wall of PFS1

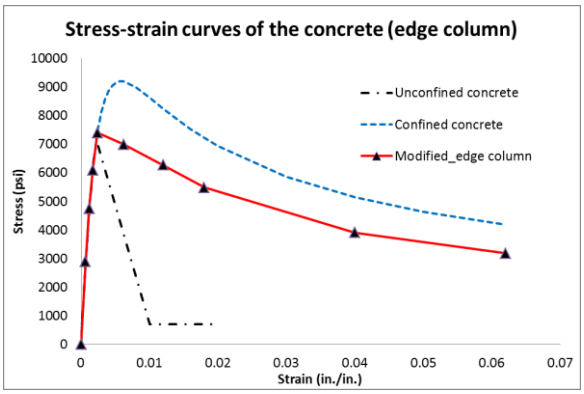

Fig. 5-13 Stress-strain response of the concrete in the edge columns of PFS1

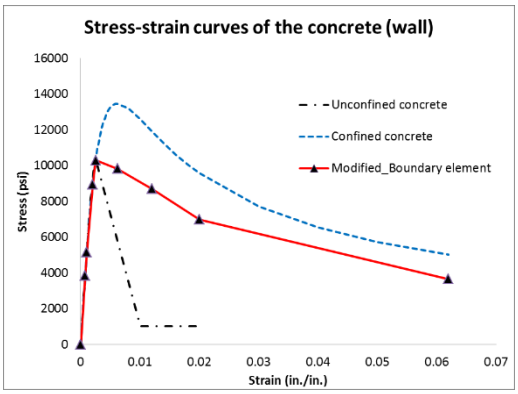

Fig. 5-14 Stress-strain response of the concrete in the wall of PFS2

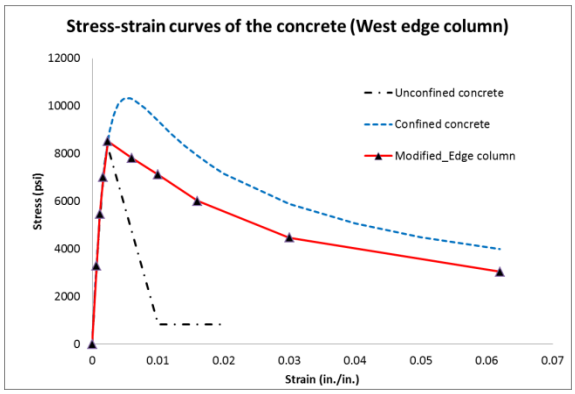

Fig. 5-15 Stress-strain response of the concrete in the west edge column of PFS2

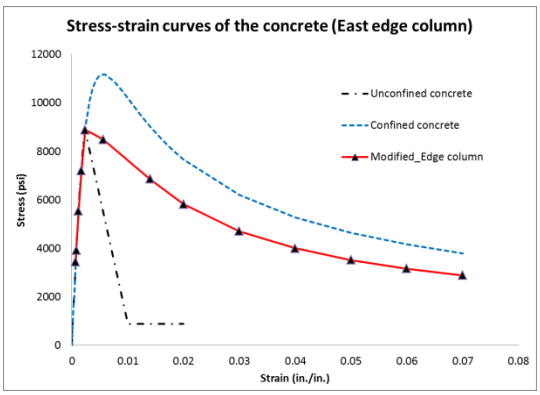

Fig. 5-16 Stress-strain response of the concrete in the east edge column of PFS2

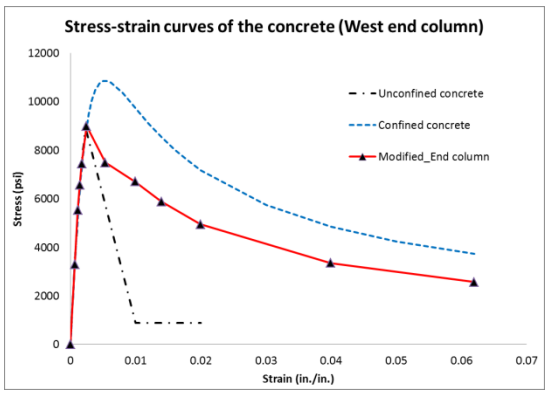

Fig. 5-17 Stress-strain response of the concrete in the west end column of PFS2

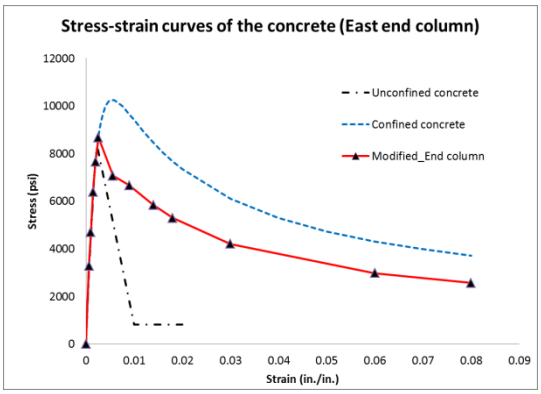

Fig. 5-18 Stress-strain response of the concrete in the east end column of PFS2

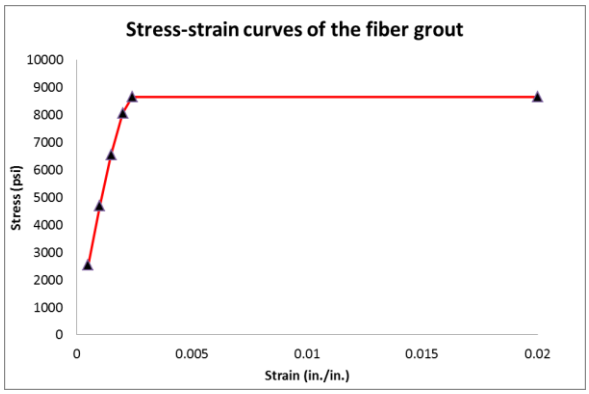

Fig. 5-19 Stress-strain response of the fiber grout material

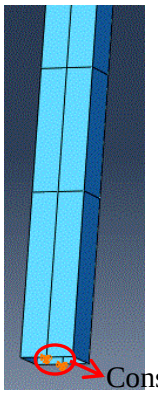

Fig. 5-20 Pin connection at the base of the side column made of a steel tube

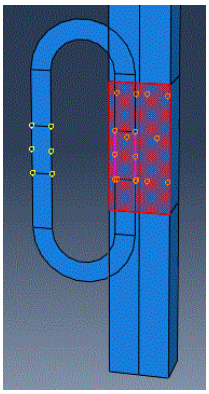

Fig. 5-21 Tie connection between an O-connector and a side column

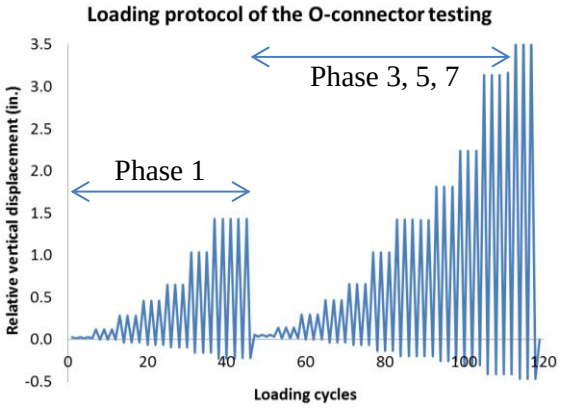

Fig. 5-22 Loading protocols for the component test for the O-connectors in the MAST tests

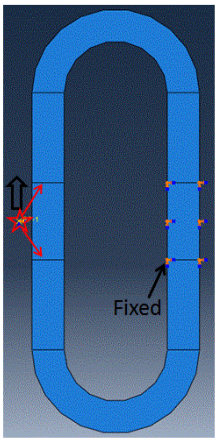

Fig. 5-23 FE modeling of an O-connector

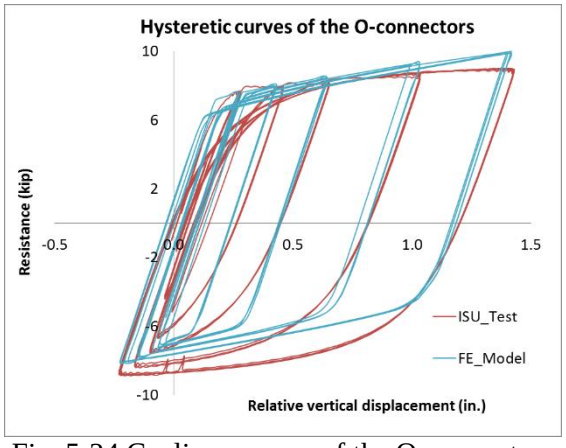

Fig. 5-24 Cyclic response of the O-connectors in Phase 1

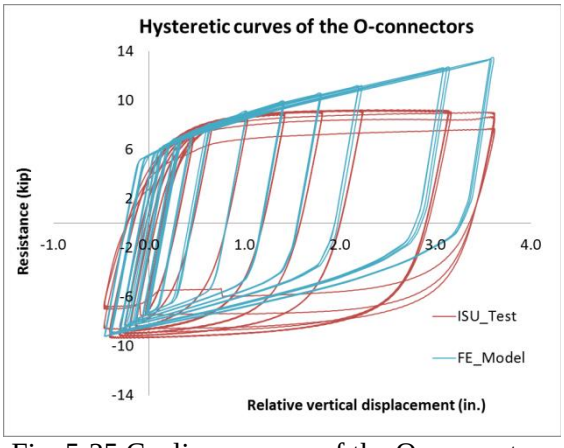

Fig. 5-25 Cyclic response of the O-connectors in Ph3, 5&7

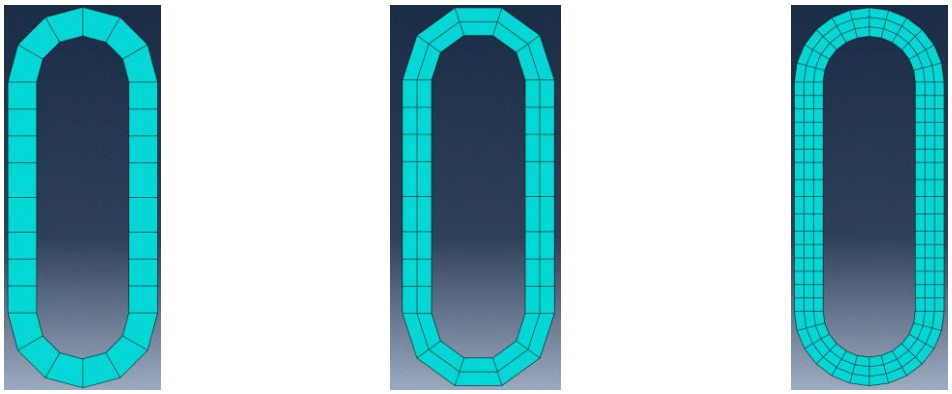

(a) Coarse meshed (b) Moderate meshed (c) Fine meshed

Fig. 5-26 Three models of O-connectors with different mesh densities

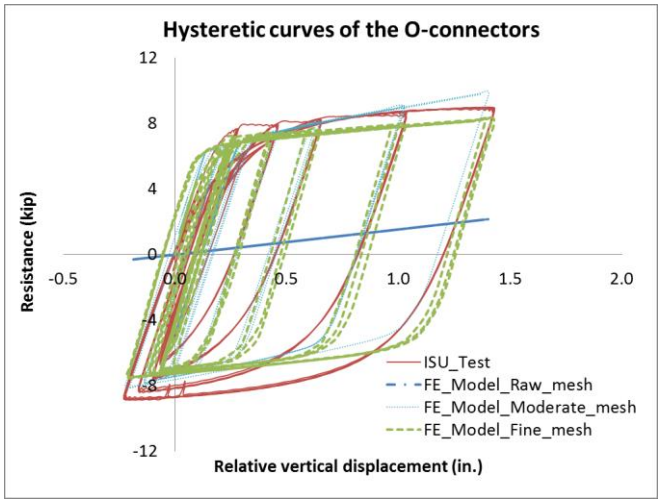

Fig. 5-27 Comparison of the analysis results from the three models with the test results

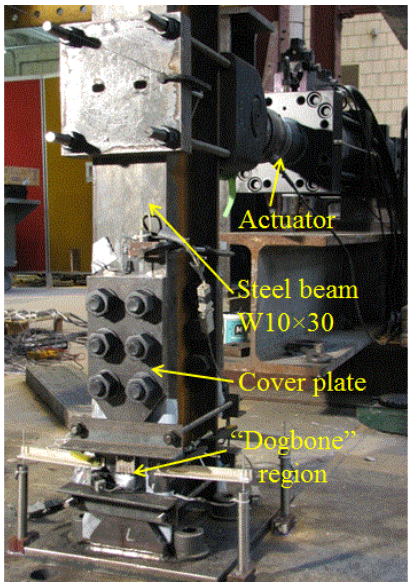

Fig. 5-28 Test setup of the component test for mega beam connections

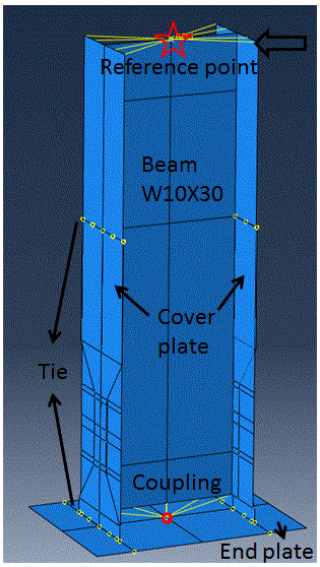

Fig. 5-29 A numerical model for the component test for mega beam connections

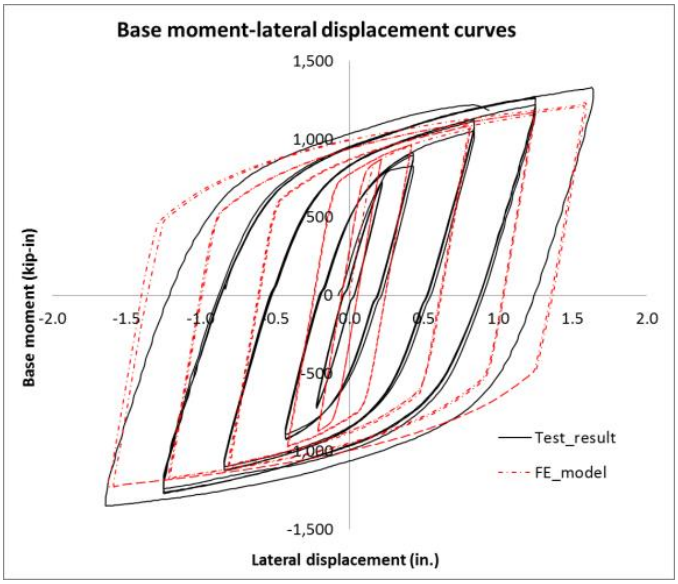

Fig. 5-30 Comparison of the simulation result and the test result for mega beams

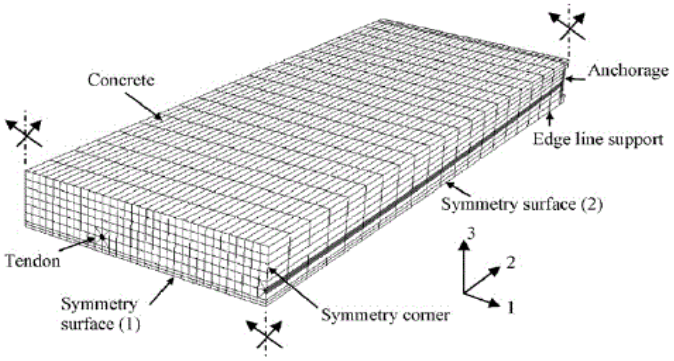

Fig. 5-31 A FE model of unbonded PT slabs with contact elements (Ellobody and Bailey 2008)

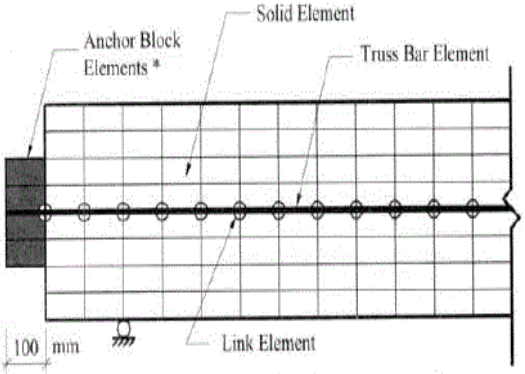

Fig. 5-32 A FE model of unbonded PT slabs with link elements (Vecchio et al. 2006)

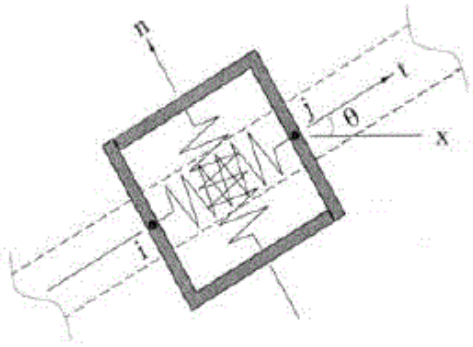

Fig. 5-33 Details of a link element (Vecchio et al. 2006)

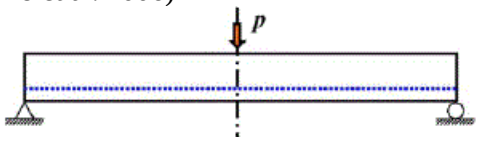

(a) A simply supported unbonded PT beam with a center load

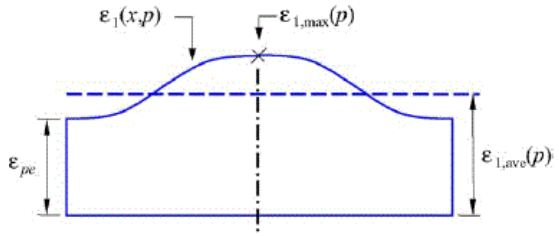

(b) Strain distribution in the strands along the length of the beam

Fig. 5-34 An example for the unique technique "adjusting stress-strain responses of PT strands" (Kwak and Kim 2006)

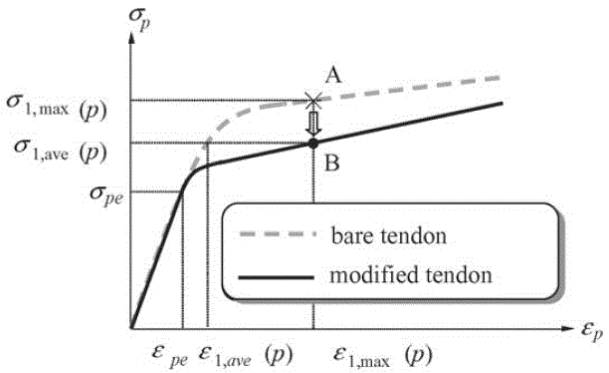

Fig. 5-35 Stress-strain responses of a bare tendon and associated modified responses (Kwak and Kim 2006)

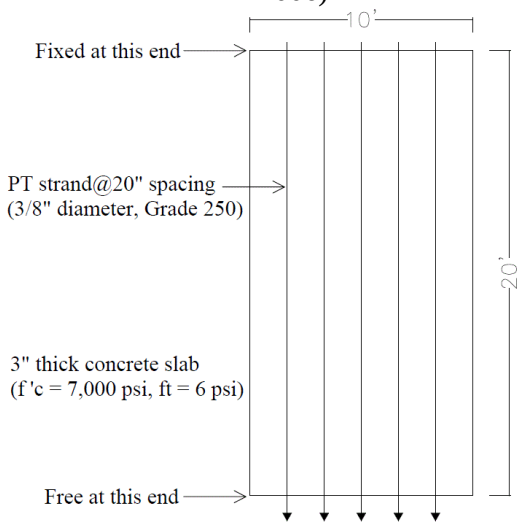

(a) Plan view of the floor slab

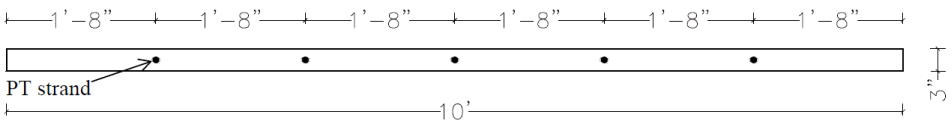

(b) Elevation view of the floor slab

Fig. 5-36 Design of a cantilever unbonded PT slab

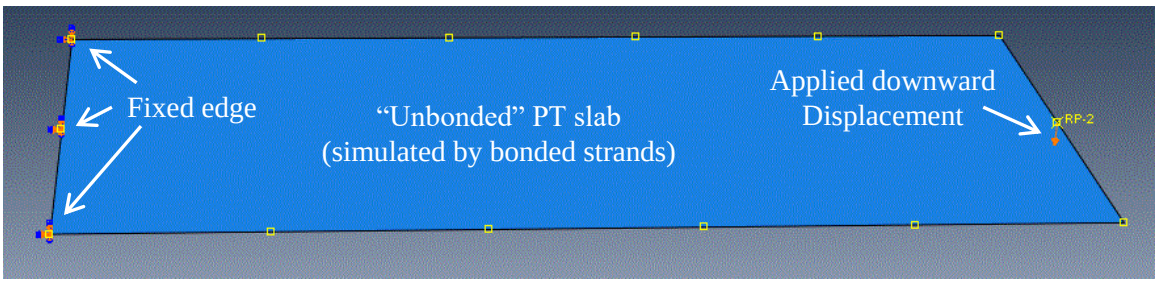

Fig. 5-37 Model of the cantilever unbonded PT slab (plan view)

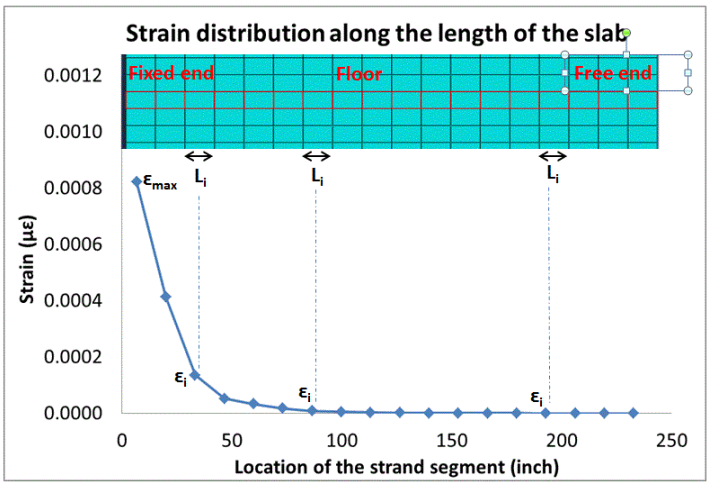

Fig. 5-38 Strain distribution in the strand along the length of the floor at 5 in. vertical deformation

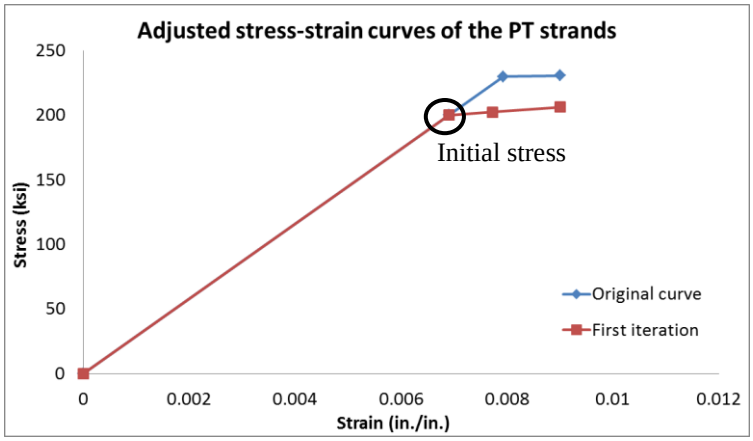

Fig. 5-39 Original stress-strain curve of the PT strand and the adjusted curve after the first run

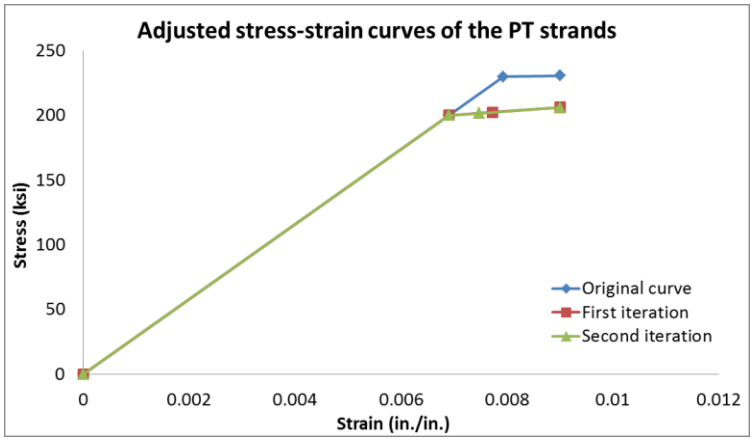

Fig. 5-40 Original stress-strain curve of the PT strand and the adjusted curves after the first and the second run

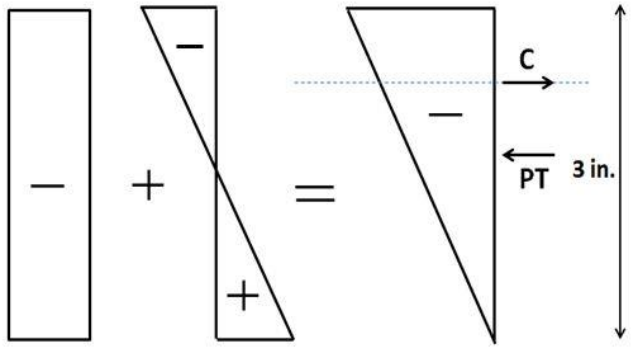

Fig. 5-41 Strain distribution along the cross section of the slab

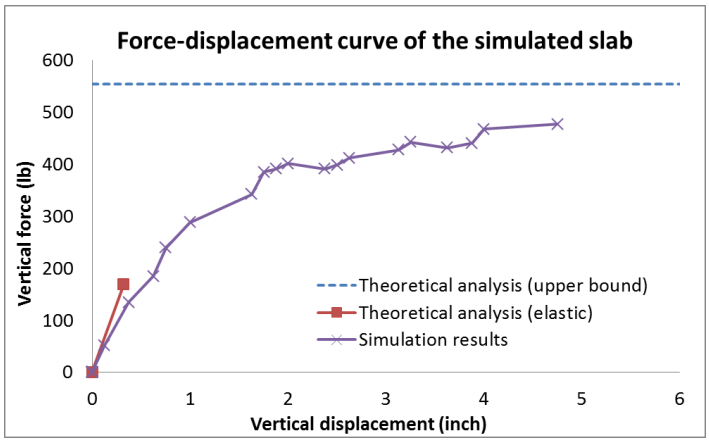

Fig. 5-42 Comparison of the simulation results and theoretical analysis

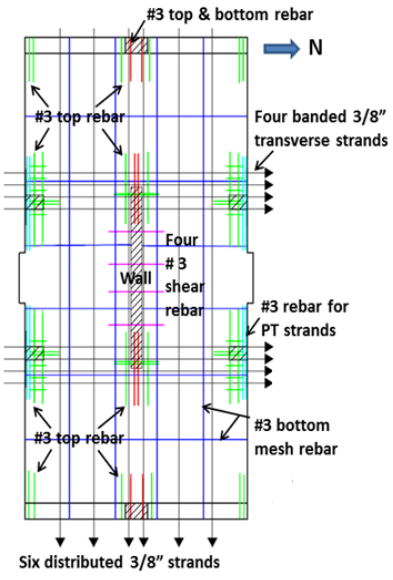

Fig. 5-43 Plan view of the unbonded PT slab

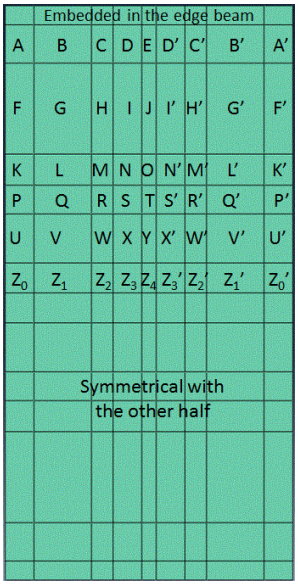

Fig. 5-44 Divided regions in the slab model

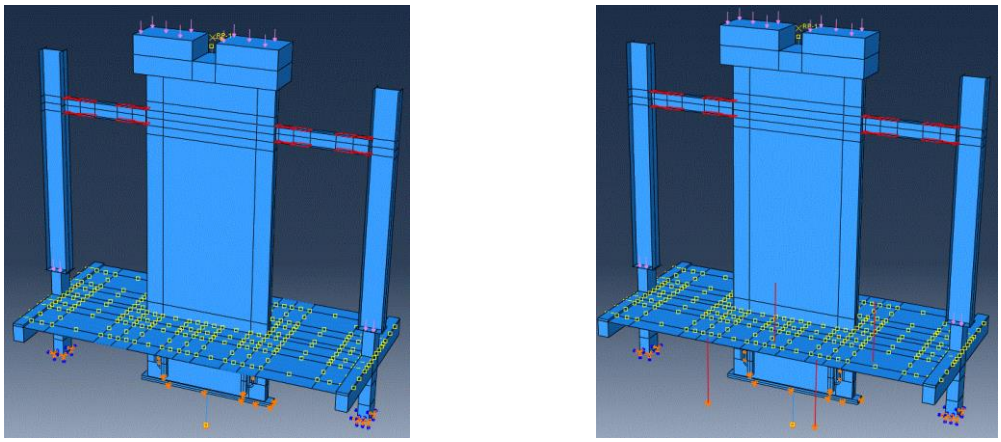

(a) Model-A PFS1 (Without props) (b) Model-A PFS1 (With props)

Fig. 5-45 Numerical models of PFS1

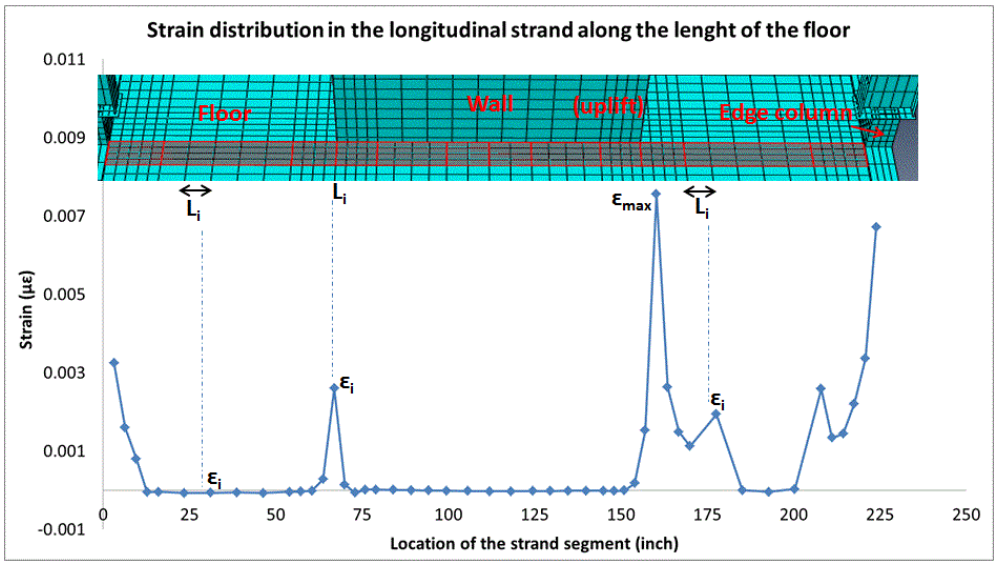

Fig. 5-46 Strain distribution in the longitudinal strand that was closest to the wall at 2% drift

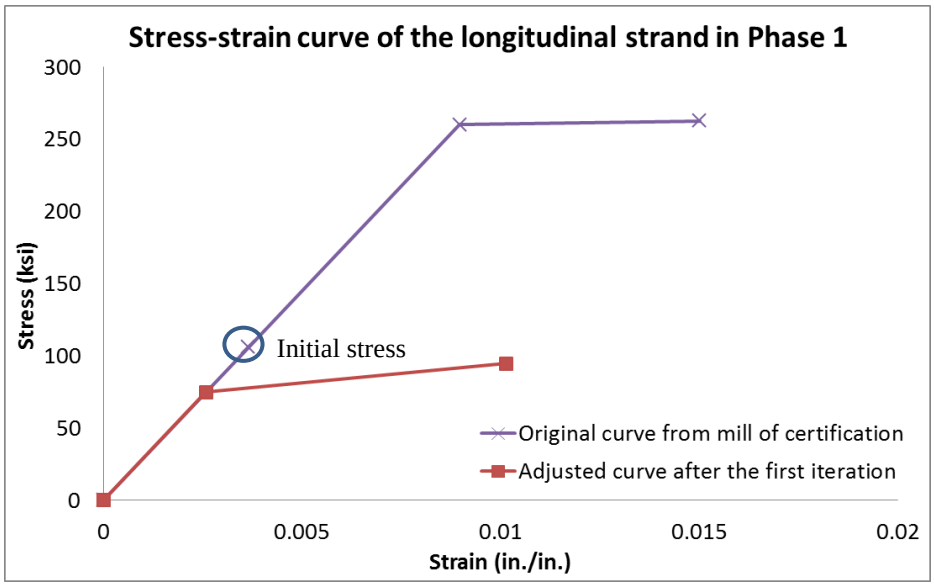

Fig. 5-47 Original stress-strain curve of the longitudinal PT strand and the adjusted curve after the first run (Phase 1)

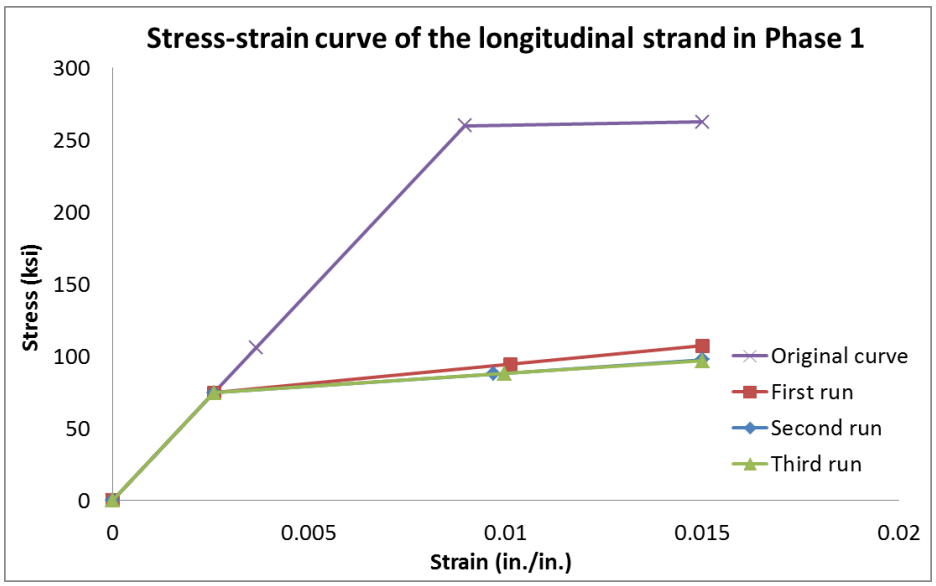

Fig. 5-48 Original stress-strain curve of the longitudinal PT strand and the adjusted curves after the first, second and third run (Phase 1)

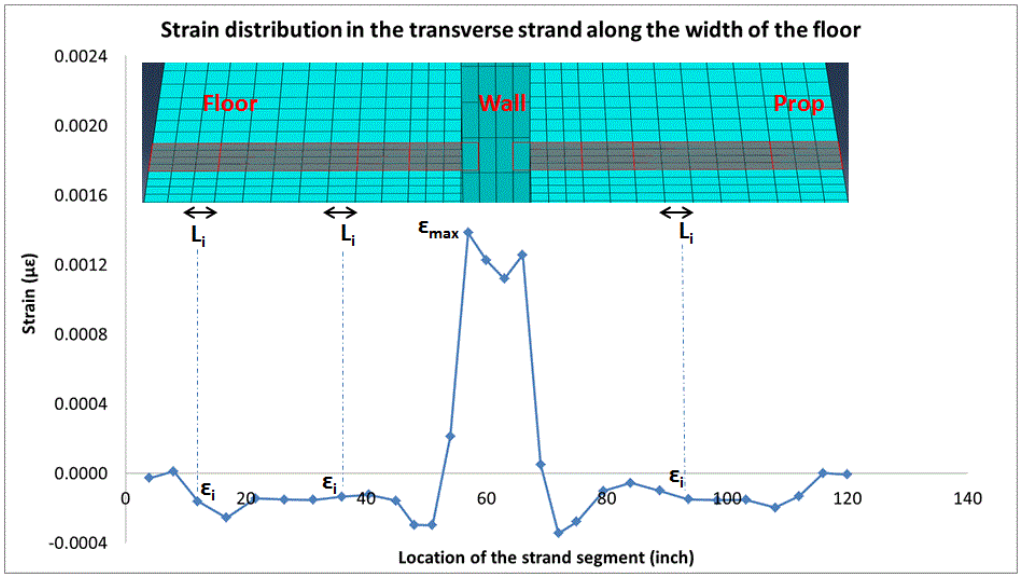

Fig. 5-49 Strain distribution in the transverse strand at 2% drift (Phase 1)

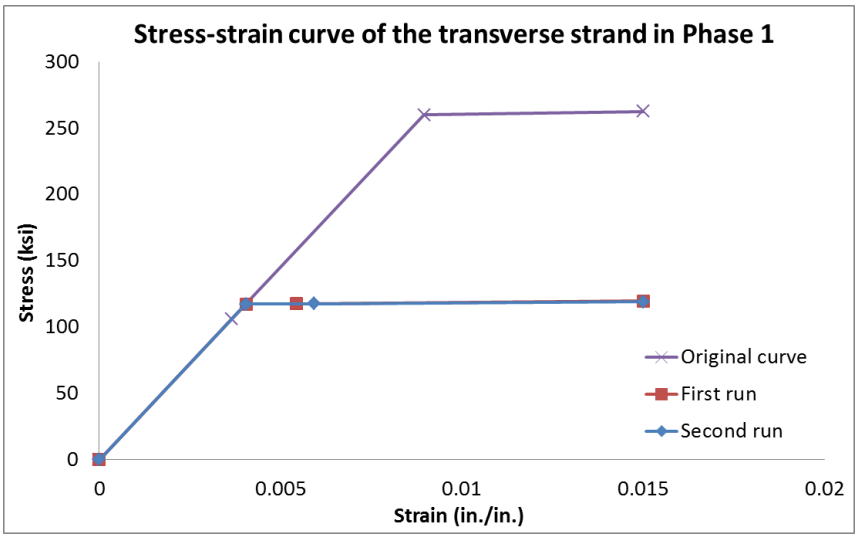

Fig. 5-50 Original stress-strain curve of the transverse PT strand and the adjusted curves after the first and second run (Phase 1)

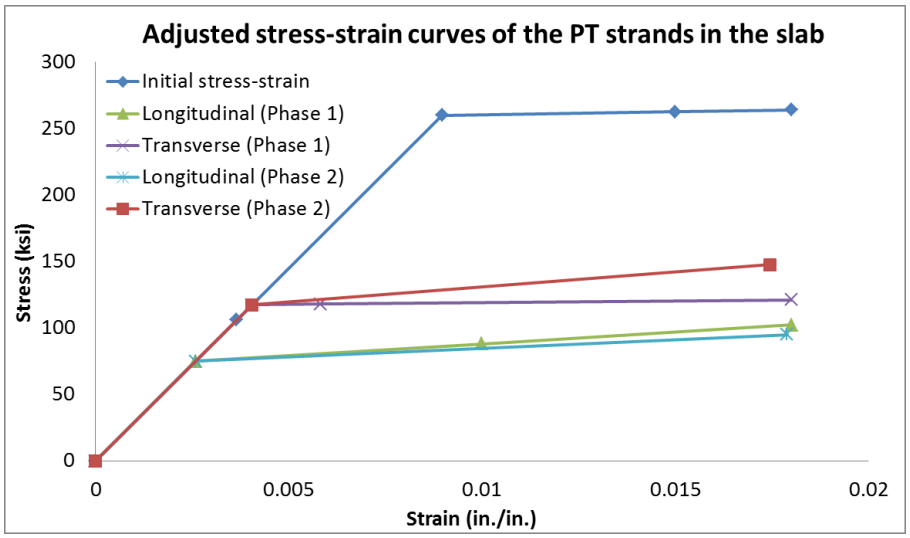

Fig. 5-51 Original stress-strain curve of the PT strands and the adjusted curves for the models

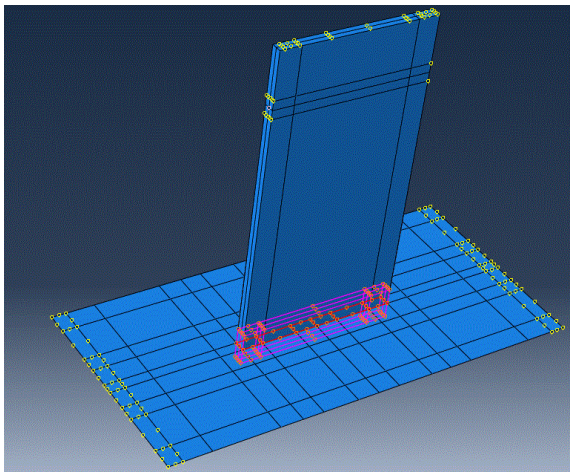
Fig. 5-52 Simulation of the rigid wall-slab connection

CHAPTER 6. Test Observations and Data Analysis for PFS1

This chapter describes the test observations and data analysis for PFS1. The numerical model described in Chapter 5 ("Model-A PFS1" without or with props) is also validated in the chapter. Section 6.1 describes the overall behavior of PFS1 in the four phases of testing. Section 6.2 through Section 6.6 describe the behavior of different structural components: rocking wall, O-connectors, unbonded PT floor, edge columns, edge beams, steel mega beams and steel columns. In each section, the damage observed in the structural component is described first, followed by the data analysis of the test and the associated results from the numerical models. Section 6.7 summarizes the conclusions from the test of PFS1.

6.1 Overall behavior

The overall behavior of PFS1 in the four phases of testing is discussed in this section, including strength, residual drift, energy dissipation capacity and base shear resistance.

6.1.1 Strength

As described in Section 4.5.1, four phases of testing were conducted on PFS1. PFS1 was under in-plane loading in the first three phases and it was under biaxial loading in the fourth phase. Props that simulated the constraint from parallel structural systems were attached to the floor after the completion of Phase 1. Severe local damage occurred to the floor slab at 3% drift in Phase 2. To continue the in-plane testing, the props were detached from the floor in Phase 3 (4% and 5% drifts). The constant axial load in the wall was removed for safety consideration in Phase 4.

Fig. 6-1 through Fig. 6-3 show the force-displacement curves of PFS1 in the first three phases of testing, respectively. The force-displacement curves measured in the four phases are superimposed in Fig. 6-4 for comparison. The flag-shaped curves demonstrated the excellent energy dissipation and reasonable self-centering behavior of PFS1.

As shown in Fig. 6-1 through Fig. 6-4, unsymmetrical behavior was observed in all phases of testing. The resistance of PFS1 was smaller when it was loaded in the negative direction (to the west). The unsymmetrical behavior observed in the in-plane tests was attributed to the behavior of the east and the west mega beams. As shown in Fig. 6-5, the moment, shear and axial load in the east and the west mega beam provided resistance to the wall rocking and contributed to the strength of the wall. When PFS1 was loaded in the positive direction (to the east), the west mega beam was subjected to a larger deformation demand due to the uplift of the west wall edge compared to the east mega beam. It was expected that the west mega beam would provide larger resistance than the east mega beam, including a larger moment resistance (M_W) and a larger moment generated by the shear force (V_W). Therefore, the resistance provided by the west mega beam was one of the main contributing factors to the strength of PFS1 when it was loaded in the positive direction. On the other hand, the resistance provided by the east mega beam was one of the main contributing factors to the strength when PFS1 was loaded in the negative direction (to the west).

As mentioned in Section 3.4.11, when installing the mega beams, the west mega beam was tightly fitted between the wall and the west steel column. It was believed that the resisting moment in the west mega beam was developed immediately when the wall was loaded in the positive direction. The behavior of the west mega beam was close to the behavior predicted from the component test. On the other hand, the east mega beam was installed between the wall and the east steel column without difficulty. It was found that the readings of the strain gages on the cover plates of the east mega beam were much smaller than expected. A lower resisting moment on the wall was generated that resulted in the lower strength of PFS1 when it was loaded in the negative direction. Numerical simulation was also conducted to investigate this unsymmetrical behavior that is described at the end of this section.

After discussing the unsymmetrical behavior observed in the test, a phase-by-phase description of the strength of PFS1 is given in the following.

The strength of PFS1 kept increasing until 2% drift in Phase 1. A small drop of the strength occurred when PFS1 was loaded towards 2.5% drift, as identified by point A in

Fig. 6-4. It was believed that it was caused by fracture of one PT strand wire in the wall at the bottom wedge plate. Buckling of the mega beam cover plates was observed at 2.5% drift in Phase 1. Some of them fractured in Phase 2 that caused the drops identified by points B and C in Fig. 6-4. The O-connectors started to fracture when PFS1 was loaded to 4% drift in Phase 3. It further reduced the strength, as identified by points D and E in Fig. 6-4. The strength of PFS1 dropped to 79% of the positive peak and 85% of the negative peak at 5% drift in Phase 3. The in-plane test was terminated at that point.

Because the axial load would generate an overturning moment in the wall in the out-of-plane direction due to P-delta effect, it was not applied to the wall due to safety consideration in Phase 4 when the biaxial loading protocol was applied. The in-plane strength of PFS1 at 4% drift in Phase 4 was only 49% of that in Phase 3. Moreover, the residual drift increased from 0.41% at the end of Phase 3 to 0.87% at the end of Phase 4. It was believed to be mainly caused by the elimination of the axial load that decreased both the strength and the self-centering capability of the wall. To be shown in Section 6.2.2, the PT force at the positive peak of 4% drift in Phase 4 was 188 kips. If the axial load 128 kips had been applied to PFS1, the resisting moment that it would generate would be 68% of that generated by the PT force (128/188×100%=68%), which would have greatly increased the resisting moment of PFS1. Moreover, the residual PT force was greatly decreased to only 59 kips when the external load applied to PFS1 was reduced to zero from the positive peak of 4% drift. If the axial load of 128 kips had been applied, the self-centering moment that it would have generated would have been about twice that generated by the PT force (128/59≈2.2). It demonstrated some advantages of using rigid wall-floor connections instead of using special vertical isolation wall-floor connections that are not able to transfer the gravity load from the floor into the wall. However, it was noteworthy that the gravity load sustained by the wall might become detrimental in the out-of-plane direction due to the P-delta effect. As shown in Fig. 6-4, the strength of PFS1 in the out-of-plane direction was much smaller than that in the in-plane direction. It was due to the small distance between the strands and the wall edges in the out-of-plane direction that provided a trivial moment arm for the PT force. Because

the axial load was not applied, the actual out-of-plane behavior of the wall was not captured in the test.

After describing the strength of PFS1 measured during the test, results from the numerical simulation are discussed below. Using the numerical techniques described in Chapter 5, three numerical models shown in Fig. 6-6, "Model-A PFS1" (without or with props) for PFS1 and "Model-B Isolated PreWEC" for the isolated PreWEC tested in PFS1, are established. The numerical model of the isolated PreWEC was developed using the same model of PFS1 ("Model-A PFS1"), but with the surrounding structures (Floor, edge columns etc.) excluded.

Fig. 6-7 shows a comparison of the envelope of the force-displacement curves of PFS1 recorded in the test with the pushover curves of PFS1 in Phase 1 (without props) and the tested isolated PreWEC from the numerical models. In Fig. 6-7, "Test results_Positive direction" represents the envelope curves when PFS1 was loaded in the positive direction. "Simulation_Model-A PFS1" and "Simulation_Model-B Isolated PreWEC" represent the pushover curves obtained from the models of PFS1 and the tested isolated PreWEC, respectively.

As shown in the figure, the pushover curve from the model of PFS1 matches well with the envelope curve of PFS1 when it was loaded in the positive direction (to the east), demonstrating the reliability of "Model-A PFS1" described in Chapter 5. Secondly, the strength of PFS1 is significantly higher than that of the tested isolated rocking-wall system. For example, the strengths of PFS1 when it was loaded in the positive and the negative direction were about 57% and 36% larger than that of the isolated rocking-wall system (Model B) at 2% drift. It was believed that the increase was generated due to the interaction between the wall and the surrounding structures (i.e. floor, edge columns and mega beams) that is discussed in detail in Section 6.4 through Section 6.6.

As discussed previously, unsymmetrical behavior of the specimen was observed during the test. It was believed that the resistance generated by the east mega beam connected to the wall did not develop as expected. To validate this assumption, Model-C was built, which represented a slight modification of Model-A, as shown in Fig. 6-8. The only change made in Model-C from Model-A was that the two cover plates of the east mega

beam connected to the wall were removed. Fig. 6-9 shows a comparison of the envelopes of the force-displacement curves of PFS1 in both positive and negative loading directions with the pushover curve of Model-C. As shown in the figure, Model-C provides a reasonable prediction of the stiffness and strength of PFS1 when it was loaded in the negative direction (to the west), justifying the aforementioned explanation of the unsymmetrical behavior. The cause of the unsymmetrical behavior is further validated in Section 6.6 when the test data of the mega beams are analyzed in detail.

6.1.2 Residual Drift and Energy Dissipation Capacity

Fig. 6-10 shows the residual displacement/drift recorded when the external lateral load applied to PFS1 was reduced to zero (named "zero load" position) at the end of each drift level. As shown in the figure, the residual drifts kept increasing in Phase 1 to the peak value of 0.58% recorded after PFS1 was loaded to 2.5% drift. The maximum residual drift recorded in Phase 2 was 0.41% recorded after the 2.5% drift cycles. The residual drift dropped to 0.33% after the 3% drift cycles, which might be attributed to the damage developed in the cover plates of the mega beams. The maximum residual drift in Phase 3 was 0.76% recorded after the 4% drift cycles. The residual drift dropped to 0.41% at the end of Phase 3, which might have been caused by the complete fracture of some cover plates and O-connectors. The residual drift increased from 0.41% at the end of Phase 3 to 0.87% at the end of Phase 4 when PFS1 was under biaxial loading. It was believed that the compromised self-centering capability of the wall was mainly caused by the removal of the axial load in the wall in Phase 4, as discussed in Section 6.1.1.

The residual drifts of PFS1 with rigid wall-floor connections were noticeable in the test, indicating that the self-centering capability of the PreWEC system might be compromised by the irreversible plastic deformations of the surrounding structures. In the following, the force-displacement behavior of the isolated PreWEC system obtained from the numerical simulation is presented and compared to PFS1.

Fig. 6-11 shows a comparison of the force-displacement curve of PFS1 recorded when it first reached the 2% design drift in Phase 1 with that of the isolated PreWEC system obtained from "Model-B." As shown in the figure, the isolated PreWEC system in the

numerical model realizes complete self-centering while PFS1 has a residual drift of 0.44% at the end of the 2% cycle, indicating that the plastic deformation incurred in the surrounding structures (i.e., mega beams, floor slab and edge columns) compromised the self-centering capability of the PreWEC system. However, the residual drift experienced by PFS1 would be deemed small compared with regular shear wall structures. Moreover, it was reported by other researchers that the residual drift of a structure at the end of a seismic excitation would typically be smaller than the maximum residual drift in the hysteresis loops obtained under quasi-static loading. This phenomenon was referred to as "shake-down" effect (Kurama 2002, Henry 2011). The residual drifts of PFS1 shown in Fig. 6-11 might become smaller following the excitations during an earthquake. Therefore, the test specimen PFS1 that contained rigid wall-floor connections through CIP construction was believed to have exhibited reasonable self-centering performance.

Under quasi-static loading, the energy dissipating capacity of a structural element can generally be represented by the area enclosed by its hysteresis loop. As shown in Fig. 6-11, the hysteresis loop of PFS1 is more than three times larger than that obtained from the numerical model of the isolated PreWEC system for the 2% cycle, indicating that the surrounding structures provided a much greater amount of energy dissipation to the test specimen.

6.1.3 Base Shear Resistance

As shown in Fig. 6-7, the strength of PFS1 was significantly larger than that of the isolated PreWEC system obtained from the numerical model. The line "Test results_Positive direction" in the figure represents the total base shear resisted by the test unit when it was loaded in the positive direction. To isolate the base shear carried by the PreWEC system in the specimen, the shear force in the edge columns needed to be subtracted. The shear force resisted by the edge columns was estimated to be 28 kip of the total base shear at 2% design drift, deduced from the estimated moments in the edge columns obtained by using multiple pairs of strain gages attached to the longitudinal reinforcement along the column height. The base shear of the tested PreWEC system was

thus approximately 110 of the total 138 kip base shear at 2% design drift, approximately 26% larger than that of the isolated PreWEC system in the numerical model.

Assuming the coefficient of friction was 0.5 at the interface between the wall and the fiber grout in accordance with Section 5.5.3 of ITG 5.2 and the vertical resisting forces from the mega beams and the floor slab were approximately equal and opposite on each end of the wall after they yielded, thereby not contributing to the normal force, the shear sliding resistance of the tested PreWEC system only exceeded the sustained base shear by a limited margin at 2% drift:

$$R_V = \mu(N_G + N_{PT}) = 0.5\times(128 + 170) = 149\ kip > 110\ kip \quad (6.1)$$

Where R_V = Base shear resistance, N_G = Axial load on the wall, N_{PT} = PT force recorded at 2% drift.

A string pot SP2_EW0 was mounted at the base of the wall to monitor the shear sliding of the wall. The location of the string pot is shown in Fig. 4-1. As shown in Fig. 6-12, when the wall was loaded to the west, the uplift at the east end of the wall had a non-negligible impact on the readings of SP2_EW0. When the wall was loaded to the east, because there was little penetration at the east end of the wall in that loading direction, the impact on the readings of SP2_EW0 was negligible. Therefore, only the readings of SP2_EW0 recorded at positive peaks when PFS1 was loaded to the east were used for analysis. Fig. 6-13 shows the readings of SP2_EW0 at the positive peak of different drift levels. As shown in the figure, the horizontal slip of the wall was negligible. For example, the maximum reading of SP2_EW0 recorded in the test was only 0.08 in. at 5% drift in Phase 3. Shear sliding failure was not observed to occur to the wall during the test.

If shear sliding of the wall had occurred in the test, the PT strands might have been distorted and fractured, which could cause severe consequences. Therefore, it is suggested that the wall-floor interaction be considered when deducing the base shear demand on the PreWEC system.

6.2 Behavior of Rocking Wall

In this section, damage to the wall and the fiber grout layer beneath the wall is described first. After describing the observed damage, a detailed description of the behavior of the wall is given, including PT forces, neutral axis depth, strain distribution, lateral deformed shape and relative wall-floor deformation.

6.2.1 Damage to the Wall and the Fiber Grout

At 0.25% drift in Phase 1, it was observed that the over-poured fiber grout that originally adhered to the wall surface detached. It was believed that the wall had been uplifted at this drift level. A vertical crack was observed in the fiber grout layer beneath the west corner of the wall at -0.25% drift, as shown in Fig. 6-14. A second vertical crack near the first one formed in the fiber grout layer at 0.75% drift.

No damage occurred to the wall until 1% drift, when horizontal cracks located above the attached O-connectors of the wall were observed on the east surface of the wall, as shown in Fig. 6-15. It was believed that when the wall rocked, the O-connectors attached to the uplifted side of the wall would deform and resist the uplift generating tensile stresses in the wall that caused the cracks.

Minor spalling of concrete cover occurred at the wall corners at 1.5% drift in Phase 1. Other than that, the majority of the wall remained intact during Phase 1. On the other hand, cracks in the fiber grout layer further developed at larger drifts in Phase 1, as shown in Fig. 6-16.

The condition of the wall remained mostly unchanged in Phase 2, even though the out-of-plane restraint to the wall from the floor became larger after the props were attached to the floor. At the end of Phase 3, the west wall corner (where a blockout opening existed) in the base block was only lightly damaged, but some damage to the fiber grout beneath the wall was observed, as shown in Fig. 6-17. It was noteworthy that because the fiber grout was confined by the pocket in the base block, the damage was not severe and the grout was deemed reusable after the test. On the other hand, minor spalling of the concrete cover occurred to the east wall corner at the end of Phase 3, as shown in Fig.

6-18. The different performance observed in the west and the east wall corner was believed to have been caused by the following two reasons.

First, to be discussed in Section 6.6, the cover plates of the east and the west mega beam that had yielded in Phase 1 might have started to strain harden in Phase 3. As mentioned in Section 6.1.1, larger strains were developed in the cover plates of the west mega beam when PFS1 was loaded to the east, compared with those in the east mega beam when PFS1 was loaded to the west. Therefore, larger moments and shear forces might be generated and transferred to the wall when PFS1 was loaded to the east, compared to those transferred to the wall when PFS1 was loaded to the west. As shown in Fig. 6-5, the larger shear forces transferred to the wall (V_W) generate a larger compression force demand on the east wall corner.

Second, the confinement effect to the fiber grout beneath the west and the east wall corner was different. The fiber grout was well confined beneath the east wall corner in the pocket. On the other hand, a blockout was formed on the west side of the base block to observe the condition of the fiber grout, as shown in Fig. 6-17. The blockout decreased the confinement effect on the fiber grout, resulting in weaker grout beneath the west corner of the wall. It was believed that the weaker fiber grout was plastified and the compression force in the west wall corner spread over a larger contact area, reducing the strains developed in the west wall corner. Smaller strains were developed in the west wall corner, causing less damage compared to the east wall corner.

After completion of the test in Phase 4, it was observed that the confined concrete core in neither the west nor the east boundary element of the wall was severely damaged, as shown in Fig. 6-19 and Fig. 6-20.

As shown in Table 3-8 , the measured strength of the fiber grout was smaller than that of the concrete in the wall. Therefore, it was expected that the fiber grout would be damaged instead of the wall, which was in accordance with the test observation presented in this section.

6.2.2 PT Forces in the Wall

Fig. 6-21 shows the PT forces in the strands of the wall recorded during the first three phases of testing. The variation of the PT forces is described phase by phase in the following.

Phase 1

Residual changes in force can be observed in Fig. 6-21 as the lines cross zero drift/displacement. As shown in the figure, the residual PT forces kept increasing until 2% drift in Phase 1 (black line). Fig. 6-22(a) shows the residual gap opening along the base of the wall at the "zero displacement position" for the first cycles at different drift levels in Phase 1. It was measured by a group of five LVDTs that were installed along the wall/base block interface, as discussed in Section 4.2.1.4. The growing values associated with the different drifts indicated that the height of the wall gradually "increased." It was observed that some of the over-poured fiber grout detached from the wall surface and was trapped in the pocket underneath the wall, causing the increased residual PT forces. Validation is given below to demonstrate that the increased PT force correlated with the recorded residual gap opening. As shown in Fig. 6-22(a), the residual gap opening of the wall was about 0.05 in. after the 1% drift cycles. The increased PT force corresponding to the 0.05 in. residual gap opening can be calculated as follows:

$$\epsilon_{1\%} = \epsilon_{initial} + \frac{\Delta_{1\%}}{L_{PT}} = \frac{F_{PT\_initial}}{E_{strand} n_{strand} A_{strand}} + \frac{\Delta_{1\%}}{L_{strands}} = \frac{112.5}{29{,}100 \times 5 \times 0.152} + \frac{0.05}{280} = 5.265 \times 10^{-4} \quad (6.2)$$

$$F_{PT\_1\%} = E_{strand} \epsilon_{1\%} n_{strand} A_{strand} = 29{,}100 \times 5.265 \times 10^{-4} \times 5 \times 0.152 = 116.4\ kips \quad (6.3)$$

Where $\epsilon_{1\%}$ = Strain in the PT strands after the 1% drift cycles, $\epsilon_{initial}$ = Initial strain in the PT strands, $\Delta_{1\%}$ = Residual gap opening recorded after the 1% drift cycles, $L_{strands}$ = Total length of the PT strands, $F_{PT\_initial}$ = Initial PT force at the beginning of the test, E_{strand} = Young's modulus of the PT strands, n_{strand} = Number of strands in the wall ; A_{strand} = Cross-sectional area of each strand, in.^{2}, $F_{PT\_1\%}$ = PT force after the 1% drift cycles

The test data showed that the PT force recorded after the 1% drift cycle was 117.9 kips. It was very close to the PT force deduced based on the residual gap opening. Therefore, it can be concluded that the increased PT force was caused by the debris trapped inside the pocket.

As shown in Fig. 6-21, noticeable increases in the PT forces were observed after the 1st peak of the 1.5% drift cycles. Fig. 6-22(b) shows the LVDT readings at the peak displacement for each cycle to 1.5% drift in Phase 1. As mentioned in Section 6.2.1, spalling of the concrete cover was observed to initiate at 1.5% drift. The spalled concrete might drop into the pocket that induced the increased PT forces at the 2nd and the 3rd peak to 1.5% drift. It further validated the conclusion that the increased PT forces were attributed to the accumulated debris in the pocket beneath the wall.

One strand wire was believed to have fractured on the way to a drift of 2.5% in Phase 1, causing a drop in the PT force shown in Fig. 6-21 and in specimen strength (Point A in Fig. 6-4). The fracture might have been caused by the uneven force distribution among the strands at the bottom wedge plate.

Phase 2 and Phase 3

As shown in Fig. 6-21, yielding of the PT strands occurred when PFS1 was loaded towards 3% drift in Phase 2. After that, the residual PT force decreased gradually in Phase 2 and Phase 3 due to the residual plastic strains accumulated in the strands. The residual PT force after the 5% drift cycles was approximately 50% of the initial PT force, as shown in Fig. 6-21.

After discussing the varied PT forces in the wall during the test, the results obtained from the numerical model of PFS1 are compared with the test results in the following.

Simulation results of the wall – PT forces

Fig. 6-23 shows a comparison of the PT forces recorded at the positive peaks of different drifts with those obtained from “Model-A PFS1” (without props). In the figure, “Test results_Positive direction” represents the envelope curve of the PT forces when PFS1 was loaded in the positive direction. “Simulation_Model-A PFS1” represents the PT forces obtained from “Model-A PFS1” (without props). As shown in the figure, the simulation results show satisfactory correlation with the experimental response.

6.2.3 Neutral Axis Depth of the Wall

As mentioned in Section 6.2.2, a group of LVDTs was used to measure the gap opening across the wall/base block interface. By plotting the LVDT readings with respect to their locations along the width of the wall, the neutral axis depth of the wall could be estimated. Fig. 6-24 shows the LVDT readings recorded at the positive peaks of different drifts in Phase 1. The readings are linearly extrapolated to the west end of the wall (-45 in.) in the figure. As shown in the figure, the readings are all positive values, thus it appears that both ends of the wall are uplifted. This interpretation obviously went against the observation in the test.

As mentioned in Section 6.2.2, the debris beneath the wall resulted in non-negligible residual readings in the LVDTs across the wall/base block interface. To obtain the N.A. depth, the residual displacements recorded at the "zero displacement position" should be subtracted from the LVDT readings recorded at the peaks. Fig. 6-25 shows the processed LVDT readings at the positive peaks of different drifts in Phase 1. As shown in the figure, the N.A. depth of the wall can be directly obtained from the curves after processing the LVDT readings.

Fig. 6-26 shows the N.A. depth of the wall in the first three phases of testing. As shown in the figure, the N.A. depths at the east wall corner (when PFS1 was loading in the positive direction) are slightly smaller than those at the west wall corner (when PFS1 was loading in the negative direction) in general, but the difference is not significant.

Fig. 6-27 shows a simplified trilinear curve proposed by Aaleti (Aaleti 2011) to predict the N.A. depth of rocking walls. An assumption was established for the simplified trilinear curve: The N.A. depth of the wall remains unchanged after 0.5% drift of the wall to higher drift levels. As shown in Fig. 6-26, the assumption that the N.A. depth does not change much after 0.5% drift seems reasonable (horizontal dotted lines are drawn from 0.5% and -0.5% drift in the figure). With this assumption, the analysis of the performance of rocking-wall systems at different drift levels can be greatly simplified. A similar assumption was adopted in Section 5.6.1.2 of ITG 5.2: the distance from the extreme compression fiber to the neutral axis shall be assumed to remain constant as θ increases

from θ_{design} to θ_{max}, where θ is the rotation of the wall, θ_{design} is the rotation of the wall at the design drift, and θ_{max} is the rotation of the wall at the maximum expected drift. The assumption was also validated by the test data.

After discussing the deduced N.A. depths of the wall in the test, the results obtained from the numerical model of PFS1 are compared with the test results in the following.

Simulation results of the wall – N.A. depth

Fig. 6-28 shows a comparison of the neutral axis depths of the wall recorded at the peaks of different drifts with those obtained from the numerical model "Model-A PFS1" (without props). In the figure, "Test results_Positive direction" represents the test results when PFS1 was loaded in the positive direction. "Simulation_Model-A PFS1" represents the results obtained from "Model-A PFS1" (without props).

As shown in the figure, the simulation results show reasonable correlation with the experimental response. At larger drifts, the numerical model slightly underestimates the N.A. depths, but the difference is not significant. For example, the N.A. depths obtained from the test and the numerical model were about 9.8 in. and 7.3 in., respectively, when the lateral drift was 2%. The difference only took up 3% of the width of the wall (90 in.).

6.2.4 Strain Distribution in the Wall

Concrete gages were placed in the corners of the wall to measure the compressive strains. The readings of the concrete gages can be used to further investigate the extent of the damage to the wall discussed in Section 6.2.1. The location of the strain gages is shown in Fig. 4-3. It was noteworthy that because the compressive strains generated during the post-tensioning operation were not recorded, the readings used below did not represent absolute strains but varied strains during the test. Assuming the initial PT force was uniformly distributed over the cross section of the wall, the initial compressive strain in the concrete of the wall is calculated as follows:

$$\varepsilon_{initial} = \frac{F_{PT\_initial}}{E_c A_g} = \frac{112.5 \times 10^6}{6410 \times 90 \times 6} \approx 32\ \mu\varepsilon \tag{6.4}$$

Where $\varepsilon_{initial}$ = Initial strain in the wall; $F_{PT\_initial}$ = Initial prestressing force in the wall recorded before the test; E_c = Young's modulus of concrete in the wall (Table 3-8); A_g = Gross cross-sectional area of the wall.

As shown above, the initial compressive strain in the concrete generated due to the initial PT force was very small. Therefore, the readings of the strain gages recorded during the test were directly used for data analysis and discussed phase by phase in the following.

Phase 1

Fig. 6-29 and Fig. 6-30 show the compressive strain distribution along the width of the wall (CG_E1/E2/E3 and CG_W1/W2/W3, respectively) when PFS1 was loaded to the positive and the negative direction in Phase 1, respectively. It was noteworthy that although straight lines were used to connect the limited data points in Fig. 6-29 and Fig. 6-30, the actual strain distribution might not be linear between two adjacent data points.

As shown in the figures, the compressive strains concentrated at the wall corners and strain compatibility was not valid at the wall base. In general, the strains in the east corner were larger than those in the west corner. It correlated with the test observation in Section 6.2.1 that the east corner was subjected to more damage.

As shown in Fig. 6-29, the readings of the strain gage that was close to the east wall end (the data points near 45 in the horizontal axis) decreased after 2% drift cycles. It might have been caused by the spalling of concrete cover in the east wall corner that initiated at 1.5% drift. On the other hand, the readings of the strain gages that were in the west wall end decreased after -1% drift cycles, as shown by rhombus markers in Fig. 6-30. The decrease might have been caused by the damaged grout beneath the west wall corner that reduced the compressive strains developed in the wall. Fig. 6-31 shows the condition of the fiber grout beneath the west and the east wall corner following the end of the test. As shown in the figure, some damage occurred to the grout beneath the west wall corner that correlated with the test observation described above.

Fig. 6-32 and Fig. 6-33 show the compressive strain distribution (CG_E1/E4 and CG_W1/W4) over 8 in. along the height of the wall, respectively. CG_E1 and CG_W1 were placed closer to the base of the wall compared with CG_E4 and CG_W4. As shown

in the two figures, the compressive strains in the concrete decreased along the height of the wall in general.

As shown in Fig. 6-32, the readings of the two strain gages at the east wall end (CG_E1/E4) decreased after 1.5% drift cycles. It might have been caused by the damage to the east wall corner that initiated at 1.5% drift. The readings of the two strain gages at the west wall end (CG_W1/W4) decreased after -1% drift cycles, as shown in Fig. 6-33. It might have been caused by the damage to the fiber grout beneath the west wall corner as mentioned previously.

Fig. 6-34 shows the tensile strain distribution in the stirrups over 38 in. along the height of the wall (SG_W1 through SG_W6). As shown in the figure, strain gage readings show that the maximum tensile strain in the stirrups in Phase 1 was only 185 $\mu\varepsilon$ at the instrumented locations. Because the tensile strains were so small, the confinement effect of the boundary elements provided little value in Phase 1. As shown in Table 3-8 , the measured concrete compressive strength of the wall was larger than that of the cube strength of the fiber grout (which might be considered confined to some extent because of the shape of the sample). The strength of the confined concrete in the wall corners would be expected to be much larger than the strength of the fiber grout. Consequently, the fiber grout was damaged instead of the concrete in the wall corners.

As shown in Fig. 6-34, the tensile strains in the stirrups that were located more than 10 in. above the wall base were very small, indicating that the confinement effect provided by those stirrups was negligible.

Phase 2

Fig. 6-35 and Fig. 6-36 show the compressive strain distribution along the width of the wall when PFS1 was loaded in the positive and the negative direction in Phase 2, respectively. Similar to the observation in Phase 1, the strains in the east corner were generally larger than those in the west corner. The maximum compressive strain recorded in the wall was 1760 $\mu\varepsilon$, similar to that recorded in Phase 1 (1800 $\mu\varepsilon$).

Fig. 6-37 and Fig. 6-38 show the compressive strain distribution in the concrete over 8 in. along the height of the wall in Phase 2. In the positive peak direction, it was observed that the compressive strain decreased along the height of the wall (from the gages located

at 2 and 8 in. from the base). In the negative loading direction, the strains remained relatively uniform over that height.

Fig. 6-39 shows the tensile strain distribution in the stirrups along the height of the wall in Phase 2. As shown in Fig. 6-39, the maximum tensile strain in the stirrups is only 260 με, indicating that the steel confinement still did not take great effect in Phase 2. Similar to Phase 1, the tensile strains in the stirrups that were located above 10 in. from the wall base were not noticeable.

Phase 3

In Phase 3, the concrete gage CG_EW1 had unreasonably large readings (about 24,000 με) at 5% drift that was beyond the measuring range (20,000 με), thus it was excluded from data analysis. Fig. 6-40 and Fig. 6-41 show the compressive strain distribution along the width of the wall when PFS1 was loaded in the positive and the negative directions, respectively. As shown in the figures, the maximum compressive strains recorded in the east and the west wall corners increased to 4100 and 3600 με, respectively. Because the PT force in the wall kept increasing at the peaks of 4% and 5% drift (shown in Fig. 6-21), the compression forces concentrated at the wall corners were larger in Phase 3 compared to those in the previous two phases. Moreover, as shown in Fig. 6-26 the N.A. depth of the wall was slightly decreased in Phase 3. Under this circumstance, a larger compression force was distributed over a smaller contact area, resulting in the increased compressive strains in the wall. Although no instrumentation was installed inside the fiber grout, it was believed that the fiber grout within the contact area was well confined in the pocket in the base block that enabled it to sustain the large compression force.

Fig. 6-42 and Fig. 6-43 show the compressive strain distribution in the concrete over 8 in. along the height of the wall in Phase 3. As shown in the two figures, the strains rapidly decreased along the height of the wall. For example, as shown in Fig. 6-43, the compressive strain decreased from -3500 με at 2 in. above the wall base to -1600 με at about 8 in. above the wall base. It was believed that the compression force at the wall corner spread out across the cross section of the wall with increased distance from the base and the high strain concentrations in the wall corners were only local behavior.

Fig. 6-44 shows the tensile strain distribution in the stirrups along the height of the wall in Phase 3. As shown in the figure, the confinement effect from the stirrups became noticeable at 5% drift. For example, the maximum tensile strain recorded in the stirrups increased to 1550 με. On the other hand, similar to the observations in Phase 1 and Phase 2, the tensile strains in the stirrups that were located higher than 10 in. above the wall base were not noticeable (e.g., the maximum recorded strain was only about 50 με).

To conclude, the maximum compressive strains recorded in the wall corners (i.e., east wall corner ~1800 με; west wall corner ~1100 με) were similar in Phase 1 and Phase 2. The N.A. depth of the wall was extended due to the weaker fiber grout that reduced the strains developed in the concrete in the wall. The steel stirrups provided little confinement effect in these two phases. When PFS1 was loaded to higher drift levels, the steel stirrups became more effective near the base of the wall. It demonstrated that even when the fiber grout was weaker than the concrete in the wall, large compressive strains might still be developed in the wall at large lateral drifts. Using steel confinement in the wall corners would be beneficial if the wall was required to remain undamaged in large seismic events.

Another finding was that the compressive strains in the wall corners decreased rapidly along the height of the wall. When large compressive strains were developed at the wall base, the decrease was more significant, indicating that the strain concentration was localized in the corners. This conclusion was also validated by the observation that the steel stirrups in the wall corners did not take effect when they were located higher than 10 in. above the wall base throughout the test. For the design of PFS1, the steel stirrups were placed over 36 in. along the height of the wall. It might be more economical to place the steel confinement over a relatively small distance in the boundary element of the wall.

Data from Krypton system

Krypton LEDs were attached to the south surface of the wall near the corner, as shown in Fig. 6-45. The 3D position of the wall at the spot where each LED was attached was recorded during the test by the Krypton camera. The relative vertical deformation between two adjacent LEDs can be deduced by processing their varied 3D positions. The

average strain between two adjacent LEDs can be deduced by dividing the relative vertical deformation by the original vertical distance between the two LEDs.

As mentioned in Section 6.2.1, spalling of the concrete cover at the east wall corner occurred after 1.5% drift. Because the LEDs were attached to the surface of the wall, spalling of the concrete might have affected the readings of the LEDs. Therefore, the strains deduced from the LEDs at 1.5% drift are used for data analysis below (rather than results at higher drifts).

Fig. 6-46 shows a comparison of the strains deduced from the LEDs near the wall edge with those recorded by concrete gages. As shown in the figure, the reliability of the concrete gage readings is validated. For example, the average readings from the two LEDs near the concrete gage at the second row (-787 and -1278 με) matched well with the concrete gage readings (-1005 με). It is also learned from the figure that the compressive strains along the height of the wall were decreasing in general. For example, the strains decreased from -1320 με (the LED in the second row) to -422 με (the LED in the sixth row) in the first column of LEDs; the strains decreased from -1427 με (the LED in the second row) to -438 με (the LED in the fifth row) in the second column of LEDs.

Fig. 6-47 shows a comparison of the strains deduced from the LEDs near the O-connectors with those recorded by concrete gages. As shown in the figure, the readings of the LEDs near the O-connectors (in the fifth and the sixth row of the second column, -1033 and -1993 με) were relatively large compared to those of adjacent LEDs. It was believed that a compression force was generated by the O-connector that increased the local compressive strains in the wall and caused the larger readings of LEDs.

It was noteworthy that some strains deduced from the LED readings were not consistent with the conclusions made above. The inconsistency might be due to the following reasons. First, the LEDs were glued to the surface of the wall, thus discrepancies might occur if the glue of some LEDs was not strong enough. Second, the consolidation condition of the concrete was highly variable in the wall corners where a great amount of steel confinement existed. It certainly would make the readings of the LEDs more variable. Last but not the least, the resolution of the LED readings was about

0.002 in. according to the product manual. When the distance between two adjacent LEDs was 1.5 in, the varied range of the deduced strains was about 1500 με, which was very large.

Simulation results of the wall – Strain distribution along the width of the wall

Fig. 6-48 shows a comparison of the strain distribution in the wall obtained at positive peaks for different drifts in the test with those obtained from "Model-A PFS1" (without props). For the test specimen, the readings from the three concrete gages at the east corner of the wall (CG_E1/E2/E3) in Phase 1 were used. For the numerical model, the vertical strains in the elements at the east corner of the wall were used, as marked in Fig. 6-49. Because the gage length of each concrete gage was similar to the total length of two vertically adjacent elements in the model, average strains of the two adjacent elements were used. In total, there were four data points from the numerical model at each drift level.

Fig. 6-48(a) shows a comparison of the strain distribution obtained from the test and that from the numerical model at small drift levels (before 0.75%). As shown in the figure, the numerical model overestimated the strains in the wall measured in the test, but the difference was not significant. It correlated with the comparison of the N.A. depths of the wall in Fig. 6-28 where the simulation results matched well with the test results before 0.75% drift in general.

Fig. 6-48(b) shows the comparison at large drift levels. As shown in the figure, the maximum strain recorded by the concrete gages in the test was about 1790 $\mu\varepsilon$ at 1.5% drift. According to the stress-strain response of the confined concrete as shown in Fig. 5-12, the strain of 1790 $\mu\varepsilon$ corresponded to a stress of 8609 *psi* in the concrete in the wall. The value was very close to the compressive strength of the grout obtained from the cube strength material test (8,650 *psi,* shown in Fig. 5-19). It was believed that when the fiber grout was weaker than the concrete in the wall, the strains that developed in the wall did not increase much after the grout had "yielded" in the test.

Different from the test results, the strains predicted by the numerical model kept increasing through 2% drift, as shown in Fig. 6-48(b). Because the softening of the confined concrete was slow, the stresses developed in each element in the wall corners

were relatively large corresponding to the large strains. This explained the findings in Section 6.2.3 that the N.A. depth of the wall predicted by the numerical model was slightly smaller than that observed in the test. The reason that caused larger strains in the wall corners in the numerical model is explained below.

Fig. 6-49 shows a portion of the model "Model-A PFS1" (without props). As shown in the figure, because the fiber grout layer was very thin, the constraint effect from the top and the bottom boundary on the elements of the fiber grout was significant.

The top boundary of the grout elements was modeled as a "rough" contact with the wall. The bottom boundary of the grout elements was "tie" constrained to the foundation (not shown in the figure). The grout elements were constrained from expanding freely in the horizontal plane on both top and bottom boundaries, indicating that they were under tri-axial compression. Under this stress condition, it was believed that the compressive strength of the grout would be greatly increased.

This conclusion was further validated by the results obtained from the numerical model. It was found that the compressive stress in the grout elements kept increasing to 13,220 psi at 2% drift. It was even larger than the compressive strength defined in uniaxial stress-strain curve of the confined concrete in the wall (10,697 psi, shown in Fig. 5-12). Because the grout was stronger than the confined concrete, larger stresses were developed in the concrete elements in the wall corners that explained the increasing strains observed in the numerical model.

To be discussed in Chapter 9, it is found that local behavior of the wall and the fiber grout does not have a great impact on the overall performance of rocking-wall structures. Therefore, although the local behavior of the wall and the fiber grout was not accurately simulated, the overall behavior of PFS1 was still well simulated by the numerical model as shown in this chapter.

6.2.5 Lateral Deformed Shape of the Wall

Five string pots (SP2_EW0, SP10_EW1, SP20_EW2, SP20_EW3 and SP30_EW4) were used to investigate the deformed shape of the wall during the test. The location of the string pots is shown in Fig. 4-1. Fig. 6-50 shows the deformed shapes of the wall at

small drift levels in Phase 1 (before 0.05% drift). As shown in the figure, the flexural deformation of the upper portion of the wall above the floor is noticeable at 0.01% and 0.03% drift. The flexural deformation was generated by the internal moments in the wall and was the major contribution factor to the lateral displacement of the wall.

At larger drift levels in Phase 1 after the wall had been uplifted, rigid body motion controlled the lateral movement of the wall, as shown in Fig. 6-51. Because PFS1 was loaded from 0.10% drift in Phase 2 and 4% in Phase 3, respectively, rigid body motion was the predominant lateral deformation mode of the wall in those two phases, as shown in Fig. 6-52 and Fig. 6-53.

Fig. 6-54 compares the readings from the top and the bottom tiltmeter in Phase 1. The location of the two tiltmeters is shown in Fig. 4-1. As shown in the figure, the top tiltmeter always had larger readings that were believed to be caused by flexural bending of the wall. Similar behavior was observed in other phases as well. Fig. 6-55 shows the percentage of the rotations caused by the flexural bending of the wall (obtained by subtracting the readings of TBW from those of TTW) relative to the total rotation of the wall on the top (measured by TTW) at the positive peaks of different drifts in Phase 1. As shown in the figure, the percentage of the rotations caused by the flexural bending of the wall rapidly decreased and was only 10% of the total rotation of the wall at 2% drift. It further validated that rigid body motion was the predominant deformation mode of the rocking wall at larger drift levels.

6.3 Behavior of O-connectors

6.3.1 Damage to the O-connectors

The readings from the strain gages (SG_WTO_U and SG_WBO_U) attached to the O-connectors indicated that local yielding occurred at 0.5% drift in Phase 1. Fig. 6-56 shows the yield lines observed at 0.75% drift in the O-connector that was attached to the north surface of the wall. The yield lines kept developing at larger drifts, as shown in Fig. 6-57 for the same O-connector. Similar damage occurred to the other O-connectors in the

test. Cracking and fracture of some of the O-connectors were observed when PFS1 was loaded to 4% drift in Phase 3.

After the four phases of testing, it was observed that all four of the O-connectors attached to the upper level of the side columns fractured but the four O-connectors attached to the lower level did not. Fig. 6-58 and Fig. 6-59 show the condition of the two O-connectors attached to the same side column. As shown in the figure, only the O-connector at the upper level fractured while the one at the lower level remained uncracked. As shown in Fig. 6-60, all side columns (emulated by steel tubes) leaned towards the center of the wall. It was believed that the O-connectors at the upper level were subjected to additional horizontal opening forces compared to the O-connectors at the lower level when the side columns were on the uplift side of the wall. Therefore, more damage occurred to the O-connectors at the upper level due to the increased deformation demand, and the damaged upper level O-connectors prevented the side columns from returning to their original upright orientation. Design recommendations for the O-connectors are given in Section 9.1.5.

6.3.2 Relative Vertical Movement of the O-connectors

Because the O-connectors yielded at small drift levels (0.5%) and the strain gage readings became unreliable after the yielding occurred, it was difficult to obtain the resisting forces provided by the O-connectors. Existing tests have demonstrated that the behavior of an O-connector can be well predicted by using numerical simulations, as long as the relative vertical movements between the O-connectors and the wall are recorded (Henry 2011). The numerical model of the O-connectors was verified by a separate component test discussed in Section 5.4.3. Two LVDTs, L2-NWOV and L2-NEOV, were used in PFS1 to measure the relative vertical deformations of the O-connectors attached to the west and the east side of the wall, respectively. Fig. 6-61 and Fig. 6-62 show the readings of L2-NWOV and L2-NEOV in Phases 1 through Phase 3.

Fig. 6-63 shows a comparison of the relative vertical displacements of the O-connectors recorded in the test with those obtained from the numerical model “Model-A PFS1” (without props). “Test results_Positive direction” and “Test results_Negative

direction" represent the readings of L2-NWOV (when PFS1 was loaded to the east) and L2-NEOV (when PFS1 was loaded to the west), respectively. "Simulation_Model-A PFS1" represents the simulation results obtained from the numerical model. As shown in the figure, the simulation results show satisfactory correlation with the experimental response.

6.4 Behavior of Unbonded PT Floor

As described in Section 3.3.2 , multiple reinforcement and PT strands of the cast-in-place unbonded PT floor went through the wall. It was expected that a rigid wall-floor connection was formed through the design. To investigate this assumption, the relative wall-floor deformation is presented in Section 6.4.1. Damage to the floor in Phase 1 through Phase 3 is presented in Section 6.4.2. The behavior of the floor in both longitudinal and transverse directions is described in detail in Section 6.4.3 through Section 6.4.8. The numerical model of the unbonded PT slab that is introduced in Section 5.5.4.4 is validated using the test data analyzed in these sections.

6.4.1 Relative Wall-Floor Deformation

As mentioned in Section 4.2.1.5, L05-FWE-V and L05-FM-V were used to monitor the relative vertical displacements between the wall and the slab (vertical shear slip). The location of the LVDTs is shown in Fig. 4-2. It was found that L05-FM-V did not function during the test, thus it was excluded from data analysis. Fig. 6-64 shows the cyclic readings of L05-FWE-V with respect to the lateral displacements of PFS1. As shown in the figure, the maximum relative vertical displacement between the wall and the floor was less than 0.02 in. There was negligible vertical shear slip between the wall and the floor in the test.

L05-FWE-H and L05-FM-H were used to monitor the relative horizontal displacements between the wall and the floor. The location of the LVDTs is also shown in Fig. 4-2. Fig. 6-65 shows the cyclic readings of L05-FWE-H with respect to the lateral displacements of PFS1. As shown in the figure, the maximum relative horizontal displacement between the wall and the floor was less than 0.005 in. The readings of L05-

FM-H were also negligible throughout the test. There was negligible horizontal shear slip between the wall and the floor in the test.

To conclude, neither vertical nor horizontal shear sliding occurred between the wall and the floor. A rigid wall-floor connection was formed during the test as assumed in design. This conclusion also validated the technique used to simulate the wall-floor connection in the numerical model. As described in Section 5.5.4.5, the portion of the floor that contained rebar and strands going through the wall was "embedded" in the wall in the model. It assumed that the "embedded" floor would not have relative displacements to the wall and the assumption matched the test observation.

6.4.2 Damage to the Unbonded PT Floor

A crack map of the bottom surface of the floor is shown in Fig. 6-66. Because of inaccessibility during the test, cracks were not marked on the top surface of the slab. The cracks on the bottom surface were marked at the first positive and negative peak drifts. Positive drifts represent that PFS1 was loaded to the east. At the positive peak drifts, the bottom surface of the slab at the east wall-floor connection and the bottom surface of the slab at the west floor-edge beam connection were in tension. At the negative peak drifts, the bottom surface of the slab at the west wall-floor connection and the bottom surface of the slab at the east floor-edge beam connection were in tension.

The crack patterns shown in Fig. 6-66 represent those initiated through Phase 2 of testing. The phases (Ph#) and the drifts when the cracks were observed to initiate are annotated in the figure. After Phase 2, no new cracks were observed to form through Phase 3. Only the existing cracks were observed to open and close. The crack patterns of the floor and the behavior of the longitudinal rebar as well as transverse rebar are discussed phase by phase in the following.

In Phase 1, a straight crack formed across the whole width of the slab at the east floor-edge beam connection at -0.25% drift, as shown in Fig. 6-67. A similar straight crack formed at the west floor-edge beam interface at 0.5% drift. Cracks started to form in the slab from the east wall face at 0.5% drift, as shown in Fig. 6-68. Similar cracks formed from the west wall face to the north and the south floor edge were observed at -0.5%

drift. At larger drift levels, cracks parallel to the existing cracks at the floor-edge beam interface were observed, as shown in Fig. 6-69. Although the moment demand on the slab was lower at the location where the new cracks formed, the moment resistance of the slab at those cross sections was smaller because the bonded reinforcement in the slab terminated there. Meanwhile, cracks started to extend from the east wall surface to the north and the south floor edges, as shown in Fig. 6-70. It was observed that the common steel anchor plate designed for the PT strands in the N-S transverse direction constrained the slab from bending locally near the anchor plate, making most of the cracks incline and extend from the wall edges to each side of the anchor plate, as shown in Fig. 6-71. Similar cracks that extended from the west wall surface to the north and the south floor edges were also observed in the test, as shown in Fig. 6-66.

All cracks were re-examined when the external loads in the crosshead decreased to zero from the peaks (termed "zero load position"). Fig. 6-72 shows the open cracks at 2.5% drift when the crack width was in excess of 0.067 inch (1.5mm). Fig. 6-73 shows the condition of the slab at "zero load position," when it was observed that most of the cracks in the floor closed because of the intact PT strands in the floor.

After the props were attached to the floor in Phase 2, no new cracks were observed until diagonal cracks started to extend from the west surface of the wall to the northeast and the southeast prop at -2% drift, as shown in Fig. 6-74. Similar diagonal cracks formed from the southwest prop and the northwest prop to the east surface of the wall at 2.5% and 3% drift, respectively.

No new cracks were observed beyond Phase 2 except that the existing cracks widened. However, concrete spalling and rebar buckling were observed at both east and west wall-floor connections at 4% drift in Phase 3, as shown in Fig. 6-75 and Fig. 6-76. Although the localized damage was severe, structural integrity of the entire floor slab was maintained because the transverse shear-friction reinforcement along the surface of the wall and the PT strands in the floor remained intact. The PT forces in the strands recorded after Phase 3 were about 100 to130% of the initial values. Fig. 6-77, Fig. 6-79 and Fig. 6-81 show the cracked slab recorded in Phase 3 (while the cracks were open at the peak drifts). Fig. 6-78, Fig. 6-80 and Fig. 6-82 show the condition of the slab after the

test. As shown in the figures, most of the cracks in the floor closed due to the residual PT forces. Fig. 6-83 and Fig. 6-84 show the top surface of the slab after the test. It was believed that the slab would be reusable after repairing the local damage.

After describing the damage to the floor observed in the test, the behavior of the structural elements in the floor are described in detail in Section 6.4.3 through Section 6.4.8. The force variation of the longitudinal and the transverse PT strands is described in Section 6.4.3. In Section 6.4.4 and Section 6.4.5, the average curvature and the strain distribution of the floor in the longitudinal direction is described first, followed by the discussion of those observed in the transverse direction in Section 6.4.6 and Section 6.4.7. The forces recorded in the props that were attached to the floor in Phase 2 are discussed in Section 6.4.8. At the end of each section, simulation results from the numerical models "Model-A PFS1" (without or with props) are compared with the associated test results to validate the reliability of the model for the unbonded PT slab.

6.4.3 Force Variation in the PT Strands

Multiple load cells were installed on the PT strands to monitor the force variation during the test. The location of the load cells is shown in Fig. 4-10. As shown in the figure, three load cells (FPTW1, FPTW2 and FPTW3) were installed on the west edge of the floor to measure the forces in the longitudinal strands; four load cells (FPTSE1 through FPTSE4) were used to measure the forces in the transverse strands.

Because PT losses occurred between the post-tensioning date and the test date, the PT forces achieved after the post-tensioning operation (shown in Section 3.4.10) were different from those measured at the beginning of the test. Table 6-1 summarizes the PT force and the stress level in each strand at the beginning of the test. Because the dimensions of the scaled floor slab were relatively small, the strands in the floor were lightly prestressed in the test compared with the typical prestress levels in PT strands in practice ($0.7f_{pu}$).

As discussed in Section 6.4.2, the floor slab was subjected to large deformations in the test. It was expected that the PT forces in both the longitudinal and transverse strands would vary due to the deformation of the floor slab. The varied PT forces in the

longitudinal strands are discussed first in the following, followed by the discussion of those in the transverse strands.

6.4.3.1 PT Force in the Longitudinal Strands

Fig. 6-85 shows the change in PT force in the longitudinal strands recorded at different positive and negative peak drifts in Phase 1 and Phase 3. Fig. 6-86 shows the results in Phase 2 when the props were attached to the floor. The horizontal axis in the figures represents the drift levels of PFS1. The vertical axis represents the changed PT force in the strands, which was equal to the measured PT force at the peak drift minus the initial PT force at the beginning of the test. As expected, the increase in the PT force was larger at higher drift levels.

As shown in Fig. 6-85, the increase in PT force was similar among all longitudinal strands when the drift levels were smaller than 2.5% in Phase 1. The increase measured by the load cell FPTW3 started to be larger than that measured by the other load cells at 1.5% drift in Phase 2, as shown in Fig. 6-86. A similar observation was found in Phase 3, when PFS1 was loaded to 4% and 5% drift as shown in Fig. 6-85. As shown in the figure, the PT strand with FPTW3 was located closest to the wall compared to the other strands. Because more damage started to occur adjacent to the wall-floor connection in Phase 2 when the props were attached to the floor, the total length of the PT strand closest to the wall was expected to be larger due to the localized larger strains in the floor, which resulted in the larger increase in PT force observed in Phase 2 and Phase 3. It was noteworthy that the largest difference of the increase in PT force between the two strands recorded by FPTW3 and FPTW1 was about 1 kip at 5% drift. It was only 9% of the total PT force in the strand measured by FPTW3, which was not significant.

As shown in Fig. 6-86, the change in PT force in the strands was approximately 0.6 to 0.8 kip at the beginning of Phase 2, indicating that the PT forces were larger than the initial PT forces after the completion of Phase 1. As discussed in Section 6.4.2, some permanent damage occurred to the slab in Phase 1 (e.g. yielding of the longitudinal rebar). It was believed that the length of the strands was elongated due to the damage to the floor, causing the increase in PT force in the strands. Similar behavior was observed in Phase 3. As shown in Fig. 6-85, the change in PT force in the strands was

approximately 1 to 1.2 kip at the beginning of Phase 3. Because the damage to the slab developed in Phase 2, the PT increase at the beginning of Phase 3 was slightly larger than that at the beginning of Phase 2.

Table 6-2 shows the percent increase in PT force relative to the initial PT force in each strand in the longitudinal direction at 2% drift in Phase 1 as well as Phase 2 and 5% drift in Phase 3. As shown in the table, the PT force in the longitudinal strands increased 23% to 38% in Phase 1 and Phase 2, and 50% to 76% in Phase 3. It was found that the vertical deformation and rotation of the floor was not negligible due to the rocking of the wall, which increased the overall length of the strands and thus resulted in increased PT forces.

It was noteworthy that the maximum stress in all longitudinal strands in Phase 1 through Phase 3 was 140 ksi, which was about $0.56f_{pu}$. Despite of the large increase in PT force, none of the longitudinal strands yielded or fractured. Because of the remaining post-tensioning forces in the floor, the structural integrity of the floor was maintained and the cracks in the floor closed upon unloading.

As shown in Table 6-2, the percentage increase in the PT force in Phase 1 was similar to that in Phase 2, indicating that the behavior of the longitudinal strands was not greatly impacted by adding the props to the floor in the transverse direction.

6.4.3.2 PT Force in the Transverse Strands

Fig. 6-87 shows the change in PT force in the transverse strands recorded at different positive and negative peak drifts in Phase 1 and Phase 3. Fig. 6-88 shows the results in Phase 2 when the props were attached to the floor. As shown in the figures, the PT increase was only noticeable when PFS1 was loaded in the negative direction. It was because the load cells FPTSE1 through FPTSE4 were installed on the transverse strands in the slab near the east wall end. When PFS1 was loaded in the negative direction (to the west), the portion of the floor connected to the east wall end was pulled up due to the uplift of the east wall end. The transverse strands in the deformed portion of the slab were elongated and thus the PT forces in the strands increased. On the other hand, when PFS1 was loaded in the positive direction (to the east), the portion of the floor connected to the east wall end stayed almost horizontal because there was little vertical movement on the

compression side of the wall. The total length of the transverse strands remained almost the same, thus there was little PT force increase in the strands.

The maximum stress in the four transverse strands was 174 ksi (recorded by FPSE3 in Phase 3), which was about $0.7f_{pu}$. None of the four transverse strands yielded or fractured during the test.

Table 6-3 shows the percent increase in PT force relative to the initial PT force in each strand in the transverse direction at -2% drift in Phase 1 as well as Phase 2 and -5% drift in Phase 3. As shown in the table, the PT forces slightly increased in Phase 1 when the props were not attached to the floor (boundary condition that simulated there was no constraint from parallel frame lines). The increase in PT force was believed to be caused by the flexural bending of the floor in the transverse direction due to the constraint from the edge beam. Not only the torsional stiffness, but also the flexural stiffness of the edge beam about the strong axis constrained the uplift of the wall, which generated the 3D effect of the floor.

After the props were attached to the floor, the increase in PT force was more noticeable, as shown in Table 6-3. It was observed that the props held down the north and the south edge of the floor that was connected to the uplift side of the wall. Under this circumstance, a great amount of flexural deformation was generated in the floor in the transverse direction. The total length of the transverse strands was increased, thus the PT forces in the strands were also increased. As shown in the table, compared with the increase in PT force in Phase 1, the increase in PT force in Phase 2 was much larger, indicating that the 3D effect of the floor became more significant after the props were attached to the floor.

As shown in Table 6-3, the increase in PT force at -5% drift in Phase 3, when the props were already removed, was comparable to that in Phase 2. It was believed that the constraint on the floor from the edge beams became more significant when the wall was loaded to higher lateral drifts. Larger flexural deformation was generated in the floor in the transverse direction, thus the PT forces were increased in the transverse strands.

6.4.3.3 Discussion of the Increase in PT Force

The increase in PT force was similar among all longitudinal strands when the props were not attached to the floor in Phase 1. After the props were attached to the floor in Phase 2, the increase in PT force in the longitudinal strand closest to the wall was larger than that in the other strands away from the wall, but the difference was not significant. It might be reasonable to assume that the distributed longitudinal strands were subjected to similar PT increase when the wall rocked.

Even when the props were not attached to the floor, the 3D constraint effect of the floor on the wall still existed due to the existence of the edge beams. As expected, attaching the props to the floor further increased the 3D constraint effect of the floor, which also increased the PT forces in the transverse strands.

The PT strands in the test structure had been lightly prestressed to provide a similar compressive stress in the scaled slab as the prototype. This was resulted because the area of the available strand could not be scaled in accordance with the dimensions of the test structure (1/3 those of the prototype). As a result of the strands being lightly prestressed, none of them were observed to yield or fracture during the test despite the large percent increase in PT force (shown in Table 6-2) that was caused by large local deformation in the floor due to the rocking of the wall. If the strands had been stressed to a higher initial prestress level, more typical of practice, they might not have remained elastic. The plastified PT strands might have lost the capability to close the cracks in the slab upon unloading. If the PT strands fractured, the structural integrity of the slab might have been impaired. To achieve the good performance of the floor slab as observed in the test, it is recommended that PT strands be lightly post-tensioned when used in rocking-wall structures.

The associated results from the numerical models of the PT floor slab are discussed below.

6.4.3.4 Simulation Results of the Slab – PT Force in the Strands

As discussed in Section 5.5.4, the technique “adjusting stress-strain responses of PT strands” was used to simulate the unbonded PT strands in the slab, because it was more computationally efficient and less vulnerable to convergence problems. The “unbonded”

strands were simulated by “bonded” strand layers. The stress-strain responses of the “bonded” strand layers were modified to reflect the “unbonded” characteristic of the strands. Different adjusted stress-strain responses were assigned to the strands in the longitudinal and the transverse directions in the model of PFS1. Moreover, the stress-strain responses of the longitudinal (or transverse) strands were different in Phase 1 and Phase 2 due to the impact from the props. Fig. 5-51 summarizes the adjusted stress-strain curves of the PT strands in the models.

Fig. 6-89 shows a comparison of the forces in the longitudinal strand closest to the wall (measured by the load cell FPTW3) in Phase 1 with those from “Model-A PFS1” (without props). As shown in the figure, the simulation results matched well with the test results. Fig. 6-90 shows a comparison of the average forces of the four banded transverse strands in Phase 1 with those from “Model-A PFS1” (without props). As shown in the figure, the forces in the simulation remained almost constant, which was in accordance with the test observation. The simulation results slightly overestimated the test results (about 3%), which was considered negligible.

Fig. 6-91 shows a comparison of the forces in the longitudinal strand closest to the wall in Phase 2 with those from “Model-A PFS1” (with props). The simulation results underestimated the test results in general. As shown in Fig. 6-86, the change in PT force in the longitudinal PT strands at the beginning of Phase 2, which can be seen at small drift levels in the figure, was about 0.6 to 0.8 kip. This initial condition was not simulated in the “Model-A PFS1” (with props) becase the pushover model did not account for the damage to PFS1 during the cyclic loading in Phase 1 of the testing. This caused the difference between the model and the test results in Phase 2 shown in Fig. 6-91.

Fig. 6-92 shows a comparison of the average forces of the four banded transverse strands in Phase 2 with those from “Model-A PFS1” (with props). As shown in the figure, the numerical model well predicted the trend of the PT forces in the strands. The largest difference between the simulation and the test results was about 9% when PFS1 was loaded to 5 in. (2% drift), which is not large.

To summarize, the numerical model using the technique "adjusting stress-strain responses of PT strands," described in Section 5.5.4, was found to be capable of simulating the unbonded PT strands in both Phase 1 and Phase 2 testing of PFS1.

After describing the behavior of the PT strands in the slab, discussions on average curvature and strain distribution of the floor, which would shed light on understanding the deformation demand on the floor, are given in the following sections. The average curvature and strain distribution of the floor in the longitudinal direction are discussed first in Section 6.4.4 and Section 6.4.5, followed by the discussion of those of the floor in the transverse direction in Section 6.4.6 and Section 6.4.7.

6.4.4 Average Curvature of the Floor in the Longitudinal Direction

As discussed in Section 4.3.1.1, multiple groups of LVDTs and string pots were used to measure the average curvature distribution at the wall-floor and the floor-edge beam connection. It was observed that the following instrumentation did not work well during the test: L05_FEG_B3 did not function well from the beginning of the test; L1_FWL1_B1 did not work after 2% drift in Phase 2; L1_FCL_T1 did not work after 2.5% drift in Phase 2. The malfunction of the LVDTs might have been caused by damage to attachments of the LVDTs to the slab in Phase 2 of testing due to slab damage in the vicinity of the attachments. The test data recorded by the instrumentation after malfunction were excluded from data analysis.

The average curvatures of the floor at the wall-floor and the floor-edge beam connection, where most of the instrumentation was placed, are presented in the following. It was noteworthy that most of the instrumentation was installed on the west half of the floor, thus only the behavior of this half of the floor is described below.

6.4.4.1 Average Curvature Distribution of the Floor at the West Wall-Floor Connection

Phase 1

Fig. 6-93 shows the average curvature distribution obtained from the 1st row of LVDTs at the west wall-floor connection when PFS1 was loaded in the positive direction (to the east) to peak drifts in Phase 1. Because the west end of the wall was uplifted, a large deformation demand on the west wall-floor connection was expected.

As shown Fig. 6-93, the average curvature decreased from the wall end to the south edge of the slab. The floor encountered localized deformation close to the wall. Fig. 6-94 shows the average curvature obtained from the 2nd row of LVDTs at the west wall-floor connection in Phase 1. As shown in the figure, the magnitude of the average curvature was much smaller than that obtained from the 1st row of LVDTs; the distribution of average curvature was larger in the region between the wall and the floor edge compared to that close to the wall. As shown in the crack map in Fig. 6-94, multiple cracks that extended from the edge of the wall existed within the coverage range of the 2nd row of LVDTs in the region between the wall and the floor edge, but there were no additional cracks within the coverage range of the 2nd row of LVDTs that were close to the wall. The crack patterns were consistent with the smaller average curvature close to the wall measured by the 2nd row of LVDTs.

To obtain average curvatures over a longer gage length, the data obtained from the 1st and the 2nd row of LVDTs were processed as follows (take L1-FWL1-T1/ L1-FWL1-B1 and L1-FWL2-T1 / L1-FWL2-B1 as an example):

$$\theta_s = \theta_{l1} + \theta_{l2} \tag{6.5}$$

$$\varphi_s = \frac{\theta_s}{s_1 + s_2} \tag{6.6}$$

Where θ_s = Rotation over a longer gage length, θ_{l1}= Local rotation obtained from the first row of LVDTs (e.g. L1-FWL1-T1/ L1-FWL1-B1), θ_{l2}= Local rotation obtained from the second row of LVDTs (e.g. L1-FWL2-T1/ L1-FWL2-B1), φ_s = Average curvature over a longer gage length, s_1 = Gage length of the first row of LVDTs (e.g. L1-FWL1-T1/ L1-FWL1-B1), s_2 = Gage length of the second row of LVDTs (e.g. L1-FWL2-T1/ L1-FWL2-B1).

Fig. 6-95 shows the average curvature over the longer gage length at the west wall-floor connection in Phase 1. As shown in the figure, the floor exhibited localized deformation close to the wall. It was consistent with the test observation described in Section 6.4.2 that damage was concentrated at the floor slab adjacent to the wall. When PFS1 was loaded in the negative direction (to the west), because the west end of the wall was at the compression side, it had little vertical movement. It was expected that the west

wall-floor connection would be subjected to a smaller deformation demand compared to that when PFS1 was loaded in the positive direction (to the east). Fig. 6-96 shows a comparison of the average curvature distribution obtained from the 1st row of LVDTs at the west wall-floor connection at 2% and -2% drift in Phase 1. As shown in the figure, the absolute average curvature at the west wall-floor connection at 2% drift is about twice that at -2% drift. Because the damage to the floor was generally caused by larger deformation in the floor, only the average curvature recorded when PFS1 was loaded in the positive direction (to the east) is discussed in the rest of this section.

Phase 2

The same procedure was followed to deduce the average curvature distribution at the west wall-floor connection when PFS2 was loaded in the positive direction (to the east) to peak drifts in Phase 2, as shown in Fig. 6-97 through Fig. 6-99. Similarly, the deformation of the slab concentrated adjacent to the wall end.

Phase 3

Severe local damage occurred to the wall-floor connection in Phase3. Some LVDTs stopped working and thus the test data could not be used for analysis in this phase.

6.4.4.2 Average Curvature Distribution of the Floor at the West Floor-Edge Beam Connection

Phase 1

Fig. 6-100 shows the average curvature distribution at the west floor-edge beam connection obtained from the 1st row of LVDTs when PFS1 was loaded in the positive direction (to the east) to peak drifts in Phase 1. As shown in the figure, the average curvature was uniformly distributed across the slab. Fig. 6-101 shows the average curvature distribution obtained from the 2nd row of LVDTs. As shown in the figure, the magnitude of the average curvature was much smaller than that obtained from the 1st row of LVDTs; the average curvature was larger in the floor close to the edge column than that at the edge of the floor. As shown in the crack map in Fig. 6-101, more parallel cracks were formed in the floor close to the edge column in general, causing the larger average curvature.

Fig. 6-102 shows the average curvature in the floor over a longer gage length at the floor-edge beam connection in Phase 1. As shown in the figure, the floor encountered uniformly distributed deformation. It was consistent with the test observation described in Section 6.4.2 that the damage was distributed across the floor-edge beam connection.

Phase 2

Fig. 6-103 through Fig. 6-105 show the average curvature distributions at the floor-edge beam connection in Phase 2. Similar to Phase 1, it was observed that the deformation was uniformly distributed across the floor-edge beam connection.

After discussing the average curvature distribution of the floor in the longitudinal direction in the test, the associated results from the numerical models are discussed in the following.

6.4.4.3 Simulation Results of the Slab – Average Curvature (longitudinal direction)

Fig. 6-106 shows a comparison of the average curvature distribution at the wall-floor connection in the longitudinal direction in Phase 1 of the test with those obtained from "Model-A PFS1" (without props). Drift levels of 0.5%, 1% and 2% were selected as representative drifts. As shown in the figure, the simulation results matched well with the test results, especially at the location close to the wall where the largest curvatures were observed. Fig. 6-107 shows a comparison of the average curvature distribution at the wall-floor connection in the longitudinal direction in Phase 2 of the test with those obtained from "Model-A PFS1" (with props). Again, the simulation provided a reasonable prediction of the test results. As shown in both figures, the simulation results demonstrate that the deformation demand on the slab concentrated at the wall-floor connection.

Fig. 6-108 shows a comparison of the average curvature distribution at the floor-edge beam connection in the longitudinal direction in Phase 1 of the test with those obtained from "Model-A PFS1" (without props). As shown in the figure, the simulation results slightly overestimated the test results, but the differences were not significant. Fig. 6-109 shows a comparison of the average curvature distribution at the floor-edge beam connection in the longitudinal direction in Phase 2 of the test with those obtained from "Model-A PFS1" (with props). The simulation also provided a reasonable prediction of

the test results. As shown in both figures, the simulation results demonstrated that the deformation demand on the slab was uniformly distributed across the floor-edge beam connection.

6.4.5 Strain Distribution of the Floor in the Longitudinal Direction

As shown in Fig. 4-12, strain gages were attached to multiple rebar in the floor slab to measure local strains in the floor. The strain distribution of the floor was investigated when the rebar was in tension. When PFS1 was loaded in the positive direction (to the east), the top rebar in the cross section of the floor at the west wall end and the bottom rebar in the cross section of the floor at the west edge beam were in tension. When PFS1 was loaded in the negative direction (to the west), the opposite occurred.

According to the strain gage readings for the rebar oriented in the longitudinal direction, initial yielding of the top rebar at the wall-floor connection and the floor-edge beam connection occurred at 0.75% and 1% drifts, respectively. Fig. 6-110 shows the strain distribution obtained from the top rebar at the cross section of the west wall-floor connection at positive drifts. As shown in the figure, local strains in the slab decreased significantly from the wall to the edge of the slab; however, it should be noted that the lines connecting the data points do not represent measured data in the figure. At larger drift cycles (e.g. 2%), it was observed that the top rebar close to the wall where SG-FWL-T1 and SG-FWL-T2 were attached had yielded while the two rebar near the prop where gages SG-FPL-T1 and SG-FPL-T2 were attached remained elastic. It correlated with the conclusion made in the previous section that the deformation of the slab concentrated close to the wall.

Fig. 6-111 shows the strain distribution obtained from the bottom rebar at the cross section of the west floor-edge beam connection at positive drifts. As shown in the figure, although the readings of the three strain gages were not similar, they all yielded at 1% drift, which correlated with the conclusion made in the previous section that the deformation of the slab was uniformly distributed at the floor-edge beam connection. The differences in strain readings may be attributed to local effects in the vicinity of the gages; the readings can be greatly influenced by the proximity of the gages to a crack.

Fig. 6-112 shows the strain distribution obtained from the bottom rebar at the cross section of the west wall-floor connection at negative drifts. Fig. 6-113 shows the strain distribution obtained from the top rebar at the cross section of the west floor-edge beam connection at negative drifts. Again, the strain gage readings validated the conclusions that the deformation of the slab concentrated close to the wall end while it was uniformly distributed along the edge beam.

After discussing the average curvature and strain distribution of the floor in the longitudinal direction, the behavior of the floor adjacent to the wall in the transverse direction is discussed in the following.

6.4.6 Average Curvature Distribution of the Floor in the Transverse Direction

As shown in Fig. 4-11, three groups of LVDTs (series FWT and FPT) were placed in the transverse direction to measure the average curvature at the wall-floor and the floor-prop connections. It was found that neither L05_FWT_T4 at the wall-floor connection nor L1_FPT_T2 at the floor-prop connection functioned well during the test. Only two groups of LVDTs were used at the wall-floor and the floor-prop connections for data analysis.

Fig. 6-114 shows the average curvature at the wall-floor connection in the transverse direction in Phase 1 and Phase 2. As shown in the figure, the average curvature deduced from the group of L1-FWT-T3/B3 was higher than that deduced from L1-FWT-T1/B1, indicating that the average curvature of the slab in the transverse direction decreased from the wall end to the edge beam.

As shown in Fig. 6-114, the average curvature was noticeable in Phase 1 even when the props were not attached to the floor. It was believed that not only the torsional stiffness, but also the flexural stiffness of the edge beam constrained the uplift of the wall, resulting in the 3D constraint effect of the floor. Similar conclusions were made when investigating the varied PT forces in the transverse strands in Section 6.4.3.2.

Fig. 6-115 shows the average curvature distribution at the floor-prop connection in the transverse direction in Phase 1 and Phase 2. As shown in the figure, the absolute magnitude of the average curvature at the floor-prop connection was very small

compared to that at the wall-floor connection. Because the props were designed to only provide axial constraint to the floor with little flexural constraint, small bending moments were generated at the floor-prop connection and thus the curvature of the slab was very small at the floor-prop connection.

Simulation of the Slab – Average curvature (transverse direction)

Fig. 6-116 shows a comparison of the average curvature distribution at the wall-floor connection in the transverse direction in Phase 1 of the test with that obtained from "Model-A PFS1" (without props). As shown in the figure, the simulation results underestimated the test results in general. It was noteworthy that because the magnitude of the average curvature in the transverse direction was small, the absolute difference shown in the figure was not large.

Fig. 6-117 shows a comparison of the average curvature distribution at the wall-floor connection in the transverse direction in Phase 2 testing with that from "Model-A PFS1" (with props). As shown in the figure, the simulation provided a reasonable prediction of the test results. Comparing Fig. 6-117 with Fig. 6-116, the simulation results validated the conclusion that the deformation demand on the slab at the wall-floor connection in the transverse direction significantly increased after the props were attached to the floor in Phase 2.

6.4.7 Strain Distribution of the Floor in the Transverse Direction

Strain gages were attached to the transverse rebar to measure the local strains in the floor slab in the transverse direction. The location of the strain gages in the slab close to the wall is shown in Fig. 6-118. Fig. 6-119 through Fig. 6-123 show the cyclic readings of these strain gages. As shown in the figures, the maximum strains in the top rebar measured by SG-FWT-T1, SG-FWT-T2 and SG-FWT-C1 were about 1500 με at 2% drift in Phase 1, indicating that the 3D constraint effect of the floor existed in Phase 1 due to existence of the edge beams. This conclusion was also made when investigating the varied PT forces in the transverse strands (Section 6.4.3.2) and the average curvature distribution of the floor in the transverse direction (Section 6.4.6).

After the props were attached to the slab in Phase 2, the maximum strains in all top rebar were larger than the yield strain of the rebar ($66.5/29000\times10^6 \approx 2290\mu\varepsilon$), indicating that this rebar had yielded. As expected, the 3D constraint effect of the floor became more significant in this phase.

For the strain gages attached to the bottom rebar (SG-FWT-B1 and SG-FWT-B2), it was found that the readings of SG-FWT-B1were much larger than those of SG-FWT-B2. The rebar where SG-FWT-B2 was attached was closer to the center of the wall, where the vertical movement of the wall was small. Therefore, the relative deformation of the slab between the wall and the edge of the slab was also small, resulting in small curvature in the floor and small strains developed in the rebar near the center of the wall.

Because the props were free to rotate in both longitudinal and transverse directions, they provided negligible flexural resistance to the floor. Therefore, it was expected that negligible moments would be generated in the floor slab at the floor-prop connection. The maximum reading of the strain gages attached to the rebar in the slab close to the props was less than 600 με. As expected, none of the transverse rebar in the slab at the floor-prop connection yielded in the test.

6.4.8 Forces in the Props in Phase 2

As discussed in Section 6.4.3 to Section 6.4.7, after props were attached to the floor in Phase 2, the 3D constraint effect of the floor on the wall became significant. A load cell was installed on each prop to measure the force variation.

Fig. 6-124 shows the load cell readings of the four props recorded at different peak drifts in Phase 2. As shown in the figure, the axial loads in the two props on the same side of the floor (east or west) were similar in general. The tensile forces recorded in each prop were about 25% to 50% larger than the compression forces recorded in the same prop. The tensile forces were generated when the portion of the slab connected to the prop was adjacent to the uplifted wall end. On the other hand, the compressive forces were generated when the portion of the slab connected to the prop was adjacent to the compression side of the wall. Because the absolute vertical movement of the slab at the uplifted side of the wall was much larger than that at the compression side of the wall, a

higher constraint effect from the props was generated and thus larger tensile forces were generated in the prop.

As shown in Fig. 6-124, the axial forces in most of the props started to decrease when PFS1 was loaded towards 1.5% drift. As mentioned in Section 6.4.7, yielding of the transverse rebar was initiated at 1.5% drift. Cracks in the floor slab also kept increasing in Phase 2. The moment resistance of the floor may have been reduced due to the increased damage to the floor, causing the decrease of the forces in the props.

By multiplying the axial forces in the prop with the distance between the prop and the wall, the resisting moments on the wall provided by the props in the transverse direction were obtained. It was found that the maximum transverse moment in Phase 2 was about twice the predicted moment resistance of the floor in the longitudinal direction at the wall-floor connection, further demonstrating the significant 3D constraint effect from the floor on the wall.

Because the design of the mega beams was based on the predicted moment resistance of the floor in the longitudinal direction (as discussed in Appendix C), it did not consider the 3D constraint effect of the floor slab. It was expected that larger resistance would be generated in the five missing floors due to constraint in the transverse direction due to the 3D interaction with the surrounding structure (e.g., adjacent columns simulated by the props.

Simulation results of the Slab – Axial forces in the Prop

Fig. 6-125 shows a comparison of the forces in the props recorded at positive peaks in Phase 2 with those from "Model-A PFS1" (with props). As shown in the figure, the simulation provided a reasonable prediction of the tensile forces in the southwest and the northwest props ("Prop_SW" and "Prop_NW"), but it underestimated the compressive forces in the southeast and the northeast props ("Prop_SE" and "Prop_NE"). It was noteworthy that because the magnitude of the compressive forces was small, the absolute difference between the forces recorded in the test and those obtained from the simulation was not significant.

6.4.9 Summary of the Behavior of the Unbonded PT Floor

A large deformation demand on the floor was concentrated at the wall-floor connection in PFS1. On the other hand, the deformation of the floor was evenly distributed at the floor-edge beam connection and the deformation demand was smaller. This conclusion can be deduced by comparing the average curvature distributions across the slab at the wall-floor connection and floor-edge beam connection in Fig. 6-93 and Fig. 6-100, respectively.

The 3D constraint effect of the floor on the wall was noticeable, but not significant in Phase 1 when the constraint from parallel structural systems was small (e.g., simulating adjacent walls rocking in phase with the tested wall). When the constraint from parallel structural systems was large (e.g., simulating adjacent frame columns constraining uplift of the slab), the 3D constraint effect of the slab was more significant (Phase 2). The strands and the rebar placed in the floor slab in the two orthogonal directions at the wall-floor connections should be considered when calculating the overall resisting moment of the floor on the wall.

After describing the behavior of the unbonded PT slab, the behavior of the edge columns and the edge beams is discussed in the next section.

6.5 Behavior of Edge Columns

In this section, damage to the edge columns observed in the test is described first. A detailed description of the behavior of the edge columns, including prestressing forces, lateral deformed shape, base rotation, curvature distribution along the height and confinement effect, is given in Section 6.5.2 through Section 6.5.6.

6.5.1 Damage to the Edge Columns

In Phase 1, flexural cracks were observed in the east edge column at 0.25% drift, as shown in Fig. 6-126. Cracks at an approximate 2 in. spacing were formed in the west edge column at 1% drift, shown in Fig. 6-127. The spacing of the cracks was similar to that of the stirrups in the edge column. Some of the cracks were extended and inclined

shear cracks formed at 1.5% drift, as shown in Fig. 6-128. Initial yielding of the longitudinal rebar in both edge columns occurred at drift levels of approximately 1%. Concrete within a height of 4 in. (half of the column depth) spalled at the corner of the west edge column at 2.5% drift, as shown in Fig. 6-129.

The damage to the edge columns did not change much in Phase 2 and Phase 3. Crushing of the concrete spread and became more severe when PFS1 was under biaxial loading in Phase 4, as shown in Fig. 6-130. It was believed that a large compression force was generated due to the biaxial bending of the edge column. The force concentrated at the corner of the edge column that caused more damage to the edge column.

6.5.2 Prestressing Force in the Edge Columns

High strength threaded rods in the edge columns were post-tensioned to emulate the gravity load from the tributary area of the edge columns. Four strain gages attached to the rods were used to measure the axial force in the rods. This method of using four strain gages to deduce the loads in the rods was validated through a component test before the assemblage test. A conversion factor was directly applied to the data acquisition system to convert the strain gage readings to the load, thus the loads in the rods were directly obtained in the test. The initial PT force in the west and the east edge columns was 24.9 and 26.5 kips, respectively.

The nominal yield strength of the 3/4 in. threaded rod was approximately 35 kips. It was obtained by multiplying the nominal yield stress (105 ksi) of the rod by the stressed cross-sectional area 0.334 in^2. Because the PT loads increased during the test due to the deformation of the edge columns, the strain gage readings were only reliable until the rods had yielded.

Fig. 6-131 shows the axial force in the east edge column versus lateral displacement of PFS1 in Phase 1. As shown in the figure, a sudden increase in PT force occurred when PFS1 was loaded to -0.75% drift (to the west). The force recorded before the sudden increase was 32.4 kips that was close to the nominal yield strength of the threaded rod. It was believed that the PT rod in the east edge column yielded at this drift level.

Fig. 6-132 shows the axial force in the west edge column versus lateral wall displacement in Phase 1. A sudden increase in PT force occurred when PFS1 was loaded to 1% drift (to the east). The force recorded before the sudden increase was 32.8 kips. It was believed that the PT rod in the west edge column yielded at this drift level.

For the two edge columns, the PT forces that emulated the gravity load from tributary areas of the floor increased about 25% to 30% (6 to 8 kips) when yielding of the threaded rods occurred. Although the increase percentage was noticeable, it was found that the absolute increased force would only generate an average stress of 0.06 to 0.08 ksi over the entire cross section of the edge column. Therefore, the increased PT force in the threaded rods did not have a great impact on the behavior of the edge columns. The gravity loads from the tributary areas of the floor were well simulated by using the PT threaded rods in the test.

6.5.3 Lateral Deformed Shapes of the Edge Columns

As shown in Fig. 4-1, three string pots (SP10-EC1, SP10-ECEB and SP2-ECBASE) were mounted along the height of the 1st story east edge column to monitor its deformed shape. Fig. 6-133 and Fig. 6-134 show the deformed shapes of the east edge column in Phase 1 and Phase 2, respectively. As expected, the east edge column was subjected to a mode of flexural bending.

SP2-ECBASE was mounted at the base of the edge column, thus the readings of SP2-ECBASE can be used to examine whether shear sliding at the column base occurred in the test. Fig. 6-135 shows the cyclic readings of SP2-ECBASE recorded in the test. As shown in the figure, the maximum horizontal movement at the column base was only 0.045 in. at 5% drift in Phase 3, indicating that shear sliding of the edge column did not occur throughout the test.

6.5.4 Rotation and Average Curvature of the Edge Columns

As shown in Fig. 4-2, LVDTs and string pots were mounted at the bottom and the top of the east edge column to measure the rotation at each end. Only the readings of the LVDTs mounted at the base of the east edge column, where damage occurred and large

curvatures were developed, were used for data analysis in the following. The method to calculate the rotations of the edge column through LVDT readings is discussed in Section 4.2.2.2.

Fig. 6-136 shows the rotation at the base of the east edge column versus the lateral displacement of PFS1. In the figure, clockwise rotations as viewed from the south of the specimen represented positive rotations, when the LVDT on the west side of the edge column had positive readings and the other LVDT on the east side of the edge column had negative readings.

Similarly, LVDTs were also used for the west edge column. Fig. 6-137 shows the rotation at the base of the west edge column. Comparing Fig. 6-136 with Fig. 6-137, the rotations of the two edge columns were similar at the base in the test.

The average curvature of the edge column was obtained by dividing the rotation of the edge column with the gage length of the LVDTs (6-1/4 in. for the east edge column and 6 in. for the west edge column). Fig. 6-138 and Fig. 6-139 show the average curvatures at the base of the east and the west edge column, respectively.

Simulation results of average curvature at the base of edge columns

Fig. 6-140 and Fig. 6-141 show a comparison of the average curvature at the base of the east and the west edge columns at positive peaks in Phase 1 in the test with those obtained from "Model-A PFS1" (without props). As shown in the figures, the simulation results matched well with the test results.

6.5.5 Curvature Distribution in the Edge Columns

As shown in Fig. 4-4 and Fig. 4-5, multiple groups of strain gages were attached to the rebar in the edge columns to monitor local curvature distribution in the edge columns. Fig. 6-142 and Fig. 6-143 show the local curvature distributions along the height of the edge columns with respect to the lateral drift of PFS1 for the east and the west edge columns, respectively. The average curvatures deduced from the LVDT readings (described in Section 6.5.4) were superimposed in the two figures as well. As shown in the figures, the average curvatures deduced from the LVDTs were larger than the local

curvatures obtained from the strain gages because the curvatures deduced from the LVDTs included the concentrated deformation at the column-base block interface.

6.5.6 Confinement Effect of the Edge Column

Fig. 6-144 through Fig. 6-146 show the cyclic readings of the strain gages attached to the stirrups recorded in Phase 1 through Phase 3. The three gages (WCOL_T1/T2/T3) were attached to the stirrups that were 2 in., 7-7/8 in. and 12 in. above the base of the edge column, respectively. As shown in the figures, the readings from WCOL_T1 were much larger than those of WCOL_T2 and WCOL_T3, indicating that the steel confinement might only have been effective close to the base of the edge column. As discussed in Section 6.5.1, concrete spalling of the edge column was observed at about 4 in. above the base. The damaged region was close to the expected plastic hinge region (half depth of the edge column). The stirrup where WCOL_T1 was attached was the only one within the plastic hinge region where the compressive strains developed in the concrete were high and the steel stirrups were more effective.

6.6 Behavior of Steel Mega Beams and Steel Columns

Because there was only one story floor slab constructed in PFS1, steel mega beams were used to simulate the constraint effect on the wall that would be provided by the five "missing" floor slabs in the "six-story" assemblage. The mega beams featured pinned connections at the ends to transmit shear and special dogbone-shaped cover plates to create a tension-compression force couple to simulate the predicted total moment resistance of the five floor slabs it was simulating. A detailed description of the mega beam is given in Section 3.3.3. Fig. 6-147 and Fig. 6-148 summarize the instrumentation on the east and the west mega beam used for data analysis, including the strain gages attached to the cover plates, the LVDTs and tiltmeters installed at the beam-wall and the beam-column connection.

In this section, damage to the mega beams is described first, followed by the data analysis of the mega beams and the associated results from the numerical models.

6.6.1 Damage to the Mega Beams

During the test, it was observed that damage to the mega beams concentrated in the cover plates, which were subjected to cyclic tension and compression. According to the results of the component test of the mega beam (discussed in Section 5.5.1), the cover plates were expected to yield at 0.5% drift.

Table 6-4 lists the drift levels when the PFS1 mega beam cover plates were observed to yield. The findings were based on the strain gage readings from gages attached to the cover plates. As shown in the table, the cover plates of the west mega beam yielded at 0.25% to 0.5% drift, and those of the east mega beam yielded at -0.5% to -1% drift. Therefore, the east mega beam did not perform as expected. It was believed that the cover plates of the east mega beam, especially at the beam-wall connection, provided less moment resistance to the wall when PFS1 was loaded in the negative direction (to the west), which caused the smaller strength of PFS1 in the negative loading direction. The moment resistances provided by the east and the west mega beam are further discussed in this section through numerical simulations.

Buckling of some cover plates was observed after the cover plates had yielded. Fig. 6-149 shows the buckling of the cover plate of the west mega beam at 1% drift in Phase 1. After cycles of tension (yielding) and compression (buckling), large local plastic strains accumulated in the cover plates and eventually caused the fracture. Fig. 6-150 shows the fracture of the cover plate of the west mega beam at 1.5% drift in Phase 2.

6.6.2 Relative Rotations of the Mega Beams

As shown in Fig. 6-147, a pair of LVDTs was mounted at the beam-wall and the beam-column connection of the east mega beam. The method to calculate the rotations at the connections by using the LVDT readings is discussed in Section 4.3.2.1. Fig. 6-151 shows the relative rotation of the east mega beam at the beam-wall (“East mega beam@Wall”) and the beam-column (“East mega beam@Column”) connection in Phase 1. As shown in the figure, the relative rotations at the beam-wall and the beam-column connections were generally smaller when PFS1 was loaded in the positive direction (to

the east) than those when PFS1 was loaded in the negative direction (to the west). The reason is explained below.

Fig. 6-152 shows a comparison of the relative rotations of the east mega beam at the beam-wall connection in the negative and the positive loading direction. As shown in Fig. 6-152(a), the relative rotation consists of the rotation of wall and that of the east mega beam that is generated due to the uplift of the wall. On the other hand, as shown in Fig. 6-152(b), the rotation of the east mega beam is negligible and only the rotation of wall contributes to the relative rotation at the beam-wall connection, because the vertical movement of the wall is negligible in the compression side. Therefore, the relative rotation of the east mega beam at the beam-wall connection was always smaller when PFS1 was loaded in the positive direction (to the east).

There were no LVDTs installed on the west mega beam due to the limited amount of LVDTs. Instead, tiltmeters were installed on the west mega beam (TBWSB) and west steel column (TBWSC), as shown in Fig. 6-148. The method to calculate the relative rotation of the west mega beam at the beam-column connection using tiltmeter readings is discussed in Section 4.3.2.1.

There was also a tiltmeter attached to the top portion of the wall the wall (TTW). Because the body of the mega beam (W10×30) was pinned-pinned connected at both ends as shown in Fig. 3-34, it was assumed that it rotated like a rigid body. The rotation on the west side of the mega beam, which was measured by the tiltmeter TBWSB, was close to that on the east side of the mega beam. This assumption would be further discussed below with the test data. By subtracting the readings of TBWSB with those of the tiltmeter TTW, the rotations of the west mega beam at the beam-wall joint was also obtained.

Fig. 6-153 shows the relative rotation of the west mega beam. As expected, the relative rotations of the west mega beam at the beam-wall and the beam-column connection were always smaller when PFS1 was loaded in the negative direction (to the west).

Fig. 6-154 shows a comparison of the rotations at the beam-wall connection of the east mega beam with those of the west mega beam. As shown in the figure, the magnitude of the rotations of the east mega beam in the negative (positive) loading direction were

similar to those of the west mega beam in the positive (negative) loading direction. For example, the rotations of the east mega beam were -0.005 and -0.023 rad at -0.25% and -1% drift, and the rotations of the west mega beam were at 0.004 and 0.023 at 0.25% and 1% drift. Therefore, the assumption that the rotation on the west side of the west mega beam (measured by the tiltmeter TBWSB) was close to that on the east side of the west mega beam seemed reasonable.

Fig. 6-155 shows a comparison of the rotations at the beam-column connection of the east mega beam with those of the west mega beam. Again, the magnitude of the rotations of the east mega beam in the negative (positive) loading direction is similar to that of the west mega beam in the positive (negative) loading direction.

Simulation results of relative rotations of the mega beams

Fig. 6-156 shows a comparison of the relative rotations of the mega beams recorded at positive peaks of different drifts in the test with those obtained from "Model-A PFS1" (without props). In the figure, "Test results_West mega beam@Wall" and "Test results_East mega beam@Wall" represent the rotations of the west and the east mega beam at the beam-wall connection. "Simulation_West mega beam@Wall" and "Simulation_East mega beam@Wall" represent the results obtained from the numerical model. As shown in the figure, the results of the numerical model matched well with the experimental response, indicating that the model successfully predicted the deformation demands on the beam-wall connections of both mega beams. Similar results were obtained for the beam-column connections of both mega beams as well.

As described in Section 5.5.1, the validated numerical model of the mega beams was expected to provide a good prediction of the moments generated in the mega beams as a function of the measured rotations. The numerical model "Model-A PFS1" predicted rotations that matched well with those measured in the tests at the same drift levels. Consequently, it was expected that the moment resistances predicted by the model in the beam-wall and the beam-column connections would be similar to those developed in the test. This prediction was found valid at the beam-wall and the beam-column connections on the west side of the wall, but not at the beam-wall connection on the east side of the

wall. This is discussed in the next section when the readings of the strain gages attached to the cover plates are analyzed to determine the moments.

6.6.3 Strains in the Cover Plates of the Mega Beams

Strain gages were attached to the cover plates of the mega beams to measure the axial strains developed in the test. The location of the strain gages is shown in Fig. 6-147 and Fig. 6-148. Because the strain gage readings became unreliable after the cover plates had yielded, only the readings recorded before yielding of the cover plates were used for data analysis in the following.

Fig. 6-157 shows the strains developed in the cover plates of the west mega beam at small drift levels. In the figure, the curves "West mega beam BOTTOM@Wall" represent the readings from SG_WBWBP_M, which was attached to the bottom cover plate of the west mega beam adjacent to the wall; the curves "West mega beam BOTTOM@Column" represent the readings from SG_WBCBP_M, which was attached to the bottom cover plate of the west mega beam adjacent to the steel column. Similar nomenclature is used for the other curves in Fig. 6-157 and Fig. 6-158.

As shown in the figure, the absolute strains in the bottom and the top cover plates at the beam-column connection ("West mega beam BOTTOM@Column" and "West mega beam TOP@Column") were similar and increasing when PFS1 was loaded to larger drifts in both loading directions. The absolute strains in the top cover plate at the beam-wall connection ("West mega beam TOP@Wall") were slightly larger than those in the bottom cover plate ("West mega beam BOTTOM@Wall") in both loading directions, but the difference was not large. The tensile/compressive stresses in the top cover plate and the compressive/tensile stresses in the bottom cover plate formed the resisting moments at the beam-wall and the beam-column connection. The results were similar to those expected from the component test (discussed in Section 5.5.1).

Fig. 6-158 shows the strains that developed in the cover plates of the east mega beam at small drift levels. As shown in the figure, the absolute strains in the bottom and the top cover plate at the beam-column connection ("East mega beam BOTTOM@Column" and

"East mega beam TOP@Column") were similar and increasing when PFS1 was loaded to larger drifts in both directions, which was as expected.

The absolute strains in the top cover plate ("East mega beam TOP@Wall") were slightly larger than those in the bottom cover plate ("West mega beam BOTTOM@Wall") in the positive loading direction, but the difference was small. However, abnormal behavior was observed in the negative loading direction. Very small strains developed in both bottom and top cover plates at the beam-wall connection, especially in the bottom cover plate. Because of this abnormal behavior, it was believed that the resisting moment generated by the east mega beam at the beam-wall connection in the negative loading direction was very small. It was noteworthy that this abnormal behavior was observed in association with the east mega beam from the beginning of the test, which might be the main cause of the lower strength of PFS1 in the negative loading direction throughout the test.

Simulation results of the strains in the cover plates

Fig. 6-159 shows a comparison of the strains in the top cover plate of the west and the east mega beam at the beam-column connection with those obtained from "Model-A PFS1" (without props). In the figure, "Test results_SG_WBCTP_M" represents the strains in the top cover plate of the west mega beam at the beam-column connection in the positive loading direction, when the west mega beam was connected to the uplift side of the wall. "Test results_SG_EBCTP_M" represents the strains in the top cover plate of the east mega beam at the beam-column connection in the negative loading direction, when the east mega beam was connected to the uplift side of the wall. "Simulation_Expected result" represents the strains in the top cover plate of the mega beam that was connected to the steel column obtained from "Model-A PFS1" (Without props).

Fig. 6-160 shows a comparison of the strains in the bottom cover plate of the west and the east mega beam at the beam-column connection with those obtained from "Model-A PFS1" (without props). In the figure, "Test results_SG_WBCBP_M" represents the strains in the bottom cover plate of the west mega beam at the beam-column connection in the positive loading direction, when the west mega beam was connected to the uplift

side of the wall. “Test results_SG_EBCBP_M” represents the strains in the bottom cover plate of the east mega beam at the beam-column connection in the negative loading direction, when the east mega beam was connected to the uplift side of the wall.. “Simulation_Expected result” represents the strains in the bottom cover plate of the mega beam that was connected to the steel column obtained from “Model-A PFS1” (Without props).

The behavior of the east mega beam was approximately symmetrical to that of the west mega beam at the beam-column connection. As shown in Fig. 6-159 and Fig. 6-160, the strains measured in the top and bottom cover plates of the west mega beam were very close to those measured in the respective top and bottom cover plates of the east mega beam, when the west/east mega beam was on the uplift side of the wall. The strains in the cover plates predicted by the numerical model “Model-A PFS1” slightly underestimated the test results, but the difference was small. It indicated that the moment resistance in the beam-column connection on both the west and the east side of the wall in the numerical model would be close to that generated in the test. The design purposes of the mega beams were realized in the beam-column connections for both the west and the east mega beam.

Fig. 6-161 shows a comparison of the strains in the top cover plate of the west and the east mega beam at the beam-wall connection with those obtained from “Model-A PFS1” (without props). In the figure, “Test results_SG_WBWTP_M” represents the strains in the top cover plate of the west mega beam at the beam-wall connection in the positive loading direction, when the west mega beam was connected to the uplift side of the wall. “Test results_SG_EBWTP_M” represents the strains in the top cover plate of the east mega beam at the beam-wall connection in the negative loading direction, when the east mega beam was connected to the uplift side of the wall. “Simulation_Expected result” represents the strains in the top cover plate of the mega beam that was connected to the uplift side of the wall obtained from “Model-A PFS1” (Without props).

Fig. 6-162 shows a comparison of the strains in the bottom cover plate of the east and the west mega beam at the beam-wall connection with those obtained from “Model-A PFS1” (without props). In the figure, “Test results_SG_WBWBP_M” represents the

strains in the bottom cover plate of the west mega beam at the beam-wall connection in the positive loading direction, when the west mega beam was connected to the uplift side of the wall. “Test results_SG_EBWBP_M” represents the strains in the bottom cover plate of the east mega beam at the beam-wall connection in the negative loading direction, when the east mega beam was connected to the uplift side of the wall. “Simulation_Expected result” represents the strains in the bottom cover plate of the mega beam that was connected to the uplift side of the wall obtained from “Model-A PFS1” (Without props).

For the west mega beam, the top cover plate of the west mega beam at the beam-wall connection yielded earlier in the test than was predicted by the model as shown in Fig. 6-161. As shown in Fig. 6-162, the strains in the bottom cover plate developed in the test were slightly larger than those predicted by the numerical model. Under this circumstance, it was expected the moment resistance in the beam-wall connection on the west side of the wall in the numerical model was slightly larger than that generated in the test. The design purpose of the west mega beam was realized.

For the east mega beam, the strains that developed in the top cover plate of the east mega beam at the beam-wall connection in the test were smaller than those predicted by the model as shown in Fig. 6-161. As shown in Fig. 6-162, the strains in the bottom cover plate of the east mega beam developed in the test were nearly zero, which were much smaller than those predicted by the numerical model. Under this circumstance, it was expected the moment resistance in the beam-wall connection on the east side of the wall was very small when PFS1 was loaded in the negative direction in the test. The design purpose of the east mega beams was not realized for this case. This observation further validated that the lower strength of PFS1 in the negative direction was mainly caused by the ineffectiveness of the east mega beam. This is consistent with the conclusion in Section 6.1.1 where Model-C investigated the removal of the two cover plates of the east mega beam connected to the wall, assuming that there was no moment resistance provided by the east mega beam. The strength of that model was consistent with that obtained for the negative loading direction; whereas the results of Model-A, with intact

cover plates was consistent with the strength of the specimen loaded in the positive direction.

The ineffectiveness of the east mega beam in the negative loading direction might have been caused by the connectivity between the steel beam and the concrete wall. As mentioned in Section 3.4.11, the west mega beam tightly fit in between the wall and the west steel column during the construction, but the east mega beam was installed between the wall and the east steel column without difficulty. The east mega beam turned out to be only functional in one loading direction under this condition.

6.6.4 Behavior of Steel Columns

The two steel columns remained elastic throughout the test. Six strain gages were attached to the top and the bottom of the east steel column. They can be used to deduce the axial forces and shear forces in the east steel column, as discussed in Section 4.3.3.

Fig. 6-163 and Fig. 6-164 show the axial force and shear force in the east steel column versus the lateral displacement of PFS1, respectively. Based on force equilibrium at the mega beam-steel column joint, the shear forces and the axial forces in the mega beam were equal to the axial forces and the shear forces in the steel column, respectively. Therefore, the shear forces and the axial forces of the east mega beam were obtained as well.

6.7 Conclusions from the Data Analysis of PFS1

The interaction between a PreWEC system and the surrounding structure was investigated in a structural assemblage that included a CIP unbonded PT floor, CIP RC edge columns, and a set of props that could be included/excluded to simulate the constraint effect of adjacent columns as opposed to adjacent PreWEC systems. The specimen (PFS1) was designed to investigate the upper bound interaction between the PreWEC system and the surrounding structure. The structure was tested quasi-statically to lateral drifts in excess of 5%. The conclusions derived from the test and the numerical simulations are as follows.

1. PFS1 that incorporated the PreWEC system and rigid-connected surrounding structure exhibited good seismic response with excellent energy dissipation and reasonable self-centering characteristic. The energy dissipation capacity of PFS1 was more than three times larger than that predicted by the numerical model of the isolated PreWEC system. The source of the increased energy dissipation was the interaction of the surrounding structure. The damage to the surrounding structure only slightly compromised the self-centering capability of the PreWEC system. The interaction between the PreWEC system and the surrounding structure is an important factor to be considered in determining the seismic performance of rocking-wall structures.

2. By comparing the test results of PFS1 with those from the numerical model of the isolated PreWEC system, it was found that the base shear of the PreWEC system in PFS1 was increased by 26% due to the wall-floor interaction at 2% design drift, which should be considered in design to avoid shear sliding of the wall.

3. Minor damage occurred to the fiber grout that was weaker than the concrete in the wall. Because the grout was confined in a pocket in the base block, the damage to the grout was not significant and the grout was reusable after the test. The N.A. depth of the wall was extended because of the weaker fiber grout. The strain demand on the boundary elements of the wall was reduced, thus little damage occurred to the wall until 3% drift.

4. When the grout was weaker than the concrete in the wall, large compressive strains still developed in the wall at large drift levels (4% and 5%). Using confinement reinforcement in the wall corners would be necessary if the wall was required to perform well after large seismic events. It was found that the compressive strains in the wall corners decreased rapidly along the height of the wall and the steel stirrups were only effective within 10 in. above the base of the wall in the test. Therefore, it might be more economical to place the steel confinement over a relatively small distance in the boundary element of the wall.

5. The rotation caused by the flexural bending of the wall represented approximately 10% of the total rotation of the wall when PFS1 was loaded to 2% design drift. Rigid body motion was the predominant lateral movement mode of the lightly post-tensioned rocking wall panel.

6. Debris of the over-poured grout and the concrete cover that spalled off the surface of the wall became trapped in the pocket of the base block. The residual PT force in the strands increased because the total length of the strands increased due to the debris. In the case of the full-scale prototype structure, the impact from the debris would be less significant because of the larger unbonded length of the PT strands.
7. Localized damage occurred in the floor slab adjacent to the wall ends. The deformation demand on the slab was concentrated at the wall-floor connection. Because the deformation demand on the slab was uniformly distributed at the floor-edge beam connections, there were only parallel cracks in the floor that occurred at the floor-edge beam interface.
8. After the localized damage to the floor adjacent to the wall ends developed, the floor became "self-debonded" from the wall and the damage did not aggravate or spread. Structural integrity of the floor was maintained because of the intact unbonded PT strands and the transverse shear-friction reinforcement. Because the strands were lightly prestressed due to scaling (larger area of strands prestressed to lower initial strains than typical), the strands remained elastic throughout the test and most cracks in the floor were observed to close at the conclusion of testing.
9. The adjacent structural systems, which were emulated by the props in the test, had little impact on the increase in PT force of the longitudinal strands in the slab. On the other hand, there was a large increase in PT force of the transverse strands in the slab due to the flexural deformation of the floor when the props were attached.
10. Because of the existence of edge beams, the 3D constraint effect of the floor slab on the rocking wall was noticeable but not very significant when there was no transverse constraint on the slab (i.e., without props, when simulating the case of parallel PreWEC systems in phase). When the parallel structural system contained frame columns, emulated by the props, the 3D constraint effect of the slab became more significant. Deduced from the axial forces recorded in the props, the maximum transverse moment resistance of the floor was about twice the predicted moment resistance of the floor in the longitudinal direction at the wall-floor connection.

11. Because the 3D constraint effect of the floor slab was not considered in the design of the mega beams, it was expected that larger resistance to the wall would be generated by the missing five floors in the prototype building. Therefore, it is recommended that the strands and the rebar placed in the floor slab in the two orthogonal directions at the wall-floor connections should be considered in calculating the overall resisting moment of the floor on the wall, especially when there is constraint close to the wall in the transverse direction in the building.

12. Although the PT forces in edge columns that emulated the gravity load from tributary areas increased about 25% to 30% in the test due to the lateral deformation of the edge columns, the corresponding increase in stress was not large in the cross section of the edge column. The gravity loads from the tributary areas of the floor were well simulated by using the PT threaded rods in the test. A plastic hinge region that was about 4 in. high (half of the column depth) formed at the base of the edge column, where damage was concentrated, large curvature was developed and confinement reinforcement was engaged in that region.

Table 6-1 PT forces and prestress level at the test date

	E–W longitudinal direction				N–S transverse direction			
	FPTW1	FPTW2	FPTW3	FPTW4	FPTSE1	FPTSE2	FPTSE3	FPTSE4
PT (*kips*)	7.6	7.0	6.1	5.4	8.7	8.1	12.1	9.7
Stress (*ksi*)	93.4	86.0	74.7	66.4	109.4	101.3	151.3	121.3
σ_s / f_{pu}^*	0.37	0.34	0.30	0.27	0.44	0.41	0.61	0.49

* $\sigma_s = F_s/A_{st}$, where A_{st} is the area of the strand (0.0813 in^2 in longitudinal strands and 0.0798 in^2 in the transverse strands according to the mill of certification). f_{pu} is the nominal strength of PT strands (250 *ksi*).

Table 6-2 Percentage increase in PT force (longitudinal direction)

Drift levels and Phases	E–W longitudinal direction (kips)			
	FPTW1	FPTW2	FPTW3	FPTW4
Phase 1@2%	25%	30%	37%	27%
Phase 2@2%	23%	27%	38%	33%
Phase 3@5%	50%	52%	76%	76%

Table 6-3 Percentage increase in PT force (transverse direction)

Drift levels and Phases	N–S transverse direction (kips)			
	FPTSE1	FPTSE2	FPTSE3	FPTSE4
Phase 1@-2%	3%	2%	2%	1%
Phase 2@-2%	15%	15%	9%	11%
Phase 3@-5%	11%	14%	15%	14%

Table 6-4 Drift levels when the cover plates of mega beams yielded

Steel beam	East mega beam (%)				West mega beam (%)			
Connection	Beam-wall		Beam-column		Beam-wall		Beam-column	
Cover	Top	Bottom	Top	Bottom	Top	Bottom	Top	Bottom
Yield*	-1.0	-0.75	-0.5	-0.5	0.25	0.5	0.5	0.25

* The yielding of all the cover plates happened in Phase 1.

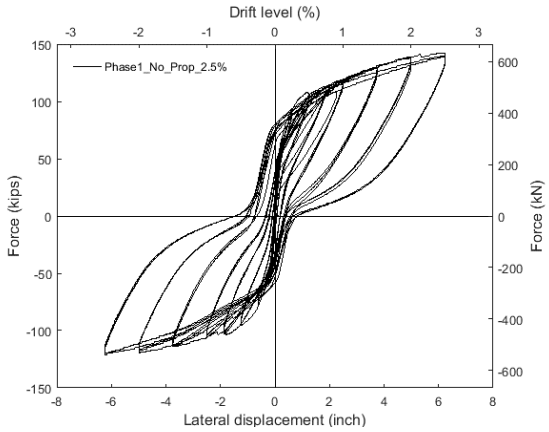

Fig. 6-1 Force-displacement response of PFS1 in Phase 1

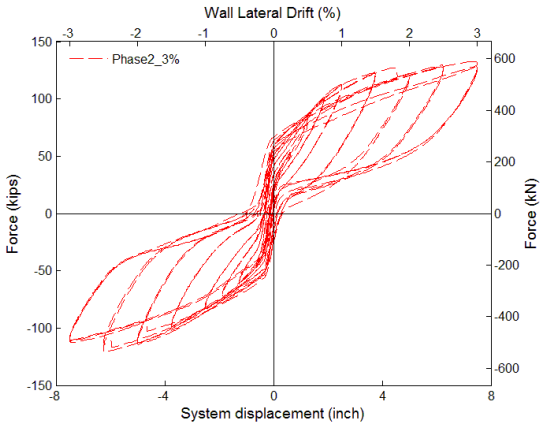

Fig. 6-2 Force-displacement response of PFS1 in Phase 2

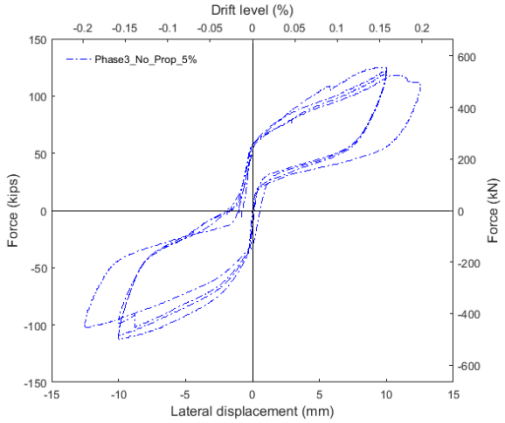

Fig. 6-3 Force-displacement response of PFS1 in Phase 3

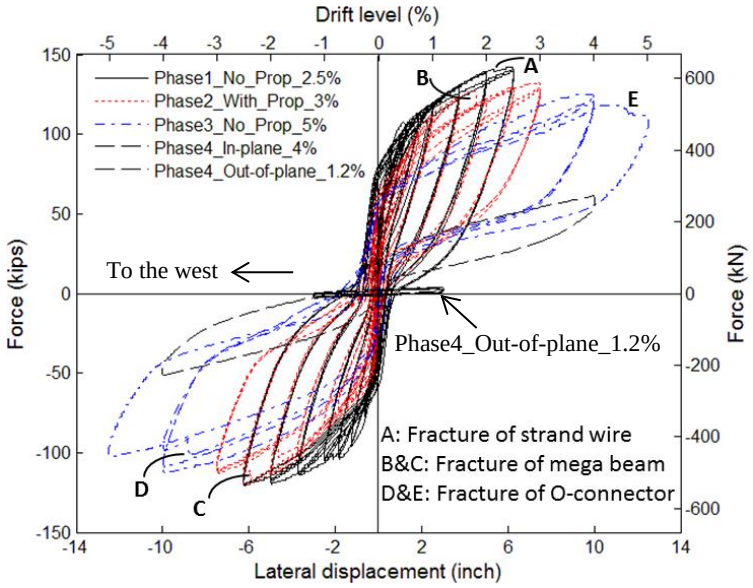

Fig. 6-4 Complete force-displacement response of PFS1 recorded in the test and the pushover curve of the isolated PreWEC system obtained from "Simulation_Model-B Isolated PreWEC"

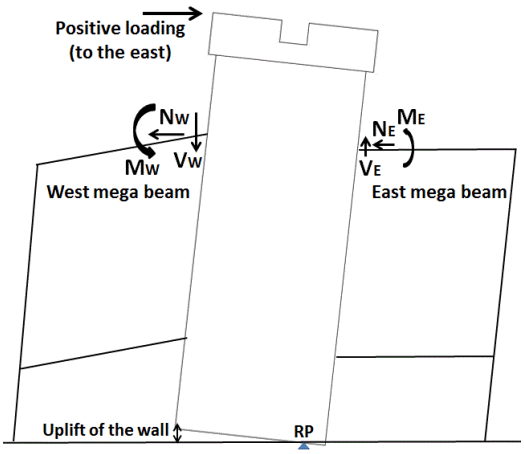

Fig. 6-5 Illustration of the resistances provided by the west and the east mega beam

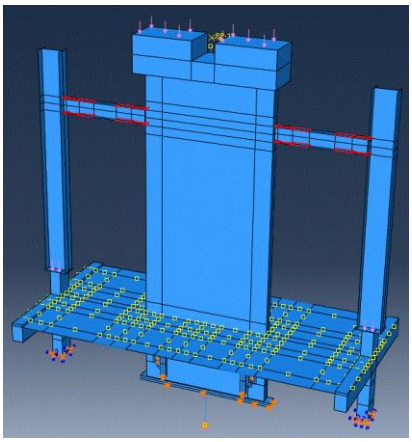

(a) Model-A of PFS1 (without props)

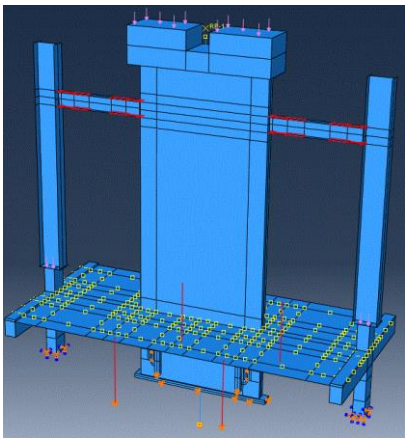

(b) Model-A of PFS1 (with props)

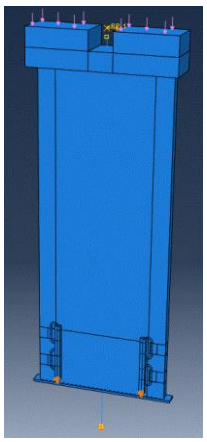

(c) Model-B of the isolated PreWEC system

Fig. 6-6 Numerical models built for PFS1 and the isolated PreWEC system

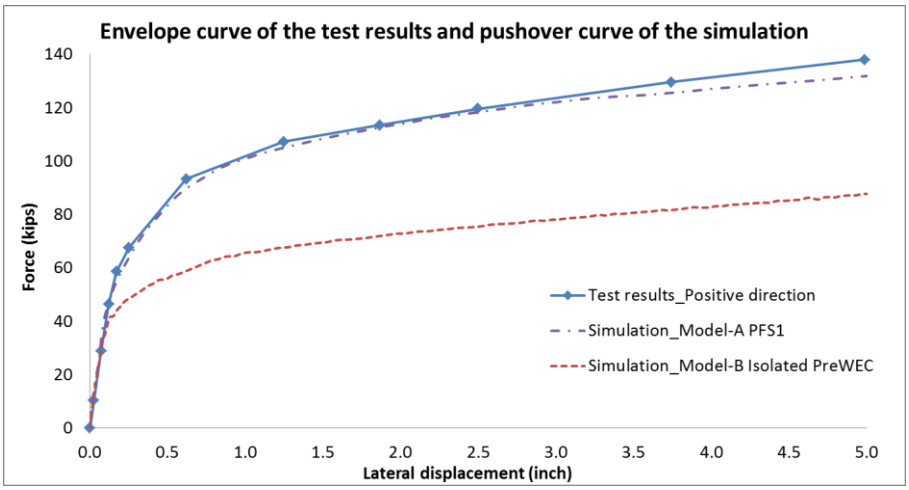

Fig. 6-7 Comparison of the envelope curve of PFS1 in the test and the pushover curves of PFS1 and the isolated PreWEC system obtained from the numerical models

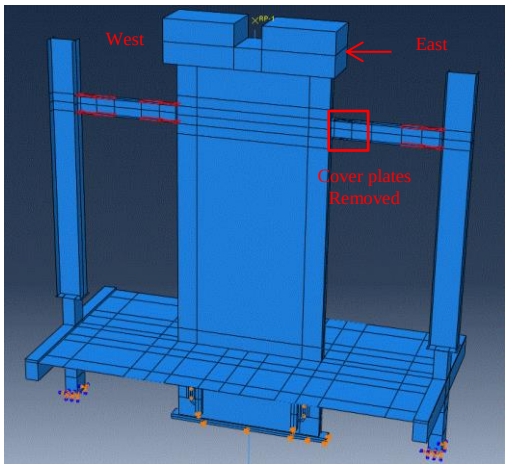

Fig. 6-8 Model-C for PFS1 (the cover plates of the east mega beam close to the wall removed)

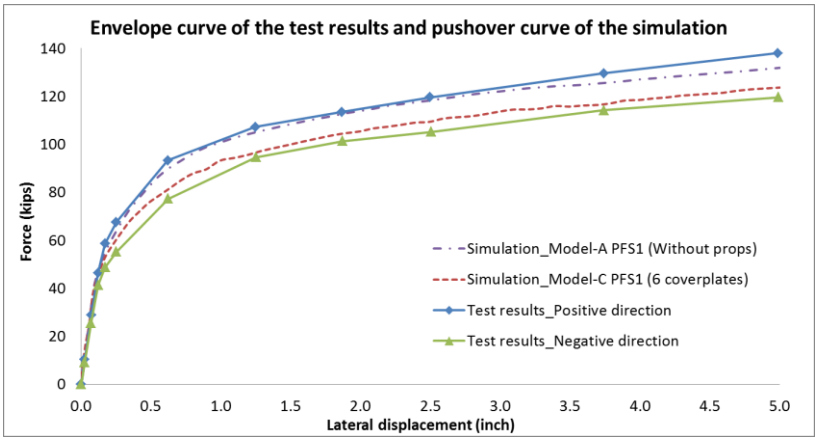

Fig. 6-9 Comparison of the envelope curves of PFS1 in both loading directions in the test with the pushover curves from Model-A and Model-C

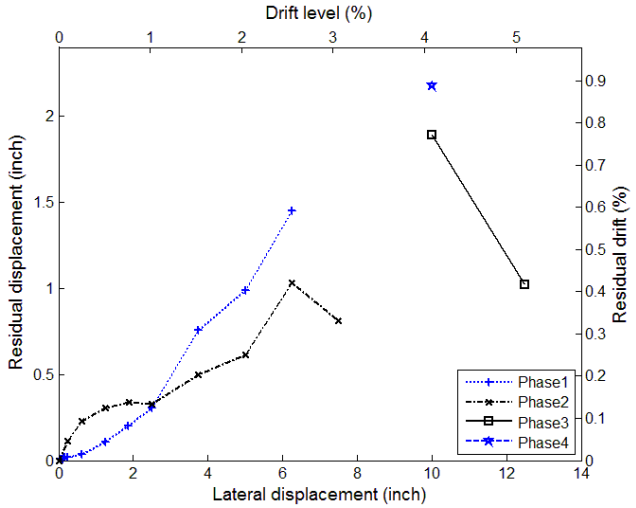

Fig. 6-10 Residual displacements/drifts of PFS1 at the "zero load" position following the last cycle of different drift levels

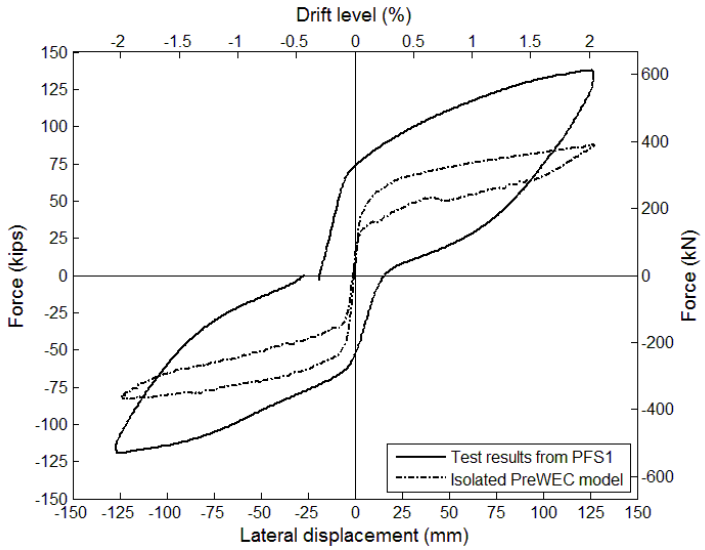

Fig. 6-11 Comparison of the force-displacement response of PFS1 with that obtained from the numerical model of the isolated PreWEC system at a 2% drift cycle

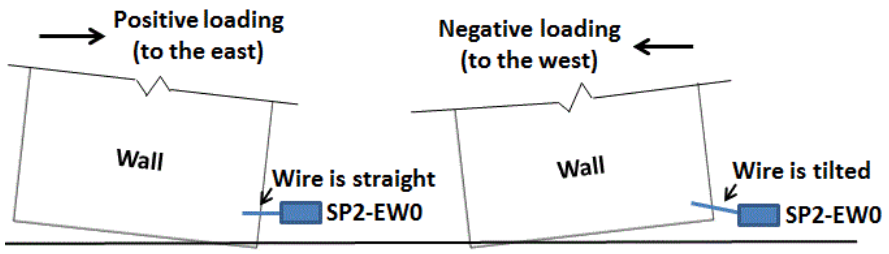

Fig. 6-12 Illustration of the measurement by SP2-EW0 in different loading directions

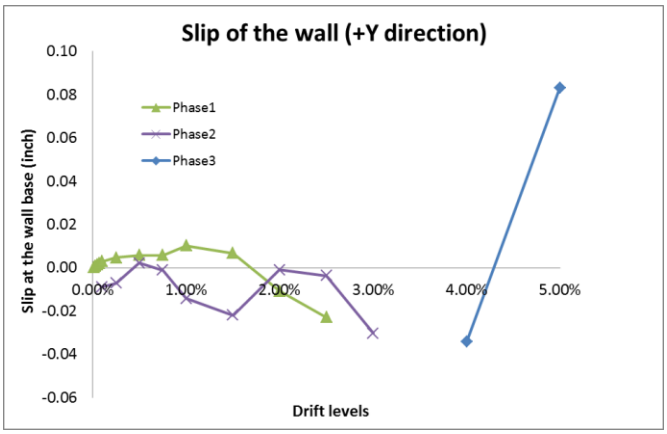

Fig. 6-13 Readings of SP2_EW0 (at the base of the wall) at positive peaks of different drift levels

Fig. 6-14 First vertical crack in the fiber grout recorded at -0.25% drift

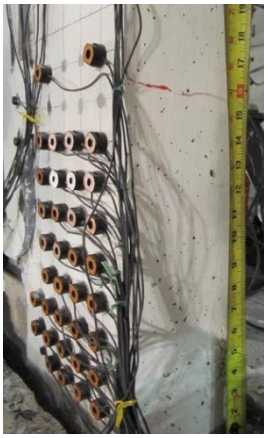
Fig. 6-15 Tensile cracks in the east surface of the wall when PFS1 was loaded to the west


Fig. 6-16 Condition of the fiber grout beneath the west wall corner at 2% drift in Phase 1

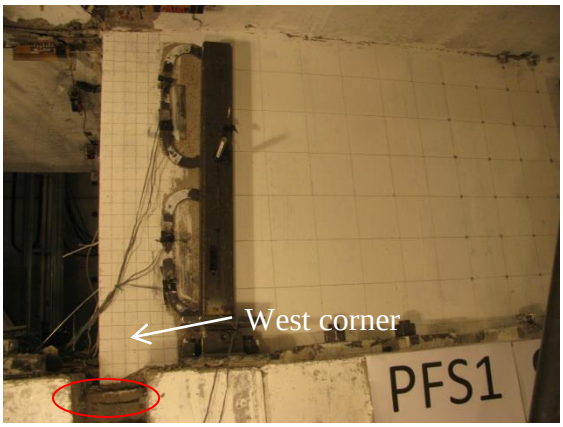

Fig. 6-17 Damage to the fiber grout beneath the west corner of the wall at the end of Phase 3

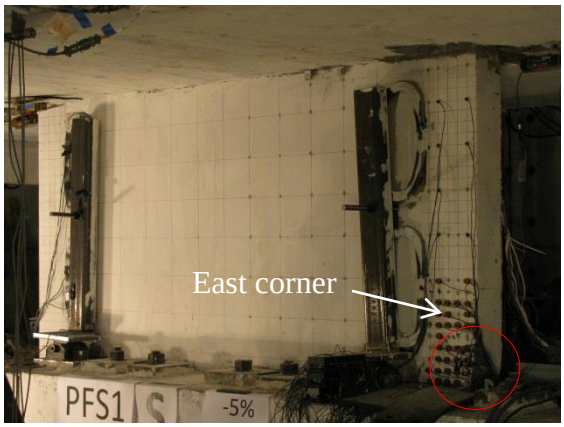

Fig. 6-18 Damage to the east wall corner at the end of Phase 3

Fig. 6-19 Condition of the east wall corner after the test

Fig. 6-20 Condition of the west wall corner after the test

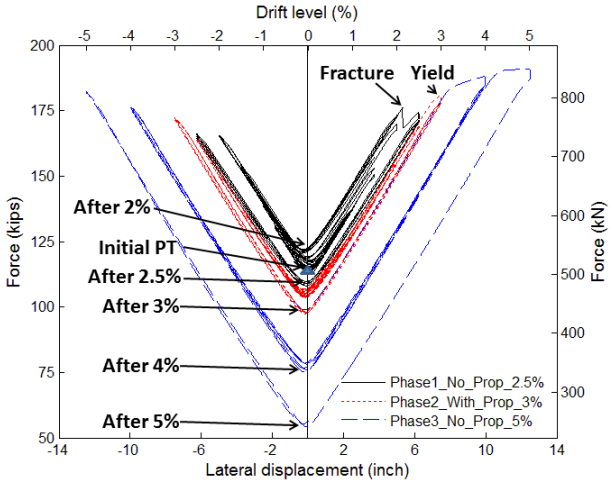

Fig. 6-21 PT force – lateral displacement response of the wall

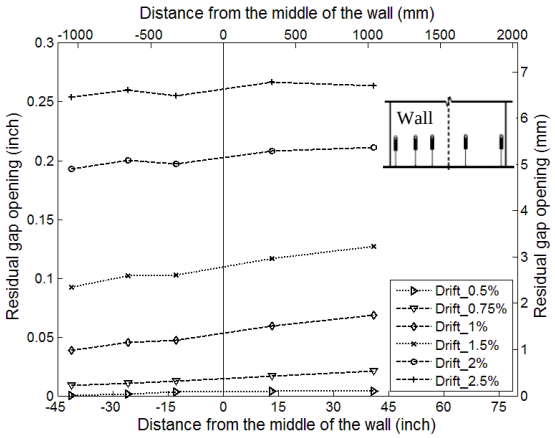

(a) Residual gap opening at positive peaks of different drifts

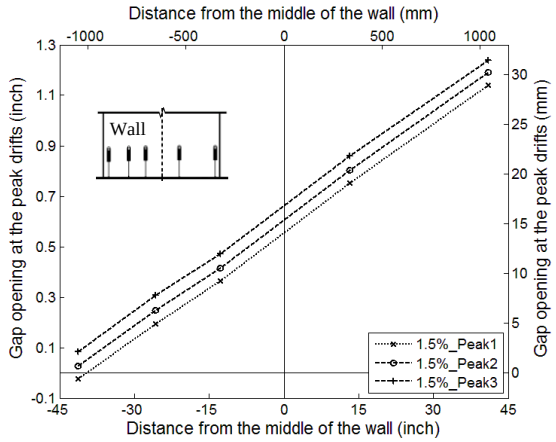

(b) Gap opening at the peak displacement in each cycle to 1.5% drift

Fig. 6-22 Readings of the LVDTs that measure the gap opening of the wall in Phase 1

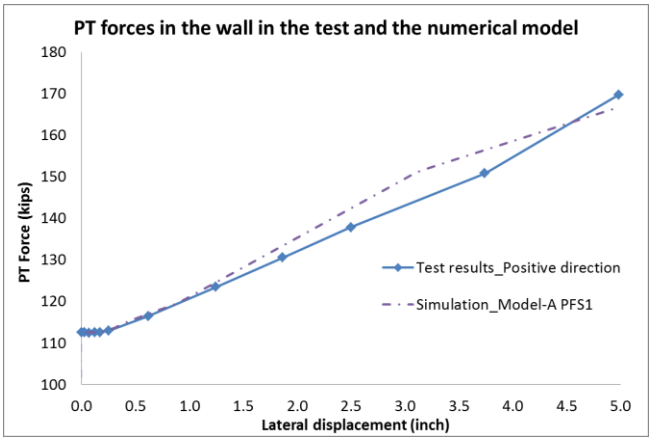

Fig. 6-23 Comparison of the PT forces recorded in the test with those obtained from "Model-A PFS1" (without props)

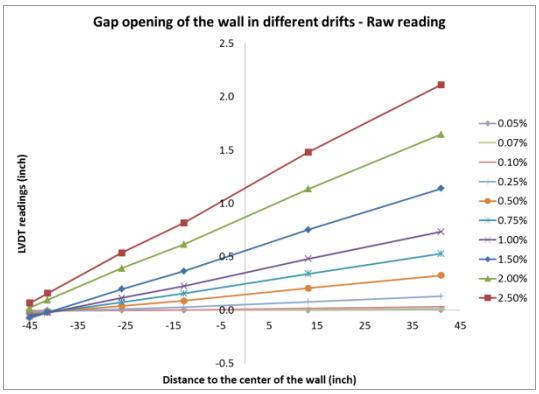

Fig. 6-24 Readings of the LVDTs at wall/base block interface at positive peaks in Phase 1

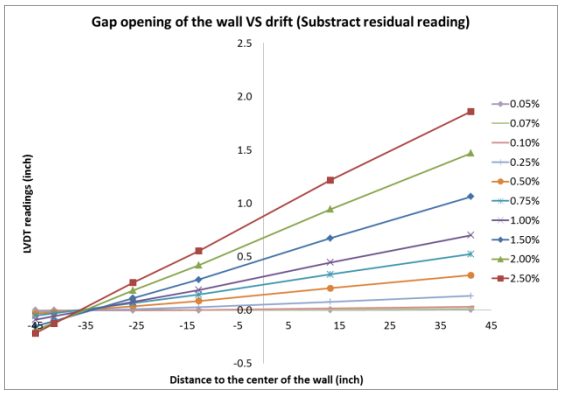

Fig. 6-25 Processed readings at wall/base block interface at positive peaks in Phase 1

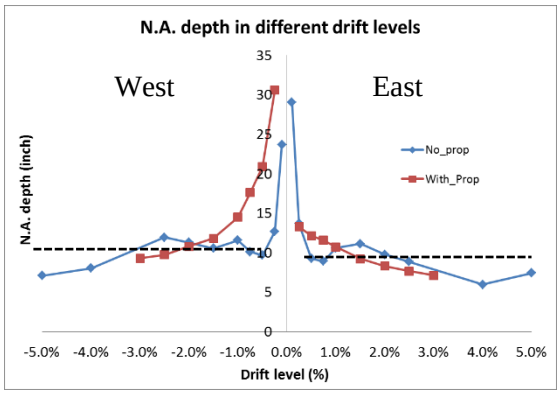

Fig. 6-26 N.A. depths of the wall at the peaks of different drifts in Phase 1 through Phase 3

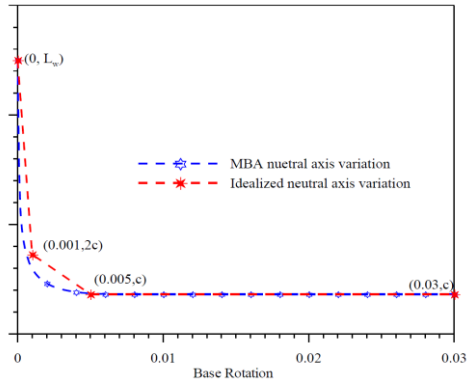

Fig. 6-27 Simplified trilinear curve for predicting N.A. depth of the wall (Aaleti 2011)

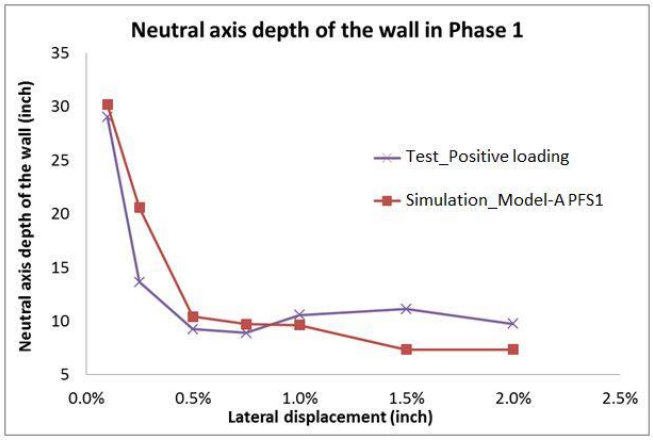

Fig. 6-28 Comparison of the N.A. depths of the wall recorded in the test with those obtained from "Model-A PFS1" (without props)

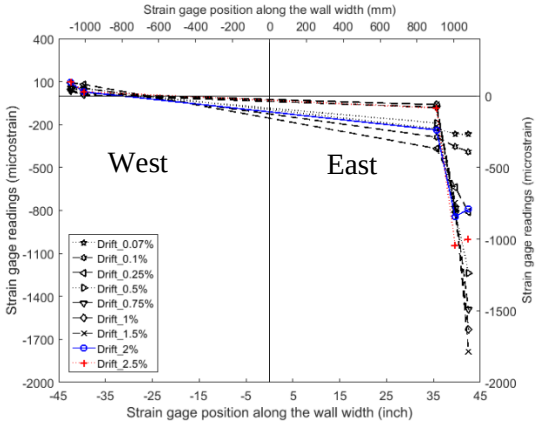

Fig. 6-29 Strain distribution along the wall width at positive peaks in Phase 1

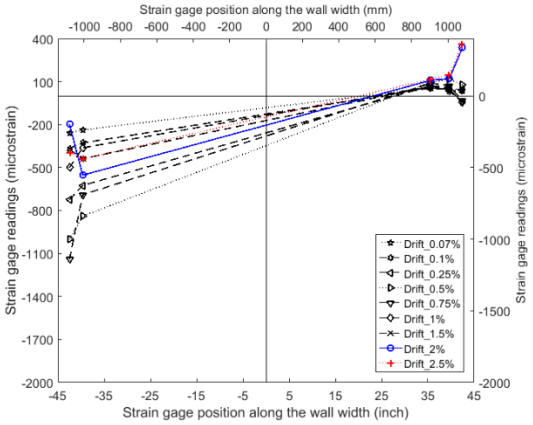

Fig. 6-30 Strain distribution along the wall width at negative peaks in Phase 1

Fig. 6-31 Condition of the fiber grout layer beneath the west and the east wall corner

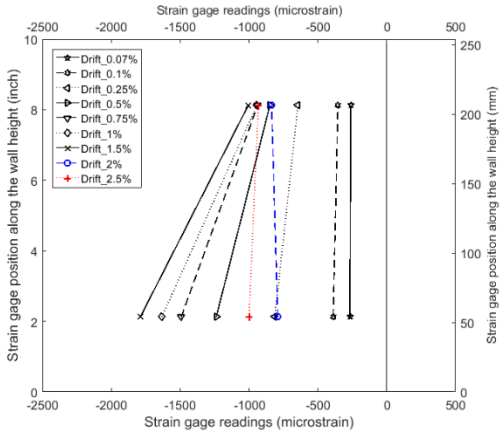

Fig. 6-32 Strain distribution along the wall height at positive peaks in Phase 1

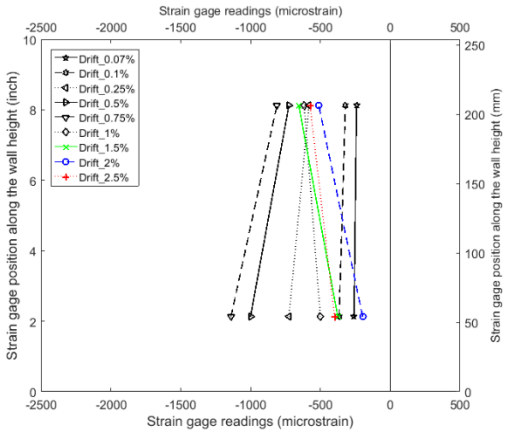

Fig. 6-33 Strain distribution along the wall height at negative peaks in Phase 1

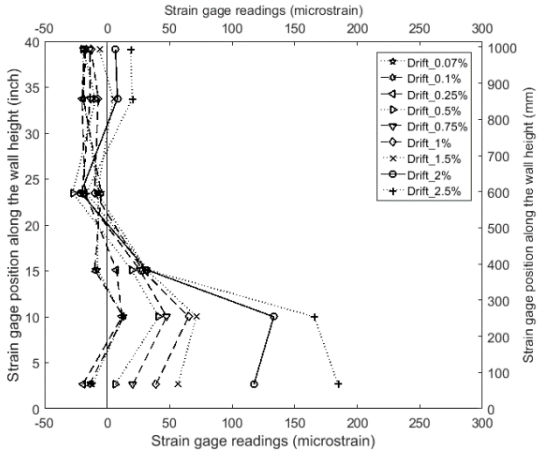

Fig. 6-34 Strain distribution in the stirrups along the wall height in Phase 1

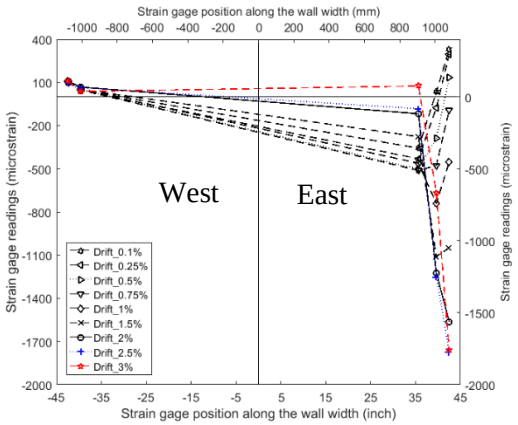

Fig. 6-35 Strain distribution along the wall width at positive peaks in Phase 2

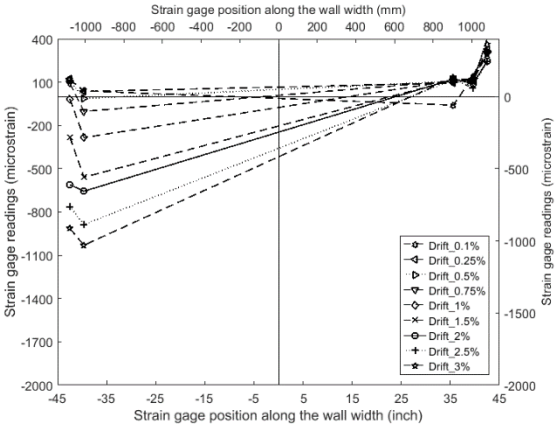

Fig. 6-36 Strain distribution along the wall width at negative peaks in Phase 2

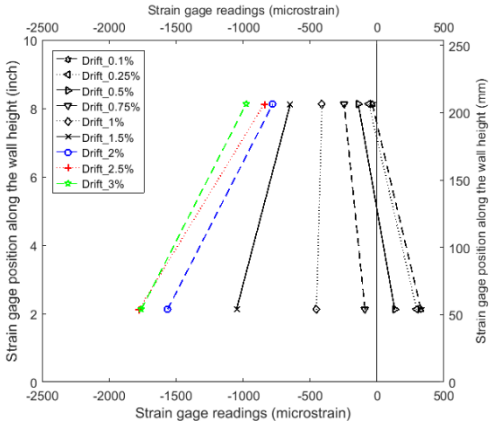

Fig. 6-37 Strain distribution along the wall height at positive peaks in Phase 2

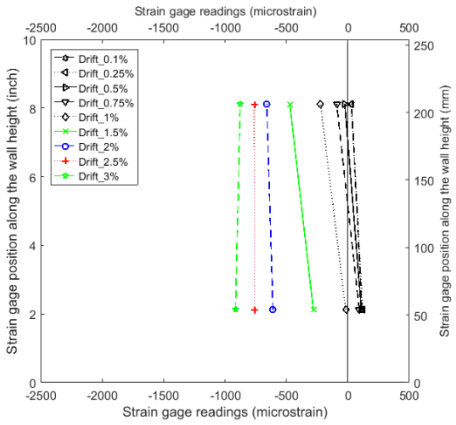

Fig. 6-38 Strain distribution along the wall height at negative peaks in Phase 2

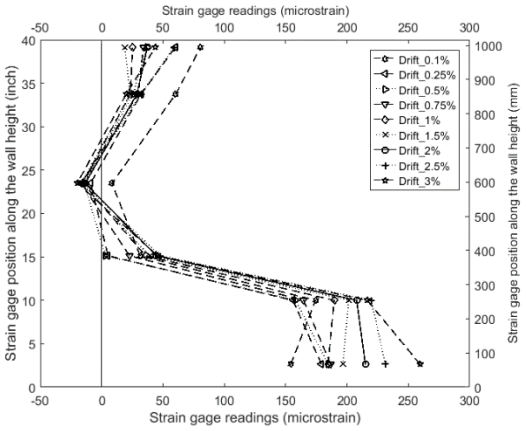

Fig. 6-39 Strain distribution in the stirrups along the wall height in Phase 2

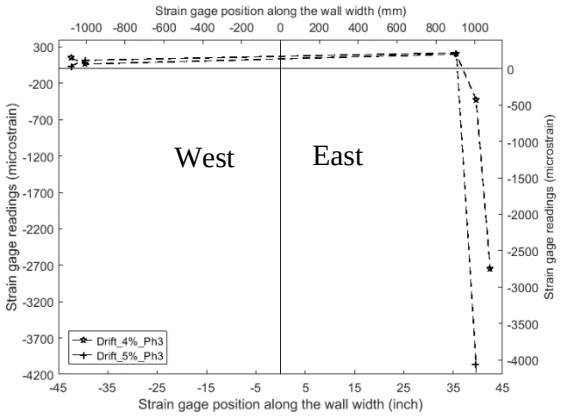

Fig. 6-40 Strain distribution along the wall width at positive peaks in Phase 3

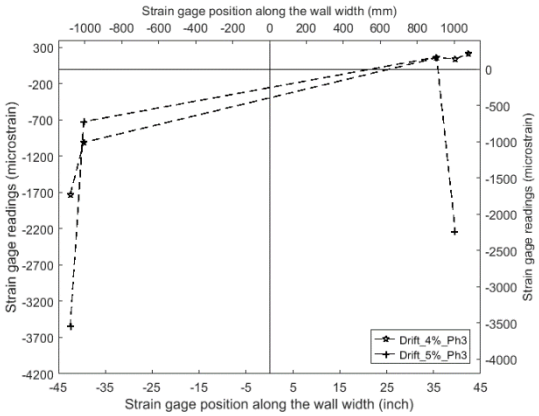

Fig. 6-41 Strain distribution along the wall width at negative peaks in Phase 3

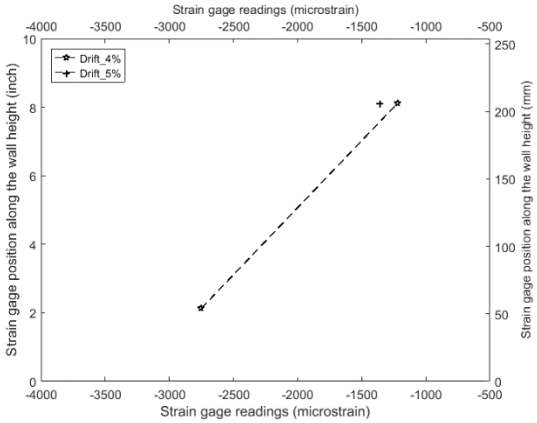

Fig. 6-42 Strain distribution along the wall height at positive peaks in Phase 3

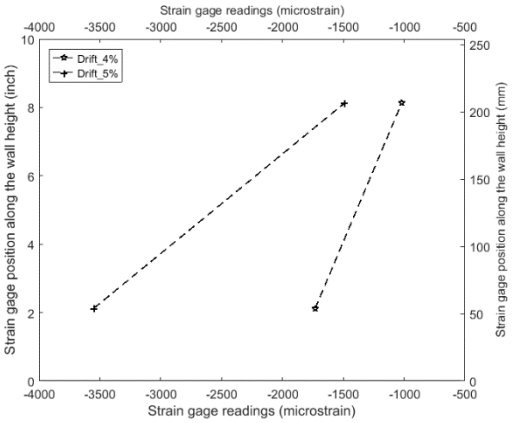

Fig. 6-43 Strain distribution along the wall height at negative peaks in Phase 3

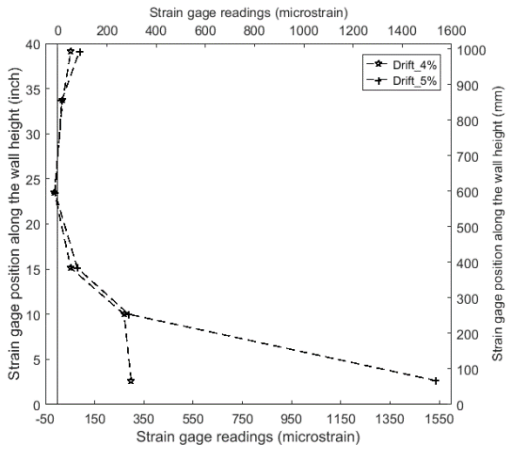

Fig. 6-44 Strain distribution in the stirrups along the wall height in Phase 3

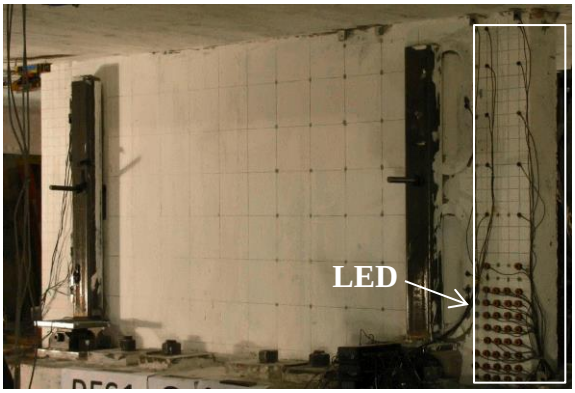

Fig. 6-45 LEDs on the wall in PFS1

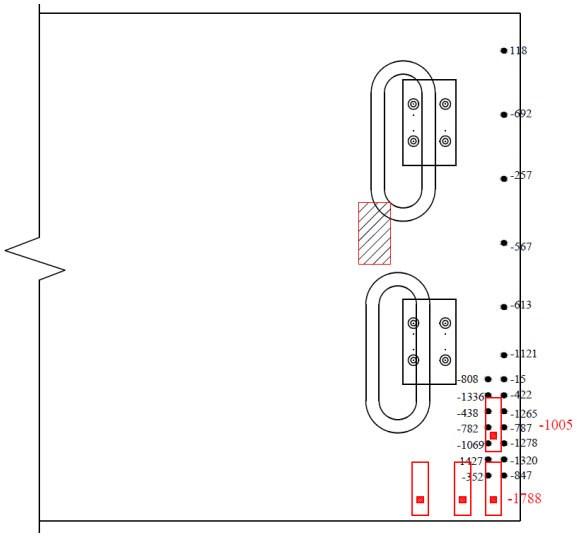

Fig. 6-46 Strains obtained from the concrete gages and the LEDs near the wall edge

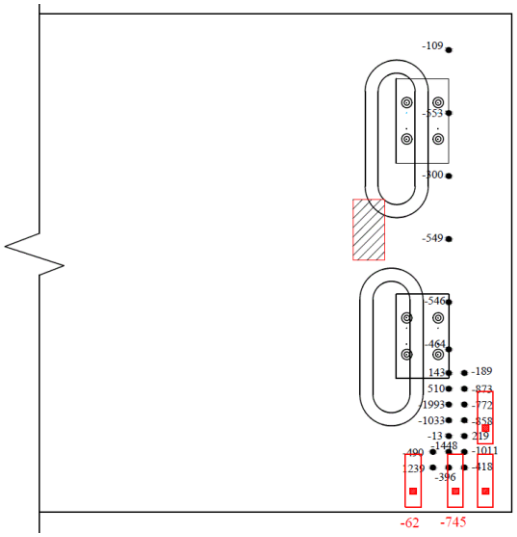

Fig. 6-47 Strains obtained from the concrete gages and the LEDs near the O-connectors

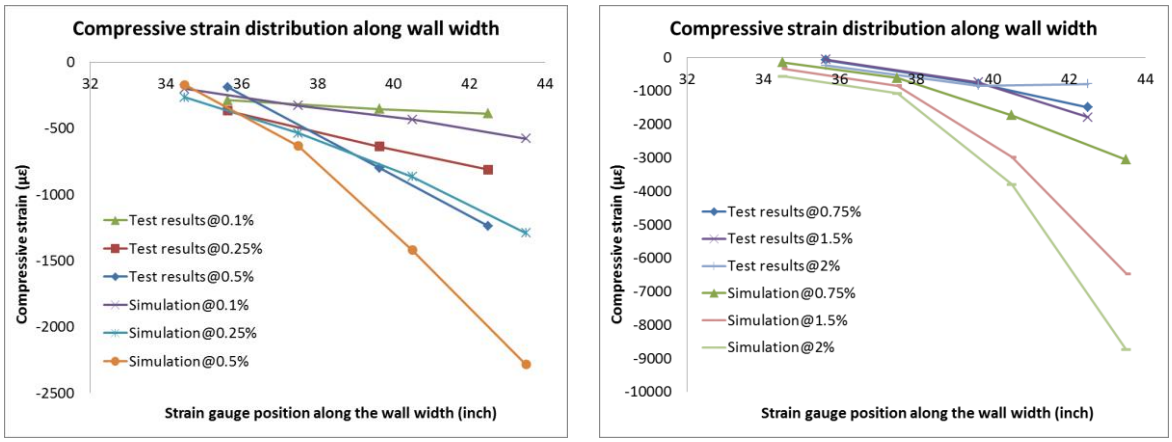

(a) At small drift levels (b) At large drift levels

Fig. 6-48 Comparison of the strain distribution in the wall corner obtained from the test with that obtained from "Model-A PFS1" (without props)

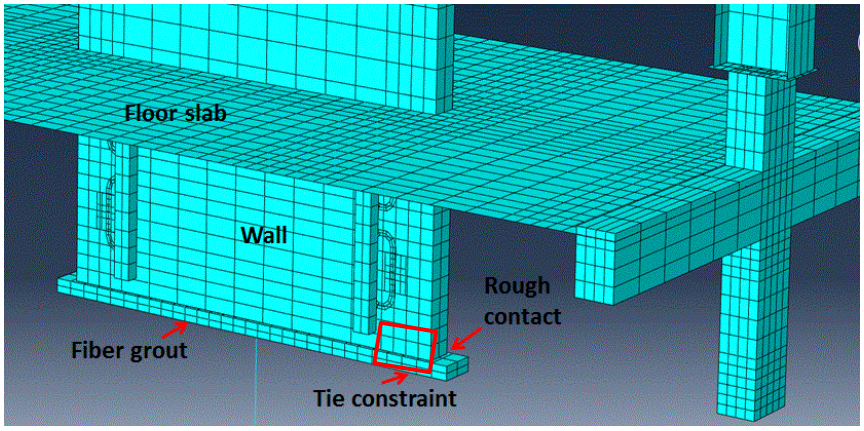

Fig. 6-49 Boundary constraint of the fiber grout elements in the numerical model

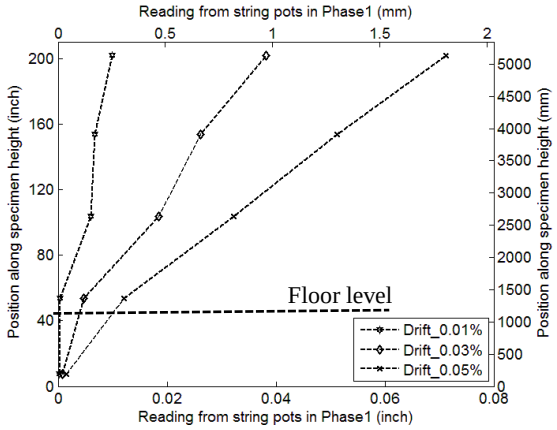

Fig. 6-50 Deformed shapes of the rocking wall at small drift levels in Phase 1

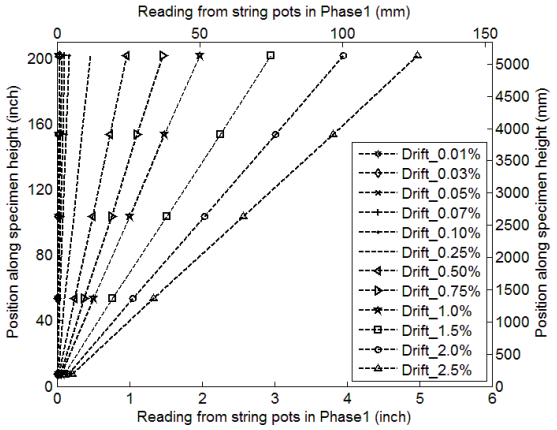

Fig. 6-51 Deformed shapes of the rocking wall at larger drift levels in Phase 1

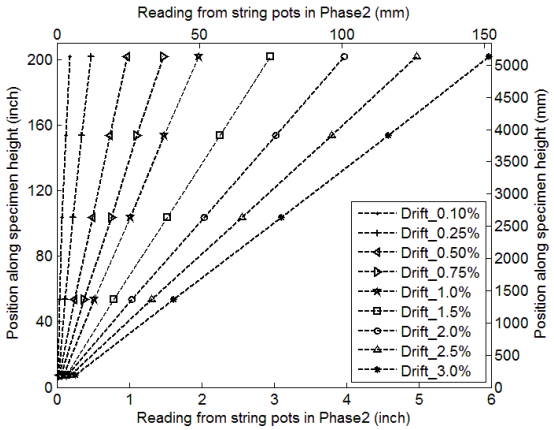

Fig. 6-52 Deformed shapes of the rocking wall in Phase 2

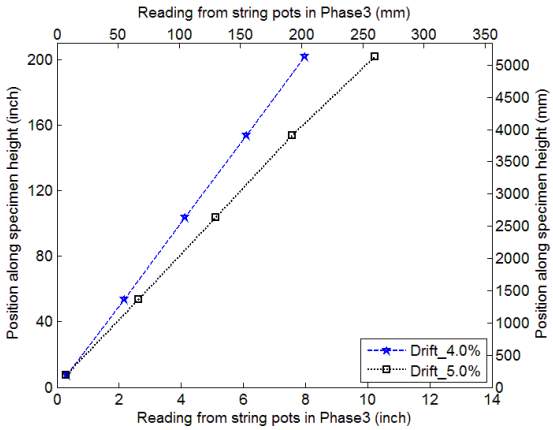

Fig. 6-53 Deformed shapes of the rocking wall in Phase 3

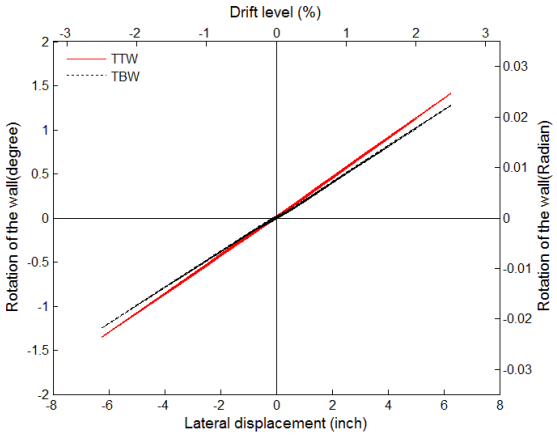

Fig. 6-54 Comparison of the rotations of the wall measured by TTW and TBW in Phase 1

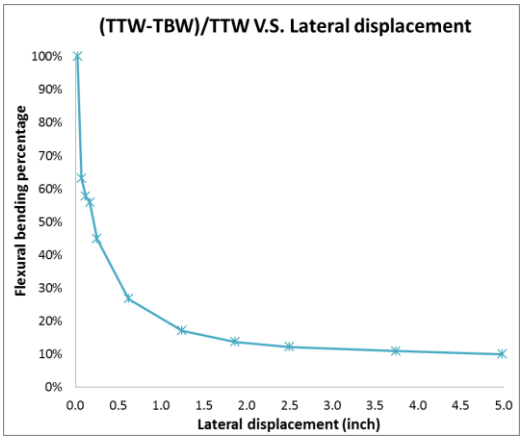

Fig. 6-55 Percentage of the flexural rotation to the total rotation of the wall in Phase 1

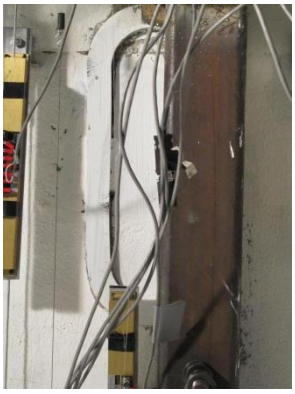

Fig. 6-56 Yield lines on the upper level O-connector at 0.75% drift

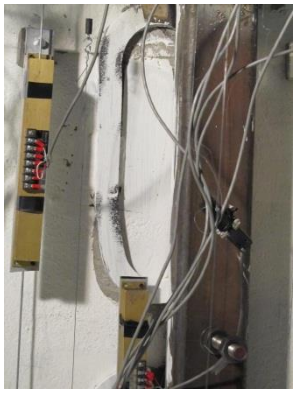

Fig. 6-57 Yield lines developed on the upper level O-connector at 2% drift

Fig. 6-58 Fractured O-connector at the upper level following the end of the test

Fig. 6-59 Uncracked O-connector at the lower level following the end of the test

Fig. 6-60 Condition of the end columns (steel tubes) following the end of the test

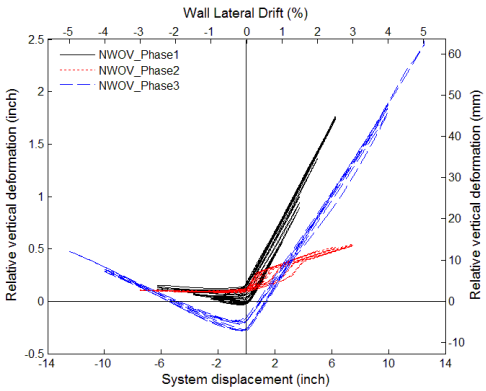

Fig. 6-61 Relative vertical displacements of the upper level O-connectors on west side of wall

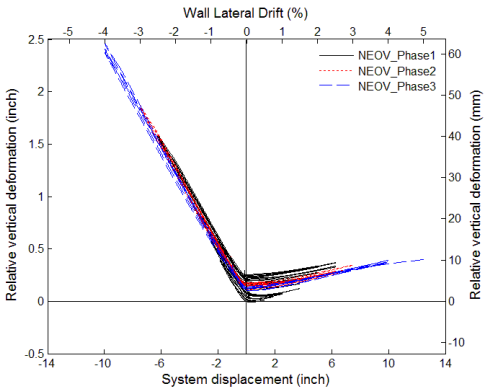

Fig. 6-62 Relative vertical displacements of the upper level O-connectors on east side of wall

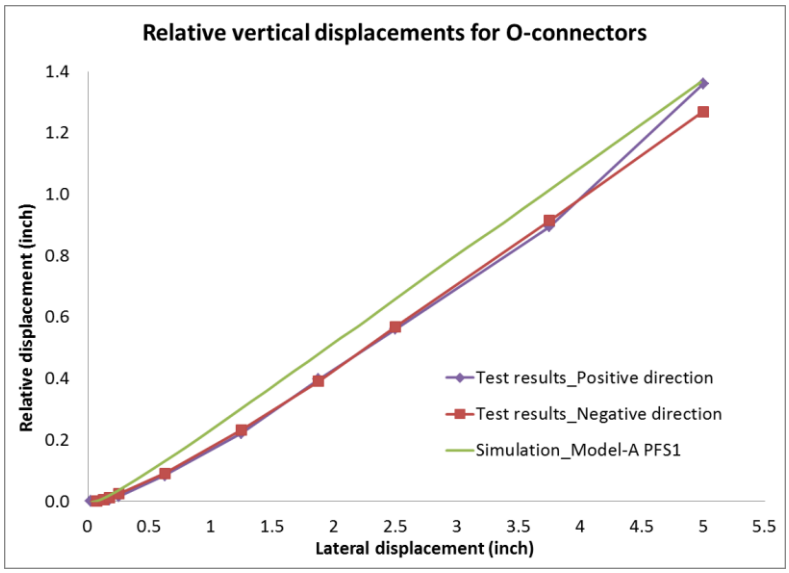

Fig. 6-63 Comparison of the relative vertical displacements of the O-connectors recorded in the test with those obtained from "Model-A PFS1" (without props)

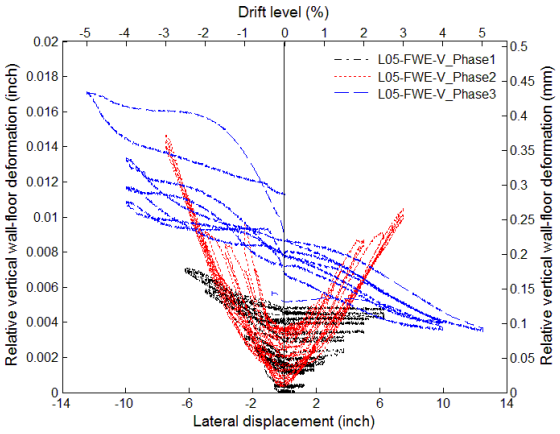

Fig. 6-64 Relative vertical deformation at wall-floor connection versus lateral wall displacement in Phase 1, 2&3

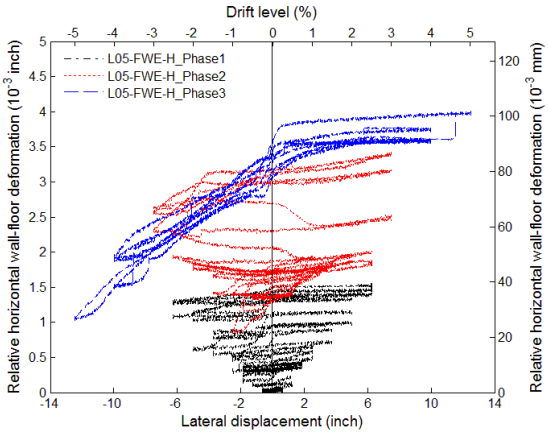

Fig. 6-65 Relative horizontal deformation at wall-floor connection versus lateral wall displacement in in Phase 1, 2&3

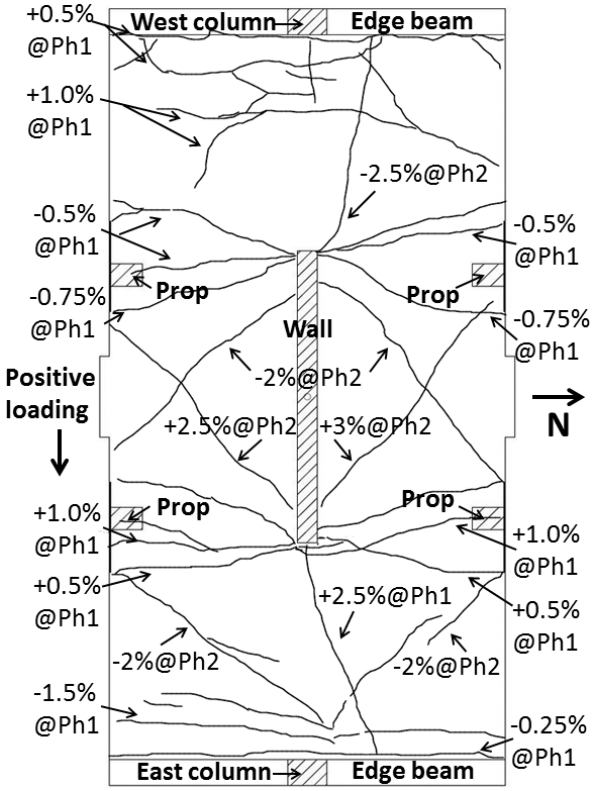

Fig. 6-66 Crack map of the floor after Phase 2

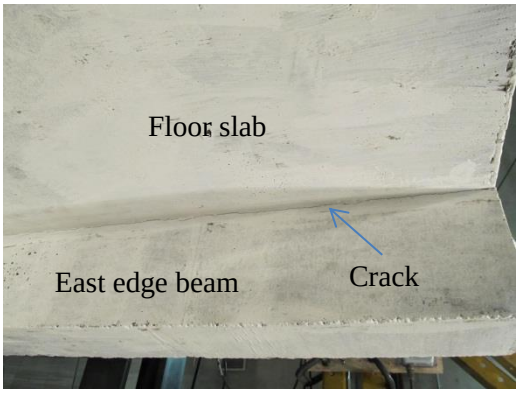

Fig. 6-67 Cracks initiating at the east floor-edge beam connection in Phase 1 (view from underside of floor)

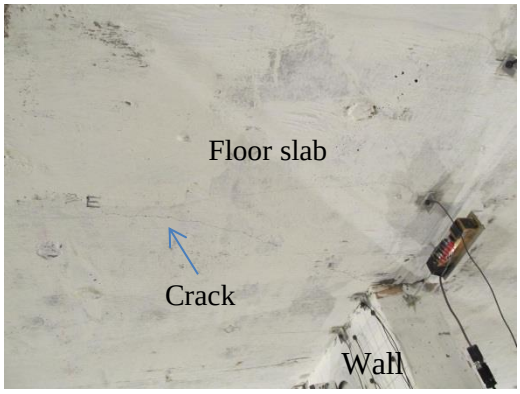

Fig. 6-68 Cracks initiating at the east wall-floor connection in Phase 1 (view from underside of floor)

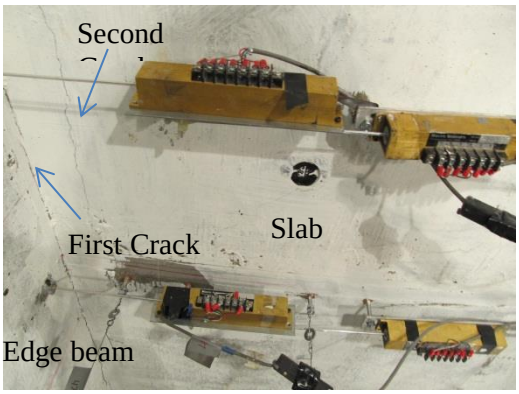

Fig. 6-69 Parallel cracks at the west floor-edge beam connection in Phase 1 (view from underside of floor)

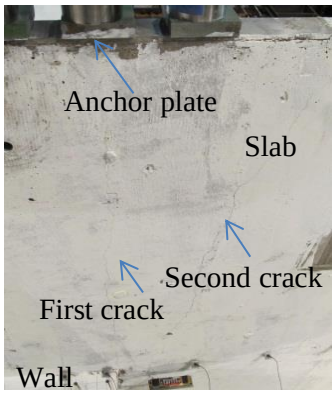

Fig. 6-70 Multiple cracks initiating from the wall at the east wall-floor connection in Phase 1 (view from underside of floor)

Fig. 6-71 Cracks in the slab extending to the end of the common anchor plate in Phase 1 (view from top of floor)

Fig. 6-72 Widely opened cracks at the east floor-edge beam connection in the slab at 2.5% drift in Phase 1 (view from underside of floor)

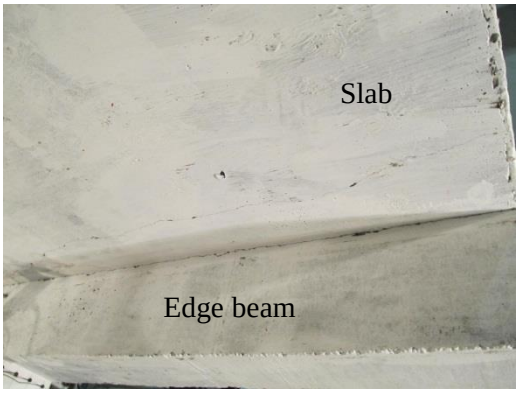

Fig. 6-73 Closed cracks in the slab at "zero load" position after 2.5% drift in Phase 1 (view from underside of floor)

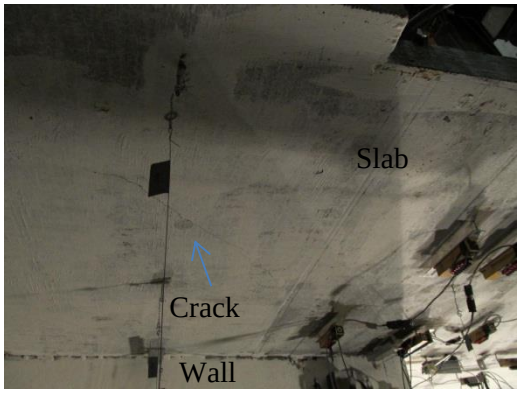

Fig. 6-74 Diagonal cracks extending from the wall to the prop in Phase 2 (view from underside of floor)

Fig. 6-75 Localized damage at the west wall-floor connection in Phase 3 (view from underside of floor)

Fig. 6-76 Localized damage at the east wall-floor connection in Phase 3 (view from underside of floor)

Fig. 6-77 Condition of the damaged bottom surface of the slab in Phase 3

Fig. 6-78 Condition of the bottom surface of the slab after the test

Fig. 6-79 Condition of the damaged top surface of the slab in Phase 3

Fig. 6-80 Condition of the top surface of the slab after the test

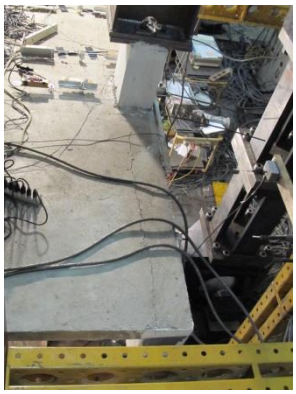

Fig. 6-81 Condition of the damaged floor-edge beam connection in Phase 3

Fig. 6-82 Condition of the slab at floor-edge beam connection after the test

Fig. 6-83 Overall condition of the top surface of the floor slab after the test

Fig. 6-84 Localized damage at the wall-floor connection after the test

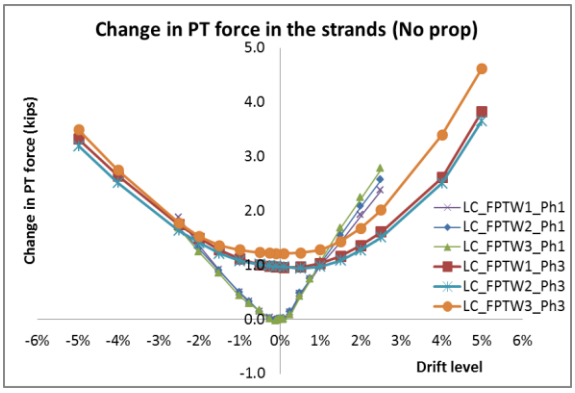

Fig. 6-85 Change in PT force in the longitudinal direction at different peak drifts (Phase 1 & 3)

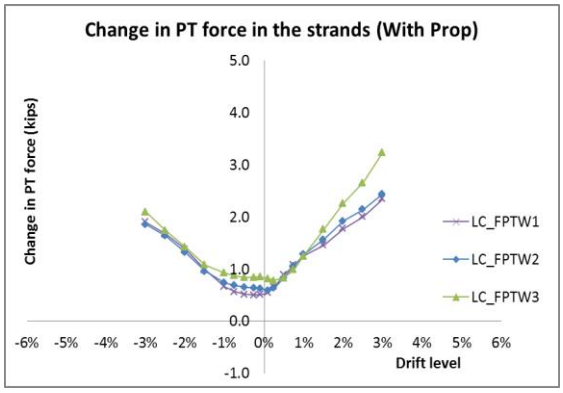

Fig. 6-86 Change in PT force in the longitudinal direction at different peak drifts (Phase 2)

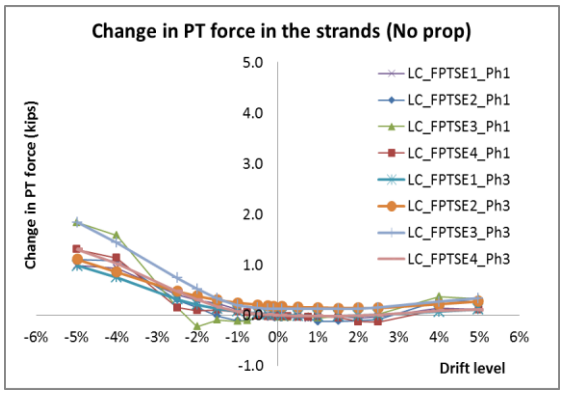

Fig. 6-87 Change in PT force in the transverse direction at different peak drifts (Phase 1 & 3)

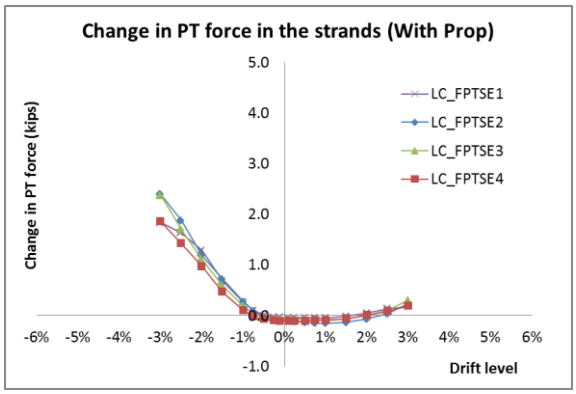

Fig. 6-88 Change in PT force in the transverse direction at different peak drifts (Phase 2)

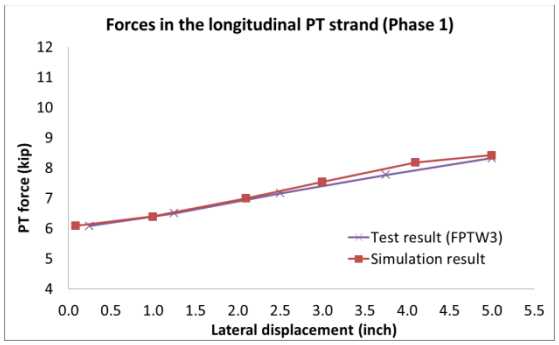

Fig. 6-89 Comparison of the forces in the longitudinal strand closest to the wall in the test with those in the model (Phase 1)

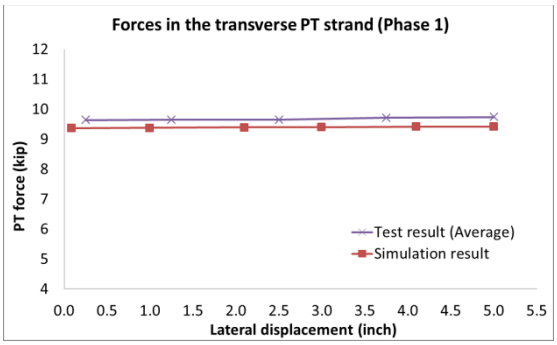

Fig. 6-90 Comparison of the average forces of the four banded transverse strand in the test with those in the numerical model (Phase 1)

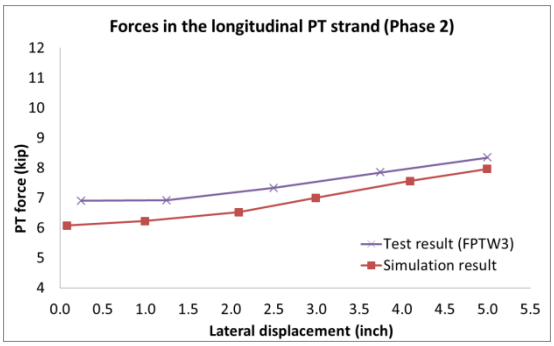

Fig. 6-91 Comparison of the forces in the longitudinal strand closest to the wall in the test with those in the numerical model (Phase 2)

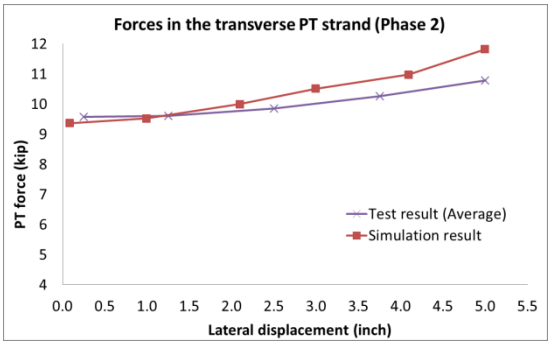

Fig. 6-92 Comparison of the average forces in the four banded transverse strand in the test with those in the numerical model (Phase 2)

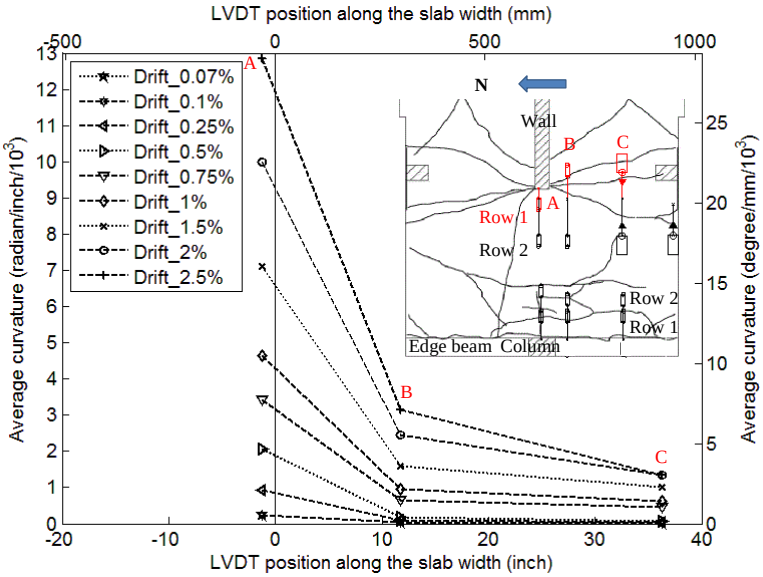

Fig. 6-93 Average curvature distribution at the wall-floor connection (1st row, Ph 1)

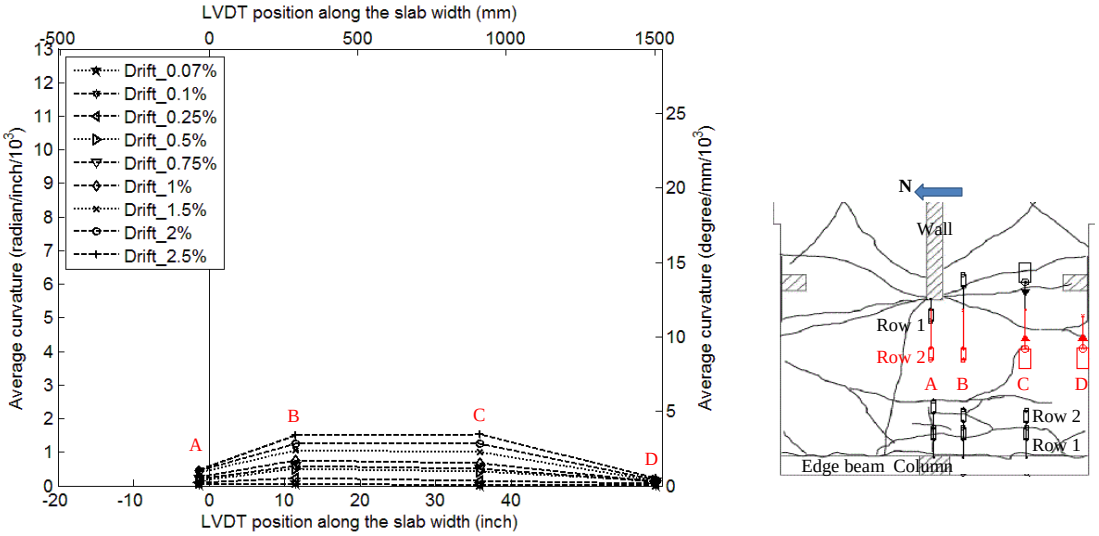

Fig. 6-94 Average curvature distribution at the wall-floor connection (2nd row, Ph1)

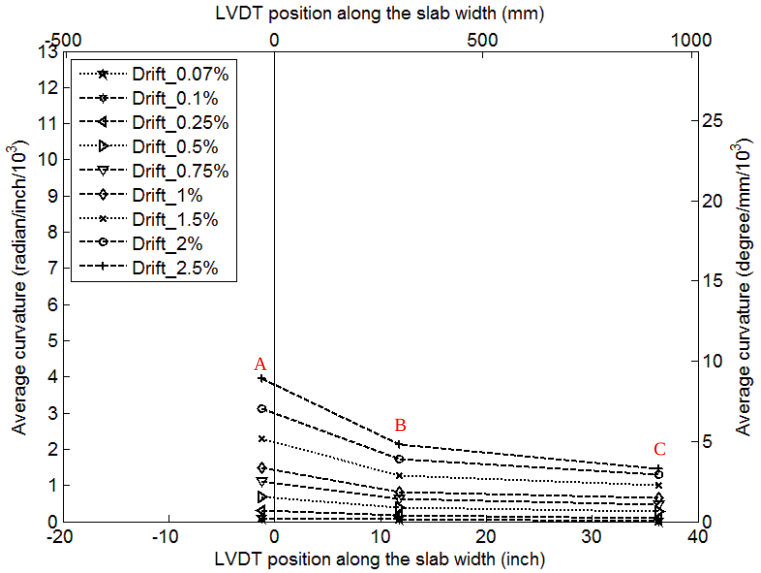

Fig. 6-95 Average curvature distribution at the wall-floor connection (1st + 2nd row, Ph1)

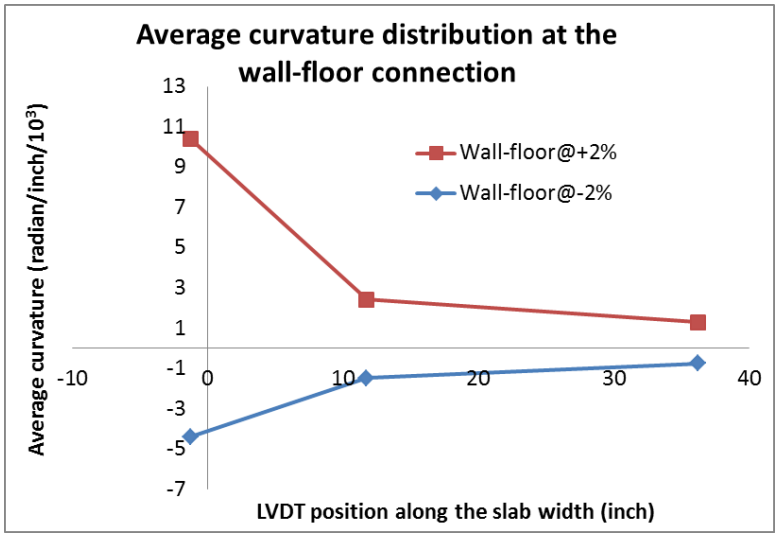

Fig. 6-96 Average curvature distribution at wall-floor connection at 2% and -2% drift (Phase 1)

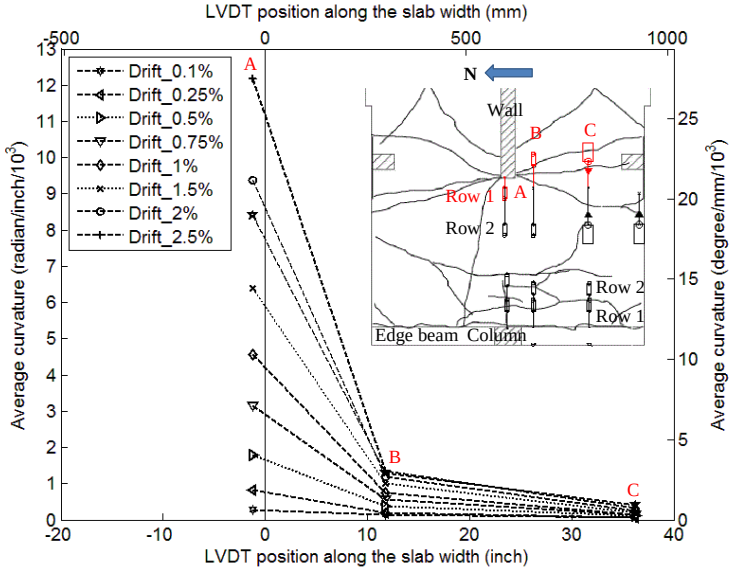

Fig. 6-97 Average curvature distribution at the wall-floor connection (1st row of LVDT, Phase 2)

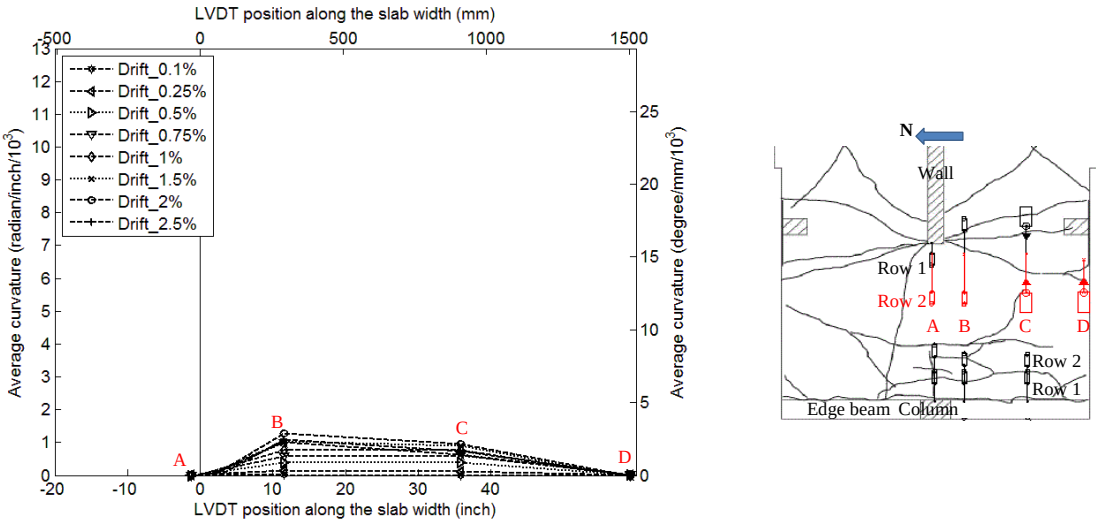

Fig. 6-98 Average curvature distribution at the wall-floor connection (2nd row of LVDT, Phase 2)

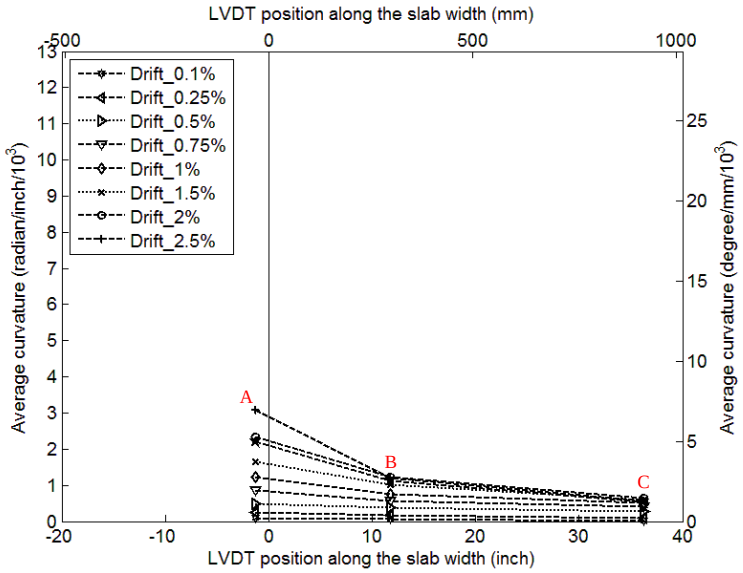

Fig. 6-99 Average curvature distribution at the wall-floor connection (1st + 2nd row, Phase 2)

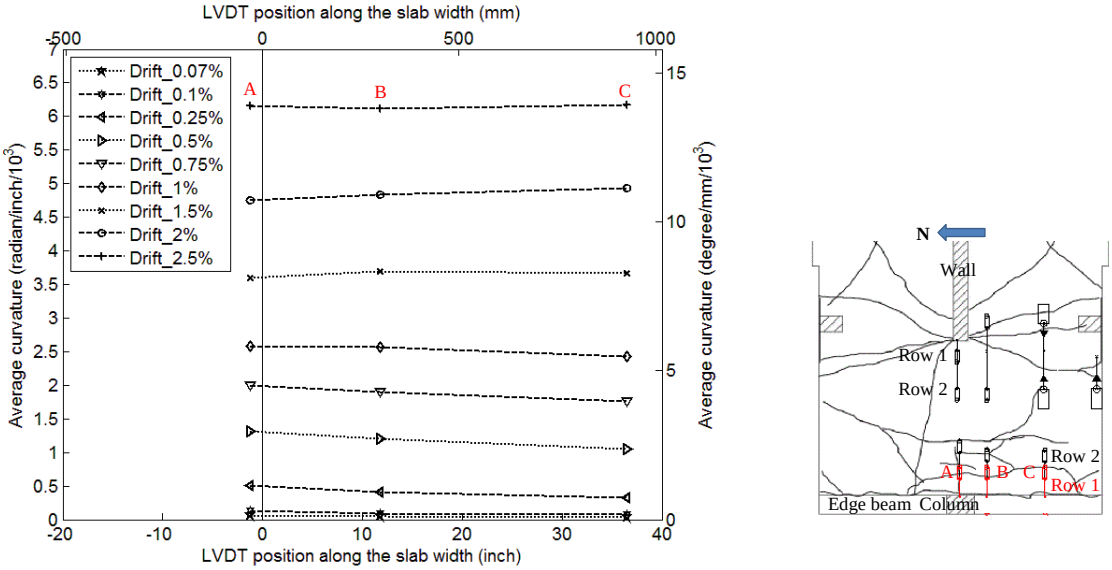

Fig. 6-100 Average curvature distribution at the floor-edge beam connection (1st row, Phase 1)

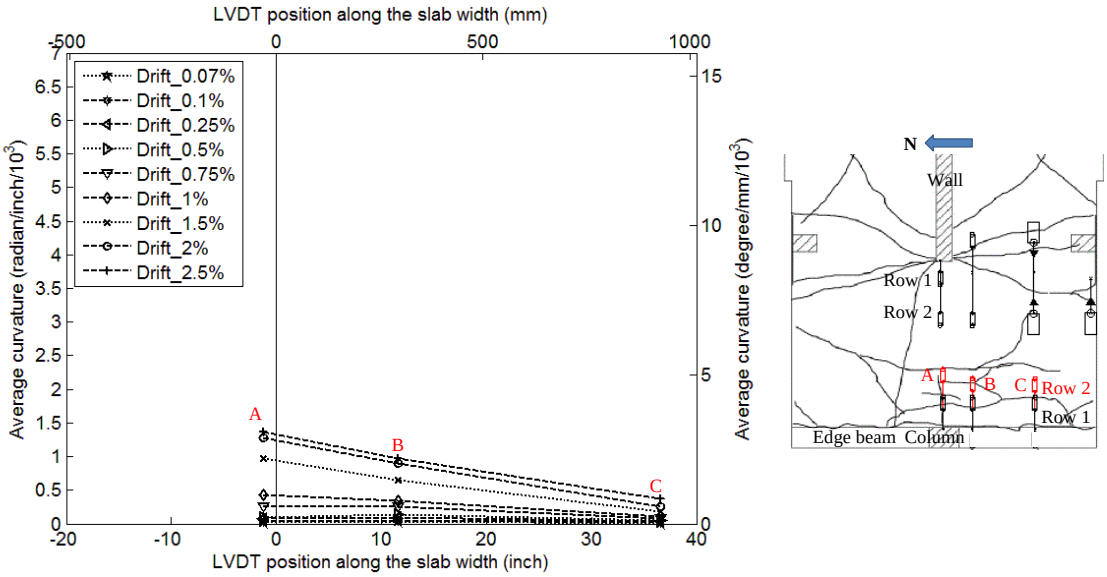

Fig. 6-101 Average curvature distribution at floor-edge beam connection (2nd row, Ph1)

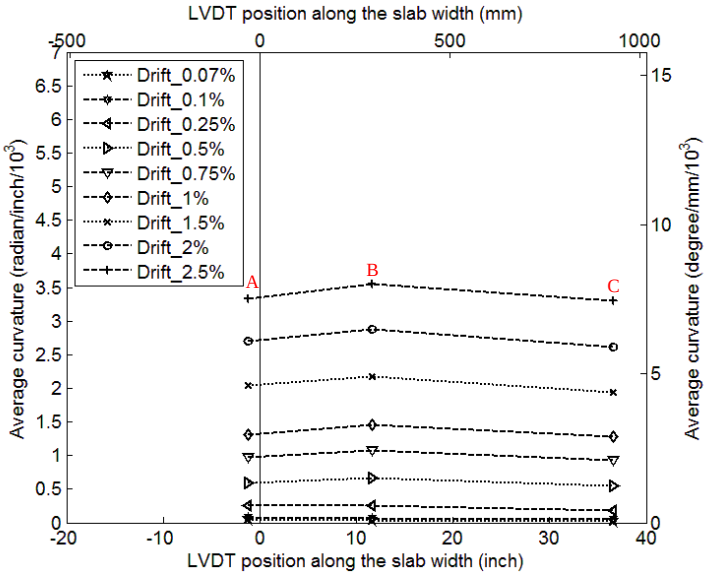

Fig. 6-102 Average curvature distribution at the floor-edge beam connection (1st + 2nd, Ph1)

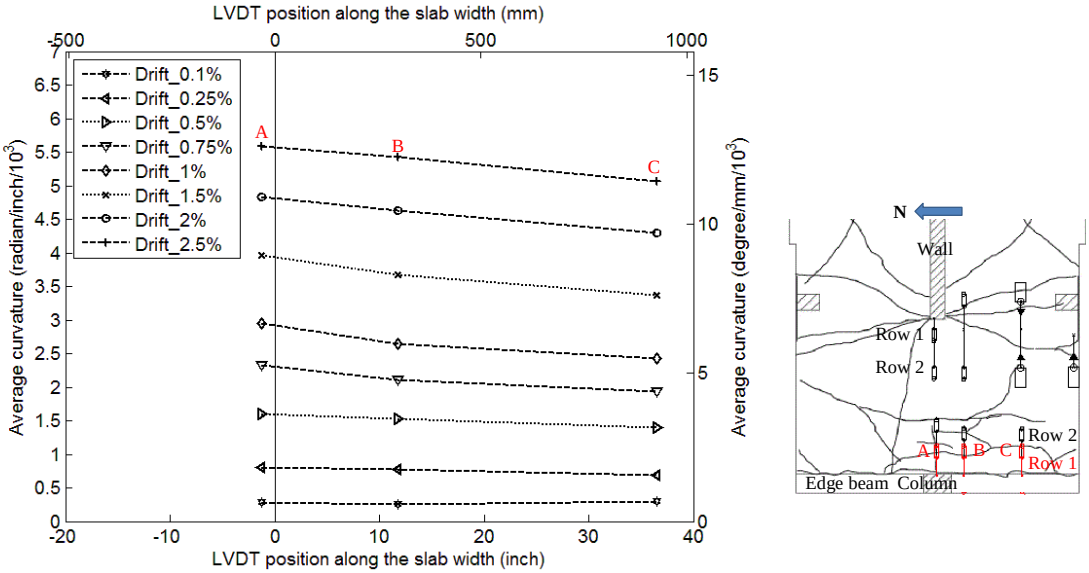

Fig. 6-103 Average curvature distribution at the floor-edge beam connection (1st row, Ph2)

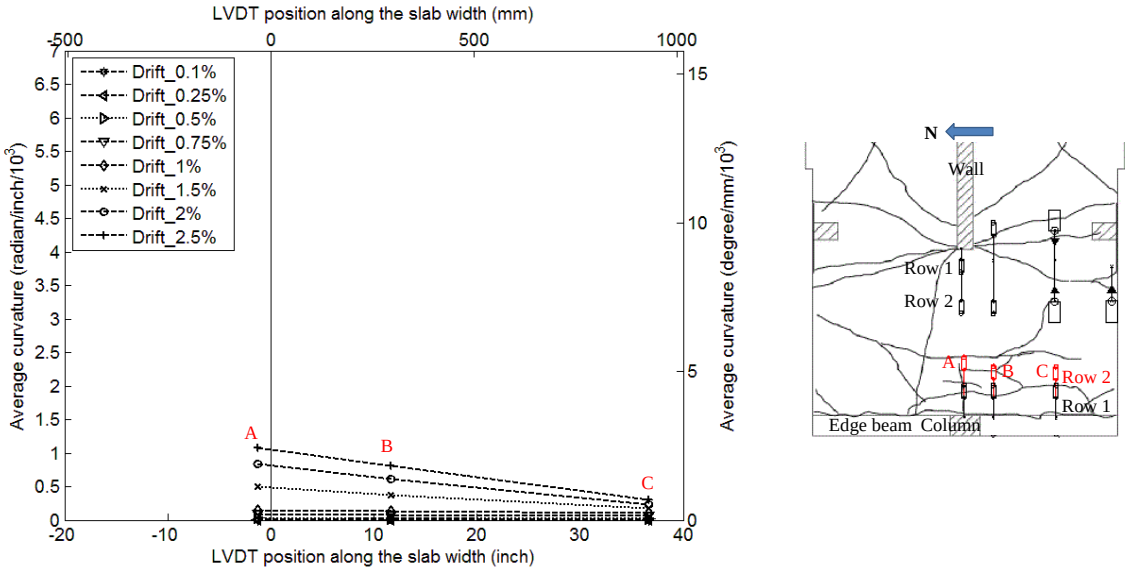

Fig. 6-104 Average curvature distribution at floor-edge beam connection (2nd row, Ph2)

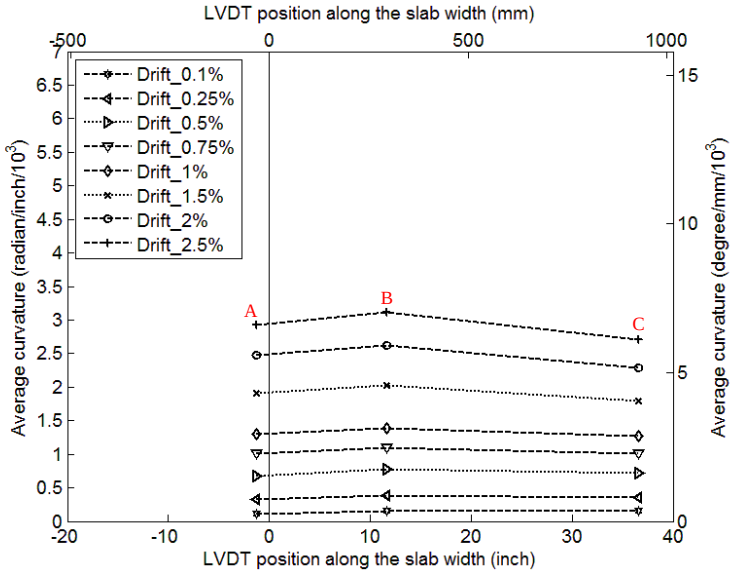

Fig. 6-105 Average curvature distribution at the floor-edge beam connection (1st + 2nd, Ph2)

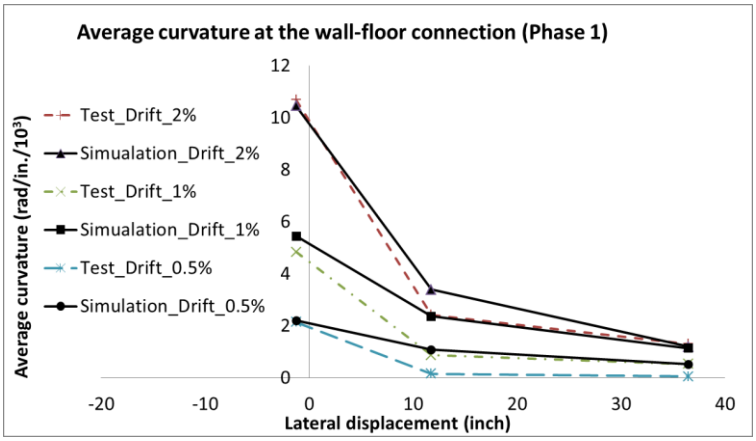

Fig. 6-106 Comparison of the average curvature distribution at the wall-floor connection in the longitudinal direction in the test with that obtained from the numerical model (Phase 1)

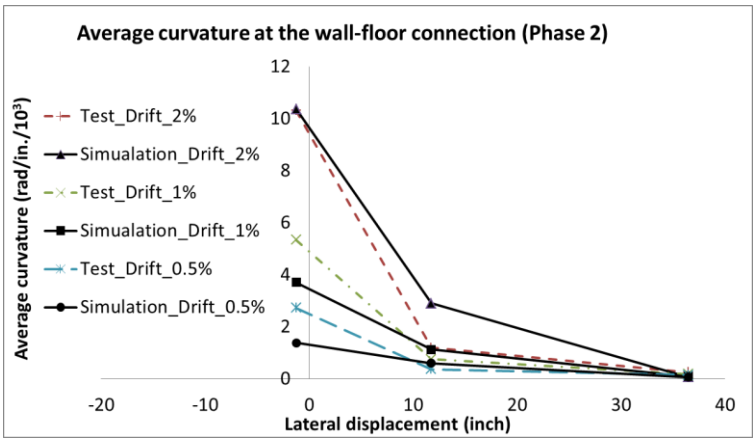

Fig. 6-107 Comparison of the average curvature distribution at the wall-floor connection in the longitudinal direction in the test with that obtained from the numerical model (Phase 2)

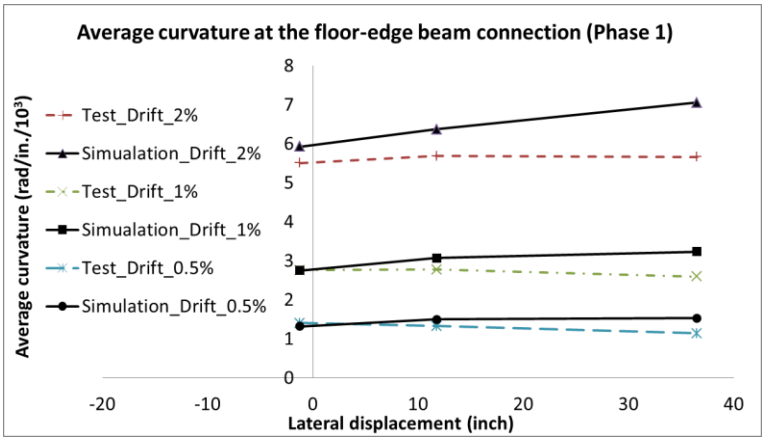

Fig. 6-108 Comparison of the average curvature distribution at the floor-edge beam connection in the longitudinal direction in the test with that obtained from the numerical model (Phase 1)

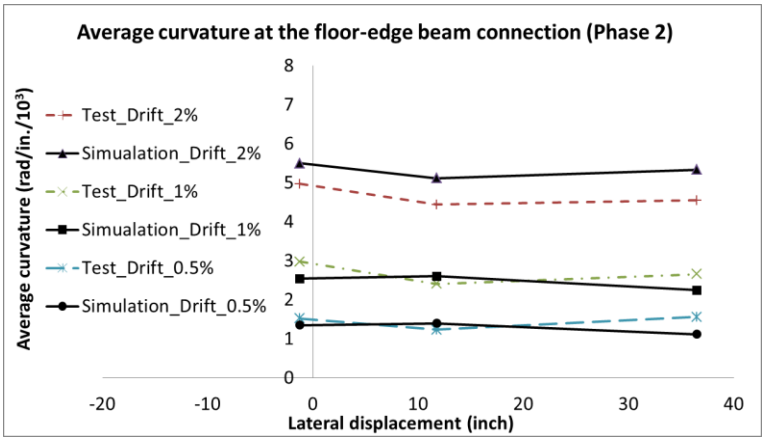

Fig. 6-109 Comparison of the average curvature distribution at the floor-edge beam connection in the longitudinal direction in the test with that obtained from the numerical model (Phase 2)

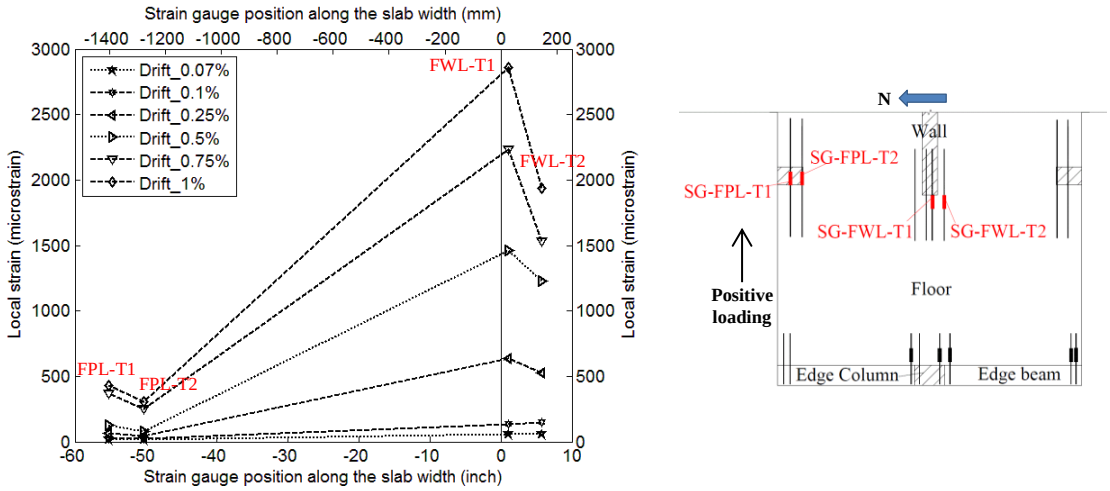

Fig. 6-110 Strain distribution at top of the west wall-floor connection at positive drifts

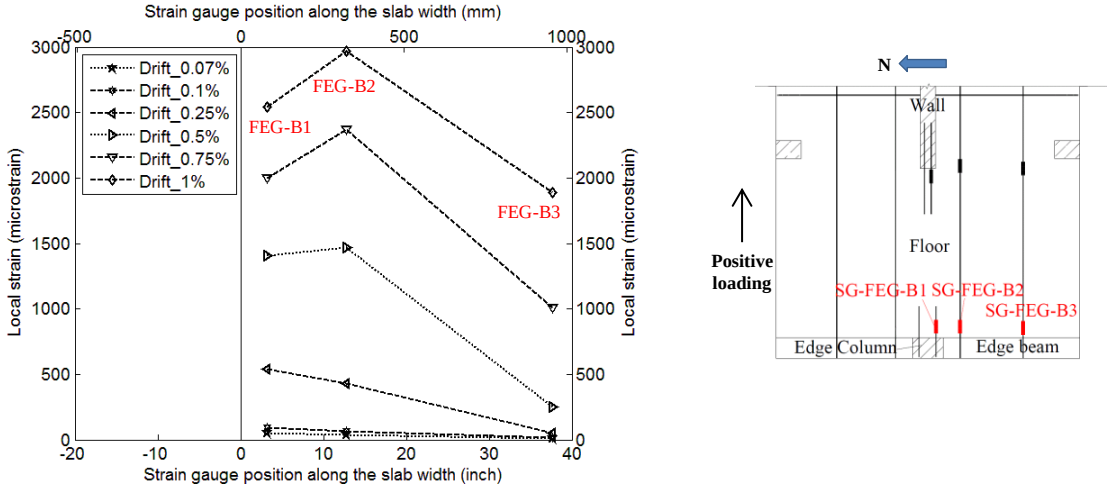

Fig. 6-111 Strain distribution at bottom of the west floor-edge beam connection at positive drifts

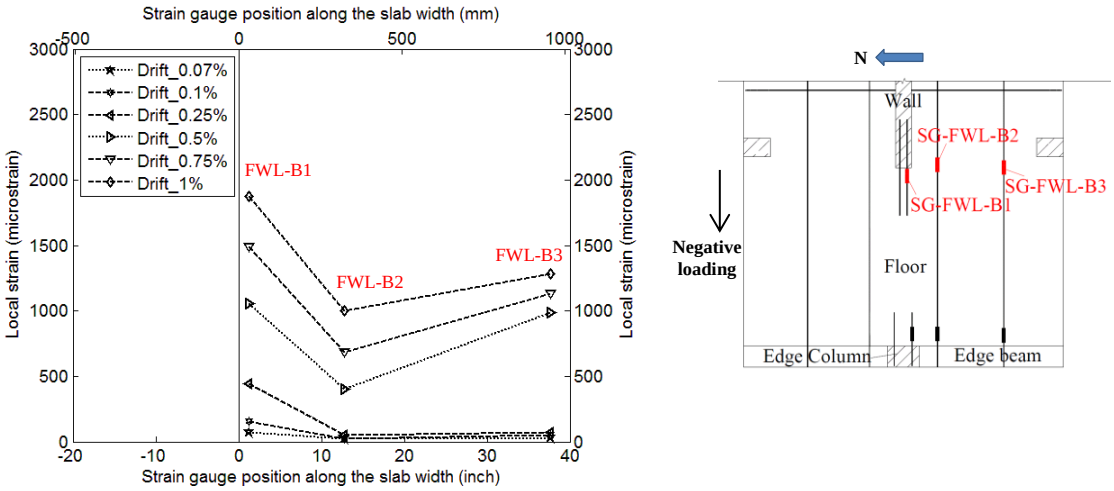

Fig. 6-112 Strain distribution at bottom of the west wall-floor connection at negative drifts

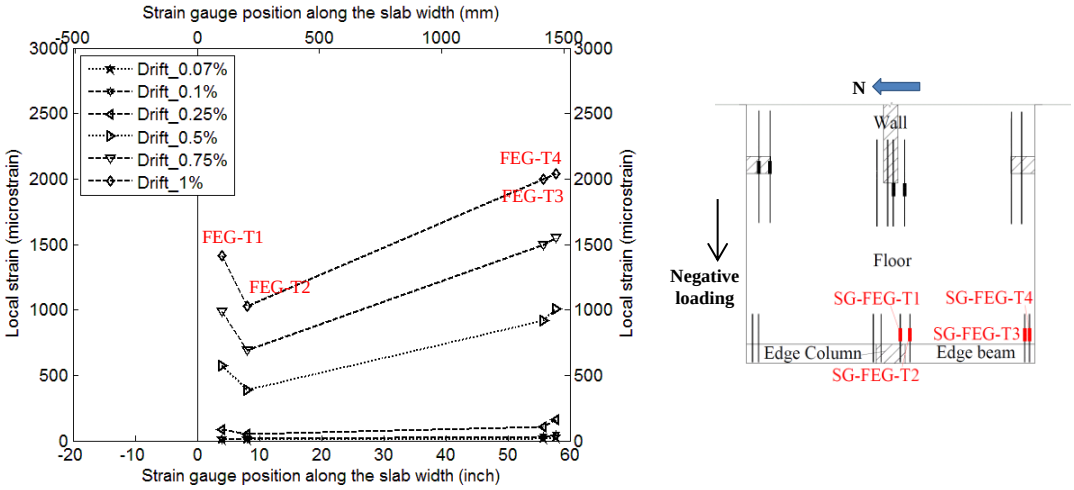

Fig. 6-113 Strain distribution at top of the west floor-edge beam connection at negative drifts

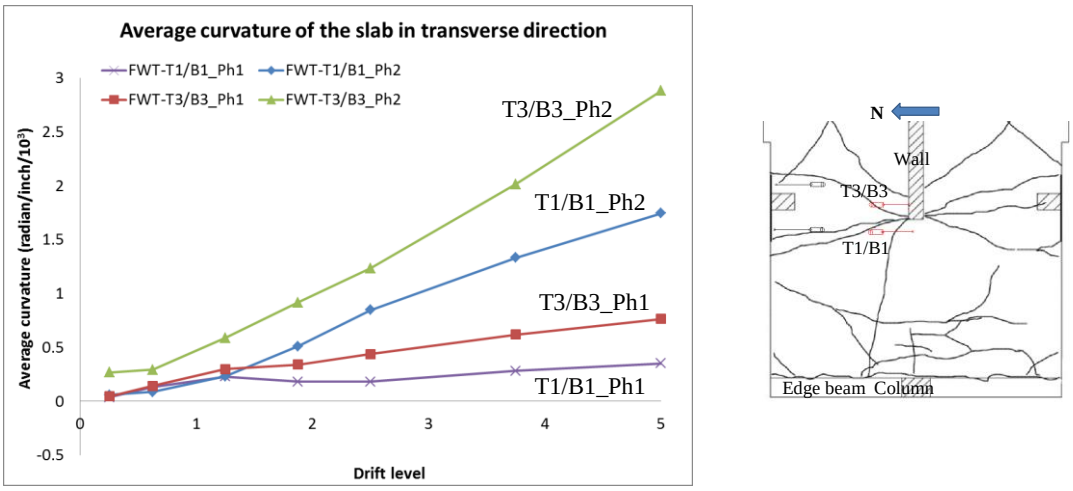

Fig. 6-114 Comparison of the average curvature distribution at the wall-floor connection in the transverse direction in Phase 1 and Phase 2

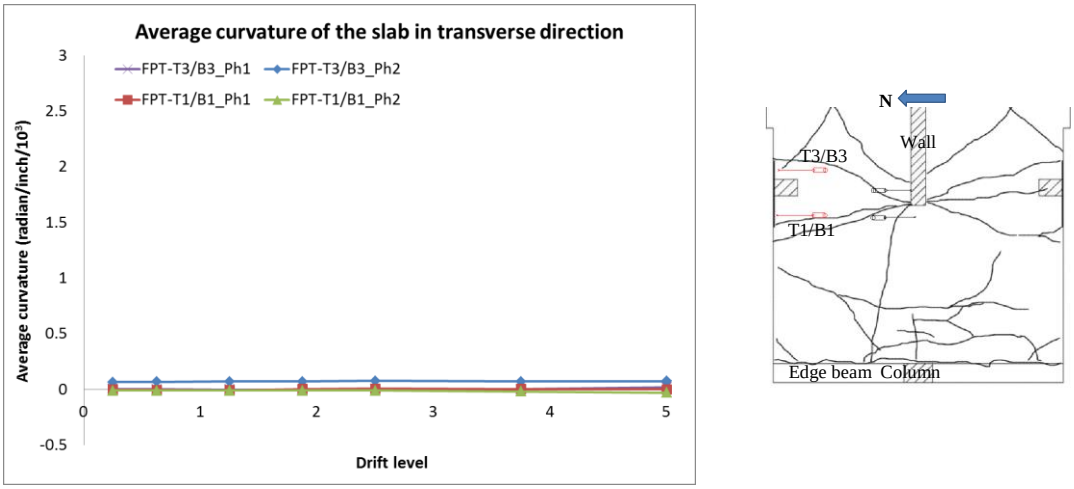

Fig. 6-115 Comparison of the average curvature distribution at the floor-prop connection in the transverse direction in Phase 1 and Phase 2

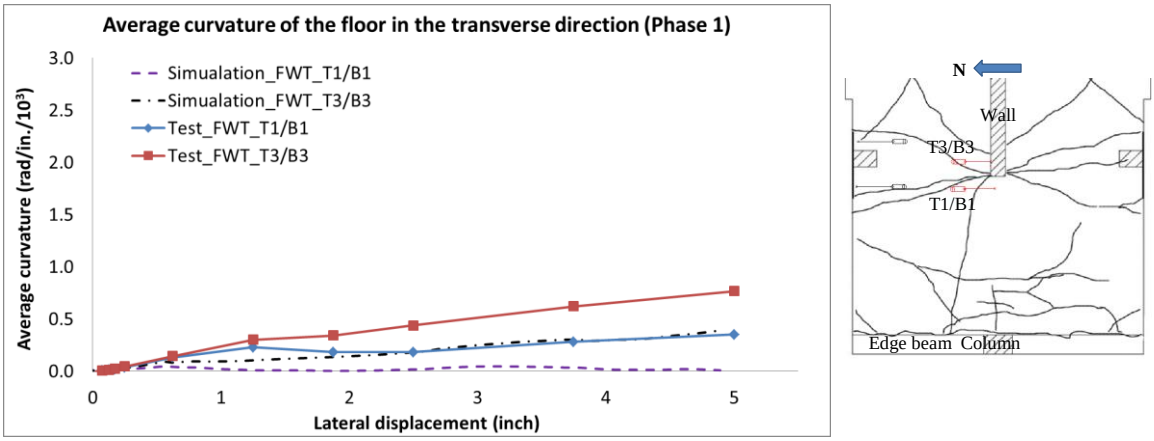

Fig. 6-116 Comparison of the average curvature distribution at the wall-floor connection in the transverse direction in the test with that obtained from the numerical model (Phaes 1)

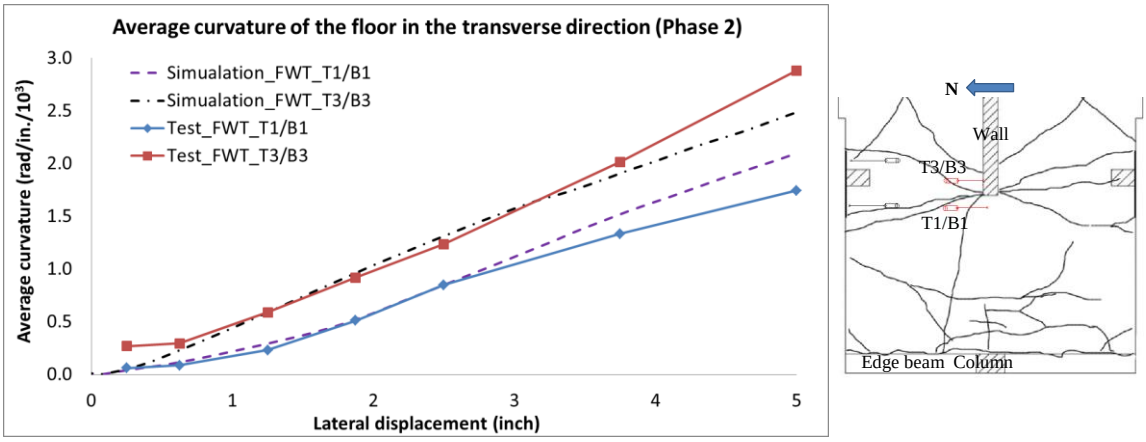

Fig. 6-117 Comparison of the average curvature distribution at the wall-floor connection in the transverse direction in the test with that obtained from the numerical model (Phaes 2)

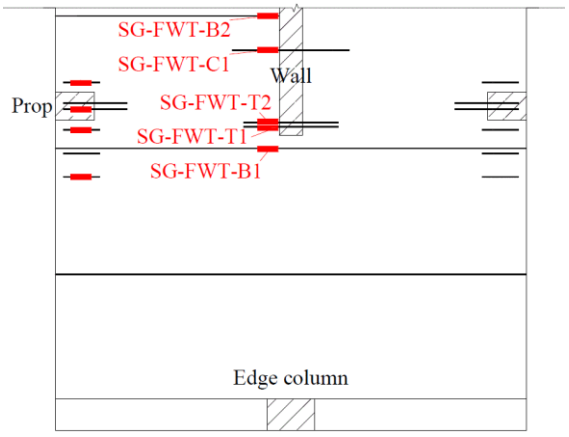

Fig. 6-118 Location of the strain gages attached to the rebar in the transverse direction

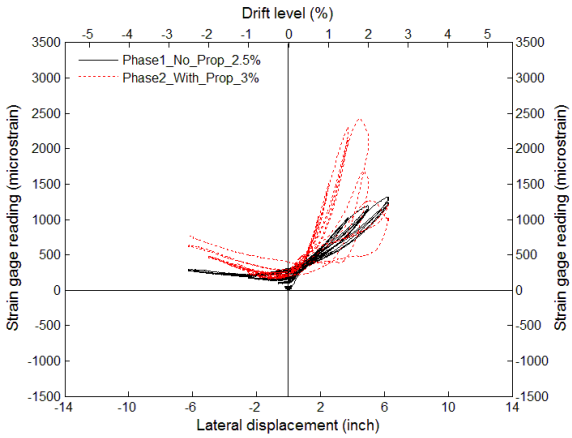

Fig. 6-119 Readings of SG-FWT-T1 in Phase 1 and Phase 2

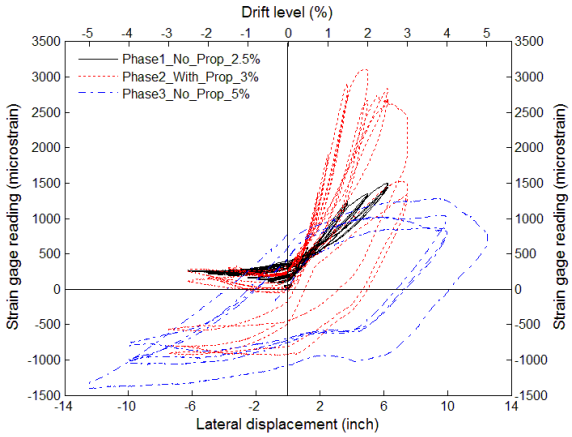

Fig. 6-120 Readings of SG-FWT-T2 in Phase 1 through Phase 3

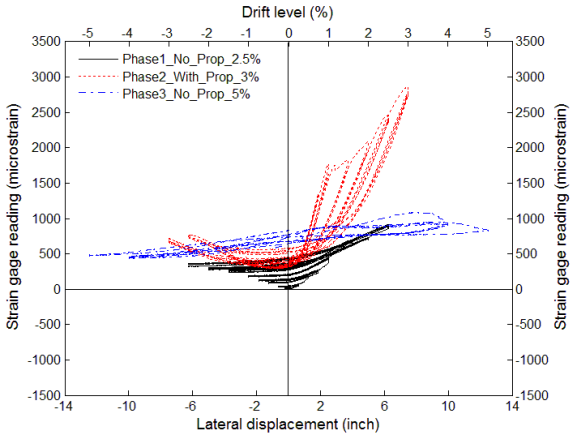

Fig. 6-121 Readings of SG-FWT-C1 in Phase 1 through Phase 3

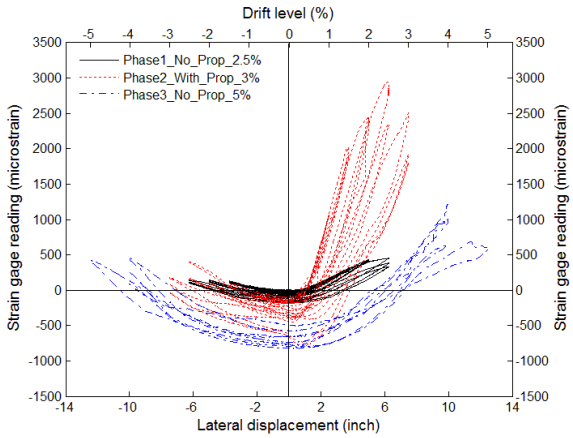

Fig. 6-122 Readings of SG-FWT-B1 in Phase 1 through Phase 3

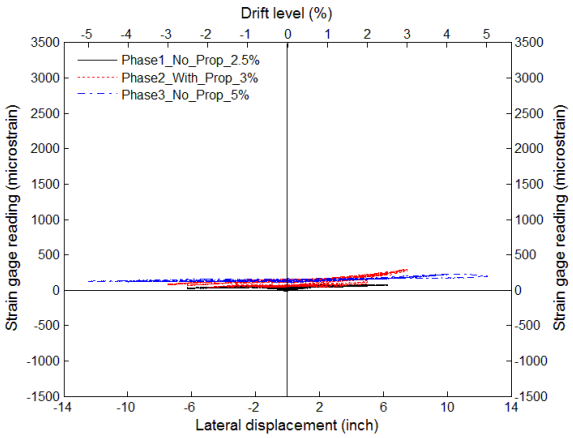

Fig. 6-123 Readings of SG-FWT-B2 in Phase 1 through Phase 3

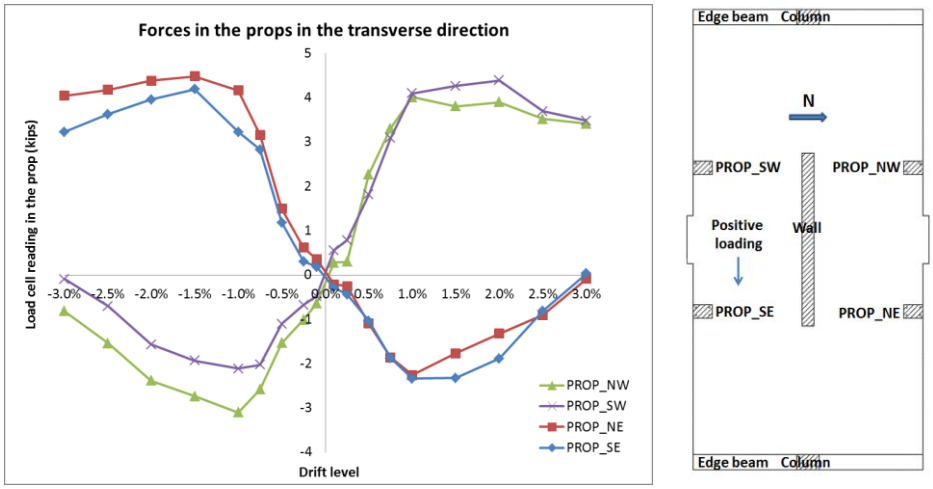

Fig. 6-124 Axial forces – lateral wall drift response of the props at different peak drifts in Phase 2

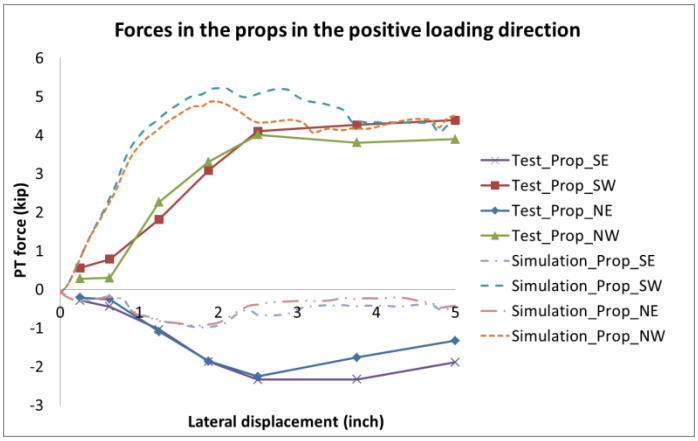

Fig. 6-125 Comparison of the forces in the props recorded in the test with those obtained from "Model-A PFS1" (with props)

Fig. 6-126 Flexural cracks at the base of the east edge column at 0.25% drift (view from north)

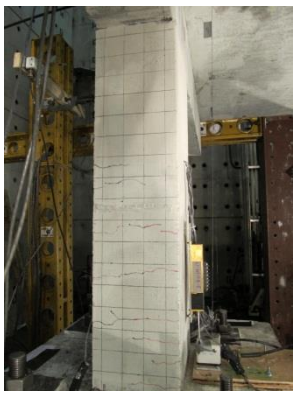

Fig. 6-127 Distributed cracks in the west edge column at 1% drift (view from south)

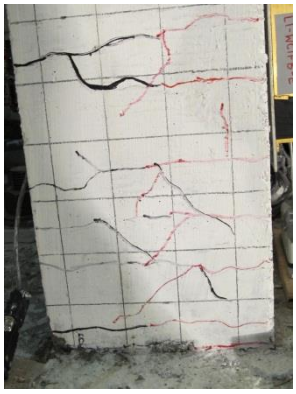

Fig. 6-128 Shear cracks in the west edge column at -1.5% drift in Phase 1 (view from south)

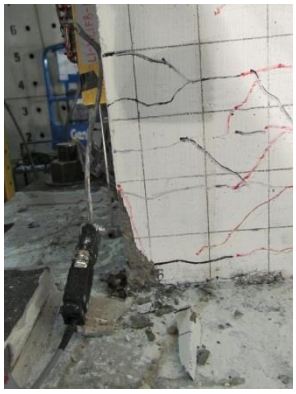

Fig. 6-129 Spalling of concrete cover in the west edge column at -2.5% drift in Phase 1 (view from south)

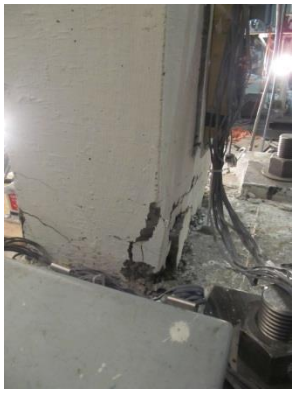

Fig. 6-130 Damage to the edge column during the biaxial loading in Phase 4

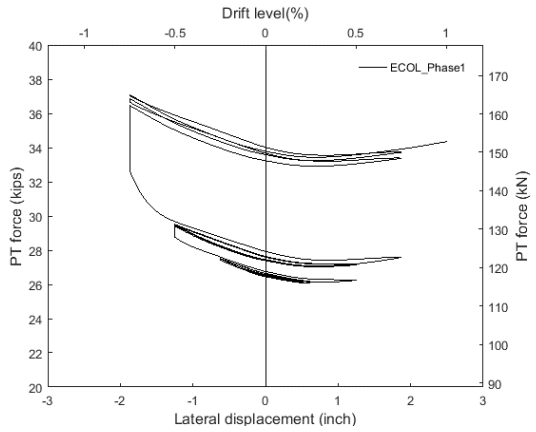

Fig. 6-131 PT force – lateral wall displacement response of the east edge column

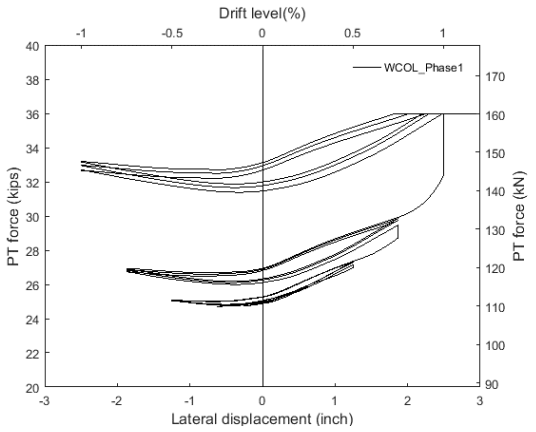

Fig. 6-132 PT force – lateral wall displacement response the west edge column

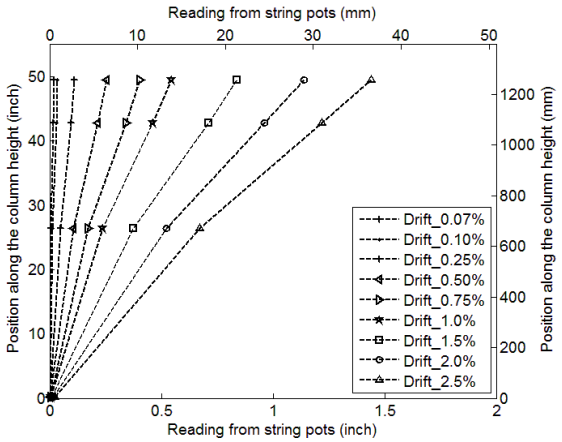

Fig. 6-133 Deformed shapes of the east edge column in Phase 1

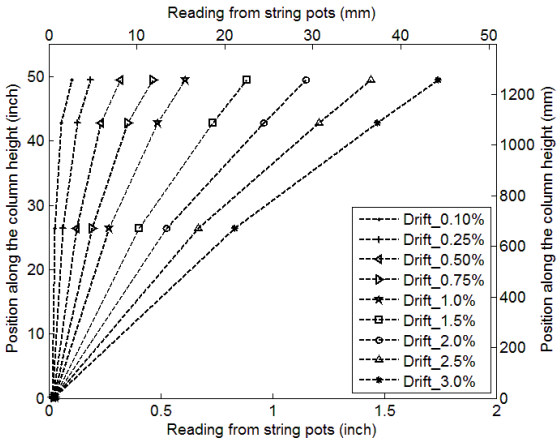

Fig. 6-134 Deformed shapes of the east edge column in Phase 2

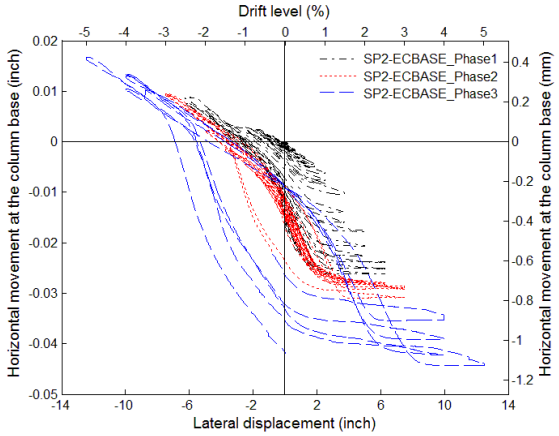

Fig. 6-135 Readings of SP2-ECBASE at the base of the east edge column in Ph1, 2&3

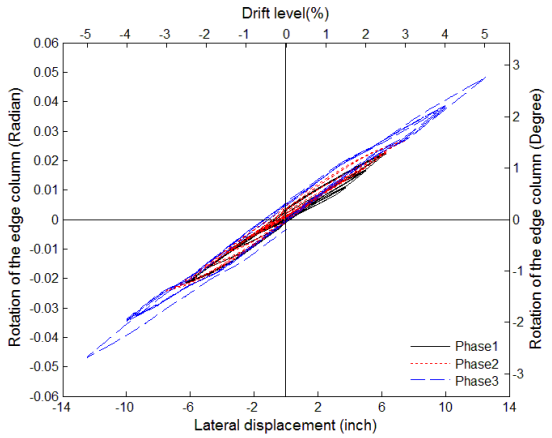

Fig. 6-136 Rotation – lateral wall displacement response at the base of the east edge column in in Ph1, 2&3

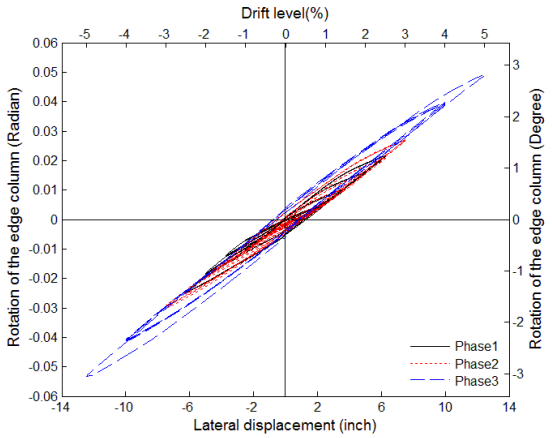

Fig. 6-137 Rotation – lateral wall displacement response at the base of the west edge column in in Ph1, 2&3

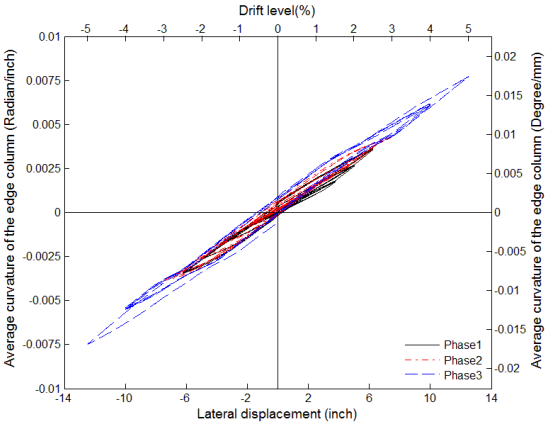

Fig. 6-138 Average curvature – lateral wall displacement response at the base of the east edge column in Ph1, 2&3

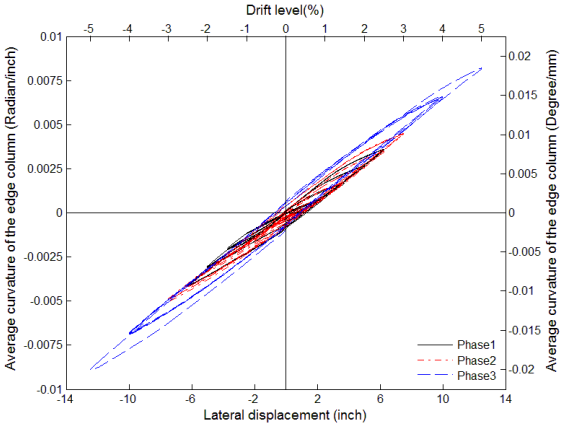

Fig. 6-139 Average curvature- lateral wall displacement response at the base of the west edge column in Ph1, 2&3

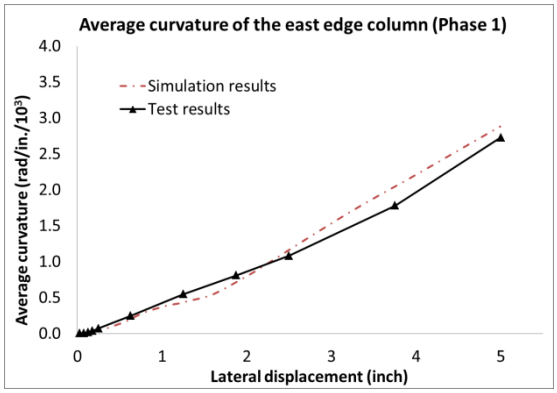

Fig. 6-140 Comparison of the average curvatures at the base of the east edge column in the test with those obtained from the model

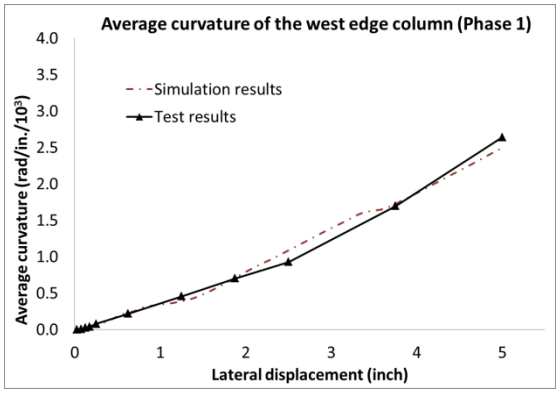

Fig. 6-141 Comparison of the average curvatures at the base of the west edge column in the test with those obtained from the model

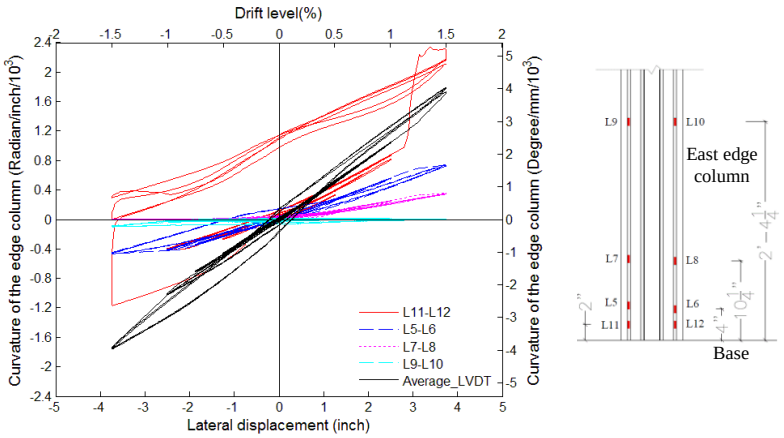

Fig. 6-142 Local curvature distribution along the height of the east edge column in Phase 1

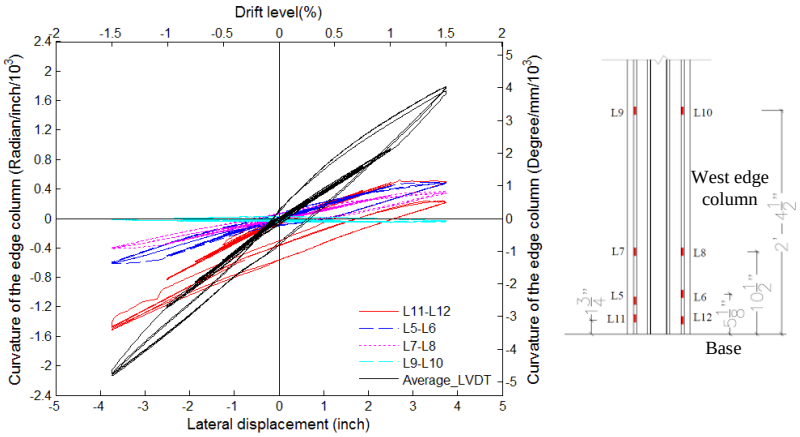

Fig. 6-143 Local curvature distribution along the height of the west edge column in Phase 1

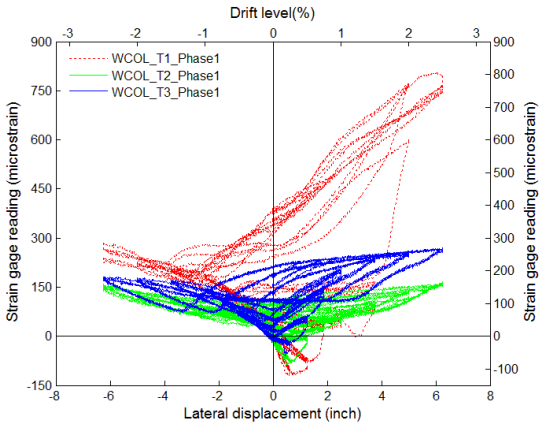

Fig. 6-144 Readings of the strain gages attached to the stirrups in Phase 1

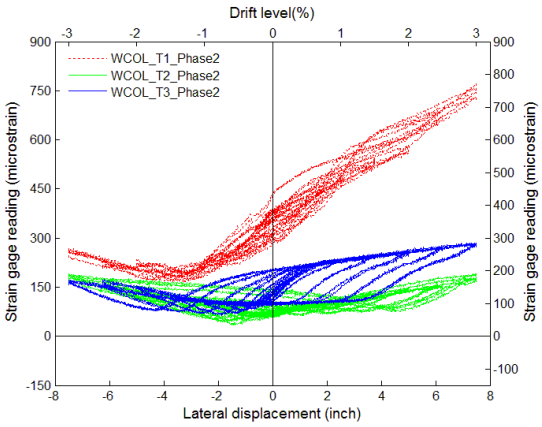

Fig. 6-145 Readings of the strain gages attached to the stirrups in Phase 2

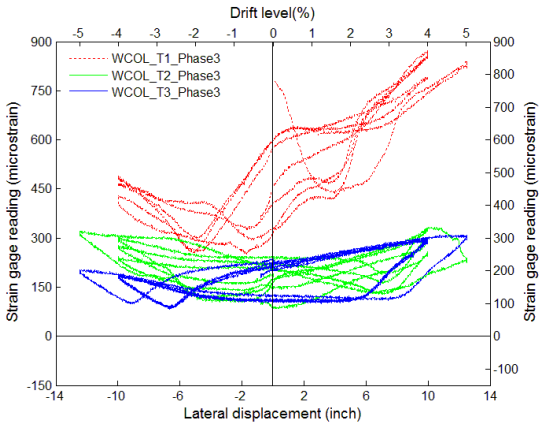

Fig. 6-146 Readings of the strain gages attached to the stirrups in Phase 3

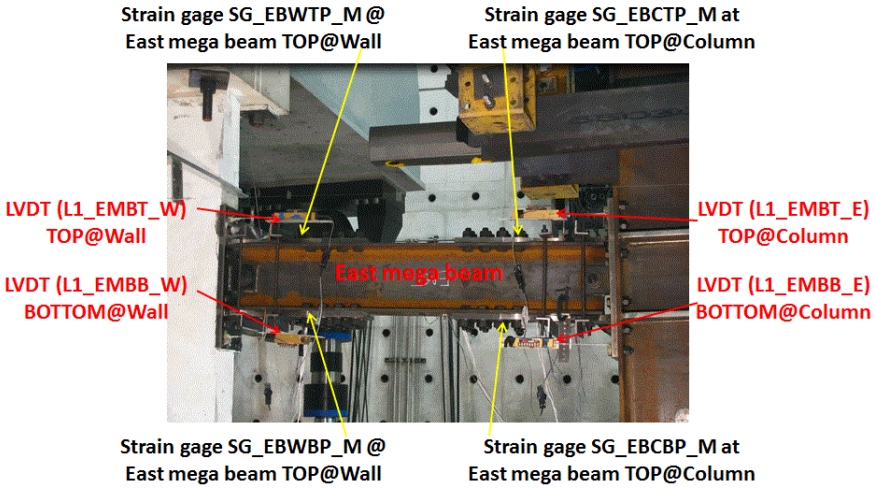

Fig. 6-147 Instrumentation on the east mega beam used for data analysis

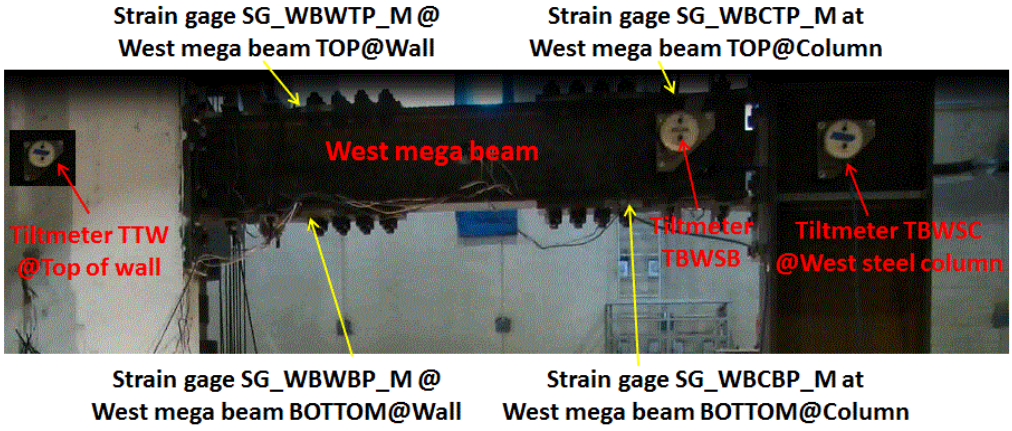

Fig. 6-148 Instrumentation on the west mega beam used for data analysis

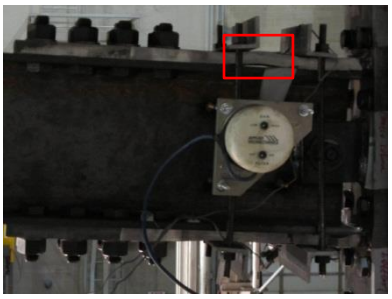

Fig. 6-149 Buckling of the cover plate of the west mega beam at 1% drift in Phase 1

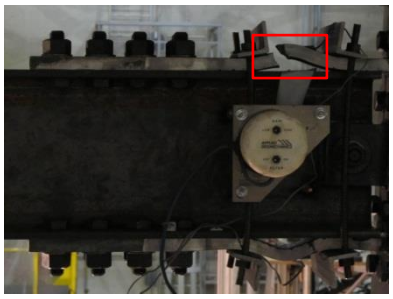

Fig. 6-150 Fracture of the cover plate of the west mega beam at 1.5% drift in Phase 2

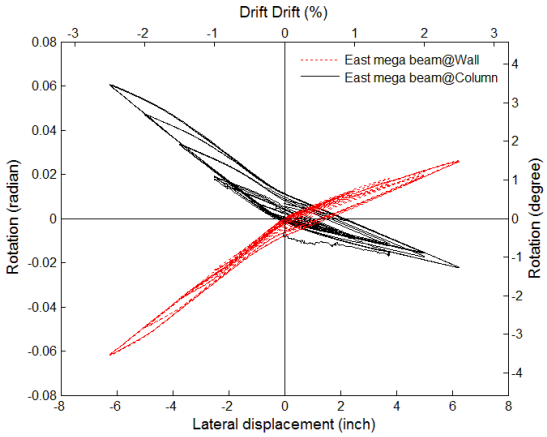

Fig. 6-151 Relative rotation – lateral wall displacement response of the east mega beam

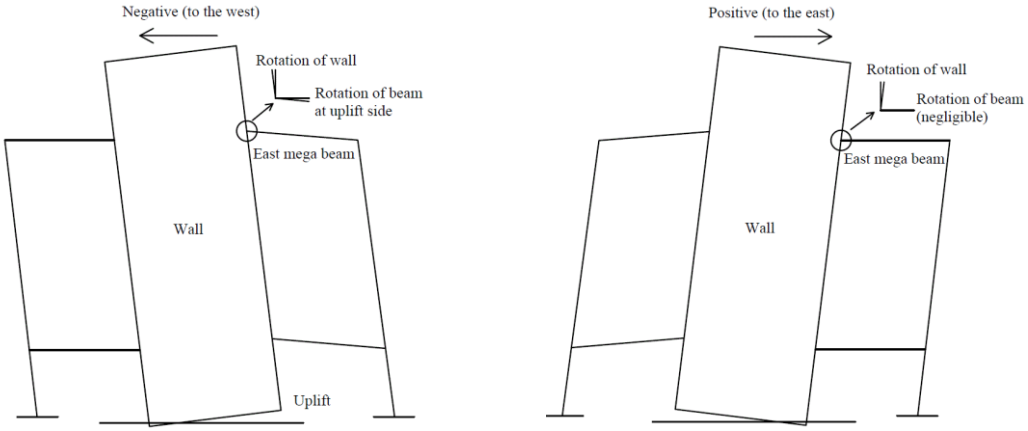

(a) Negative loading direction (b) Positive loading direction

Fig. 6-152 Illustration of the relative rotations of the east mega beam at the beam-wall connection

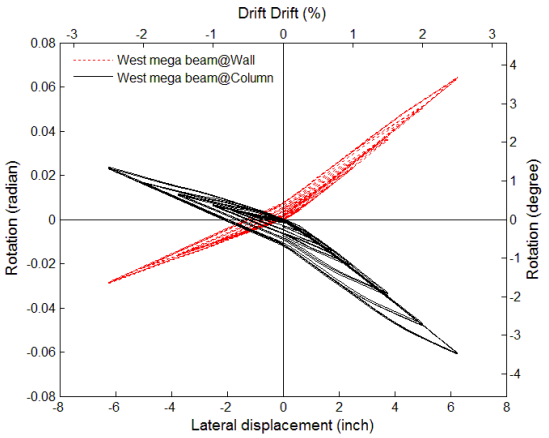

Fig. 6-153 Relative rotation – lateral wall displacement response of the west mega beam at the beam-wall and the beam-column connection in Phase 1

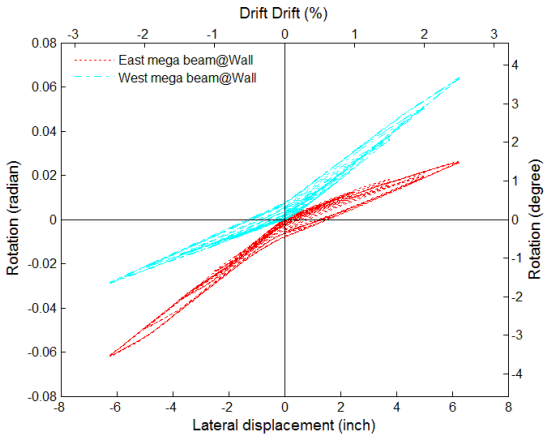

Fig. 6-154 Comparison of the rotations at the beam-wall connection of the east mega beam with those of the west mega beam

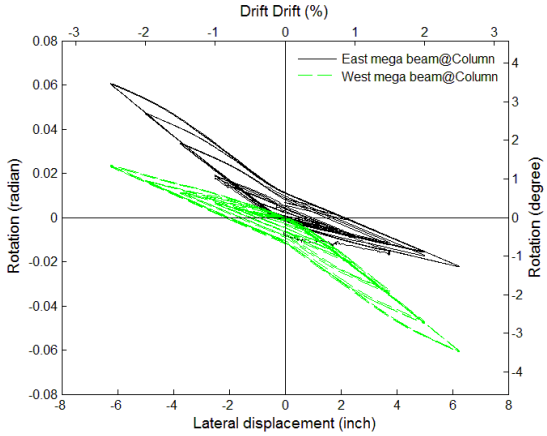

Fig. 6-155 Comparison of the rotations at the beam-column connection of the east mega beam with those of the west mega beam

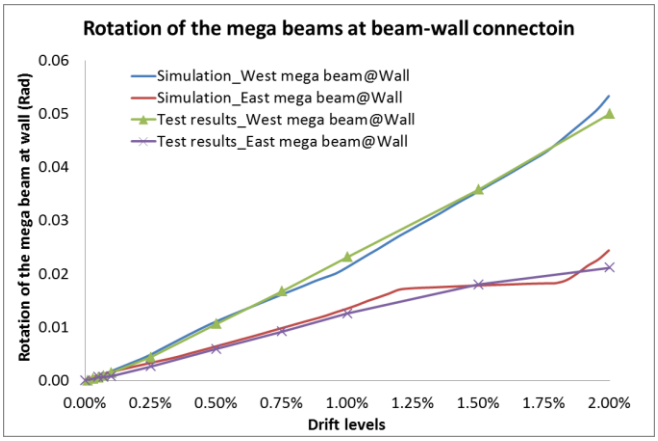

Fig. 6-156 Relative rotations of the mega beams in the test with those obtained from simulation

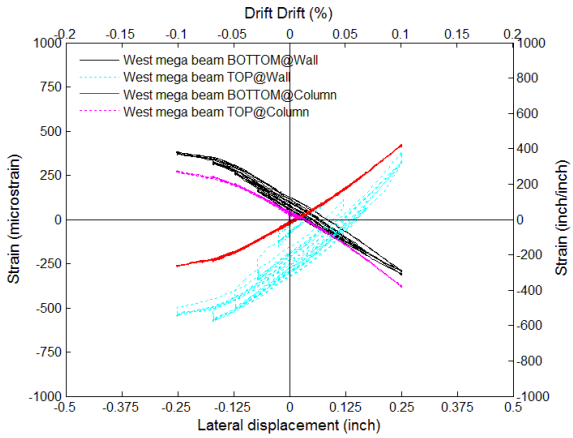

Fig. 6-157 Readings of the strains in the west mega beam cover plates at the beam-column connection

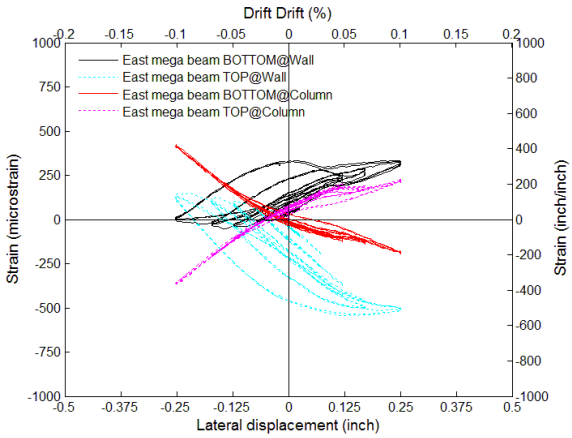

Fig. 6-158 Readings of the strains in the east mega beam cover plates at the beam-column connection

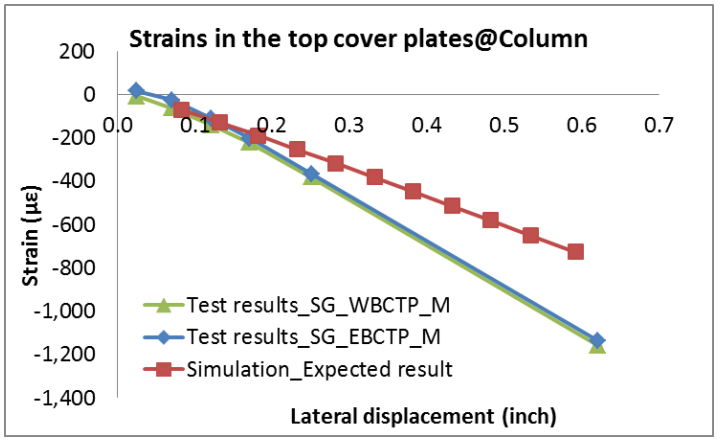

Fig. 6-159 Comparison of the strains in the top cover plate of the east and the west mega beam at the beam-column connection with those obtained from "Model-A PFS1" (without props)

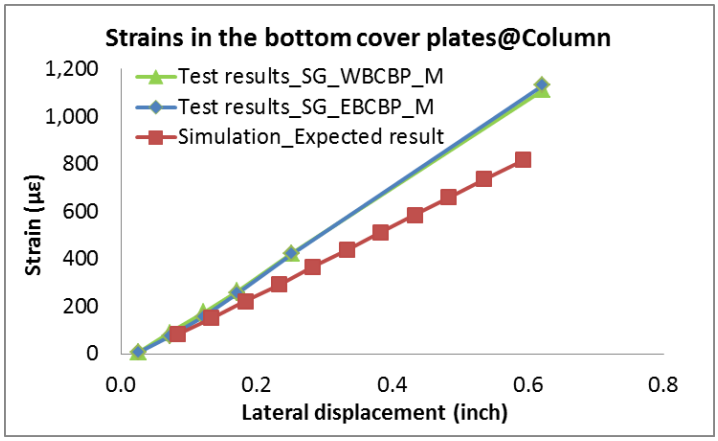

Fig. 6-160 Comparison of the strains in the bottom cover plate of the east and the west mega beam at the beam-column connection with those obtained from "Model-A PFS1" (without props)

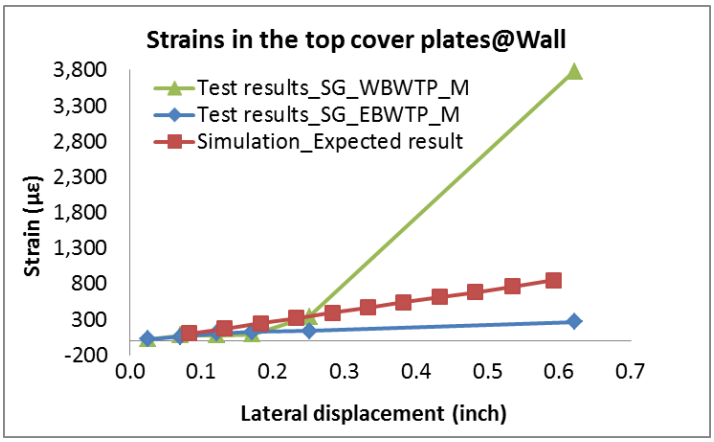

Fig. 6-161 Comparison of the strains in the top cover plate of the east and the west mega beam at the beam-wall connection with those obtained from "Model-A PFS1" (without props)

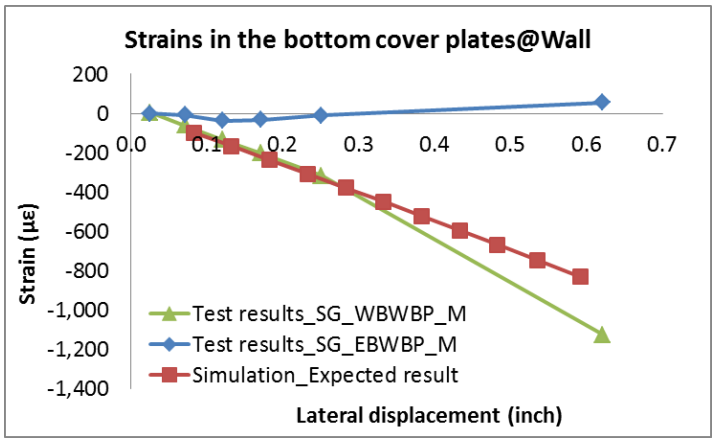

Fig. 6-162 Comparison of the strains in the bottom cover plate of the east and the west mega beam at the beam-wall connection with those obtained from "Model-A PFS1" (without props)

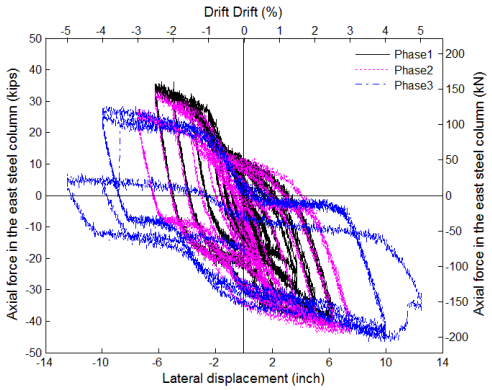

Fig. 6-163 Axial force – lateral wall displacement response of the east steel column in the test

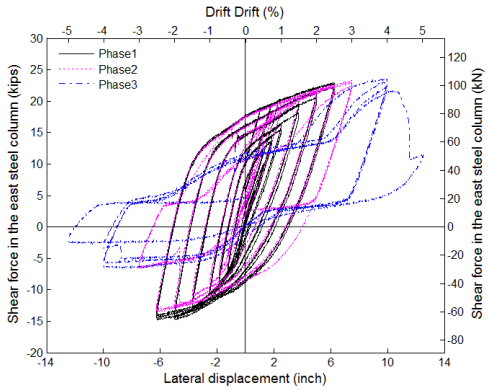

Fig. 6-164 Shear force – lateral wall displacement response of the east steel column in the test

CHAPTER 7. Test Observations and Data Analysis for PFS2

This chapter describes the test observations and data analysis for PFS2. Section 7.1 describes the overall behavior of PFS2 in the twelve phases of testing. Section 7.2 through Section 7.7 describe the behavior of different structural components, including rocking wall, fiber grout, end columns, O-connectors, precast floor, edge columns, and mega steel trusses. In each section, the damage observed in the structural component is described first, followed by the data analysis of the test. Section 7.8 summarizes the conclusions from PFS2.

7.1 Overall behavior of PFS2

The overall behavior of PFS2 is discussed in this section, including the strength, residual drift, and base shear resistance.

7.1.1 Strength

7.1.1.1 Phases of Testing

PFS2 was subjected to twelve phases of testing that featured different boundary conditions and loading protocols. A summary of the phases is given below. A detailed description is given in Section 4.5.2.

In Phase 1 and 2, the base plates of the edge columns were not tightened to the base block and the edge columns were expected to behave like rocking columns. Props were not attached to the transverse beams in Phase 1, but were attached in Phase 2. The presence of props emulated an adjacent frame line featuring columns; the absence of props emulated an adjacent rocking-wall system. In Phase 3 and 4, the base plates of the edge columns were tightened to the base block. This fixed column base connection remained until Phase 9. Props were not attached to the transverse beams in Phase 3, but were attached in Phase 4. In Phase 5, PFS2 was loaded to higher drift levels (4%).

PFS2 was subjected to biaxial loading in Phase 6. One cycle of a “butterfly-shaped” loading pattern was applied to 2% drift and two cycles of a “butterfly-shaped” loading pattern to 3% drift were conducted in this phase. The test resumed in-plane loading in

Phase 7 during which PFS2 was loaded to 5% drift. Two BS Italia connections were torched in Phase 8 and PFS2 was again loaded to 5% drift in this phase. Before Phase 9 began, the second story steel mega trusses were removed.

To investigate the behavior of an isolated rocking wall panel, the impact from the surrounding structures was minimized in Phase 10: the props were removed; the PT forces in the rods in the edge columns and the PreWEC end columns were removed; the nuts that tightened the base plates of the edge columns to the base block were removed and all O-connectors were torched. PFS2 was again loaded to 5% drift in this phase.

The isolated wall panel was subjected to biaxial loading in Phase 11. The following loading protocols were conducted in sequence: one cycle of "butterfly-shaped" loading to 2% drift; one cycle of in-plane loading to 3%; one cycle of "butterfly-shaped" and "cloverleaf-shaped" loading to 3% drift; a half cycle of "butterfly-shaped" loading to 3% drift and a cycle of "butterfly-shaped" loading to 4% drift.

No axial load was applied to the wall in Phase 1 through Phase 11. A constant axial load (96.8 kips) was applied to the wall in Phase 12 to investigate the impact from the gravity loads on the wall. PFS2 was loaded to 2% drift in this phase.

In-plane behavior of PFS2 in Phases 1 through 5, Phases 7 through 10 and Phase 12 is discussed first in this section, followed by discussions of the biaxial behavior of PFS2 in Phase 6 and that of the isolated rocking wall panel in Phase 11.

7.1.1.2 In-plane Behavior

Fig. 7-1 shows the force-displacement curves of PFS2 in the first two phases of testing. The only difference in these two phases was that props were attached to the transverse beams in Phase 2 but not in Phase 1. As shown in the figure, the constraint effect from the props had little impact on the overall behavior of PFS2 by comparing the curves in the last cycle of Phase 1 with those of Phase 2. The readings from the load cells showed that the axial forces in the props were all smaller than 1 kip in Phase 2, further demonstrating that the constraint effect was not significant. The props were attached to the transverse beams that were connected to the PreWEC end columns. Because the width of the end columns was small, the uplift of the end columns was small when they rocked, inducing little axial deformation demand on the props and thus negligible axial

forces in the props. It was believed that each frame line of such a structure in a prototype building would behave relatively independently because the impact from the structural elements in parallel frame lines was small.

Fig. 7-2 shows a comparison of the force-displacement curve in Phase 1 with that in Phase 3. The only difference in these two phases was that rocking edge column base connections were used in Phase 1 while fixed-base edge column base connections were used in Phase 3. As shown in the figure, the strength of PFS2 increased approximately 2.5% at 2% drift in Phase 3 compared with that in the last cycle of 2% drift in Phase 1. Similarly, a small increase in strength (3%) can be observed by comparing the hysteresis curves with props in Phase 2 (rocking edge columns) with those in Phase 4 (fixed-base edge columns), as shown in Fig. 7-3. To be discussed in Section 7.6, the moment resistance of the fixed-base edge columns was larger than that of the rocking edge columns, which contributed to the increased overall strength. Because the strength of the entire specimen was mainly provided by the wall, whose stiffness was much larger than that of the edge columns, the increase in overall strength was small.

Fig. 7-4 shows the force-displacement curves recorded in Phase 4, Phase 5 and Phase 7. In these phases, the boundary conditions were the same with props attached and fixed-base edge columns being used. The strength of PFS2 reached the peak at 4% drift in Phase 5 and dropped approximately 10% at 4% drift in Phase 7. It was believed that some of the O-connectors fractured after Phase 5, which reduced the strength of PFS2.

Fig. 7-5 shows a comparison of the force-displacement curve of PFS2 in the last cycle of 5% drift in Phase 7 with that in the first cycle of 5 % drift in Phase 8. The only difference in these two phases was that two of the four BS Italia connections were torched before Phase 8. As shown in the figure, the force-displacement curves in the two phases are similar. It was believed that the resistance from the PreWEC system and the surrounding structures did not change much under these two conditions. Because the shear resistance of each full-scale BS Italia connector was much larger than the expected shear force transferred in the test, it was believed that even when there were only two BS-Italia connections left in Phase 8, the slab was still successfully isolated from the vertical movement of the wall. Therefore, the overall behavior of PFS2 was similar in these two

phases. The amount of shear force transferred by each BS-Italia connection is discussed in Section 7.5.3.

Fig. 7-6 shows a comparison of the force-displacement curve of PFS2 in the first cycle of 5% drift in Phase 9 (steel tubes removed) with that in the last cycle of 5% drift in Phase 8 (steel tubes attached). As shown in the figure, the removal of the steel trusses (steel tubes) did not have noticeable impact on the overall strength of PFS2.

Fig. 7-7 shows a comparison of the force-displacement curve of PFS2 in the first cycle of 5% drift in Phase 10 with that in the last cycle of 5% drift in Phase 9. In Phase 10, only the rocking wall panel contributed to the strength of the entire specimen. As shown in the figure, the strength of PFS2 at 5% drift in Phase 10 was approximately 12% lower than that in Phase 9 that was caused by the removal of the surrounding structures. The surrounding structures did not contribute much to the strength of PFS2.

Because the BS Italia connections only transferred horizontal shear forces, the gravity loads from the tributary area of the wall were sustained by the end columns instead of the wall in PFS2 in the first eleven phases of testing. In Phase 12, a constant axial load was applied to the wall through the crosshead to investigate the impact on the overall behavior if the gravity load had been transferred to the wall in PFS2. Fig. 7-8 shows a comparison of the force-displacement curve of PFS2 in Phase 12 with that in Phase 11. As shown in the figure, the strength of the wall greatly increased in Phase 12. Because the width of the wall was much larger than that of the end columns, the gravity loads sustained by the wall provided a great amount of resisting moment due to a much longer lever arm of the wall. It demonstrated the advantage of transferring the gravity load to the wall instead of the end columns that was realized by using rigid wall-floor connections (discussed in Chapter 6).

After discussing the behavior of PFS2 under in-plane loading, the behavior of PFS2 under biaxial loading in Phase 6 and Phase 11 is discussed below.

7.1.1.3 Biaxial Behavior

In Phase 6 when PFS2 was under biaxial loading, it was found that the upper portion of the wall (above the first story floor) bent in the out-of-plane direction while the lower portion of the wall (below the first story floor) remained relatively straight. Fig. 7-9

shows the deformed shape of the wall in Phase 6. Fig. 7-10 compares the out-of-plane rotations of the wall above and below the floor that were recorded by the tiltmeter TTW and TBW. The location of TTW and TBW is shown in Fig. 4-15. As shown in Fig. 7-10, the readings recorded by TTW are much larger than TBW that further validates the observation in Fig. 7-9. It was believed that the edge columns and props constrained the lower portion of the wall from bending in the out-of-plane direction. However, there was no constraint to the wall above the floor and the out-of-plane stiffness of the wall was relatively small, the out-of-plane displacement of PFS2 was mainly provided by the flexural bending of the upper portion of the wall instead of rocking of the wall. The purpose of investigating the out-of-plane behavior of PFS2 was not fully realized in Phase 6 due to the limitation of the boundary conditions to the elements of the test specimen not attached to the crosshead.

In Phase 11, because the props were removed and the deboned edge columns as well as end columns provided little resistance to the wall, it was expected that there was little out-of-plane constraint to the wall in this phase. Fig. 7-11 compares the out-of-plane rotations of the wall above and below the floor recorded by TTW and TBW. As shown in the figure, the readings of TTW are only slightly larger than those of TBW that was likely due to the flexural deformation of the wall. The rocking behavior of the wall in the out-of-plane direction was the dominant factor in this phase. Fig. 7-12 shows the force-displacement curves of PFS2 in both the in-plane and the out-of-plane directions in Phase 11. The drop in in-plane strength at peak drifts occurred as PFS2 was held at that in-plane drift level and loaded in the out-of-plane direction. Similar to PFS1, the strength of the wall in the out-of-plane direction was much smaller than that in the in-plane direction.

7.1.2 Residual Drift

Fig. 7-13 summarizes the residual displacement/drift of PFS2 recorded at the end of each drift level when it was under in-plane loading.

Because of the usage of BS-Italia connections that isolated the floor from the vertical movement of the wall, it was expected that the constraint effect from the surrounding structure would be small. As shown in the figure, the maximum residual drift in Phase 1

was only 0.08% (corresponding to 0.2 in. lateral displacement at the top of PFS2), indicating that the surrounding structures did not compromise the self-centering capability of the rocking wall.

One cycle of loading (2% drift) was applied in Phase 2 when the pinned-pinned props were attached to the floor. As shown in Fig. 7-13, the residual drift did not change (the marker for Phase 2 was coincident with that for Phase 1 at 2% drift). Because the out-of-plane deformation of the floor was small due to the use of the BS Italia connections, it was expected that the 3D constraint effect of the floor would be small and the structural elements in the adjacent frame line would have little impact on the tested wall frame.

In Phase 3, the rocking edge column base connections that were used in Phase 1 and Phase 2 were changed to fixed edge column base connections. Yielding of some of the rebar in the fixed-base edge columns was expected to hinder the self-centering of the wall. However, as shown in Fig. 7-13, the maximum residual drift in Phase 3 was 0.055%, which is still considered negligible. It was believed that because the stiffness and the strength of the edge columns were much smaller than those of the wall, the impact from the plastified edge columns on the self-centering capability of the wall would not be significant.

One cycle of loading (2% drift) was conducted in Phase 4 with props attached and fixed-base edge columns used. The residual drift of PFS2 was 0.049% in Phase 4, which was close to that recorded in Phase 3. Again, adding props had little impact on the overall behavior of PFS2.

As shown in Fig. 7-13, the residual drift greatly increased when PFS2 was loaded to 4% drift in Phase 5. To be shown in Fig. 7-32 in Section 7.2.3, the PT strands started to yield at 3% drift. The residual PT force recorded when PFS2 was unloaded from the peak of 4% drift in Phase 5 was greatly reduced such that it greatly decreased the self-centering capability of the wall and resulted in the subsequent increased residual drift.

As shown in Fig. 7-13, the residual drift of PFS2 reached the peak (0.152%) after the 4% cycles in Phase 7, but it dropped to 0.088% after the 5% cycles in Phase 7. It was believed to be mainly caused by the complete fracture of some of the O-connectors that reduced the resisting moment on the wall. The residual drift of PFS2 did not change

much after Phase 7, when it went through the largest lateral drift cycles (5%) in the test. In Phase 8 through Phase 12, it was observed that the further loss of the residual PT force was small (e.g., the PT loss was only 1.5% of the residual PT force recorded at the end of Phase 7), indicating that the further decrease of the self-centering capability of the wall was negligible in these phases.

7.1.3 Base Shear Resistance

A numerical model of the isolated rocking-wall system tested in PFS2, including the wall, the end columns and the O-connectors, was built as described in Chapter 5. Fig. 7-14 shows a comparison of the envelope curve of PFS2 in Phase 1 with the pushover curve obtained from the numerical model. As shown in the figure, the base shear of PFS2 was only slightly larger than that of the isolated rocking-wall system (e.g., approximately 4% larger at 2% drift). Because the precast floor was successfully isolated from the vertical movement of the wall (to be discussed in Section 7.5.1), it was believed that the surrounding structure had little contribution to the strength of PFS2. The higher base shear was believed to be mainly contributed by the shear resistance of the edge columns.

SP2_EW0 was attached to the east corner of the wall to monitor the shear sliding of the wall as shown in Fig. 4-15. Similar to the discussion of PFS1 in Section 6.1.3, when PFS2 was loaded to the east, little penetration occurred to the east wall end and there was little impact on the readings of SP2_EW0 due to rocking of the wall. The readings of SP2_EW0 recorded when PFS2 was loaded to the east were used for analysis. Fig. 7-15 shows the horizontal movement of the wall at the base at different positive peaks up to 5% drift. As shown in the figure, the slip of the wall was negligible and shear sliding failure was not observed in the test.

7.1.4 Summary of the Overall Behavior of PFS2

As discussed in Section 7.1.1 and Section 7.1.2, the props and the surrounding structure did not have significant impact on the overall in-plane behavior of PFS2 (Phase 1 and Phase 2). The strength of PFS2 was slightly increased after rocking edge columns were changed to fixed-base edge columns (Phase 3 and Phase 4). The strength of PFS2

reached the maximum value at the first peak of 4% drift in Phase 5. Some of the O-connectors fractured after the 4% drift cycles and the strength of PFS2 started to decrease. In Phase 6 when PFS2 was under biaxial loading, out-of-plane flexural bending occurred to the unconstrained portion of the wall above the floor. The actual out-of-plane behavior of PFS2 was not realized in this phase. The strength of PFS2 remained stable at 5% drift in Phase 7 and it only decreased about 10%. The operation of torching two BS Italia connections (Phase 8) and removing the steel trusses (Phase 9) did not have a significant impact on the overall behavior. After Phase 9, the surrounding structures were removed and the strength of PFS2 decreased approximately 12% (Phase 10). In Phase 11, it was observed that the isolated wall panel rocked in both in-plane and out-of-plane directions. The strength of the wall in the out-of-plane direction was much smaller than that in the in-plane direction. A constant axial load was applied to the wall in Phase 12 and PFS2 was loaded in the in-plane direction. Compared to the previous phases when the gravity loads were sustained by the end columns, the applied axial load increased the in-plane strength of PFS2 by 26% in this phase.

The residual drift of PFS2 was small throughout the test. It was believed that because the BS Italia connections successfully isolated the precast floor from the wall, the surrounding structures had a very small impact on the self-centering capability of the rocking-wall system. Through the numerical simulation, it was observed that the base shear of PFS2 was only slightly larger than that of the isolated rocking-wall system tested in PFS2, further validating that the surrounding structure had little impact on the overall behavior of the entire specimen. Shear slip of the wall was not observed in the test.

To avoid lengthy descriptions in the following sections, only damage observed in different structural components is described phase by phase in the following sections. For data analysis purposes, Phases 1, 4, 5 and 7 were chosen as representative testing phases. Phase 1 was the first loading phase of the test (no props and with rocking columns), and the other phases used in the data analysis, Phases 4, 5 and 7, all featured props attached and fixed-base edge columns used.

7.2 Behavior of Rocking Wall and Fiber Grout

In this section, the damage that occurred to the wall and the fiber grout beneath the wall in the twelve phases of testing is described first. After describing the observed damage, the behavior of the wall panel in representative phases (Phase 1, 4, 5 and 7) is described in detail, including PT forces, neutral axis depth, strain distribution and lateral motion of the wall.

7.2.1 Damage Observed in the Wall

In Phase 1, a horizontal crack was observed at the wall/fiber grout interface near the east corner of the wall at -0.25% drift (when PFS2 was loaded to the west), as shown in Fig. 7-16. Because the fiber grout was over-poured to be 1/2 in. higher than the bottom of the wall, the observation indicated that the wall might have been uplifted and separated from the fiber grout. The width of the crack became wider and some over-poured grout spalled onto the base block at higher drifts (e.g. 0.5%), as shown in Fig. 7-17. It should be noted that the dark-colored sections in the photo were where the white wash or concrete film spalled off the steel angles armoring the corner of the walls.

In Phase 2, no additional damage was observed until -2% drift when a segment of concrete cover (7 in. wide) spalled off the wall as shown in Fig. 7-18. The damage might have been caused by local stress concentration as explained below.

The spalling was located approximately 20 in. away from the east end of the wall where the contact area between the wall and the fiber grout was reduced due to the existence of embedded dowel rebar that extended across the wall/base block interface. As shown in Fig. 3-92, four dowel rebar embedded in the bottom of the wall were used to prevent out-of-plane movement of the wall during construction and during out-of-plane lateral loading. One of the dowel rebar was located 20 in. away from the wall where the spalling of the concrete was observed.

A 4-in. square piece of foam was placed around each embedded dowel rebar to serve as a “dam” and to prevent the grout from bonding with the rebar. Because the wall was only 6 in. thick and the foam was much less stiff than the grout, there was only 1 in. grout

bearing beneath the wall in the regions where the dowel rebar were located. A local stress concentration developed when the wall contacted the grout and might have caused the spalling of the concrete cover. Although the concrete spalling might have been prevented in the prototype building because of the increased bearing areas provided by thicker full-scale walls, it is recommended that a barrier with a smaller footprint (e.g., foam tube around the dowel rebar) be used beneath the wall to avoid the stress concentration.

In Phase 3, two horizontal cracks were observed at a height of 27 in. from the bottom of the wall at 2% drift as shown in Fig. 7-19. The cracks were located above the O-connector attachment to the wall, originating from the west end of the wall and extending towards the center of the wall. When the wall rocked, the O-connectors on the uplifted side of the wall restrained the uplift and generated local tensile strains in the wall that caused the cracking. Similar observations are shown in Fig. 6-15 during the test of PFS1.

No additional damage was observed in the wall in Phase 4. After the first four phases of testing up to 2% drift levels, little damage was observed in the wall corners. Because the fiber grout used in PFS2 was of the same brand as that used in PFS1 and the fabrication procedure was similar, it was believed that the grout was also weaker than the concrete in the wall. Therefore, damage occurred to the fiber grout instead of the wall (discussed in detail in Section 7.2.2). In Phase 5, flaking of the concrete cover occurred in the wall corners when PFS2 was loaded to higher lateral drifts (4%) as shown in Fig. 7-20 and Fig. 7-21. Little damage occurred to the concrete core in the wall corners.

In Phase 6 when PFS2 was under biaxial loading, cracks were observed on the north surface of the wall near the second story O-connectors, as shown in Fig. 7-22. It should be noted that the lines shown in the figures were added to highlight the observed cracks for clarity. As discussed in Section 7.1.1, the upper portion of the wall above the floor slab bent in the out-of-plane direction due to the constraint from the surrounding structure that were not loaded by the crosshead. Flexural bending in the out-of-plane direction was generated in the wall that caused the cracking. Damage to the wall near the second story O-connectors was also observed, as shown in Fig. 7-23 and Fig. 7-24. It was believed that when the wall bent in the out-of-plane direction, the O-connectors generated an out-of-

plane force in the wall that pulled out the concrete. The O-connectors were connected to both the laterally loaded wall and the unloaded end column.

In Phase 7, the damage in the wall corners became more severe when PFS2 was loaded to 5% drift, as shown in Fig. 7-25.

At 5% drift, there was some separation observed between the steel channel and the concrete at the base of the wall, as shown in Fig. 7-26. The compression forces that transferred through the steel channel at the tip of the wall may have caused the stiff channel to remain straight, while the concrete connected with the other end of the steel channel (far from the tip of the wall) moved upwards due to the uplift of the wall. Consequently, separation occurred between the end of the steel channel (far from the tip of the wall) and and the surrounding concrete.

During Phase 8 through Phase 12, no further damage to the wall was observed. Overall, most of the wall remained intact after 5% drift despite of the minor concrete spalling at the base of the wall.

7.2.2 Damage Observed in the Fiber Grout beneath the Wall

A layer of 8 in. wide, 1-1/4 in. deep and 94 in. long fiber grout was poured above the base block. The grout layer was 2 in. wider than the 6-in. thick wall in the out-of-plane direction. The grout extended 2 in. beyond the east end of the east end column and the west end of the west end column in the in-plane direction.

In Phase 1, the over-poured fiber grout detached from the surface of the wall and spalled onto the base block when the wall uplifted, as shown in Fig. 7-27. There was no other noticeable damage to the fiber grout beneath the wall until 2.5% drift in Phase 5, as shown in Fig. 7-28. A great amount of concrete debris fell on the fiber grout layer at larger drifts in Phase 5, making it difficult to examine the condition of the grout subsequently during the test. The debris was removed following the end of the test. Fig. 7-29 and Fig. 7-30 show the condition of the fiber grout beneath the east and the west corner of the wall. As shown in the figures, the damage of the grout beneath the wall was not severe.

7.2.3 PT Forces in the Wall

Different from PFS1, no pocket existed in the base block of PFS2 and the fiber grout was directly poured onto the base block. When the wall uplifted, the fiber grout spalled onto the base block instead of being trapped in the pocket as observed in PFS1. Fig. 7-31 shows the residual gap opening in Phase 1. As shown in the figure, the absolute residual gap opening was negligible (smaller than 0.009 in.) even at drifts of 2%. There was little fiber grout or concrete cover debris that deposited beneath the wall.

Fig. 7-32 shows the PT forces recorded in the representative phases (Phase 1, 4, 5 and 7). As shown in the figure, the residual PT forces in the wall remained almost constant before 2% drift in Phase 1. Yielding of the strands occurred when PFS2 was loaded to 3% drift level in Phase 5. It satisfied the requirement in Section 4.4.7 of ITG-5.2 that the strands should not yield at design drifts (e.g., 2%). The residual PT force kept decreasing after yielding as the wall was subjected to larger drift levels. It was approximately 69% of the initial PT force at the end of Phase 7. Fracture of the strand wires did not occur in PFS2.

7.2.4 Neutral Axis Depth of the Wall

Similar to PFS1, a group of LVDTs was used to measure the gap opening across the wall/base block interface. By plotting the LVDT readings with respect to the locations of the LVDTs along the width of the wall, the neutral axis (N.A.) depth of the wall could be obtained. Fig. 7-33 shows the LVDT readings recorded at different positive peaks in Phase 1. The readings were linearly extrapolated to the position at the east end of the wall (abscissa equals to 34 in.) in the figure. The N.A. depth can be directly deduced from the figure. It was different from PFS1 where the debris became trapped in the pocket, which resulted in a non-negligible residual gap opening of the wall and the LVDT readings had to be processed to deduce the N.A. depth, as discussed in Section 6.2.3.

Fig. 7-34 shows the N.A. depth of the wall in the representative phases. Table 7-1 lists the values. In general, the N.A. depth recorded during the positive loading (at the east wall corner) was similar to that recorded during the negative loading (at the west wall

corner). The assumption proposed by Aaleti (2011) that the N.A. depth did not change much after 0.5% drift was not very accurate. On the other hand, the assumption that the N.A. depth did not change much after the design drift (assumed to be 2%) was reasonable when PFS2 was loaded in the positive or the negative direction (ITG 2009).

7.2.5 Strain Distribution in the Wall

Multiple groups of strain gages were used to investigate the force flow in the wall. The location of the gages is shown in Fig. 4-17. Because CG_CEWB2 were not functioning during the test, the second row of the concrete gages (CG_EWBC2 /CG_CEWB2 /CG_CWWB3) was excluded from the data analysis.

More concrete gages were placed in the west corner than the east corner of the wall. In the following sections, data analysis is only conducted when PFS2 was loaded in the negative direction and the west wall corner was in contact with the fiber grout.

Phase 1

Fig. 7-35 shows the compressive strain distribution along the width of the wall near the base measured by CG_EWBC1-1/1-2/1-3, CG_CEWB1, CG_CWWB1, and CG_WWBC1-1 when PFS2 was loaded to the negative peak in Phase 1. Fig. 7-36 and Fig. 7-37 show the readings from the 3rd and the 4th row of concrete gages from the bottom of the wall (CG_EWBC3/ CG_CEWB3/ CG_CWWB3 and CG_EWBC4/CG_CEWB4/CG_CWWB4). Although straight lines are used to connect the limited data points in Fig. 7-35 through Fig. 7-37, the actual strain distribution might not be linear between two adjacent data points. Fig. 7-38 shows the tensile strains in the stirrups distributed along the height of the wall (SG_WWB_T1 through SG_WWB_T6).

As shown in Fig. 7-35 and Fig. 7-38, the maximum concrete compressive strain and the maximum stirrup tensile strain were only 2290 and 528 $\mu\varepsilon$, respectively. The confinement effect of the boundary elements provided limited value in Phase 1. Similar to PFS1, the compressive strength of the confined concrete in the wall corners was believed to be larger than that of the fiber grout beneath the wall. The weaker fiber grout was plastified instead of the concrete in the wall corners, resulting in an extended N.A. depth and small compressive strains in the wall. The extended N.A. depth of the wall is

further discussed in Section 9.1.2. It was also observed in Fig. 7-38 that the tensile strains that developed in the stirrups located above 10 in. from the wall base were very small, indicating that the compressive stresses that concentrated at the wall corner along the base block distributed with the width of the wall over its height.

As shown in Fig. 7-35, the readings of the strain gage closest to the wall ends (abscissa equal to -34 in.) kept increasing in Phase 1. This was different from the observation in PFS1 where the strain gage reading closest to the west wall end (abscissa equals to -45 in. in Fig. 6-30) dropped after -0.75% drift. Different from PFS1 where the concrete cover spalled before 2% drift, no damage to the wall corners was observed at 2% drift in PFS2. Therefore, the strains in the wall end kept increasing at higher drift levels when the concentrated compression force in the wall corners increased due to the increased PT force (shown in Fig. 7-32) and the decreased N.A. depth (shown in Fig. 7-34).

Phase 4, Phase 5 and Phase 7

Fig. 7-39 shows the compressive strain distribution along the width of the wall near the bottom of the wall in Phase 4 and 5. The readings of the concrete gages close to the wall end surpassed the reliable measurement range of the gages (20,000 με) at 5% drift in Phase 7, thus they were not used for the analysis. Fig. 7-40 and Fig. 7-41 show the readings from the 3rd and the 4th row of concrete gages. Fig. 7-42 shows the tensile strains in the stirrups distributed along the height of the wall. Test data from Phase 7 is included in Fig. 7-40 through Fig. 7-42.

As shown in Fig. 7-39 and Fig. 7-42, the maximum concrete compressive strain and the maximum tensile strain in the stirrup were approximately 4,560 με and 780 με in Phase 5. The confinement effect from the stirrups became noticeable, but not significant. Again, the tensile strains were small in the stirrups located above 10 in. from the wall base. The maximum reading above that height was only approximately 100 με at 4% drift in Phase 5, further validating the conclusion that the compression force at the corner distributed across the width of the wall along the height of the wall.

After describing the strain distribution in the wall, an in-depth discussion of the force flow in the rocking wall is given below.

Disturbed region and Bernoulli region in the rocking wall

When the wall rocked about the corners, it was expected that the compression force would concentrate at the wall corners and spread to the rest of the wall with height. According to Saint Venant's Principle, the wall can be divided into disturbed and undisturbed (i.e., Bernoulli) regions where plane sections remain plane. The height of the disturbed region was expected to be approximately equal to the width of the wall (68 in.).

As shown in Fig. 7-36 and Fig. 7-40, strain compatibility was not valid across the wall section where the 3rd row of concrete gages was located (17 in. above the base of the wall). On the other hand, strain compatibility was approximately valid (shown in Fig. 7-37 and Fig. 7-41) at the cross section where the 4th row of concrete gages was located (148 in. above the base of the wall). Although there were some local disturbances created by the O-connectors and the steel trusses, the prediction that the height of the disturbed region was about 68 in. according to the Saint Venant's Principle seemed reasonable to explain the test observation.

Strain distribution along the height of the wall

Fig. 7-43 and Fig. 7-44 show the compressive strain distribution at the wall corner along the height of the wall (CG_EWBC1-1, CG_EWBC2 and CG_EWBC3) in Phase 1 and Phase 4 and 5, respectively. Similar to PFS1, it was found that the strains rapidly decreased along the height of the wall. For example, as shown in Fig. 7-44, the compressive strain decreased from -4600 με at 4 in. above the wall base to -1400 με at about 9 in. above the wall base. The observation further demonstrated that the compression force spread in the disturbed region at the wall corners and the strain concentration in the wall corners was a local behavior.

Data from Krypton system

The Krypton LEDs that were attached to the first story of the wall are shown in Fig. 7-45. As shown in the figure, the LEDs were distributed over a large region of the wall to enable determination of the average strain distribution over the region.

Fig. 7-46 shows a comparison of the distributed strains in the wall deduced from the LEDs with those recorded by the concrete gages at 1.5% drift in Phase 1. As shown in the figure, the compressive strains spread from the wall corner to a larger cross section along

the height of the wall in general. For example, the strains decreased from -5150 με (the LED in the first row and first column) to -432 με (the LED in the first row and sixth column) in the horizontal direction. In the vertical direction, the strains decreased from -432 με (the LED in the first row and sixth column) to -49 με (the LED in the third row and sixth column); the strains changed from a small tensile strain 44 με (the LED in the third row and seventh column, not within compression zone) to a compressive strain -167 με (the LED in the seventh row and seventh column, within compression zone) in the vertical direction.

7.2.6 Lateral Motion of the Rocking Wall

Deformed shape of the wall

Four string pots (SP2_EW0, SP20_EW2, SP20_EW3 and SP30_EW4) were placed along the height of the wall to investigate its deformed shape. The location of the string pots is shown in Fig. 4-15. Fig. 7-47 shows the deformed shape of the wall at low drift levels in Phase 1 (before 0.10% drift). As shown in the figure, the flexural bending of the upper half of the wall above the floor was noticeable before the wall uplifted at approximately 0.05% drift. The flexural deformation generated by the internal moment in the wall was the major contributor to the lateral displacement of the wall at the low drift levels. At higher drift levels in Phase 1 after the wall uplifted, rigid body motion dominated the lateral movement of the wall, as shown in Fig. 7-48.

Because PFS2 was loaded from 2% drift in Phase 4, 2.5% drift in Phase 5 and 4% drift in Phase 7, rigid body motion was the dominant lateral deformation mode of the wall at the peaks in those phases, as shown in Fig. 7-49. Similar conclusions were obtained in the test of PFS1.

Flexural deformation of the wall

Fig. 7-50 compares the readings recorded by the tiltmeter TTW and TBW in Phase 1. Similar to the observation in PFS1, the readings in TTW that was attached to the top portion of the wall were always larger than those in TBW, which was believed to be mainly contributed by the flexural bending of the wall. The behavior was also observed when PFS2 was loaded to larger drifts.

7.3 Behavior of the End Columns and the Transverse Beams

The two PreWEC end columns placed adjacent to the wall ends extended above the first story floor. Because of the use of BS Italia connections, the gravity loads from the tributary area of the wall were transferred to the end columns instead of the wall in PFS2. The end columns are critical structural components in the rocking-wall structures using this type of special wall-floor connections, sustaining the gravity loads and connecting with the O-connectors. It should be noted that the gravity loads were simulated by post-tensioned unbonded threaded rod in the end columns in the test.

This section describes the damage that occurred to the end columns and the fiber grout beneath the end columns, followed by the discussion of the PT forces, strain distribution, confinement effect, lateral motion and rotation of the end columns in representative phases. The behavior of the transverse beams is also briefly discussed.

7.3.1 Damage to the End Columns

In Phase 1, minor concrete cover spalled off the east corner of the east end column at 1.5% drift, as shown in Fig. 7-51. Spalling of the concrete was also observed in the west corner of the west end column at -1.5% drift in Phase 1, as shown in Fig. 7-52. The observed damage is explained below. Fig. 7-53 illustrates the force flow in the end columns. As shown in the figure, when the wall was loaded to the east, the east end column displaced laterally and rotated about the east corner. The resistance from the O-connectors attached to the east side of the wall provided compressive forces in the east end column. Combining with the PT force in the east end column that emulated the gravity load from tributary areas of the wall, a relatively large compression force was generated in the east corner of the east end column and caused the concrete spalling. On the other hand, the resistance from the O-connectors attached to the west side of the wall provided tensile forces in the west end column. The tensile forces counteracted the PT force in the west end column and thus reduced the compression force in the corner. No concrete spalling was observed in the east corner of the west end column. Instead, the west corner of the west end column was damaged when PFS2 was loaded to the west.

In Phase 2 through Phase 4 when the largest lateral drift was the same as that in Phase 1 (2%), the extent of the damage to both end columns did not change much. Despite minor concrete cover spalling, the damage to the end columns was not significant.

In Phase 5, other than the damage to the east corner, flaking of the concrete was also observed in the west corner of the east end column at -4% drift, as shown in Fig. 7-54. Similarly, some damage to the east corner of the west end column was observed at 4% drift. As shown in Fig. 7-55, the concrete cover within 2 in. from the base of the column (i.e., one marked grid) spalled off.

Fig. 7-56 shows the damage to the east corner of the west end column viewing from a different angle. It is noteworthy that a void is observed in the figure. As discussed in Section 3.6.6, a consolidation issue was encountered during the fabrication of the west end column (shown in Fig. 3-135). Although high strength grout was used to fill the void, it appeared that the void was not completely filled, which reduced the cross section of the west end column and resulted in the damage.

The damage to the end columns remained unchanged in Phase 6. In Phase 7, minor concrete spalling was observed in the west corner of the east end column, as shown in Fig. 7-57. Some of the concrete core of the west end column spalled as shown in Fig. 7-58. As will be discussed in Section 7.3.4, the PT clamping force in the west end column decreased significantly due to the loss of the concrete core. In Phase 10, it was observed that the west end column started to lose contact with the fiber grout as shown in Fig. 7-59. It was believed that the reduced PT clamping force due to the spalling of the base of the west end column was exceeded by the tensile force provided by the O-connectors. Consequently, the PT threaded rod was not able to tie down the west end column to the grout subsequently. The gravity loads sustained by the end columns were emulated by post-tensioned forces in the end columns in the test. In the prototype building, it was expected that the gravity loads would still exist to clamp the end columns to the foundation.

Fig. 7-60 and Fig. 7-61 show the condition of the east and the west end column following the end of the test. In the east end column, the concrete that was approximately 1-1/2 in. deep from the surface of the east corner had spalled. Minor concrete cover

spalled in the west corner of the east end column. In the west end column, the concrete that was approximately 4 in. deep from the surface of the east corner and 3 in. deep from the surface of the west corner had spalled. The more severe damage to the west end column might have been a result of its poor concrete quality that was shown in Fig. 3-135 and discussed in Section 3.6.6.

7.3.2 Damage to the Transverse Beams

No damage to the transverse beams was observed until Phase 6, when the props were attached to the transverse beams and PFS2 was subjected to biaxial loading. Cracks in the bottom surface of the beam adjacent to the beam-column joint were observed, as shown in Fig. 7-62. Cracks in the top surface of the beam were not marked during the test due to the accessibility issue. It was believed that the out-of-plane movement of the wall was restrained by the props. Resisting moments were generated by the axial tension/compression forces in the props that caused the concrete cracking observed at the beam/column joint.

7.3.3 Damage to the Fiber Grout beneath the End Columns

No damage to the fiber grout beneath the end columns was observed in Phase 1. In Phase 2, an inclined crack in the fiber grout beneath the east end column was observed at 2% drift, as shown in Fig. 7-63. The crack in the grout was almost parallel to the boundary of the concrete cover that had spalled off at the east corner of the east end column. A similar inclined crack occurred in the top corner of the fiber grout beneath the west end column at- 2% drift in Phase 2, as shown in Fig. 7-64.

During the construction, a piece of square wood block was placed beneath the center of each end column to prevent the grout from filling the hole reserved for the unbonded PT rod. Because the wood block was less stiff than the fiber grout, a discontinuity existed in the grout bearing. When the end column rocked on the fiber grout, a resultant inclined force was generated in the fiber grout layer that was formed by combining the vertical compression and the horizontal shear force at the base of the end column. The inclined cracks were caused by the resultant force.

In Phase 5, the inclined crack shown in Fig. 7-63 developed into a through crack across the entire depth of the fiber grout layer at 2.5% drift, as shown in Fig. 7-65. Similarly, the inclined crack shown in Fig. 7-64 eventually split off the upper corner of the grout as shown in Fig. 7-66.

Fig. 7-67 and Fig. 7-68 show the condition of the fiber grout beneath the east and the west end column, respectively, following the end of the test. Compared with the condition of the grout beneath the wall (Fig. 7-29 and Fig. 7-30), the damage in the grout layer beneath the end columns was much more severe. It was noteworthy that the wood blocks in the fiber grout layer beneath the wall were located far from the wall corners. Because the grout bearing was continuous, no noticeable damage occurred to the fiber grout beneath the wall corners. Therefore, it is recommended that a spacer with a narrower profile be placed beneath the end columns around the PT rods to avoid the damage.

7.3.4 Prestressing Forces in the End Columns

A load cell was installed on each end column to monitor the force variation in the PT during the tests. The initial PT force in the west and the east end column was 62 and 61 kips, respectively, at the beginning of the test. The expected yield force of the threaded rod was 115 kips according to the mill of certification.

Fig. 7-69 shows the PT force in the west end column in Phase 1. Unsymmetrical behavior is observed in the figure. In general, the PT force was larger in the west column when PFS2 was loaded in the positive direction. For example, the PT force at 2% drift was 74 kips and it was 67 kips at -2% drift in the first cycle. As shown in Fig. 7-53, when PFS2 was loaded to the east (positive direction), the O-connectors attached to the west side of the wall generated uplift forces in the west end column. On the other hand, the O-connectors generated compressive forces in the west end column when PFS2 was loaded to the west (negative direction). The total force in the east corner of the west end column, which consisted of the clamping PT force and the compressive forces from the O-connectors, was larger when PFS2 was loaded to the west (negative direction), resulting in a larger N.A. depth of the west end column at the west corner. It led to a smaller

distance between the PT threaded rod and the rotation point, resulting in a smaller elongation of the PT rod and thus a smaller PT force recorded in the negative direction.

As shown in Fig. 7-69, the PT force started to decrease from the first to the third peak of 1.5% drift in the negative direction. The decrease might be attributed to the damage to the west corner developed at 1.5% drift as shown in Fig. 7-52.

Fig. 7-70 shows the axial force recorded in the east end column in Phase 1. The PT force dropped from 65 kip to 57 kip when PFS2 was held still in the first cycle of 1.5% drift. As shown in Fig. 7-51, concrete cover in the east corner of the east end column spalled off at 1.5% drift. Under this circumstance, the rotation point of the end column moved towards the center of the end column and the distance between the PT threaded rod and the rotation point was reduced. The elongation of the PT threaded rod was reduced due to the decreased lever arm of the PT force that resulted in decreased PT forces in the threaded rod. As shown in the figure, the PT forces keep decreasing at the second and the third peak of the 1.5% drift cycles and all the three cycles of 2% drift as well. The smallest PT force recorded at the third peak of 2% drift was 47 kips, which was even smaller than the initial PT force (61 kips). It was observed that the fiber grout beneath the east corner of the east end column was also damaged in Phase 1. When the end column rocked on the damaged grout, the height of the east end column (i.e. the elongation of the PT rod) was further decreased, which reduced the PT force from its initial value.

Fig. 7-71 shows the PT forces recorded in the west end column in the representative phases. The PT forces dropped significantly in Phase 5, when the damage to the west end column quickly developed in Phase 5 as discussed in Section 7.3.1. It was believed that the spalling of the concrete core in the west end column reduced the height of the west end column (i.e. the elongation of the PT rod), which reduced the PT forces. The PT forces dropped to zero in Phase 7, indicating that the threaded rods completely lost the capability to clamp the west end column to the base block. It explained the observation shown in Fig. 7-59 that the west end column was picked up in Phase 7. Again, it was expected that the gravity loads would still exist in the prototype building, which might clamp the end columns to the foundation.

Fig. 7-72 shows the PT forces recorded in the east end column in the representative phases. Similar to the observation shown in Fig. 7-70, the PT forces kept decreasing when PFS2 was loaded in the positive direction (to the east). As shown in Fig. 7-54, the fiber grout beneath the east corner was completely split off in Phase 5. When the end column rocked about the east corner, it was expected that the height of the east end column (i.e. the elongation of the PT rod) was reduced due to the loss of the grout that caused the decrease of the PT forces.

Fig. 7-73 and Fig. 7-74 compare the impact from the damaged grout and the damaged concrete core on the overall behavior of rocking walls and end columns. As shown in Fig. 7-73, the N.A. depth of the end column was relatively small compared with that of the rocking wall. Once the fiber grout split off and was lost, the end column was more likely to rotate on the foundation below the fiber grout, which reduced the height of the end column (i.e., elongation of the PT rod). Similarly, because the elongation of the PT rod was relatively small due to the small width of the end column, the loss of the concrete core would greatly reduce the height of the end column (i.e., elongation of the PT rod) compared to that of the wall, as shown in Fig. 7-74. The PT clamping forces in the end columns would be greatly reduced in both conditions.

When the clamping PT force was smaller than the tensile forces provided by the O-connectors, the end columns were pulled up by the wall. Under this circumstance, the relative vertical deformation between the end columns and the O-connectors would be greatly reduced, resulting in smaller resistances and less energy dissipation from the O-connectors. Moreover, the pulled up end columns generated additional out-of-plane deformation demands on the floor and caused damage to the floor.

To reduce the damage, special detailing is recommended to highly confine the concrete at the base of the end columns, such as installing steel tubes around the base or steel angles in the corners. It is also recommended the selected grout should be highly ductile to avoid being split off and remain in place beneath the end columns.

7.3.5 Strain Distribution in the End Columns

Four concrete strain gages were used in each end column to investigate the compressive strain distribution. Three steel strain gages were attached to the stirrups to monitor the confinement effect along the height of the end column. The location of the strain gages is shown in Fig. 4-25 through Fig. 4-28.

It was noteworthy that when the end columns were prestressed, neither the concrete strain gages nor steel strain gages were attached to the data acquisition system yet. The strains generated during the post-tensioning operation were not recorded. The actual strain in the concrete where a concrete gage was located should be calculated by adding the initial compressive strain to the recorded concrete gage readings. However, it was found that the initial strain was relatively small compared to the compressive strains recorded in the test. For example, assuming the initial prestressing force was uniformly distributed over the cross section of the west end column, the initial compressive strain in the concrete is calculated below:

$$\varepsilon_{initial} = \frac{F_{initial\_rod}}{E_c(A_g - A_{PT\_hole})} = \frac{62 \times 10^6}{5242 \times (10 \times 6 - 0.25 \times 2.5 \times 2.5\pi)} = 215\ \mu\epsilon \quad (7.1)$$

Where $\varepsilon_{initial}$ = Initial strain in the west end column; $F_{initial\_rod}$ = Initial force in rods in end columns; E_c = Young's modulus of concrete in the west end column (Table 3-8); A_g = Gross cross-sectional area of the west end column; A_{PT_hole} = Cross-sectional area of the PVC pipe of 2-1/2 in. diameter for the PT rod.

In this section, the strain gage readings recorded during the test were directly used for data analysis for simplicity.

Phase 1

Fig. 7-75 shows the readings from the concrete gages embedded near the base of the east end column in Phase 1. CG-E-ECOL-L1 was placed 1-3/4 in. away from the west surface and 1 in. above the base plate. CG-E-ECOL-L2 and CG-E-ECOL-L3 were placed 1-7/8 in. and 2 in. away from the east surface; both were 1-1/2 in. above the base plate.

As shown in the figure, the maximum compressive strain recorded by CG-E-ECOL-L2 and CG-E-ECOL-L3 in the east corner of the east end column was approximately 1,600 με, which was half of the maximum usable compressive strain (0.003) assumed in Section 10.2.3 in ACI 318-11.

Fig. 7-76 shows the readings of CG-E-ECOL-L2 and CG-E-ECOL-L3 in the first cycle of 1.5% drift in Phase 1. Noticeable increase of the compressive strains was observed when PFS2 was held still at the first peak of 1.5% drift cycles. As discussed in Section 7.3.1, damage to the east corner of the east end column and the fiber grout beneath the corner was observed at this drift cycle. It was believed that the compression force in the east end column was redistributed to the undamaged region where the two gages were embedded that caused the noticeable increase of the readings.

Fig. 7-77 shows the readings from the concrete gages located near the base of the west end column in Phase 1. CG-W-ECOL-L1 and CG-W-ECOL-L2 were placed 1-1/2 in. and 1 in. away from the west surface; both were 1-1/2 in. above the base. CG-W-ECOL-L3 was placed 1-1/2 in. away from the east surface and 1 in. above the base.

As shown in the figure, the maximum compressive strain recorded by the concrete gages CG-W-ECOL-L2 and CG-W-ECOL-L3 in the east corner of the west end column was approximately 6,000 με. It was approximately twice the maximum usable strain (0.003). As shown in Fig. 7-56, a void existed in the west end column due to the consolidation issue. A stress concentration might have occurred in the local region where the two concrete gages were located and caused the larger readings.

Phase 4, Phase 5 and Phase 7

The readings of the concrete gages in both end columns did not change much in Phase 4, when the maximum drift was the same as that in Phase 1 (2%).

Fig. 7-78 shows the readings of CG-E-ECOL-L1 and CG-E-ECOL-L2 in the east end column in Phase 5. Comparing Fig. 7-78 with Fig. 7-75, the maximum reading of CG-E-ECOL-L2, which was located in the east corner, dropped from -1,600 με to -500 με. As shown in Fig. 7-57, a great amount of concrete spalled off the east corner of the east end column. It was believed that the compression zone of the end column shifted towards the

center of the end column due to the damage and was further away from the region where CG-E-ECOL-L2 was located.

Damage to the west end column became severe at higher drift levels in Phase 5. Because readings from most concrete gages in the west end column exceeded the reliable measurement range (i.e., 20,000 με), they were excluded from the data analysis herein.

7.3.6 Confinement Effect of the Stirrup

As shown in Fig. 4-25 and Fig. 4-27, strain gages were attached to the stirrups at the base of both end columns to monitor the confinement effect. SG_E_ECOL_T2 in the east end column was broken during the fabrication and it was excluded from the analysis. Abnormal negative readings were recorded by SG_W_ECOL_T1 in the west end column, thus it was also excluded from the analysis.

Fig. 7-79 and Fig. 7-80 show the tensile strains in the stirrups in the east and the west end columns, respectively. As shown in Fig. 7-79, the tensile strains in the first stirrup (T1, 5/8 in. above the column base) were larger than those in the fourth stirrup (T3, 5-1/2 in. above the column base) in general. The readings of T1 greatly increased to 1,190 με at 1.5% drift, but decreased to 450 με when PFS2 was held still at the first peak of the 1.5% drift. As shown in Fig. 7-70, the PT force dropped when PFS2 was held still at the peak of the 1.5% drift due to the concrete spalling at the east corner of the east end column. It was believed that the confinement effect was reduced because the decreased PT force reduced the compression force at the corner and the concrete that spall from the core reduced the pressure on the transverse reinforcement. As shown in Fig. 7-80, the tensile strain in the second stirrup (T2, 2-1/8 in. above the column base) was approximately twice of that in the fourth stirrup (T3, 5-1/2 in. above the column base).

Fig. 7-81 and Fig. 7-82 show the strain gage readings in the east and the west end column in Phase 5, respectively. As shown in Fig. 7-81, the tensile strains in the first stirrup of the east end column increased but those in the fourth stirrup did not change much. Similar behavior was observed in the west end column, as shown in Fig. 7-82.

To conclude, the confinement effect was much more significant near the base of the end columns and it became less effective beyond the base. Because the localized

compression force in the corners spread out to the entire cross section above the base, the maximum compressive strain in the concrete rapidly decreased along the height of the end column. According to the test data, it was found that the steel confinement located at 5 in. above the base (approximately half of the end column width) became less effective.

7.3.7 Lateral Motion of End Columns

Four string pots (SP10_1EC, SP10_2EC, SP10_3EC and SP10_4EC) were used to investigate the deformed shape of the west end column in the test. The location of the string pots is shown in Fig. 4-15. Fig. 7-83 shows the deformed shapes of the end column at low drift levels in Phase 1 (before 0.10% drift). As shown in the figure, the lateral movement in the upper half of the end column above the floor was much larger than that in the lower half. The end column was directly joined to the wall through O-connectors, as shown in Fig. 7-84. When the upper portion of the wall above the floor bent in the in-plane direction before the wall was uplifted, the wall provided a lateral force on the end columns through the O-connectors. Before the end column was uplifted, the lateral displacement at the top of the end column was mainly caused by the flexural deformation of the end column, as shown in Fig. 7-83.

At higher drift levels in Phase 1 when the end column started to rock in phase with the wall, rigid body motion controlled the lateral movement of the wall, as shown in Fig. 7-85. When PFS2 was loaded to 2% drift in Phase 4, from 2.5% to 4% drift in Phase 5, and from 4% to 5% drift in Phase 7, rigid body motion was the predominant lateral deformation mode of the end column, as shown in Fig. 7-86.

7.3.8 Rotation of the East End Column

A tiltmeter TBEC was installed on the east end column to measure its rotation. The location of the tiltmeter is shown in Fig. 4-15. Fig. 7-87 compares the rotations of the end column with those of the wall at the peaks of different drifts in Phase 1. As shown in the figure, the rotations of the end column were similar to those of the wall, indicating that the end column rocked in phase with the wall. The conclusion is further validated in Fig. 7-88, when PFS2 was loaded to higher drift levels in Phase 5 and Phase 7.

7.3.9 Steel Angles Affixed to the Transverse Beams

Steel angles were attached to the transverse beams and the edge beams to support the precast planks. DCDT2, DCDT3 and DCDT4 were used to measure the deformation of the steel angles. The locations of the DCDTs are shown in Fig. 4-16. The body of each of the DCDTs was attached to one leg of the angle and the core of the DCDT was attached to the other leg. The DCDT measured the relative opening or closing of the steel angle.

Fig. 7-89 shows the readings of DCDT3 in the representative phases. The readings of DCDT2 and DCDT4 were similar to those of DCDT3.

As shown in the figure, only the closing of the steel angle (negative readings) was observed in the test and it was negligible (e.g., smaller than 0.012 in. at 5% drift in Phase 7).

The precast planks were connected to the transverse/edge beams by steel straps on the top and sat on the steel angles directly. Because the planks were not fixed to the steel angles, the planks were observed to be picked up by the steel straps and lose contact with the steel angles during the test, as shown in Fig. 7-90.

7.4 Behavior of the O-connectors

7.4.1 Damage to the O-connectors

Yield lines in some O-connectors were observed at 0.75% drift in Phase1, as shown in Fig. 7-91. Readings from the strain gages attached to the O-connectors also indicated that the O-connectors started to yield at this drift level. At higher drift levels, damage occurred to the O-connectors at the weld, as shown in Fig. 7-92. Cracks started to develop in some O-connectors at 4% drift in Phase 5, as shown in Fig. 7-93.

The development of the cracks in the O-connectors was not predictable. Some O-connectors completely failed while others were only partially failed. As an example, both legs of the O-connector shown in Fig. 7-94 completely fractured such that it was not capable of providing any resistance to the wall or dissipating energy. As another example, one half of the O-connector (U-shaped on the top) shown in Fig. 7-95 fractured and the other half (U-shaped on the bottom) did not. The “half-fractured” O-connector

was still capable of generating resistance to the wall and dissipating energy. Different from PFS1 where the O-connectors that were placed at higher levels had more damage than those at lower levels, fracture of the O-connectors was observed at both higher and lower levels in PFS2.

7.4.2 Relative Vertical Movement of the O-connectors

As discussed in Section 6.3.2, existing tests have shown that the behavior of an O-connector can be well predicted by numerical models as long as its relative vertical deformations are recorded. In PFS2, only one LVDT was used to measure the relative vertical deformations of the O-connectors due to the limited amount of instrumentation. That LVDT was placed near the O-connector that was on the north surface of wall at the first floor (west side). Fig. 7-96 shows the relative vertical deformations recorded in Phase 1. Fig. 7-97 shows the relative vertical deformations recorded in Phase 4, Phase 5 and Phase 7. As shown in the figures, the O-connector on the west side of the wall was subjected to a much larger relative deformation when PFS2 was loaded in the positive direction (to the east) than when PFS2 was loaded in the negative direction (to the west). This was because the O-connector was on the uplifted side of the wall in that situation. Because of the limited stroke (4 in.), the LVDT stopped functioning properly when PFS2 was loaded towards 5% drift.

7.5 Behavior of Precast Floor

Because of the use of BS Italia connections, it was expected that the precast floor would be isolated from the vertical movement of the wall when it rocked. In this section, the relative displacement between the wall and the floor is described first to validate the design assumption that the floor would be isolated from the vertical movement. Damage to the precast floor is described in Section 7.5.2. After that a detailed description of the behavior of the precast floor in representative phases (Phase 1, 4, 5 and 7) is given, including the horizontal force transfer, rotation of the planks and performance of the plank-plank connections (JVI Mini V).

7.5.1 Relative Displacement between the Wall and the Floor

Fig. 7-98 shows the marker lines of different colors that were drawn on the wall along the bottom edge of the floor at different drift levels. As shown in the figure, the lines are located at different heights, indicating that relative vertical displacements observed between the wall and the floor. Fig. 7-99 shows the wall-floor interface at 4% drift in Phase 5, when the wall was loaded to the east. As shown in the figure, half of the slotted channel embedded in the east side of the wall is visible while the channel in the west side of the wall is barely visible. These observations show that when the wall rocked, the floor was not picked up by the wall and remained relatively horizontal.

Two LVDTs (L1-FWE-V and L1-FM-V) were used to measure the relative vertical displacement between the wall and the floor. The location of the LVDTs is shown in Fig. 4-15. It was found that L1-FM-V did not function well during the test, thus only L1-FWE-V was used for data analysis. Fig. 7-100 shows the cyclic readings of L1-FWE-V with respect to the lateral displacement of PFS2 in Phase 1. As shown in the figure, relative vertical displacements between the wall and the floor existed and increased when PFS2 was loaded to larger lateral drifts. Unsymmetrical behavior was also observed in the figure. As shown in Fig. 4-15, the LVDT L1-FWE-V was not placed in the center of the wall but to the west of the center of the wall. As expected, the uplift of the wall at the location where the LVDT was attached would be larger when PFS2 was loaded to the east (in the positive direction). Than that when PFS2 was loaded to the west (in the negative direction).

The extent of the isolation (fully or partial) between the wall and the floor is investigated in the following. Assuming the floor was completely isolated from the vertical uplift of the wall, Fig. 7-101 illustrates the relative vertical displacement between the wall and the slab when the wall was loaded to the east. The relative vertical displacement is equal to the uplift of the wall (Δ_{uplift_wall}) minus the uplift of the slab (Δ_{uplift_slab}), which is generated due to the uplift of the end column (Δ_{uplift_endcol}). Δ_{uplift_wall} can be predicted by multiplying the drift angle (θ) with the distance between L1-FWE-V and the rotation point, which is equal to $S_{L1\_FWE\_V}$ (40 in.) minus the N.A. depth of the

wall (c, discussed in Section 7.2.4). Because the width of the end column is relatively small, Δ_{uplift_endcol} can be directly calculated by multiplying the drift angle (θ) by the width of the end column (w_{Ecol} = 10 in.) for simplicity. The estimated relative vertical displacement ($\Delta_{relative\_disp}$) at the location of L1_FWE_V is calculated as follows:

$$\begin{aligned}\Delta_{relative\_disp} &= \Delta_{uplift\_wall} - \Delta_{uplift\_slab} \\ &= (s_{L1\_FWE\_V} - c)\theta - \frac{w_{wall} - s_{L1\_FWE\_V}}{w_{wall}}\Delta_{uplift\_endcol} \\ &= (40 - c)\theta - \frac{68 - 40}{68}(w_{Ecol}\theta) \approx (36 - c)\theta\end{aligned} \quad (7.2)$$

Fig. 7-102 compares the readings of L1-FWE-V recorded in the test with $\Delta_{relative\_disp}$ estimated by using the equation above at positive peaks of different drifts in Phase 1, 5 and 7. As shown in the figure, the estimated values matched well with the readings of L1-FWE-V, indicating that the floor was fully isolated from the vertical uplift of the wall by using the BS Italia connections. The design purpose was fulfilled.

Although the floor was fully isolated from the vertical movement of the wall, some damage to the precast floor was still observed during the test, which is described in the following sections.

7.5.2 Damage to the Precast Floor

The precast floor consisted of planks, BS Italia connections, strap plates and JVI Mini V connectors. Performance of the four components is discussed below.

Planks

No damage occurred to the planks in Phase 1 (with rocking edge columns and without props) and Phase 2 (with rocking edge columns and with props). At 0.75% drift in Phase 3 (with fixed-base edge columns and without props), cracks were observed in the two planks that were directly connected to the wall by BS Italia connections (marked as Plank 4 in Fig. 3-104) as shown in Fig. 7-103 and Fig. 7-104. The cracks were approximately 20 in. away from the edge of the floor and extended perpendicular to the wall.

As shown in Fig. 3-108, two U-shaped rebar (marked in red) were placed around the embedded plates of the strap plates (marked in cyan). They were terminated at

approximately 17-1/2 in. away from the edge of the floor. It was believed that the observed cracks were caused by the discontinuity of the rebar at the location where the tensile stress in the rebar was transferred to the surrounding concrete. Because the cracks did not grow in the following phases of testing, the damage was negligible. No cracks were observed in the other planks.

BS Italia connections

Fig. 7-105 shows the condition of the BS Italia connections at 4% drift in Phase 5. No cracks or fracture of the connections were observed in the test. Shown in Section 7.5.3, the horizontal force transferred by each BS Italia connection was much smaller than its design capacity, which explains the undamaged condition of the BS Italia connections.

Strap plates

No damage occurred to the strap plates in Phase 1 through Phase 4. When PFS2 was loaded to higher drift levels (3% and 4%) in Phase 5, yield lines were observed in the strap plates across the plank-edge beam and the plank-transverse beam connection, as shown in Fig. 7-106 and Fig. 7-107. Although the planks were successfully isolated from the vertical movement of the wall, the strap plates were still subjected to flexural bending due to the non-negligible rotations of the planks. The rotation demand on the strap plates is discussed in detail in Section 7.5.4.

JVI Mini V connectors

JVI Mini V connectors were used as plank-plank connections in the test. Fig. 7-108 shows the condition of the connector following the end of the test. No damage was observed to occur to the JVI Mini V connectors and the concrete of the planks adjacent to the connectors. As expected, the JVI Mini V connectors remained elastic throughout the test.

7.5.3 Horizontal Forces Transferred by the BS Italia Connections

A component test that focused on investigating the performance of BS Italia connections was conducted at Iowa State University before the test of PFS2 (Watkins 2014). The test setup is shown in Fig. 7-109. As shown in the figure, an isolated rocking wall panel (without energy dissipating elements) was loaded through two “floor tubes”

(shown in yellow) attached to the wall and connected to a horizontal actuator. Four BS Italia connections (marked as “Connector” in the figure) were welded to the floor tubes to transfer the horizontal force to the wall.

The results of the component test showed that when each BS Italia connection sustained a 26 kip horizontal force, the floor was fully isolated from the uplift of the wall at 2% lateral drift. The BS Italia connection was capable of sliding 1 in. along the vertical slot channel. The V-shaped connector got jammed in the channel when the vertical sliding demand was larger than 1 in., causing unexpected flexural bending of the floor tubes. Under this circumstance, the BS Italia connections failed to isolate the floor tubes from the vertical movement of the wall.

It was believed that when the V-shaped connector transferred the load between the floor and the wall, the connector stud compressed the surface of the slot channel. A friction force was generated on the surface that constrained the vertical sliding of the connector stud. Therefore, the amount of the maximum horizontal force transferred by each BS Italia connection was a key factor to be considered in the design.

In the test of PFS2, strain gages were attached to both top and bottom surfaces of the steel straps to measure the horizontal forces transferred between the wall and the floor. The location of the strain gages is shown in Fig. 4-30.

Using the readings from the strain gages (SG_P19_A5, SG_P20_A6, SG_P23_A5, SG_P24_A6, SG_P27_A5, SG_P28_A6, SG_P35_Y, SG_P36_A6, SG_P39_A5, SG_P40_A5, SG_P43_A3 and SG_P44_A6) that were attached to the strap plates at the west floor-transverse beam connection, the horizontal forces transferred between the floor and the west side of the wall in Phase 1, Phase 4, and Phase 5 were deduced and are shown in Fig. 7-110 through Fig. 7-112. The method to calculate the horizontal force transferred by each steel strap was discussed in Section 4.4.2.

As shown in Fig. 7-110, the maximum horizontal force transferred between the floor and the west side of the wall was 7.7 kips in the positive loading direction and 9.8 kips in the negative loading direction in Phase 1.

After the base plate of the edge column was tied down to the base block in Phase 4, the maximum horizontal force transferred between the floor and the west side of the wall

increased to 16.0 kips in the positive loading direction and 15.4 kip in the negative loading direction, as shown in Fig. 7-111. To be shown in Fig. 7-144 in Section 7.6.5, the moment resistance of the fixed-base edge column was approximately twice of that of the rocking edge column. The fixed-base edge columns provided a larger resistance to the wall and increased the transferred horizontal forces. The behavior of the edge columns is discussed in detail in Section 7.6.

As shown in Fig. 7-112, the maximum transferred force was slightly larger in both positive and negative loading directions when PFS2 was loaded to higher drift levels in Phase 5 (e.g. 18.2 kips at 3% and -18.7 kips at -4% drift). It was believed after the fixed-base edge columns had yielded in Phase 4, the moment resistance of the edge columns slightly increased due to the strain hardening effect of the rebar that provided a larger resistance to the wall.

Comparing Fig. 7-112 with Fig. 7-111, the residual displacements of the edge columns (identified as the displacements at which the curves crossed the horizontal axis) were greatly increased at higher drift levels (3% and 4%) in Phase 5 due to the damage developed in the edge columns.

Because the strap plates yielded in Phase 5, it was found that the strain gages attached to some strap plates started to generate abnormal readings. The data in the following phases of testing were not used for data analysis.

To conclude, the maximum horizontal force transferred between the floor and the west side of the wall was approximately 19 kips in Phase 1 through Phase 5. Assuming the force was evenly distributed to the two BS Italia connections, the force that each connection sustained was 9.5 kips. It was about one third of the nominal shear resistance of the BS Italia connection (26 kips). With this amount of transferred load, the connector stud successfully slid up to 1.5 inch along the slotted channel at 5% drift. It showed that the connector stud was capable of sliding a larger distance when the force transferred by each BS-Italia connection was smaller than the nominal shear resistance (26 kips).

As shown in Fig. 7-101, the vertical sliding demand on each BS Italia connection was directly related to the location of the BS Italia connection placed in the wall. The arrangement of the BS Italia connections is another key factor to be considered in design.

Design recommendations for this type of special wall-floor connection are given in Section 9.3.1.

7.5.4 Rotation at the Floor-Edge Beam and the Floor-Transverse Beam Connections

As discussed in 7.5.2, yield lines on the strap plate across the floor-edge beam and the floor-transverse beam connections were observed in Phase 5, as shown in Fig. 7-106 and Fig. 7-107. As discussed in Section 7.5.3, the maximum horizontal force transferred between the floor and the west side of the wall was approximately 19 kips in Phase 5, which was small compared to the yield strength of one strap plate:

$$F_{y\_strap} = f_y A_{strap} = 47 \times 0.375 \times 4 = 70.5\ kips \quad (7.3)$$

Where F_{y_strap} = Yield strength of a strap plate; f_y = Yield stress of the strap plate (shown in Table 3-7); A_{strap} = Cross-sectional area of a strap plate.

There were eight strap plates across each floor-edge beam (floor-transverse beam) connection, thus the maximum axial tension/compression force sustained by each strap plate would be much smaller than its yield strength. Assuming the maximum horizontal force (19 kips) was evenly distributed to the eight strap plates, it was calculated that the stress in each of the eight strap plates would only be 19/8/(0.375×4)=1.6 ksi. Therefore, yielding of the strap plates was not caused by the horizontal force transferred between the wall and the floor.

As shown in Fig. 7-101, although the floor was isolated from the vertical movement of the wall, the strap plates at the floor-transverse beam connections were subjected to flexural bending due to the rotations of the end columns that rocked in phase with the wall. Similarly, the strap plates at the floor-edge beam connections were also subjected to flexural bending due to the rotation of the edge columns. It was believed that yielding of the strap plates was caused by the rotation demand on the strap plates. The behavior of the strap plates observed in the test is explained below.

Four groups of LVDTs (Series of FCL and MFCL) were used to investigate the rotation demand on the strap plates across the floor-edge beam connections. Six groups of LVDTs (Series of FWL1, FWL and MFWL) were used across the floor-transverse beam connections. L1-FWL-T4/B4 and L1-FWL-T5/B5 measured the rotations between the

center planks (planks with BS Italia connections) and the transverse beam. LVDTs L1-FWL-T1/B1, L1-FWL1-T2/B2, L1-FWL-T3/B3 and L1-MFWL-T2/B2 measured the rotations between three of the four west edge planks (without BS Italia connections) and the transverse beam. The location of the LVDTs is shown in Fig. 4-29. It was found that L1-FWL-T1 did not function well during the test, thus the group of L1-FWL-T1/B1 was excluded from data analysis.

Phase 1

Yielding of the strap plates was not observed in Phase 1. Fig. 7-113 shows the rotations of the strap plates across the plank-edge beam connection in Phase 1. As shown in the figure, the rotations were uniformly distributed. For example, the largest rotation was recorded by FCL-T3/B3 (0.0228 rad) and the smallest was recorded by FCL-T1/B1 (0.0213 rad) at 2% drift. The difference between the largest and the smallest values was very small. Because the edge beam was much stiffer than the strap plates, the torsional deformations of the edge beam caused by the moment resistance of the strap plates was relatively small, rendering the uniformly distributed rotations of the strap plates across the plank-edge beam connections.

Fig. 7-114 and Fig. 7-115 show the rotations of the strap plates across the edge plank-transverse beam and the center plank-transverse beam connections in Phase 1. As shown in the figures, the rotations of the strap plates near the end column were similar to those of the strap plates further away from the end column. For example, the largest rotation recorded by MFWL-T2/B2 was 0.0214 rad, which was only 13% larger than the smallest rotation recorded by FWL-T3/B3 (0.0187 rad) at 2% drift. Again, because of the existence of relatively stiff transverse beams, uniformly distributed rotations of the strap plates across the plank-transverse beam connection were generated.

Before calculating the moments in the strap plates caused by the recorded rotations, the yield moment resistance of a strap plate is calculated first. As shown previously, the stress in each strap plate caused by the resultant axial tension/compression force was only 1.6 ksi even with the maximum horizontal force transferred between the floor and the wall. To simplify the yield moment calculation, the small resultant axial tension/compression force in the strap plate was neglected.

$$M_{strap\_y} = f_y \frac{I_{strap}}{t/2} = 47 \times \frac{0.375^3 \times 4/12}{0.375/2} \approx 4.4\ kip - in \tag{7.4}$$

Where M_{strap_y} = Moment resistance of a strap plate; I_{strap} = Moment of inertia of a strap plate; t = Thickness of strap plates. The calculated yielding moment resistance is used below to judge the condition of the strap plates.

Fig. 7-116 illustrates the rotations of the strap plates that generated the moments. Assuming a constant moment was distributed along the short length of the strap plate and the strap plate remained elastic, the rotation of the strap (α_{strap}) would be calculated as follows:

$$\alpha_{strap} = \int \varphi_{strap} dL = \int \frac{M_{strap}}{E_s I_{strap}} dL = \frac{M_{strap} L_{strap}}{E_s I_{strap}} \tag{7.5}$$

Transform Eq. (7.5):

$$M_{strap} = \frac{\alpha_{strap} E_s I_{strap}}{L_{strap}} \tag{7.6}$$

Where α_{strap} = Rotation of the strap plate due to flexural bending; M_{strap} = Moment in the strap plate; E_s = Young's modulus of the strap plate; L_{strap} = Length of the strap plate between the weld and the edge of the plank.

The largest rotations recorded at the plank-edge beam and the plank-transverse beam connections in Phase 1 were 0.0228 and 0.0214 rad, respectively. The maximum moments generated in the strap plates in Phase 1 are calculated using Eq. (7.6) as follows:

$$M_{strap\_eb} = \frac{\alpha_{strap\_eb} E_s I_{strap}}{L_{s\_eb}} = \frac{0.0228 \times 29000 \times 0.375^3 \times 4/12}{4.25} \approx 2.6\ kip - in < M_{strap\_y} = 4.4\ kip - in \tag{7.7}$$

$$M_{strap\_tb} = \frac{\alpha_{strap\_tb} E_s I_{strap}}{L_{s\_tb}} = \frac{0.0214 \times 29000 \times 0.375^3 \times 4/12}{4.5} \approx 2.4\ kip - in < M_{strap\_y} = 4.4\ kip - in \tag{7.8}$$

Where M_{strap_eb} = Moments generated in the strap plate at the floor-edge beam connection; α_{strap_eb} = Maximum rotation of the strap plate at the floor-edge beam connection; L_{s_eb} = Length of the strap plate between the end of the strap and the edge of

the plank at the floor-edge beam connection; M_{strap_tb} = Moments generated in the strap plate at the floor-transverse beam connection; α_{strap_tb} = Maximum rotation of the strap plate at the floor-transverse beam connection; L_{s_tb} = Length of the strap plate between the end of the strap plate and the edge of the plank at the floor-transverse beam connection.

As shown above, it was verified through the calculation that yielding of the strap plates would not occur in Phase 1, which matched the test observation in Phase 1.

Phase 5

Yielding of the strap plates was observed in Phase 5. It was found that the maximum rotations of the strap plates recorded at the plank-edge beam and the plank-transverse beam connections were 0.0483 rad and 0.0393 rad in Phase 5, respectively. Assume the strap plates remained elastic and use Eq. (7.6) to calculate the moments in the strap plates:

$$M_{strap\_eb} = \frac{\alpha_{strap\_eb} E_s I_{strap}}{L_{s\_eb}} = \frac{0.0483 \times 29000 \times 0.375^3 \times 4/12}{4.25} \approx 5.5\ kip-in > M_{strap\_y} = 4.4\ kip-in \quad (7.9)$$

$$M_{strap\_tb} = \frac{\alpha_{strap\_tb} E_s I_{strap}}{L_{s\_tb}} = \frac{0.0393 \times 29000 \times 0.375^3 \times 4/12}{4.5} \approx 4.4\ kip-in = M_{strap_y} = 4.4\ kip-in \quad (7.10)$$

As demonstrated above, the strap plates at both the floor-edge beam and the floor-transverse beam connections would yield in Phase 5. It matched the test observation in Phase 5.

To conclude, although the planks were successfully isolated from the vertical movement of the wall during the test, the strap plates connecting the planks to the edge beams and the transverse beams yielded due to the rotation demand on the planks. Although yielding of the strap plates occurred at relatively large drift levels in the test of PFS2 (after 2% drift), it might need to be considered when designing rocking-wall structures with different structural configurations. Design recommendations for the strap plates are given in Section 9.3.2.

7.5.5 Tensile Opening and Shear Slip of JVI Mini V Connectors

Six LVDTs were used to monitor the potential tensile opening (L05_FL_2, L05_FL_4 and L05_FL_6) and in-plane shear slip (L05_FL_1, L05_FL_3 and L05_FL_5) of the plank-plank connections. The locations of the LVDTs are shown in Fig. 4-29.

The maximum reading of L05_FL_2, L05_FL_4 and L05_FL_6 was only 0.014 in. in the twelve phases of testing, indicating that no tensile opening occurred with respect to the JVI Mini V connectors. Similarly, the maximum reading of L05_FL_1, L05_FL_3 and L05_FL_5 was only 0.004 in. during the twelve phases of testing, indicating that no shear slip occurred in association with the JVI Mini V connectors. The connectors performed as expected during the test.

7.6 Behavior of Edge Columns and Edge Beams

In this section, damage to the end columns and the edge beams in all phases is described first, followed by a detailed description of the behavior of the edge columns, including PT forces, strain distribution, confinement effect, rotations, average curvatures, local curvatures, and shear slip. Because some strain gages attached to the rebar stopped functioning after the rebar had yielded in Phase 3, Phase 3 instead of Phase 4 is chosen as one of the representative phases in this section. The behavior of the edge beams is briefly discussed at the end of this section.

7.6.1 Damage to the Edge Columns and the Edge Beams

In Phase 1 and Phase 2, the nuts of the threaded rods were not installed and the base plates of the edge columns were not tightened to the fiber grout layer, as shown in Fig. 7-117. At 0.75% drift in Phase 1, an opening between the base plate and the fiber grout layer was observed, as shown in Fig. 7-118. The opening became larger at 2% drift in Phase 1, as shown in Fig. 7-119. No cracks were observed in the body of the edge columns in Phase 1 and Phase 2.

After the base plate was tightened to the fiber grout layer in Phase 3, cracks in the body of the west edge column were observed at 0.07% drift, as shown in Fig. 7-120. The

cracks kept developing at larger drifts in Phase 3, as shown in Fig. 7-121. The spacing of the cracks was approximately 2 in., which was equal to the spacing of the transverse confining reinforcement in the edge column. Spalling of the concrete cover in the edge columns was observed at 4% drift in Phase 5, as shown in at Fig. 7-122. Fracture of the weld at the base of the rebar was observed through the damaged concrete, as shown in Fig. 7-123. Separation between the concrete and the base plate was also observed, as shown Fig. 7-124. The damage to the edge column became more severe in Phase 6 and buckling of the rebar was observed, as shown in Fig. 7-125. Fig. 7-126 and Fig. 7-127 show the condition of the east and the west edge column after 5% drift in Phase 8, respectively. As shown in the figures, crushing of the concrete concentrated within 4 in. above the base plate, which was half of the depth of the edge column (8 in.). Some of the rebar that buckled in previous cycles fractured.

At the beginning of Phase 10, the edge columns were changed to rocking columns by removing the post-tensioning forces in the edge columns and the nuts that clamped the base plates to the base blocks, as shown in Fig. 7-128. Fig. 7-129 and Fig. 7-130 show the condition of the east and the west edge column after cleaning the debris at the base. Damage to the two edge columns is summarized in Fig. 7-131.

It should be noted that the rebar cages of the edge columns were assembled in the MAST laboratory and some strain gages were attached to the rebar before being shipped to the precasting plant. The assembled cage was welded to the steel plate in the plant. However, it was very difficult to hold the heavy cage stable in place and there were some accessibility problems with the gaged rebar during the welding operation. Therefore, the quality of the weld between the rebar and the steel plate was not reliable, which might have contributed to the fracture of the welds between the rebar and the base plate.

Learning from the precasters, the recommended construction procedure for precast columns is to first weld short rebar to the steel plate, then insert the welded bars anchoring the plate into the column such that the bars welded to the plate form noncontact lap splices with the longitudinal rebar in the column cage. It was believed that the recommended fabrication procedure would lead to better weld quality and alleviate some of the observed damage to the edge columns.

7.6.2 Prestressing Force in the Edge Columns

A 1 in. diameter threaded rod was post-tensioned to emulate the gravity load from tributary areas of the edge column. The nominal tensile strength of the threaded rod was approximately 64 kips according to the mill certification. A load cell was installed on each edge column to measure the PT force variation.

The initial PT forces in the east and the west edge columns were both 28.7 kips at the beginning of the test. As mentioned in Section 7.6.1, little damage occurred to the edge columns in Phase 1 when the base plates of the edge columns were not tightened to the base block. Fig. 7-132 shows a comparison of the axial forceS in the east and the west edge column versus lateral displacement of PFS2 in Phase 1. As shown in the figure, the axial forces in the two edge columns were similar in general; the PT forces in each edge column recorded in the positive loading were similar to those recorded during the negative loading. It was believed that there were few moments and shear forces generated in the steel mega trusses and the precast planks, which were pinned-pinned connected at both ends, the impact from them on the edge columns was small. Therefore, symmetrical PT forces were recorded in each edge column in different loading directions, and the PT forces of the east edge column were similar to those of the west edge column in the same drift level.

Fig. 7-133 shows a comparison of the axial forces in the east and the west edge columns versus lateral displacement of PFS2 in Phase 7, when considerable damage occurred to both edge columns. As shown in the figure, the largest difference of the PT forces in the east and the west edge column occurred at -5% drift in Phase 7 (it was 40.7 kip in the west edge column and 38.2 kip in the east edge column). Again, the difference was only about 7%, which was not large.

The maximum PT force in the west edge column at -5% drift in Phase 7 (40.7 kips) was approximately 42% larger than the initial PT force. Because the PT force was designed to simulate the constant gravity load transferred to the edge column, the increased PT force appeared to contradict the design purpose. However, it was noteworthy that the absolute increase of the PT forces was not large. For example, the

maximum increase (e.g., 40.7-28.7=12 kips) would only generate an average stress of 0.12 ksi over the entire cross section of the edge column. It was believed that the increased stress would not have a great impact on the behavior of the edge columns. Therefore, the gravity load transferred to the edge columns was reasonably simulated by using the post-tensioned threaded rods.

7.6.3 Compressive Strain and Confinement Effect in Edge Columns

Four concrete strain gages were placed at the base of each edge column to measure compressive strains in the concrete. Three steel strain gages were attached to the stirrups to monitor the confinement effect. The location of the strain gages is shown in Fig. 4-20 and Fig. 4-21. Before the test, it was found that multiple strain gages in the east edge column were broken during the construction, including CG-E-GCOL-L2, CG-E-GCOL-L4, SG-ECOL-T1, SG-ECOL-T2, and SG-WCOL-T3. On the other hand, only CG-W-GCOL-L3 and SG-WCOL-T2 were not functioning in the west edge column. It was believed that damage to the strain gages was mainly caused during welding of the longitudinal rebar to the base plate. The west edge column is selected as representative and analyzed in this section.

Concrete resistive strain gages CG-W_GCOL_L1 and CG-W_GCOL_L2 were located approximately 1-1/2 in. above the base plate. Concrete resistive strain gage CG-W_GCOL_L4 was located approximately 12-1/2 in. above the base plate. Steel resistive strain gages SG-WCOL-T1 and SG-WCOL-T3 were attached to the stirrups located 1-5/8 in. and 7-1/4 in. above the base plate.

It was noteworthy that when the edge columns were prestressed, neither the concrete strain gages nor steel strain gages were attached to the data acquisition system yet. The strains generated during the post-tensioning operation were not recorded. For example, assuming the initial prestressing force was uniformly distributed over the cross section of the west edge column, the initial compressive strain in the concrete is calculated as follows:

$$\varepsilon_{initial} = \frac{F_{initial\_rod}}{E_c(A_g - A_{PT\_hole})} = \frac{28.7\times10^6}{5328\times(12\times8 - 0.25\times2.5\times2.5\pi)} = 59\mu\epsilon \quad (7.11)$$

Where $\varepsilon_{initial}$ = Initial strain in edge column; $F_{initial\_rod}$ = Initial force in rods in edge columns; E_c = Young's modulus of concrete in the edge column (Table 3-8); A_g = Gross cross-sectional area of the edge column; A_{PT_hole} = Cross-sectional area of the PVC pipe.

Because the initial strain was relatively small compared to the compressive strains recorded in the test, the readings of the strain gages recorded during the test were directly used for data analysis in the following sections.

Phase 1

Fig. 7-134 shows the readings of the three concrete gages recorded in Phase 1. As shown in the figure, the maximum compressive strain in Phase 1 was only 310 $\mu\varepsilon$ recorded by CG-W-GCOL-L2. The compressive strains in the concrete were small, indicating that the compression force was distributed over a relatively large region in the cross section of the edge column where the gage CG-W-GCOL-L2 was located. Fig. 7-135 shows the readings of the two steel strain gages on the transverse reinforcement recorded in Phase 1. As shown in the figure, the readings were small, indicating that there were few tensile strains developed in the stirrups and the stirrups provided little confinement effect in Phase 1.

Phase 3

In Phase 3, the rocking edge columns were changed to fixed-base edge columns by tightening the base plates to the base block Fig. 7-136 shows the readings of the three concrete gages recorded in Phase 3. The readings of CG-W-GCOL-L2 recorded in Phase 1 are superimposed in Fig. 7-136 for comparison. As shown in the figure, the tensile strains in the concrete increased significantly, which explains the concrete cracking in the body of the edge columns in Phase 3. As shown in the figure, the compressive strain measured by CG-W-GCOL-L2 increased from 310 $\mu\varepsilon$ at 2% drift in Phase 1 to 934 $\mu\varepsilon$ at 2% drift in Phase 3, indicating that flexural deformations of the edge column greatly increased in Phase 3.

Fig. 7-137 shows the readings of the two steel strain gages on the transverse reinforcement recorded in Phase 3 with the readings of SG-WCOL-T1 recorded in Phase 1 superimposed for comparison. As shown in the figure, the readings of SG-WCOL-T1 were much larger than those of SG-WCOL-T3. As expected, the confinement effect was more significant near the base of the edge column. As shown in the figure, the confinement effect became more significant due to the larger compressive strains developed in the concrete in Phase 3. In the fixed-base edge columns, the resultant compression force of the compression zone was equal to the sum of the post-tensioned force that emulated gravity loads and the tensile forces in the longitudinal rebar. It would be larger than that in the rocking edge columns where the resultant compression force of the compression zone was mostly equal to the post-tensioned force.

After discussing the compressive strain and confinement effect in the edge columns, rotation, average and local curvatures of the edge columns are discussed in the following sections.

7.6.4 Rotation and Average Curvature of the Edge Columns

7.6.4.1 Rotation of the West Edge Column

As shown in Fig. 4-16, two groups of LVDTs (L1-WC1FB-E/L1-WC1FB-W and DCDT5/DCDT8) were installed at the base of the west edge column. In the in-plane direction, the total rotation of the west edge column was measured by L1-WC1FB-E/L1-WC1FB-W and the rotation of the base plate was measured by DCDT5/DCDT8. The rotation of the body of the edge column was obtained by subtracting the rotation of the base plate from the total rotation. It should be noted that the LVDTs L1-WC1FB-E/L1-WC1FB-W were placed at 10-1/2 in. above the base plate, thus they were measuring the rotations between the edge columns and the base block over that distance.

Fig. 7-138 and Fig. 7-139 show the total rotation at the base of the west edge column (WGcol_Total), the rotation of the body of the edge column (WGcol_Column) and the rotation of the base plate (WGcol_Plate) in Phase 1 and Phase 3, respectively. As shown in Fig. 7-138, the majority of the total rotation in Phase 1 was contributed by the rotation

of the base plate (e.g., 80% at 2% drift). The rest of the total rotation was provided by flexural bending of the edge column.

As shown in Fig. 7-139, the majority of the total rotation in Phase 3 (i.e., with the base of the columns bolted) was contributed by flexural bending of the edge column (e.g., 76% at 2% drift). It was noteworthy that even after the base plate was tied down to the base block by the threaded rods, the rotation of base plate was still noticeable due to the elongation of the threaded rods. If a precast fixed-base edge column and a cast-in-place edge column of the same height were laterally displaced to the same drift level, the deformation demand on the body of the precast edge column would be smaller because of the rotation of the base plate. Under this circumstance, it was expected that the stiffness of the precast edge columns would be smaller than that of the fixed-base edge columns at the same lateral displacement and less damage would occur to the precast edge columns.

7.6.4.2 Average Curvature of the West Edge Column

The average curvature of the edge column at the base was obtained by dividing the rotations of the body of the edge column with the gage length of the LVDTs. Fig. 7-140 shows a comparison of the average curvatures at the base of the west edge column in Phase 1 and Phase 3. As shown in the figure, the average curvatures of the west edge column in Phase 1 were significantly smaller than those in Phase 3, when flexural deformations were greatly increased in the west edge column.

7.6.5 Local Curvature of Edge Columns

Multiple groups of strain gages were attached to the longitudinal rebar in the edge columns to investigate the local curvature distribution along the height of the edge columns. The location of the strain gages is shown in Fig. 4-18 through Fig. 4-21. The strain gages were attached to the rebar when assembling the steel cages in the laboratory, and then the gaged steel cages were shipped to the precasting plant. It was found that multiple strain gages were damaged during the shipment and the welding operation, including: SG_EGCOL_L2, SG_EGCOL_L4 and SG_EGCOL_L8 in the east edge column, and SG_WGCOL_L1, SG_WGCOL_L2, SG_WGCOL_L7 and

SG_WGCOL_L9 in the west edge column. In this section, the east edge column was used for data analysis.

Fig. 7-141 shows a comparison of the readings of SG_EGCOL_L3 in Phase 1 and Phase 3. SG_EGCOL_L3 was attached to the rebar that was 3-1/2 in. above the base plate. As shown in the figure, the strains in the rebar were much larger in Phase 3 than those in Phase 1. Moreover, the residual strains recorded when the curves cross the horizontal axis in Phase 1 were close to zero, but they were non-negligible in Phase 3. It was believed that after the base plate of the edge column was tightened to the base block in Phase 3, the internal moment at the base of the edge column greatly increased because of the increased flexural deformations, resulting in the larger strains in the rebar. Plastic deformations were generated in the rebar after they yielded in Phase 3.

Fig. 7-142 shows the readings of SG_EGCOL_L7 and SG_ECOL_L14 recorded in Phase 1, Phase 3 and Phase 7. SG_EGCOL_L7 was attached to the rebar close to the top of the first story edge column and SG_ECOL_L14 was attached to the rebar close to the bottom of the second story edge column. As shown in the figure, the strains were much smaller than the yielding strain of the rebar (approximately 2300 $\mu\varepsilon$). The yielding strain was deduced from the yield stress of the No.3 rebar listed in Table 3-7 ($66.5/29000\times10^6$). Therefore, the longitudinal rebar remained elastic at those locations even after the edge columns were rigidly connected to the base block and displaced to large lateral drifts (e.g. 5%). As expected, plasticity of the edge column only occurred at the column base.

Local curvatures of the edge column could be deduced using the strain gages attached to two longitudinal rebar located on the opposite sides of the edge column. The deduction is described in detail in Section 4.2.2.3. Fig. 7-143 shows the local curvatures in the east edge column in Phase 1 and Phase 3 deduced by using the strain gage pair SG_EGCOL_L5/SG_EGCOL_L6. The reason for choosing this strain gage pair was that it was located right above the region (7-1/2 in. above the base plate) where the readings of the strain gages greatly exceeded the yielding strains before 2% drift due to the yielding of the rebar. It was more reliable to use the readings of the strain gage pair SG_EGCOL_L5/SG_EGCOL_L6, which were not excessively larger than the yielding strains. Once the local curvatures were obtained, the local moments at the base of the

edge column could be deduced through sectional analysis. The software framework OpenSees (Open System for Earthquake Engineering Simulation) was used for the sectional analysis. The code used in OpenSees is listed in Appendix E. By combining the deduced moment at 7-1/2 in. above the base plate with the recorded rotation response between the edge column and the base block over 10-1/2 in. gage length (Section 7.6.4.1), the moment-rotation curve of the east edge column at the base was obtained (Fig. 7-144). As shown in the figure, the residual rotations recorded when the curves crossed the horizontal axis were close to zero in Phase 1, indicating that the east edge column was capable of self-centering. Under this circumstance, the whole specimen was almost "self-centered" and close to "damage-free" (the damage to the replaceable O-connectors was deemed acceptable; no fracture was observed in this phase). Fast reoccupation of the structure after seismic events could be realized.

As shown in Fig. 7-144, the residual rotations were non-negligible in Phase 3. It was believed that the irreversible plastic deformations of the edge column, which included yielding of the rebar and spalling of the concrete, resisted the edge column from self-centering. The damaged edge column also resisted the wall from self-centering that might increase the residual drift of the entire specimen. The damaged edge columns needed to be repaired before reoccupying the structure.

As shown in Fig. 7-144, the moment resistance and the energy dissipating capacity of the rocking edge column were smaller than those of the fixed-base edge column, which was as expected. The purpose of using different details for the edge column base connections (untightening or tightening to the base block) was to provide alternative options for designers and to investigate the corresponding behavior of the edge columns. In the prototype building, the post-tensioning forces in the edge columns would be replaced by gravity loads. However, post-tensioning rods would be required in the rocking edge column case to provide moment resistance. The amount of PT forces could be scaled to provide similar moment resistance as fixed-base edge columns. To enhance the energy dissipation of the rocking edge columns, external "fuses" that serve a similar function as the O-connectors could be attached to the rocking edge columns to increase their energy dissipating capacity. As an example, Fig. 7-145 shows steel angles attached

to the edge column with one leg welded to the steel base plate and the other leg bolt-connected to the foundation. When the edge column rocks, the deformed steel angles would not only increase the strength of the edge column, but would also help dissipate energy through hysteretic damping.

7.6.6 Shear Slip of Edge Columns

A string pot SP2_ECBASE was installed at the base of the east edge column to monitor the shear slip. The location of the string pot is shown in Fig. 4-15. Fig. 7-146 shows the cyclic readings of SP2-ECBASE in Phase 1 and Phase 3. As shown in the figure, the absolute horizontal movements in both phases were very small (e.g. smaller than 0.04 in. at 2% drift), indicating that slip did not occur in either phase.

In Phase 1 when the base plate of the edge column was not tightened to the base block (shown in Fig. 7-119), it was believed that the lateral movement recorded by SP2-ECBASE was mainly contributed by the rocking of the east edge column. A friction force was generated at the base plate/grout interface by the PT clamping force. It resisted the shear sliding of the edge column. Moreover, the threaded rods with one end being embedded in the base block and the other end protruding through the holes in the base plate also restrained the shear sliding of the edge column.

In Phase 3 when the base plate of the edge column was tightened to the base block (shown in Fig. 7-120), because a large friction force was generated by both the PT clamping force and the tie-down forces from the four threaded rods, shear sliding of the edge column was more unlikely to occur. As expected, the lateral movement recorded by SP2-ECBASE is much smaller in Phase 3, as shown in Fig. 7-146.

7.6.7 Behavior of the Edge Beams

No noticeable damage to the edge beams was observed throughout the test. Similar to the observation at the plank-transverse beam connection in Fig. 7-90, the planks lost contact with the steel angle affixed to the edge beam during the test, as shown in Fig. 7-147.

7.7 Behavior of Mega Trusses

"Mega trusses" were emulated by steel tubes pin-connected to the wall. The mega trusses were expected to rotate like rigid bodies without being subjected to any flexural bending. Two strain gages were attached to both ends of each steel truss to measure the axial forces in the truss. The location of the strain gages is shown in Fig. 4-22. The maximum reading of all strain gages was smaller than 120 με when PFS2 was loaded to 5% lateral drifts in Phase 7. As expected, the steel trusses remained elastic throughout the test.

7.8 Conclusions from the Data Analysis of PFS2

A large-scale precast structural assemblage (PFS2) was tested under pseudo-static loading to investigate the performance of rocking-wall structures using vertically isolating wall/floor connections to minimize the wall-floor interaction. The rocking-wall system used in PFS2 was the Precast Wall with End Columns (termed "PreWEC") system. It consisted of a non-bearing rocking wall, rocking end columns adjacent to the wall that carried gravity loads, and energy dissipating elements "O-connectors" attached to the wall and the end columns. The surrounding structures included precast edge columns and a precast floor system formed by untopped planks. Special wall-floor connections (BS Italia connections) were used to isolate the floor from the vertical movement of the wall.

PFS2 was tested to lateral drifts in excess of 5%. The conclusions derived from the data analysis and the numerical simulations are as follows:

1. PFS2 exhibited excellent self-centering performance. The precast floor was successfully isolated from the vertical movement of the wall by using the BS Italia connections. Because the wall-floor interaction was greatly reduced, the self-centering capability of PFS2 was not compromised by the surrounding structure. The base shear of PFS2 was only 4% larger than that of the isolated PreWEC system obtained from the numerical simulation.

2. When the floor was isolated from the vertical movement of the wall, the structural system in the adjacent frame lines, which was emulated by props in the test, had little impact on the behavior of the tested PreWEC system.
3. When rocking edge columns were used along with the rocking wall, the entire specimen was almost “damage-free” at 2% design drift. Immediate re-occupation of the structure was feasible under this condition.
4. A disturbed region existed near the base of the wall within the first story, where the concentrated compression force spread out from the corner of the wall with height. The test data was in accord with the assumption that the height of the disturbed region was equal to the length of the wall, which was proposed based on Saint Venant’s Principle. Bernoulli theory (i.e., plane sections remain plane) was valid at higher levels in the wall, which was beyond the disturbed region.
5. Damage occurred to the ends of the fiber grout layer. The damage might have been caused by the inclined shear force generated by the compression force and the horizontal shear force concentrated at the corners of the end columns. Damage also occurred to the fiber grout beneath the end columns due to the discontinuity in the grout bearing. It is recommended that a spacer with a narrower profile be placed beneath the end columns around the PT rods to reduce the damage.
6. Damage occurred to the base of the east end column. The overall length of the PT rods was reduced due to the spalling of the concrete at the corners and the loss of the fiber grout beneath the end columns. The PT clamping forces in the end columns were greatly reduced in the test, causing the end columns being picked up and the effectiveness of the O-connectors being nullified. To avoid damage to the concrete core, it is recommended that special detailing should be used around the edge column base. The strain gage readings showed that the height of the stress concentration region in the end columns was small. Steel channels could be placed at the corners to protect the concrete. Note that the picking up of the end columns might not occur in the prototype structure due to the gravity load effects.
7. The precast floor performed well throughout the test. Little damage occurred to the precast planks and the BS Italia connections. Yielding of the strap plates in the precast

floor was observed only after 2.5% drift. It was validated that the yielding was caused by the deformation demands on the strap plates due to the rotations of the end columns and the edge columns.

8. The precast floor was successfully isolated from the vertical movement of the wall at 5% drift (corresponding to 1.5 in. relative vertical displacement), when the maximum force transferred by each BS Italia connection was approximately one third of its design capacity.

9. After the base plates of the edge columns were tightened to the base block, damage occurred to the edge columns. Premature fracture of the welds between the rebar and the base plate was observed in the test. It was believed that the fracture was mainly contributed by poor quality weld due to limited accessibility/congestion in the weld region. It is recommended that an alternate detail be used (welding dowel bars to embed plates).

10. Compared with fixed-base edge columns, rocking edge columns had the advantage of "damage-free" and "self-centered." External replaceable energy dissipating elements can be installed at the base of the rocking edge column to increase its moment resistance and energy dissipating capacity.

Table 7-1 N.A. depth of the specimen PFS2

Testing phases	Phase 1						Phase 4	Phase 5			Phase 7
Drift level (%)	0.25	0.5	0.75	1.0	1.5	2.0	2.0	2.5	3.0	4.0	5.0
Positive loading (in.)	12.3	9.4	8.0	7.2	6.4	6.1	6.2	5.7	5.5	5.1	5.2
Negative loading (in.)	9.7	8.6	8.1	7.9	7.5	7.2	7.4	7.2	7.1	6.9	7.3

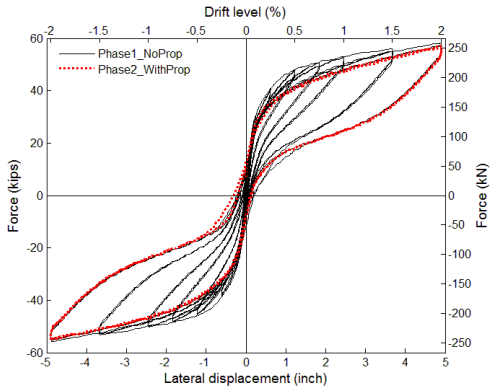

Fig. 7-1 Force-displacement response in Phase 1 (without props) and Phase 2 (with props)

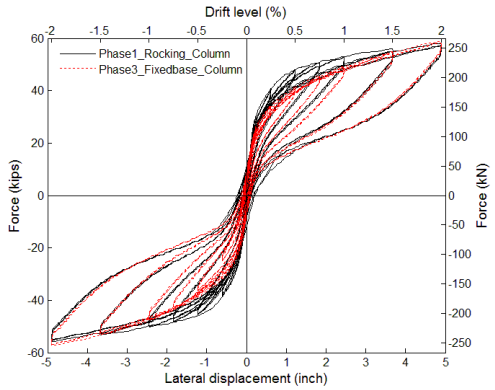

Fig. 7-2 Force-displacement response in Phase 1 (rocking edge columns) and Phase 3 (fixed-base edge columns)

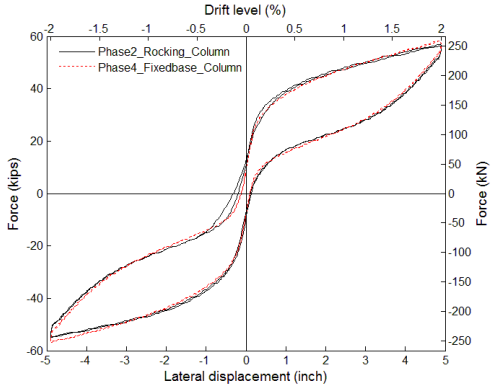

Fig. 7-3 Force-displacement response in Phase 2 (rocking edge columns) and Phase 4 (fixed-base edge columns)

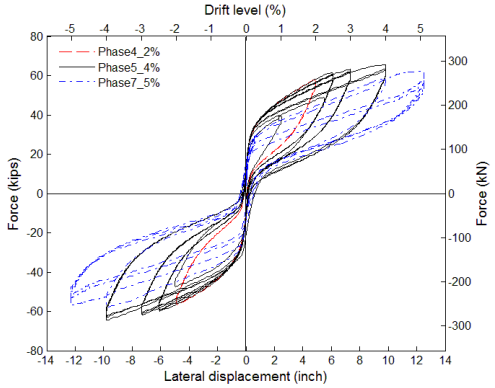

Fig. 7-4 Force-displacement response in Phase 4, 5&7 (with props and fixed-base edge columns)

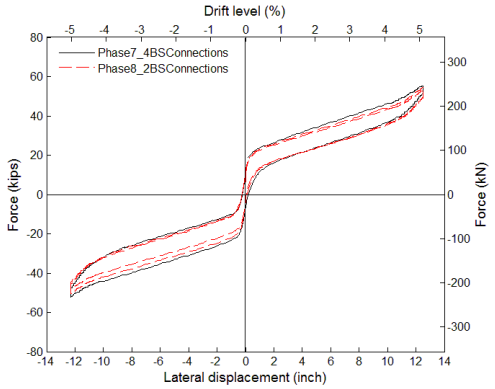

Fig. 7-5 Force-displacement response in Phase 7 (four BS Italia connections) and Phase 8 (two BS Italia connections)

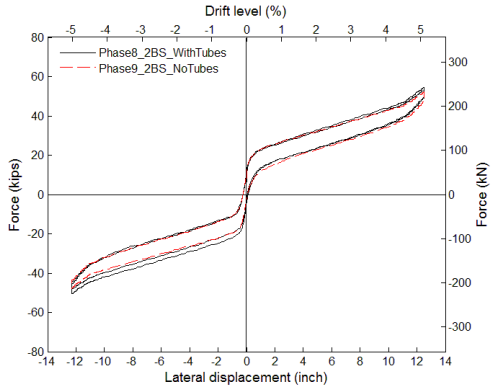

Fig. 7-6 Force-displacement response in Phase 8 (With steel tubes) and Phase 9 (No Steel tubes)

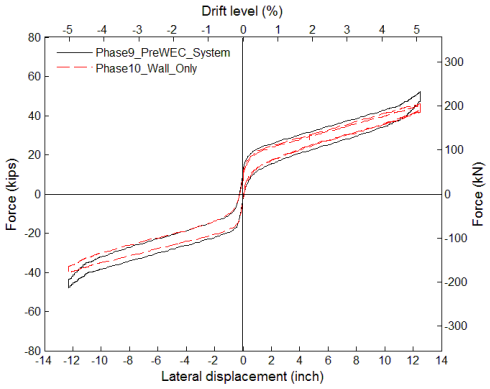

Fig. 7-7 Force-displacement response in Phase 9 (PFS2) and Phase 10 (wall only)

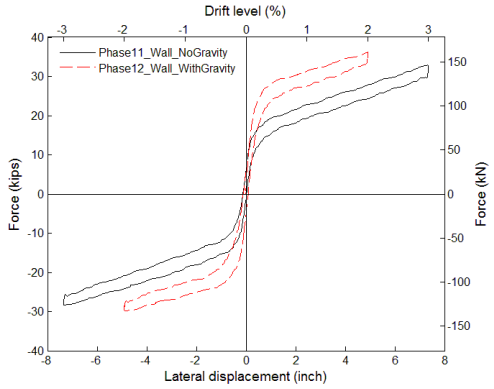

Fig. 7-8 Force-displacement response in the 3% in-plane loading in Phase 11 (without gravity loads in the wall) and Phase 12 (with gravity loads in the wall)

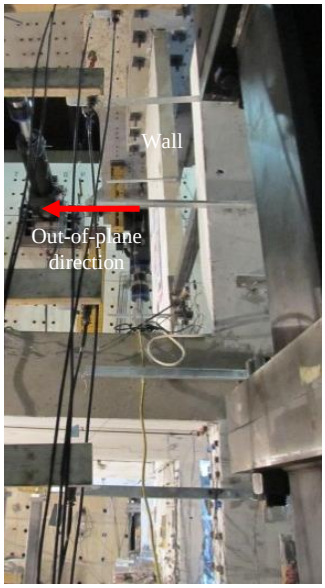

Fig. 7-9 Bending of the wall in Phase 6

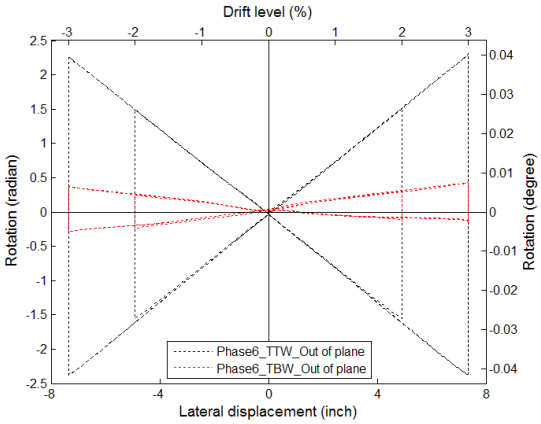

Fig. 7-10 Rotation-lateral wall displacement response of the top and bottom tiltmeters on the wall (Phase 6)

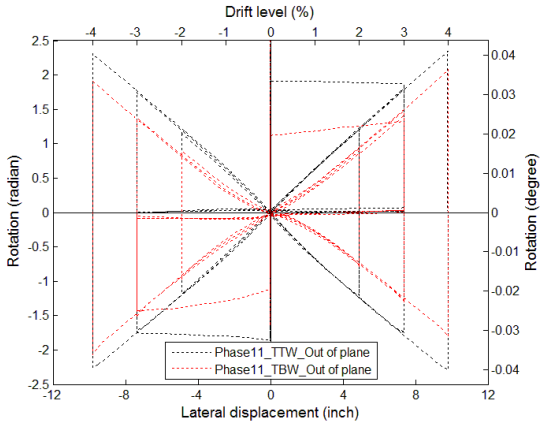

Fig. 7-11 Rotation – lateral wall displacement response of the tiltmeters in Phase 11

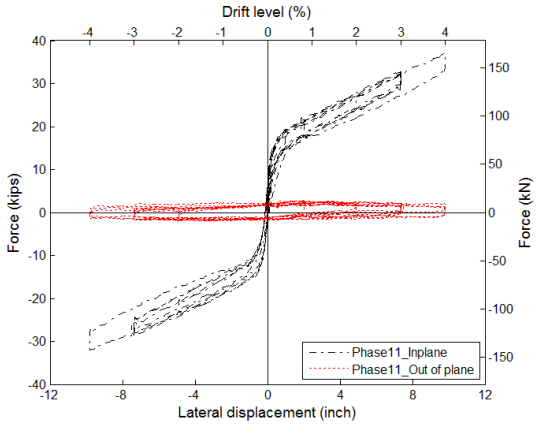

Fig. 7-12 Force-displacement response of PFS2 under biaxial loading in Phase 11

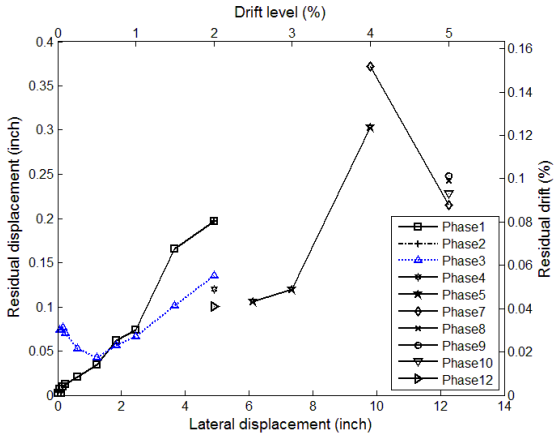

Fig. 7-13 Residual displacements/drifts recorded in the in-plane phases

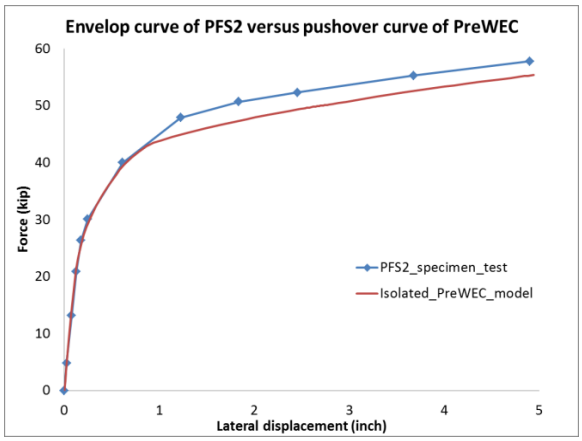

Fig. 7-14 Comparison of the envelope curve of PFS2 and the pushover curve of the isolated PreWEC from the model

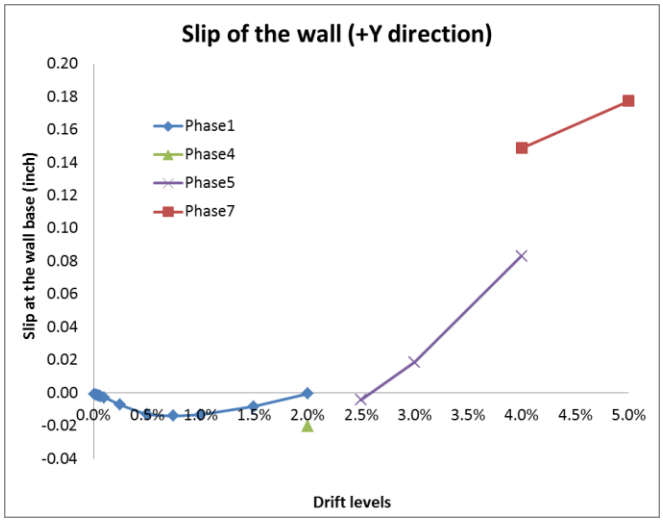

Fig. 7-15 Slip of the wall at different drift levels in PFS2 testing

Fig. 7-16 Horizontal crack at the east wall corner at -0.25% drift (view from south)

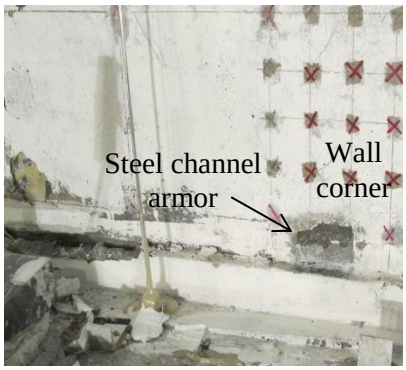

Fig. 7-17 Spalling of fiber grout at 0.5% drift

Fig. 7-18 Concrete over spalling in the wall at -2% drift in Phase 2

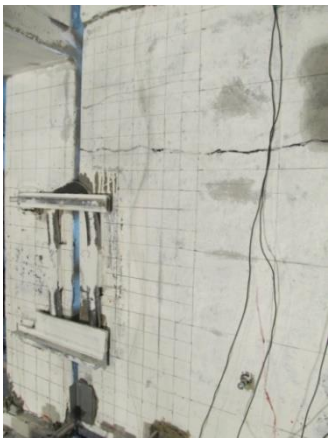

Fig. 7-19 Horizontal cracks in the wall at 2% drift in Phase 3

Fig. 7-20 Damage to the concrete cover in the west wall corner at 4% in Phase 5

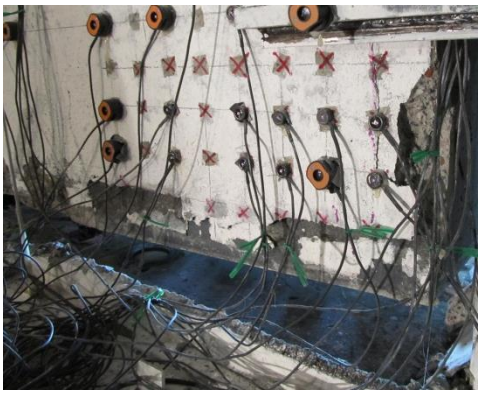

Fig. 7-21 Damage to the concrete cover in the east wall corner at 4% in Phase 5

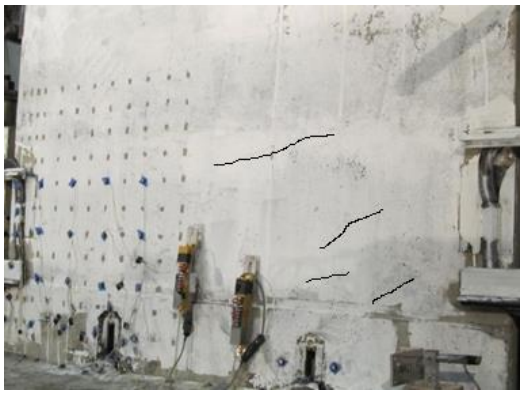

Fig. 7-22 Inclined cracks on the north surface of the wall in Phase 6

Fig. 7-23 Cracks initiated near the 2nd story northeast O-connector at 3% drift in Phase 6 (view from north)

Fig. 7-24 Concrete spalling near the 2nd story northeast O-connector at 3% drift in Phase 6 (view from south)

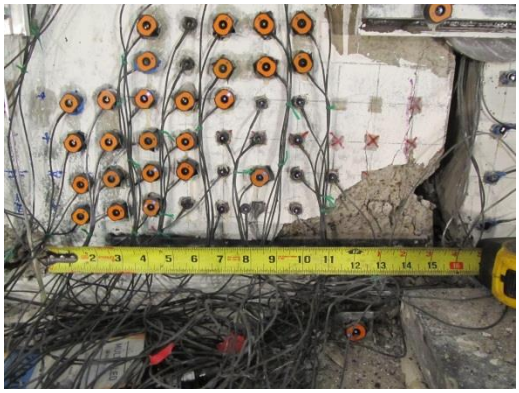

Fig. 7-25 Damage in the east corner of the wall after 5% drift in Phase 7

Fig. 7-26 Separation between the steel channel and the concrete in wall corner

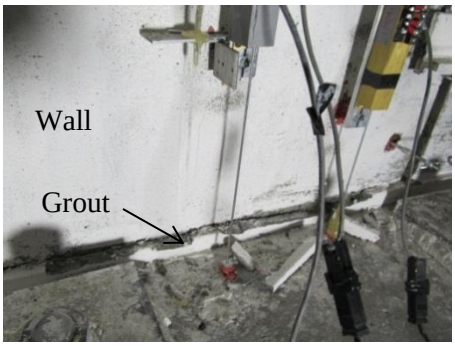

Fig. 7-27 Spalling of the over-poured fiber grout at 0.75% drift in Phase 1

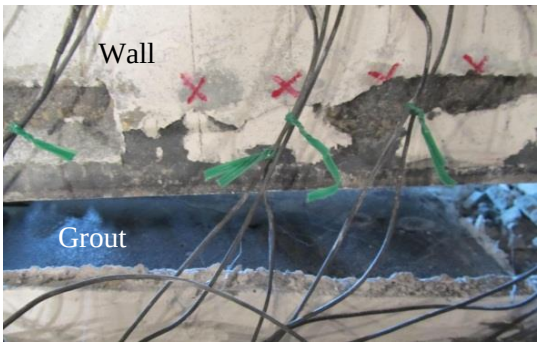

Fig. 7-28 Fiber grout beneath the east corner of the wall at -2.5% drift in Phase 5

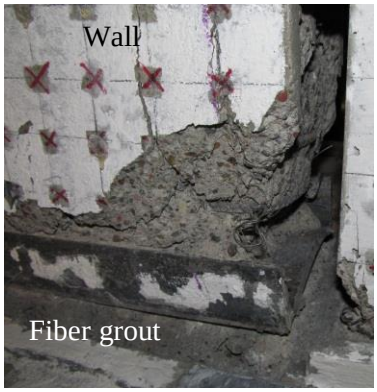

Fig. 7-29 Condition of fiber grout beneath the east corner of the wall after the test

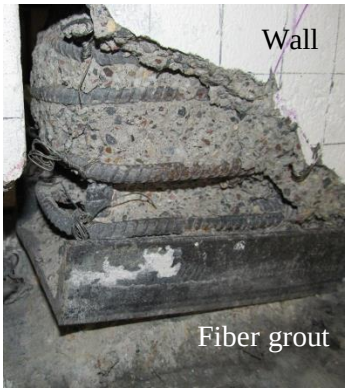

Fig. 7-30 Condition of fiber grout beneath the west corner of the wall after the test

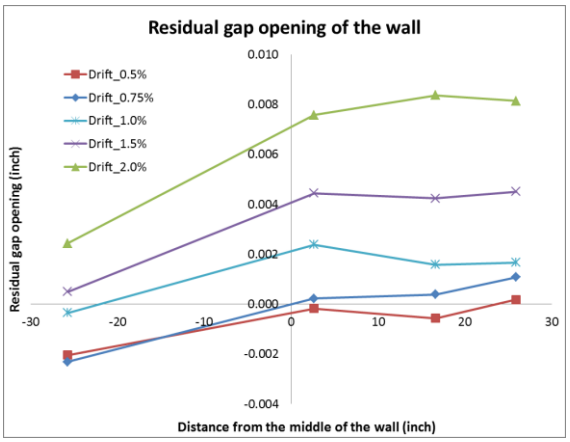

Fig. 7-31 Residual gap opening at different drift levels in Phase 1

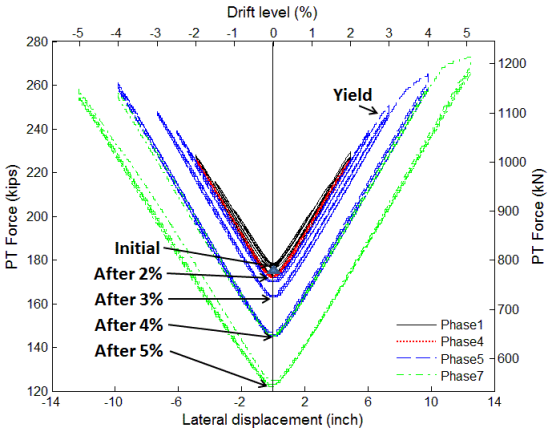

Fig. 7-32 PT force – lateral displacement response of the wall

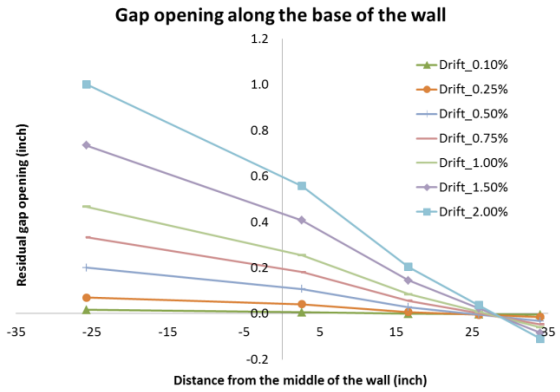

Fig. 7-33 Readings of the LVDTs at wall/base block interface at positive peaks

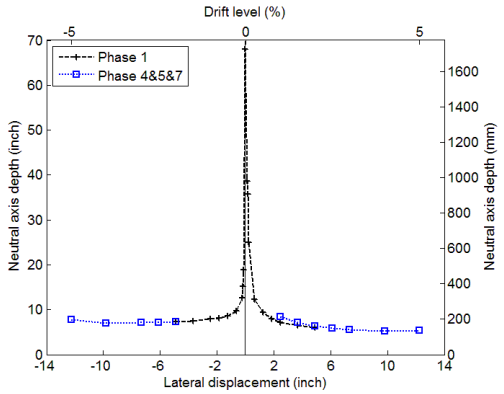

Fig. 7-34 N.A. depth of the wall at peak drifts in Phase 1, 4, 5&7

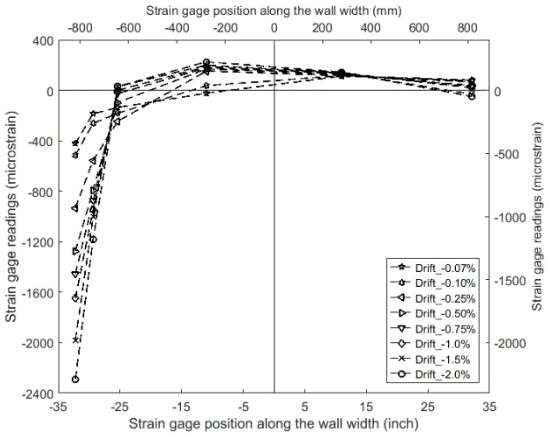

Fig. 7-35 Strain distribution along the wall width (1st row 1-1/2 in. above the wall base, negative peaks in Ph1)

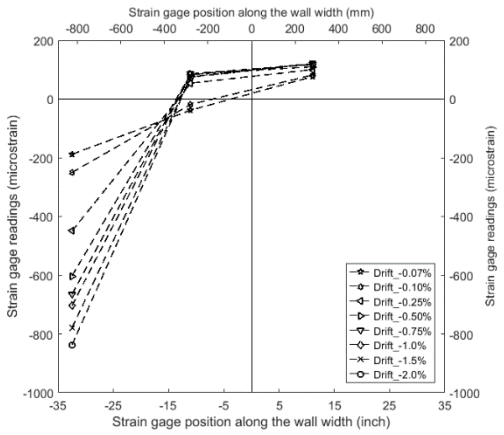

Fig. 7-36 Strain distribution along the wall width (3rd row 16-7/8 in. above the wall base, negative peaks Ph1)

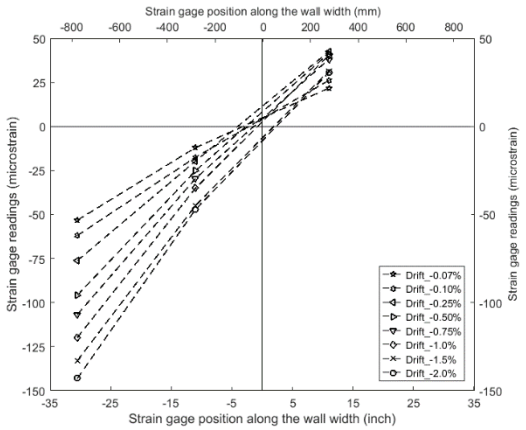

Fig. 7-37 Strain distribution along the wall width (4th row 147-7/8 in. above the wall base, negative peaks in Phase 1)

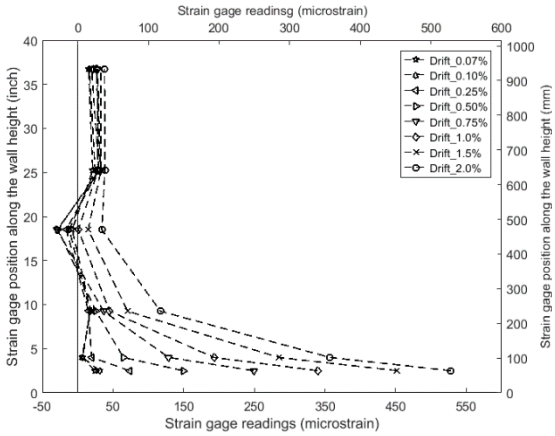

Fig. 7-38 Strains in the stirrups along the height of the wall in Phase 1

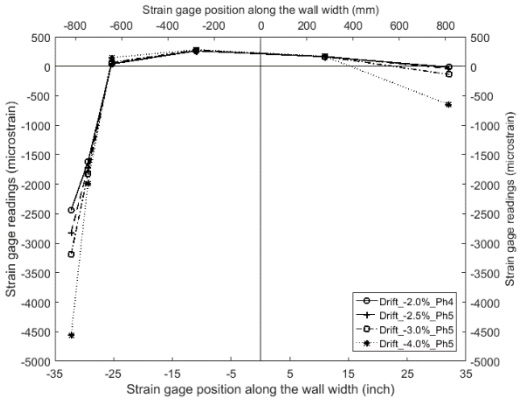

Fig. 7-39 Strain distribution along the wall width (1st row, negative peaks in Ph4&5)

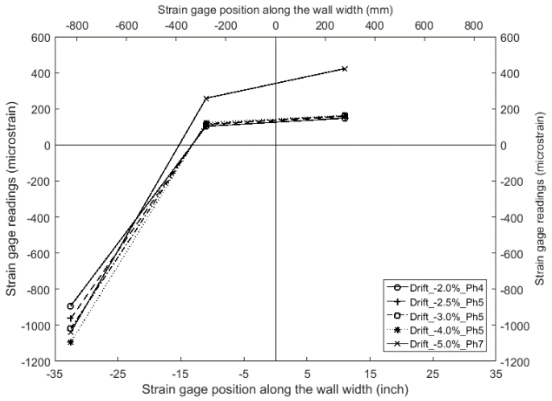

Fig. 7-40 Strain distribution along the wall width (3rd row, negative peaks in Ph4, 5&7)

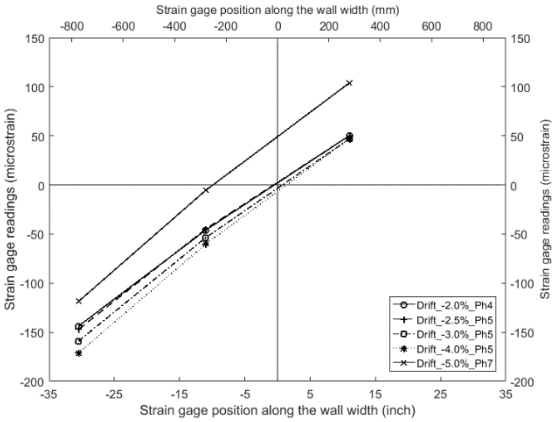

Fig. 7-41 Strain distribution along the wall width (4th row, negative peaks in Ph4, 5&7)

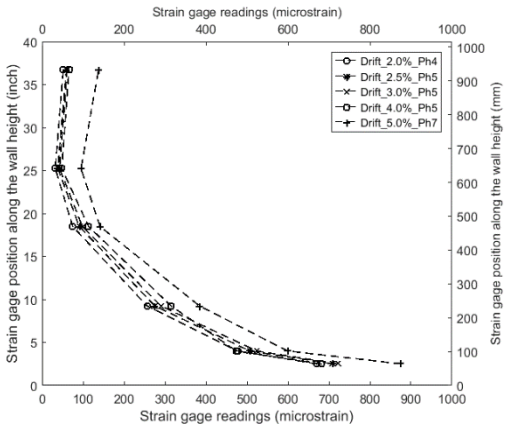

Fig. 7-42 Strain in the stirrups distributed along the height of the wall in Ph4, 5&7

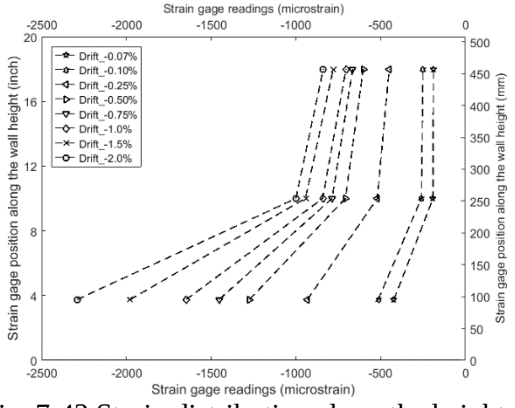

Fig. 7-43 Strain distribution along the height of the wall in Phase 1

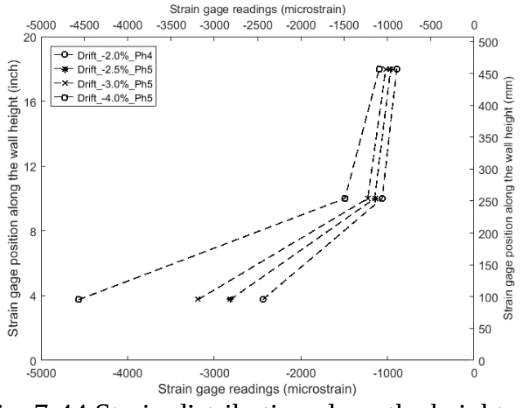

Fig. 7-44 Strain distribution along the height of the wall in Ph4&5

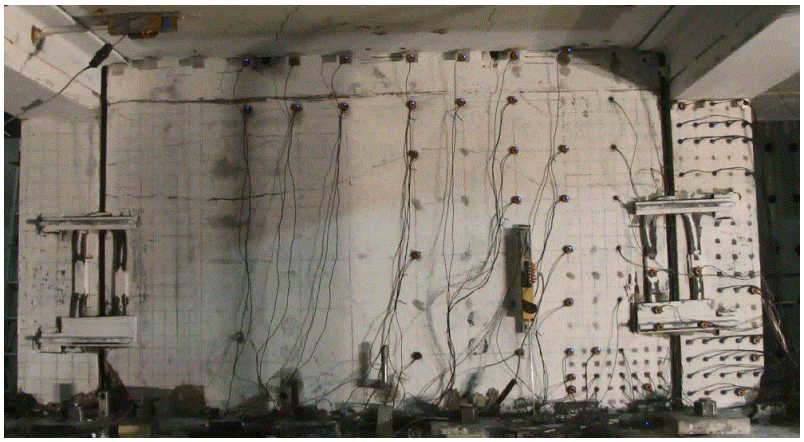

Fig. 7-45 LEDs on the wall in PFS2 in Phase 5

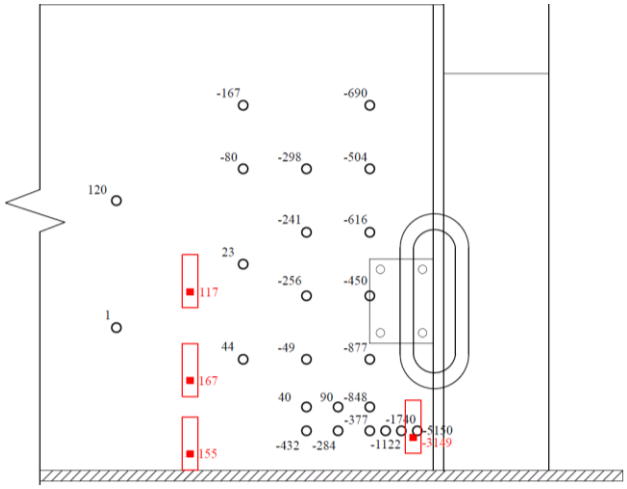

Fig. 7-46 Strains obtained from the concrete gages and LEDs on the wall at 1.5% drift in Phase 1

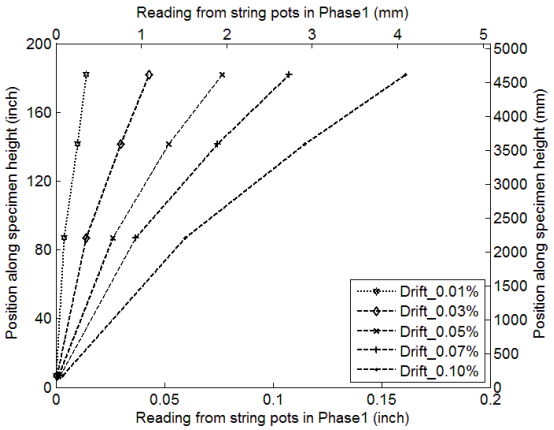

Fig. 7-47 Deformed shape of the wall at low drift levels in Phase 1

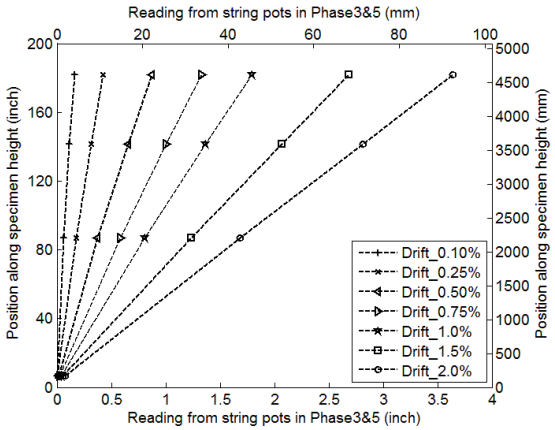

Fig. 7-48 Deformed shape of the wall at high drift levels in Phase 1

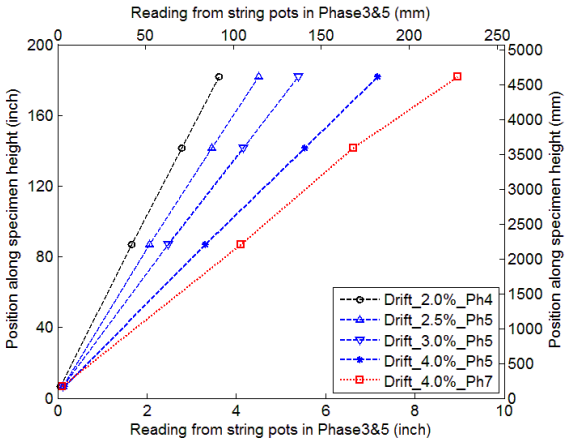

Fig. 7-49 Deformed shape of the wall in Ph4, 5&7

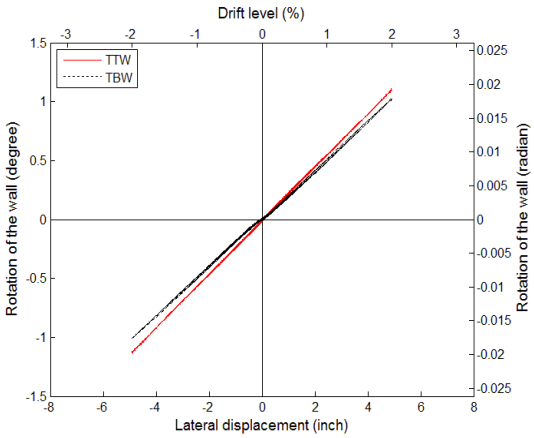

Fig. 7-50 Rotation – lateral displacement response of the wall in Phase 1

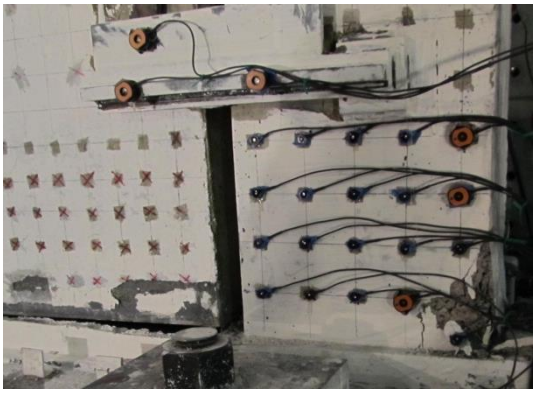

Fig. 7-51 Damage in the east corner of the east end column at 1.5% drift cycle in Phase 1 (view from south)

Fig. 7-52 Damage in the west corner of the west end column at -1.5% drift in Phase 1

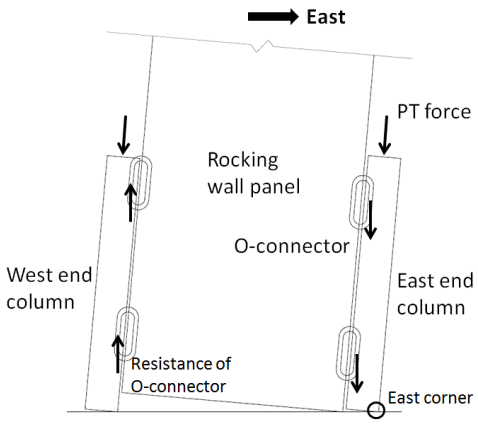

Fig. 7-53 Force flow in end columns

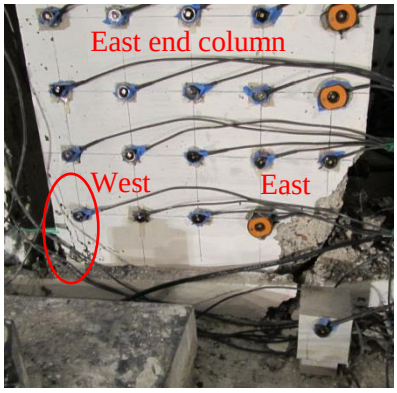

Fig. 7-54 Damage in the east end column at -4% drift in Phase 5 (view from south)

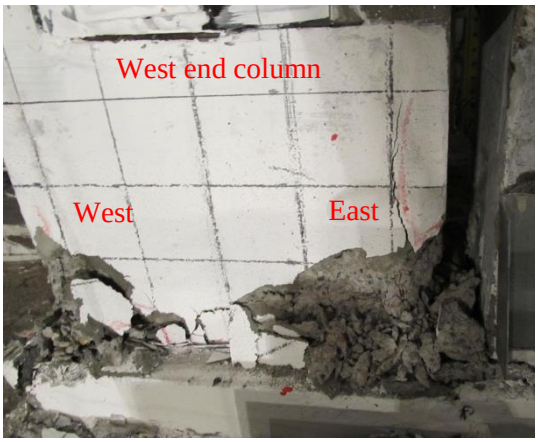

Fig. 7-55 Damage in the west end column at 4% drift in Phase 5 (view from south)

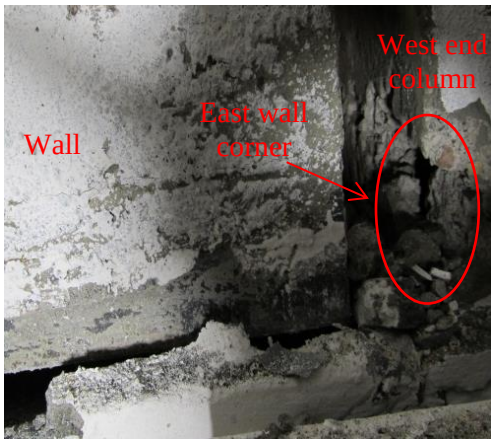

Fig. 7-56 Damage in the east corner of the west end column in Phase 5 (view from north)

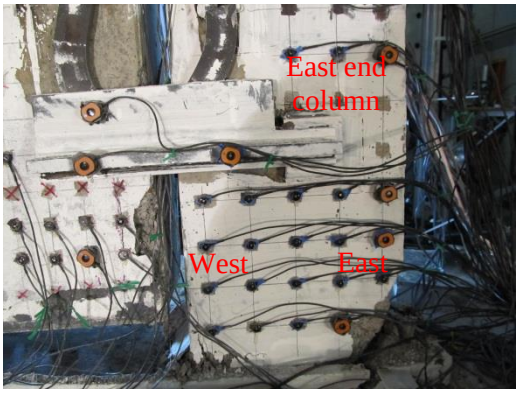

Fig. 7-57 Damage to the east end column at -5% drift in Phase 7

Fig. 7-58 Damage to the west end column at the peak of 5% drift in Phase 7

Fig. 7-59 West end column being picked up at 5% drift in Phase 10

Fig. 7-60 The condition of the east end column after the test (view from north)

Fig. 7-61 The condition of the west end column after the test (view from south)

Fig. 7-62 Tensile cracks in the bottom of the transverse beam at 3% drift in Phase 6

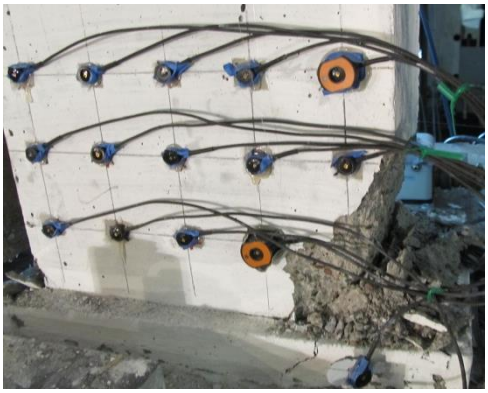

Fig. 7-63 Damage of the fiber grout beneath the east corner of the east end column at 2% in Phase 2 (view from south)

Fig. 7-64 Damage of the fiber grout beneath the west corner of the west end column at -2% in Phase 2 (view from south)

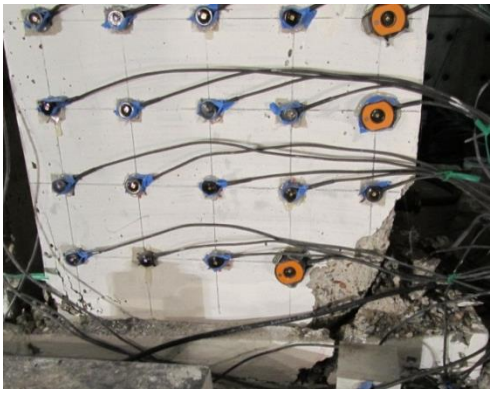

Fig. 7-65 Through crack in the fiber grout beneath the east corner of the east end column at 2.5% in Phase 5

Fig. 7-66 Spalling of the upper corner of the fiber grout beneath the east corner of the east end column at 2.5% in Phase 5

Fig. 7-67 Condition of fiber grout layer beneath the east end column after the test

Fig. 7-68 Condition of fiber grout layer beneath the west end column after the test

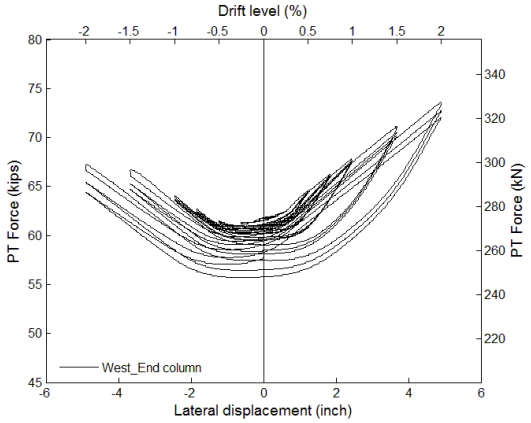

Fig. 7-69 PT force – lateral wall displacement response of the west end column in Phase 1

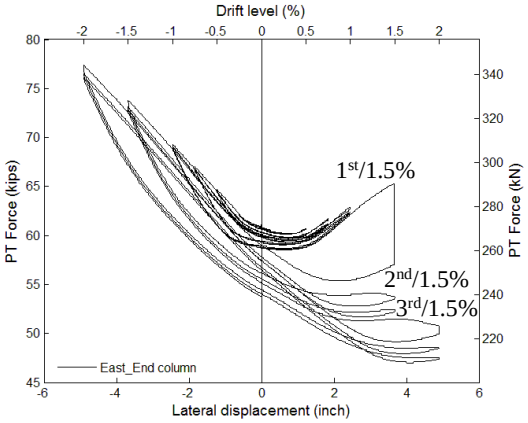

Fig. 7-70 PT force – lateral wall displacement response of the east end column in Phase 1

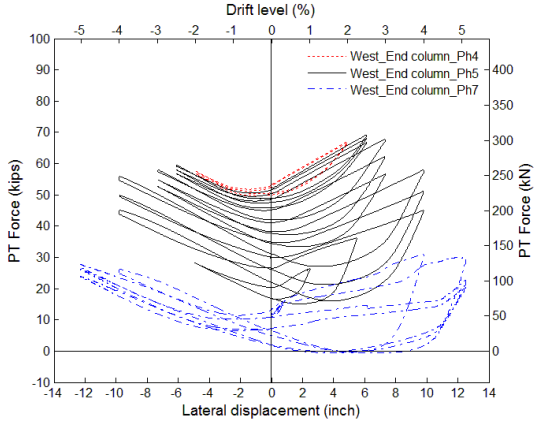

Fig. 7-71 PT force – lateral wall displacement response of the west end column in Ph4, 5&7

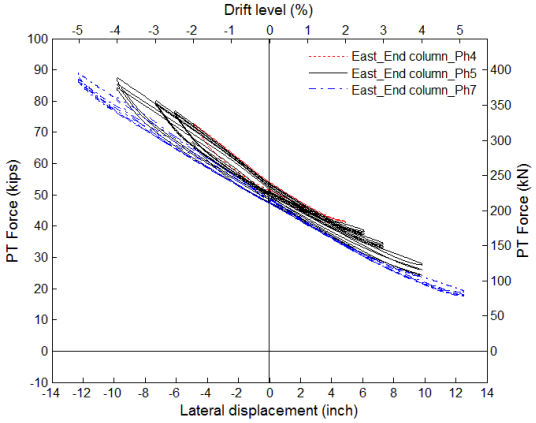

Fig. 7-72 PT force – lateral wall displacement response of the east end column in Ph4, 5&7

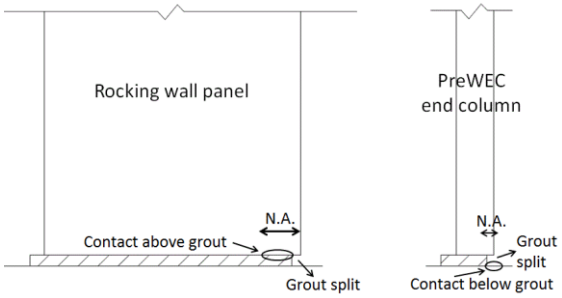

Fig. 7-73 Impact from split grout on rocking wall panel and PreWEC end column

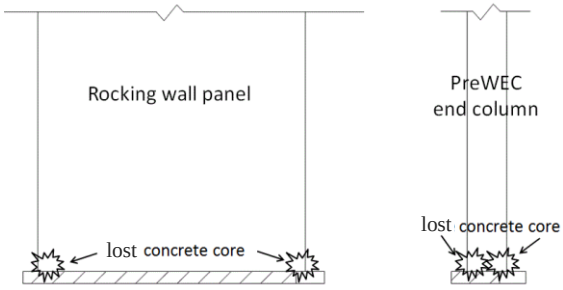

Fig. 7-74 Impact from damaged concrete on rocking wall panel and PreWEC end column

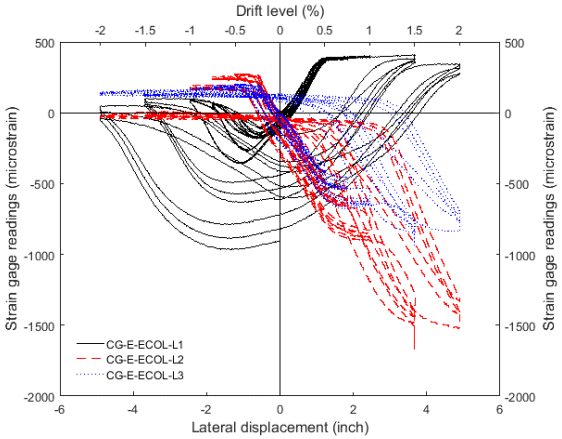

Fig. 7-75 Readings of the concrete gages near the bottom of the east end column in Phase 1

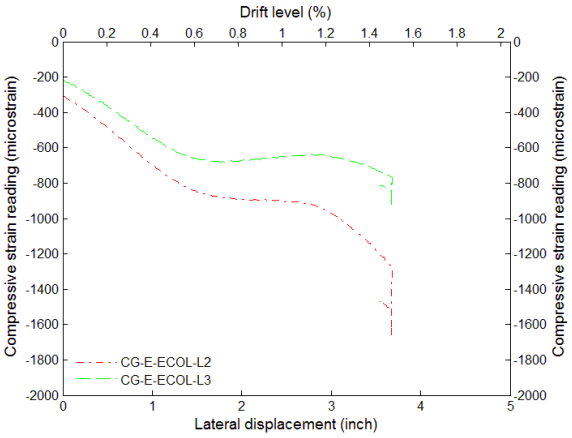

Fig. 7-76 Readings of CG-E-ECOL-L2/L3 at the 1st cycle of 1.5% drift in Phase 1

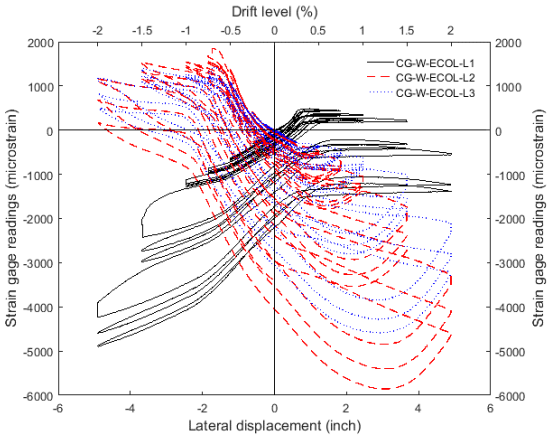

Fig. 7-77 Readings of the concrete gages near the bottom of the west end column in Phase 1

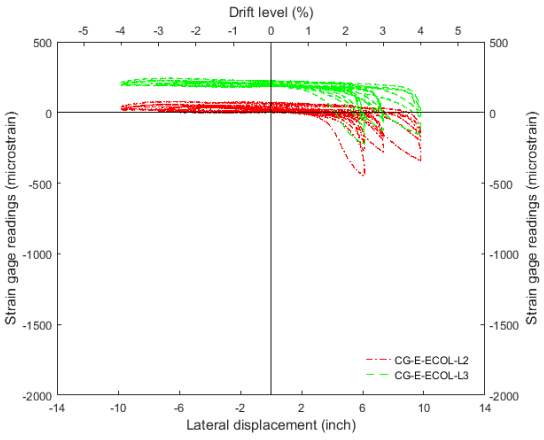

Fig. 7-78 Readings of the concrete gages near the bottom of the east end column in Phase 5

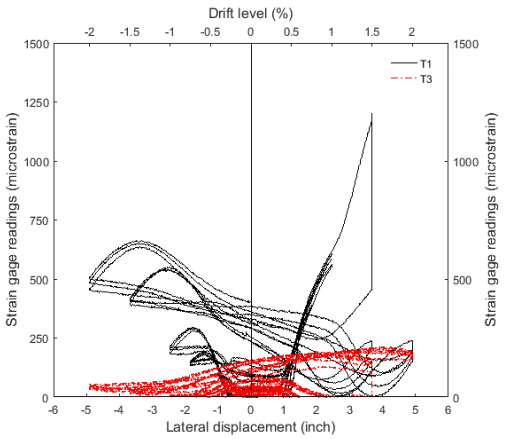

Fig. 7-79 Tensile strain readings of the stirrups in the east end column in Phase 1

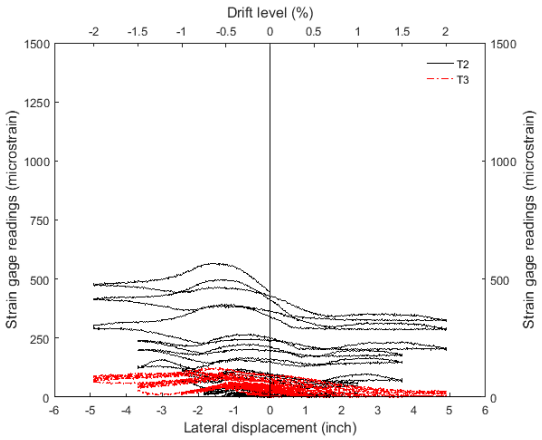

Fig. 7-80 Tensile strain readings of the stirrups in the west end column in Phase 1

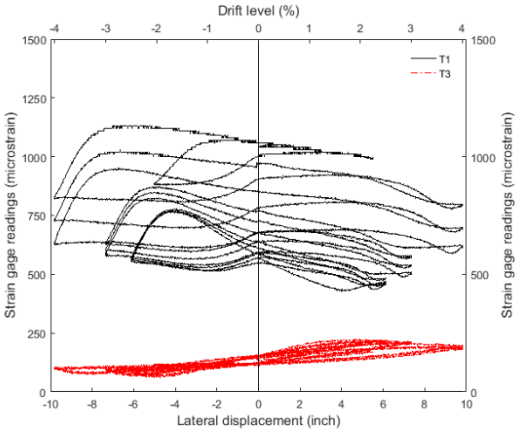

Fig. 7-81 Tensile strain readings of the stirrups in the east end column in Phase 5

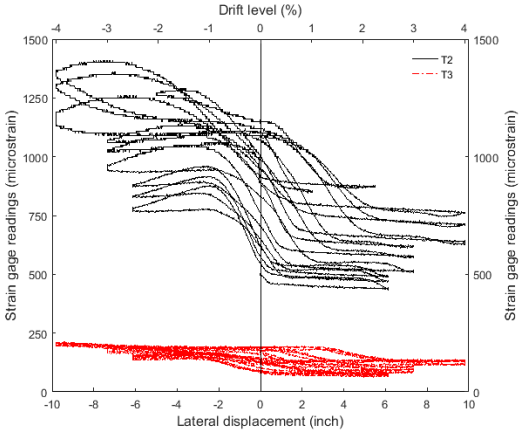

Fig. 7-82 Tensile strain readings of the stirrups in the west end column in Phase 5

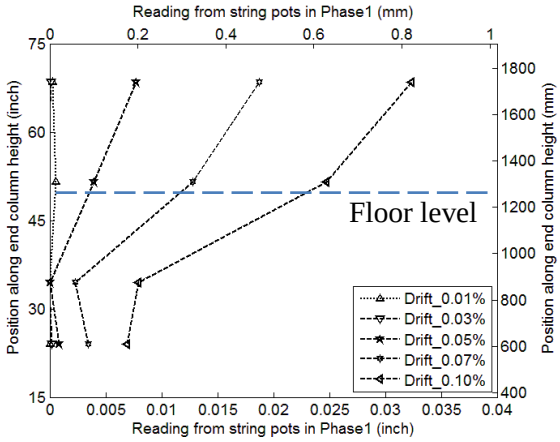

Fig. 7-83 Deformed shape of the west end column at low drift levels in Phase 1

Fig. 7-84 O-connectors connecting the wall and the end column

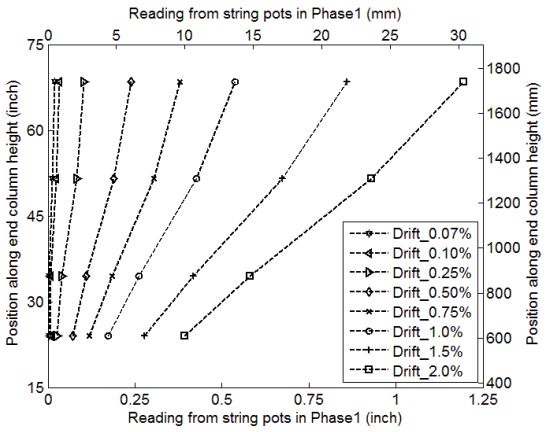

Fig. 7-85 Deformed shape of the west end column in Phase 1

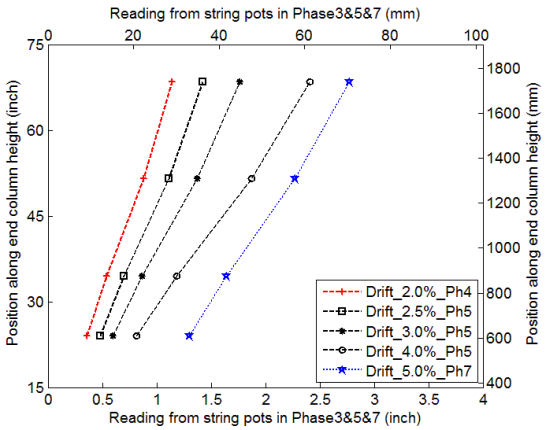

Fig. 7-86 Deformed shape of the west end column at low drift levels in Phase 4, 5&7

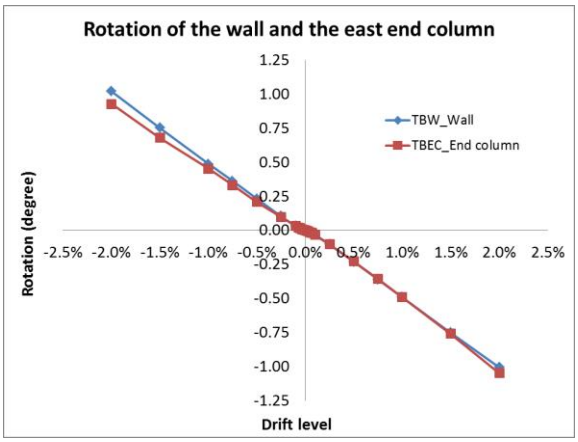

Fig. 7-87 Rotations of the end column and the wall at different peaks in Phase 1

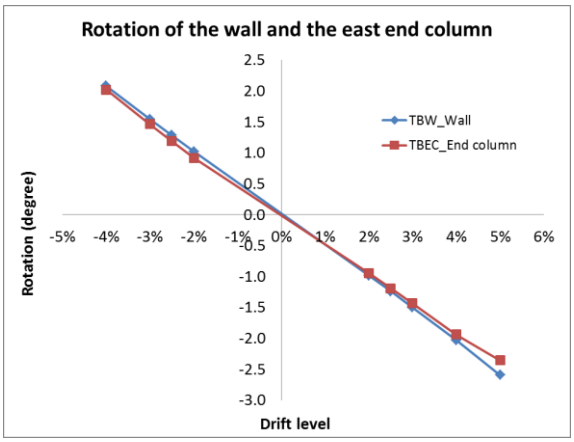

Fig. 7-88 Rotations of the end column and the wall at different peaks in Phase 5 and 7

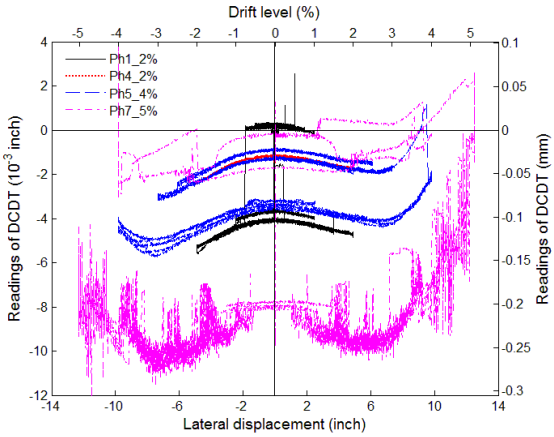

Fig. 7-89 Relative deformation of steel angles

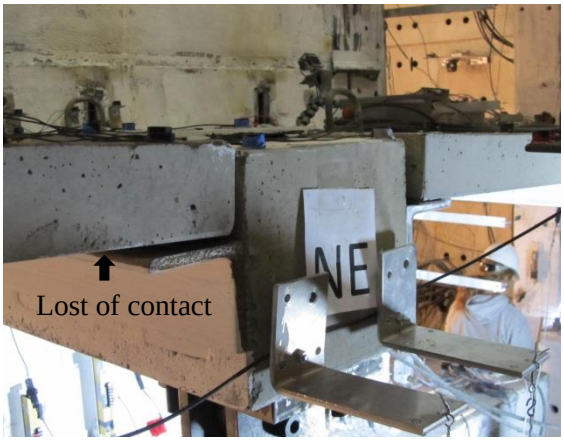

Fig. 7-90 Contact loss between the planks and the steel angle affixed to the transverse beam

Fig. 7-91 Yield lines on the O-connector at 0.75% drift in Phase 1

Fig. 7-92 Crack initiated at the weld of the O-connector

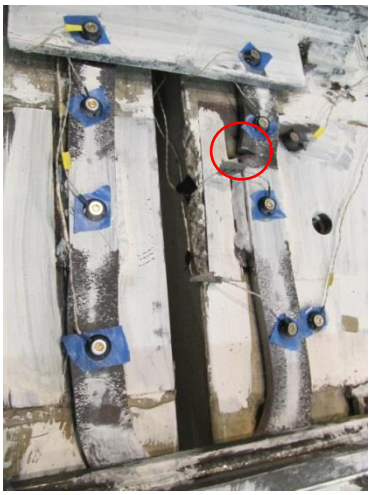

Fig. 7-93 Crack formed near the weld at 4% drift in Phase 5

Fig. 7-94 Complete fracture of an O-connector at 5% drift in Phase 8

Fig. 7-95 “Half-fractured” O-connector at 5% drift in Phase 8

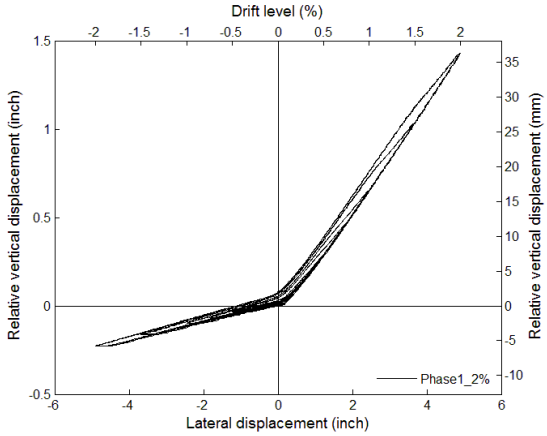

Fig. 7-96 Relative vertical displacement of the O-connector in Phase 1

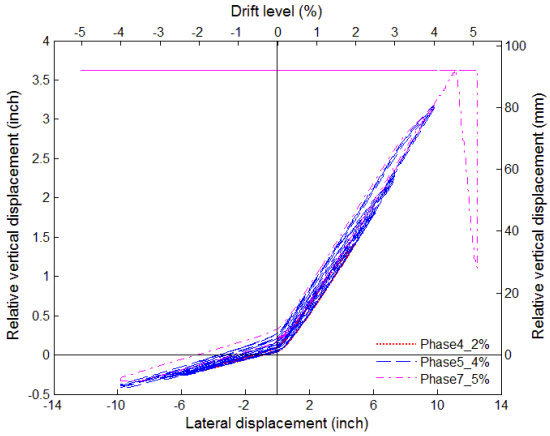

Fig. 7-97 Relative vertical displacement of the O-connector in Phase 4, 5&7

Fig. 7-98 Marker lines drawn along the bottom of the planks in different drift levels

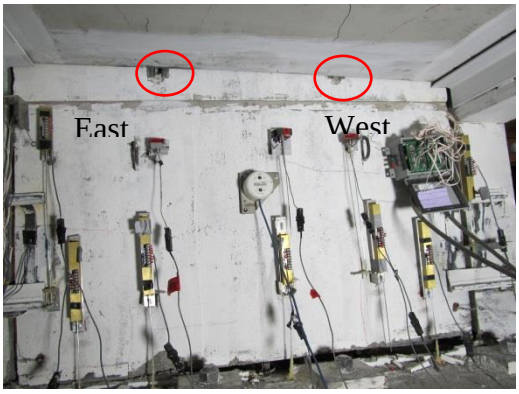

Fig. 7-99 Relative movement between the wall and the floor at 4% drift in Phase 5

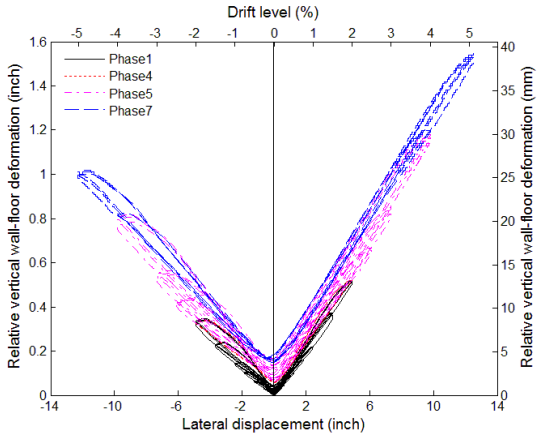

Fig. 7-100 Relative vertical deformation at the wall-floor connection in Ph1, 4, 5&7

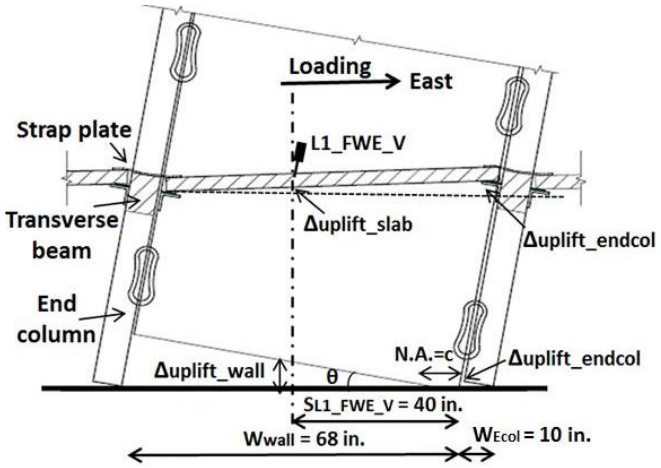

Fig. 7-101 Illustration of the equation for predicting the relative wall/floor displacement

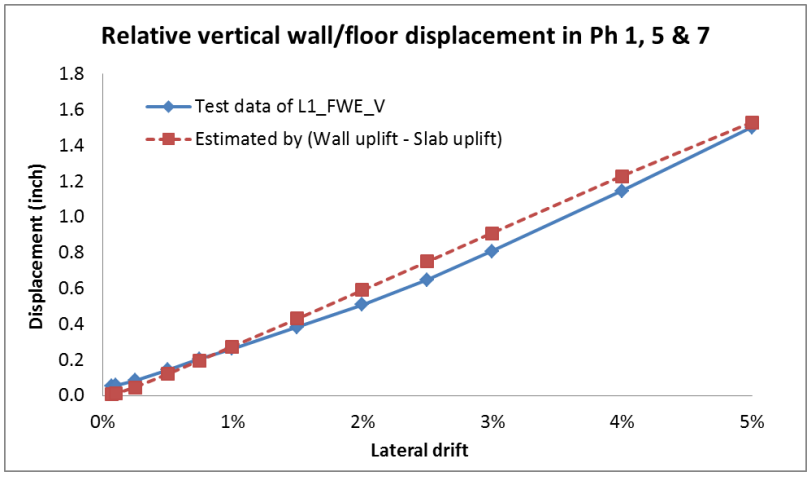

Fig. 7-102 Comparison of the relative vertical wall-floor displacement with the uplift of the wall in Phase 1, 5&7

Fig. 7-103 Cracks in the south middle plank at 0.75% drift in Phase 3

Fig. 7-104 Cracks in the north middle plank at 0.75% drift in Phase 3

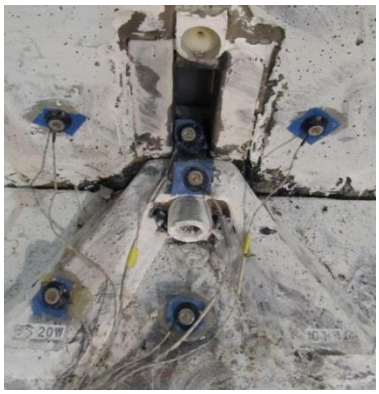

Fig. 7-105 Condition of the BS Italia connection at 4% drift in Phase 5

Fig. 7-106 Yield lines in the strap across plank-edge beam connection at 3% drift in Phase 5

Fig. 7-107 Yield lines in the strap across plank-transverse beam connection at 4% drift in Phase 5

Fig. 7-108 Condition of the JVI Mini V connector after the test

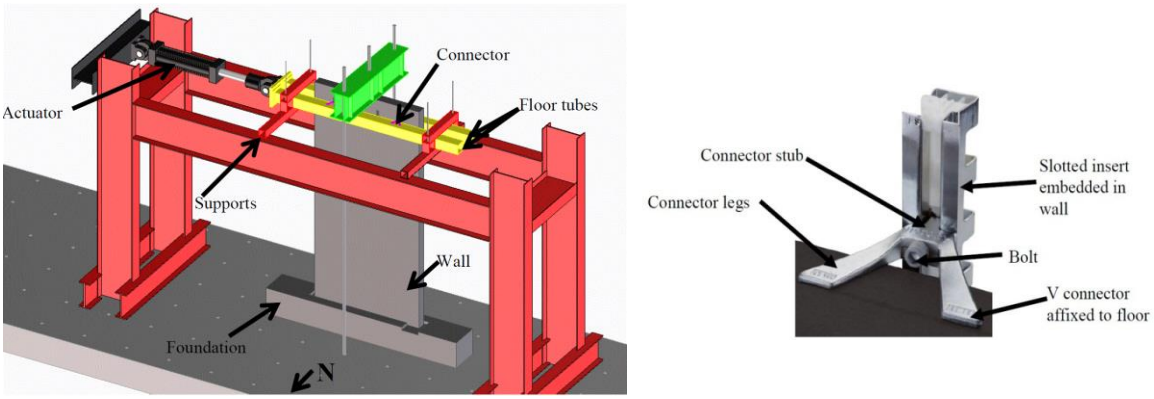

Fig. 7-109 Assemblage test including wall, floor tubes and Victory connections (Watkins 2014)

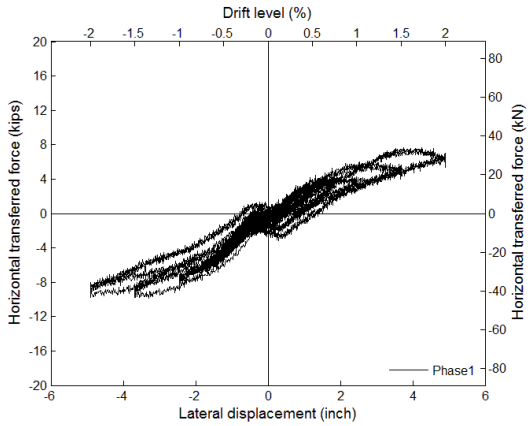

Fig. 7-110 Horizontal forces transferred between the wall and the floor in Phase 1

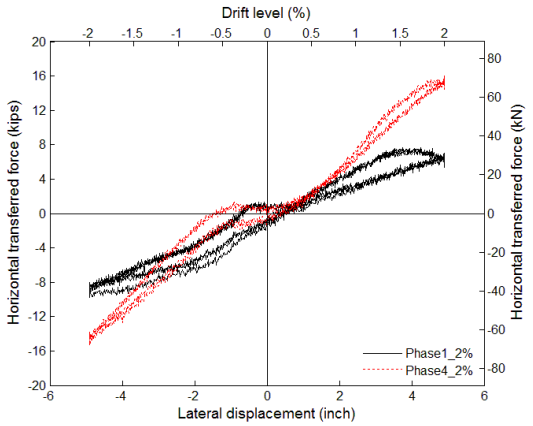

Fig. 7-111 Horizontal forces transferred between the wall and the floor in Phase 4

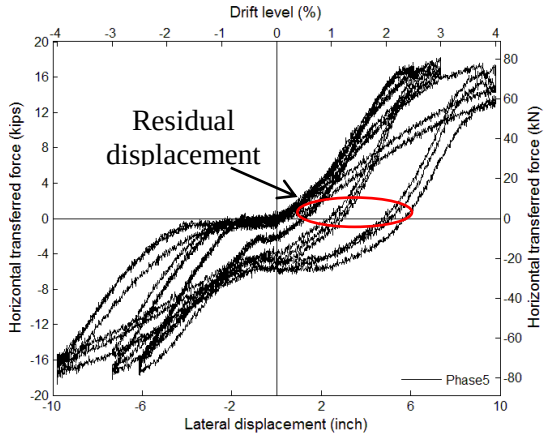

Fig. 7-112 Horizontal forces transferred between the wall and the floor in Phase 5

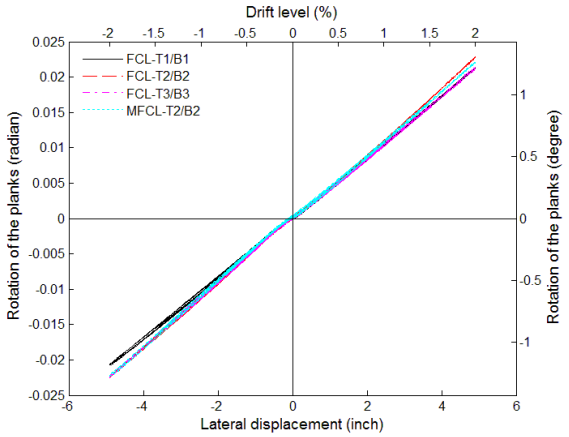

Fig. 7-113 Rotations of edge planks across the plank-edge beam connections in Phase 1

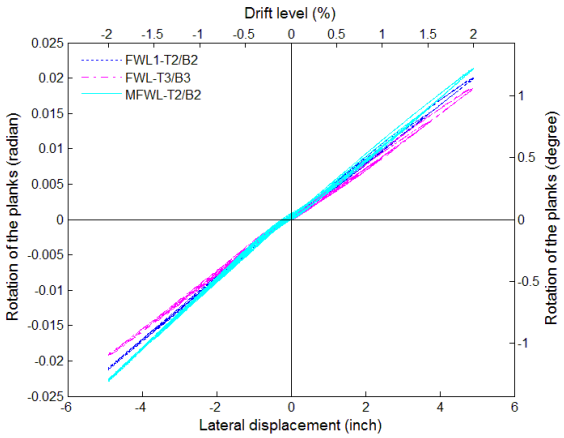

Fig. 7-114 Rotations of edge planks across plank-transverse beam connections in Phase 1

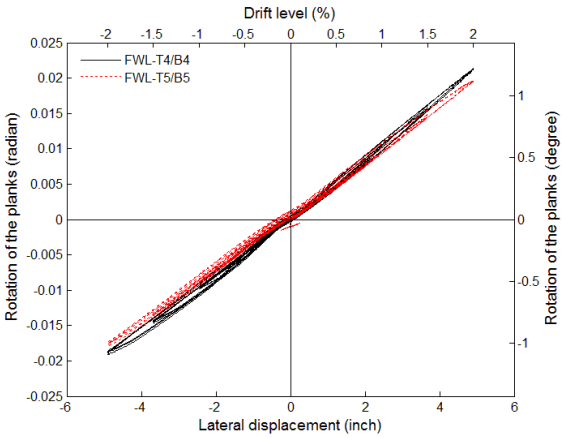

Fig. 7-115 Rotations of center planks across plank-transverse beam connections in Phase 1

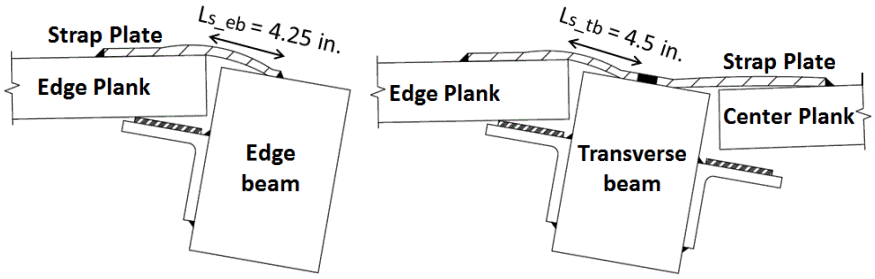

Fig. 7-116 Rotation demand on the strap plates

Fig. 7-117 Detail of the rocking column base connection

Fig. 7-118 Opening between the base plate and the fiber grout layer at 0.75% drift in Phase 1

Fig. 7-119 Opening between the base plate and the fiber grout at 2% drift in Phase 1

Fig. 7-120 Cracks in the fixed-base west edge column at 0.07% drift in Phase 3

Fig. 7-121 Cracks distributed along the edge column at 1.5% drift in Phase 3

Fig. 7-122 Crushing of the concrete cover in the edge column at 4% drift in Phase 5

Fig. 7-123 Fracture of the weld of the rebar observed at 4% drift in Phase 5

Fig. 7-124 Separation between the edge column and the base plate at 4% drift in Phase 5

Fig. 7-125 Damage to the east edge column base at 2% butterfly loading in Phase 6

Fig. 7-126 Conditions of the east edge column after 5% drift in Phase 8

Fig. 7-127 Conditions of the west column after 5% drift in Phase 8

Fig. 7-128 Uplift of the column in Phase 10

Fig. 7-129 Crushing of the concrete core and fracture of the rebar at the east column base

Fig. 7-130 Fracture of the weld for the rebar at the west column base

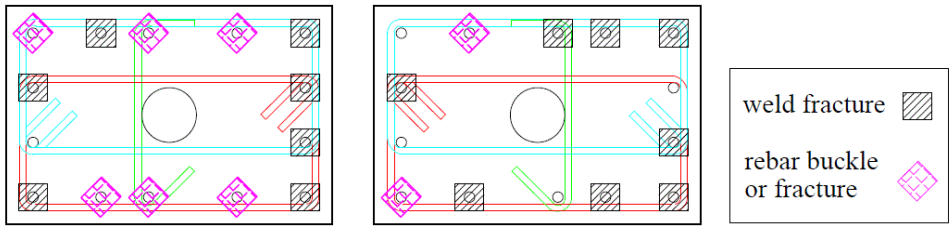

Fig. 7-131 Summary of the damage at the base of the east and the west column after the test

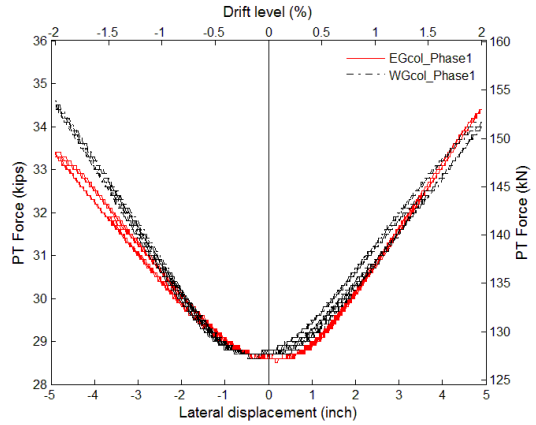

Fig. 7-132 PT force – lateral wall displacement response in the east and the west edge column in Phase 1

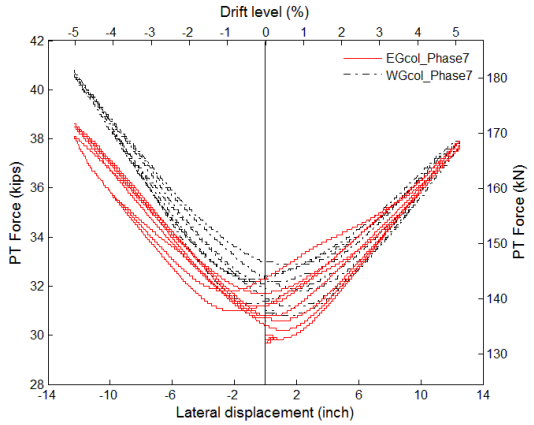

Fig. 7-133 PT force – lateral wall displacement response in the east and the west edge column in Phase 7

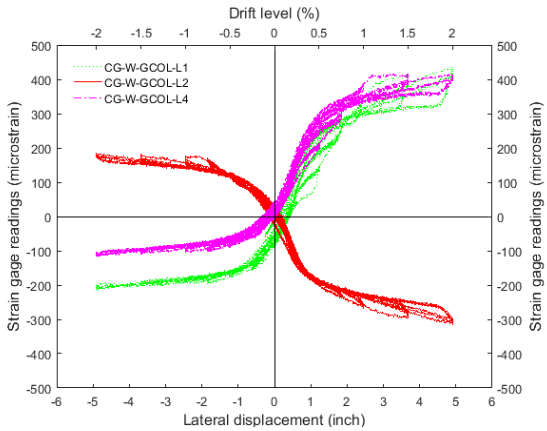

Fig. 7-134 Concrete strain – lateral wall displacement response in the west edge column in Phase 1

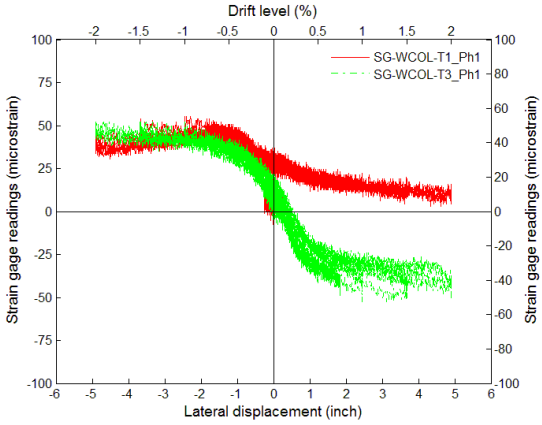

Fig. 7-135 Transverse reinforcement strain - lateral wall displacement response in the west edge column in Phase 1

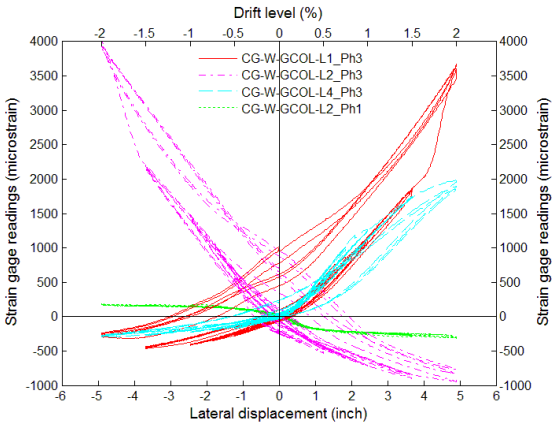

Fig. 7-136 Concrete strain – lateral wall displacement response in the west edge column in Phase 3

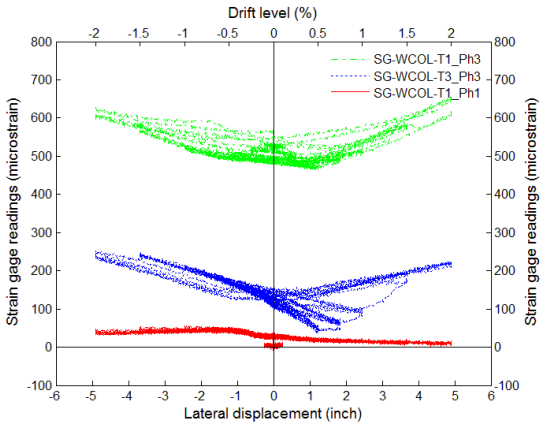

Fig. 7-137 Transverse reinforcement strain – lateral lateral wall displacement response in the west edge column in Phase 3

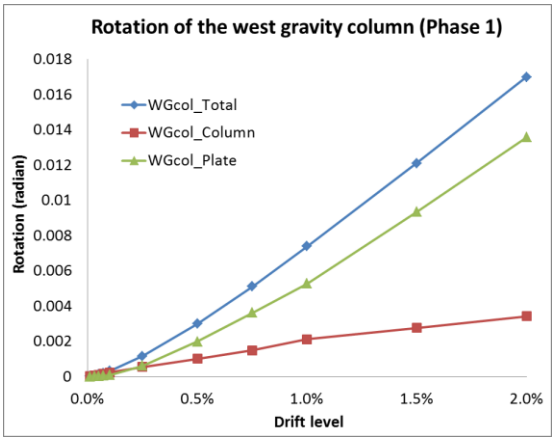

Fig. 7-138 Rotation of the west edge column base at different drifts in Phase 1

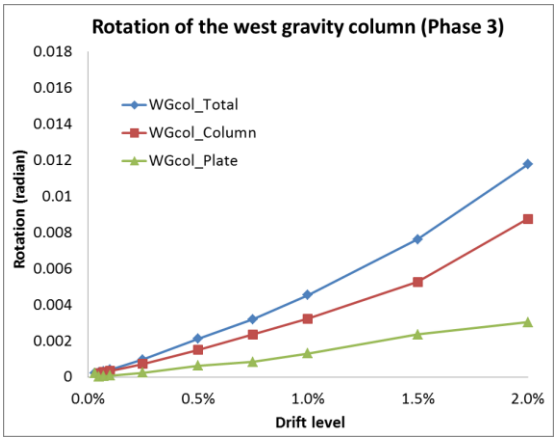

Fig. 7-139 Rotation of the west edge column base at different drifts in Phase 3

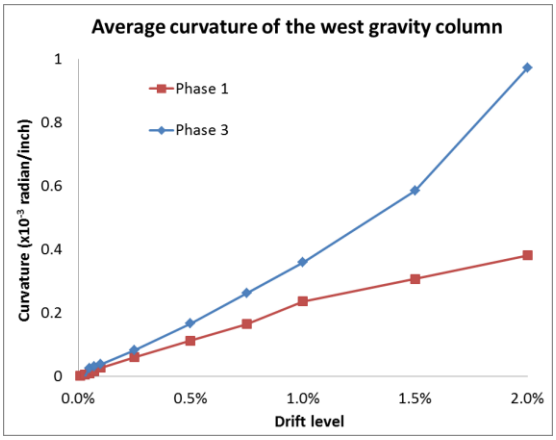

Fig. 7-140 Average curvatures at the west column base in Phase 1 and Phase 3

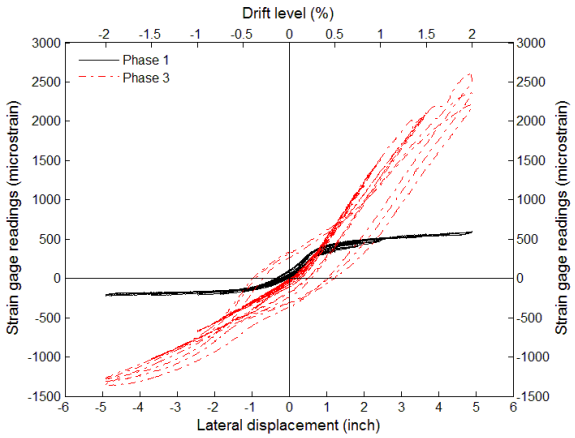

Fig. 7-141 Readings of SG_EGCOL_L3 in Phase 1 and Phase 3

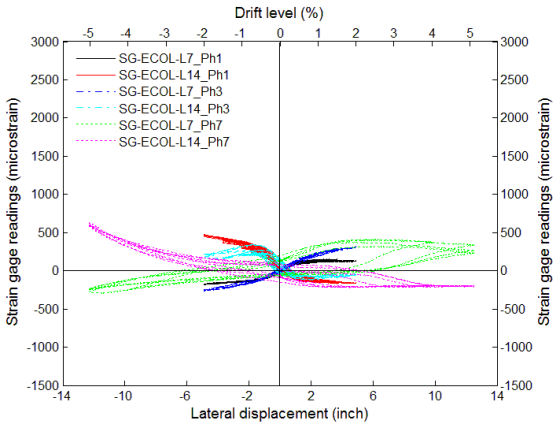

Fig. 7-142 Readings of SG_EGCOL_L7 and SG_ECOL_L14 in Phase 1, 3&7

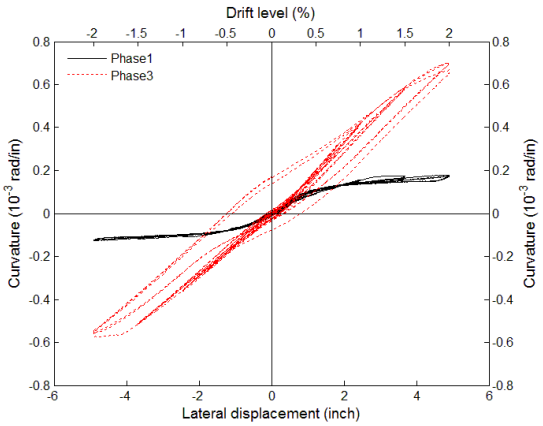

Fig. 7-143 Curvature – lateral wall displacement response of local curvature in the east edge column in Ph1&3

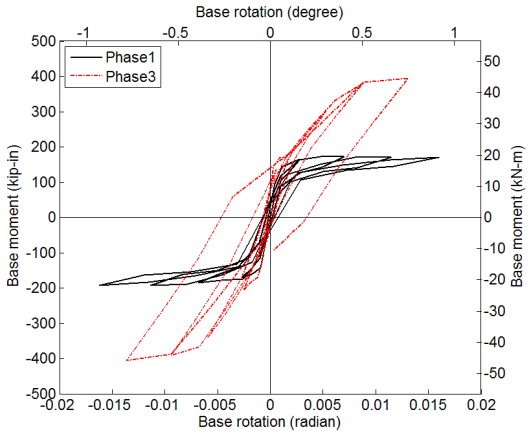

Fig. 7-144 Moment-rotation curves of the east edge column in Phase 1 and Phase 3

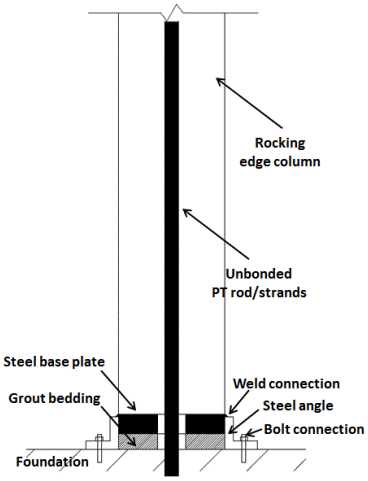

Fig. 7-145 Rocking edge column with energy dissipating elements

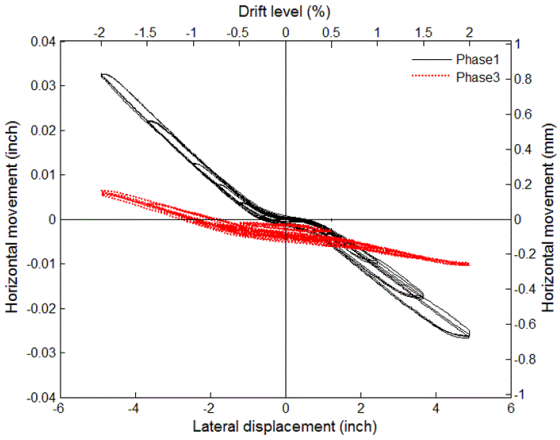

Fig. 7-146 Horizontal movement – lateral wall displacement response at the base of the east edge column in Phase 3

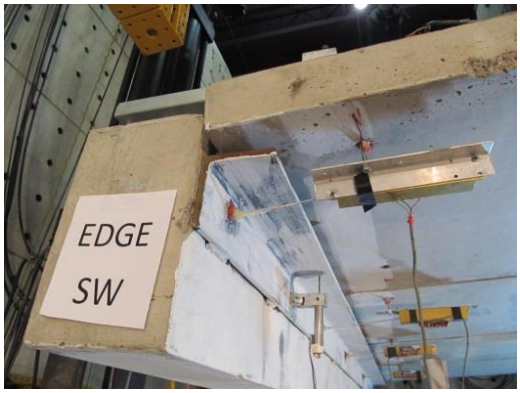

Fig. 7-147 Contact loss between the planks and the steel angle affixed to the edge beam

CHAPTER 8. Comparison of PFS1 and PFS2

As mentioned in Section 3.5.1, the base moment of the PreWEC system used in PFS1 was designed to be only 4% larger than that of the PreWEC system used in PFS2. Therefore, a direct comparison of PFS1 and PFS2 was made possible to investigate the impact from the surrounding structure on the overall behavior of rocking-wall structures using different types of wall-floor connections. A general comparison of the two specimens including their design purposes, structural components, and construction techniques is given in Section 8.1. The overall behavior of the two specimens, including stiffness, strength and self-centering capabilities, is compared and analyzed in Section 8.2 and Section 8.3. The damage to the two specimens observed in the tests are compared and discussed in Section 8.4. A summary of the conclusions made in this chapter is given in Section 8.5.

8.1 General Comparison of PFS1 and PFS2

As discussed in Chapter 3, the interaction between PreWEC systems and surrounding structures was designed to be maximized in PFS1 but minimized in PFS2 primarily through the selection of different floor systems in the two specimens. The differences between PFS1 and PFS2 are summarized in Table 8-1.

As shown in the table, the types of PreWEC systems used in PFS1 and PFS2 were different. In PFS1, four short steel tubes were used as the PreWEC end columns. The steel tubes were placed adjacent to the front and the back surface of the wall, thus it might be more appropriate to call them side columns. The steel tubes were pinned-connected to the base block through clevis hinges. Two energy dissipating components (O-connectors) were connected to each steel tube. In PFS2, two precast reinforced concrete (RC) columns were used as the PreWEC end columns. The RC columns were placed adjacent to each end of the wall and clamped to the base block through post-tensioned threaded rods. Four O-connectors were connected to each RC column.

The most remarkable difference between PFS1 and PFS2 was the adopted wall-floor connections. A cast-in-place (CIP) unbonded post-tensioned slab was constructed in

PFS1. Multiple rebar and PT strands in the slab went through the wall, thus a rigid wall-floor connection was formed through CIP construction of the slab. In PFS2, a precast floor system was formed by using multiple pieces of solid planks. Special precast wall-floor connections that were designed to isolate the floor from the vertical movement of the wall were used in PFS2.

Because of the usage of different wall-floor connections, the gravity load transfer path in PFS1 was not the same as that in PFS2. In PFS1, the gravity loads on the floor were directly transferred to the wall through the rigid wall-floor connection. It was realized by applying an axial load, which was equal to the sum of the gravity loads from the tributary areas of the six floors, to the specimen through the MAST crosshead. On the other hand, in PFS2, the gravity loads on the floor were transferred to the PreWEC end columns due to the usage of the special wall-floor connections that vertically isolated the floor from the wall. The gravity load was emulated by introducing prestress forces equal to the gravity loads from the tributary areas of the six floors. Therefore, the loads on each end column in PFS2 were approximately half of those on the wall in PFS1.

Because of the usage of different wall-floor connections, it was expected that the constraint effect from surrounding structures (i.e. floor systems, edge beams and edge columns) on the PreWEC systems would also be different. Gravity load transfer path and constraint effect from the surrounding structures were two key factors that greatly impacted the overall and the local behavior of the rocking-wall structures. They are discussed thoroughly in later sections of this chapter.

Because only the first-story floor slab was constructed in both tests, concepts of "mega beams/mega trusses" were introduced to simulate the missing floor slabs from the other five stories in the scaled prototype building. Steel beams with cover plates that were fixed-connected at both ends were used in PFS1. In PFS2, steel tubes pinned-connected at the ends were used. Consistent with the floor systems in the respective structures, flexural resistance was developed at the ends of the mega beams in PFS1 but not at the ends of the mega trusses in PFS2.

Rigid floor-edge beam connections and fixed edge column base connections were formed through CIP construction in PFS1. In PFS2, the precast planks were supported on

steel angles affixed to the edge beams (transverse beams) and were connected across the top by strap plates. Because there would be little flexural resistance generated at the floor-edge beam (floor-transverse beam) connections, the connections behaved like pinned connections. Two different base connections were investigated with the edge columns in PFS2. By untightening/tightening the column base plates to the base block, both rocking and fixed edge column base connections were realized and tested in PFS2. Some of the construction techniques were different in the fabrication of PFS1 and PF2. In PFS1, fiber grout was poured into a pocket in the base block. The pocket prevented potentially excessive shear sliding of the wall and provided constraint to the fiber grout that increased its strength and ductility. Although having a pocket in the base block was beneficial, it increased the time and difficulty of construction. In PFS2, there was no pocket in the base block of the wall. The fiber grout was directly placed above the base block, which simplified the construction practice.

Four rebar dowels were embedded at the bottom of the wall and extended across the wall/base block interface in PFS2. They were embedded in wall and unbonded to the base block. This configuration was believed to better facilitate fabrication tolerances. Because if the bars in the base block were offset, it would be difficult to drill holes to align the dowels in wall due to relatively thin web of wall. The dowels were used to provide detailing that might be used in the prototype structure to prevent lateral movement at the base of the wall during construction and out-of-plane slip of the wall during service when loaded in the transverse direction, particularly without the pocket in the base block to help provide stability. This detailing was not used in PFS1. The impact from using different construction techniques in the tests is discussed in detail in Section 8.4.

Testing phases selected for comparison

As discussed in Section 4.5, multiple phases of testing were conducted in both tests. To make the comparison feasible, only some phases are selected as explained below.

During the test of PFS1, one strand wire in the wall was believed to have fractured when PFS1 was loaded towards 2.5% drift in Phase 1, causing some permanent PT loss in the strands. Moreover, non-negligible damage also occurred to the CIP slab, mega beams, O-connectors and fixed-base edge columns at the end of Phase 1. The initial

condition of PFS1 in Phase 2 and Phase 3 was changed due to the PT loss and the damage to the surrounding structure.

During the test of PFS2, the specimen was loaded to 2% drift without props and with rocking edge columns being used in Phase 1. Although the entire specimen was almost "damage-free" in Phase 1, the initial condition of PFS2 in the following phases of testing was changed due to the yielding of the replaceable O-connectors.

Because it was more reasonable to compare the behavior of PFS1 and PFS2 when the initial conditions of the two specimens were similar, only the test data recorded before 2% drift in Phase 1 of PFS1 and that recorded in Phase 1 of PFS2 was used for analysis in Section 8.2 and Section 8.3, including the stiffness, strength and self-centering capabilities of the two specimens. The damage to the two specimens observed in the test is compared and analyzed in Section 8.4.

8.2 Stiffness and Strength

8.2.1 Stiffness

Fig. 8-1 shows a comparison of the secant stiffness of PFS1 with that of PFS2 at different drift levels. The secant stiffness was calculated by dividing the lateral external force input to the specimen with the lateral displacement recorded on top of the specimen. As shown in the figure, the secant stiffness of PFS1 was much larger than that of PFS2 at the same drift level.

The secant stiffnesses of PFS1 and PFS2 at different positive drifts are listed in Table 8-2. As shown in the table, the initial secant stiffness of PFS1 was about 2.2 times that of PFS2 at 0.01% drift. At this small drift level, the walls in neither specimen had experienced uplift yet, thus the O-connectors and the surrounding structure had little deformation and contributed little to the initial stiffness of the entire specimen. It was believed that the initial stiffness of the specimen was mainly contributed by the flexural stiffness of the wall.

The walls were clamped to the base blocks by the initial axial forces in the walls. In PFS1, the initial axial force (257 kips) consisted of a constant axial load applied to the wall (128 kips), an initial PT force (113 kips) and self-weight of the wall (16 kips). In PFS2, the initial axial force (190 kips) consisted of an initial PT force (177 kips) and self-weight of the wall (13 kips). Assuming the action lines of the initial axial forces in the walls passed through the centroid of the wall, the P-delta effect (geometry nonlinearity) was negligible when the lateral drift of the wall was very small (0.01%). The wall would behave like a cantilever wall with a fixed base connection. The initial flexural stiffness of the walls in PFS1 and PFS2 are calculated as follows:

$$PFS1:\ k_w = \frac{3E_cI_w}{{H_w}^3} = \frac{3\times6410\times6\times90^3}{12\times249.5^3} = 1353.6\ kip/in \tag{8.1}$$

$$PFS2:\ k_w = \frac{3E_cI_w}{{H_w}^3} = \frac{3\times5586\times6\times68^3}{12\times245^3} = 537.3\ kip/in \tag{8.2}$$

Where k_w= Lateral stiffness of the wall in PFS1 and PFS2;

As shown above, the lateral stiffness of the wall in PFS1 (416 kip/in) was approximately 2.5 times that in PFS2 (190 kip/in). It was close to the test result (2.2). As shown in the equations above, the width of the wall in PFS1 (90 in.) was larger than that in PFS2 (68 in.), which caused the larger initial secant stiffness of PFS1.

The difference in the width of the wall was attributed to the PreWEC system selected in the tests. The overall widths of the PreWEC system in PFS1 and PFS2 were the same (90 in.) in both structures. In PFS1, the four side columns were placed adjacent to the N and S wall surfaces and did not take up space in the plane of the wall panel, thus the width of the wall was the full 90 in. For PFS2, two end columns of 10 in. wide were placed at each end of the wall and took up the space in the plane of the wall. Therefore, the width of the wall in PFS2 was reduced to 68 in. Consequently, the smaller dimension of the wall resulted in its smaller initial stiffness.

8.2.2 Strength

Fig. 8-2 shows a comparison of the base moment-lateral displacement envelope curve of PFS1 with that of PFS2. As mentioned in Section 4.5, external lateral loads generated to achieve the programmed lateral displacements and external lateral resisting moments slaved to the external loads were applied to the top of the wall in the tests. The base moment of the specimen (PFS1 or PFS2) was calculated through multiplying the applied lateral load with the height of the wall and then subtracting the result by the slaved lateral resisting moment. As shown in Fig. 8-2, the base moment of PFS1 was much larger than that of PFS2 at the same drift level. Table 8-3 lists the calculated base moment resistance of PFS1 and PFS2.

As mentioned previously, the base moment of the PreWEC system used in PFS1 was only 4% larger than that of the PreWEC system used in PFS2. As shown in Table 8-3, the base moment of PFS1 was about 143% larger than that of PFS2 at 2% drift. It was believed that the difference was caused by two key factors: gravity load transfer paths and constraint effect from the surrounding structure. Further explanation of the difference in strength of PFS1 and PFS2 is provided in the following.

Fig. 8-3 shows the force flow in the wall of PFS1 when it was loaded to the east. Table 8-4 summarizes the annotations in Fig. 8-3. As shown in the figure, when the external lateral force (F_{ET}) and the lateral moment (M_{ET}) were applied to the specimen, the following resisting moments were generated: the resisting moment (M_N and M_W) generated by the gravity loads carried by the wall (F_N) and the self-weight of the wall and the top block (W_W); the resisting moment (M_{PT}) generated by the PT force (F_{PT}); the resisting moments (M_{O_E} and M_{O_W}) generated by the east and the west O-connectors and the resisting moment (M_{SU}) generated by the surrounding structure (i.e. steel mega beams, unbonded PT floor and edge columns).

Fig. 8-4 shows the force flow in the wall of PFS2 when PFS2 was loaded to the east. Table 8-5 summarizes the annotations in Fig. 8-4. As shown in the figure, when the external lateral force (F_{ET}) and the lateral moment (M_{ET}) were applied to the specimen, the following resisting moments were generated: the resisting moment (M_W) generated by

the self-weight of the wall and the top block (W_W); the resisting moment (M_{PT}) generated by the PT force (F_{PT}); the resisting moments (M_{O_E} and M_{O_W}) generated by the east and the west O-connectors and the resisting moment (M_{SU}) generated by the surrounding structure (i.e. steel mega trusses, precast floor and edge columns).

In both PFS1 and PFS2, the resisting moments (M_N and M_W) generated by F_N and W_W were calculated through multiplying the total force ($F_N + W_W$) by the distance between the wall center and the action line of the resultant compression force (d_{NWPT}). Because the PT strands were located in the middle of the wall, the action line of the PT force was the same as that of F_N (W_W) and the resisting moment provided by the PT force was $F_{PT}d_{NWPT}$. As discussed in Section 6.2.1 and Section 7.2.1, there was little damage to the concrete in the wall corners and the confinement effect of the boundary elements was not significant in Phase 1 of both tests. Under this circumstance, the stress distribution over the contact region was between linear elastic and Whitney stress block assumptions. The moment arm d_{NWPT} in PFS1 and PFS2 is calculated using Whitney stress block assumptions as regulated in ACI 318-11:

$$PFS1: \quad d_{NWPT} = \frac{w_{WALL}}{2} - \frac{\beta_1 c}{2} = \frac{90}{2} - \frac{0.65c}{2} = 45 - 0.325c \tag{8.3}$$

$$PFS2: \quad d_{NWPT} = \frac{w_{WALL}}{2} - \frac{\beta_1 c}{2} = \frac{68}{2} - \frac{0.65c}{2} = 34 - 0.325c \tag{8.4}$$

Where c = Neutral axis depth of the walls (summarized in Section 6.2.3 for PFS1 and Section 7.2.4 for PFS2), β_1 = Equivalent rectangular block constant. As shown in Table 3-8, the measured strength of the concrete in the wall in PFS1 and PFS2 was 8.3 and 8.8 kip, respectively. β_1 was 0.65 according to Section 10.2.7.3 in ACI 318-11. When the stress distribution over the contact region is assumed to be linear elastic, the coefficient 0.325 shown in the above two equaitons becomes 1/3 (i.e., 0.333).

The resisting moments (M_{O_E} and M_{O_W}) generated by the O-connectors were calculated through multiplying the vertical resisting forces (R_{O_E} and R_{O_W}) from the east and the west O-connectors by the associated distance (d_{O_E} and d_{O_W}) between the O-connectors and the action line of the resultant compression force. The calculation of d_{O_E} (d_{O_W}) and R_{O_E} (R_{O_W}) of the east and the west O-connectors is discussed below.

As shown in Fig. 8-3, d_{O_E} and d_{O_W} in PFS1 are calculated:

$$d_{O\_E} = S_{O\_E} - \frac{\beta c}{2} = 9 - 0.325c; \tag{8.5}$$

$$d_{O\_W} = w_{WALL} - S_{O\_W} - \frac{\beta c}{2} = 90 - 9 - \frac{0.65c}{2} = 81 - 0.325c; \tag{8.6}$$

As shown in Fig. 8-4, d_{O_E} and d_{O_W} in PFS2 are calculated as follows:

$$d_{O\_E} = S_{O\_E} - \frac{\beta c}{2} = 2.5 - 0.325c; \tag{8.7}$$

$$d_{O\_W} = w_{WALL} - S_{O\_W} - \frac{\beta c}{2} = 68 - 2.5 - \frac{0.65c}{2} = 65.5 - 0.325c; \tag{8.8}$$

Where S_{O_E} = Distance between the east O-connectors and the adjacent wall end; S_{O_W} = Distance between the west O-connectors and the adjacent wall ends.

To obtain the vertical resisting forces R_{O_E} and R_{O_W}, the numerical model of the O-connectors was used. The model had been calibrated through a component test of the O-connectors, as discussed in Section 5.4.3. The relative vertical movements of the O-connectors, summarized in Section 6.3.2 for PFS1 and Section 7.4.2 for PFS2, were applied to the numerical model to obtain the vertical resisting forces R_{O_E} and R_{O_W}.

Because there was limited instrumentation on the surrounding structure in both specimens, it was difficult to obtain the contributions from each structural component to the total resisting moment of the surrounding structure (M_{SU}) (i.e. steel mega beams, floors and edge columns in PFS1; steel trusses, floors and edge columns in PFS2). Instead, the total resisting moment (M_{SU}) in either PFS1 or PFS2 was considered as a whole and calculated based on the equilibrium between the external moment and the internal moment. As shown in Fig. 8-3 and Fig. 8-4, when the moment equilibrium of the wall is established about the action line of the resultant compression force at the wall corner, M_{SU} is calculated through subtracting the external moment provided by the external loads (F_{ET} and M_{ET}) by the sum of M_N, M_{PT}, M_{O_E} and M_{O_W} at the base of the wall:

$$\begin{aligned} M_{SU} &= M_{BASE} - M_N - M_W - M_{PT} - M_{O\_E} - M_{O\_W} \\ &= F_{crosshead} H_w + M_{slaved} - M_N - M_W - M_{PT} - M_{O\_E} \\ &\quad - M_{O\_W} \end{aligned} \tag{8.9}$$

Where M_{BASE} = Moment at the base of the wall generated by the applied external loads and external moments; $F_{crosshead}$ = Concentrated lateral force applied to the crosshead, H_w = Height from the top of the top block to the bottom of the wall (250 in. for PFS1 and 245 in. for PFS2); M_{slaved} = External moments applied to the wall through the crosshead. In both PFS1 and PFS2, as described in Section 4.5, M_{slaved} was slaved to the applied external loads ($M_{slaved} = -3.48F_{crosshead}$).

Fig. 8-5 and Fig. 8-6 show the portion of the resisting moment contributed by different structural components at the positive peaks in PFS1 and PFS2, respectively. Table 8-6 lists the resisting moment from each structural component in PFS1 and PFS2at 2% drift.

As shown in Fig. 8-5, the "Gravity loads" and the "PT force" contributed the majority of the resisting moment at the beginning of the test of PFS1. After the wall was uplifted, the "O-connectors" and "Surrounding structures" started to be involved in resisting the external loads, thus their resisting moments increased at larger drift levels. Correspondingly, the contribution from the "Gravity loads" and "PT force" decreased at larger drift levels.

The increased rate of the contribution from the surrounding structure dropped at 0.25% drift, when the cover plates of the west mega beam had yielded as shown in Table 6-4. The increased rate of the contribution from the O-connectors dropped at 0.5% drift, when the O-connectors started to yield as mentioned in Section 6.3.1. It was noteworthy that the absolute resisting moment provided by "Gravity loads" remained relatively constant after 0.5% drift, when the N.A. depth of the wall did not change much at the drifts larger than 0.5%, as shown in Fig. 6-26. Because the overall strength of PFS1 kept increasing to 2% drift, the contribution from the "Gravity loads" was decreasing. On the other hand, the absolute resisting moment provided by the "PT force" kept increasing because of the increased PT forces after 0.5% drift, it was found that the contribution from the "PT force" did not change much at the drifts larger than 0.5%, as shown in Fig. 8-5. At 2% drift in Phase 1 of PFS1, the relative contributions to the resisting moment from the gravity loads, the PT force, the O-connectors and the surrounding structures were 23%, 25%, 10% and 42%, respectively.

As shown in Fig. 8-6, the PT force contributed the majority of the resisting moment at the beginning of the test of PFS2 (e.g. 72% at 0.05% drift). Similar to PFS1, after the wall was uplifted, the "O-connectors" provided more resisting moments at larger drifts. The increase rate of the contribution from the O-connectors started to decrease at 0.25% drift and remained almost constant after 0.5% drift, when they started to yield as mentioned in Section 7.4.1. The contribution from the "Gravity loads" and "Surrounding structures" slightly decreased at larger drifts. At 2% drift in Phase 1 of PFS2, the contribution portion from the gravity loads, the PT force, the O-connectors and the surrounding structures were 6%, 62%, 23% and 9%, respectively.

As shown in Table 8-6, the resisting moments provided by the PT force and the O-connectors in PFS1 were similar to those in PFS2. However, the resisting moments provided by the gravity loads and the surrounding structure in PFS1 were much larger than those in PFS2, making the base moment of PFS1 about 143% larger than that of PFS2 at 2% drift. The resisting moments from the two sources are further analyzed below.

The gravity loads on the floor were directly transferred to the wall in PFS1, but they were sustained by the two PreWEC end columns in PFS2 due to the use of the special vertical movement isolation connections, which would not be able to transfer gravity loads from the floor to the wall. Because the width of the wall in PFS1 (90 in.) was much larger than that of the end columns in PFS2 (10 in.), the moment arm of the gravity load in the wall was much larger than that in the end columns, which contributed to the much larger resisting moment in PFS1 shown in Table 8-6.

As shown in Fig. 8-3, the resisting moments from the surrounding structure (M_{SU}) included the following in PFS1: the concentrated moments at the wall-mega beam and the wall-floor connections (M_{MB_W} , M_{MB_E}, M_{SLAB_W} and M_{SLAB_E}), the resisting moments generated by the shear couples in the mega beams and the floor (V_{MB_W} and V_{MB_E}, V_{SLAB_W} and V_{SLAB_E}), and the resisting moments generated by the axial forces in the mega beams and the floor (N_{MB_W} and N_{MB_E}, N_{SLAB_W} and N_{SLAB_E}). In PFS2, there were few moments or shear couples generated in the mega trusses and the precast floor. As shown in Fig. 8-4, only the resisting moments generated by the axial forces in the mega trusses

and the floor (N_{MT_W} and N_{MT_E}, N_{BS_W} and N_{BS_E}) contributed to the resisting moments from the surrounding structure (M_{SU}) in PFS2. Therefore, the resisting moments from the surrounding structure in PFS1 were greatly larger than those in PFS2, as shown in Table 8-6.

It was noteworthy that the difference in gravity load transfer path and constraint effect from the surrounding structure were both related to the different wall-floor connections used in PFS1 and PFS2. Therefore, the selection of wall-floor connections is the essential factor to be considered during the design of rocking-wall structures.

8.3 Self-centering Behavior

8.3.1 Self-Centering Performance of PFS1 and PFS2

The force-displacement curves of PFS1 and PFS2 in Phase 1 are superimposed in Fig. 8-7. Fig. 8-8 shows a comparison of the residual displacement/drift of the two specimens recorded at the end of different drift levels. As shown in Fig. 8-7 and Fig. 8-8, the self-centering performance of PFS2 was better than that of PFS1.

Investigation of the self-centering performance of PFS1 and PFS2 is presented in the following sections. Sources of self-centering moments are discussed in Section 8.3.2. Sources of self-centering-resisting moments are discussed in Section 8.3.3. In Section 8.3.4, a general criterion is proposed to ensure the self-centering of rocking-wall structures.

8.3.2 Sources of Self-Centering Moment

8.3.2.1 Self-Centering Moments in PFS1

When PFS1 was unloaded from the peak at each drift level, the moment (M_N) generated by the gravity loads in the wall (F_N), the moment (M_W) generated by the self-weight of the wall and the top block (W_W), and the moment (M_{PT}) generated by the clamping PT force in the strands (F_{PT}) always facilitated the self-centering of the specimen.

When the O-connectors and the surrounding structure (i.e. mega beams, unbonded PT floor and edge columns) remained elastic, they also facilitated the self-centering of the specimen when PFS1 was unloaded from the peak. However, once these structural components had yielded, they started to resist the rocking wall returning to its upright position due to the irreversible plastic deformations. The self-centering-resisting sources in PFS1 are discussed in detail in Section 8.3.3.1.

The self-centering moments from F_N, W_W and F_{PT} were calculated through multiplying the forces by the horizontal distance between the wall center and the action line of the resultant compression force at the wall corner, which was determined by the N.A. depth of the wall. Using the test data recorded in the last cycle of 2% drift, Fig. 8-9 shows the the self-centering moments generated by F_N, W_W and F_{PT} in PFS1. As shown in the figure, the moments generated by "PT force," "Gravity load" and "Self-weight" slowly decreased when PFS1 was unloaded from the peak displacement; the decreasing rate of the moments generated by "PT force" was larger than that of the moments generated by "Gravity load" and "Self-weight." It was noteworthy that the moments did not change direction in any quadrant of the figure, indicating that they always facilitated the self-centering of the specimen during the course of unloading.

8.3.2.2 Self-Centering Moments in PFS2

When PFS2 was unloaded from the peak at each drift level, the moment (M_W) generated by the self-weight of the wall and the top block (W_W) and the moment (M_{PT}) generated by the clamping PT force in the strands (F_{PT}) always facilitated the self-centering of the specimen. Different from PFS1, the gravity loads on the floors in PFS2 were transferred to the PreWEC end columns instead of the wall, thus they did not contribute to the self-centering of the wall.

Similar to PFS1, the O-connectors and the surrounding structure (i.e. mega trusses, precast floor and edge columns) only facilitated the self-centering of the specimen when they were elastic, but started to resist the self-centering of the rocking wall once they had yielded. The self-centering-resisting sources in PFS2 are discussed in detail in Section 8.3.3.2. Using the test data recorded in the third cycle of 2% drift, Fig. 8-10 shows the self-centering moments generated by W_W and F_{PT} in PFS2.

8.3.2.3 Discussion on the Self-Centering Moments in PFS1 and PFS2

Comparing Fig. 8-9 with Fig. 8-10, it is obvious that the sum of the self-centering moments in PFS1 was larger than that in PFS2 because of the contribution from the moment generated by the gravity loads in the wall. The contribution from the "Gravity load" and the "PT force" to the self-centering capability of the specimens is further discussed below.

As shown in Fig. 8-9 and Fig. 8-10, the self-centering moments provided by the "PT force" decreased faster than those provided by "Gravity load" during the course of unloading. It was because the elongation of the PT strands was decreased when the gap opening at the wall/base block interface was reduced during the course of unloading. Under this circumstance, the PT forces in the strands were also reduced. If the PT strands of the wall had yielded or fractured at the peaks of large drifts, the PT forces would be further reduced during the course of unloading due to the plastic elongation of the strands. Therefore, although both the "PT force" and the "Gravity load" facilitated the self-centering of the wall, the self-centering moments generated by the constant "Gravity load" were more reliable than those generated by the "PT force." From this point of view, rigid wall-floor connections that transfer both horizontal shear and gravity loads on the floor to the wall have some advantages over special vertical movement isolated connections that only transfer the horizontal shear of the floor to the wall.

It was noteworthy that the gravity loads on the floor were transferred to the PreWEC end columns in PFS2. The width of the end columns was much smaller compared to that of the wall, thus the action line of the gravity loads in a real system might be out of bounds of the end columns, generating overturning moments instead of self-centering moments on the end columns due to P-Delta effect. This was not the case in the test structure because the gravity load effect was simulated by an unbonded PT threaded rod.

To conclude, the self-centering moments in PFS1 were larger than those in PFS2 due to the contribution from the moments generated by the gravity loads in the wall. Compared to "PT force," the self-centering moments provided by "Gravity load" were more reliable in rocking-wall structures.

After describing the sources of self-centering moments in PFS1 and PFS2, the self-centering-resisting moments in the two specimens are discussed in the next section.

8.3.3 Sources of Self-Centering-Resisting Moment

8.3.3.1 Self-Centering-Resisting Moments in PFS1

As mentioned in the previous sections, once the O-connectors and the surrounding structure had yielded, they started to resist the self-centering of the wall during the course of unloading due to the irreversible plastic deformations.

The self-centering-resisting moments included M_{O_E} and M_{O_W} generated by the O-connectors (R_{O_W} and R_{O_E}) and the resisting moments generated by the surrounding structure (M_{SU}), which consisted of the concentrated moments at the wall-mega beam and the wall-floor connections (M_{MB_W} , M_{MB_E} , M_{SLAB_W} and M_{SLAB_E}), the moments generated by the shear couples in the mega beams and the floor (V_{MB_W} and V_{MB_E}, V_{SLAB_W} and V_{SLAB_E}), and the moments generated by the axial forces in the mega beams and the axial forces in the floor (N_{MB_W} and N_{MB_E}, N_{SLAB_W} and N_{SLAB_E}). The resisting moments generated by the west and the east O-connectors are discussed first.

O-connectors

By applying the relative vertical displacements recorded by the LVDTs (L2_NWOV and L2_NEOV, shown in Fig. 6-61 and Fig. 6-62) to the numerical model of the O-connectors (validated in Section 5.4.3), the resisting forces from the O-connectors was obtained. The associated resisting moments (M_{O_E} and M_{O_W}) were calculated through multiplying the resisting forces by the horizontal distances between the O-connectors and the action line of the resultant compression forces at the wall corners. Fig. 8-11 shows the resisting moments generated by the west and the east O-connectors in the last cycle of 2% drift. As shown in the figure, the resisting moment from the "West O-connectors" rapidly decreased to zero when PFS1 was unloaded from the positive peak. It changed direction and started to resist the wall from self-centering.

It was noteworthy that the resisting moment of the "West O-connectors" became negligible when the specimen was loaded in the negative direction. It was because the west O-connectors were adjacent to the compressive side of the wall when the specimen

was loaded in the negative direction (to the west), the distance between the west O-connector and the action line of the resultant compression forces at the west wall corner was very small. The resisting moments of the west O-connectors were greatly reduced due to the small moment arm of the resisting forces in the west O-connectors.

When PFS1 was unloaded from the negative peak, the moments of the "East O-connectors" started to resist the wall from self-centering after the elastic unloading of the east O-connectors. Similar to the west O-connectors, the resisting moments of the east O-connectors were greatly reduced when PFS1 was loaded in the positive direction (to the east).

Surrounding structures

It was difficult to obtain the resisting moments from each structural component of the surrounding structure due to limited instrumentation. Instead, the resisting moments from the surrounding structure are treated as a whole. Based on the moment equilibrium established in Eqn. (8.9) in Section 8.2.2, the resisting moments from the surrounding structure were obtained after calculating the moments provided by external loads and those provided by O-connectors. Fig. 8-12 shows the resisting moments from the surrounding structure. As shown in the figure, when the specimen was unloaded from the positive peak displacement, the moments from the surrounding structure quickly decreased to zero and then increased in the reverse direction that resisted the rocking wall from self-centering. Similar behavior was observed when the specimen was unloaded from the negative peak displacement.

8.3.3.2 Self-Centering-Resisting Moments in PFS2

In PFS2, the self-centering-resisting moments included M_{E_O} *and* M_{W_O} generated by the O-connectors and the resisting moments generated by the surrounding structure (M_{SU}), which consisted of the moments generated by the axial forces in the mega trusses and the axial forces in the precast floor (N_{MT_W} and N_{MT_E}, N_{BS_W} and N_{BS_E}).

O-connectors

One LVDT was used in PFS2 to measure the relative vertical deformation of the O-connectors. The LVDT (L2-NWOV) was mounted on the O-connectors attached to the west end of the wall. By applying the cyclic readings of L2-NWOV (Fig. 7-96) to the

numerical model of the O-connectors, the resisting forces from the O-connectors was obtained. Fig. 8-13 shows the resisting moments generated by the O-connectors in the third cycle of 2% drift.

Surrounding structures

Similar to PFS1, Eqn. (8.9) in Section 8.2.2 was used to deduce the resisting moments provided by the surrounding structure. Because there was no LVDT mounted on the O-connectors attached to the east side of the wall, their resisting moments were not obtained. However, it was noteworthy that when PFS2 was loaded in the positive direction (to the east), the O-connectors attached to the east end of the wall were adjacent to the compression side of the wall and their resisting moments were negligible. Therefore, it was reasonably accurate to neglect the contribution from the O-connectors attached to the east end of the wall in Eqn. (8.9) when the specimen was loaded in the positive direction. The resisting moments provided by the surrounding structure in the third positive half cycle of 2% cycle are shown in Fig. 8-14.

8.3.3.3 Discussion on the Self-Centering-Resisting Moments in PFS1 and PFS2

Comparing Fig. 8-12 with Fig. 8-14, it is obvious that the self-centering-resisting moments provided by the surrounding structure in PFS1 were much larger than those in PFS2. In PFS1 where rigid wall-floor connections were used, damage to the O-connectors, the unbonded PT floors, the mega beams and the edge columns all contributed to the self-centering-resisting moments. On the other hand, in PFS2 where the special vertical movement isolated connections were used, the entire specimen was almost “damage-free” except the O-connectors, thus the resistances to the self-centering of the wall were much smaller.

8.3.4 General Criterion to Ensure Self-Centering of Rocking-Wall Structures

As shown in Fig. 8-8, the residual drift of PFS2 was smaller than that of PFS1after similar peak drift levels, indicating that the self-centering performance of PFS2 was superior to that of PFS1.

As discussed in Section 8.3.2.3, compared with rigid wall-floor connections (PFS1), it was disadvantageous to use special vertical movement isolated connections (PFS2)

because the gravity loads transferred to the end columns had little contribution to the self-centering of the entire structure. On the other hand, as discussed in Section 8.3.3.3, less damage occurred to the surrounding structure in PFS2, resulting in smaller resistances to the self-centering of the entire structure. Pros and cons existed when using either type of wall-floor connections. In-depth study of the self-centering performance of PFS1 and PFS2 is given in the following.

Table 8-7 lists the base moments calculated from the external loads (M_{BASE}), and internal moments (M_N, M_W, M_{PT}, M_O and M_{SU}) at -0.4% drift when both PFS1 and PFS2 were unloaded from the third negative peak of 2% drift. The methods to calculate the moments in Table 8-7 are described in detail in Section 8.2.2 and are not repeated here. As shown in the table, the base moment provided by the external loads (M_{BASE}) was close to zero in PFS1, thus 0.4% was considered as the residual drift after the 2% drift cycles in PFS1. On the other hand, the base moment provided by the external loads in PFS2 still existed, indicating that PFS2 was still under the course of unloading such that its residual drift was smaller than 0.4%. It was found that the residual drift was only 0.08% after the 2% drift cycles in PFS2.

As shown in the table, although the gravity loads in the wall provided more self-centering moment (M_N) in PFS1 compared with PFS2 (4354-1 = 4353 kip-in), the self-centering-resisting moment from the surrounding structure (M_{SU}) in PFS1 was larger than that of PFS2 (7866-909 = 6957 kip-in). Compared to PFS2, the increased self-centering-resisting moment was about 60% larger than the increased self-centering moment in PFS1, resulting in the larger residual drifts in PFS1.

A general criterion developed based on moment equilibrium, which is applicable when either type of wall-floor connection system is used, is proposed below to ensure the self-centering of rocking-wall structures:

$$\frac{M_{PT\_i} + M_N + M_W}{\alpha_0 M_E + \beta_0 M_S} \geq 1 \tag{8.10}$$

Where M_{PT_i}= Moment provided by initial effective PT forces; M_N= Moment provided by the gravity loads on the floors transferred to the wall; M_W= Moment provided by the self-weight of the wall; α_0= Overstrength factor for the energy dissipating elements; M_E=

Maximum moment provided by the energy dissipating elements; β_0= Overstrength factor of the surrounding structure; M_S= Maximum moment provided by the surrounding structure.

As shown in Eqn. (8.10), the impact from gravity load transfer path and constraint effect from the surrounding structure are considered by including the self-centering moment from gravity loads (M_N) and the self-centering-resisting moment from the surrounding structure (M_S). Therefore, Eqn. (8.10) is applicable to rocking-wall structures using either rigid wall-floor connections or precast vertical movement isolated connections. Three important factors considered in Eqn. (8.10) are explained in the following.

Drift Level when Moment Equilibrium Established

As shown in Fig. 8-9 and Fig. 8-10, the self-centering moments provided by the PT forces, the gravity loads in the walls and the self-weight of the walls decreased at smaller drift levels because the moment arms of the self-centering forces (PT forces, gravity loads and self-weight) reduced due to the increased neutral axis depth of the walls as the walls returned to the upright position. Therefore, it was more conservative to examine the self-centering performance of rocking-wall structures at a relatively small drift level. In Eqn. (8.10), it was recommended that the moment equilibrium condition should be examined at the maximum residual drift limit of rocking-wall structures instead of the design drift or the regulated maximum drift limit. The maximum residual drift limit of rocking-wall structures is further discussed below.

The following maximum residual drift limit was proposed (Rahman and Sritharan 2006) as the acceptable limit of rocking-wall structures at four earthquake intensity levels: 0.1% (EQ-I), 0.3% (EQ-II), 0.5% (EQ-III), and 0.75% (EQ-IV), where EQ-III was the design level earthquake and EQ-IV was the maximum considered earthquake. The maximum residual drift limit suitable for Eqn. (8.10) could be selected based on specific performance requirements of rocking-wall structures, which might vary in the design.

Initial Effective PT Force

The gravity loads in the wall and the self-weight of the wall were assumed to remain constant when the structures were loaded or unloaded in earthquake events. On the other

hand, because the elongation of the PT strands in the wall decreases during the course of unloading, the PT force in the wall kept decreasing and was close to the initial effective PT force at the maximum residual drift limit. To be conservative and simple, it was recommended to use the moment calculated by the initial effective PT force in the wall (M_{PT_i}) in Eqn. (8.10).

Maximum Self-Centering-Resisting Moments

As shown in Fig. 8-11 through Fig. 8-14, the self-centering-resisting moments from the O-connectors and the surrounding structure kept increasing when the specimens were unloaded to their upright position (the curves across the vertical axis in the figures). Due to complexity of the hysteric behavior that was deformation-history dependent, it was difficult to determine the self-centering-resisting moments generated by different structural components at the maximum residual drift limit. To be conservative and simple, it was recommended that the maximum moments that could be developed by the energy dissipating elements (M_E) and the surrounding structure (M_S) should be used in Eqn. (8.10). The introduction of the overstrength factors (α_0 and β_0), which would vary with different structural components, further increased the safety factor of Eqn. (8.10).

After comparing the stiffness, the strength and the self-centering performance of PFS1 and PFS2, damage to different structural components in the two specimens, including the PreWEC systems, fiber grout layers, floor systems, mega beams/trusses, and edge columns, is compared and analyzed in the next section.

8.4 Damage to PFS1 and PFS2

8.4.1 PreWEC System

8.4.1.1 Wall Panels

Fig. 8-15 and Fig. 8-16 show the condition of the wall corners at 2% drift (Phase 1) in PFS1 and PFS2, respectively. As shown in the figures, little damage occurred to the walls in both tests.

Although there was little damage to the wall corners in PFS2, some damage was observed near the center of the wall base, as shown in Fig. 8-17. As discussed in Section

7.2.1, the damage was caused by local stress concentrations in the wall due to the existence of the dowel rebar across the wall/base block interface. The dowel rebar was not used in the wall in PFS1, thus the center of the wall base remained intact at the end of the test, as shown in Fig. 8-18.

Cracks in the walls were observed in both PFS1 and PFS2, as shown in Fig. 6-15 and Fig. 7-19. The cracks were observed above the attachment of at least the lower level O-connectors in both tests. It was believed that the cracks were caused by local tensile stresses in the wall generated by the resistances of the O-connectors. That is, when the wall tried to uplift and was restrained by the O-connectors, local tensile stresses developed just above the connectors. Because the resistances of the O-connectors only slightly increased once they had yielded, the tensile cracks in the walls did not grow after the yielding of the O-connectors in the two tests (PFS1: 0.5%, PFS2: 0.75%).

8.4.1.2 O-connectors

In PFS1, the width of the wall was 90 in. with four side columns used to connect the O-connectors. The total width of the PreWEC system in PFS2 was also 90 in., but that included two 10 in. wide end columns used to connect the O-connectors. A 1 in. gap was reserved between each side of the wall in PFS2 and the adjacent end column so the actual PFS2 precast wall width was 68 in.

Because of the different styles of PreWEC systems used in the two specimens, the distance between the O-connectors and the farther end of the wall in PFS1 was different from that in PFS2. For example, the distance between the O-connectors attached to the west side of the wall and the east end of the wall was 81-1/2 in. in PFS1. In PFS2, the distance between the O-connectors attached to the west side of the wall and the east end of the wall was 65-1/2 in.

Fig. 8-19 shows a comparison of the readings of L2_NWOV in PFS1 with those in PFS2. The LVDT L2_NWOV was installed on the O-connectors that were attached to the west side of the wall in both tests. As shown in the figure, the O-connectors were subjected to unsymmetrical deformation in both specimens with larger deformation at positive drifts (when the specimens were loaded to the east) and much smaller deformation at negative drifts (when the specimens were loaded to the west). It was

obvious that the O-connectors would only be subjected to larger vertical deformation when they were on the uplifted side of the wall.

As shown in Fig. 8-19, the O-connectors in PFS1 were subjected to larger vertical deformations than those in PFS2 at the same positive drift. It was mainly because the distance between the O-connectors and the farther end of the wall in PFS1 (81-1/2 in.) was 16 in. larger than that in PFS2 (65-1/2 in.). Because of the larger relative vertical deformation, it was expected that the O-connectors in PFS1 would provide larger vertical resistances than those in PFS2 at the same drift level. It was also expected that the O-connectors in PFS1 would yield earlier than those in PFS2, which was validated by the test results (PFS1: 0.5%, PFS2: 0.75%).

8.4.1.3 End Columns

As shown in Fig. 3-16, four steel tubes, which are 4 in. wide, 3 in. deep and 1/4 in. thick, were used as the end columns to connect the O-connectors in PFS1. The steel tubes were pinned-connected at the base. They remained elastic throughout the test.

As shown in Fig. 3-88, two reinforced concrete end columns were placed adjacent to each end of the wall to connect the O-connectors in PFS2. The end columns sat on the fiber grout above the base block and were clamped to the base block by prestressed threaded rods. Different from PFS1, the end columns in PFS2 also carried the gravity loads from tributary floor areas of the wall that greatly increased the compression force demand in the end columns. As discussed in Section 7.3.1, spalling of concrete cover occurred to the end columns at 1.5% drift and damage to the end columns became more severe at larger drift levels. To ensure the end columns perform properly, design recommendations of the end columns are given in Section 9.1.6.

8.4.2 Fiber Grout Layer

In PFS1, the fiber grout was poured into a pocket in the base block, as shown in Fig. 3-50. In PFS2, the fiber grout was directly poured above the base block, as shown in Fig. 3-121.

Fig. 8-20 and Fig. 8-21 show the condition of the fiber grout beneath the corners of the wall after the test of PFS1. As shown in the figures, because the fiber grout was confined

in the pocket, damage to the grout was not significant in general. Some vertical cracks occurred to the grout beneath the west corner of the wall, where the confining effect was reduced due to the blockout, as shown in Fig. 8-20. It was expected that the minor damaged grout was reusable after the test.

Fig. 8-22 and Fig. 8-23 show the condition of the fiber grout beneath the west and the east corners of the wall after the test of PFS2. Compared to the condition of the fiber grout in PFS1, it was obvious that damage to the grout beneath the wall corners was much greater in PFS2. It should be noted that besides the grout not being confined in a pocket in PFS2, PFS2 was also subjected to many more cycles of loading than PFS1, which could have contributed to the greater amount of damage observed in the grout of PFS2 at the end of the test.

Fig. 8-24 and Fig. 8-25 show the condition of the fiber grout beneath the west and the east end column at 4% drift in Phase 5 of PFS2. As shown in Fig. 8-24, the upper corner of the grout was completely split off at the west end. An inclined crack developed across the full depth of the grout at the east end, as shown in Fig. 8-25. After the completion of the test, it was observed that a great amount of fiber grout beneath the ends columns was completely lost, as shown in Fig. 8-26 and Fig. 8-27. As explained in Section 7.3.3, the wood spacers shown in Fig. 8-26 and Fig. 8-27 caused discontinuity in the fiber grout bearing, which was believed to be the main cause of the poor performance of the fiber grout at larger drifts. The damaged grout would need to be replaced for future usage. Design recommendations for the fiber grout layer are given in Section 9.1.3.

8.4.3 Floor Systems

A cast-in-place unbonded post-tensioned floor slab was used in PFS1 and it was rigid-connected to the wall. As discussed in Section 6.4.2, cracks were initiated at the floor-edge beam and the wall-floor connections at -0.25% and 0.5% drift, respectively. The bonded reinforcement in the slab yielded at the floor-edge beam and the wall-floor connection at 0.75% and 1% drift, respectively. Concrete spalling and rebar buckling were observed at both east and west wall-floor connections at 4% drift. Although the local damage to the wall-floor connections was severe, most of the cracks in the floor

closed upon unloading due to the residual PT forces provided by the strands that remained elastic throughout the test. It was expected that the slab was reusable after repairing the localized damage.

It was found that the damage to the floor slab was caused by the rotation demand on the wall-floor connections that was generated due to the rotation and the uplift of the wall. Design recommendations of the rigid wall-floor connections are given in Section 9.2.

Two steel beams with cover plates were used to simulate the longitudinal resistance of the five missing CIP unbonded PT slabs in PFS1. A tension-compression force couple was generated by the special dogbone-shaped cover plates of the mega beam that simulated the moment resistance of the five missing slabs. Yielding, buckling and fracture of the cover plates were observed during the test of PFS1.

A precast floor slab that consisted of solid planks was used in PFS2. The planks sat on steel angles affixed to the edge beams and the transverse beams. The planks were connected to the edge beams as well as the transverse beams through steel strap plates on the top. In the test of PFS2, the floor slab was successfully isolated from the uplift of the wall because of the usage of the special vertical movement isolated connections. Compared with the CIP floor slab in PFS1, the damage to the precast floor was much lighter in PFS2. There was no damage to the special vertical movement isolated connections. Minor cracks occurred in the solid planks. The cracks were formed at the location where the two U-shaped rebar around the embedded plates of the strap plates terminated in the slab. It was believed that the cracks were caused by the tensile stress in the surrounding concrete that was transferred from the U-shaped rebar. The strap plates at the floor-edge beam and the floor-transverse beam connections remained elastic until 3% drift. The slab was believed to be reusable without repair after the test. To ensure the precast floor system would perform as expected, design recommendations of the vertical movement isolated connections and the strap plates at the plank-beam connections are given in Section 9.3.1 and Section 9.3.2, respectively.

Because the precast planks were connected to the wall through vertical movement isolated connections and pinned-connected to the transverse beams as well as the edge

beams, the constraint from the precast floor on the wall was small. Two steel tubes that were pinned-connected to the wall and the edge columns were used to simulate the five missing floors in PFS2. They remained elastic throughout the test.

8.4.4 Edge Columns

CIP edge columns and edge beams were built in PFS1. The longitudinal reinforcement of the edge columns was continuous into the base block, forming rigid column base connections. The first story edge column and the edge beam were cast together with the unbonded post-tensioned floor slab, forming rigid floor-edge beam connections. The edge columns were also post-tensioned with a high strength unbonded 3/4 in. threaded rod to simulate the gravity load in the edge columns. During the test, flexural cracks in both edge columns initiated at 0.25% drift in Phase 1. Initial yielding of the longitudinal reinforcement in the edge columns occurred at approximately 1% drift. Spalling of the concrete cover at the corners was observed at 2.5% drift in Phase 1.

Precast edge column and edge beam assemblages were used in PFS2The longitudinal rebar of the precast edge column were welded to a steel base plate that was connected to the base block through four threaded rods. The edge columns were also post-tensioned with a high strength unbonded 1 in. threaded rod to simulate the gravity load in the edge columns. In Phase 1 and Phase 2 of PFS2, the nuts of the threaded rods were not attached, thus the base plate was not tightened to the base block. No cracks were observed in the edge columns in these two phases. It was believed that the edge columns behaved like rocking columns, thus negligible tensile strains developed in the edge columns through Phase 2.

In Phase 3, the base plates were tightened to the base block by putting back the nuts of the threaded rods. Cracks in the edge columns were initiated at 0.07% drift. Initial yielding of the longitudinal reinforcement occurred at approximately 1.5% in Phase 3. Crushing of the concrete cover, buckling of the rebar and fracture of the weld between the rebar and the base plate occurred to the edge columns at 4% drift in Phase 5.

It was noteworthy that the behavior of the fixed-base edge columns in PFS2 was different from that in PFS1. Two factors that contributed to the difference are discussed in the following.

It was noteworthy that the behavior of the fixed-base edge columns in PFS2 was different from that in PFS1. Two factors that contributed to the difference are discussed in the following.

8.4.4.1 Deformation Demand

In PFS1, the CIP edge columns were rigidly connected to the base block and the unbonded PT slab. Therefore, the lateral displacement of the structure imposed large deformation demands on the edge column. The deformation demands imposed on the edge columns in PFS2 were not as severe as those in PFS1 even when the edge columns were attached to the base block by clamping the column base plate to the base block through tightening the nuts as discussed in Section 7.6.4. In that condition, the rotation of the base plate was still noticeable (i.e., rotation of the base plate contributed 26% of the total rotation at the base of the west edge column at 2% drift). The rigid body rotation of the base plate contributed a significant portion of the lateral displacement at the top of the edge column relieving some of the flexural bending in the columns.

8.4.4.2 Axial loads

In PFS1, damage occurred to the steel mega beams and the CIP floor slab at both wall-mega beam (wall-floor) and mega beam-steel column (floor-edge beam) connections. Flexural moments and shear forces were generated at these connections.

Based on the force equilibriums established at the mega beam-steel column and the floor-edge beam connections, the sum of the shear forces in the mega beams and those in the floor slab was equal to the additional axial force in the edge columns. A tension force was generated in the edge column that was adjacent to the uplifted side of the wall and a compression force was generated in the edge column that was adjacent to the compression side of the wall. For example, as shown in Fig. 6-163, a compression force approximately 32.9 kips was transferred to the east edge column at 2% drift in Phase 1.

On the other hand, a tension force of approximately 33.3 kips was transferred to the east edge column at -2% drift in Phase 1.

Near the top of the first story east edge column, strain gages (SG_ECOL_L9 and SG_ECOL_L10) attached to the longitudinal rebar (which remained elastic) were used to deduce the axial load in the edge columns. It was found that the total axial load in the first story east edge column was -71 kip at 2% drift and 16 kip at -2% drift.

The strain gages (SG_ECOL_L5 and SG_ECOL_L6) attached to the longitudinal rebar near the base of the first story east edge column remained functional through 2% drift in Phase 1. By analyzing the readings from these two strain gages it was found that the flexural moment in the east edge column was 605 kip-in at 2% drift and 237 kip-in at -2% drift. The location of the strain gages is shown in Fig. 4-4.

The strain gage SG_EGCOL_L8 attached to the longitudinal rebar near the top of the first story east edge column was broken before the test of PFS2, thus it could not be used to deduce the axial load. In PFS2, because the east steel tube was pinned-pinned connected to the east edge column and the wall, the moments and the shears generated in the steel tube were expected to be negligible. It was also expected that the moment and the shear generated in the precast floor would be small, because both plank-edge beam and plank-transverse beam connections were close to pinned connections. Therefore, the axial forces generated in the east edge column by the east steel tube and the precast floor slab would be small. Under this circumstance, the axial load in the first story east edge column at 2% drift could be calculated by summing the PT force at 2% drift (measured by the load cell, 32.6 kips) with the self-weight of the edge column (6.3 kips), which was approximately 39 kips.

By analyzing the readings of the strain gages (SG_EGOL_L5 and SG_EGCOL_L6) attached to the longitudinal rebar near the base of the first story east edge column, it was found that the flexural moment in the east edge column was 513 kips at 2% drift and 444 kips at -2% drift. Different from PFS1, the flexural moment in the east edge column deduced in the positive loading direction was similar to that deduced in the negative loading direction.

Assuming the maximum usable strain of the concrete was 0.003 as specified in ACI-318-11, Fig. 8-28 shows the P-M curve of the east edge column obtained through sectional analysis in OpenSees. The data points that represent the axial forces and the moments in the east edge column in PFS1 and PFS2 at 2% and -2% drift are also included in the figure. As shown in the figure, the additional compression/tension force generated by the steel mega beam and the rigid-connected CIP floor increased/decreased the moment resistance of the edge column in PFS1. On the other hand, because there were negligible additional axial forces generated in the edge column in PFS2, the impact from the steel tubes and the precast floor slab on the edge column was not significant.

8.5 Conclusions from the Comparison of PFS1 and PFS2

Two rocking-wall structural assemblages (PFS1 and PFS2) were successfully tested under pseudo-static loading in the MAST laboratory. The two specimens were designed to investigate the upper bound and the lower bound interaction between PreWEC systems and surrounding structure.

In PFS1, a PreWEC system and CIP surrounding structure were built to investigate the upper bound interaction. The rigid wall-floor connection was formed through CIP construction, which promoted the wall-floor interaction. In PFS2, a PreWEC system and precast surrounding structure were built to investigate the lower bound interaction. Special precast vertical movement isolated connections were used as the wall-floor connections, which greatly reduced the wall-floor interaction. Because the base moment of the PreWEC system in PFS1 was designed to be similar to that in PFS2, a direct comparison of PFS1 and PFS2 would shed light on the investigation of the impact on the behavior of rocking-wall structures using different types of wall-floor connections. The conclusions derived from the test observations and the data analysis are as follows:

1. The initial secant stiffness of PFS1 was about 2.2 times that of PFS2. Because of the different styles of PreWEC systems used in PFS1 and PFS2, the width of the wall in PFS1 was larger than that in PFS2 and caused the larger initial secant stiffness of PFS1.

2. The base moment of PFS1 was much larger than that of PFS2 at the same drift level. Gravity load transfer path and constraint effect from surrounding structures were the two key factors that contributed to the difference.

3. Both PFS1 and PFS2 demonstrated reasonable self-centering performance. Because of the contribution from the gravity loads carried by the wall, the self-centering capacity of the wall in PFS1 was larger than that in PFS2. However, the self-centering performance of PFS1 was inferior to that of PFS2 due to the additional constraint from the damaged surrounding structure.

4. A general criterion, which accounts for gravity load transfer path and constraint effect from surrounding structure, is proposed to ensure the self-centering of rocking-wall structures. It is recommended that the criterion be examined at the maximum residual drift limit, which is selected based on performance requirements of the rocking-wall structures. To be conservative, it is recommended that the self-centering moment provided by initial effective PT forces and the maximum self-centering-resisting moment developed by the energy dissipating elements and the surrounding structure be used in evaluating the criterion.

5. Little damage occurred to the wall corners in both specimens at 2% design drift. Some damage was observed near the center of the wall base in PFS2, which was caused by discontinuity in the fiber grout near the dowel rebar in the wall across the wall/base block interface. Cracks in the walls were observed above the points of attachment of the O-connectors in both specimens, which were believed to be caused by local tensile forces generated by the O-connectors resisting the uplift of the walls.

6. Unsymmetrical deformations occurred in the O-connectors in both specimens. Compared with PFS2, the O-connectors in PFS1 were subjected to larger vertical deformations, thus they provided larger vertical resistances at the same drift level and yielded at smaller drift levels.

7. The PreWEC end columns that were pinned-connected to the base block remained elastic in PFS1. A great amount of damage occurred to the PreWEC end columns in PFS2 due to the large compression demand generated by the combined PT forces and the resistance from the connected O-connectors.

8. Minor damage occurred to the fiber grout in PFS1 that was confined in a pocket in the base block. The fiber grout was directly poured above the base block in PFS2. Much more damage occurred to the fiber grout beneath the wall and the end columns in PFS2. The damaged grout would have needed to be replaced for future usage.
9. Multiple cracks and localized damage occurred to the wall-floor connections in PFS1. Most cracks subsequently closed upon unloading because of the residual PT forces provided by the strands in the slab that remained elastic throughout the test. It was believed that the CIP floor was reusable after repair. On the other hand, little damage occurred to the precast floor in PFS2. It was believed that the precast floor was reusable without repair after the test.
10. Damage to the CIP edge columns occurred from 0.25% drift in PFS1. In PFS2, damage occurred to the precast edge columns only after the steel base plates of the edge columns were tightened to the base block.
11. The deformation demand on the edge columns in PFS2 was smaller than that in PFS1 due to the rigid body rotation of the steel base plate. The additional axial forces generated by the CIP floor and the steel mega beams had a non-negligible impact on the moment resistances of the edge column in PFS1 while the impact was negligible in PFS2 in which the precast floor and the steel trusses were pinned-pinned connected to the wall and the edge columns.

Table 8-1 Differences between PFS1 and PFS2

Specimens	PFS1	PFS2
Rocking-wall system	PreWEC with side columns made of short steel tubes	PreWEC with end columns made of RC columns
O-connectors (8 total)	Two O-connectors connected to each of four side columns	Four O-connectors connected to each of two end columns
Floor system	Cast-in-place (CIP) unbonded post-tensioned slab	Precast slab formed by solid RC planks
Wall-floor connections	Rigid wall-floor connections formed by CIP concrete	Precast connections that isolated the floor from vertical movement of wall
Second story components	Steel beams with cover plates, fixed connections at both ends	Steel trusses made of tubes, pinned connections at both ends
Edge beams and edge columns	Rigid floor-edge beam connections; CIP RC columns with fixed-base connections	Pinned-pinned floor-edge beam (transverse beam) connections; Precast RC columns with rocking/fixed-base connections
Rebar across wall-grout interface	None	Four rebar across the wall/base block interface (embedded in the wall and unbonded to the base block)
Fiber grout layer	Fiber grout poured in a pocket in the base block (confined)	Fiber grout directly placed above the base block (unconfined)

Table 8-2 Secant stiffness of the two specimens at different positive drifts (unit: kip/in)

Drift	0.01%	0.05%	0.07%	0.1%	0.25%	0.5%	0.75%	1%	1.5%	2%
PFS1	416	384	335	269	150	86	61	48	35	28
PFS2	190	168	151	122	65	39	28	21	15	12

Table 8-3 Base moment resistance of the two specimens at different positive drifts (unit: kip-in)

Drift	0.01%	0.05%	0.07%	0.1%	0.25%	0.5%	0.75%	1%	1.5%	2%
PFS1	2157	9729	12199	14118	19475	22268	23551	24818	26930	28624
PFS2	991	4284	5410	6209	8197	9747	10297	10724	11359	11758

Table 8-4 Summary of the annotations in Fig. 8-3

Components	Name	Annotation
Wall panel	F_N	Gravity loads carried by the wall
	F_{PT}	Post-tensioned force on the wall
	W_W	Self-weight of the wall and the top block
West O-connectors	R_{O_W}	Resisting force in each of the four O-connectors on the west side of the wall (far from the rotation point)
East O-connectors	R_{O_E}	Resisting force in each of the four O-connectors on the east side of the wall (near the rotation point)
West mega beam	M_{MB_W}	Resisting moment at the wall - west mega beam connection
	N_{MB_W}	Axial force in the west mega beam
	V_{MB_W}	Shear force in the west mega beam
East mega beam	M_{MB_E}	Resisting moment at the wall - east mega beam connection
	N_{MB_E}	Axial force in the east mega beam
	V_{MB_E}	Shear force in the east mega beam
West wall-floor connection	M_{SLAB_W}	Resisting moment at the west wall-floor connection
	N_{SLAB_W}	Axial force in the west wall-floor connection
	V_{SLAB_W}	Shear force in the west wall-floor connection
East wall-floor connection	M_{SLAB_E}	Resisting moment at the east wall-floor connection
	N_{SLAB_E}	Axial force in the east wall-floor connection
	V_{SLAB_E}	Shear force in the east wall-floor connection

Table 8-5 Summary of the annotations in Fig. 8-4

Components	Name	Annotation
Wall panel	F_{PT}	Post-tensioned force on the wall
	W_W	Self-weight of the wall and the top block
West O-connectors	R_{O_W}	Resisting force in each of the four O-connectors on the west side of the wall (far from the rotation point)
East O-connectors	R_{O_E}	Resisting force in each of the four O-connectors on the east side of the wall (near the rotation point)
West mega tube	N_{MT_W}	Axial force in the west mega tube
East mega tube	N_{MT_E}	Axial force in the east mega tube
West BS Italia	N_{SLAB_W}	Axial force transferred by the west BS connections
East BS Italia	N_{SLAB_E}	Axial force transferred by the east BS connections

Table 8-6 Contribution of the resisting moment in PFS1 and PFS2 at 2% drift provided by different structural components (unit: kip-in)

Specimen	Gravity loads (kip-in)	PT force (kip-in)	O-connectors (kip-in)	Surrounding structure (kip-in)	Total (kip-in)
PFS1	6473 (23%)	7086 (25%)	2770 (10%)	12295 (42%)	28624
PFS2	745 (6%)	7338 (62%)	2689 (23%)	985 (9%)	11758

* Number in parenthesis represents contribution percentage to the total resisting moment

Table 8-7 External moments and internal moments in PFS1 and PFS2 at -0.4% drift during the unloading in the third cycle of 2% drift (unit: kip-in))

Specimen	M_{BASE}	M_N	M_W	M_{PT}	M_O*	M_{SU}
PFS1	38	4354	918	4271	-1715	-7866
PFS2	-3104	1	682	5368	-2038	-909

* M_O represents the sum of the moments provided by all O-connectors (M_{O_E} + M_{O_W})

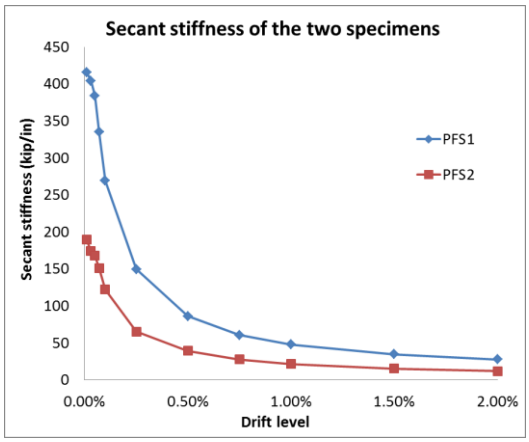

Fig. 8-1 Comparison of the secant stiffness of PFS1 and PFS2 in Phase 1

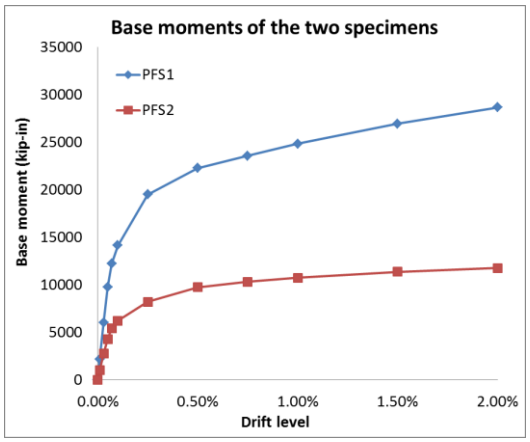

Fig. 8-2 Comparison of the base moments of PFS1 and PFS2 in Phase 1

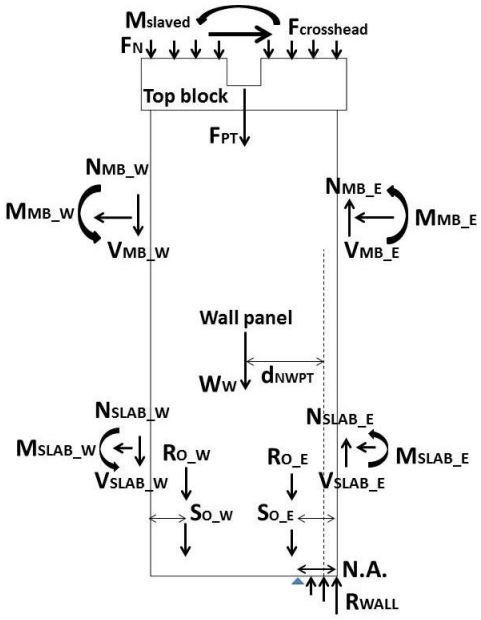

Fig. 8-3 Illustration of the force flow in the wall of PFS1

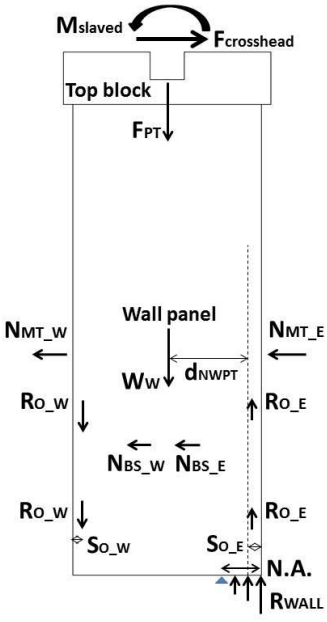

Fig. 8-4 Illustration of the force flow in the wall of PFS2

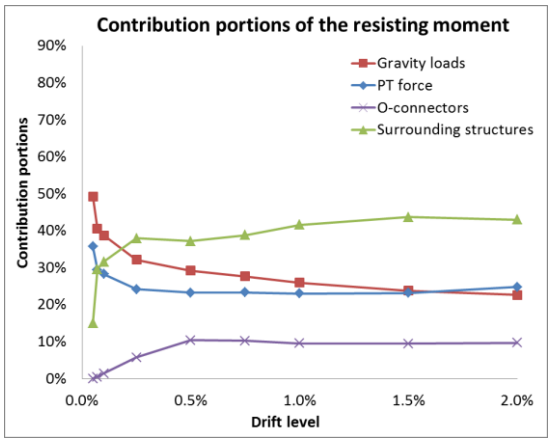

Fig. 8-5 Contribution to the resisting moment provided by different components in PFS1

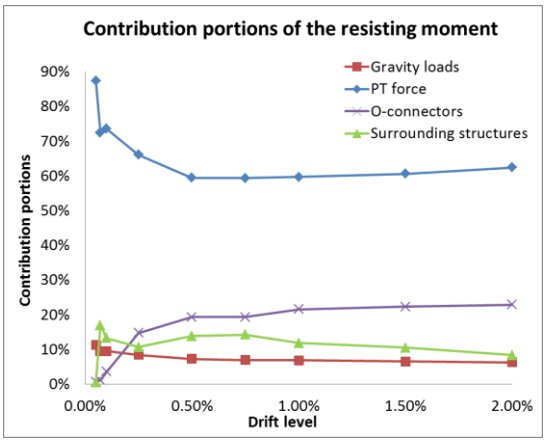

Fig. 8-6 Contribution to the resisting moment provided by different components in PFS2

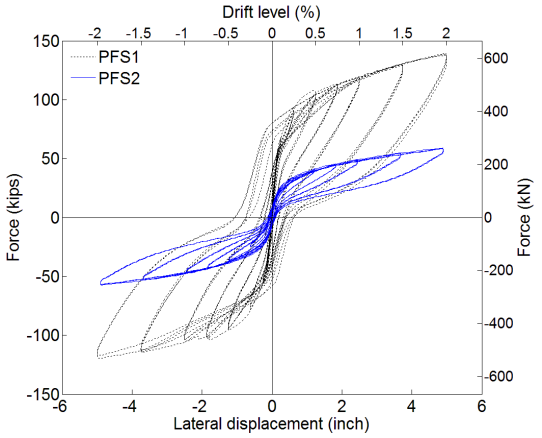

Fig. 8-7 Comparison of force-dislacement curves of PFS1 and PFS2 in Phase 1

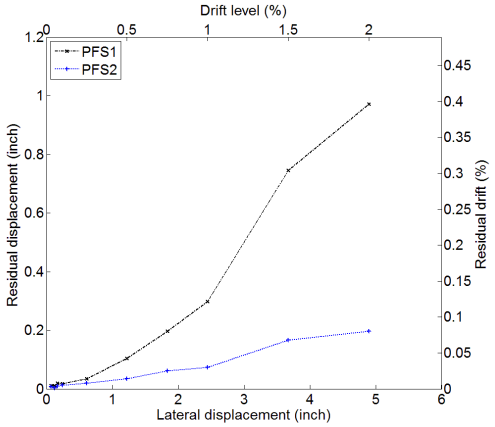

Fig. 8-8 Comparison of the residual displacements/drifts of PFS1 and PFS2

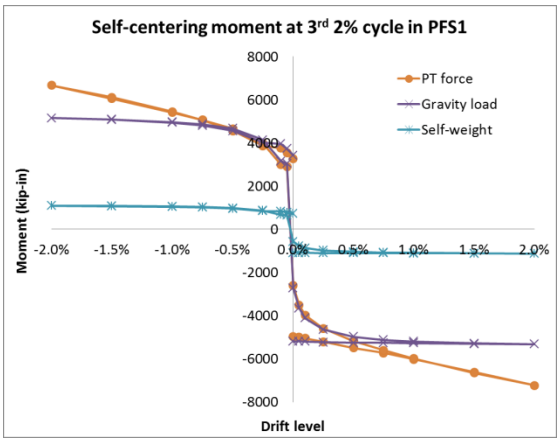

Fig. 8-9 Self-centering moments – lateral wall drift response of PFS1

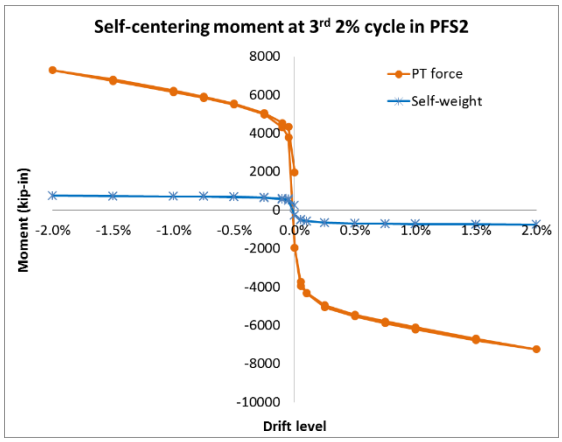

Fig. 8-10 Self-centering moments – lateral wall drift response of PFS2

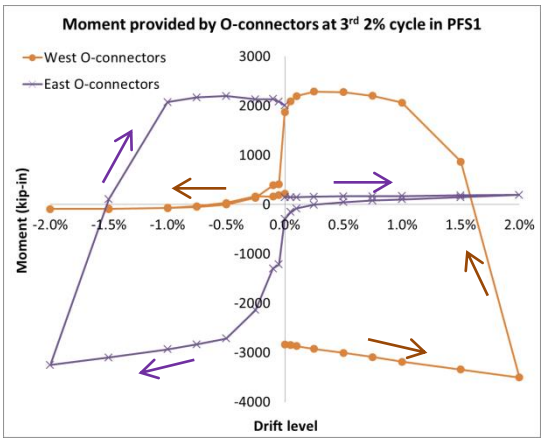

Fig. 8-11 Moments generated by the O-connectors in the third cycle of 2% drift in PFS1

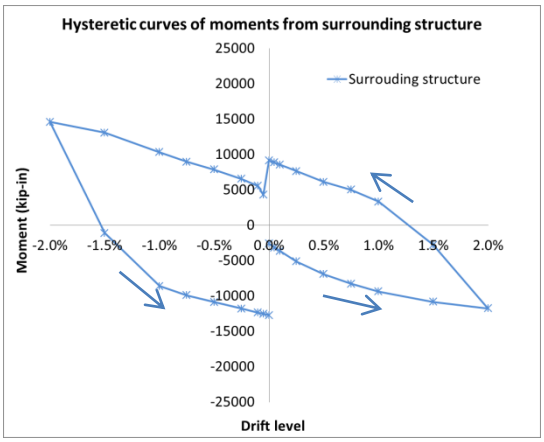

Fig. 8-12 Moments generated by the surrounding structure in the third cycle of 2% drift in PFS1

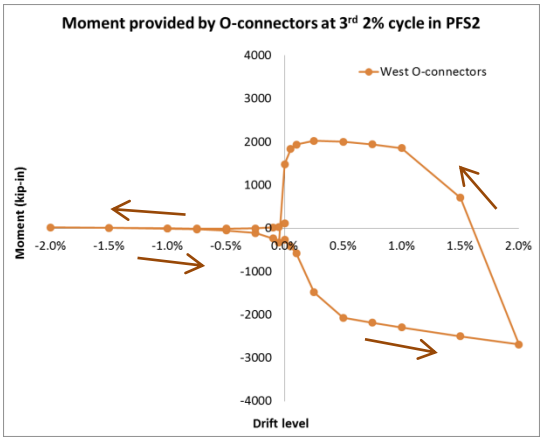

Fig. 8-13 Moments generated by the O-connectors (west side of the wall) in the third cycle of 2% drift in PFS2

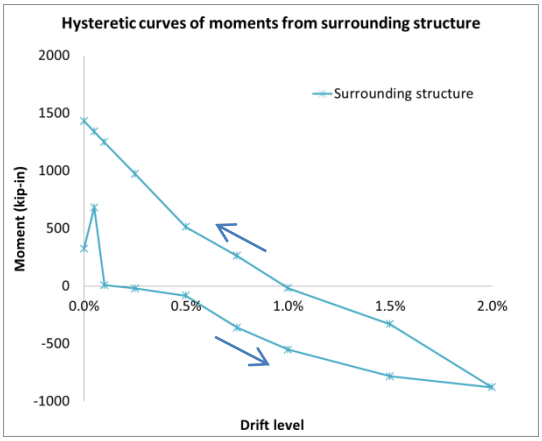

Fig. 8-14 Moments generated by the surrounding structure in the third positive half cycle of 2% drift in PFS2

Fig. 8-15 Condition of the west wall corner in PFS1 at 2% drift in Phase 1

Fig. 8-16 Condition of the west wall corner in PFS2 at 2% drift in Phase 1

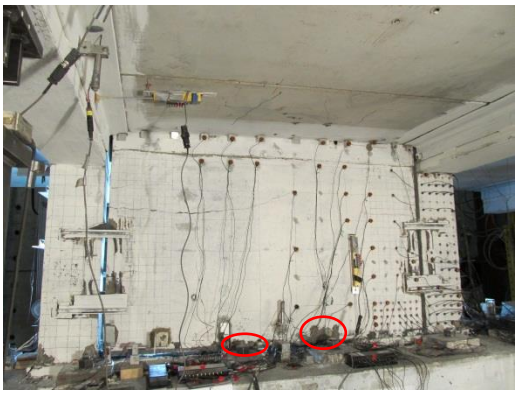

Fig. 8-17 Damage to the center of the wall base during the test of PFS2

Fig. 8-18 Condition of the wall panel after the test of PFS1

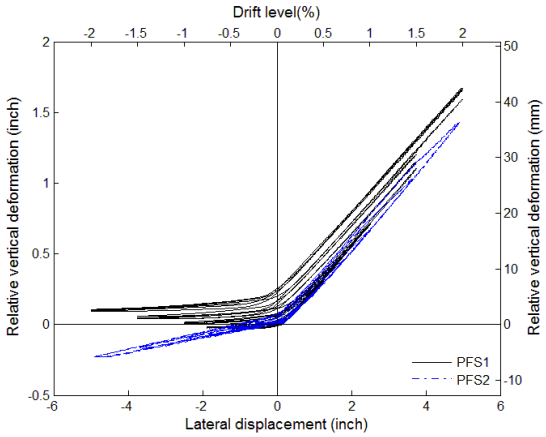

Fig. 8-19 Relative vertical deformation – lateral wall displacement response of the O-connectors attached to the west side of the wall in PFS1 and PFS2

Fig. 8-20 Condition of fiber grout beneath the west corner of the wall after the test of PFS1

Fig. 8-21 Condition of fiber grout beneath the east corner of the wall after the test of PFS1

Fig. 8-22 Condition of the fiber grout beneath the west wall corner after the test of PFS2

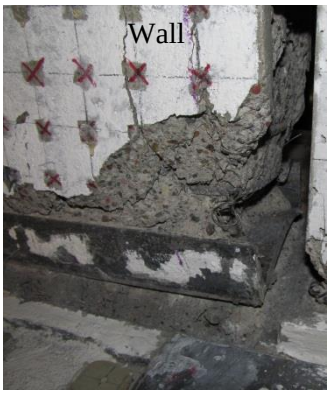

Fig. 8-23 Condition of the fiber grout beneath the east wall corner after the test of PFS2

Fig. 8-24 Condition of the fiber grout beneath the west end column after 4% drift in Phase 5 of PFS2

Fig. 8-25 Condition of the fiber grout beneath the east end column after 4% drift in Phase 5 of PFS2

Fig. 8-26 Condition of the fiber grout beneath the west end column after the test of PFS2

Fig. 8-27 Condition of the fiber grout beneath the east end column after the test of PFS2

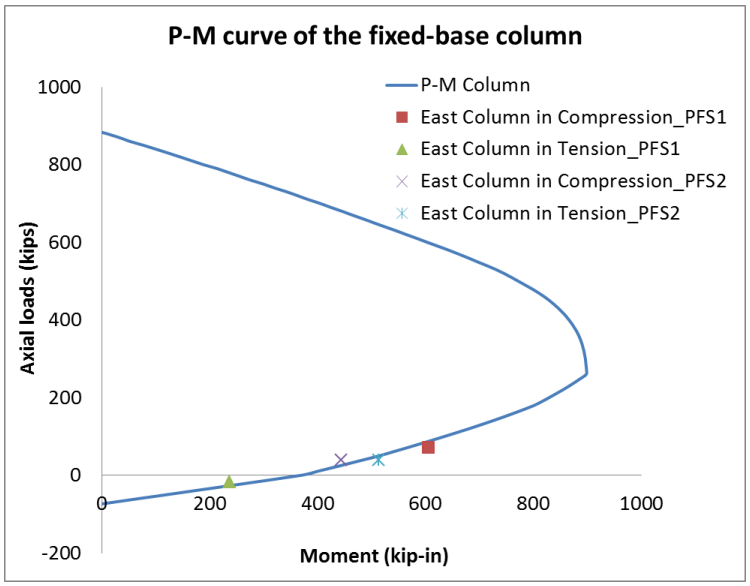

Fig. 8-28 P-M curve of the edge columns with data points representing the axial force and the moment in the east edge column in PFS1 and PFS2 at 2% and -2% drift (Note: positive axial loads represent compression forces

CHAPTER 9. Design Recommendations

In this chapter, design recommendations for PreWEC systems, including rocking walls, fiber grout, O-connectors and end columns, are described in Section 9.1. For rocking-wall structures using rigid wall-floor connections, design recommendations for cast-in-place floors are provided in Section 9.2. For rocking-wall structures using the special vertical movement isolated connections, design recommendations for the special precast wall-floor connections and the plank-beam connections are described in Section 9.3.

9.1 Design Recommendation for PreWEC Systems

Existing design guidelines for rocking walls (ITG-5.2) are discussed in Section 2.4.2. It was found that some essential design parameters were not included in the design guidelines, such as the amount of longitudinal rebar in the wall and the height of the steel confinement in the wall corners.

The design details of the rocking walls in existing experimental studies are summarized in Table 2-2. As shown in the table, inconsistencies exist between the design details adopted in past tests and those recommended in ITG-5.2 (Brian and Kurama 2009, Schoettler 2010, Aaleti and Sritharan 2011), such as the dimension, the spacing and the width of the steel confinement in the wall corners. For those design parameters that were not included in ITG-5.2 as mentioned previously, they were generally determined based on the counterpart recommendations for special structural walls in ACI 318-11. Neither ITG-5.2 nor the past experiments considered the interaction between the rocking-wall system and the surrounding structure, which has proven to have a great impact on the behavior of rocking-wall structures depending on the selected type of wall-floor connections in Chapter 6 in this dissertation.

In this section, the force flow in a rocking wall panel is described first, followed by discussion of the grout layer interface between the rocking wall and the foundation. Design recommendations for different structural components of PreWEC systems, including rocking wall panels, O-connectors and PreWEC end columns, are provided in Section 9.1.4 through Section 9.1.6.

9.1.1 Force Flow in Rocking Wall Panels

Strain distributions in rocking wall panels have been discussed in Section 6.2.4 (PFS1) and Section 7.2.5 (PFS2). A summary of the test observations is given in the following.

9.1.1.1 Disturbed Region in the Wall Panel

Fig. 6-29 and Fig. 6-30 (PFS1) show the compressive strain distribution across the width of the wall at 2 in. above the base. It should be noted that the strains plotted in this dissertation represent the changes in strain observed from the beginning of the tests. These strains do not include any initial strains generated prior to testing (e.g., from post-tensioning the wall). As shown in the figures, strain compatibility does not appear valid near the base of the wall; very small tensile strains (less than 100 $\mu\varepsilon$) were recorded in the region of the wall that was far from the compression side. These strains represent the unloading of the initial precompression (i.e., ~32 $\mu\varepsilon$ in Section 6.2.4) in the wall as it underwent uplift. Similar conclusions can be drawn from Fig. 7-35 and Fig. 7-36 (PFS2).

Due to the unbonded PT tendon, strain compatibility did not exist between the tendon and the concrete. It was believed that a disturbed region existed in the ground story of the wall. The compression was concentrated where the wall contacted the grout and the wall was unstressed at the base where there was uplift because the tension was provided through the unbonded PT. The concentrated compression force in the wall corner spread out across the wall with height. Local effects were created near the attachment of the O-connectors and other attachments (e.g., mega beams/trusses).

9.1.1.2 Undisturbed Region in the Wall Panel

As shown in Fig. 7-37 (PFS2), strain compatibility was valid at the cross section where the fourth row of concrete strain gages (CG-CWWB4, CG-CEWB4 and CG-EWBC4 in Fig. 4-17) was located (148 in. above the base of the wall). Strain was linearly distributed across the width of the wall. It was believed that the cross section was in an undisturbed region of the wall.

9.1.1.3 Height of the Disturbed Region

As shown in Fig. 7-36, strain compatibility was not valid at the cross section where the third row of concrete strain gages was located (17 in. above the base of the wall). It

indicated that the height of the disturbed region in the wall was larger than 17 in. in PFS2. As mentioned previously, an undisturbed region exists at 148 in. above the base of the wall. It could be concluded that the height of the disturbed region was larger than 17 in. and smaller than 148 in. Because the width of the wall in PFS2 (68 in.) was within the range of 17 to 148 in., it might be reasonable to expect the height of the disturbed region to extend approximately 68 in. in accordance with St. Venant's Principle.

9.1.1.4 Comparison of the Force Flow in Rocking Walls and Special Structural Walls

Summarizing the discussions above, the force flow in a typical rocking wall panel is shown in Fig. 9-1. As shown in the figure, a disturbed region exists near the base of the rocking wall panel where structural discontinuity exists across the wall/foundation interface. In the disturbed region, concentrated compression forces spread out from the small contact region at the base of the wall to a larger area in the wall with height from the base. The neutral axis depth of the wall increases along the height of the wall. As shown in Fig. 9-1, the moment resistance of the wall near the base is formed by a force couple that consists of the tensile force in the PT strands and the resultant compression force in the cross section of the wall. Without gravity loads or other external axial loads, the tensile forces in the unbonded PT strands are constant and must equal the resultant compression forces in the wall. As shown in Fig. 9-1, the action lines of the compression forces vary because of the varied stress distribution in the disturbed region, causing different moment arms of the force couple and thus different moment resistances at different cross sections of the wall.

For comparison purposes, Fig. 9-2 shows the force flow in a special structural wall that is specified in Section 21.9 of ACI 318-11. As shown in the figure, the tensile forces in a special structural wall are primarily provided by the longitudinal bar through bond with the concrete. The location of the resultant tension and compression do not vary much from cross section to cross section (that is, the neutral axis depth remains relatively constant); whereas, the tensile forces in the reinforcement and compression forces in the concrete vary with the sectional moment.

To conclude, the force flow in a rocking wall panel is significantly different from that in a special structural wall. It might be unreasonable to use the recommendations for

special structural walls in ACI-318 to design rocking wall panels. Design recommendations of the rocking walls are given in Section 9.1.4.

9.1.2 Impact from Grout Bearing on the Rocking Wall Behavior

Existing design guidelines for rocking walls (ITG-5.2) required that the specified strength of the grout beneath the wall should not be less than f'_c, where f'_c was the specified strength of unconfined concrete (ITG 2009). The grout was originally designed to be stronger than the concrete in the wall in PFS1 and PFS2. However, the results from the material tests of PFS1 indicated that the strength of the grout was about 30% lower than its nominal strength, while the strength of the concrete was about 70% larger than its nominal strength. Because material tests were not conducted for the grout used in PFS2, it was assumed that the compressive strength of the grout was similar to that used in PFS1 (8647 psi). The assumption was reasonable because the grout of the same brand was used and the fabrication operation of the fiber grout was the same in the two tests. Consequently, the grout was believed to be weaker than the concrete in the wall in both tests.

Learning from the precast manufacturers, the over-strength of concrete in precast walls is commonplace in the industry. It results because precasters desire to have a fast turnaround time on the precasting bed to produce more products. This is accomplished by achieving high early strength concrete to facilitate the early release of the prestressing strands. As a result, the concrete compressive strength of the wall can be significantly higher than that specified in design, and it is likely to be stronger than that of the specified strength of the grout layer. In the following, the isolated PreWEC system tested in PFS2 is selected as an example to investigate the impact from the grout bearing on the rocking wall. The reason for selecting PFS2 instead of PFS1 was that there was little interaction between the wall and the surrounding structure in PFS2, thus it was simplier to calculate the total compression force at the corner of the wall.

In the following, the actual strength of the grout was first used to calculate the N.A. depth of the wall and the associated moment resistance of the PreWEC system. Second, the N.A. depth of the wall and the associated moment resistance were calculated using

the strength of the confined concrete in the wall corners and the strength of the nominal unconfined concrete. The obtained results are then compared and discussed at the end of the section. It was noteworthy that in the three cases described below, the grout layer was assumed to be made of ductile material (e.g. fiber grout, not mortar etc.), thus sudden losses of the grout bearing were prevented.

9.1.2.1 Grout Weaker than the Wall

The total compression force in the wall corners at 2% drift is calculated first. The initial PT force in the wall was 177 kip in Phase 1 ($F_{PT\_initial}$). The PT force in the wall recorded at 2% drift (N_{PT}) was 230 kip in the test. Because the four O-connectors that were away from the compression side of the wall had yielded, each of them provided approximately 9 kip vertical resisting force (R_{YO}) in the wall. The resisting force was obtained from the numerical simulation shown in Fig. 5-27. Because the relative vertical deformation of the other four O-connectors close to the compression side of the wall was very small, their resisting forces were negligible and not considered. The total weight of the top block and the wall (W_w) was 13 kip. Because of the usage of the special vertical movement isolated connections, the surrounding structure had little contribution to the vertical compression forces at the wall corners. The total compression force P_{total} at the wall corners is calculated as:

$$P_{total} = N_{PT} + 4R_{YO} + W_w = 230 + 9\times4 + 13 = 279\ kip \quad (9.1)$$

Due to the difficulty in installing instrumentation in the thin grout layer, there is no information in the literature or from the tests of PFS1 and PFS2 about the strain distribution in the grout bearing beneath rocking walls. Because of the existence of steel fibers, it was expected that the fiber grout material was ductile and its softening after peak strength was slow. It was assumed that the property of the fiber grout was similar to that of the confined concrete.

It was proposed by Paulay and Priestley that the equivalent stress block parameters for confined concrete, α_c and β_c, were equal to 0.9 and 1.0, respectively (Paulay and Priestley 1992). Similar values were adopted in the design guidelines ITG-5.2 (ITG 2009). In Section 5.6.3.8 of ITG-5.2, it was assumed that the concrete stress of $0.92f'_{cc}$ was uniformly distributed over an equivalent rectangular compression zone extending a

distance of $0.96c$ from the extreme concrete compression fiber, where f'_{cc} was the specified strength of confined concrete in the wall corners and c was the N.A. depth of the wall. Therefore, the assumption specified in ITG 5.2 might also be suitable for the fiber grout bearings. The fiber grout stress of $0.92f'_g$ was uniformly distributed over an equivalent compression zone assumed to be $0.96c$ at the wall/grout interface. The neutral axis depth of the wall can then be calculated by using the strength of the fiber grout as shown below:

$$0.96c = \frac{P_{total}}{0.92f'_g t} = \frac{279}{0.92\times 8.647\times 6} \approx 5.8" \;\rightarrow\; c \approx 6.1" \tag{9.2}$$

Where f'_g = Compressive strength of the grout (Table 3-8), t = Thickness of the wall.

As shown in Table 7-1, the neutral axis depth of the wall was 6.1 in. when PFS2 was loaded to 2% drift in Phase 1. The result was deduced by using the test data from a row of LVDTs attached across the wall/base block interface. The result calculated from Eq. (9.2) matched well with the test result.

After calculating the neutral axis depth of the wall, the PT force in the wall at 2% drift is re-examined below. As shown in Fig. 9-3, the elongation of the PT strands (Δ_{PT}) is calculated as:

$$\Delta_{PT} = \theta\left(\frac{w_{wall}}{2} - c\right) = 0.02\times\left(\frac{68}{2} - 6.1\right) = 0.56" \tag{9.3}$$

The corresponding stress in the PT strands at 2% would be:

$$\begin{aligned}\sigma_{strand} &= \frac{F_{PT\_initial}}{n_{strand}A_{strand}} + E_{strand}\frac{\Delta_{PT}}{L_{strands}} \\ &= \frac{177}{7\times 0.153} + 29100\times\frac{0.56}{275} \approx 224\ ksi\end{aligned} \tag{9.4}$$

The stress was smaller than the yield strength of the strands (256 ksi), thus he strands did not yield at 2% drift. The expected force in the strands at 2% drift ($N_{PT\_2\%}$) was:

$$\begin{aligned}N_{PT\_2\%} &= \sigma_{strand}n_{strand}A_{strand} = 224\times 7\times 0.153 \approx 240\ kip > N_{PT} \\ &= 230\ kip\end{aligned} \tag{9.5}$$

As shown above, the PT force predicted by using the calculated N.A. depth of the wall was about 10 kip larger than that recorded at 2% drift in the test (230 kip). It was believed that the difference might be caused by the slip of the strands in the test. Because

the difference was less than 5% of the recorded PT force, it was still reasonable to use Eq. (9.3) through Eq. (9.5) to deduce the PT force in the wall after the N.A. depth of the wall was calculated.

Fig. 9-3 illustrates the forces distributed at the base of the wall. As shown in the figure, the moment resistance of the PreWEC system (M_{PreWEC}) is calculated as follows:

$$\begin{aligned} M_{PreWEC} &= (N_{PT} + W_w)\left(\frac{w_{wall}}{2} - \frac{0.96c}{2}\right) \\ &\quad + 4R_{YO}\left(w_{wall} - d_{O\_W} - \frac{0.96c}{2}\right) \\ &= (230 + 13)\left(\frac{68}{2} - \frac{5.8}{2}\right) + 4{\times}9\left(68 - 2.5 - \frac{5.8}{2}\right) \\ &= 9{,}811\ kip - in \end{aligned} \tag{9.6}$$

Where d_{O_W} = Distance between the O-connectors attached to the west side of the wall and the adjacent edge of the wall.

9.1.2.2 Grout Stronger than the Wall

If the grout were stronger than the confined concrete in the wall corners, the N.A. depth of the wall should be calculated using the strength of the confined concrete in the wall. The strength of the confined concrete in the wall corners was 13.47 ksi in PFS2. It was calculated by using the measured strength of concrete (Table 3-8) and the Mander model (described in detail in Section 5.3.2.2).

By several iteration trials, it was assumed that the neutral axis depth of the wall was 4 in. The same procedure described above was used to deduce the PT force in the wall at 2% drift. The assumed 4 in. neutral axis depth of the wall is verified at the end of this section. Because there was no test data in this study associated with stronger grout, the results cannot be validated.

The elongation of the PT strands is calculated as:

$$\Delta_{PT} = \theta\left(\frac{w_{wall}}{2} - c\right) = 0.02{\times}\left(\frac{68}{2} - 4\right) = 0.6" \tag{9.7}$$

The stress in the PT strands at 2% drift is:

$$\sigma_{strand} = \frac{F_{PT\_initial}}{n_{strand}A_{strand}} + E_{strand}\frac{\Delta_{PT}}{L_{strands}} = \frac{177}{7\times0.153} + 29100\times\frac{0.6}{275} \approx 229\ ksi < f_{py} = 256\ ksi \quad (9.8)$$

Because the strands did not yield, the force in the PT strands at 2% drift is:

$$N_{PT} = \sigma_{strand}n_{strand}A_{strand} - N_{slip} = 229\times7\times0.153 - 10 \approx 235\ kip \quad (9.9)$$

It was noteworthy that the same amount of PT slip was included above by subtracting N_{slip} in Eq. (9.9).

The assumed neutral axis depth is re-examined below:

$$0.96c = \frac{N_{PT} + 4R_{YO} + W_w}{0.92f'_{cc}t} = \frac{235 + 9\times4 + 13}{0.92\times13.47\times6} \approx 3.8" \ \rightarrow \ c \approx 4" \quad (9.10)$$

As shown in Eq. (9.10), the calculated neutral axis depth of the wall was very close to the assumed value, thus the assumption was valid. The associated moment resistance of the PreWEC system is calculated:

$$\begin{aligned} M_{PreWEC} &= (N_{PT} + W_w)\left(\frac{w_{wall}}{2} - \frac{0.96c}{2}\right) \\ &\quad + 4R_{YO}\left(w_{wall} - d_{O\_W} - \frac{0.96c}{2}\right) \\ &= (235 + 13)\left(\frac{68}{2} - \frac{4}{2}\right) + 4\times9\left(68 - 2.5 - \frac{4}{2}\right) \\ &= 10{,}222\ kip - in \end{aligned} \quad (9.11)$$

9.1.2.3 Design Results

During the design, the nominal strength of the concrete in the wall (6 ksi) might be directly used to calculate the moment resistance of the PreWEC system. After several iteration trials, it was assumed that the neutral axis depth of the wall was 12 in. The elongation of the PT strands (Δ_{PT}) is calculated:

$$\Delta_{PT} = \theta\left(\frac{w_{wall}}{2} - c\right) = 0.02\times(\frac{68}{2} - 12) = 0.44" \quad (9.12)$$

The stress in the PT strands at 2% drift is:

$$\sigma_{strand} = \frac{F_{PT\_initial}}{n_{strand}A_{strand}} + E_{strand}\frac{\Delta_{PT}}{L_{strands}} = \frac{177}{7\times0.153} + 29100\times\frac{0.44}{275} \approx 212\ ksi < f_{py} = 256\ ksi \quad (9.13)$$

The force in the PT strands at 2% drift is (the same amount of PT slip is included):

$$N_{PT} = \sigma_{strand}n_{strand}A_{strand} - N_{slip} = 212\times7\times0.153 - 10 \approx 217\ kip \quad (9.14)$$

The assumed neutral axis depth is examined below:

$$0.75c = \frac{N_{PT} + 4R_{YO} + W_w}{0.85f'_c t} = \frac{217 + 9\times4 + 13}{0.85\times6\times6} \approx 8.7" \rightarrow c \approx 11.6" \quad (9.15)$$

Therefore, the assumed neutral axis depth of the wall was valid. The associated moment resistance of the PreWEC system (M_{RO}) is calculated:

$$M_{PreWEC} = (N_{PT} + W_w)\left(\frac{w_{wall}}{2} - \frac{0.75c}{2}\right) + 4F_O\left(w_{wall} - d_{O\_W} - \frac{0.75c}{2}\right) = (217 + 13)\left(\frac{68}{2} - \frac{8.7}{2}\right) + 4\times9\left(68 - 2.5 - \frac{8.7}{2}\right) = 9{,}021\ kip - in \quad (9.16)$$

9.1.2.4 Comparison and Discussion

Table 9-1 summarizes the results in Section 9.1.2.1 through Section 9.1.2.3. As shown in the table, the N.A. depth of the wall recorded at 2% drift in the test (Case 1) was approximately 33% larger than that in Case 2 and 90% smaller than that in Case 3. However, because the N.A. depth is only a small fraction of the width of the wall (6% to 17% in the three cases), the moment arm of the PT strands and the PT force in the wall in Case 1 were close to those in Case 2 and Case 3, as shown in the table. It was found that the moment resistance of the PreWEC system in the test (Case 1) was only 4% smaller than that in Case 2 and 8% larger than that in Case 3.

As mentioned in Section 2.4.3.2, it was also suggested by other researchers (Rahman and Restrepo 2000) that the N.A. depth of the rocking wall should be restricted to within

15% of the width of the wall to ensure hysteretic response stability and geometrical stability. A larger N.A. depth is associated with a larger compression force, and consequently, the wall is more susceptible to buckling. Therefore, the conclusion that the N.A. depth was only a small fraction of the width of the rocking wall was generally applicable in the design of rocking-wall structures. Under this circumstance, it was believed that the strength of the grout layer did not have a great impact on the moment resistance of the PreWEC system.

When the nominal strength of the concrete was used for design purposes (Case 3), the moment resistance of the PreWEC system was approximately 12% smaller than that obtained in the test (Case 1), which was conservative. Therefore, it was acceptable to use the nominal strength of the concrete to design the rocking walls.

9.1.3 Design Recommendation for Grout Bearing beneath PreWEC Systems

Multiple factors that should be considered in the design of grout bearings beneath PreWEC systems are described in this section.

9.1.3.1 Economical Consideration

No matter which was stronger, the grout layer or the confined concrete, once one of them "plastified," the concentrated compression force in the wall corner had to be spread over a larger area that might increase the neutral axis depth of the wall and decrease the moment resistance of the wall. In other words, the impact from the grout on the overall behavior of the wall was similar to that from the confined concrete in the wall corners. Therefore, it might be more economical to select the grout that has similar strength to the confined concrete, which is explained below.

The products of fiber grout materials were scarce and expensive in the market. Generally, the cost of the fiber grout materials was higher when the required strength of the grout was larger. If the strength of the concrete in the wall is specified in the design, it may not be economical to select the grout to be stronger than the confined concrete in the wall corners.

9.1.3.2 Construction of the Grout Bearing

The grout bearing could be constructed by pouring the grout materials into a pocket in the foundation (similar to PFS1). The grout would be expected to have increased strength and ductility due to the confinement provided by the pocket. Even if the grout were weaker than the confined concrete in the wall corners, it would remain in the pocket even after it was plastified or crushed. Because the damaged grout still contacted with the wall and provided resistance, abrupt change in the N.A. depth of the wall or sudden drop in the strength of the wall would be prevented.

The grout bearing could also be constructed by directly pouring the grout materials above the foundation (similar to PF2), which can greatly simplify the construction. Under this circumstance, it is essential to select ductile materials for the grout bearing (e.g., fiber grout).

9.1.4 Design Recommendation for Rocking Wall Panels

After discussing the design recommendations for the grout bearing, design recommendations for rocking wall panels are given in this section, including longitudinal reinforcement, shear reinforcement, shear sliding resistances and boundary elements in the wall corners.

9.1.4.1 Longitudinal Reinforcement

As shown in Table 2-2, because there were no appropriate design guidelines, the amount of longitudinal reinforcement in the walls were designed in different ways in the three existing tests by previous researchers (Brian et al. 2009, Schoettler 2010, Aaleti and Sritharan 2011).

Because the longitudinal reinforcement in the wall contributed little to the strength of the wall, the required amount of longitudinal reinforcement was not decided by the strength demand but other design considerations in practice, such as minimum shrinkage and temperature reinforcement (Section 7.12 of ACI 318-11), minimum shear reinforcement (Section 21.9.2.1 of ACI 318-11), and local considerations.

Examples of local behaviors that should be considered in determining the amount and the arrangement of the longitudinal reinforcement in the wall include tensile stresses

generated from the O-connector anchorage and the wall-floor connection. As shown in Fig. 6-15 (PFS1) and Fig. 7-19 (PFS2), tensile cracks formed in the walls near the O-connectors. It was believed that local tensile strains were generated in the wall due to the resistances of the O-connectors to the uplift of the wall. Therefore, an appropriate amount of longitudinal reinforcement should be placed in the wall near the O-connections to control the cracking of the wall. The amount of wall reinforcement can be determined based on the maximum resistance expected to be provided by the O-connectors.

When rigid wall-floor connections were used in rocking-wall structures, it was recommended that longitudinal reinforcement should be placed in the wall near the wall-floor connections, where local tensile strains might be generated due to the vertical forces transferred to the wall from the floors.

Because the longitudinal reinforcement could help sustain the concentrated compression force in the wall corners, it was recommended to place an appropriate amount of reinforcement in the boundary elements that would alleviate some of the damage to the concrete.

9.1.4.2 Shear Reinforcement and Shear Sliding Resistance

As shown in Table 2-2, the shear reinforcement used in the “ND” test and the “NCREE” test was designed based on existing guidelines (ITG-5.2) for rocking walls (ITG 2009). However, the design guidelines in ITG-5.2 did not account for the interaction between rocking-wall systems and surrounding structures, because it was developed based on experimental studies of isolated rocking-wall systems and rocking-wall structures using special vertical movement isolated connections.

As discussed in Section 6.1.3, the base shear of the PreWEC system in the test of PFS1 was significantly higher than that of the isolated PreWEC system predicted by numerical simulation, which was mainly caused by the interaction between the PreWEC system and the surrounding structures. It was suggested that the interaction should be considered when deducing the base shear demand on the wall, which was used to design the required amount of shear reinforcement in the wall and examine the shear sliding resistance of the wall.

9.1.4.3 Steel Confinement in the Wall Corners

As discussed in Section 9.1.2, the strength of the grout bearing has a direct impact on the strains developed in the wall corners. When the grout bearing was weaker than the confined concrete in the wall corners, the grout instead of the wall was primarily damaged, as observed in both PFS1 and PFS2. On the other hand, if the grout bearing was stronger than the confined concrete in the wall corners, it was expected that large strains would be developed in the concrete that might cause the damage to the concrete. Design recommendation for the steel confinement in the wall corners under the two conditions is provided below.

Fiber grout weaker than the confined concrete in the wall corners

As discussed in Section 6.2.4 and Section 7.2.5, the maximum tensile strain in the steel stirrups measured at 2% drift in PFS1 and PFS2 were only 185 and 528 $\mu\varepsilon$, respectively. It indicated that the confinement effect was not significant at small drift levels.

When the walls were loaded to larger drifts (4% and 5%), the strains in the concrete in the wall corners greatly increased and the confinement effect from the stirrups became noticeable. For example, as shown in Fig. 6-44, the largest tensile strain in the stirrups measured at 5% drift in PFS1 increased to 1550 $\mu\varepsilon$; as shown in Fig. 7-42, the largest tensile strain in the stirrups measured at 5% drift in PFS2 increased to 880 $\mu\varepsilon$.

Fig. 9-4 shows the condition of the steel angle in the wall corner at the end of the test of PFS1. As shown in the figure, the web of the steel channel was subjected to inwards flexural bending during test. It was believed that the spalled concrete cover of the wall and the concrete debris dropped from the wall-floor connection fell into the pocket in the base block and were trapped below the steel channel. When the steel channel sat above the debris, the web of the steel channel was bent because of the compressive resistance of the confined powdered debris. The large compressive strains developed in the wall above the interface caused the steel confinement to take effect.

Although there was no pocket in the base block in PFS2, some concrete that spalled from the wall and the end columns still fell beneath the steel channel. It was also observed that the web of the steel channel in the wall in PFS2 was bent, as shown in Fig.

9-5. Similarly, the large compressive strains would be developed in the wall under this circumstance and the steel confinement would take effect.

In summary, the steel confinement was not effective at small drifts when the grout bearing was weaker than the confined concrete in the wall corners due to the increased neutral axis depth associated with the weaker grout. The steel confinement would take effect at large drifts because of the debris underneath the wall corners. Therefore, it was recommended that some steel confinement should still be placed in the wall corners to be conservative. The amount of required steel confinement could be determined according to the design procedure proposed below under the condition that the fiber grout was stronger than the confined concrete.

Fiber grout stronger than the confined concrete in the wall corners

When the fiber grout beneath the wall is stronger than the confined concrete in the wall corners, large compressive strains would be developed in the concrete. It is essential to place the steel confinement in the wall corners to prevent excessive spalling of the concrete. The following design recommendation is provided, including the height, the width, and the amount of the steel confinement.

(1) Assumptions

Several assumptions were made to simplify the determination of the steel confinement requirement.

First, the O-connectors and the surrounding structures were not initially considered, but are discussed at the end of this section.

Second, an unstressed region was assumed to exist at the base of the wall due to the unbonded nature of the PT strands, as shown in Fig. 9-1. It was assumed that there were no forces developed in the concrete and the rebar in the unstressed region.

Third, it was assumed that the amount of the post-tensioned strands in the wall was already determined before designing the steel confinement. In general, the required post-tensioning forces in the wall could be determined based on the base moment demand on the wall (Aaleti 2011). The amount of the post-tensioned strands could be roughly determined to provide the required PT forces in the wall with an appropriate initial prestress in the strands.

Fourth, it was assumed that the distribution of the moments in the wall, which is associated with the lateral loads transferred to the wall, could be obtained using the force-based design approach. Therefore, the base moment demand on the wall was determined.

(2) Height of the steel confinement h_{cc}

a. Theoretical determination

It is acknowledged that steel confinement does not take effect until after the compressive strain in the concrete exceeds the maximum usable strain (e.g., 0.003, Section 10.2.3 of ACI 318-11) because the transverse confining reinforcement provides a passive confining effect on the concrete. It is only effective after the lateral expansion of the concrete increases relative to that of the reinforcement due to the increased Poisson effect as the concrete becomes damaged.

As shown in Fig. 9-1, a disturbed region existed in the lower story of the wall, where the concentrated compression force at the wall/foundation interface spread out with distance from the base. Fig. 6-43 and Fig. 7-44 show the strain distribution in the concrete along the height of the wall in PFS1 and PFS2, respectively. As shown in the figures, at 5% drift in PFS1 and 4% drift in PFS2, the recorded strain was larger than 0.003 in the concrete at 2 in. (PFS1) and 4 in. (PFS2) above the base of the wall while it was smaller than 0.003 at 8 in. (PFS1) and 10 in. (PFS2) above the base of the wall. Fig. 6-44 and Fig. 7-42 show the tensile strains in the steel stirrups placed along the height of the wall in PFS1 and PFS2. As shown in the figures, at 5% drift in PFS1 and 4% drift in PFS2, the tensile strains in the stirrup at 2-1/2 in. (PFS1) and 3 in. (PFS2) above the base of the wall were much larger than those in the stirrups located approximately 10 in. above the base of the wall in both tests.

In summary, the concentrated compression force quickly spread out in the disturbed region from the wall/foundation interface, reducing the compressive strains in the extreme concrete fiber at the cross sections that were farther away from the base of the wall. This indicates that the steel confinement might not be needed or effective in the cross sections where the strain in the extreme compressive concrete fiber are smaller than 0.003.

A cut-off section for the steel confinement should be at the height of the section where the strain in the extreme compressive concrete fiber is estimated to be less than or equal to 0.003. The steel confinement should be placed between the base of the wall and the cut-off section in the disturbed region at the wall corners. Assuming the equivalent stress block parameters for confined concrete, α and β, were 0.92 and 0.96 according to the existing design guidelines ITG-5.2 (ITG 2009). Establishing the force and the moment equilibrium at the base of the wall and the potential cut-off section, the following equations can be established:

$$P_{total} = N_{PT} + N_G + W_w \tag{9.17}$$

$$c_{base} = \frac{P_{total}}{\alpha_c \beta_c f'_{cc} t} = \frac{P_{total}}{0.96 \times 0.92 f'_{cc} t_w} \tag{9.18}$$

$$M_{BASE} = P_{total}\left(\frac{w_{wall}}{2} - \frac{0.96 c_{base}}{2}\right) = P_{total}\left(\frac{w_{wall}}{2} - \frac{P_{total}}{1.84 f'_{cc} t}\right); \tag{9.19}$$

Where N_{PT} = PT forces in the wall, N_G = Gravity loads transferred to the wall; W_w= Self-weight of the wall; c_{base} = Neutral axis depth at the base of the wall; P_{total} = Total compression force at the corner of the wall; M_{BASE} = Moment at the base of the wall. It was noteworthy that Eq. (9.17) was established based on the first and the second assumption: the O-connectors and the surrounding structures were not considered in the deduction; there were no forces developed in the concrete and the rebar in the unstressed region.

At the cut-off section where the steel confinement would not be present, the equivalent stress block parameters for unconfined concrete, α and β were used according to ACI 318-11. Similarly, establishing the force and the moment equilibrium at the cut-off section, the following two equations can be established:

$$c_{cut-off} = \frac{P_{total}}{0.85 \beta f'_c t} \tag{9.20}$$

$$M_{cut-off} = P_{total}\left(\frac{w_{wall}}{2} - \frac{\beta c_{cut-off}}{2}\right) = P_{total}\left(\frac{w_{wall}}{2} - \frac{P_{total}}{1.7 f'_c t}\right); \tag{9.21}$$

Where $c_{cut-off}$ = Neutral axis depth at the cut-off section of the wall; $M_{cut-off}$ = Moment at the cut-off section of the wall. It should be noted that the total compression force P_{total} used in Eq. (9.20) at the cut-off section was the same as that at the corner of

the wall, because P_{total} was equal to the tensile force in the strands that did not change in the wall.

Because the PT forces in the wall, N_{PT}, would vary when the wall was loaded to different drift levels, the total compression force at the corner of the wall, P_{total}, in Eq. (9.17) through Eq. (9.21) would change correspondingly. To be conservative, it was assumed that all the strands in the wall reached their tensile strength (e.g. 270 ksi for Grade 270 strand). Because the amount of the PT strands in the wall was already determined as described in the third assumption above, the total compression force P_{total} was determined, thus the moment at the base of the wall (M_{BASE}) and that at the cut-off section of the wall ($M_{cut-off}$) could be determined through Eq. (9.19) and Eq. (9.21). Because the distribution of the lateral moments on the wall was obtained based on the force-based design as described in the fourth assumption above, the distance between the base of the wall and the cut-off section (h_{cc}) could be obtained once M_{BASE} and $M_{cut-off}$ were known. The theoretical deduction described above could be used to provide a conservative prediction of the height of the steel confinement required in the disturbed region.

b. Empirical prediction

Some empirical equations were proposed by other researchers to provide an estimation of the height of the strain concentration (H_{cr}) at the wall corners. Although it was different from the required height of the steel confinement (h_{cc}) defined above, it might provide a rough estimation of h_{cc}.

It was recommended by Perez that nonlinear behavior of the concrete in compression was concentrated at a distance $H_{cr} = \min(2t_w^{''}, 2c^{''})$ above the wall base (Perez et al. 2007). In the expression, $t_w^{''}$ was the distance between the centerline of steel confinement in the direction of wall thickness; $c^{''}$ was the neutral axis depth of the wall measured from centerline of steel confinement at the design drift. It was suggested by Restrepo and Rahman that $H_{cr} = c$, where c was the neutral axis depth of the wall at design drift (Restrepo and Rahman 2007). After reviewing existing experimental results of rocking

walls, Gavridou suggested that $H_{cr} = \min(1.5t, c)$, where t was the thickness of the wall (Gavridou 2015).

In the following, the test results obtained from PFS1 and PFS3 were compared to the results predicted based on these empirical equations. It was noteworthy that these empirical equations were all based on the assumption that larger strains were developed in the confined concrete in the wall. This assumption was only valid for PFS1 and PFS2 at large drifts. The neutral axis depth of PFS1 and PFS2 at 5% drift was taken for comparison below. For both PFS1 and PFS2, the thickness of the wall t was 6 in; the distance between the centerline of steel confinement to the wall end was 11/16 in. (1/2 in. concrete cover + $d_{b\#3}$/2). As shown in Fig. 6-44 and Fig. 7-42, the tensile strains developed in the stirrups located approximately10 in. above the base of the wall were very small in both tests. Based on this observation, it was assumed that the height of strain concentration H_{cr} was less than or equal to 10 in. in PFS1 and PFS2.

Table 9-2 shows a comparison of the height of strain concentration in the tests of PFS1 and PFS2 with those recommended in the existing literature. As shown in the table, the results from the existing empirical equations show reasonable correlation with the test results; the equation proposed by Perez, provides the best result. It might be reasonable to use this equation to provide a rough estimation of the required height of the steel confinement.

c. Maximum strain in the extreme compressive concrete fiber

Once the required height of the steel confinement was determined, the maximum strain in the extreme compressive concrete fiber at the base of the wall could be determined. Fig. 9-6 illustrates the deformation of the wall at the wall corner and the expected compressive strain distribution along the height of the wall. A horizontal line was drawn in the figure to represent the cut-off section where the strain in the concrete was equal to 0.003. To calculate the maximum strain in the extreme compressive concrete fiber at the base of the wall, three assumptions were made. First, the compression force at the wall corners spread out, thus the strains decreased significantly along the height of the wall. This assumption was validated with test data shown in Fig. 6-43 (PFS1) and Fig. 7-44 (PFS2). Second, although the strains decreased quickly as shown in Fig. 9-6 (similar

behavior was observed in Fig. 7-44), it was conservatively assumed that the compressive strains linearly decreased along the height of the wall. Third, it was assumed that only the strains which were larger than 0.003 (in the confined region at the base of the wall) contributed to shortening of the wall at the tip. As shown in Fig. 9-6, it was believed that the compressive strains in the unconfined concrete were much smaller than those in the confined concrete, contributing little to the shortening of the wall. The shortening of the wall at the wall tip was then equal to the sum of the strains within h_{cc} multiplied by the elemental length of the strains.

The following equation is proposed to deduce the maximum strain in the extreme compressive concrete fiber:

$$\frac{\epsilon_{conc} + 0.003}{2} h_{cc} = \theta c \ \rightarrow \epsilon_{conc} = \frac{2\theta c}{h_{cc}} - 0.003 \tag{9.22}$$

Where ϵ_{conc}= Maximum strain in the extreme compressive concrete fiber; θ = Rotation of the wall, determined based on the performance requirement of the wall; c = Neutral axis depth of the wall when the rotation of the wall is θ.

(3) Width of the steel confinement

The width of the steel confinement was determined based on the neutral axis depth of the wall and the compressive strain distribution over the neutral axis depth. To deduce the neutral axis depth of rocking walls, (9.18) adopted in the existing design guidelines ITG-5.2 (ITG 2009) could be used.

Fig. 6-29 and Fig. 7-35 show the compressive strain distribution at the corners of the walls in PFS1 and PFS2, respectively. As shown in the figures, a linear distribution of the compressive strain is valid in general. It might be reasonable to assume that plane sections remained plane in the contact region.

As described in Section 2.4.3.3, an equation, which assumed a linear distribution of compressive strain over the contact region, was proposed to determine the width of the steel confinement:

$$l_{cr} = c(1 - \frac{\epsilon_{unconf}}{\epsilon_{conc}}) \tag{9.23}$$

Where l_{cr}= Width of the steel confinement; ϵ_{unconf}= Crushing strain of the unconfined concrete (e.g. 0.003); ϵ_{conc}= Maximum strain in the extreme compressive concrete fiber. Similar to the deduction of the height of the steel confinement, it was assumed in Eq. (9.23) that the steel confinement might not be needed in the region where the strains in the concrete fibers were smaller than 0.003.

(4) The amount of the steel confinement

Once the maximum strain in the extreme compressive concrete fiber ϵ_{conc} was obtained through Eq. (9.22), the amount of the steel confinement required in the wall corners could be calculated using existing confinement models. For example, if the confinement model proposed by Mander et al. (1988) was selected, the following equation could be used:

$$\rho_{cc} = \frac{(\varepsilon_{conc} - 0.004) f_{cc}^{'}}{1.4 f_{yt} \varepsilon_{su}} \tag{9.24}$$

Where ρ_{cc} = Volumetric ratio of the steel confinement to the concrete core, f'_{cc} = Strength of the confined concrete, f_{yt} = Yield strength of the steel confinement, ε_{su} = Ultimate strain of the steel confinement. Because f'_{cc} is dependent on the value of ρ_{cc}, an iterative process would be needed to solve Eq. (9.24).

(5) Impact from the O-connectors

The impact from the O-connectors on the design of the boundary elements was different in the two types of PreWEC systems. For the PreWEC system with two end columns adjacent to the wall, once the O-connectors had yielded, the vertical resistances provided by the O-connectors at each end of the wall were approximately equal and opposite, as shown in Fig. 8-4. It was believed that the O-connectors would not introduce any significant axial force on the wall corners (Henry et al. 2016).

For the PreWEC system with four side columns on the front and the back of the wall, because the vertical resistances provided by the O-connectors on each side of the wall were in the same direction as shown in Fig. 8-3, it was believed that the vertical resistances provided by the O-connectors would provide additional axial forces on the wall corners. Under this circumstance, the additional axial forces provided by the O-connectors should be included in Eq. (9.17):

$$P_{total} = N_{PT} + N_G + W_w + \sum R_{YO} \tag{9.25}$$

Where $\sum R_{YO}$ = Sum of the resisting forces from the O-connectors

For both types of PreWEC systems, the O-connectors provided additional moment resistance to the rocking-wall structures. It was assumed that all of the O-connectors were located above the cut-off section of the wall. To account for the additional moment resistance of the provided by the O-connectors, Eq. (9.19) and Eq. (9.21) are changed to:

$$M_{BASE} = P_{total}\left(\frac{w_{wall}}{2} - \frac{P_{total}}{1.84f'_{cc}t}\right) + \sum M_O\,; \tag{9.26}$$

$$M_{cut-off} = P_{total}\left(\frac{w_{wall}}{2} - \frac{P_{total}}{1.7f'_{c}t}\right) + \sum M_O\,; \tag{9.27}$$

Where $\sum M_O$ = Sum of the resisting moments from the O-connectors

(6) Impact from the surrounding structures

When the special vertical movement isolated connections were used as the wall-floor connections in the rocking-wall structures, there were no additional axial forces introduced on the wall corners as long as the special wall-floor connections functioned properly.

In the rocking-wall structures with rigid wall-floor connections, because the deformation demand on the floor connected to the uplifted side of the wall was different from that connected to the compression side of the wall, the moment resistance in the floor generated at different sides of the wall would be different. Because different shear forces would be generated at different sides of the wall, it was expected that an additional axial load would be generated at the wall corners.

It was found that the rigid-connected floor slab would yield at relatively small drift levels in rocking-wall structures (e.g. 0.75% drift in PFS1). Once the floors had yielded, if the strain hardening effect of the floors was not significant (i.e., the moment resistances of the floors would not greatly increase after the yielding), the vertical resistances provided by the floors connected to each side of the wall would be approximately equal and opposite, as shown in Fig. 8-3. It is similar to the case of the O-connectors connected to each side of the wall as described previously. Under this circumstance, Eq. (9.25) would still be valid.

For the PreWEC systems using either type of wall-floor connections, the floor slabs would provide additional moment resistance to the rocking-wall structures. In general, the floor slabs would be located above the expected cut-off section of the wall. Eq. (9.26) and Eq. (9.27) are changed to:

$$M_{BASE} = P_{total}\left(\frac{w_{wall}}{2} - \frac{P_{total}}{1.84f'_{cc}t}\right) + \sum M_O + \sum M_{SU}\,; \tag{9.28}$$

$$M_{cut-off} = P_{total}\left(\frac{w_{wall}}{2} - \frac{P_{total}}{1.7f'_{c}t}\right) + \sum M_O + \sum M_{SU}\,; \tag{9.29}$$

Where $\sum M_{SU}$ = Sum of the resisting moments from the floor slabs. It was expected that M_{SU} in the rocking-wall structures with rigid wall-floor connections would be much larger than that in the rocking-wall structures with special vertical movement isolated connections.

Following the same procedure described previously, the height of the steel confinement h_{cc} could be deduced based on Eq. (9.28) and Eq. (9.29). Using Eq. (9.22), the maximum strain in the extreme compressive concrete fiber ϵ_{conc} could be deduced. Once ϵ_{conc} was obtained, the width and the amount of the steel confinement could be obtained through Eq. (9.23) and Eq. (9.24).

9.1.5 Design Recommendation for O-connectors

The O-connectors, which are connected to the wall and end columns in PreWEC systems, are used as energy dissipating elements in rocking-wall structures. When the wall rocks, the O-connectors deform due to the relative vertical deformation between the wall and the end columns, dissipating energy through hysteretic damping. In this section, the arrangement of the O-connectors is discussed first, followed by the discussion of the behavior of the O-connectors under combined vertical and horizontal deformation demand.

9.1.5.1 Arrangement of the O-connectors

The O-connectors could be installed only at the first story of the wall (e.g. PFS1) or at different stories of the wall (e.g. PFS2). Because the relative vertical deformation is only related to the horizontal distance between the attachment point of the O-connectors and

the rotation point of the wall, it would be similar for the O-connectors installed at different stories along the height of the wall. Under this circumstance, the performance of the O-connectors installed at different stories would be similar. Therefore, the arrangement of the O-connectors was not restricted, but was open to the designers in practice. Generally, it may be convenient, as well as more desirable to the architects, to install all the required O-connectors within a single story and keep the surface of the wall clear at the other stories. It should be noted that a large concentrated force could be generated at the attachment points between the O-connectors and the wall, thus an appropriate amount of vertical reinforcement should be used around the O-connectors to carry their tensile resistance forces to the wall.

9.1.5.2 Behavior of the O-connectors under Combined Deformations

When the wall rocked, the end columns were pushed or pulled laterally by the wall in the horizontal direction. If the end columns did not rock in phase with the wall, relative horizontal displacement might exist between the wall and the end columns. As shown in Fig. 6-60, it was observed that the steel tube end columns, which were actually side columns in PFS1, leaned towards the center of the wall at the end of the test, indicating that the O-connectors placed on the upper level were subjected to horizontal opening in the test of PFS1. This phenomenon was not observed in the test of PFS2 with the end columns extending above the floor and constrained to rock in phase with the wall. In the following, the behavior of the O-connectors under combined vertical and horizontal deformation is investigated using the numerical model validated in Section 5.4.3.

Three monotonic loading protocols were applied to the numerical model. In the first protocol, the O-connector was only subjected to vertical deformation up to 2.4 in. In the second protocol, the O-connector was subjected to vertical deformation up to 2.4 in. and additional 1 in. horizontal opening. In the third protocol, the O-connector was subjected to vertical deformation up to 2.4 in. and additional 2 in. horizontal opening. Fig. 9-7 shows a comparison of the simulation results in the three cases. As shown in the figure, compared with the first case, the vertical resistance of the O-connector decreased slightly (4%) when it was subjected to 2.4 in. vertical deformation and an additional 1 in. horizontal opening; the vertical resistance of the O-connector decreased noticeably (22%)

when it was subjected to 2.4 in. vertical deformation with an additional 2 in. horizontal opening. It was obvious that the performance of the O-connectors would be better and more predictable if they were only subjected to relative vertical deformation. To satisfy this requirement, the end columns should rock in phase with the wall, which is discussed in the next section.

9.1.6 Design Recommendation for PreWEC End Columns

Two different styles of PreWEC systems are investigated in this dissertation. For the PreWEC system used in PFS1, four steel tubes were used as the end columns. They were placed adjacent to the front and the back surface of the wall (named "side columns" in this section). The O-connectors were welded to the surface of the steel tubes. For the PreWEC system used in PFS2, two precast reinforcement concrete (RC) columns were used as the end columns. They were placed adjacent to each end of the wall. The O-connectors were welded to the steel plates pre-embedded in the RC columns. Design recommendations for the side columns and the end columns are given below.

9.1.6.1 Side Columns

As discussed in Section 9.1.5.2, the vertical resistances provided by the O-connectors are decreased if they are subjected to horizontal opening. It was recommended that the side columns should extend above the floor slabs. Under this circumstance, the side columns would be bounded by the floor slab on each story and rock in phase with the wall, eliminating the horizontal deformation demand on the O-connectors. Because the side columns might bear on the floor during rocking of the wall, protection materials (e.g. rubber) should be placed between the side columns and the floor.

It was observed by other researchers that out-of-plane buckling could occur to the O-connectors, as shown in Fig. 9-8 (Henry 2011). In PFS1, the O-connectors were placed between the surface of the wall and that of the steel tubes (side columns), thus they were constrained by the wall and the steel tubes and out-of-plane buckling was prevented. Because forces might be generated by the O-connectors that push the steel tubes in the out-of-plane direction, a threaded rod running through the front steel tube, the wall and the back steel tube was used to connect the three together. The through hole in the wall,

which was located between the top and the bottom plate in the wall, is shown in Fig. 3-20. A through hole was cut in the steel tube to accommodate the threaded rod, as shown in Fig. 3-23(c).

It was noteworthy that if the steel tubes extended above the floor slab as recommended previously, they would also be bounded by the floor slab in the out-of-plane direction. Under this circumstance, it was unnecessary to use the aforementioned method in PFS1 to reduce the out-of-plane bending of the steel tubes. The construction of the PreWEC system could be greatly simplified.

9.1.6.2 End Columns

Different from the side columns in PFS1 that were only used to connect the O-connectors, the end columns in PFS2 served two purposes: connect the O-connectors and carry the gravity loads from the tributary areas of the wall. Design recommendations for the end columns are provided below.

PT force in the end columns

Because the width of the end columns was generally small, the moment arm between the PT force in the end column and the resultant compression force at the corner of the end column was small. Therefore, the end columns contributed little to the moment resistance of the entire PreWEC system. It might not be effective to employ large PT forces in end columns. Furthermore, when the O-connectors imposed resisting forces that compressed the end columns, the sum of the PT forces, the gravity loads carried by the end columns and the resisting forces from the O-connectors was large, which might damage the corner of end columns. As shown in Fig. 7-63, damage occurred to the east corner of the east end column when the wall was loaded to the east and the east O-connectors generated a compression force on the east end column. Similar observation is shown in Fig. 7-64. Damage occurred to the west corner of the west end column when the wall was loaded to the west and the west O-connectors generated a compression force on the west end column. Therefore, it was recommended that the initial PT force in the end columns should be close to the lower bound PT force.

The lower bound initial PT force was determined when the O-connectors pulled up the end columns. As shown in Fig. 7-59, the O-connectors attached to the west side of the

wall pulled the west end column up when PFS2 was loaded to the east. To prevent the end columns from losing contact with base block, the summed force of the clamping force from the PT threaded rod and the gravity load carried by the end column (self-weight included) should exceed the resisting forces from the O-connectors.

Because the gravity loads carried by the end columns might exceed the resisting forces from the O-connectors, no PT forces were required under this circumstance according to the force equilibrium condition of the end column. However, moment equilibrium condition of the end columns should also be considered when determining the lower bound PT force. The action line of the gravity load might be out of the bound of the end columns, generating an overturning moment in the end columns due to the P-delta effect. Although horizontal resisting forces would be provided by the wall to resist the end columns from overturning, it was recommended that the end column should be capable of self-centering itself for conservative considerations. Therefore, it was recommended that the self-centering moment provided by the PT forces in the end columns should exceed the overturning moments generated by the gravity loads and the resisting forces from the O-connectors at the design drift level.

In summary, the lower bound initial PT forces in the end columns should be the larger of the two values deduced based on the force and the moment equilibrium condition.

Special details to protect the base of end columns

As discussed in Section 7.3.1, a great amount of damage occurred to the corners of the end columns after 3% drift. Once the end columns were damaged, the PT forces that clamped the end columns to the base block greatly decreased. In the test, the damaged west end column was picked up by the wall due to the loss of the clamping forces that made the connected O-connectors useless. Moreover, the uplifted end columns would generate an additional vertical deformation demand on the floor that might cause damage to the floor. It was recommended that special detailing should be used to protect the base of the end columns. For example, steel angles could be installed at the corners to highly confine the concrete in column base, similar to the detail used in the rocking wall corners.

Other design recommendation for the end columns

Because the gravity loads on the floors were transferred to the end columns, they would extend above the floor slabs and were bounded by the floor slab at each story. The end columns would rock in phase with the wall, thus the horizontal deformation demand on the O-connectors was eliminated. Due to the constraint from the floor slabs, the end columns would not be subject to excessive out-of-plane deformation either.

It was recommended that two steel straps be installed for each O-connector to prevent it from buckling in the out-of-plane direction. This design was used in PFS2 as shown in Fig. 3-97, and none of the O-connectors buckled in the test. A wider strap should be used for the bottom strap; otherwise the deformed O-connectors might be outside the bound of the strap due to the uplift of the wall.

9.2 Design Recommendation for Rigid Wall-Floor Connections

One disadvantage of using rigid wall-floor connections in rocking-wall structures was potential damage to floor slabs compared to using vertical movement isolated connections. It was noteworthy that in test specimen PFS1, with the slab continuously attached to the wall, that the observed floor damage was localized near the wall ends as shown in Fig. 6-75 and Fig. 6-76. The localized damage was believed to have been caused by the high deformation demand on the floor at the uplifted side of the wall. A simplified linear elastic 2D analytical model was proposed to investigate the factors that induced the moment demand on the floor slab in the longitudinal direction, as shown in Fig. 9-9. The 3D effect of the floor was not considered in this 2D model for simplicity. The slab was modeled by two beam elements connecting the wall and the columns. The small axial deformation of the columns was neglected. The wall was assumed to rock like a rigid body about the corner. An elastic slope-deflection equation was established to calculate the concentrated moment demand on the floor at the wall-floor connection (M_{slab}):

$$M_{slab} = 4i_{slab}\theta + 2i_{slab}\beta - 6i_{slab}\frac{-\Delta}{L} \tag{9.30}$$

$$\Delta = s\theta \tag{9.31}$$

$$i_{slab} = \frac{E_c I_{slab}}{L_{slab}} \tag{9.32}$$

Where θ = Rotation of the wall; β = Rotation at the top of the column; L_{slab}= Span of the slab; Δ = Vertical deformation of the floor at the wall end (equal to the wall uplift); s = Horizontal distance between the wall-floor connection and the rotation point of the wall; i_{slab} = Flexural stiffness of the floor; E_c = Young's modulus of concrete; I_{slab}= Moment of inertia of the floor.

As shown in Eqn. (9.30), the moment demand on the floor at the wall-floor connection is generated due to the rotation of the wall as well as the columns, and the uplift of the wall. It was mainly related to the flexural stiffness of the slab as well as the columns, and the width of the wall. When the slab and the columns were more flexible and the wall was narrower, the moment demand on the floor would be smaller.

If the geometric dimensions of the structure were fixed in the design, changing the location of the wall-floor connection might be a way to reduce the moment demand on the floor. Because high deformation demand exists at the wall ends, if the strands and the rebar in the floor that ran transversely through the wall were placed towards the wall center and the floor was debonded at the wall ends, i_{slab} would become smaller because of the larger span; L_{slab} and Δ would be smaller due to the smaller distance to the neutral axis of the wall *s*, greatly reducing the moment generated at the wall-floor connection. Using the geometry of the test specimen PFS1 and assuming equal rotations of the wall and the columns for simplicity (i.e. $\theta = \beta$), as an example, the wall-floor moment demand would decrease by 50% if the wall-floor connection was moved to the center of the wall.

Although the 3D effect of the floor was not considered in this 2D model, it was expected that the moment demand on the floor in the transverse direction would also decrease because of the reduced Δ. Therefore, connecting the floor towards the middle of the wall could be an effective way to alleviate some of the damage to the slab. It was noteworthy that in the test specimen PFS1, the slab locally "self-debonded" from the wall after damage occurred to the wall ends. The damage was neither aggravated nor spread, which might be due to the decreased moment demand on other portions of the floor.

It was noteworthy that other design factors should also be considered, including the constraint from parallel adjacent structural systems, the capability to transfer both the gravity load and shear force through a smaller region, and the structural integrity requirements of the wall-floor connection.

9.3 Design Recommendation for Structures Assembled by Precast Members

9.3.1 Recommendation for Precast Wall-Floor Connections

Existing tests have demonstrated that the vertical movement isolated connections might not slide well even when the shear transferred by the connection is under its nominal shear capacity (Moroder et al. 2014, Watkins et al. 2014). When the connections transfer shear forces, a great amount of friction can be generated in the connections that may affect their ability to slide. If the surfaces of the embedded channel become damaged (e.g., dented) due to the transferred shear, smooth vertical sliding of the connector would become more difficult.

It was noteworthy that when the wall rocked in the out-of-plane direction, tension forces might also be generated in the precast wall-floor connections that increase the vertical friction forces in the channel. Similarly, the surfaces of the embedded channel might become damaged (e.g., dented).

Therefore, it is recommended that specific component tests be conducted to investigate the vertical sliding behavior for these types of connections under combined shear and tension forces. Materials of low friction coefficient should be used on the channel surfaces (e.g., Teflon) and the embedded slot channel should be made from stiff materials that are resistant to damage such as denting (Watkins 2014). The number of wall-floor connections should be determined based on their reliable shear and tension capacities under which the floor system is able to be fully isolated from the vertical movement of the wall.

Arrangement of the precast wall-floor connections is another important factor in the design. In the DSDM project (Schoettler 2010), the vertical movement isolated connections got jammed during the shaking table test of the rocking-wall structure

because the vertical sliding stroke of the channel in the wall was limited. If the vertical sliding stroke of the wall-floor connections ran out, the floor would not be fully isolated from the vertical movement of the wall.

The maximum relative vertical displacement for each wall-floor connection should be equal to its distance to the farther end of the wall multiplied by the maximum expected rotation of the wall, which is close to the lateral drift of the wall because the wall rocks like a rigid body. To decrease the stroke demand during cyclic loadings, it is recommended to place the connections close to the middle of the wall. However, spacing of the connections should not be too small because of the concern of the concrete in the wall being pulled-out in the out-of-plane direction. Minimum spacing should be regulated for different types of connections through specific component tests. Because the relative vertical sliding of the connector stud is in the same direction (towards the bottom of the channel) during cyclic loading, the connector of the special connection affixed to the floor (e.g. V-shape plate of BS Italia connections) should be placed close to the top of the channel in the wall to maximize its available stroke.

9.3.2 Recommendation for Plank-Beam Connections

As discussed in Section 7.5.2, although the planks were successfully isolated from the vertical movement of the wall in the test of PFS2, the strap plates across the plank-beam connections yielded at 3% drift in Phase 5. It was concluded in Section 7.5.4 that the yielding of the strap plates was caused by the relative rotation demand on the strap plates. In the following, an equation is proposed to predict the rotation demand on the strap plates at the plank-transverse beam and the plank-edge beam connection.

Fig. 9-10 illustrates the rotation demand on the strap plates at the plank-transverse beam and the plank-edge beam connection. The edge columns are considered as "rocking columns" in the figure, which is similar to the condition in Phase 1 of PFS2. As shown in the figure, rotation of the strap plates at the plank-transverse beam connection consists of two parts: rotation of the end column (α_{Endcol}) and rotation of the plank (β_{Wplank} for the west edge plank, β_{Eplank} for the east edge plank). Similarly, rotation of the strap plates at

the plank-edge beam connection consists of rotation of the edge column ($\alpha_{Edgecol}$) and rotation of the plank (β_{Wplank} and β_{Eplank}, respectively).

Assuming the end column and the edge column rocked in phase with the wall, rotation of the end column α_{Endcol} and that of the edge column $\alpha_{Edgecol}$ are both equal to the rotation of the wall. Rotation of the planks is caused by the relative vertical displacement at the two ends. As shown in Fig. 9-10, for the west edge plank, the east end of the plank is uplifted due to the uplift of the west end column; the west end of the plank remains almost horizontal because the west edge column has negligible vertical deformation close to its compression side.

For the east edge plank, the east end of the plank uplifts due to the uplift of the east edge column; the west end of the plank remains almost horizontal because the east end column has negligible vertical deformation close to its compression side.

The following equation is proposed to provide an upper bound estimation for the rotation of the strap plates at the plank-transverse beam and the plank-edge beam connections:

$$\begin{aligned}\alpha_{strap} &= \alpha_{Endcol} + max\left\{\beta_{Wplank}, \beta_{Eplank}\right\} \\ &= \theta + \frac{max\left\{\Delta_{uplift\_endcol}, \Delta_{uplift\_edgecol}\right\}}{L_{slab}} \\ &= \theta + \frac{max\left\{w_{Ecol}, w_{Edgecol}\right\}}{L_{slab}}\theta\end{aligned} \tag{9.33}$$

Where α_{strap} = Rotation of the strap; β_{Wplank} = Rotation of the west edge plank; β_{Eplank} = Rotation of the east edge plank; θ = Rotation of the wall (equal to lateral drift of the wall); Δ_{uplift_endcol} = Uplift of end columns; $\Delta_{uplift\_edgecol}$ = Uplift of edge columns; L_{slab} = Span of the slab; w_{Ecol} = Width of end columns; $w_{Edgecol}$ = Width of edge columns.

For the specimen PFS2, L_{slab} = 68 in.; w_{Ecol} = 10 in.; $w_{Edgecol}$ = 8 in. Substitute the values into Eq. (9.33): $\alpha_{strap} \approx 1.15\theta_{wall}$

Fig. 9-11 shows a comparison of the maximum rotations of the strap plates at the plank-edge beam connection (recorded by FCL-T2/B2) and the plank-transverse beam

(recorded by MFWL-T2/B2) in Phase 1 with the results predicted by Eq. (9.33). As shown in the figure, the maximum rotations at the plank-edge beam connection predicted by Eq. (9.33) (curve FCL-T2/B2_Ph1) are similar to those recorded at the plank-transverse beam connection (curve MFWL-T2/B2) in the test. Eq. (9.33) provides a good prediction of the rotations measured at both plank-edge beam and plank-transverse beam connections.

Fixed edge column base connections might be more typically used in practice, which was similar to the condition in Phase 4 of PFS2. Fig. 9-12 shows a comparison of the maximum rotations of the strap plates at the plank-edge beam connection (recorded by FCL-T2/B2) and the plank-transverse beam (recorded by MFWL-T2/B2) in Phase 4 with the results predicted by Eq. (9.33). As shown in the figure, Eq. (9.33) provides a conservative prediction for the rotation of the strap plates at the plank-transverse beam connection (Curves "MFWL-T2/B2_Ph4"), but it underestimates the rotation of the strap plates at the plank-edge beam connection (Curves "FCL-T2/B2_Ph4").

As mentioned previously, Eq. (9.33) was established based on the assumption that the edge columns rocked in phase with the wall and the rotation of the edge columns was similar to that of the wall. However, when the edge columns were fixed-connected to the base block, flexural bending became the dominant deformation mode of the edge columns. More investigation is provided below through a simplified analytical model of the edge columns.

For simplicity, Fig. 9-13 shows the deformed shapes of a rocking column and a fixed-base cantilever column. The height of the two columns is the same (H_{col}). When the two columns remain elastic and are laterally displaced by the same distance (D_{slab}), the rotation at the top of the rocking column (α_{rcol}) is calculated as follows:

$$\alpha_{rcol} = \frac{D_{slab}}{H_{col}} \tag{9.34}$$

On the other hand, the rotation at the top of the fixed-base column (α_{fcol}) is calculated as:

$$\alpha_{fcol} = \frac{FH_{col}^2}{2E_cI_{col}} \tag{9.35}$$

The lateral displacement at the top of the fixed-base column is calculated and transformed:

$$D_{slab} = \frac{FH_{col}^3}{3E_cI_{col}} \rightarrow \frac{FH_{col}^2}{2E_cI_{col}} = \frac{3D_{slab}}{2H_{col}} \rightarrow \alpha_{fcol} = \frac{3D_{slab}}{2H_{col}} = \frac{3}{2}\alpha_{rcol} \quad (9.36)$$

Where F = Lateral force on top of the column, E_c = Young's modulus of the concrete; I_{col} = Moment inertia of the column

As shown above, the rotation at the top of the fixed-base column is 50% larger than that of the rocking column, when the columns remain elastic and are laterally displaced by the same amount of distance at the top, D_{slab}.

After a plastic hinge is developed at the bottom of the fixed-base column, as shown in Fig. 9-14, the rotation at the top of the fixed-base column (α_{fcol}) is calculated and transformed (the small elastic deformation of the column is neglected):

$$D_{slab} = D_{elastic} + D_{plastic} \approx \alpha_{fcol}(H_{col} - L_{hinge})$$
$$\rightarrow \alpha_{fcol} = \frac{D_{slab}}{H_{col} - L_{hinge}} > \alpha_{rcol} = \frac{D_{slab}}{H_{col}} \quad (9.37)$$

Where $D_{elastic}$ = Elastic deformation at the top of the column; $D_{plastic}$ = Plastic deformation at the top of the column; L_{hinge} = Plastic hinge length of the column

As shown Eq. (9.37), the rotation at the top of the fixed-base column is still larger than that of the rocking column. The analysis proved two test observations. First, the rotation of the strap plates at the plank-edge beam connection was larger than that at the plank-transverse beam connection due to the larger rotation at the top of the fixed-base edge column compared to that of the rocking end column. Second, Eq. (9.33) underestimates the rotation demand on the strap plates at the floor-edge beam connection when the edge columns are fixed connected to the foundation.

To better estimate the rotation demands on the strap plates with either rocking edge columns or fixed-base edge columns being used in rocking-wall structures, an amplification coefficient μ is introduced into Eq. (9.33) as shown below:

$$\alpha_{strap} = \alpha_{Edgecol} + max\left\{\beta_{Wplank}, \beta_{Eplank}\right\}$$
$$= \mu\theta + \frac{max\{\Delta_{uplift\_endcol}, \Delta_{uplift\_edgecol}\}}{L_{slab}}$$
$$= (\mu + \frac{max\{w_{Ecol}, w_{Edgecol}\}}{L_{slab}})\theta \quad (9.38)$$
$$\mu = \begin{cases} 1.0, & rocking\ edge\ column \\ 1.2, & fixed-base\ edge\ column \end{cases}$$

Fig. 9-15 shows a comparison of the rotations of the strap plates at the plank-edge beam and the plank-transverse beam connection in Phase 4 with the results predicted by Eq. (9.38). Based on Eq. (9.36) when the edge columns were assumed to be elastic, the ratio between the fixed-base and the rocking column rotations was 1.5. As shown in the figure, Eq. (9.38) provides a close and conservative prediction of the rotation demand on the strap plates with the μ factors of 1.0 and 1.2 as given with Eq. (9.38) (i.e., column rotation ratio of 1.2).

The following equation is proposed in Section 7.5.4 to calculate the moment in the strap plates generated due to the rotation demand:

$$M_{strap} = \frac{\alpha_{strap} E_s I_{strap}}{L_{strap}} \quad (9.39)$$

Where α_{strap} = Rotation of the strap plate due to flexural bending; M_{strap} = Moment in the strap; E_s = Young's modulus of the strap; L_{strap} = Length of the strap between the weld and the edge of the plank.

Substituting Eq. (9.38)into Eq. (9.39), the moment demand on the strap plates is obtained:

$$M_{strap} = \left(\mu + \frac{max\{w_{Ecol}, w_{Edgecol}\}}{L_{slab}}\right)\frac{E_s I_{strap}}{L_{strap}}\theta; \quad (9.40)$$
$$\mu = \begin{cases} 1.0, & rocking\ edge\ column \\ 1.2, & fixed-base\ edge\ column \end{cases}$$

As shown in Eq. (9.40), the moment demand on the strap plates can be directly calculated based on the geometry of the structure and the drift level of the wall. It can be easily used in practice to design the strap plates.

A gap is always reserved at plank-beam connections to provide construction tolerance, as shown in Fig. 3-112 and Fig. 3-113. When determining the dimension of the gap, the relative plank-beam rotation should be considered to avoid collision when the gap closes, which is not included in current design guidance. Minimum dimensions can be determined through multiplying the thickness of the precast slabs by the maximum relative rotation predicted from Eq. (9.38).

During the cyclic loading, the gap would close in one loading direction and the gap would open in the opposite loading direction. It was observed that the planks lost contact with the steel angle support during the test but remained inside the bound of the steel angle support, as shown in Fig. 7-147. To prevent the planks from rotating outside the bound, the contact length between the plank and the steel angle should be larger than the dimension of the gap.

Table 9-1 Results of the three cases

Case number	Description of the case	c (in)	d^*_{NWPT} (in)	N^{**}_{PT} (kip)	M_{PreWEC} (kip-in)
Case 1	Grout weaker than concrete; Use actual strength of fiber grout (8,647 psi)	6.1	31	230	9,811
Case 2	Grout stronger than concrete; Use strength of confined concrete (13,470 psi)	4.1	32	235	10,222
Case 3	Grout stronger than concrete; Use nominal strength of unconfined concrete (6,000 psi)	11.6	30	217	9,021

* d_{NWPT} is the distance between the wall centroid and the action line of resultant compression force at the wall corners.
** The PT loss due to the slip of the strands was subtracted during the calculation of N_{PT}

Table 9-2 Strain concentration heights in the tests and the existing recommendations (unit: in.)

Test specimens	Test results	Perez			Restrepo	Gavridou	
		$2.0t''_w$	$2.0c''$	min $(2.0t''_w, 2.0c'')$	c	$1.5t_w$	min $(1.5t_w, c)$
PFS1	10	9.3	13.4	9.3	7.4	9	7.4
PFS2	10	9.3	9.2	9.2	5.3	9	5.3

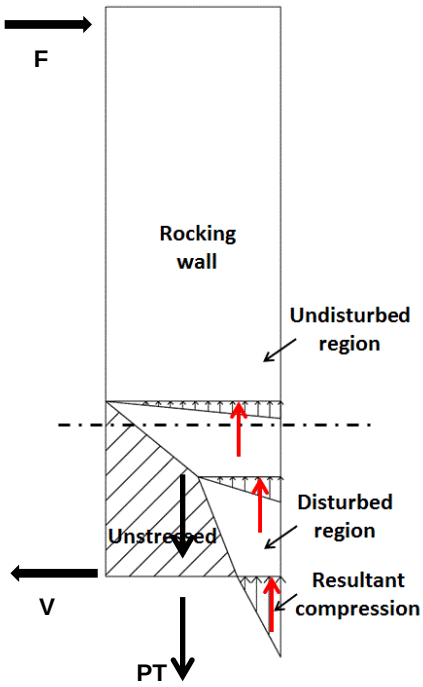

Fig. 9-1 Strain distribution in a rocking wall (Base shear not shown for clarity)

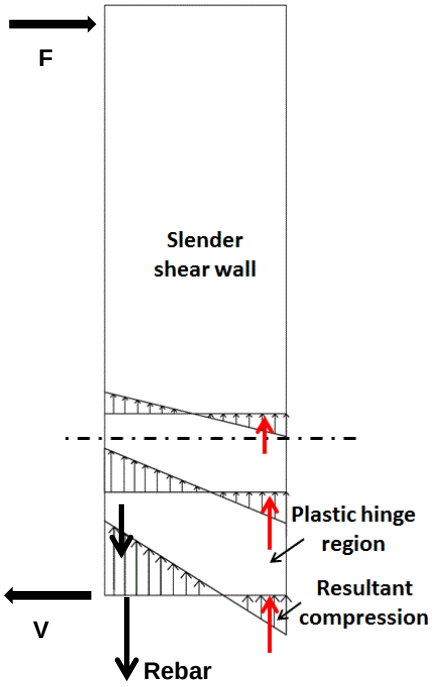

Fig. 9-2 Strain distribution in a structural wall (Base shear not shown for clarity)

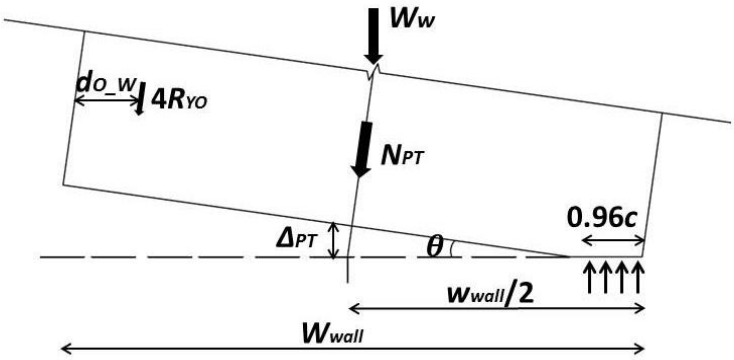

Fig. 9-3 Free body diagram of the wall and the O-connectors

Fig. 9-4 Bending of the steel angle in the wall at the end of the test of PFS1

Fig. 9-5 Bending of the steel angle in the wall at the end of the test of PFS2

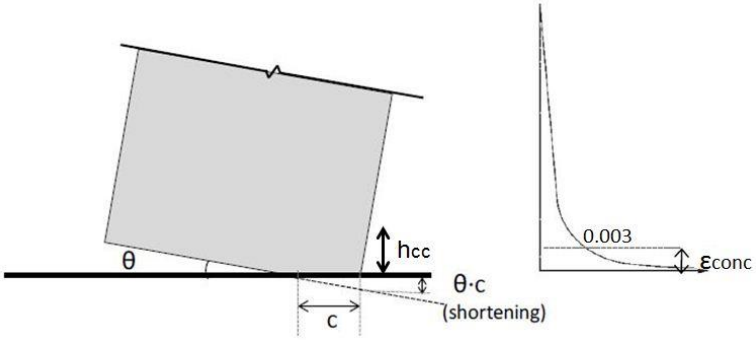

Fig. 9-6 Illustration of the deformation at the wall corner and the compressive strain distribution along the height of the wall

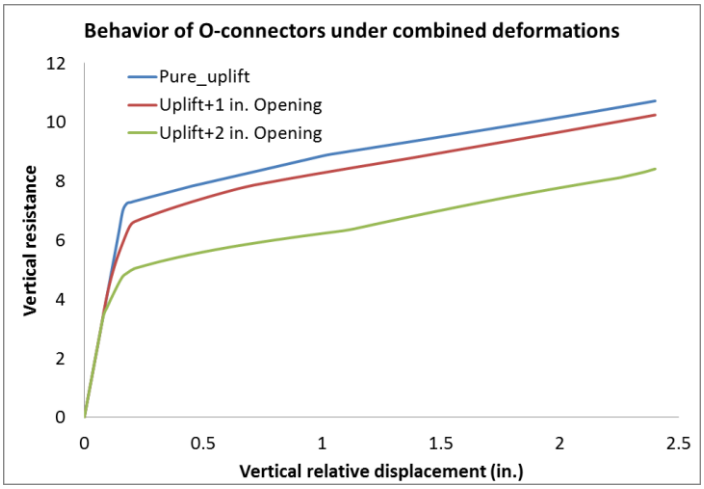

Fig. 9-7 Vertical resistances of O-connectors under different loading conditions

Fig. 9-8 Buckling of the O-connectors in the component test (Henry 2011)

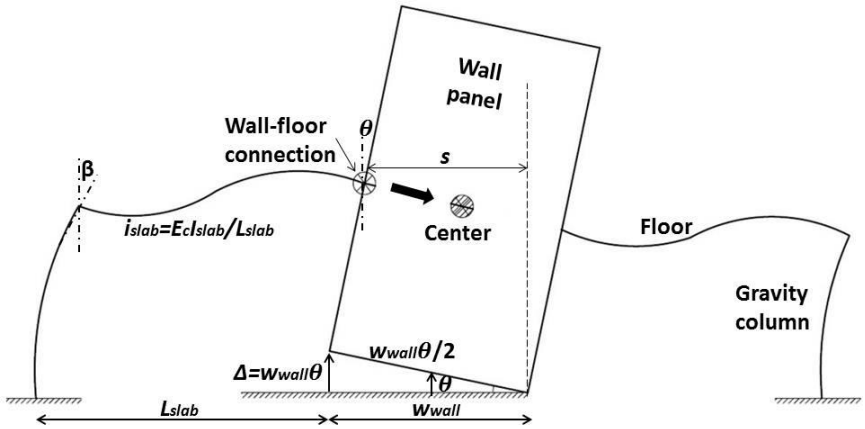

Fig. 9-9 Simplified 2D analytical model

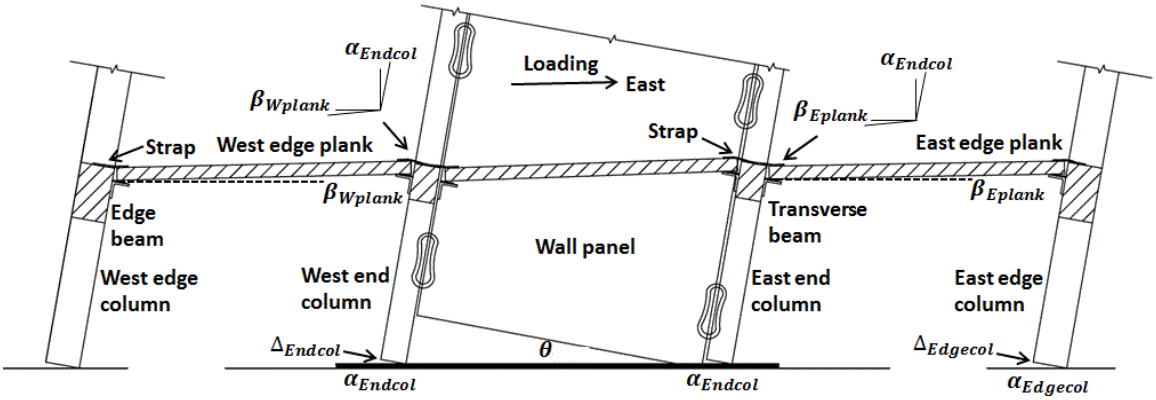

Fig. 9-10 Illustration of the rotation demand on the strap plates at the plank-transverse beam and the plank-edge beam connections

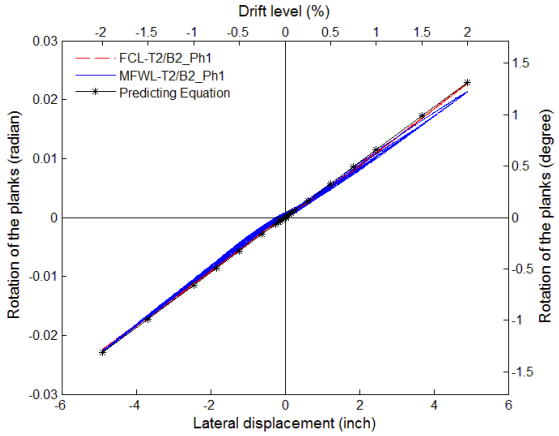

Fig. 9-11 Comparison of the rotations of the strap plates at the plank-edge beam and the plank-transverse beam connection in Phase 1 with the results predicted by Eq. (9.33)

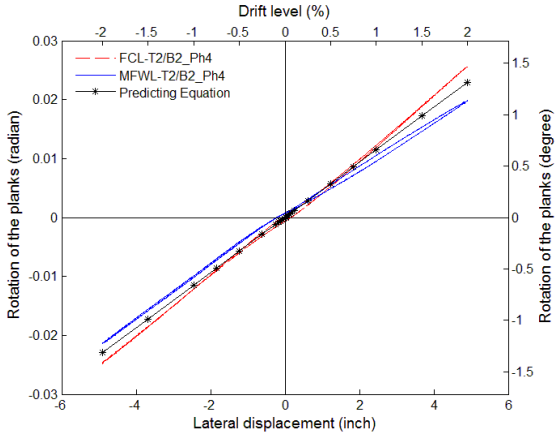

Fig. 9-12 Comparison of the rotations of the strap plates at the plank-edge beam and the plank-transverse beam connection in Phase 4 with the results predicted by Eq. (9.33)

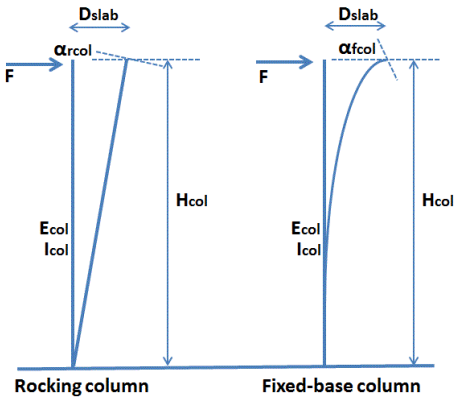

Fig. 9-13 Deformed shapes of a rocking column and a fixed-base column (elastic)

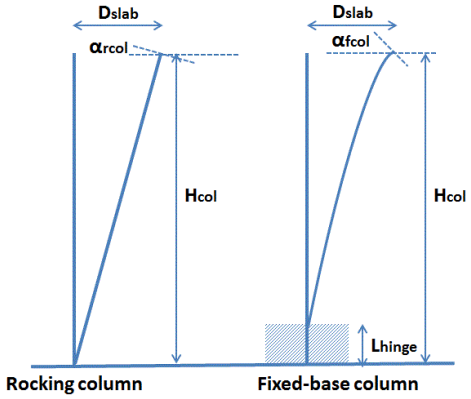

Fig. 9-14 Deformed shapes of a rocking column and a fixed-base column (plastic)

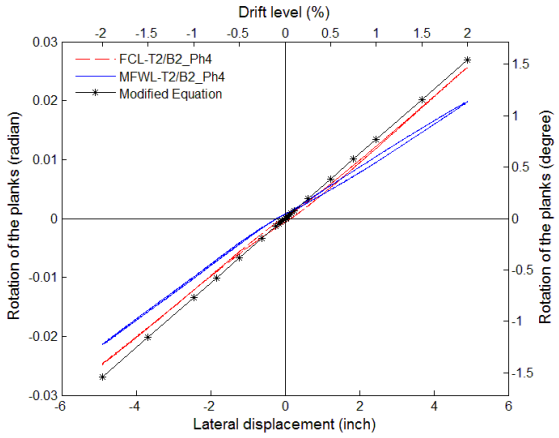

Fig. 9-15 Comparison of the rotations of the strap plates at the plank-edge beam and the plank-transverse beam connection in Phase 4 with the results predicted by Eq. (9.38)

CHAPTER 10. Summary and Conclusions

Rocking-wall systems are innovative structural systems that have been proposed and investigated for decades. Housner (1963) conducted the first significant research of rocking behavior of tall structures that survived in the 1960 Chilean earthquake. A jointed US-Japan research project PRESSS (PREcast Seismic Structural Systems) was initiated in 1990's that featured both experimental and theoretical studies of rocking-wall systems (Priestley et al. 1999). A great amount of experimental studies of rocking-wall systems had been conducted since then. Previous tests had demonstrated the excellent self-centering performance of rocking-wall systems, and their energy dissipation capacities by using them in combination with yielding elements (Schultz and Magana 1996, Restrepo and Rahman 2007, Brian et al. 2009, Schoettler 2010, Aaleti and Sritharan 2011). However, this innovative structural system was not popularized in practice. One of the main reasons was that there was limited effort had been put into investigating the interaction mechanism between rocking-wall systems and surrounding structures (e.g. floors and columns), as stated in Chapter 1.

Chapter 2 provides a literature review of existing experimental and numerical studies on rocking-wall structures. The literature review provides the following findings:

- Jointed wall systems, hybrid wall systems and Precast Wall with End Columns (PreWEC) systems are three types of isolated rocking-wall systems that have been mainly investigated to date. PreWEC systems have provided improved performance compared to jointed wall systems and hybrid wall systems with better design efficiency, reduced cost, and replaceable energy dissipating elements.
- Three computational techniques (lumped plasticity, fiber-based and solid element-based) have been mainly used to simulate rocking-wall systems. Despite high computational cost, solid element-based models have been primarily used for simulation to capture the overall and local behavior of rocking-wall systems.

- Only limited experimental studies of rocking-wall structures were found in the literature, including PRESSS project (Priestley et al. 1999), DSDM project (Schoettler 2010) and E-Defense testing (Nagae et al. 2011). Due to the complexity and diverse purposes of these tests, no systematic studies focusing on the interaction mechanism between rocking-wall systems and surrounding structures have been conducted.
- Current design guidelines of rocking-wall systems (ITG 5-2) were not complete (e.g., height of the steel confinement and the amount of longitudinal reinforcement required in the wall). Inconsistencies existed between the design guidelines and the design of rocking-wall systems practically used in the existing experiments (e.g., width of the steel confinement).

To overcome the limitations mentioned above and popularize the rocking-wall systems in practice, two large-scale rocking-wall structural assemblages (PFS1 and PFS2) that included PreWEC systems and surrounding structures were tested. The rocking-wall structural assemblages were selected to bound the potential interaction of the surrounding structure with the rocking wall. PFS1 represented an upper bound interaction and PFS2 represented a lower bound interaction that was designed to isolate the vertical uplift of the rocking wall from the floor to avoid potential damage to the floor system.

Chapter 3 provides a description of the two specimens PFS1 and PFS2. In PFS1, the PreWEC system consisted of a precast rocking wall that carried gravity loads (i.e., bearing wall), four end columns made of short steel tubes to attach energy dissipating elements (O-connectors) to the wall. The surrounding structure included cast-in-place edge columns and an unbonded post-tensioned (PT) floor system. Rigid wall-floor connections were formed in PFS1 by having multiple rebar and strands in the cast-in-place slab pass through the wall. Because only the first story unbonded PT slab was constructed as a representative floor to simplify the construction of the test specimen, a set of “mega beams” was implemented in the specimen to simulate the constraint of the five missing upper-story CIP floors of the prototype building on the wall.

In PFS2, the PreWEC system consisted of a precast non-bearing rocking wall, O-connectors were attached between the wall and two end columns adjacent to and in the

plane of the wall that provided a unique gravity load transfer path for the precast rocking-wall structures. The surrounding structure included precast edge columns and a floor system formed by precast untopped planks. Special precast connections (BS-Italia) that isolated the floor from the vertical movement of the wall were used as the wall-floor connections. A set of "mega trusses" were implemented in the specimen to simulate the constraint of the five missing upper-story precast floors of the prototype building on the wall.

Chapter 3 also provides a detailed description of the construction procedure of the two specimens. Different techniques were used during the construction of the two specimens. In PFS1, the floors and the edge columns were cast together in the laboratory with the precast wall set in place. In PFS2, all structural members, including the wall, the end columns and the floor slab, were precast members and assembled in the laboratory. Because there were very few rocking-wall structures that had been built in practice, it was believed that the detailed description of the construction procedure would be useful for other researchers and practicing engineers. The material properties of PFS1 and PFS2 are summarized at the end of that chapter.

Chapter 4 provides a description of the instrumentation plans and loading protocols of the two specimens. The types of instrumentation used in the tests, the purposes of the instrumentation and the associated data processing methods are presented. With various combinations of boundary conditions (with or without props, etc.) and loading directions (in-plane or biaxial), PFS1 and PFS2 featured four and twelve phases of testing, respectively. The data generated by the instrumentation were used for analysis in Chapter 6 through Chapter 8.

Because the amount of available instrumentation was limited for such large and complicated structural assemblages, only parts of the specimens were instrumented. Numerical simulation was used to further understand the behavior of the specimens, which is described in Chapter 5.

In PFS1, a numerical model of the entire specimen was built. To improve the accuracy of the model, available results from specific component tests of O-connectors and mega beams were used to calibrate the model. To numerically simulate the "unbonded"

characteristic of the unbonded post-tensioned slab, the method of "Adjusting stress-strain responses of PT strands" was used. To validate the method, a numerical model of a cantilever unbonded PT slab was built using commercial software ABAQUS. Results obtained from the numerical model showed satisfactory consistency with those from theoretical analysis of a cantilever PT slab.

In PFS2, only the numerical model of the isolated PreWEC system was built instead of the entire specimen. By comparing the results from the numerical model with the test results of PFS2, the effectiveness of the vertical movement isolation connections (BS-Italia) used in PFS2 is investigated in Chapter 7.

A summary of the main conclusions from the two tests is given below (Chapter 6 through Chapter 8), followed by design recommendations proposed for rocking-wall structures (Chapter 9). This chapter concludes with suggestions for future research of rocking-wall structures.

10.1 Conclusions from PFS1 – Chapter 6

10.1.1 Overall Behavior of PFS1

The specimen PFS1 exhibited good seismic response with excellent energy dissipation and reasonable self-centering characteristics. Unsymmetrical behavior of PFS1 was observed in the test with a smaller base moment being generated when PFS1 was loaded in the negative direction (to the west). By investigating the altered numerical model of PFS1 with two cover plates of the east mega beam being removed, it was shown that the unsymmetrical behavior was caused by the ineffectiveness of the east mega beam. It was believed that the mega beams behaved normally when PFS1 was loaded in the positive direction (to the west). By comparing the behavior of PFS1 in the positive loading direction with that from the numerical model of the isolated PreWEC system, it was found that the base shear of the PreWEC system was increased by 26% in PFS1 because of the wall-floor interaction at 2% design drift. The energy dissipating capacity of PFS1 was more than three times larger than that of the isolated PreWEC system, which was contributed by the surrounding structure. Compared with the isolated PreWEC system

that realized complete self-centering, PFS1 had 0.44% residual drift at the end of the 2% cycle. The residual drift was still considered small compared with regular shear wall structures. The damage that occurred to the surrounding structure only slightly compromised the self-centering capability of the PreWEC system.

10.1.2 Behavior of Structural Components

10.1.2.1 PreWEC System

Little damage occurred to the wall throughout the test. Instead, minor damage occurred to the fiber grout in the pocket of the base block. The material tests revealed that the actual strength of the fiber grout was smaller than that of the concrete in the wall. Therefore, the N.A. depth of the wall was extended. Because the concentrated compression force spread over a larger contact area, the strain demand on the boundary elements of the wall was reduced and less damage occurred to the wall.

Debris of the over-poured grout and the concrete cover that spalled off the wall surface became trapped in the pocket of the base block. The height of the wall was increased due to the debris that increased the residual PT force in the wall. Slip and unexpected fracture of one strand wire occurred in the test.

10.1.2.2 Unbonded PT Slab

Localized severe damage concentrated at the floor slab adjacent to the wall, while minor parallel cracks were uniformly distributed at the floor-edge beam interface. It was believed that the deformation demand on the slab concentrated close to the wall end and more uniformly distributed along the edge beam. After the localized damage to the floor adjacent to the wall ends was fully developed, the floor became “self-debonded” from the wall and the damage did not aggravate or spread. Most cracks in the floor closed after the test and structural integrity of the floor was maintained because of the intact transverse shear-friction reinforcement and the unbonded PT strands had not yielded.

The 3D constraint effect of the floor slab on the rocking wall was noticeable because of the existence of edge beams. But the effect was not significant when no transverse constraint was imposed (i.e., when simulating the case of parallel PreWEC systems in phase, without “props”). When the parallel structural system contained frame columns,

emulated by attaching props to the slab, the 3D effect became more significant. The rebar in the slab that ran in the transverse direction (perpendicular to the wall) and went through the wall started to yield, and the PT force of the transverse strands greatly increased. On the other hand, it was found that the constraint from adjacent structural systems that were emulated by adding the props had little impact on the PT forces of the strands in the slab running in the longitudinal direction (parallel to the wall).

10.1.2.3 Edge Columns

Initial yielding of the longitudinal rebar in both edge columns occurred at drift levels of approximately 1%. Concrete within half of the column depth crushed at the corner at 2.5% drift levels. Crushing of the concrete in the edge column corners became more severe when the specimen was under biaxial loading. The PT forces which emulated the gravity load on the edge column increased about 25% to 30% due to the lateral deformation of the edge columns, but the magnitude of the increased stress over the cross section of the edge column was not large and did not have a great impact on the behavior of the edge columns.

10.2 Conclusions from PFS2 – Chapter 7

10.2.1 Overall Behaviors of PFS2

In PFS2, it was validated that the precast floor was successfully isolated from the vertical movement of the rocking wall. By comparing the envelope of the force-displacement curves of the specimen recorded in the test with the pushover curve of the isolated PreWEC system from the numerical model, it was found that the base shear of the PreWEC system only increased by 4% at 2% design drift. The wall-floor interaction was greatly reduced when the special precast wall-floor connections (BS Italia) were properly designed and used in rocking-wall structures. It was also found that the structural system in the adjacent frame line, which was simulated by props, had little impact on the in-plane behaviors of the tested PreWEC system with the usage of BS-Italia connections.

PFS2 exhibited excellent self-centering performance throughout the test. The residual drift of PFS2 was only 0.08% at 2% design drift, which was negligible. Moreover, it was observed that the entire specimen was almost "damage-free" at 2% design drift when "rocking" edge columns were used. Yielding of the replaceable energy dissipating O-connectors, spalling of the concrete cover in the wall (end columns) and cracking of the fiber grout layer were deemed repairable. Immediate re-occupation of the rocking-wall structure would be feasible after a seismic event.

10.2.2 Behaviors of the Structural Components

10.2.2.1 PreWEC System

Because there were many more strain gages installed in the wall in PFS2, several assumptions of rocking walls were examined using the instrumentation. First, it was proven that a disturbed region existed near the wall base where the concentrated compression forces spread out. Second, the strain gage readings did not conflict with the assumption that the height of the disturbed region was equal to the width of the wall, which was proposed based on St. Venant's Principle. Third, the assumption found in existing literature (Restrepo and Rahman 2007) that constant compressive strains were distributed over a distance equivalent to the N.A. depth of the wall above the foundation was not accurate.

Some damage occurred to the ends of the fiber grout layer in PFS2. It was believed that the damage was caused by inclined shear forces that were generated by combining the concentrated compression forces and horizontal shear forces near the corners of the end columns. Damage to the fiber grout layer beneath the end columns was also observed. It was believed that the wood spacers used for blockout around the PT rods caused discontinuity in the fiber grout layer and contributed to the damage.

Crushing of the concrete core occurred at the base of the end columns under combined gravity loads, PT clamping forces and resistances of O-connectors when the specimen was loaded to 4% drift. The damage was attributed to the following causes. First, the quality of the concrete in the end columns was poor due to consolidation issues encountered during fabrication. Second, the PT force provided by the PT threaded rods

increased by 45% when the end columns were displaced to 4% drift, which greatly increased the compression forces concentrated at the corners of end columns. It was noteworthy that the end columns were only two-story high in the test to simplify the construction. If it was six-story high as scaled from the prototype structure, it was believed that the PT increase would be much smaller because the unbonded length of the threaded rod would be greatly extended.

The overall length of the PT rods was reduced when the spalling of concrete and the loss of fiber grout beneath the end columns occurred. Because the elongation of the PT rods was relatively small due to relatively small end column widths, the decrease of the overall length caused a great reduction of the PT clamping forces in the end columns. It was observed that one of the two end columns lost contact with the fiber grout and was picked up by the wall during the test. It was noteworthy that the gravity loads sustained by the end columns were simulated by the PT forces in the threaded rods in the test. In practice, the end columns might not be picked up by the wall because of the existence of the sustained gravity loads, even after the PT clamping force was lost. However, even in the prototype building, PT clamping forces are required to facilitate self-centering of the end columns. Real gravity load effects in the prototype building could generate overturning in the end columns due to the P-delta effect.

10.2.2.2 Precast Floor

The precast floor performed very well throughout the test. Little damage occurred to the precast planks, the plank-to-plank connections (JVI Mini V) and the wall-floor connections (BS Italia). Test data showed that the connector stud of BS Italia connections successfully slid up to 1.5 in. along the slotted insert in the wall at 5% drift, when the shear force transferred by each BS-Italia connection (9 kip) was about one third of its nominal shear capacity. It was noteworthy that the past component test of the BS Italia connections (Watkins 2016) indicated that they were only able to slide 1 in. along the slotted insert when the transferred shear force was 26 kip. It appeared that the connection was capable of sliding a larger distance when the transferred force of the BS-Italia connection was smaller.

Yielding of the strap plates across beam-plank connections did not occur until 3% drift. The yielding was mainly caused by the rotation demands on the strap plates that were generated due to the rocking of end columns. None of the strap plates fractured during the test. It was recommended that cast-in-place (CIP) composite-topping slab and CIP topping slab should be used for precast buildings in regions of moderate to high seismicity in ACI 318-11. The precast untopped slabs are not recommended in buildings assigned to Seismic Design Categories D, E, and F according to current design codes. The excellent behaviors of the precast untopped slab observed in the test provided proof of its potential application in high seismic regions.

10.2.2.3 Edge Columns

When the edge columns were laterally displaced with the nuts of the bolts not being tightened at the base, a concentrated opening formed between the base plate and the grout layer. The edge columns behaved like “rocking columns.” No cracks occurred in the edge columns when PFS2 was laterally displaced to 2% drift. After the base plates of the edge columns were fixed to the base block through tightening the bolts, it was found that rotation of the base plates still existed in the test due to the stretching of the rods. The rotation of the base plates contributed 26% of the total rotation at the column base at 2% drift. Cracking and flaking of the concrete in the edge columns was observed to occur. Early fracture of the weld between the longitudinal rebar and the base plate was observed during the test. The damage was believed to have been mainly caused by a weld of poor quality generated due to difficulty in welding the reinforcement to the base plates in the precast columns. It is recommended that four rods be prewelded to the base plate and subsequently inserted into the column cage prior to casting to avoid the difficulty in welding within the cage; similar to the technique used to attach the angles to the wall corners. Welding within the cage was further complicated in the edge columns because strain gages were located in the vicinity of the welds. Compared with fixed-base edge columns, rocking edge columns had the advantage of “damage-free.”

10.3 Conclusions from Comparison of PFS1 and PFS2 – Chapter 8

In PFS1, four short steel tubes were used as the end columns and O-connectors were directly welded to the steel tubes. In PFS2, two reinforced concrete precast columns were used as the end columns and O-connectors were welded to the steel plates pre-embedded in the precast end columns. Although the types of PreWEC systems used were different, the base moment of the PreWEC system in PFS1 was only 4% larger than that in PFS2 according to the design. On the basis of the PreWEC systems with similar strengths, different floor systems and wall-floor connections were used in PFS1 and PFS2 to maximize and minimize the wall-floor interaction. A direct comparison of the two specimens was conducted to investigate the seismic performance of rocking-wall structures under these two extreme conditions in Chapter 8.

10.3.1 Stiffness and Strength

Before the rocking walls uplifted, the initial secant stiffness of PFS1 was about 2.2 times that of PFS2. Because the two end columns were placed next to the ends of the wall in PFS2, the width of the wall in PFS2 was about 25% smaller than that in PFS1, causing the smaller initial stiffness.

At the same drift levels, the base moment of PFS1 was much larger than that of PFS2. Gravity load transfer paths and the constraint effect from surrounding structure were the two key factors contributing to the difference.

The gravity loads from the floors were directly transferred to the wall in PFS1, while they were transferred to the two end columns in PFS2 because of the usage of the vertical movement isolation floor connections to the wall. The width of the wall (90 in.) in PFS1 was much larger than that of the end columns (10 in.) in PFS2. The moment arm of the gravity loads in PFS1 was much larger than that in PFS2, which provided a much larger resisting moment and greatly increased the strength of PFS1. Because the width of the end columns was relatively short, the gravity loads might generate overturning moments in the end columns due to P-delta effects, which would actually reduce the resisting moment of the PreWEC system.

In PFS1, the resisting moments generated by the surrounding structure included the concentrated moments at the mega beam-wall and floor-wall connections, the resisting moments generated by the shears in the mega beams and the floor, and the resisting moments generated by the axial forces in the mega beams and the floor. They contributed to the strength of PFS1. On the other hand, because the steel tubes and the precast floor in PFS2 were pinned-pinned connected at the ends, few resisting moments and shear forces were generated. Only the resisting moments generated by the axial forces in the steel tubes of the mega-truss and the floor contributed to the strength of PFS2, which were relatively small.

Compared to the rocking-wall structures using rigid wall-floor connections, the stiffness and strength of the rocking-wall structures using special precast wall-floor connections were smaller. To limit the lateral deflections and provide sufficient strength, it was believed that larger PT forces in the wall, wall panels with a larger length, or more PreWEC systems would be required as the lateral resisting systems in rocking-wall structures using special precast wall-floor connections.

10.3.2 Self-centering Performance

Both specimens demonstrated reasonable self-centering performance. Although the self-centering capacity of the wall in PFS1 was larger because of the contribution from the gravity loads carried by the wall, the self-centering performance of PFS1 was inferior to that of PFS2 due to the additional constraint from the damaged surrounding structure.

10.3.3 Damage to the Structures

10.3.3.1 PreWEC System

Little damage occurred to the wall corners in both specimens. Cracking and fracture of the O-connectors were observed only after 4% drift in both tests, indicating that they were capable of providing stable energy dissipation until high drift levels.

The steel tubes that were used as end columns remained elastic in PFS1. A great amount of damage occurred to the RC end columns in PFS2 due to the large compression demand and the concrete of poor quality in the end columns.

10.3.3.2 Fiber Grout Layer

In PFS1, minor damage occurred to the fiber grout that was confined in the pocket of the base block. In PFS2, the fiber grout was directly poured above the base block. A great amount of damage to the fiber grout beneath the end columns was observed, which caused the severe loss of the clamping PT forces in the end columns.

10.3.3.3 Floor Systems

Localized damage occurred to the CIP floor at the wall-floor connections in PFS1. Other than the severe localized damage near the wall tips, most cracks in the floor subsequently closed upon unloading because of the residual PT forces provided by the PT strands, which remained elastic in the test. The floor was believed to be reusable after local repair. On the other hand, little damage occurred to the precast planks, the precast wall-floor connections (BS-Italia), the plank-to-plank (JVI Mini V) and the strap plates across plank-beam connections in PFS2. The precast floor was believed to be reusable immediately after a seismic event.

10.3.3.4 Edge Columns

Damage to the CIP edge columns was observed from the beginning of the test in PFS1. Damage to the precast edge columns in PFS2 was observed only after the steel base plates of the columns were tightened to the base block. The additional axial forces generated by the CIP floor and the steel mega beams had a non-negligible impact on the moment resistance of the edge column in PFS1. The deformation demand on the edge columns in PFS2 was smaller than that in PFS1 due to the rigid body rotation of the steel base plate. Additional axial tensile forces would be generated in the edge column that was adjacent to the uplifted side of the wall, which reduced the moment resistance of the edge column. The impact was not significant in PFS2 because few axial forces were generated by the pinned-pinned connected precast floor and steel tubes.

10.4 Design Recommendations of Rocking-Wall Structures – Chapter 9

10.4.1 Selection of Wall-Floor Connections

The comparison of PFS1 and PFS2 clearly proved that the performance of rocking-wall structures was greatly impacted by the interaction between PreWEC systems and surrounding structures, which was mainly affected by the selection of the type of wall-floor connections. Pros and cons existed for the rocking-wall structures with either rigid wall-floor connections or special precast isolation connections as summarized below.

The advantages of rocking-wall structures with rigid wall-floor connections include:

- The gravity loads sustained by the wall contribute to the strength of the PreWEC system; the constraint effect from surrounding structures further increases the strength of the entire structure
- The gravity loads sustained by the wall contribute to the self-centering capacity of the entire structure
- The CIP construction techniques are typical and acceptable in regions of moderate to high seismicity

The disadvantages include:

- Damage to the surrounding structures is not negligible and impaired the self-centering performance of the entire structure; repair work is required after seismic events
- Advanced structural analysis is required to determine the resisting forces generated by the constraint effect from surrounding structures
- The contribution from the gravity loads to the strength of the structure might be nullified during vertical seismic excitations
- The construction speed may be slower than that of an entire precast system

For rocking-wall structures with special precast isolation connections, the advantages include:

- Damage to the surrounding structures is negligible; fast reoccupation of the structure is possible after seismic events

- Performance of the entire rocking-wall structure is more predictable because of the elimination of wall-floor interaction
- The construction speed is fast because most of the structural members are precast

The disadvantages include:

- Additional gravity load transfer paths are required in the structures that might reduce the flexibility in floor-plan layout and space planning
- Because the gravity loads were not sustained by the wall and contributed little to the strength, the initial PT force required in each wall might be very large and more PreWEC systems might be required for the lateral resisting systems
- The performance of the entire structure relies on the special precast wall-floor connections; experimental tests of the connections under reasonable loading conditions are required to decide the reliable functionality of the connections
- The usage of precast construction techniques is limited in regions of moderate to high seismicity by current codes

Although it would be arbitrary to claim one type of connection was superior to the other, the performance of rocking-wall structures evaluated above would be beneficial for the practicing engineers to make the selection based on the unique conditions associated with each project.

10.4.2 Self-Centering Criterion

The residual drifts of both specimens were reasonably small in the tests. It demonstrated that the self-centering performance of rocking-wall structures would be realized if they were properly designed, no matter which type of wall-floor connections were used.

A general criterion, which accounted for the impact from gravity load transfer path and constraint effect from surrounding structure, was proposed to ensure the self-centering of rocking-wall structures. The criterion shown below was applicable when either type of wall-floor connection system is used in rocking-wall structures.

$$\frac{M_{PT\_i} + M_N + M_W}{\alpha_0 M_E + \beta_0 M_S} \geq 1 \quad (10.1)$$

Where M_{PT_i}= moment provided by initial effective PT force; M_N= moment provided by the gravity loads sustained by the wall (self-weight excluded); M_W= moment provided by the self-weight; α_0= overstrength factor for the energy dissipating elements; M_E= maximum moment provided by the energy dissipating elements; β_0= overstrength factor for the surrounding structural system; M_S= maximum moment provided by surrounding structure.

The criterion should be examined at the maximum residual drift limits, which was determined based on performance requirements of the rocking-wall structures. To be conservative, the moment provided by initial effective PT force and maximum moment that could be developed by energy dissipating elements and surrounding structure should be used in the criterion.

10.4.3 Design of the PreWEC Systems

10.4.3.1 Rocking Wall Panels

Because the tensile strains developed in the walls were relatively small, the amount of longitudinal reinforcement in the wall could be selected based on the minimum required shrinkage and temperature reinforcement (Section 7.12 of ACI 318-11) and minimum required shear reinforcement in the wall (Section 21.9.2.1 of ACI 318-11).

In rocking-wall structures with rigid wall-floor connections, the wall-floor interaction should be considered when deducing the base shear demand on the wall, which was used to design shear reinforcement in the wall. Shear sliding of the rocking walls should also be examined to prevent the distortion of the unbonded PT strands in the wall.

When the grout beneath the wall was weaker than the concrete in the wall, the steel confinement provided little values at small drifts, but it took effect at large drifts. It was recommended that some steel confinement should still be placed in the wall corners. When the grout beneath the wall was stronger than the concrete in the wall, a proper amount of the steel confinement should be placed in the wall corners. Design

recommendation of the steel confinement was provided, including the height, the width and the required amount in the wall corners.

10.4.3.2 End Columns

To reduce the damage to the end columns, it was recommended that the lower bound PT forces should be applied to the end columns. Both force and moment equilibrium conditions should be considered to determine the lower bound PT forces in the end columns. To avoid the end columns of the PreWEC system from being picked up, which would nullify the O-connectors and cause damage to secondary structural elements, special detailing should be used around the edge column base. Steel channels can be placed at the corners of the column for protection.

10.4.4 Selection and Placement of Fiber grout

The N.A. depth of the rocking wall was suggested to be restricted to within 15% of the wall length to ensure hysteretic response stability and geometrical stability (Rahman and Restrepo 2000). A larger N.A. depth is associated with a larger compression force, and consequently, the wall is more susceptible to buckling. It was found from theoretical deduction that having a grout layer stronger or weaker than the concrete in the walls did not have a great impact on the overall behavior of the wall when the N.A. depth of the wall was only a small fraction of the length of the wall. Under this circumstance, it was more economical to select the grout that has similar strength to the confined concrete.

When the grout was placed in a pocket in the foundation, the grout would remain in the pocket even after it was plastified or crushed. Abrupt change in the N.A. depth of the wall or sudden drop in the strength of the wall was prevented. When the fiber grout was directly poured above the foundation to simplify the construction, it was essential to select ductile materials for the grout bearing (e.g. fiber grout). Small spacers used to blockout grout around the PT strands or the dowel rebar should be made from stiff materials to reduce the discontinuity in the grout. It was also recommended that dowel bars should be embedded in the wall and placed across the wall/foundation interface to prevent the out-of-plane movement of the wall.

When the end columns of the PreWEC systems are used to sustain the gravity loads in rocking-wall structures, it is recommended to place the grout in the pocket beneath the end columns, which increases its ductility and prevents the severe loss of the PT clamping forces caused by the split of the grout.

10.4.5 Rigid-connected Surrounding Structures

Connecting the CIP floor towards the center of the wall was an effective way to alleviate some of the damage to the slab without changing geometric dimensions of the structure. To prevent yielding of the strands in the unbonded PT slab caused by large floor deformations, it was recommended to lightly prestress the floor strands in the rocking-wall structures. Both the longitudinal and transverse resisting moment capacity of the floor at the wall-floor connections should be considered when analyzing the constraint effect of the floor on the rocking wall in the design.

10.4.6 Vertically Isolated Surrounding Structures

The special precast wall-floor connections that isolated the floor from the vertical movement of the wall were the key components to realize the expected performance of rocking-wall structures. The number of wall-floor connections should be determined based on the reliable shear and tension capacities under which floor system is able to be fully isolated from the uplift of the wall, while reliably transferring the lateral forces into the wall. Specific component tests should be conducted by the manufacturers to obtain these design parameters of the product.

The precast wall-floor connections should be placed toward the wall center to limit the required range of vertical travel the connector must slide under cyclic loading. Because the relative vertical sliding of the connector stud is always in the same direction (towards the bottom of the channel) during cyclic loading, the connector of the special connection affixed to the floor (e.g. V-shape plate of BS Italia connections) should be offset to be close to the top of the channel in the wall to maximize its available stroke. Materials of low friction coefficient should be coated on the connector stud. The slotted insert

embedded in the wall should be thickened and made from hardened steel to avoid deformations/dents.

Steel straps at plank-beam connections might yield due to the rotation demand caused by the rotation of the end columns and edge columns. Equations were proposed to estimate the rotations and the associated moment demands on the strap plates.

10.5 Recommendations for Future Research

The two large-scale tests of rocking-wall structures presented in this dissertation provided valuable information to investigate the interaction between rocking-wall systems and surrounding structures. During the course of the investigation, some issues were encountered and deserved further studies, as summarized in the following.

- Because the gravity loads sustained by the end columns were emulated by PT forces in the end columns, the P-delta effect on the end columns was not experienced in the test. Moreover, the concrete in the end columns was poor due to construction issues and the end columns were only two-story high in the test. The actual performance of the end columns was not well evaluated by the test. Because the end columns provided a unique gravity load transfer path to rocking-wall structures using special precast wall-floor connections, it is recommended to conduct more experimental and numerical simulations of the end columns to further investigate their behavior.
- The method of "Adjusting stress-strain responses of PT strands" to simulate the unbonded PT slab is justified in this dissertation. The method is applicable in most of the commercial software for finite element analysis. Parametric studies can be conducted to investigate the optimal span-to-depth ratio, reinforcement ratio and initial prestress of the strands in the unbonded PT slab in rocking-wall structures.
- Due to the limitation of the test program, the behaviors of the rocking-wall structures under biaxial loading were not well emulated. To study the actual out-of-plane behaviors, it is recommended to conduct experimental and numerical

studies of rocking-wall structures that include floor slabs of all stories and realize the proper boundary conditions of the structures.

Bibliography

Aaleti, S., and Sritharan, S. (2009). "A simplified analysis method for characterizing unbonded post-tensioned precast wall systems." *Eng. Struct.*, 31(12), 2966–2975.

Aaleti, S., and Sritharan, S. (2011). Performance Verication of the PreWEC Concept and Development of Seismic Design Guildelines. *ISU-ERI-Ames Report ERI-10347*, Department of Civil, Construction and Environmental Engineering, Iowa State University, Ames, IA

ABAQUS user manual 6.11. Dassault Systems, Inc. 2011

ACI (American Concrete Institute) (2005). "Building code requirement for reinforced concrete." *ACI 318-05,* Farmington Hills, MI.

ACI (American Concrete Institute) (2011). "Building code requirement for reinforced concrete." *ACI 318-11,* Farmington Hills, MI.

ACI (American Concrete Institute) (2011). "Guide for Design of Slab-Column Connections in Monolithic Concrete Structures" *ACI 352.1R-11,* Farmington Hills, MI.

Belleri, A., Schoettler, M.J., Restrepo, J.I., and Fleischman, R.B. (2014). "Dynamic Behavior of Rocking and Hybrid Cantilever Walls in a Precast Concrete Building." *ACI Struct. J.*, 111(3), 661–671.

Belleri, A., Torquati, M., and Riva, P. (2013). "Finitie Element Modeling of 'Rocking Walls.'" *Proc., 4th ECCOMAS Thematic Conference on Computational Methods in Stuctural Dynamics and Earthquake Engineering*, Kos Island, Greece.

Brian, J.S., and Kurama, Y. (2009). "Design of hybrid precast concrete walls for seismic regions." Structures Congress 2009: Don't Mess with Structural Engineers-Expanding Our Role, *ASCE*, Reston, VA, 1–10.

Brian J.S., Kurama Y.C. and McGinnis, M. J. (2011). "Design and Measured Behavior of a Hybrid Precast Concrete Wall Specimen for Seismic Regions." *J. Struct. Eng.*, 137(10),1052-1062

Burns, N.H., Charney, F.A., Vine, W.R. (1978). Tests of one-way posttensioned slabs with unbonded tendons. *PCI J.* (September–October), 66–83.

Chang, G.A., and Mander, J.B. (1994). Seismic Energy Based Fatigue Damage Analysis of Bridge Columns: Part 1- Evaluation of Seismic Capacity. *Technical Report NCEER-94-0006*, Department of Civil Engineering, State University of New York at Buffalo, Buffalo, NY

Ellobody, E. and Bailey, C. G. (2009), "Modelling of unbonded post-tensioned concrete slabs under fire conditions" *Fire Safety J.*, Vol. 44, 159-167.

Erkmen B. and Schultz A. E. (2007). "Self-centering behavior of unbonded precast concrete shear walls" *Earthquake Resistance and Engineering Structures VI*, 185-194.

Gavridou, S. (2015). "Shake Table Testing and Analytical Modeling of a Full-Scale, Four-Story Unbonded Post-Tensioned Concrete Wall Building," *Ph.D. thesis*, University of California, Los Angeles, United States

Henry, R. S. (2011). "Self-centering Precast Concrete Walls for Buildings in Regions with Low to High Seismicity," *Ph.D. thesis*, University of Auckland, Aucland, New Zealand

Henry, R.S., Sritharan, S. and Ingham J.M. (2016). "Finite element analysis of the PreWEC self-centering concrete wall system" *Eng. Struct.*, 115, 28–41.

Henry, R.S., Sritharan, S. and Ingham J.M. (2016). "Residual drift analyses of realistic self-centering concrete wall systems" *Earthquakes and Structures*, 10(2), 409–428.

Holden, T. , Restrepo, J. and Mander, B.J. (2003). "Seismic Performance of Precast Reinforced and Prestressed Concrete Walls." *J. Struct. Eng.*, 129(3),286-296

Housner, G. W. (1963) Behavior of inverted pendulum structures during earthquakes. *Seismological Society of America - Bulletin*, 53(2), 403-417.

Huang, Y. (2012). "Finite Element Method for Post-Tensioned Prestressed Concrete Structures," *Ph.D. thesis*, University of Oklahoma, Norman, Oklahoma

ITG. (2007). Acceptance Criteria for Special Unbonded Post-Tensioned Precast Structural Walls Based on Validation Testing and Commentary. *ACI ITG-5.2-09*, Farmington Hills, MI.

ITG. (2009). Requirements for Design of a Special Unbonded Post-Tensioned Precast Shear Wall Satisfying ACI ITG-5.1 and Commentary. *ACI ITG-5.2-09*, Farmington Hills, MI.

Kurama, Y. C. (2002). "Hybrid post-tensioned precast concrete walls for use in seismic regions" *PCI J.*, 47(5), 36-59.

Kurama, Y., Sause R., Pessiki S., and Lu L.W. (1999). "Lateral Load Behavior and Seismic Design of Unbonded Post-Tensioned Precast Concrete Walls" *ACI Struct. J.*, 96(4), 622–632.

Kwak, H. G. and Kim, J. H. (2006), "Numerical models for prestressing tendons in containment structures" *Nuclear Engineering and Design*, Vol. 236, 1061-1080.

Lee, J., and Fenves G. L. (1998). Plastic-Damage Model for Cyclic Loading of Concrete Structures. *Journal of Engineering Mechanics*, vol. 124, no.8, pp. 892–900, 1998.

Lou, T. J., Lopes, S.M.R. and Lopes, A. V. (2013), "Nonlinear and thime-dependent analysis of continuous unbonded prestressed concrete beams" *Computers and Structures*, Vol. 119, 166-176.

Lubliner J., Oliver J., Oller S., and Oñate E. (1989). A Plastic-Damage Model for Concrete. *International Journal of Solids and Structures*, vol. 25, pp. 299–329, 1989.

Mander, J. B., Priestley, M. J. N., and Park, R. (1988) Theoretical stress-strain model for confined concrete. *J. Struct. Eng.*, 114(8), 1804-1826.

Moroder, D., Sarti, F., Palermo, A., and Pampanin, S. (2014). Experimental investigation of wall-to-floor connections in post-tensioned timber buildings. *NZSEE Conference*, 2014.

Nagae,T., Kenlchl, T., Wallace J., Ghannoum, W., Moehle, J. SR. Design and Instrumentation of the 2010 E-Defense Four-Story Reinforced Concrete and Post-Tensioned Concrete Buildings. 2011.

Nagae T, Tahara K, Fukuyama K, Matsumori T, Wallace J. Test Results of Four-Story Reinforced Concrete and Post-Tensioned Concrete Buildings : The 2010 E-Defense Shaking Table Test. *15th WCEE*, 2012.

Paulay, T., and Priestley, M. J. N. (1992). Seismic design of reinforced concrete and masonry buildings, Wiley, New York.

PCI (Precast Concrete Institute). (2004). "PCI Design Handbook: Precast and Prestressed Concrete." Chicago, IL.

Perez, F. K. (2004). "Experimental and Analytical Lateral Load Response of Unbonded Post-Tensioned Precast Concrete Walls" *Ph.D. thesis*, Lehigh University, Bethlehem, Pennsylvania

Perez, F.J., Sause R., and Pessiki S. (2007). "Analytical and Experimental Lateral Load Behavior of Unbonded Posttensioned Precast Concrete Walls" *J. Struct. Eng.*, 133(11), 1531-1540

Prakash, G.H. Powell, DRAIN-2DX-Version 1.02 – User Guide, *Report No. UCB/SEMM-93/17*, Civil Eng. Dept., University of California at Berkeley, CA, 1993

Priestley, M. J. N., Sritharan, S., Conley, J. R., and Pampanin, S. (1999). "Preliminary Results and Conclusions From the PRESSS Five-Story Precast Concrete Test Building." *PCI J.*, 44(6), 42–67.

Rahman, M. A., and Sritharan, S. (2006). "An Evaluation of Force-based Design vs. Direct Displacement-based Design of Jointed Precast Post-tensioned Wall Systems." *Earthquake Engineering and Engineering Vibration*, 5(2), 285-296

Restrepo, J. I., and Rahman, M. A. (2007). "Seismic Performance of Self-Centering Structural Walls Incorporating Energy Dissipators." *J. Struct. Eng.*, 133(11),1560-1570

Roh, H. and Reinhorn, A.M. (2009). “Analytical modeling of rocking elements” *Eng. Struct.*, 31, 1179 –1189.

Schoettler, M. J., Belleri, A., Zhang, D., Restrepo, J. I., and Fleischman, R. B. (2008). “Preliminary results of the testing for the development of a diaphragm seismic design methodology.” *PCI J.*, 54(1),100-124.

Schoettler M.J. (2010). “Seismic Demands in Precast Concrete Diaphragms,” *Ph.D. thesis*, University of California, San Diego, San Diego, CA

Schultz, A.E. and Magana, R.A. “Seismic Behavior of Connections in Precast Concrete Walls.” Paper No. SP 162-12, Mete A. Sozen Symposium (273-311), *ACI SP 162*, ACI, Farmington Hills, MI, 1996

Smith, B. J., Kurama, Y. C., and Mcginnis, M. J. (2011). “Design and Measured Behavior of a Hybrid Precast Concrete Wall Specimen for Seismic Regions.” *J. Struct. Eng.*, 137(10), 1052–1062.

Sritharan, S., Aaleti S., Henry R.S., Liu K.Y. and Tsai K.C. (2015). “Precast concrete wall with end columns (PreWEC) for earthquake resistant design” *Earthquake Engineering and Structural Dynamics*, 44(12), 2075–2092.

Tanyeri A, Moehle J, Nagae T. Seismic Performance and Modeling of Post-Tensioned, Precast Concrete Shear Walls. *PCI J.* 2013;65:1–15.

Thomas, D.J. and Sritharan, S. (2004) An evaluation of seismic design guidelines proposed for precast jointed wall systems. *ISU-ERI-Ames Report ERI-04643*, Department of Civil, Construction and Environmental Engineering, Iowa State University, Ames, IA

Tuna, Z., Gavridou, S., and Wallace, J. (2012). “2010 E-Defense Four-Story Reinforced Concrete and Post-Tensioned Buildings–Preliminary Comparative Study of Experimental and Analytical Results.” *Proc., 15th World Conference on Earthquake Engineering Conf.*, Lisboa, Portugal

Vecchio, F. J., Gauvreau P., and Liu, K. (2006). “Modeling of Unbonded Post-Tensioned Concrete Beams Critical in Shear” *ACI Struct. J.*, 103(1), 57–64

Watkins, J., Sritharan, S., and Henry, R.S. (2014). An Experimenal Investigation of a Wall-to-Floor Connector for Self-Centering Walls. *10th U.S. National Conference on Earthquake Engineering*, Anchorage, Alaska

Wood, S., Wright, J., and Moehle, J. (1987). “The 1985 Chile earthquake, observations on earthquake-resistant construction in Vina del Mar. ” Civil Engineering Studies, *Structural Research Series No. 532*, Univ.of Illinois, Urbana, Ill.

Zhang, Y. F. and Wang, Z.H. (2000). “Seismic Behavior of Reinforced Concrete Shear Walls Subjected to High Axial Loading.” *ACI Struct. J.*, 97(5), 739–750.

Appendix A: Details of the Props

Props were used in PFS1 and PFS2 to simulate a boundary condition case where adjacent frame lines to the rocking wall frame (test specimen) would be columns. The props, as columns, restricted the uplift of the floor slab. Some of the tests on PFS1 and PFS2 were run with props to simulate the condition of the adjacent column frame line, and some tests were run without props. In the latter case, the free edge boundary condition simulated adjacent rocking wall frame lines rocking in phase. Fig. A-1 through Fig. A-8 show the prop details.

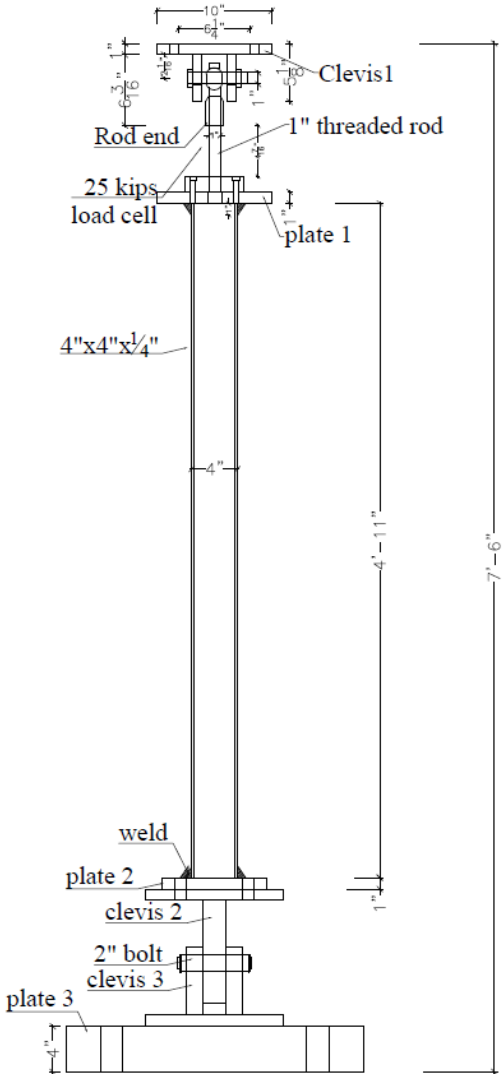

Fig. A-1 Detail of the props

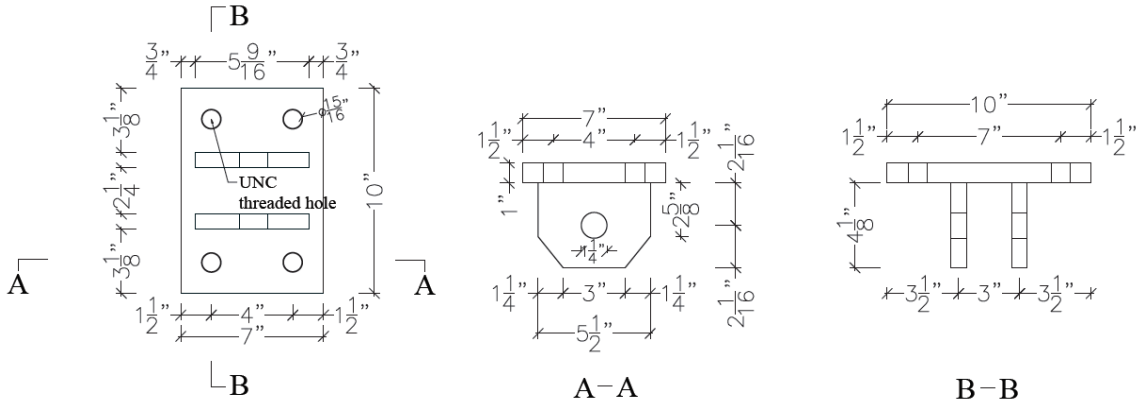

Fig. A-2 Detail of the Clevis1

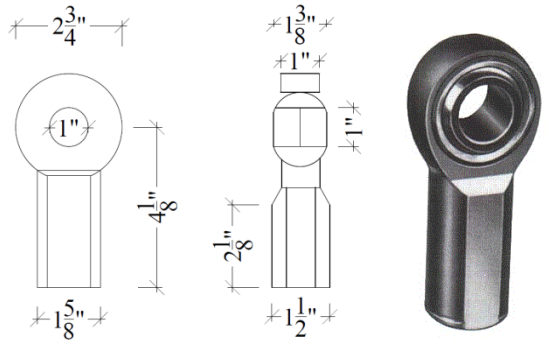

Fig. A-3 Rod end (Aurora Company product kw-16-1)

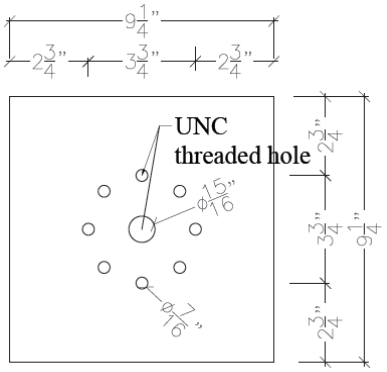

Fig. A-4 Detail of Plate 1 (connected pipe and 1” strut)

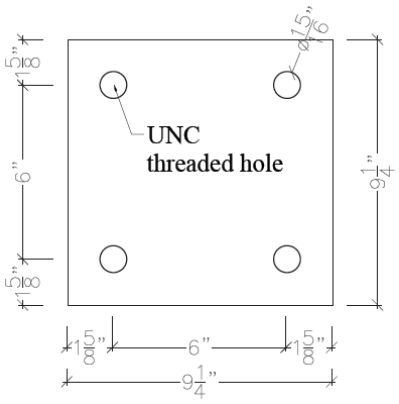

Fig. A-5 Detail of Plate 2 (connected pipe and clevis 2)

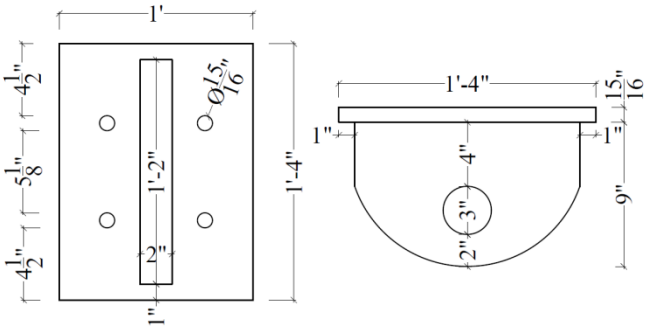

Fig. A-6 Detail of Clevis 2

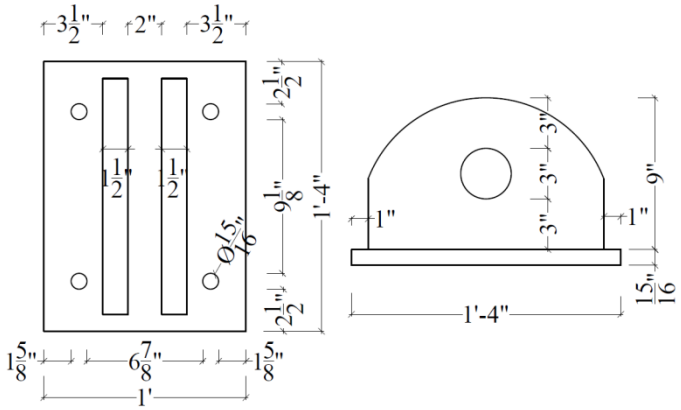

Fig. A-7 Detail of Clevis 3

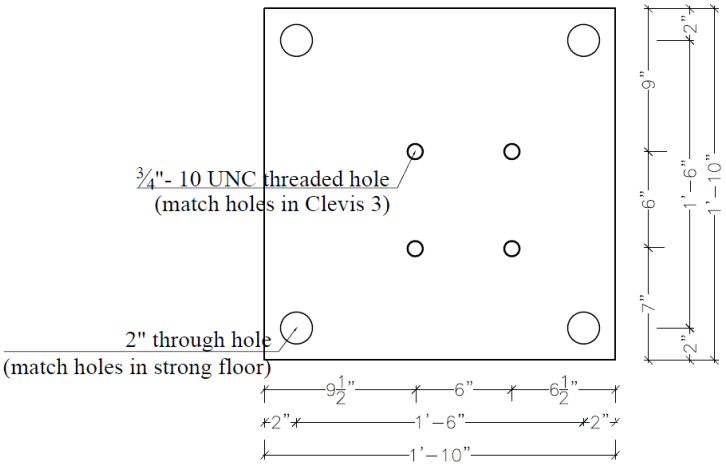

Fig. A-8 Detail of Plate 3 (4 in. thick)

Appendix B: Base Moment Resistance of the Rocking-Wall Systems

This appendix describes calculation of the base moment resistance of the rocking-wall system for PFS1 and PFS2. In the case of PFS1, the base moment capacity was considered with and without the effect of the gravity load on the wall in Appendix B1 and B2, respectively. In the case of PFS2, the base moment capacity was considered with gravity load sustained by the end columns in Appendix B3.

The following assumptions were made when calculating the base moment resistance of the rocking-wall systems:

(1) The resistance of the O-connectors was related to the relative vertical deformation of the O-connectors. The following relation equations are obtained from the component tests (Henry 2011):

When $\Delta_O < 0.15$ in., the O-connectors were elastic: $R_O = 43.3\Delta_O$

When $\Delta_O \geq 0.15$ in., the O-connectors were hardening: $R_O = 6.5 + 0.87(\Delta_O - 0.15)$

When $\Delta_O \geq 3.6$ in., the O-connectors reached a plateau: $R_O = 9.5\ kips$ It was noteworthy that the dimensions of the O-connectors used in PFS1 were similar to those in the component test mentioned above. These relation equations were used during the design.

(2) In PFS1, the location of the O-connections was 8.5 in. away from the end of the wall. In PFS2, the location of the O-connections was 2.5 in. away from the end of the wall.

(3) The strength of the Gr 270 strands was (PCI 2008):

When $\varepsilon_{strand} < 0.0085$, $\sigma_{strand} = 29000\varepsilon_{strand}$

When $\varepsilon_{strand} > 0.0085$, $\sigma_{strand} = 270 - \frac{0.04}{\varepsilon_{strand} - 0.007}$

(4) Gr 270 1/2 in. diameter 7-wire strands were used in both tests. Five strands were used in the rocking wall of PFS1 and seven were used in PFS2. The length of the PT strands in both PFS1 and PFS2 was 280 in.

(5) Nominal strength of the unconfined concrete in the walls in PFS1 and PFS2 was 6 ksi. Nominal strength of the unconfined concrete in the end columns in PFS2 was 5 ksi.

Strength of the confined concrete was taken as 1.35 times the unconfined concrete strength. Equivalent compressive stress blocks were assumed at the corners of the walls and at the corners of the end columns. The coefficient 1.35 and the coefficients of the stress blocks α and β were calculated in the following (Aaleti 2011):

$$\alpha = \frac{2\times(0.98 - 0.0022f_c')r}{r - 1 + 2^r}; \beta = 0.96;\ r = 1.24 + 0.01\times\frac{(f_c' - 4.0)}{0.25}$$

$$f_c' = 6\ ksi, r = 1.24 + 0.01\times\frac{(6-4.0)}{0.25} = 1.32;\ \alpha = \frac{2\times(0.98 - 0.0022\times6)\times1.32}{1.32 - 1 + 2^{1.32}}$$

$$\approx 0.91;$$

$$f_c' = 5\ ksi, r = 1.24 + 0.01\times\frac{(5-4.0)}{0.25} = 1.28;\ \alpha = \frac{2\times(0.98 - 0.0022\times5)\times1.28}{1.28 - 1 + 2^{1.28}}$$

$$\approx 0.92;$$

(7) The self-weight of the wall and the top block in PFS1 and PFS2 were:

$$PFS1: W = \rho_G(V_{TB} + V_{WALL}) = \frac{150\times[(25\times99\times26 - 16\times13\times26) + 224\times90\times6]}{12\times12\times12\times1000}$$

$$\approx 16\ kips$$

$$PFS2: W = \rho_G(V_{TB} + V_{WALL}) = \frac{150\times[(25\times99\times26 - 16\times13\times26) + 224\times68\times6]}{12\times12\times12\times1000}$$

$$\approx 13\ kips$$

Where the unit weight of concrete was taken as 150 lbs/ft^3 and the lengths are given in inches.

(8) The gravity load transferred to the wall was 128 kips in PFS1. The same amount of gravity load was evenly transferred to the two end columns adjacent to the wall in PFS2.

(9) Side columns (four steel tubes) were used in PFS1. The steel tubes were pin-connected to the base block, thus they did not contribute to the moment resistance of the rocking-wall system. End columns (two reinforced concrete precast columns) were used in PFS2. The precast columns were clamped to the base block by prestressed threaded rods and behaved like rocking columns. They contributed to the moment resistance of the rocking-wall system and should be included.

B1: PFS1 (gravity load sustained by the wall not included)

In this section, calculations are presented to show that the strands would remain elastic to the design drift of 2% and the nominal moment resistance capacity of the wall at the design drift satisfied the required design moment.

Five strands at an initial prestress of $0.58f_{pu}$ were selected in PFS1. The gravity load sustained by the wall is not considered in this section. Fig. B-1 shows the load distribution in the rocking-wall system. Assuming the N.A. depth of the wall was 5.6 in. at 2% design drift, the elongation of the PT strand was:

$$\Delta_{design\_2\%} = \left(\frac{w_{wall}}{2} - c_{design\_wall}\right) \times \theta = \left(\frac{90}{2} - 5.6\right) \times 0.02 \approx 0.79\ in.$$

The stress of the PT strands at 2% drift was:

$$\sigma_{design\_2\%} = \sigma_{initial} + \frac{\Delta_{design\_2\%}}{L_{strands}} = 0.58f_{pu} + E_{strand}\frac{\Delta_{design\_2\%}}{L_{strands}}$$

$$= 0.58 \times 270 + 29000 \times \frac{0.79}{280} = 238\ ksi < f_{py} = 29000 \times 0.0085$$

$$= 246.5\ ksi$$

The PT strands did not yield at 2% design drift, which satisfied the requirement in ITG-5.2 (ITG 2009).

The relative vertical deformation of each O-connector away from the rotation point was:

$$\Delta_{FO} = \left(w_{wall} - s_{FO} - c_{design\_wall}\right) \times \theta = (90 - 8.5 - 5.6) \times 0.02 \approx 1.52\ in.$$

The vertical resistance from each O-connector away from the rotation point was:

$$R_{FO} = 6.5 + 0.87(\Delta_{FO} - 0.15) = 6.5 + 0.87 \times (1.52 - 0.15) \approx 7.7\ kips$$

The relative vertical deformation of each O-connector adjacent to the rotation point was:

$$\Delta_{NO} = \left(s_{FO} - c_{design\_wall}\right) \times \theta = (8.5 - 5.6) \times 0.02 = 0.058\ in.$$

The vertical resistance from each O-connector adjacent to the rotation point was:

$$R_{NO} = 43.3\Delta_{NO} \approx 2.5\ kips$$

When the axial load applied to the wall (128 kip) was not included, the N.A. depth of the wall was:

$$c_{design\_wall} = \frac{F_{wall-2\%} + W_{wall} + n_{FO}R_{FO} + n_{NO}R_{NO}}{\alpha\beta f'_{cc} t}$$

$$= \frac{238\times5\times0.153 + 16 + 4\times7.7 + 4\times2.5}{0.91\times0.96\times1.35\times6.0\times6} \approx 5.6\ in. = 5.6\ in., O.K.$$

The assumed N.A. depth was valid. The moment resistance of the rocking-wall system about the centroid of the compressive stress block (inverted triangle mark in Fig. B-1) was:

$$M_{design\_wall} = (F_{wall-2\%} + W_{wall})\left(\frac{w_{wall}}{2} - \frac{\beta c_{design\_wall}}{2}\right)$$

$$+ n_{FO}R_{FO}\left(w_{wall} - s_{FO} - \frac{\beta c_{design\_wall}}{2}\right)$$

$$+ n_{NO}R_{NO}\left(s_{NO} - \frac{\beta c_{design\_wall}}{2}\right)$$

$$= (238\times5\times0.153 + 16)\left(\frac{90}{2} - \frac{0.96\times5.6}{2}\right)$$

$$+ 4\times7.7\times\left(90 - 8.5 - \frac{0.96\times5.6}{2}\right) + 4\times2.5\times\left(8.5 - \frac{0.96\times5.6}{2}\right)$$

$$= 10{,}866\ kip - in$$

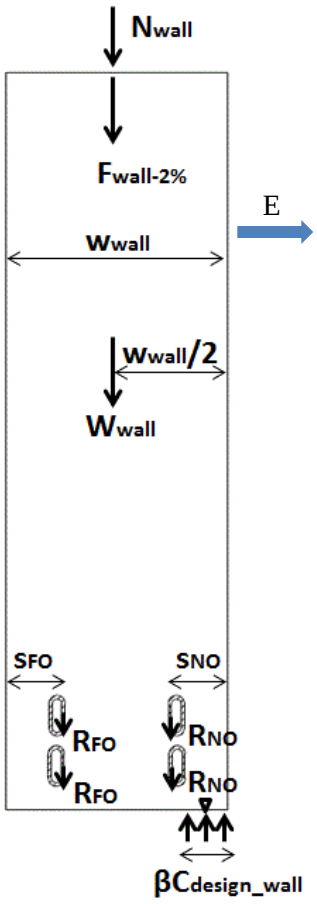

Fig. B-1 Load distribution in the rocking-wall system

B2: PFS1 (gravity load sustained by the wall included)

In this section, the gravity load sustained by the wall is considered.

Assuming the N.A. depth of the wall was 8.5 in. at 2% design drift, the elongation of the PT strand was:

$$\Delta_{design\_2\%} = \left(\frac{w_{wall}}{2} - c_{design\_wall}\right) \times \theta = \left(\frac{90}{2} - 8.5\right) \times 0.02 = 0.73\ in.$$

The stress of the PT strands at 2% drift was:

$$\sigma_{design\_2\%} = \sigma_{initial} + \frac{\Delta_{design\_2\%}}{L_{strands}} = 0.58 f_{pu} + E_{strand} \frac{\Delta_{design\_2\%}}{L_{strands}}$$

$$= 0.58 \times 270 + 29000 \times \frac{0.73}{280} = 232\ ksi < f_{py} = 29000 \times 0.0085$$

$$= 246.5\ ksi$$

The PT strands did not yield at 2% design drift, which satisfied the requirement in ITG-5.2 (ITG 2009).

The relative vertical deformation of each O-connector away from the rotation point was:

$$\Delta_{FO} = \left(w_{wall} - s_{FO} - c_{design\_wall}\right) \times \theta = (90 - 8.5 - 8.5) \times 0.02 = 1.46\ in.$$

The vertical resistance from each O-connector away from the rotation point was:

$$R_{FO} = 6.5 + 0.87(\Delta_{FO} - 0.15) = 6.5 + 0.87 \times (1.46 - 0.15) \approx 7.6\ kips$$

The relative vertical deformation of each O-connector adjacent to the rotation point was:

$$\Delta_{NO} = \left(s_{FO} - c_{design\_wall}\right) \times \theta = (8.5 - 8.5) \times 0.02 = 0\ in.$$

The vertical resistance from each O-connector adjacent to the rotation point was:

$$R_{NO} = 43.3\Delta_{NO} = 0\ kips$$

The axial load applied to the wall was 128 kip and the self-weight of the wall and the top block was 16 kips. The N.A. depth of the wall was:

$$c_{design\_wall} = \frac{F_{wall-2\%} + W_{wall} + N_{wall} + n_{FO}R_{FO} + n_{NO}R_{NO}}{\alpha\beta f'_{cc} t}$$

$$= \frac{232 \times 5 \times 0.153 + 16 + 128 + 4 \times 7.6 + 4 \times 0}{0.91 \times 0.96 \times 1.35 \times 6.0 \times 6} \approx 8.3\ in. \approx 8.5\ in., O.K.$$

The assumed N.A. depth was valid. As shown in Fig. B-1, the moment resistance of the rocking-wall system about the centroid of the compressive stress block was:

$$M_{design\_wall} = (F_{wall-2\%} + W_{wall} + N_{wall}) \left(\frac{w_{wall}}{2} - \frac{\beta c_{design\_wall}}{2}\right)$$

$$+ n_{FO}R_{FO} \left(w_{wall} - s_{FO} - \frac{\beta c_{design\_wall}}{2}\right)$$

$$+ n_{NO}R_{NO} \left(s_{NO} - \frac{\beta c_{design\_wall}}{2}\right)$$

$$= (232 \times 5 \times 0.153 + 16 + 128) \left(\frac{90}{2} - \frac{0.96 \times 8.5}{2}\right)$$

$$+ 4 \times 7.6 \times \left(90 - 8.5 - \frac{0.96 \times 8.5}{2}\right) + 0 = 15{,}509\ kip - in$$

B3: PFS2 (gravity load sustained by the end columns included)

The wall in PFS2 was a nonbearing wall. The gravity loads were carried by the two end columns adjacent to the wall. In this section, calculations are presented to show that the strands would remain elastic to the design drift of 2% and the nominal moment resistance capacity of the wall at the design drift satisfied the required design moment. Seven strands at an initial prestress of $0.65f_{pu}$ were selected in PFS2.

Assuming the N.A. depth of the wall was 6.7 in. at 2% drift, the elongation of the PT strand was:

$$\Delta_{design\_2\%} = \left(\frac{w_{wall}}{2} - c_{design\_wall}\right) \times \theta = \left(\frac{68}{2} - 6.7\right) \times 0.02 = 0.55\ in.$$

The stress of the PT strands at 2% drift was:

$$\sigma_{design\_2\%} = \sigma_{initial\_design} + \frac{\Delta_{design\_2\%}}{L_{strands}} = 0.65f_{pu} + E_{strand}\frac{\Delta_{design\_2\%}}{L_{strands}}$$

$$= 0.65 \times 270 + 29000 \times \frac{0.55}{280} = 232\ ksi < f_{py} = 29000 \times 0.0085$$

$$= 246.5\ ksi$$

The PT strands did not yield at 2% design drift, which satisfied the requirement in ITG-5.2 (ITG 2009).

The relative vertical deformation of each O-connector away from the rotation point was:

$$\Delta_{FO} = \left(w_{wall} - s_{FO} - c_{design\_wall}\right) \times \theta = (68 - 2.5 - 6.7) \times 0.02 \approx 1.18\ in.$$

The vertical resistance from each O-connector away from the rotation point was:

$$R_{FO} = 6.5 + 0.87(\Delta_{FO} - 0.15) = 6.5 + 0.87 \times (1.18 - 0.15) \approx 7.4\ kips$$

The relative vertical deformation of each O-connector adjacent to the rotation point was:

$$\Delta_{NO} = \left(c_{design\_wall} - s_{FO}\right) \times \theta = (6.7 - 2.5) \times 0.02 = 0.08\ in.$$

The vertical resistance from each O-connector adjacent to the rotation point was:

$$R_{NO} = 43.3\Delta_{NO} \approx 3.6\ kips$$

The axial load input to the wall was zero and the self-weight of the wall and the top block was 13 kips. The N.A. depth of the wall was:

$$c_{design\_wall} = \frac{F_{wall-2\%} + W_{wall} + n_{FO}R_{FO} + n_{NO}R_{NO}}{\alpha\beta f'_{cc} t}$$

$$= \frac{232\times7\times0.153 + 13 + 4\times7.4 - 4\times3.6}{0.91\times0.96\times1.35\times6.0\times6} \approx 6.5\ in. \approx 6.7\ in., O.K.$$

The assumed N.A. depth was valid. As shown in Fig. B-2, the moment resistance of the rocking-wall system about the centroid of the compressive stress block (inverted triangle mark in Fig. B-2) was:

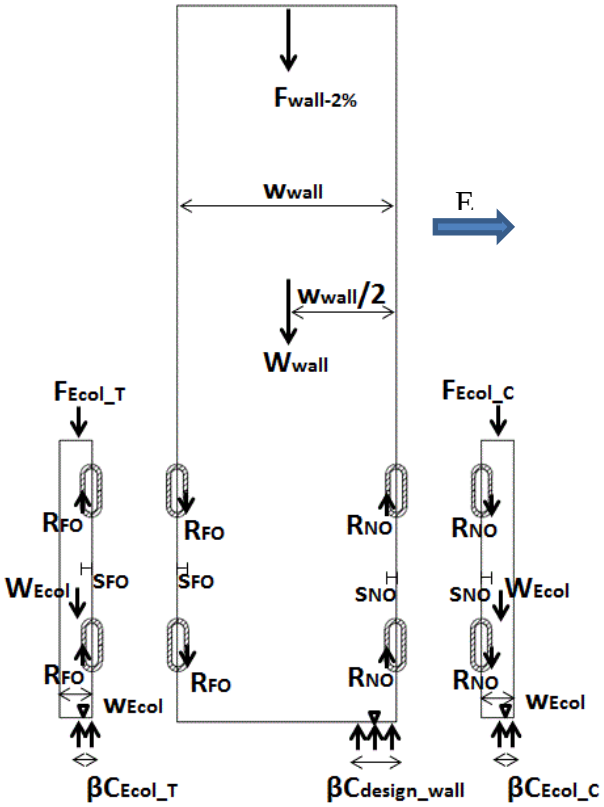

Fig. B-2 Load distribution in the rocking-wall system in PFS2

$$M_{design\_wall} = (F_{wall-2\%} + W_{wall})\left(\frac{w_{wall}}{2} - \frac{\beta c_{design\_wall}}{2}\right) + n_{FO}R_{FO}\left(w_{wall} - s_{FO} - \frac{\beta c_{design\_wall}}{2}\right) + n_{NO}R_{NO}\left(s_{NO} - \frac{\beta c_{design\_wall}}{2}\right)$$
$$= (232\times7\times0.153 + 13)\left(\frac{68}{2} - \frac{0.96\times6.7}{2}\right) + 4\times7.4\times\left(68 - 2.5 - \frac{0.96\times6.7}{2}\right) - 4\times3.6\times\left(2.5 - \frac{0.96\times6.7}{2}\right)$$
$$= 9{,}903\ kip - in$$

As shown in Fig. B-2, other than the moment resistance of the rocking wall and the O-connectors, the two end columns also contributed to the moment resistance of the rocking-wall system. The self-weight of each end column was:

$$W_{Ecol} = \rho_G V_{Ecol} = 150\times10\times6\times78/1728000 \approx 0.4 \text{ kips};$$

The prestress forces in the rods of both end columns were 64 kips, which was used to simulate the gravity load carried by the end column as discussed in detail in Section 3.5.2. The length of the rods was 126-1/2 in. As shown in Fig. B-2, the resisting forces from the O-connectors compressed the end column located near the compressed wall end. Assume the N.A. depth of the right end column was 2.5 in. at 2% drift, the elongation of the prestressed rod was:

$$\Delta_{rod\_2\%} = \left(\frac{w_{Ecol}}{2} - c_{design\_Ecol}\right)\times\theta = \left(\frac{10}{2} - 2.5\right)\times0.02 = 0.05\ in.$$

The stress of the prestressed rod at 2% drift was:

$$\sigma_{rod\_2\%} = \sigma_{initial\_rod} + \frac{\Delta_{rod\_2\%}}{L_{rod}} = \frac{F_{initial\_rod}}{A_{rod}} + E_{rod}\frac{\Delta_{rod\_2\%}}{L_{rod}}$$
$$= \frac{64}{1.045} + 29000\times\frac{0.05}{126.5} \approx 72.7\ ksi < f_{y-rod} = 110\ ksi$$

The prestressed rod did not yield at 2% drift. The N.A. depth of the right end column was:

$$c_{Ecol\_C} = \frac{F_{Ecol\_C} + W_{Ecol} + n_{NO}R_{NO}}{\alpha\beta f'_{cc}t} = \frac{\sigma_{rod\_2\%}A_{rod} + W_{Ecol} + n_{NO}R_{NO}}{\alpha\beta f'_{cc}t}$$

$$= \frac{72.7 \times 1.045 + 0.4 + 4\times 3.6}{0.92\times 0.96\times 1.35\times 5.0\times 6} \approx 2.5\ in. = 2.5\ in., O.K.$$

The assumed N.A. depth was valid. The moment resistance of the right end column about the centroid of the compressive stress block (inverted triangle mark in Fig. B-2) was:

$$M_{Ecol\_C} = \left(F_{Ecol\_C} + W_{Ecol}\right)\left(\frac{w_{Ecol}}{2} - \frac{\beta c_{Ecol\_C}}{2}\right) + n_{NO}R_{NO}\left(w_{Ecol} - s_{NO} - \frac{\beta c_{Ecol\_C}}{2}\right)$$

$$= (72.7\times 1.045 + 0.4)\left(\frac{10}{2} - \frac{0.96\times 2.5}{2}\right)$$

$$+ 4\times 3.6\times\left(10 - 2.5 - \frac{0.96\times 2.5}{2}\right) \approx 381\ kip - in$$

For the west end column near the uplift wall end, the resisting forces from the O-connectors pulled the end column up. Assuming the N.A. depth of the end column was 1.5 in. at 2% drift, the elongation of the prestressed rod was:

$$\Delta_{rod\_2\%} = \left(\frac{w_{Ecol}}{2} - c_{design\_Ecol}\right)\times\theta = \left(\frac{10}{2} - 1.5\right)\times 0.02 = 0.07\ in.$$

The stress of the prestressed rod at 2% drift was:

$$\sigma_{rod\_2\%} = \sigma_{initial\_rod} + \frac{\Delta_{rod\_2\%}}{L_{rod}} = \frac{F_{initial\_rod}}{A_{rod}} + E_{rod}\frac{\Delta_{rod\_2\%}}{L_{rod}}$$

$$= \frac{64}{1.045} + 29000\times\frac{0.07}{126.5} \approx 77.3\ ksi < f_{y-rod} = 110\ ksi$$

The prestressed rod did not yield at 2% drift. The N.A. depth of the left end column was:

$$c_{Ecol\_T} = \frac{F_{Ecol\_T} + W_{Ecol} - n_{FO}R_{FO}}{\alpha\beta f'_{cc}t} = \frac{\sigma_{rod\_2\%}A_{rod} + W_{Ecol} - n_{FO}R_{FO}}{\alpha\beta f'_{cc}t}$$

$$= \frac{77.3 \times 1.045 + 0.4 - 4\times 7.4}{0.92\times 0.96\times 1.35\times 5.0\times 6} \approx 1.4\ in. \approx 1.5\ in., O.K.$$

The assumed N.A. depth was valid. The moment resistance of the right end column about the centroid of the compressive stress block (inverted triangle mark in the Fig. B-2) was:

$$M_{Ecol\_T} = \left(F_{Ecol\_T} + W_{Ecol}\right)\left(\frac{w_{Ecol}}{2} - \frac{\beta c_{Ecol\_T}}{2}\right) - n_{FO}R_{FO}\left(s_{FO} - \frac{\beta c_{Ecol\_T}}{2}\right)$$

$$= (77.3\times 1.045 + 0.4)\left(\frac{10}{2} - \frac{0.96\times 1.5}{2}\right) - 4\times 7.4\times\left(2.5 - \frac{0.96\times 1.5}{2}\right)$$

$$\approx 295\ kip - in$$

To conclude, the total moment resistance of the PreWEC system in PFS2 was:

$$M_{PreWEC} = M_{design\_wall} + M_{Ecol\_C} + M_{Ecol\_T} = 9903 + 381 + 295 = 10{,}579\ kip - in$$

The percentage of moment carried by the end columns represented 6.5% of the total moment resistance of the PreWEC system as shown below.

$$\frac{M_{Ecol\_C} + M_{Ecol\_T}}{M_{PreWEC}}\times 100\% = \frac{381 + 295}{10579}\times 100\% = \ 6.4\%$$

Appendix C: Moment Resistance of the Unbonded Post-Tensioned Slab

In the test specimens, only the first floor systems were constructed. Mega beams and steel trusses were used to simulate the remaining five floors in PFS1 and PFS2, respectively. In the case of PFS1, this required the mega beams to provide a moment resistance that would be equivalent to that of the five floors. This appendix summarizes determination of the yield moment resistance of the unbonded PT slab at two cross sections: floor-edge beam and wall-floor sections. Only the negative moment resistance was calculated (i.e., top-of-the-slab in tension case) for both sections because that provided the largest yield moments due to the greater concentration of reinforcement at the top of the section at those locations. The entire width of the slab was assumed to be effective in calculating the moment resistance. Strain compatibility was only valid for the concrete and the discrete bonded reinforcement. Because the PT strands were unbonded, strain compatibility could not be used to determine the stress in the strands. To determine the expected stress in the strands at the yield moment, the initial strand stress and nominal prestress at failure, f_{ps}, were determined.

In the E-W in-plane direction, the prototype design required: $F_{design\_slab} = 13$ kip/ft. After scaling, the PT force in the specimen was 13/3=4.3 kip/ft.

In the PFS1 floor slab, six 7-wire Grade 250 ksi 3/8 in. PT strands were used. The nominal area of a 3/8 in. strand is 0.08 in^2. The initial stress in the strands was $0.36f_{pu}$ = 90 ksi, which provided a PT force per unit length of $0.36f_{pu} \times n \times A / L$ = 90 × 6 × 0.08 / 10 ft. = 4.3 kip/ft. The effective PT force in each 3/8" strand was determined to be 90ksi × 0.08in^2 = 7.2 kips.

According to Section 18.7.2 of ACI 318-11, the stress in the prestressing steel at nominal flexural strength, f_{ps}, can be approximated by using Equation 18-3 if f_{se} is at least $0.5f_{pu}$ for unbonded PT in a member with a span to depth ratio of at least 35. The slab was 3 in. thick and 10 ft. wide. The span to depth ratio was approximately 40 (distance from the column to the center of the wall was approximately 10 ft.). The tested PT slab met the span-to-depth criteria to use the approximation, but it did not meet the criteria in terms of

the prestress level (i.e., f_{se} was only 0.36 f_{pu}). Although the approximation did not directly apply, it was used as an estimate of the prestress level at nominal strength.

Because the unbonded PT strands had a curved profile along the length of the slab, its moment contribution was dependent on its position within the cross section of the slab. The yield moments at the floor-edge beam and wall-floor connections are calculated in the following.

Slab yield moment at floor-edge beam connection - For the slab-edge beam connection, the PT strands was in the middle of the cross section. The stress in the prestressing steel at nominal flexural strength, f_{ps}, was calculated below:

$$\rho_p = \frac{A_{ps}}{bd_p} = \frac{n_{PT\_slab}A_{PT\_slab}}{bd_p} = \frac{6\times0.08}{10'\times12"\times(3" - 1.5")} = 2.67\times10^{-3}$$

$$f_{ps} = f_{se} + 10{,}000 + \frac{f_c'}{300\rho_p} = 90{,}000 + 10{,}000 + \frac{5{,}000}{300\times2.67\times10^{-3}} \approx 106\ ksi$$

Because the PT stress in the unbonded tendon was expected to remain nearly the same during the deformation of the slab, the PT force $f_{ps}A_{ps} = 106\times6\times0.08 \approx 51\ kip$ was used to estimate the yielding moment of the floor system.

Other than the PT strands, bonded reinforcement (8 #3) was placed at the top of the slab and bonded reinforcement (2 #3) as well as mesh reinforcement (4 #3) on the bottom of the slab. Because the width of the slab was large, it was assumed that the concrete would be in the linear elastic range when the mild reinforcement yielded. When the top bonded reinforcement yielded, the bottom reinforcement may be elastic in either tension or compression; it was assumed to be elastic in compression as an initial assumption. Fig. B-3 shows the assumed force distribution through the depth of the slab.

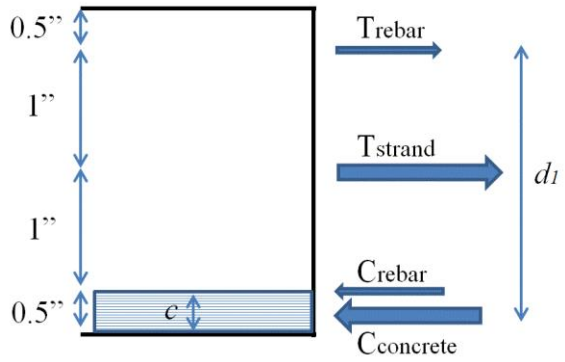

Fig. C-1 Assumed force distribution in the slab at yield moment

Assuming the distance from the top bonded reinforcement to the N.A. is d_1, then the curvature of the cross section when the top bonded reinforcement yielded was:

$$\varphi = \frac{\varepsilon_y}{d_1} = \frac{60/29{,}000}{d_1} = \frac{2.07\times10^{-3}}{d_1}$$

The strain in the bottom reinforcement was:

$$\varepsilon_b = \varphi(d_1 - 1 - 1)$$

The strain in the extreme compressive concrete fiber was:

$$\varepsilon_c = \varphi(2.5 - d_1)$$

The force equilibrium of the cross section:

$$1/2\times10'\times12in/ft\times(2.5 - d_1)\times E_c\times\varphi(2.5 - d_1) + 29000\varphi(d_1 - 2)\times6\times0.11$$
$$= 60\times8\times0.11 + 51$$

Where E_c = 4030 ksi, the assumed modulus of elasticity for concrete with f'_c of 5000 psi. Solve for d_1,

$$d_1 \approx 1.87”;\ \ \varphi = \frac{2.069\times10^{-3}}{d_1} = 1.11\times10^{-3};$$

$$\varepsilon_b = \varphi(d_1 - 2) = -1.44\times10^{-4} < -\varepsilon_y = -2.069\times10^{-3}$$

$$\varepsilon_c = \varphi(2.5 - d_1) = 6.97\times10^{-4}$$

$$\sigma_c = 6.97\times10^{-4}\times4030 \approx 2.8\ ksi = 0.56f'_c > 0.45f'_c$$

The assumptions that the bottom reinforcement was in compression and not yielded were valid. The assumption of the triangular distribution of the compression stress in the concrete was not quite valid, but it was deemed to be a reasonable approximation.

The yielding moment at the floor-edge beam connection was then calculated:

$$M_y = 60\times8\times0.11\times d_1 + 51\times(d_1 - 1) - 29000\varphi(2 - d_1)\times6\times0.11\times(2 - d_1)$$
$$\approx 143\ kip - in$$

<u>*Slab yield moment at wall-floor connection*</u> - For the wall-floor connection, the PT strands were at the top of the cross section (1/2 in. away from the floor surface). The stress in the prestressing steel at nominal flexural strength, f_{ps}, was calculated below:

$$\rho_p = \frac{A_{ps}}{bd_p} = \frac{n_{PT\_slab}A_{PT\_slab}}{bd_p} = \frac{6\times0.08}{10'\times12"\times(3" - 0.5")} = 1.6\times10^{-3}$$

$$f_{ps} = f_{se} + 10{,}000 + \frac{f_c'}{300\rho_p} = 90{,}000 + 10{,}000 + \frac{5{,}000}{300\times2.67\times10^{-3}} \approx 110\ ksi$$

The PT force $f_{ps}A_{ps} = 110\times6\times0.08 \approx 53\ kip$ was used to estimate the yielding moment of the floor system at the wall-floor connection.

Similar to the floor-edge beam connection, bonded reinforcement (8 #3) were placed at the top of the slab and bonded reinforcement (2 #3) as well as mesh reinforcement (4 #3) on the bottom of the slab. As for the wall-floor yield moment calculation, the concrete was assumed to be linear elastic and the bottom reinforcement was assumed to be elastic in compression. The force equilibrium of the cross section was established:

$$1/2\times10'\times12in/ft\times(2.5 - d_1)\times E_c\times\varphi(2.5 - d_1) + 29000\varphi(d_1 - 2)\times6\times0.11$$
$$= 60\times8\times0.11 + 53$$

Solve for d_1:

$$d_1 \approx 1.86";\ \ \varphi = \frac{2.069\times10^{-3}}{d_1} = 1.11\times10^{-3};$$

$$\varepsilon_b = \varphi(d_1 - 2) = -1.51\times10^{-4} < -\varepsilon_y = -2.069\times10^{-3}$$

$$\varepsilon_c = \varphi(2.5 - d_1) = 7.06\times10^{-4}$$

$$\sigma_c = 6.97\times10^{-4}\times4030 \approx 2.9\ ksi = 0.58f'_c > 0.45f'_c$$

Again, the assumptions that the bottom reinforcement was in compression and not yielded were valid. The assumption of the triangular distribution of the compression stress in the concrete was not quite valid, but it was deemed to be a reasonable approximation. These results were the same as obtained for the floor-edge beam case.

The yielding moment at the wall-floor connection was then calculated as follows:

$$M_y = 60\times8\times0.11\times d_1 + 53\times(d_1 - 0) - 29000\varphi(2 - d_1)\times6\times0.11\times(2 - d_1)$$
$$\approx 197\ kip - in$$

At the wall-floor connection, the PT was higher in the section and thus provided the section with a higher yield moment. When designing the mega beam, the moment resistance of the floor at the wall-floor connection is used to provide larger constraint to the wall.

Appendix D: Information of the Instrumentation in PFS1 and PFS2

A great amount of instrumentation was used in the tests, including load cell, tiltmeter, Linear Variable Differential Transformer (LVDT), string pot, Direct Current Displacement Transducer (DCDT), strain gages and concrete gages. Detailed information of the instrumentation in PFS1 and PFS2 is provided in Table D-1 and Table D-2, respectively. It is noteworthy that in the two tables, the as built position of the instrumentation is measured based on the coordination systems established in Fig. 4-1 through Fig. 4-14 (PFS1) and Fig. 4-15 through Fig. 4-30 (PFS2). The gage length of the string pots and the LVDTs represent the distance between the two attach points of each instrumentation.

Table D-1 Instrumentation in PFS1

Sensor Label	Sensor Type	As built Position			Position Units	Sensor Units	Gage Length	
		X	Y	Z			Value	Units
SP2-EW0	Stringpot	-3	36.75	49	in	in		in
SP10-EW1	Stringpot	0	45	95	in	in		in
SP20-EW2	Stringpot	0	45	145.5	in	in		in
SP20-EW3	Stringpot	0	45	195.375	in	in		in
SP30-EW4	Stringpot	0	45	243.5	in	in		in
SP20-ESC2	Stringpot	3	123.75	141.5	in	in		in
SP20-ESC3	Stringpot	3	123.75	193.5	in	in		in
SP30-ESC4	Stringpot	3	123.75	242.5	in	in		in
SP10-NEF-LROT	Stringpot	-54.125	119.5	87.625	in	in		in
SP10-SEF-LROT	Stringpot	54	119.5	87.875	in	in		in

Sensor Label	Sensor Type	As built Position			Position Units	Sensor Units	Gage Length	
		X	Y	Z			Value	Units
SP10-EC1	Stringpot	0	119.5	94.5	in	in		in
SP10-ECEB	Stringpot	0	119.5	71.375	in	in		in
SP2-ECBASE	Stringpot	0	119.5	45.25	in	in		in
SP10-WC1	Stringpot	0	-120.25	93.25	in	in		in
SP10_FL1	Stringpot	-1.75	-48.625	0	in	in		in
SP10_FL2	Stringpot	-1.75	-62.125	0	in	in		in
SP5_FL3	Stringpot	-1.75	-77.875	0	in	in		in
SP5_FL4	Stringpot	-1.75	-97.25	0	in	in		in
SP2_FL5	Stringpot	-1.75	-109	0	in	in		in
SP5_FL6	Stringpot	-29.375	-108	0	in	in		in
SP5_FL10	Stringpot	-46.75	-36.875	0	in	in		in
SP5_FL11	Stringpot	-29.75	-36.875	0	in	in		in
SP10_FL12	Stringpot	-6	-36.625	0	in	in		in
SP5_FL13	Stringpot	-29.625	-78.25	0	in	in		in
SP5_FL14	Stringpot	-57.625	-0.125	0	in	in		in
SP5_FL15	Stringpot	-29.875	-0.375	0	in	in		in
SP5_FL16	Stringpot	-6.25	-0.125	0	in	in	8.5	in
SP2-FWL1-T3	Stringpot	36.5	-49.625	3.75	in	in	8.5	in
SP2-FWL1-B3	Stringpot	36.5	-49.625	-3.875	in	in	8.5	in
SP2-FWL2-T3	Stringpot	36.5	-49.625	4	in	in	8.5	in
SP2-FWL2-B3	Stringpot	36.5	-49.625	-4.25	in	in	8	in
SP2-FWL2-T4	Stringpot	58.5	-52.125	4.375	in	in	8	in
SP2-FWL2-B4	Stringpot	58.5	-52.125	-3.75	in	in	8	in

Sensor Label	Sensor Type	As built Position			Position Units	Sensor Units	Gage Length	
		X	Y	Z			Value	Units
SP2-EC1FT-E	Stringpot	0	119.5	75.875	in	in	8	in
SP2-EC1FT-W	Stringpot	0	109.75	45	in	in	8	in
L1-EMBT_E	LVDT	0	106.375	244.25	in	in	6	in
L1-EMBT_W	LVDT	0	46	244.5	in	in	6	in
L1-EMBB_E	LVDT	0	106.375	224.75	in	in	6	in
L1-EMBB_W	LVDT	0	46	225	in	in	6	in
L05-EGB2FB-W	LVDT	10.75	113.375	93	in	in	7	in
L05-EGB2FB-E	LVDT	11.125	117.75	93	in	in	7	in
L05-EC2FB-F-W	LVDT	55	113.375	93	in	in	7	in
L05-EC2FB-F-E	LVDT	54.875	117.75	93	in	in	7	in
L05-EC2FB-W	LVDT	32.875	113.375	93	in	in	7	in
L05-EC2FB-E	LVDT	32.875	117.75	93	in	in	7	in
L1-EC1FB-E	LVDT	0	120.75	45	in	in	6.75	in
L1-EC1FB-W	LVDT	0	109.75	45	in	in	5.875	in
L2-EW1	LVDT	-3	41.25	45	in	in	6.75	in
L2-EW2	LVDT	-3	25.75	45	in	in	7.25	in
L1-EW3	LVDT	-3	12.75	45	in	in	7.5	in
L2-WW1	LVDT	-3	-41	45	in	in	7.75	in
L2-WW2	LVDT	-3	-26	45	in	in	7.75	in
L1-WW3	LVDT	-3	-13.25	45	in	in	7.75	in
L05-FWE_V	LVDT	3	12.875	93	in	in	1.5	in
L05-FWE_H	LVDT	3	11	93	in	in	2.25	in

Sensor Label	Sensor Type	As built Position			Position Units	Sensor Units	Gage Length	
		X	Y	Z			Value	Units
L05-FM_V	LVDT	3	-13	93	in	in	1.5	in
L05-FM_H	LVDT	3	-10.5	94.5	in	in	1.25	in
L01-NE-WE	LVDT	-3	12.75	45	in	in	31.125	in
L01-NE-WM	LVDT	-3	-26	45	in	in	31.75	in
L01-NE-EM	LVDT	-3	-13.25	45	in	in	31.5	in
L05-NW-EE	LVDT	-3	-41	45	in	in	31.5	in
L2_NWOV	LVDT	-3	-33.25	82.5	in	in	5.75	in
L2_NEOV	LVDT	-3	33.25	80.875	in	in	4.25	in
L1-WC1FB-E	LVDT	0	-110.75	45	in	in	5.875	in
L1-WC1FB-W	LVDT	0	-121.5	45	in	in	6	in
L1-FCL-T1	LVDT	0	-111.75	2	in	in	7.625	in
L1-FCL-B1	LVDT	0	-111.75	-2.25	in	in	7.625	in
L1-FCL-T2	LVDT	-1.25	-104.125	2	in	in	11	in
L1-FCL-B2	LVDT	-1.25	-104.125	-2.25	in	in	11	in
L1-FEG-T1	LVDT	11.75	-104.25	2	in	in	9.5	in
L1-FEG-B1	LVDT	12.75	-111.75	-2	in	in	7.5	in
L05-FEG-T2	LVDT	36.5	-104.25	1.875	in	in	9.25	in
L05-FEG-B2	LVDT	37.75	-111.75	-2	in	in	7.5	in
L05-FEG-T3	LVDT	59.125	-104.375	2	in	in	9.625	in
L05-FEG-B3	LVDT	58	-111.75	-1.75	in	in	7.375	in
L05-FCE-T1	LVDT	11.75	-104.25	2	in	in	7.5	in
L05-FCE-B1	LVDT	11.75	-104.25	-2.125	in	in	7.5	in
L05-FCE-T2	LVDT	36.5	-104.25	2	in	in	7.375	in

Sensor Label	Sensor Type	As built Position			Position Units	Sensor Units	Gage Length	
		X	Y	Z			Value	Units
L05-FCE-B2	LVDT	36.5	-104.25	-2.25	in	in	7.375	in
L1-FWL1-T1	LVDT	-0.75	-45	2	in	in	4.375	in
L1-FWL1-B1	LVDT	-0.75	-45	-2	in	in	4.375	in
L1-FWL1-T2	LVDT	11.75	-49.75	2	in	in	10.125	in
L1-FWL1-B2	LVDT	11.75	-49.75	-2	in	in	10.125	in
L01-FWL1-T4	LVDT	58.5	-52.125	2.125	in	in	14.25	in
L1-FWL2-T1	LVDT	-1.25	-49.375	2	in	in	16.25	in
L1-FWL2-B1	LVDT	-1.25	-49.375	-2	in	in	16.25	in
L05-FWL2-T2	LVDT	11.75	-49.75	2	in	in	16.125	in
L05-FWL2-B2	LVDT	11.75	-49.75	-2	in	in	16.125	in
L1-FWT-T1	LVDT	-1.75	-49.375	2	in	in		in
L05-FWT-B1	LVDT	-1.75	-49.375	-2.125	in	in		in
L1-FWT-T3	LVDT	-3	-38.25	2	in	in		in
L1-FWT-B3	LVDT	-3	-38.25	-1.75	in	in		in
L05-FWT-T4	LVDT	-3	-24.25	1.75	in	in		in
L05-FWT-B4	LVDT	-3	-24.25	-2	in	in		in
L05-FPT-T1	LVDT	-58.625	-48.75	2	in	in		in
L05-FPT-B1	LVDT	-58.625	-48.75	-1.75	in	in		in
L1-FPT-T2	LVDT	-58.625	-36.5	1.875	in	in		in
L05-FPT-T3	LVDT	-58	-30	2	in	in		in
L05-FPT-B3	LVDT	-58	-30	-2	in	in		in
L05-EFWL-T	LVDT	-0.125	45	2	in	in		in
L05-EFWL-B	LVDT	-0.125	45	-1.75	in	in		in

Sensor Label	Sensor Type	As built Position			Position Units	Sensor Units	Gage Length	
		X	Y	Z			Value	Units
L05-EFCL-T	LVDT	-0.25	112	2	in	in		in
L05-EFCL-B	LVDT	-0.25	112	-2	in	in		
WALL_PT_400K	Load Cell	0	0	278	in	kip		
PROP-SE	Load Cell	-55	37.5	73.5	in	kip		
PROP-SW	Load Cell	-55	-37.5	73.5	in	kip		
PROP-NE	Load Cell	55	37.5	73.5	in	kip		
PROP-NW	Load Cell	55	-37.5	73.5	in	kip		
LC-FPTW1	Load Cell	41	-120	1.5	in	kip		
LC-FPTW2	Load Cell	23	-120	1.5	in	kip		
LC-FPTW3	Load Cell	4	-120	1.5	in	kip		
LC-FPTW4	Load Cell	4	120	1.5	in	kip		
LC-FPTSE1	Load Cell	60	51.5	1.5	in	kip		
LC-FPTSE2	Load Cell	60	45.5	1.5	in	kip		
LC-FPTSE3	Load Cell	60	39.5	1.5	in	kip		
LC-FPTSE4	Load Cell	60	33.5	1.5	in	kip		
TTW_5959_X	Inclinometer	3	-0.25	253.5	in	°		
TBW_5960_X	Inclinometer	3	0	74.5	in	°		
TBWSC_5928_X	Inclinometer	0	-116.25	234.25	in	°		
TBWSB_5963_X	Inclinometer	0	-100	234.25	in	°		
TBEC_5961_X	Inclinometer	-6	116.25	64.125	in	°		

Sensor Label	Sensor Type	As built Position			Position Units	Sensor Units	Gage Length	
		X	Y	Z			Value	Units
CG_WWBC_L1	Strain Gage	0	42.5	2.125	in	µstrain		
CG_WWBC_L2	Strain Gage	0	39.625	2.125	in	µstrain		
CG_WWBC_L3	Strain Gage	0	35.625	2.125	in	µstrain		
CG_WWBC_L4	Strain Gage	0	42.5	8.125	in	µstrain		
CG_EWBC_L1	Strain Gage	0	-42.5	2.125	in	µstrain		
CG_EWBC_L2	Strain Gage	0	-39.625	2.125	in	µstrain		
CG_EWBC_L3	Strain Gage	0	-35.625	2.125	in	µstrain		
CG_EWBC_L4	Strain Gage	0	-42.5	8.125	in	µstrain		
SG_WWB_T1	Strain Gage	0	38.5	2.625	in	µstrain		
SG_WWB_T2	Strain Gage	0	38.5	10	in	µstrain		
SG_WWB_T3	Strain Gage	0	38.5	15.125	in	µstrain		
SG_WWB_T4	Strain Gage	0	38.5	23.5	in	µstrain		
SG_WWB_T5	Strain Gage	0	38.5	33.75	in	µstrain		
SG_WWB_T6	Strain Gage	0	38.5	39.125	in	µstrain		
SG_EWB_T1	Strain Gage	0	-38.5	2.875	in	µstrain		
SG_EWB_T2	Strain Gage	0	-38.5	9.75	in	µstrain		
SG-ECOL-L1	Strain Gage	-0.75	-3	-0.5	in	µstrain		
SG-ECOL-L2	Strain Gage	-0.75	3	-0.5	in	µstrain		
SG-ECOL-L3	Strain Gage	-0.75	-3	3.5	in	µstrain		
SG-ECOL-L4	Strain Gage	-0.75	3	3.5	in	µstrain		
SG-ECOL-L5	Strain Gage	-0.75	-3	4.5	in	µstrain		
SG-ECOL-L6	Strain Gage	-0.75	3	4	in	µstrain		
SG-ECOL-L7	Strain Gage	-0.75	-3	10.5	in	µstrain		

Sensor Label	Sensor Type	As built Position			Position Units	Sensor Units	Gage Length	
		X	Y	Z			Value	Units
SG-ECOL-L8	Strain Gage	-0.75	3	10.25	in	µstrain		
SG-ECOL-L9	Strain Gage	-0.75	-3	28.25	in	µstrain		
SG-ECOL-L10	Strain Gage	-0.75	3	28.25	in	µstrain		
SG-ECOL-L11	Strain Gage	-0.75	-3	2	in	µstrain		
SG-ECOL-L12-PY	Strain Gage	-2.5	-1.25	2	in	µstrain		
SG-ECOL-L13	Strain Gage	-0.75	3	2	in	µstrain		
SG-ECOL-L15	Strain Gage	-0.75	-2.5	49	in	µstrain		
SG-ECOL-L16	Strain Gage	-0.75	3	49	in	µstrain		
SG-WCOL-L1	Strain Gage	0.5	2.75	-0.5	in	µstrain		
SG-WCOL-L2	Strain Gage	0.5	-2.75	-0.5	in	µstrain		
SG-WCOL-L3	Strain Gage	0.5	2.75	3.5	in	µstrain		
SG-WCOL-L4	Strain Gage	0.5	-2.75	3.5	in	µstrain		
SG-WCOL-L5	Strain Gage	0.5	2.75	4.25	in	µstrain		
SG-WCOL-L6	Strain Gage	0.5	-2.75	5.125	in	µstrain		
SG-WCOL-L7	Strain Gage	0.5	2.75	10.5	in	µstrain		
SG-WCOL-L8	Strain Gage	0.5	-2.75	10.5	in	µstrain		
SG-WCOL-L9	Strain Gage	0.5	2.75	28.5	in	µstrain		
SG-WCOL-L10	Strain Gage	0.5	-2.75	28.5	in	µstrain		
SG-WCOL-L11	Strain Gage	0.5	2.75	2	in	µstrain		
SG-WCOL-L12-PY	Strain Gage	0.5	-2.75	1.75	in	µstrain		
SG-WCOL-L13	Strain Gage	-4.75	-2.75	1.75	in	µstrain		
SG-WCOL-L15	Strain Gage	0.5	2.75	49	in	µstrain		
SG-WCOL-L16	Strain Gage	0.5	-2.75	49	in	µstrain		

Sensor Label	Sensor Type	As built Position			Position Units	Sensor Units	Gage Length	
		X	Y	Z			Value	Units
SG-WCOL-T1	Strain Gage	0	-6	2.25	in	µstrain		
SG-WCOL-T2	Strain Gage	0	-6	8.25	in	µstrain		
SG-WCOL-T3	Strain Gage	0	-6	12	in	µstrain		
SG-FEG-T0-Y	Strain Gage	-7.25	-109	1.625	in	µstrain		
SG-FEG-T1-Y	Strain Gage	4	-108.5	1.375	in	µstrain		
SG-FEG-B1-Y	Strain Gage	3.25	-109	0.75	in	µstrain		
SG-FEG-T2-Y	Strain Gage	8	-108	1.75	in	µstrain		
SG-FEG-B2-Y	Strain Gage	12.75	-107.5	0.625	in	µstrain		
SG-FEG-B3	Strain Gage	37.625	-108	1.25	in	µstrain		
SG-FEG-T3	Strain Gage	55.75	-108	2.375	in	µstrain		
SG-FEG-T4	Strain Gage	57.75	-108	2.375	in	µstrain		
SG-FEGE-B1-Y	Strain Gage	12.75	-94.375	0.875	in	µstrain		
SG-FEGE-B2	Strain Gage	37.625	-94.25	1	in	µstrain		
CG-L-SW	Strain Gage	30.125	-77.75	1.5	in	µstrain		
CG-L-WM	Strain Gage	0.125	-77.5	1.5	in	µstrain		
CG-L-NW	Strain Gage	-29.875	-78.25	1.5	in	µstrain		
SG-FWL-B3	Strain Gage	37.625	-45	0.75	in	µstrain		
SG-FWL-B2-Y	Strain Gage	12.75	-44	0.75	in	µstrain		
SG-FWL-T2-Y	Strain Gage	5.75	-46	2.25	in	µstrain		
SG-FWL-B1-Y	Strain Gage	1.25	-46	0.5	in	µstrain		
SG-FWL-T1-Y	Strain Gage	1	-46	2.25	in	µstrain		
SG-FWT-B1	Strain Gage	-4	-48	1.25	in	µstrain		
SG-FWT-T1-Y	Strain Gage	-4	-42.5	1.75	in	µstrain		

Sensor Label	Sensor Type	As built Position			Position Units	Sensor Units	Gage Length	
		X	Y	Z			Value	Units
SG-FWT-T2-Y	Strain Gage	-4	-41.5	1.75	in	µstrain		
SG-FWT-C1-Y	Strain Gage	-4	-23.5	1.5	in	µstrain		
SG-FWT-B2	Strain Gage	-13.5	-17	1.25	in	µstrain		
CG-T-SW	Strain Gage	31.5	-43.375	1.5	in	µstrain		
CG-T-NW	Strain Gage	-31.5	-43.5	1.5	in	µstrain		
SG-FPT-B2-Y	Strain Gage	-49.5	-50.5	0.125	in	µstrain		
SG-FPT-T1-Y	Strain Gage	-49.5	-50.5	2.5	in	µstrain		
SG-FPT-B1-Y	Strain Gage	-49.5	-48.25	1	in	µstrain		
SG-FPT-T2-3-Y	Strain Gage	-49.5	-38.5	1.5	in	µstrain		
SG-FPT-T2-Y	Strain Gage	-49.5	-37.875	2.25	in	µstrain		
SG-FPT-B3-Y	Strain Gage	-49.5	-37.875	0.125	in	µstrain		
SG-FPT-T3-Y	Strain Gage	-49.5	-31.25	2.375	in	µstrain		
SG-FPT-B4-Y	Strain Gage	-49.5	-31.25	0.125	in	µstrain		
SG-FPT-B5	Strain Gage	-49.625	-17	1	in	µstrain		
SG-FPL-T2-Y	Strain Gage	-50.25	-38.5	2	in	µstrain		
SG-FPL-T1-Y	Strain Gage	-54.875	-37.5	2.125	in	µstrain		
CG-T-SE	Strain Gage	31.375	43.5	1.5	in	µstrain		
CG-T-NE	Strain Gage	-31.375	43.625	1.5	in	µstrain		
SG-EFWL-T-Y	Strain Gage	1	46	2.25	in	µstrain		
SG-EFWT-T2-Y	Strain Gage	-4	41.5	1.75	in	µstrain		
SG-EFWT-T1-Y	Strain Gage	-4	43.5	1.75	in	µstrain		
CG-L-SE	Strain Gage	30	77.625	1.5	in	µstrain		
CG-L-EM	Strain Gage	0	77	1.5	in	µstrain		

Sensor Label	Sensor Type	As built Position			Position Units	Sensor Units	Gage Length	
		X	Y	Z			Value	Units
CG-L-NE	Strain Gage	-30	77.5	1.5	in	µstrain		
SG-EFCL-B-Y	Strain Gage	2	109	0.75	in	µstrain		
SG-EBCTP-M	Strain Gage	0	99.5	240.75	in	µstrain		
SG-EBCTP-E	Strain Gage	-0.5	99.5	240.75	in	µstrain		
SG-EBCBTF	Strain Gage	-2.3	99.5	240.75	in	µstrain		
SG-EBMT	Strain Gage	0	76.125	240	in	µstrain		
SG-EBWTP-M	Strain Gage	0	52.625	241	in	µstrain		
SG-EBWTP-E	Strain Gage	-0.5	52.625	241	in	µstrain		
SG-EBCBP-M	Strain Gage	0	99.5	228.25	in	µstrain		
SG-EBCBP-E	Strain Gage	0.5625	99.5	228.25	in	µstrain		
SG-EBCBBF	Strain Gage	2.25	99.5	228.25	in	µstrain		
SG-EBMB	Strain Gage	0	76.125	229.375	in	µstrain		
SG-EBWBP-M	Strain Gage	0	52.75	228.5	in	µstrain		
SG-EBWBP-E	Strain Gage	0.5625	52.75	228.5	in	µstrain		
FRA-EBC-V	Strain Gage	0.15625	99.5	234.5	in	µstrain		
FRA-EBC-I	Strain Gage	0.15625	99.5	234.5	in	µstrain		
FRA-EBC-H	Strain Gage	0.15625	99.5	234.5	in	µstrain		
FRA-EBM-V	Strain Gage	0.15625	76.125	234.625	in	µstrain		
FRA-EBM-I	Strain Gage	0.15625	76.125	234.625	in	µstrain		
FRA-EBM-H	Strain Gage	0.15625	76.125	234.625	in	µstrain		
FRA-EBW-V	Strain Gage	0.15625	52.625	234.75	in	µstrain		
FRA-EBW-I	Strain Gage	0.15625	52.625	234.75	in	µstrain		
FRA-EBW-H	Strain Gage	0.15625	52.625	234.75	in	µstrain		

Sensor Label	Sensor Type	As built Position			Position Units	Sensor Units	Gage Length	
		X	Y	Z			Value	Units
SG-ESCTTF	Strain Gage	0	123.75	214.125	in	µstrain		
SG-ESCTBF	Strain Gage	0	107.375	214.125	in	µstrain		
SG-ESCTW-N	Strain Gage	-0.38	115.5	214.125	in	µstrain		
SG-ESCBTF	Strain Gage	0	123.75	119.125	in	µstrain		
SG-ESCBBF	Strain Gage	0	107.375	119.125	in	µstrain		
SG-ESCBW-N	Strain Gage	-0.38	115.5	119.125	in	µstrain		
SG-WBWTP-M	Strain Gage	0	-53	240.875	in	µstrain		
SG-WBCTP-M	Strain Gage	0	-99.75	240.5	in	µstrain		
SG-WBWBP-M	Strain Gage	0	-53	228.375	in	µstrain		
SG-WBCBP-M	Strain Gage	0	-99.875	228	in	µstrain		
FRA-WBM-V	Strain Gage	0.15625	-76.5	234.5	in	µstrain		
FRA-WBM-I	Strain Gage	0.15625	-76.5	234.5	in	µstrain		
FRA-WBM-H	Strain Gage	0.15625	-76.5	234.5	in	µstrain		
SG_WTO_U	Strain Gage	9.25	-36	81.125	in	µstrain		
SG_WTO_UC	Strain Gage	9.25	-36.5	81.125	in	µstrain		
SG_WTO_D	Strain Gage	9.25	-36	75.625	in	µstrain		
SG_WBO_U	Strain Gage	9.25	-36	61	in	µstrain		
SG_WBO_UC	Strain Gage	9.25	-36.5	61	in	µstrain		
SG_WBO_D	Strain Gage	9.25	-36	55.5	in	µstrain		
SG_WHSS_W	Strain Gage	5.875	-29.25	50.5	in	µstrain		
SG_WHSS_E	Strain Gage	5.875	-33.25	50.5	in	µstrain		
SG_SE_PROP1	Strain Gage	55	37.5	66	in	µstrain		
SG_SE_PROP2	Strain Gage	55	37.5	66	in	µstrain		

Sensor Label	Sensor Type	As built Position			Position Units	Sensor Units	Gage Length	
		X	Y	Z			Value	Units
SG_SE_PROP3	Strain Gage	55	37.5	20.5	in	µstrain		
SG_SE_PROP4	Strain Gage	55	37.5	20.5	in	µstrain		

Table D-2 Instrumentation in PFS2

Sensor Label	Sensor Type	As built Position			Position Units	Sensor Units	Gage Length	
		X	Y	Z			Value	Units
SP10-EC1	Stringpot	0	120.5	87.75	in	in	36	in
SP10-EC2	Stringpot	0	120.5	116.25	in	in	36	in
SP20-EC3	Stringpot	0	120.5	139.75	in	in	36	in
SP2-EW0	Stringpot	-3	31	51.5	in	in	30.5	in
SP20-EW2	Stringpot	0	34	132	in	in	123	in
SP20-EW3	Stringpot	0	34	186.5	in	in	122.75	in
SP20-EW4	Stringpot	0	34	226.75	in	in	121.5	in
SP10-SEF-LROT	Stringpot	53.5	120.5	87.75	in	in	112.375	in
SP10-NEF-LROT	Stringpot	-54.25	120.5	87.5	in	in	77.5	in
SP5-ECEB	Stringpot	0	120.5	71	in	in	36	in
SP2-ECBASE	Stringpot	0	120.5	47.875	in	in	36	in
SP10-1EC	Stringpot	0	-45	69	in	in	18.125	in
SP10-2EC	Stringpot	0	-45	79.5	in	in	18.125	in
SP10-3EC	Stringpot	0	-45	96.5	in	in	18.125	in
SP10-4EC	Stringpot	0	-45	113.75	in	in	18.125	in
SP2-WW0	Stringpot	-3	-31	50.75	in	in	31	in
SP10-WC1	Stringpot	0	-120	87.75	in	in	10.5	in

Sensor Label	Sensor Type	As built Position			Position Units	Sensor Units	Gage Length	
		X	Y	Z			Value	Units
SP10-WCOLE-U	Stringpot	-54	-120	92	in	in	26.625	in
SP10-WCOLE-D	Stringpot	-54	-120	82	in	in	26.5	in
SP10-WCOLJ-U	Stringpot	0	-120	92.25	in	in	46.5	in
SP10-WCOLJ-D	Stringpot	0	-120	82.5	in	in	46	in
SP10-TB1	Stringpot	-7.75	36.75	84	in	in		
SP10-TB3	Stringpot	-32.5	37.125	84	in	in		
SP10-TB4	Stringpot	-32.5	43	84	in	in		
SP10-TB5	Stringpot	-60	36.875	84	in	in		
SP10-TB6	Stringpot	-60	43	84	in	in		
L1-EMBT_E	LVDT	0	112.5	146	in	in	8.5	in
L1-EMBT_W	LVDT	0	34	145.75	in	in	8.5	in
L1-EMBB_E	LVDT	0	112.5	134.25	in	in	8.5	in
L1-EMBB_W	LVDT	0	34	134	in	in	8.5	in
L05-EGB2FB-E	LVDT	-9	-14.125	113.5	in	in	8	in
L05-EGB2FB-W	LVDT	-9	-14.125	118.5	in	in	8	in
L05-EC2FB-E	LVDT	-35.875	-35.875	113.5	in	in	8	in
L05-EC2FB-W	LVDT	-35.75	-35.75	118.75	in	in	8	in
L05-EC2FB-F-E	LVDT	-58.125	-58.125	113.5	in	in	8	in
L05-EC2FB-F-W	LVDT	-57.75	-57.75	119	in	in	8	in
L05_EC1FT_E	LVDT	0	120.5	76.625	in	in	6.25	in
L05-EC1FT-W	LVDT	0	112.5	77	in	in	5.875	in
L1_EC1FB_E	LVDT	0	122.75	45	in	in	12.75	in

Sensor Label	Sensor Type	As built Position			Position Units	Sensor Units	Gage Length	
		X	Y	Z			Value	Units
L1_EC1FB_W	LVDT	0	110.5	45	in	in	12	in
L05_NW_EE	LVDT	-3	29.25	56.5	in	in	20.5	in
L01-NW-EM	LVDT	-3	15.375	56.5	in	in	20.5	in
L01-NW-WM	LVDT	-3	-2.5	56.5	in	in	20.5	in
L01_NW_WE	LVDT	-3	-15	56.625	in	in	20.5	in
L2-EW1	LVDT	-3	25.875	45	in	in	8	in
L2-EW2	LVDT	-3	16.625	45	in	in	11.5	in
L1-CW	LVDT	-3	-2.625	45	in	in	11.5	in
L2-WW1	LVDT	-3	-25.75	45	in	in	8.5	in
L2-WW2	LVDT	-3	-17.5	45	in	in	11.625	in
L2-NWOV	LVDT	-3	-39.25	62.75	in	in	3.75	in
L1-WC1B-1	LVDT	0	-121.5	45	in	in	11.625	in
L1-WC1B-2	LVDT	0	-110.625	45	in	in	11.75	in
L05-WCOL_S	LVDT	6	-116	57.25	in	in	6	in
L05-WCOL_N	LVDT	-6	-116	57.25	in	in	6	in
L2-WOP_E	LVDT	3	16.75	45	in	in	12.125	in
L1-FWE-V	LVDT	3	-1.625	99	in	in	3	in
L1-FM-V	LVDT	3	6	96	in	in	3	in
L1-FCL-T1	LVDT	2.125	-112	2	in	in	9	in
L05-FCL-T2	LVDT	27	-118.25	1.75	in	in	15.125	in
L1-FCL-T3	LVDT	57	-118.5	2.125	in	in	14.5	in
L05_FL_1	LVDT	33.75	-99.5	2	in	in	9.25	in
L05_FL_2	LVDT	26.75	-78.625	2.125	in	in	7	in

Sensor Label	Sensor Type	As built Position			Position Units	Sensor Units	Gage Length	
		X	Y	Z			Value	Units
L05_FL_3	LVDT	3.25	-99.5	1.5	in	in	9.125	in
L05_FL_4	LVDT	-3.5	-79.25	2	in	in	6.75	in
L05_FL_5	LVDT	26.75	-12.25	1.5	in	in	9.125	in
L05_FL_6	LVDT	26.5	0.5	1.75	in	in	7.25	in
L05-MFCL-T2	LVDT	-28.75	-118.125	2	in	in	14.25	in
L1-MFWL-T2	LVDT	-27.25	-38	2	in	in	14.75	in
L1-FWL1-T1	LVDT	1.5	-45	2.625	in	in	7.125	in
L1-FWL1-T2	LVDT	26.75	-37.875	1.75	in	in	14.75	in
L1-FWL-T3	LVDT	57.5	-38.125	1.875	in	in	14.5	in
L1-FWL-T4	LVDT	26.75	-37.875	1.75	in	in	10.625	in
L1-FWL-T5	LVDT	57.5	-38.125	1.75	in	in	10.625	in
L1-FCL-B1	LVDT	2.5	-112	-2	in	in	7.375	in
L1-FCL-B2	LVDT	26.75	-112	-2.125	in	in	7.375	in
L1-FCL-B3	LVDT	56.5	-112	-1.75	in	in	7.5	in
L05-MFCL-B2	LVDT	-28.5	-112	-2	in	in	7.75	in
L1-MFWL-B2	LVDT	-27	-45	-2	in	in	7	in
L1-FWL-B1	LVDT	2	-45	-1.875	in	in	6.875	in
L1-FWL-B2	LVDT	27	-45	-2	in	in	6.75	in
L1-FWL-B3	LVDT	57.5	-45	-1.875	in	in	7.125	in
L1-FWL-B4	LVDT	27	-35	-2	in	in	7.375	in
L1-FWL-B5	LVDT	57.375	-35	-2.125	in	in	7.25	in
DCDT1	DCDT	3	-11.375	50	in	in	3	in

Sensor Label	Sensor Type	As built Position			Position Units	Sensor Units	Gage Length	
		X	Y	Z			Value	Units
DCDT2	DCDT	0	32.375	89.5	in	in	1.25	in
DCDT3	DCDT	0	109.5	90	in	in	1.625	in
DCDT4	DCDT	0	47.875	89.5	in	in	0.875	in
DCDT5	DCDT	0	-110.125	45	in	in	0.5	in
DCDT6	DCDT	0	-32.75	49.75	in	in	3	in
DCDT8	DCDT	0	-122.875	45	in	in	0.625	in
DCDT9	DCDT	3	39	93.25	in	in	2.625	in
DCDT10	DCDT	3	0	45	in	in	5.125	in
DCDT11	DCDT	3	-28.125	45	in	in	3.625	in
TBEGC_X	Inclinometer	-6	116.5	65	in	°		
TBEC_X	Inclinometer	-3	40	77.75	in	°		
TTW_X	Inclinometer	-3	0.25	225.5	in	°		
TBW_X	Inclinometer	-3	0	77	in	°		
TBWSB_X	Inclinometer	-2	-91.625	139.5	in	°		
LC_400K	Load Cell	0	0	278.25	in	kip		
LC_EGRAV	Load Cell	0	116.5	156.75	in	kip		
LC_EEND	Load Cell	0	40	124.25	in	kip		
LC-WEND	Load Cell	0	-40	124.25	in	kip		
LC-WGRAV	Load Cell	0	-116	156.75	in	kip		
SE_PROP	Load Cell	63	40	91.375	in	kip		
SW_PROP	Load Cell	57	40	74	in	kip		

Sensor Label	Sensor Type	As built Position			Position Units	Sensor Units	Gage Length	
		X	Y	Z			Value	Units
NW_PROP	Load Cell	-57	-40	74	in	kip		
NE_PROP	Load Cell	-63	-40	91.375	in	kip		
CG-EWBC1-1	Strain Gage	0	-32.25	2.625	in	µstrain		
CG-EWBC1-2	Strain Gage	0	-29.375	2.375	in	µstrain		
CG-EWBC1-3	Strain Gage	0	-25.375	2.375	in	µstrain		
CG-EWBC2	Strain Gage	0	-31.625	9	in	µstrain		
CG-EWBC3	Strain Gage	0	-32.5	17	in	µstrain		
CG-EWBC4	Strain Gage	0	-30.5	148	in	µstrain		
CG-EWBC5	Strain Gage	0	-30.5	208	in	µstrain		
CG-CEWB1	Strain Gage	0	-11	1.375	in	µstrain		
CG-CEWB2	Strain Gage	0	-11	8	in	µstrain		
CG-CEWB3	Strain Gage	0	-11	16.625	in	µstrain		
CG-CEWB4	Strain Gage	0	-11	148	in	µstrain		
CG-CEWB5	Strain Gage	0	-11	208	in	µstrain		
CG-CWWB1	Strain Gage	0	11	1.625	in	µstrain		
CG-CWWB2	Strain Gage	0	11	8.625	in	µstrain		
CG-CWW_B3	Strain Gage	0	11	17	in	µstrain		
CG-CWWB4	Strain Gage	0	11	148.375	in	µstrain		
CG-CWWB5	Strain Gage	0	11	208.375	in	µstrain		
CG-WWBC1-1	Strain Gage	0	32.125	3.125	in	µstrain		
SG-WWB-T1	Strain Gage	2.5	26.75	2.5	in	µstrain		
SG-WWB-T2	Strain Gage	2.5	26.75	4	in	µstrain		

Sensor Label	Sensor Type	As built Position			Position Units	Sensor Units	Gage Length	
		X	Y	Z			Value	Units
SG-WWB-T3	Strain Gage	2.5	26.75	9.25	in	µstrain		
SG-WWB-T4	Strain Gage	2.5	26.75	18.5	in	µstrain		
SG-WWB-T5	Strain Gage	2.5	26.75	25.25	in	µstrain		
SG-WWB-T6	Strain Gage	2.5	26.25	36.75	in	µstrain		
CG-EWEI	Strain Gage	0	-17.125	48.125	in	µstrain		
CG-EWMI	Strain Gage	0	-10.875	48.125	in	µstrain		
CG-WWM1	Strain Gage	0	10.875	48.125	in	µstrain		
CG-WWE1	Strain Gage	0	17.125	48.125	in	µstrain		
CG-E_ECOL-L1	Strain Gage	-1	3.25	1.25	in	µstrain		
CG-E_ECOL-L2	Strain Gage	-1	-3.125	1.75	in	µstrain		
CG-E_ECOL-L3	Strain Gage	1.125	-3	1.875	in	µstrain		
CG-E_ECOL-L4	Strain Gage	1	3.5	10.25	in	µstrain		
SG-E_ECOL-T1	Strain Gage	0	0	0.625	in	µstrain		
SG-E_ECOL-T2	Strain Gage	0	0	2.125	in	µstrain		
SG-E_ECOL-T3	Strain Gage	0	0	5.5	in	µstrain		
CG_W_ECOL-L1	Strain Gage	-1	-3.5	1.625	in	µstrain		
CG_W_ECOL-L2	Strain Gage	-1	3.5	1.125	in	µstrain		
CG_W_ECOL-L3	Strain Gage	1	3.5	1	in	µstrain		
CG_W_ECOL-L4	Strain Gage	-0.875	-3.5	10	in	µstrain		
SG-W_ECOL-T1	Strain Gage	0	0	0.5	in	µstrain		
SG-W_ECOL-T2	Strain Gage	0	0	2.125	in	µstrain		
SG-W_ECOL-T3	Strain Gage	0	0	5.5	in	µstrain		
SG-ECOL-T1	Strain Gage	0.25	0	1.25	in	µstrain		

Sensor Label	Sensor Type	As built Position			Position Units	Sensor Units	Gage Length	
		X	Y	Z			Value	Units
SG-ECOL-T2	Strain Gage	0.25	0	3.125	in	µstrain		
SG-ECOL-T3	Strain Gage	0.25	0	6.375	in	µstrain		
SG-EGCOL-L1	Strain Gage	0	3	1.25	in	µstrain		
SG-EGCOL-L2	Strain Gage	0	-3	1.25	in	µstrain		
SG-EGCOL-L3	Strain Gage	0	3	3.5	in	µstrain		
SG-EGCOL-L4	Strain Gage	0	-3	3.5	in	µstrain		
SG-EGCOL-L5	Strain Gage	0	3	7.5	in	µstrain		
SG-EGCOL-L6	Strain Gage	0	-3	7.5	in	µstrain		
SG-EGCOL-L7	Strain Gage	0	3	31.5	in	µstrain		
SG-EGCOL-L8	Strain Gage	0	-3	31.5	in	µstrain		
SG-ECOL-L14	Strain Gage	0	-3	48	in	µstrain		
SG-ECOL-L15	Strain Gage	0	3	48	in	µstrain		
CG_E_GCOL-L1	Strain Gage	-4	2.75	3	in	µstrain		
CG_E_GCOL-L2	Strain Gage	-4	-2.75	3	in	µstrain		
CG_E_GCOL-L3	Strain Gage	3.75	-2.75	12.5	in	µstrain		
CG_E_GCOL-L4	Strain Gage	-4	2.75	13	in	µstrain		
SG-WCOL-T1	Strain Gage	0.25	0	1.625	in	µstrain		
SG-WCOL-T2	Strain Gage	0.25	0	3.375	in	µstrain		
SG-WCOL-T3	Strain Gage	0.25	0	7.25	in	µstrain		
SG-WGCOL-L1	Strain Gage	0	3	0.875	in	µstrain		
SG-WGCOL-L2	Strain Gage	0	-3	0.875	in	µstrain		
SG-WGCOL-L3	Strain Gage	0	3	2.875	in	µstrain		
SG-WGCOL-L4	Strain Gage	0	-3	2.875	in	µstrain		

Sensor Label	Sensor Type	As built Position			Position Units	Sensor Units	Gage Length	
		X	Y	Z			Value	Units
SG-WGCOL-L5	Strain Gage	0	3	6.875	in	µstrain		
SG-WGCOL-L6	Strain Gage	0	-3	6.875	in	µstrain		
SG-WGCOL-L7	Strain Gage	0	3	31	in	µstrain		
SG-WGCOL-L8	Strain Gage	0	-3	31	in	µstrain		
SG-WGCOL-L9	Strain Gage	0	3	47.5	in	µstrain		
SG-WGCOL-L10	Strain Gage	0	-3	47.5	in	µstrain		
CG-W_GCOL-L1	Strain Gage	-4	2.75	1.125	in	µstrain		
CG-W_GCOL-L2	Strain Gage	-4	-2.875	1.125	in	µstrain		
CG-W_GCOL-L3	Strain Gage	4.25	-2.75	12.25	in	µstrain		
CG-W_GCOL-L4	Strain Gage	-4	2.875	12.125	in	µstrain		
SG_TRANB_1	Strain Gage	-6	3	46	in	µstrain		
SG_TRANB_3	Strain Gage	-5.5	3	39	in	µstrain		
SG_TRANB_4	Strain Gage	-5.5	3	39	in	µstrain		
SG_P1_Y	Strain Gage	49.5	-113.125	120.1875	in	µstrain		
SG_P2_A6	Strain Gage	49.5	-113.125	119.8125	in	µstrain		
SG_P3_Y	Strain Gage	39.75	-112.75	120.1875	in	µstrain		
SG_P4_A6	Strain Gage	39.75	-112.75	119.8125	in	µstrain		
SG_P5_Y	Strain Gage	19.25	-113.125	120.1875	in	µstrain		
SG_P6_A6	Strain Gage	19.25	-113.125	119.8125	in	µstrain		
SG_P7_Y	Strain Gage	9.25	-113	120.1875	in	µstrain		
SG_P8_A6	Strain Gage	9.25	-113	119.8125	in	µstrain		
SG_P9_A3	Strain Gage	-11	-113	120.1875	in	µstrain		
SG_P10_A6	Strain Gage	-11	-113	119.8125	in	µstrain		

Sensor Label	Sensor Type	As built Position			Position Units	Sensor Units	Gage Length	
		X	Y	Z			Value	Units
SG_P11_A6	Strain Gage	-20.75	-113	120.1875	in	µstrain		
SG_P13_A6	Strain Gage	-41.25	-113	120.1875	in	µstrain		
SG_P15_A3	Strain Gage	-51.25	-113.125	120.1875	in	µstrain		
SG_P16_A3	Strain Gage	-51.25	-113.125	119.8125	in	µstrain		
SG_P17_A5	Strain Gage	50.25	-44.5	120.1875	in	µstrain		
SG_P18_A6	Strain Gage	50.25	-44.5	119.8125	in	µstrain		
SG_P19_A5	Strain Gage	50.25	-35.5	120.1875	in	µstrain		
SG_P20_A6	Strain Gage	50.25	-35.5	119.8125	in	µstrain		
SG_P21_A5	Strain Gage	40.75	-44.5	120.1875	in	µstrain		
SG_P22_A6	Strain Gage	40.75	-44.5	119.8125	in	µstrain		
SG_P23_A5	Strain Gage	40.75	-35.5	120.1875	in	µstrain		
SG_P24_A6	Strain Gage	40.75	-35.5	119.8125	in	µstrain		
SG_P25_A5	Strain Gage	20.875	-44.5	120.1875	in	µstrain		
SG_P26_A6	Strain Gage	20.875	-44.5	119.8125	in	µstrain		
SG_P27_A5	Strain Gage	20.875	-35.5	120.1875	in	µstrain		
SG_P28_A6	Strain Gage	20.875	-35.5	119.8125	in	µstrain		
SG_P29_A5	Strain Gage	10.875	-47.25	120.1875	in	µstrain		
SG_P30_A6	Strain Gage	10.875	-47.25	119.8125	in	µstrain		
SG_P31_Y	Strain Gage	10.875	-44.25	120.1875	in	µstrain		
SG_P32_A6	Strain Gage	10.875	-44.25	119.8125	in	µstrain		
SG_P33_Y	Strain Gage	10.875	-35.25	120.1875	in	µstrain		
SG_P34_A6	Strain Gage	10.875	-35.25	119.8125	in	µstrain		
SG_P35_Y	Strain Gage	10.875	-32.25	120.1875	in	µstrain		

Sensor Label	Sensor Type	As built Position			Position Units	Sensor Units	Gage Length	
		X	Y	Z			Value	Units
SG_P36_A6	Strain Gage	10.875	-32.25	119.8125	in	µstrain		
SG_P37_A5	Strain Gage	-10.625	-44.5	120.1875	in	µstrain		
SG_P38_A6	Strain Gage	-10.625	-44.5	119.8125	in	µstrain		
SG_P39_A5	Strain Gage	-10.625	-35.5	120.1875	in	µstrain		
SG_P40_A6	Strain Gage	-10.625	-35.5	119.8125	in	µstrain		
SG_P41_A3	Strain Gage	-50.125	-47.25	120.1875	in	µstrain		
SG_P42_A6	Strain Gage	-50.125	-44.25	119.8125	in	µstrain		
SG_P43_A3	Strain Gage	-50.125	-35.25	120.1875	in	µstrain		
SG_P44_A6	Strain Gage	-50.125	-32.25	119.8125	in	µstrain		
SG_P45_Y	Strain Gage	50.625	35.5	120.1875	in	µstrain		
SG_P46_A6	Strain Gage	50.625	35.5	119.8125	in	µstrain		
SG_P47_A5	Strain Gage	50.625	44.5	120.1875	in	µstrain		
SG_P48_A6	Strain Gage	50.625	44.5	119.8125	in	µstrain		
SG_P50_A6	Strain Gage	20.75	35.5	120.1875	in	µstrain		
SG_P52_A6	Strain Gage	20.75	44.5	120.1875	in	µstrain		
SG_P54_A6	Strain Gage	10.5	35.5	120.1875	in	µstrain		
SG_P56_A6	Strain Gage	10.5	44.5	120.1875	in	µstrain		
SG_P57_A5	Strain Gage	-10.75	35.5	120.1875	in	µstrain		
SG_P58_A6	Strain Gage	-10.75	35.5	119.8125	in	µstrain		
SG_P59_A5	Strain Gage	-10.75	44.5	120.1875	in	µstrain		
SG_P60_A6	Strain Gage	-10.75	44.5	119.8125	in	µstrain		
SG_P61_A3	Strain Gage	50.5	113	120.1875	in	µstrain		
SG_P62_A6	Strain Gage	50.5	113	119.8125	in	µstrain		

Sensor Label	Sensor Type	As built Position			Position Units	Sensor Units	Gage Length	
		X	Y	Z			Value	Units
SG_P63_A3	Strain Gage	-10.25	113	120.1875	in	µstrain		
SG_P64_A6	Strain Gage	-10.25	113	119.8125	in	µstrain		
CG_PL_1	Strain Gage	-22.375	12.625	92	in	µstrain		
CG_PL_2	Strain Gage	-22.375	57.375	92	in	µstrain		
CG_PL_3	Strain Gage	-4	7	92	in	µstrain		
CG_PL_4	Strain Gage	-4	28.5	92	in	µstrain		
CG_PL_5	Strain Gage	-5.5	35.75	92	in	µstrain		
CG_PL_6	Strain Gage	-5.375	56.25	92	in	µstrain		
CG_PL_7	Strain Gage	-23.25	14.5	92	in	µstrain		
CG_PL_8	Strain Gage	-6	14.75	92	in	µstrain		
SG_PBS1	Strain Gage	-1.25	15	92	in	µstrain		
SG_PBS2	Strain Gage	-7	15	92	in	µstrain		
SG_PBS3	Strain Gage	-1.25	26	92	in	µstrain		
SG_PBS4	Strain Gage	-7	26	92	in	µstrain		
SG_PBS5	Strain Gage	-1.25	43	92	in	µstrain		
SG_PBS6	Strain Gage	-7	43	92	in	µstrain		
SG_PBS7	Strain Gage	-1.25	54	92	in	µstrain		
SG_PBS8	Strain Gage	-7	54	92	in	µstrain		
SG_NE_PROP_T_S	Strain Gage	-54.5	40	66.5	in	µstrain		
SG_NE_PROP_T_N	Strain Gage	-59.5	40	66.5	in	µstrain		
SG_NE_PROP_T_E	Strain Gage	-57	42.5	66.5	in	µstrain		
SG_NE_PROP_T_W	Strain Gage	-57	37.5	66.5	in	µstrain		
SG_NE_PROP_B_S	Strain Gage	-54.5	40	23.5	in	µstrain		

Sensor Label	Sensor Type	As built Position			Position Units	Sensor Units	Gage Length	
		X	Y	Z			Value	Units
SG_NE_PROP_B_N	Strain Gage	-59.5	40	23.5	in	µstrain		
SG_NE_PROP_B_E	Strain Gage	-57	42.5	23.5	in	µstrain		
SG_NE_PROP_B_W	Strain Gage	-57	37.5	23.5	in	µstrain		
SG_1FOWALL_E	Strain Gage	-3.4375	32.125	67	in	µstrain		
SG_1FOCOL_E	Strain Gage	-3.4375	36.125	67	in	µstrain		
SG_1FOWALL_M	Strain Gage	-3.4375	31.5	67	in	µstrain		
SG_2FOWALL_E	Strain Gage	-3.4375	32.125	113	in	µstrain		
SG_2FOCOL_E	Strain Gage	-3.4375	36.125	113	in	µstrain		
SG_2FOWALL_M	Strain Gage	-3.4375	31.5	113	in	µstrain		
SG_WTRCOL_N	Strain Gage	-2	-103.5	140	in	µstrain		
SG_WTRCOL_S	Strain Gage	2	-103.5	140	in	µstrain		
SG_WTRWALL_N	Strain Gage	-2	-42.5	140	in	µstrain		
SG_WTRWALL_S	Strain Gage	2	-42.5	140	in	µstrain		
SG_ETRCOL_N	Strain Gage	-2	104	140	in	µstrain		
SG_ETRCOL_S	Strain Gage	2	104	140	in	µstrain		
SG_ETRWALL_N	Strain Gage	-2	42.5	140	in	µstrain		
SG_ETRWALL_S	Strain Gage	2	42.5	140	in	µstrain		

Appendix E: Sectional Analysis of the Edge Column

This appendix describes calculation of moment resistances of edge columns in PFS1 and PFS2. An axial load of 180 kips that was equal to the gravity loads from the tributary floor was applied to the edge column. The moment-curvature curve of the edge column was obtained through the analysis. The code input to the OpenSees is shown below.

```
wipe
model basic -ndm 2 -ndf 3
# ----- Define variables of section dimension and material property:
# Units: kips, in
set fy 60;     # Yield stress
set E 29000.0;    # Young's modulus of steel
set colWidth 36; # Width of the column
set colDepth 24; # Depth of the column
set cover 1.5;     # Concrete cover
set holew 6;   # width of the center hole
set holed 6;   # depth of the center hole
```

```
set stirrup 0.5; # diameter of no.4 stirrup
set As    1.0;   # area of no. 9 rebar
set dia   1.128; # diameter of No.9 rebar
set y1 [expr $colDepth/2.0]; # Centroid of column in Y direction
set z1 [expr $colWidth/2.0]; # Centroid of column in Z direction
# Define two nodes at (0,0): it is a cross section (zero length)
node 1 0.0 0.0
node 2 0.0 0.0
# Fix all degrees of freedom, except bending at 2nd node and axial displacement
fix 1 1 1 1
fix 2 0 1 0
# Generate materials:
# Concrete07 uses Mander Model. Expression of the constitutive law is listed on the website
# Core concrete:
# uniaxialMaterial Concrete07 $matTag $fc $ec $Ec $ft $et $xp $xn $r --unconfined concrete
  uniaxialMaterial Concrete07 1       -5 -0.0021 4511 0.53 0.000235 2 2.3 4.8
```

```
# uniaxialMaterial Concrete07 $matTag $fc $ec $Ec $ft $et $xp $xn $r --- for confined concrete
  uniaxialMaterial Concrete07 2        -7.9 -0.00814 4511 0.53 0.000235 2 30 1.3
# Reinforcing steel: --- strain hardening is taken account (0.01 need to be considered)
# uniaxialMaterial Steel01 $matTag $Fy $E0 $b   <$a1 $a2 $a3 $a4>
  uniaxialMaterial Steel01 3       $fy $E 0.01
# section Fiber $secTag {
  section Fiber 1 {
  # patch rect $matTag $numSubdivY $numSubdivZ $yI  $zI  $yJ $zJ define left band of unconfined concrete cover (stirrup)
  patch rect 1       128          1          -$y1 -$z1 $y1 [expr -$z1+$cover+$stirrup/2.0]
  # patch rect $matTag $numSubdivY $numSubdivZ $yI  $zI  $yJ $zJ --- define right band of unconfined concrete cover (stirrup)
    patch rect 1       128          1          -$y1 [expr $z1-$cover-$stirrup/2.0] $y1 $z1
  # patch rect $matTag $numSubdivY $numSubdivZ $yI  $zI  $yJ $zJ --- define bottom band of unconfined concrete cover (stirrup)
    patch rect 1       15          1      -$y1 [expr -$z1+$cover+$stirrup/2.0] [expr -$y1+$cover+$stirrup/2.0] [expr $z1-$cover-$stirrup/2.0]
  # patch rect $matTag $numSubdivY $numSubdivZ $yI  $zI  $yJ $zJ --- define top band of unconfined concrete cover (stirrup)
    patch rect 1       15          1          [expr $y1-$cover-$stirrup/2.0] [expr -$z1+$cover+$stirrup/2.0] $y1 [expr $z1-$cover-$stirrup/2.0]
  # patch rect $matTag $numSubdivY $numSubdivZ $yI  $zI  $yJ $zJ - confined concrete core. In Y direction, 6.75/27=0.25" per band
```

patch rect 2 98 1 [expr -$y1+$cover+$stirrup/2.0] [expr -$z1+$cover+$stirrup/2.0] [expr $y1-$cover-$stirrup/2.0] [expr -$holew/2.0]

patch rect $matTag $numSubdivY $numSubdivZ $yI $zI $yJ $zJ - confined concrete core. In Y direction, 6.75/27=0.25" per band

patch rect 2 33 1 [expr $holed/2.0] [expr -$holew/2.0] [expr $y1-$cover-$stirrup/2.0] [expr $holew/2.0]

patch rect $matTag $numSubdivY $numSubdivZ $yI $zI $yJ $zJ - confined concrete core. In Y direction, 6.75/27=0.25" per band

patch rect 2 33 1 [expr -$y1+$cover+$stirrup/2.0] [expr -$holew/2.0] [expr -$holed/2.0] [expr $holew/2.0]

patch rect $matTag $numSubdivY $numSubdivZ $yI $zI $yJ $zJ - confined concrete core. In Y direction, 6.75/27=0.25" per band

patch rect 2 98 1 [expr -$y1+$cover+$stirrup/2.0] [expr $holew/2.0] [expr $y1-$cover-$stirrup/2.0] [expr $z1-$cover-$stirrup/2.0]

Create the reinforcing fibers: --- bottom layer rebar 5#3; top layer rebar 5#3; center layer 2#3; center layer 2#3 .
The position here NEGLECT the diameter of stirrup.

layer straight $matTag $numFiber $areaFiber $yStart $zStart $yEnd $zEnd

layer straight 3 5 $As [expr -$y1+$cover+$stirrup+$dia/2.0] [expr -$z1+$cover+$stirrup+$dia/2.0] [expr -$y1+$cover+$stirrup+$dia/2.0] [expr $z1-$cover-$stirrup-$dia/2.0]

layer straight 3 2 $As [expr -$y1+$cover+$stirrup+$dia/2.0+1.75] [expr -$z1+$cover+$stirrup+$dia/2.0] [expr -$y1+$cover+$stirrup+$dia/2.0+1.75] [expr $z1-$cover-$stirrup-$dia/2.0]

layer straight 3 2 $As [expr $y1-$cover-$stirrup-$dia/2.0-1.75] [expr -$z1+$cover+$stirrup+$dia/2.0] [expr $y1-$cover-$stirrup-$dia/2.0-1.75] [expr $z1-$cover-$stirrup-$dia/2.0]

layer straight 3 5 $As [expr $y1-$cover-$stirrup-$dia/2.0] [expr -$z1+$cover+$stirrup+$dia/2.0] [expr $y1-$cover-$stirrup-$dia/2.0] [expr $z1-$cover-$stirrup-$dia/2.0] }

```
# Define element: zerolengthSection L=1, strain=elongation/1; curvature=rotation/1
# element zeroLengthSection $eleTag $iNode $jNode $secTag <-orient $x1 $x2 $x3 $yp1 $yp2 $yp3>
  element zeroLengthSection 1       1      2      1        -orient 1 0 0 0 1 0
# Set axial load
set axialLoad -180
# print axial load value on the screen:
puts "axialLoad: $axialLoad"
# Define constant axial load
pattern Plain 1 "Constant" {    load 2 $axialLoad 0.0 0.0}
# Create recorder
 recorder Node -file curvature.out -time -node 2 -dof 3 disp
 recorder Node -file moment.out -time -node 1 -dof 3 reaction
# Define analysis parameters
integrator LoadControl 0
system ProfileSPD
test RelativeEnergyIncr 1.0e-5 15
```

```
numberer Plain
constraints Plain
algorithm Newton
analysis Static
# Do one analysis to apply axial load
set okaxial [analyze 1]
puts $okaxial
if {$okaxial <0 } { puts "FE divergence."; exit}
loadConst -time 0.0
# Define stepsize, and number of steps
#set Kyestimate [expr $fy/$E/0.6/($colDepth-$cover)];
# Rough guess of the yield curvature. Determine loading step size - (fy/E)/(0.6d)
#set dK [expr $Kyestimate*0.02];          # Rotation (or curvature) increment is #set to be 2% of estimated yield curvature above
#set numstep 2000;                        # The total curvature solving is 2%x2000=40 #times the estimated yield curvature
set dK0 -1E-6;
# Define loading pattern: specify the input moment is at node 2, not other patterns
```

```
#pattern Plain $patternTag $tsTag {}
pattern Plain 2 "Linear" {       load 2 0.0 0.0 1.0}
set currentDisp 0;
set ok 0;
set fileID1 [open "Phase3_wcol34_curvature.txt" r+];
set peakDisp [read $fileID1]
set fileID2 [open "history_label.txt" r+];
set cyclelabel [read $fileID2];
```